Magmatisme mafique et minéralisations Sb-Au dans le domaine Centre Armoricain : contrôles spatio-temporels et implications metallogéniques

Anthony Pochon

▶ **To cite this version:**

Anthony Pochon. Magmatisme mafique et minéralisations Sb-Au dans le domaine Centre Armoricain : contrôles spatio-temporels et implications metallogéniques. Sciences de la Terre. Université de Rennes, 2017. Français. NNT : 2017REN1S101 . tel-01755499

HAL Id: tel-01755499
https://theses.hal.science/tel-01755499

Submitted on 30 Mar 2018

HAL is a multi-disciplinary open access archive for the deposit and dissemination of scientific research documents, whether they are published or not. The documents may come from teaching and research institutions in France or abroad, or from public or private research centers.

L'archive ouverte pluridisciplinaire **HAL**, est destinée au dépôt et à la diffusion de documents scientifiques de niveau recherche, publiés ou non, émanant des établissements d'enseignement et de recherche français ou étrangers, des laboratoires publics ou privés.

ANNÉE 2017

UNIVERSITÉ DE RENNES 1

UNIVERSITE BRETAGNE LOIRE

THÈSE / UNIVERSITÉ DE RENNES 1
sous le sceau de l'Université Bretagne Loire

pour le grade de

DOCTEUR DE L'UNIVERSITÉ DE RENNES 1

Mention : Sciences de la Terre

Ecole doctorale EGAAL

présentée par

Anthony Pochon

Préparée à l'unité de recherche Géosciences Rennes – UMR 6118
OSUR (Observatoire des sciences de l'Univers)
UFR Sciences et Propriétés de la Matière

Magmatisme mafique et minéralisations à Sb-Au dans le domaine Centre Armoricain: contrôles spatio-temporels et implications métallogéniques

Thèse soutenue à Rennes
le 18 décembre 2017

devant le jury composé de :

Laurence ROBB
Professeur, University of Oxford / *rapporteur*

Patrick LEDRU
Vice President Exploration, Areva Resources Canada Inc / *rapporteur*

Georges BEAUDOIN
Professeur, Université Laval / *examinateur*

Eric MARCOUX
Professeur, Université d'Orléans / *examinateur*

Marie-Christine BOIRON
Chargé de recherche, Université de Lorraine / *examinatrice*

Michel BALLEVRE
Professeur, Université de Rennes 1 / *examinateur*

Denis GAPAIS
Directeur de recherche, Université de Rennes 1 / *directeur de thèse*

Eric GLOAGUEN
Ingénieur géologue, BRGM / *co-directeur de thèse*

Remerciements

Pour commencer, mes remerciements vont vers mes deux directeurs de thèse Denis et Eric pour leurs conseils, la confiance et la liberté dont j'ai bénéficié tout au long de cette thèse et même depuis le master 2. Eric, tu m'as initié à la géologie bretonne (avec Denis et Charles bien entendu) et surtout à la métallogénie de l'or et de l'antimoine. La thèse a pu voir le jour notamment avec ton dossier « choukroute » sur l'antimoine armoricain. Denis, tu m'as accueilli à Géosciences Rennes et tu m'as inculqué la « recherche rennaise » et appris à écrire mon premier papier. Tu m'as également permis de participer à tous les congrès où je désirais aller notamment en me prêtant (souvent d'ailleurs) tes propres crédits de recherche. Un grand merci au troisième directeur officieux de cette thèse, Yannick. Ta bonne humeur, ton enthousiasme et tes compétences de géologue de terrain, de structuraliste, de métallogéniste, de pétrologue, de numéricien… m'ont été d'un grand secours durant ces trois ans. Grâce à toi je sais reconnaitre les graptolites (« private joke »). Ton super-fourgon nous a ouvert les portes de toutes les carrières bretonnes et on aura appris ensemble qu'il ne faut pas laisser le gyrophare allumé toute une matinée sinon on reste bloqué dans la fosse. Un grand merci aussi à Flo et Charlie qui étaient là dès le début et qui ont également activement contribué à cette thèse.

Merci également à Philippe et Marc, j'ai adoré travailler et discuter avec vous, vous êtes également plus que des collaborateurs comme en témoignent nos nombreuses discussions tournebridesques. Grâce à cela, des papiers et un projet au Canada ont vu le jour. De plus, nos séjours à Nancy et à Yokohama resteront gravés dans ma mémoire. Encore merci Marc d'avoir rameuté une troupe de policiers japonais armés jusqu'aux dents autour de notre appart'.

Je remercie également les membres du jury qui ont accepté d'évaluer mon travail et de participer à notre petite excursion de terrain pré-soutenance de thèse. Laurence, j'ai été ravi d'apprendre que le comté est votre fromage préféré. Patrick, Georges et Marie-Christine, j'espère que vous avez apprécié la soirée « roupettes à queues » au port du Crouesty. Eric M., merci pour le cadeau de thèse dédicacé. Michel, merci d'avoir guidé l'excursion du dimanche matin à Port-Navalo et promis je ne sous-estimerai plus la faille de Nort-sur-Erdre.

Voilà le tant attendu paragraphe sur le 127... Merci à Crevette, Blondark et Vicky d'avoir accepté l'unique XY du bureau réservé aux XX depuis tant d'années. Pour être exact, tout a commencé au 14B avec Blondark (qui s'appelait Solenn à l'époque). Nos discussions endiablés qui au début tournait autour de « bonjour, au revoir, t'as pas une gomme ?... » m'ont poussé à me retirer dans le 127 (quand on m'a obligé à fuir le 14B) vers une personne qui respire la joie de vivre (à savoir Blondark d'où son nom). Puis il y a également Crevette alias Caro que tout rennais connait et

qui ne passe pas inaperçu dans le labo (j'en profite pour dire qu'on t'entend dans tout le labo avec tes talons, c'est relativement agaçant !!!!). Elle m'a aussi grandement persuadé de choisir ma retraite dans le 127 (et non je ne me suis pas transformé en pochonne comme tu l'espérais). Ainsi est né le savant mélange du 127 : l'énergie inépuisable de Caro (comme quoi une alimentation à base de carotte, de laitue et d'alcool fait ses preuves), la noirceur plus noire que noir de Solenn, le calme inébranlable de Vicky devant tant de bêtises humaines, les meurtres en série de pochon junior – charmant petit poisson capable des pires atrocités (le portrait craché de son père adoptif), les parties de tarots compulsives, les mails d'amours… bref un environnement de travail idéal pour rédiger une thèse !

Comme tout le monde le sait, un travail de thèse n'est pas le travail d'une seule personne et je voudrais remercier toutes les personnes avec qui j'ai travaillé (de près ou de loin) : Guillaume pour l'initiation à la géophysique, Xavier et Sylvain pour les lames minces, Yann pour le broyage, David pour les analyses Sm-Nd, Marie-Anne pour la gestion administrative et les ordres de mission fait à la dernière minute, Damien pour m'avoir donné accès aux collections du musée Géosciences Rennes, Cécile, Christian et Guirec pour notre échappée à la recherche de dolérite. Merci également à tous ceux avec qui j'ai pu discuter de manière enrichissante : Pierre, Pavel, Ben, Marc, Gilles, Thierry, Pipo, Johann…Merci aux « québécois » Fx, Arnaud, Emilie, Anne-Aurélie, Dany et Philippe pour votre accueil à Québec et à Chicoutimi.

Mes derniers remerciements s'adressent aux copains, copines ou juste connaissances de passage, de Rennes ou d'ailleurs, avec qui j'ai pu partager des moments comme boire des bières, squatter les pots de thèses, fumer des clopes, des choses saines quoi… : Christophe-san, notre semaine au Japon restera dans mes souvenirs comme notre super soirée au Yumi bar à chanter toute la nuit ou encore notre balade autour du Fuji-sama, Benoit, Benj, Arthur, Nathan, Céline, Ben, Harold l'abrasif, Etienne, Flo, Thomas, Thomas, Pavloch', James, Pierre, Olivier, Thibaut, Jean-mi, Yann, Victorien, Julien, Julien, Jul's, Florent, Bouboule, Foufouille, Babou, Elise, Hélène, Charlotte, Marie, Sophie,…et je m'excuse pour tous ceux que j'ai oublié. Merci à toi Auré pour m'avoir accompagné dans ma vie pendant près de 4 ans et avoir contribué indirectement à cette thèse. Petit séquence kitsch…mille mercis à ma famille pour m'avoir accompagné jusqu'ici, ma petite sœur Carla, mon petit frère Valentin et surtout à vous Papa et Maman votre fiston préféré ;-) vous remercie du plus profond de son cœur.

Cette thèse a été financée par la région Bretagne et le BRGM

Résumé

Au sein de la croûte terrestre, une grande partie des processus de mobilisation et redistribution des métaux résulte de circulations de fluides à grande échelle. Par conséquent, c'est un paramètre clé dans la formation de nombreux types de gisements variés. Les zones de déformation étant les vecteurs principaux des circulations de fluides, la plupart des gisements d'or (Au) et d'antimoine (Sb) se retrouvent localisés au sein des ceintures orogéniques. Le Massif Armoricain constitue un segment de la chaîne varisque ouest-européenne et contient de nombreux gisements à Sb-Au. L'objectif de cette thèse est à la fois de fournir de nouvelles contraintes sur la genèse des minéralisations varisques à Sb-Au et d'améliorer l'état des connaissances sur les processus critiques à l'origine des circulations de fluides minéralisatrices. Ainsi, une analyse des relations spatiales et des analyses structurales, géochronologiques et géochimiques ont été réalisées sur les gisements à Sb-Au du Domaine Centre Armoricain (DCA) et sur le gisement du Semnon en particulier.

Une grande partie des gisements à Sb-Au est spatialement associée à des zones denses et relativement magnétiques suggérant la présence de corps mafiques/ultramafiques en profondeur. Cela est supporté par les nombreuses occurrences de dykes et sills de dolérites à travers toute la région. Ces dykes et sills sont issus d'un important évènement magmatique mafique mis en place à 360 Ma durant un changement drastique de la dynamique de convergence, passant de la subduction continentale à l'initiation de la collision. Les minéralisations à Sb-Au du DCA sont précoces dans l'histoire Carbonifère de la chaîne varisque armoricaine. Par conséquent, la plupart des minéralisations du DCA ne sont pas associées à l'évènement hydrothermal minéralisateur tardi-Carbonifère, bien connu dans la chaîne varisque européenne, en particulier au sein des zones internes de la chaîne tel que le Massif Central français. Au-delà du fait que cet évènement hydrothemal à Sb-Au soit précoce, la mise en place d'un magmatisme mafique généralisé dans la croûte supérieure du DCA est synchrone avec les minéralisations à Sb-Au et apparait comme un paramètre essentiel dans la mobilisation de circulations de fluides minéralisateurs advectifs.

A plus grande échelle, la mise en place d'un magmatisme mafique couplée à la circulation de fluides hydrothermaux à Sb-Au met en lumière et améliore nos connaissances sur les processus hydrothermaux, magmatiques et tectoniques d'échelle lithosphérique gouvernant l'hydrothermalisme porteur de métaux. Par conséquent, ces résultats ouvrent de nouvelles perspectives pour l'exploration minière, notamment dans la recherche de nouveaux gisements d'antimoine et d'or au sein de la chaîne varisque européenne.

Abstract

Through the Earth's crust, a major part of the mobilization and the redistribution processes of metals are the result of large-scale fluid flows. Consequently, it is a key factor in the formation of various types of mineral deposits. Because deformation zones are the principal vector for fluid flows, most hydrothermal antimony (Sb) and gold (Au) deposits are localized in orogenic deformed belts. As a western part of the European Variscan belt, the Armorican Massif hosts several Sb-Au deposits. The purpose of this work is to provide new constraints on the genesis of these Variscan Sb-Au mineralization and to improve our knowledge about critical processes for hydrothermal mineralizing fluid flows. For these reasons, spatial relationships, structural, geochemical and geochronological investigations were performed on the Sb-Au deposits from the Central Armorican Domain (CAD), the Le Semnon Sb-Au deposit in particular.

A major part of Sb-Au deposits are spatially associated with high-density and magnetic zones reflecting the presence of mafic/ultramafic bodies at depth and that is supported by numerous occurrences of dolerite dykes and sills throughout the region. These dykes and sills are issued from an important mafic magmatic event at *ca*. 360 Ma emplaced during a plate dynamic shift from continental subduction to incipient collision stage. Sb-Au mineralization from the CAD belongs to the early Carboniferous history within the Variscan framework. Consequently, most of Sb-Au mineralization (at least in the CAD) is not related to the Late Carboniferous hydrothermal mineralizing event, well-identified in the Variscan southernmost internal zones and especially in the French Massif Central. Beyond that early hydrothermal event, the widespread emplacement of a mafic magmatism in the CAD upper crust is coeval with Sb-Au mineralization and appears as a major trigger for highly advective mineralizing fluid flows.

At a larger scale, mafic magmatism emplacement coupled with early Carboniferous Sb-Au hydrothermal fluid flows highlights and improves our knowledge of lithospheric-scale tectonics, magmatic and hydrothermal processes governing such metal-bearing hydrothermalism. As a consequence, those results provide a new framework for future mining exploration of antimony and gold deposits in the European Variscan belt.

Table des matières

Introduction générale 1

Partie 1 – Antimoine, Or et Massif Armoricain 9

1. Généralités sur l'antimoine 11

2. Les minéralisations antimonifères et aurifères au sein de la chaine Varisque 18

3. Le Massif Armoricain : contexte géologique et métallogénique 22

Partie 2 – Analyse spatiale : réexamen des facteurs géologiques contrôlant la localisation des gisements à Sb-Au 31

Article #1 : "Antimony deposits in the Variscan Armorican belt, a link with mafic intrusives?" 34

Partie 3 – Le magmatisme mafique du Massif Armoricain : contraintes temporelles et signification 45

Article #2 : "U-Pb LA-ICP-MS dating of apatite in mafic rocks: Evidence for a major magmatic event at the Devonian-Carboniferous boundary in the Armorican Massif (France)" 48

Données complémentaires : Datation U-Pb sur zircon et apatite d'un magmatisme anté-varisque 71

Partie 4 – Les minéralisations Sb-Au de Bretagne Centrale : implications métallogéniques et tectoniques 79

Article #3 : "Metal mobility during hydrothermal breakdown of Fe-Ti oxides: insights from Sb-Au mineralizing event (Variscan Armorican Massif, France)" 82

Article #4 : "Hydrothermal history of Variscan Sb-Au mineralisation: insight from Central Brittany (France)" 111

Données complémentaires : étude des inclusions fluides du gisement Sb-Au de la Lucette 154

Partie 5 – Intégration des minéralisations Sb-Au dans l'évolution géodynamique du Massif Armoricain 167

1. Minéralisations Sb-Au : témoins de circulations de fluides à l'échelle régionale 169

Article #5 : "An Early Carboniferous Sb-Au mineralizing peak in a long-lived hydrothermal history: major tectono-magmatic implications for the Armorican Massif (France)"

2. Datation de l'indice aurifère de Beslé : témoin de circulation de fluides localisée le long de la branche Nord du CSA 186

3. Apport des signatures isotopiques Sr-Nd sur la source du magmatisme mafique 190

4. Intégration des données dans l'évolution géodynamique du Massif Armoricain à 360 Ma 194

Conclusions générales 203

Références bibliographiques 213

Annexes 231

Introduction générale

Une grande partie des gisements métallifères dans le monde sont d'origine hydrothermale, à l'exception des gisements purement liés à des processus magmatiques (e.g. les gisements de métaux Cr, Ni, Cu, PGE associés aux roches mafiques/ultramafiques, certaines disséminations dans des intrusifs acides à intermédiaires), des gisements supergènes ou encore des placers. Ces gisements hydrothermaux sont le produit d'interactions complexes entre des fluides et des roches de composition et d'origine variés. La circulation de fluides joue un rôle majeur dans la redistribution des éléments chimiques, notamment les métaux, lors des processus géologiques à l'échelle de la lithosphère. En effet, les métaux – à l'exception du fer – sont généralement en traces et très peu concentrés au sein de la croûte terrestre. Ainsi la formation d'un gisement métallifère nécessite souvent un facteur de concentration extrême des métaux qui le compose. Cette concentration est uniquement rendue possible par la circulation de fluides qui représentent les vecteurs principaux du transport des métaux de la source à la zone de dépôt. Pour ce faire, les fluides ont également la capacité d'extraire les métaux (i.e. les mettre en solution) d'une roche source et de les déposer au sein d'une zone favorable au piégeage de ceux-ci (appelé communément un piège). Les fluides ont donc un rôle essentiel tant ils sont omniprésents sur Terre, notamment dans les zones de convergences.

Comprendre les processus à l'origine des fluides minéralisateurs n'est jamais chose aisée. En effet, les conditions physico-chimiques nécessaires qui contrôlent la mobilisation des fluides et leurs capacités à extraire les métaux d'une roche source et les reprécipiter au sein d'un piège sont nombreuses et parfois difficile à évaluer. D'autant plus que, dans la plupart des cas, nous ne disposons que de moyens indirects d'investigations et d'informations parcellaires, comme par exemple l'altération hydrothermale des roches qui témoignent du passage d'un fluide à un instant donné. De plus, les fluides peuvent provenir de différentes sources comme par exemple : les fluides météoriques qui dérivent de la surface, les fluides provenant de l'eau de mer, les fluides magmatiques ou encore les fluides métamorphiques. Pour retracer l'histoire géologique d'un gisement, il est donc indispensable de caractériser à minima les fluides responsables du dépôt de la minéralisation. Néanmoins, il est tout aussi indispensable de comprendre les processus capables de mobiliser et de drainer des quantités de fluides suffisantes pour la formation d'un gisement. Ces mécanismes sont généralement liés à des gradients thermiques et/ou de pression et sont souvent associés à la déformation des roches, qui est considérée comme un acteur majeur de la circulation des fluides dans la croûte (e.g. Beach 1976; Etheridge et al. 1983; Fyfe et al. 1978; Sibson et al. 1975) mais également dans le manteau (e.g. Précigout et al. 2017). Les zones de cisaillement et les failles apparaissent comme un système de plomberie naturel favorisant la circulation des fluides, notamment en augmentant la perméabilité des roches ou en la fracturant. La datation des circulations de fluides (i.e. un évènement hydrothermal) est également nécessaire afin de pouvoir

replacer le cadre géologique d'un gisement dans un contexte géodynamique global de plus grande échelle. Cependant, bien que les méthodes de datation aient considérablement évoluées ces dernières années, cela reste encore un challenge. En effet, les systèmes minéralisés résultent souvent d'une histoire polyphasée qu'il est difficile de retracer et de démêler. De plus, les minéralisations sont parfois affectées par d'autres circulations de fluides postérieures et totalement déconnectés de leur histoire. Il apparait donc que la compréhension d'un système minéralisé et la conceptualisation d'un modèle générique nécessite d'étudier les roches environnantes qui enregistrent l'altération hydrothermale lors du passage des fluides, la minéralisation elle-même, la géométrie de la plomberie ainsi que le timing d'un ou plusieurs évènements hydrothermaux.

Les gisements d'or (Au), auxquels sont souvent associées des minéralisations à antimoine (Sb), sont les gisements les plus étudiés à travers le monde, notamment pour la valeur marchande de l'or et les enjeux sociétaux qui en découlent. Dans le monde, la majorité des gisements à Sb ± Au sont hydrothermaux et de type épigénétique (Obolensky et al. 2007) et résultent de processus capables de mobiliser de grandes quantités de fluides, tant les facteurs d'enrichissement sont extrêmes pour ces métaux (~3000 à 100000 fois la concentration moyenne de la croûte continentale pour l'or, Cathelineau et al. 2011). Ces types de gisements (i.e. filoniens et stratoïdes) peuvent se rencontrer dans la plupart des contextes géologiques et présentent des styles de minéralisations très variés en raison de la grande variabilité de leurs roches encaissantes, de leurs drains (i.e. zones de cisaillement) et de la source des fluides. Par conséquent, il n'existe pas de modèle global de genèse qui fasse consensus tant la diversité des gisements est grande. Néanmoins, de nombreux gisements à Sb ± Au présentent des caractéristiques similaires comme dans le cas de la chaîne varisque ouest-européenne où ils semblent être spatialement associés à de grandes zones de cisaillements et de failles d'échelle crustale et d'âge tardi-varisque (e.g. Massif Central français, Bellot et al. 2003; Bouchot et al. 2005). Si de nombreuses études ont permis de contraindre les sources des fluides, les âges et les processus de mobilisation de ces métaux des minéralisations aurifères et antimonifères du Massif Central français (MCF), les minéralisations Sb ± Au armoricaines ne bénéficient pas de cette chance et restent encore mal comprises.

A l'instar du MCF, le Massif Armoricain est un segment de la chaine varisque ouest européenne et constitue une grande province métallogénique française, notamment pour l'antimoine et l'or. De la fin du 19ème au début du 20ème siècle, environ 62000 t Sb et 20t Au ont ainsi été extraites de gisements filoniens hydrothermaux. La célèbre mine et gisement géant (Laznicka 2010) de La Lucette a fourni environ 68 % de la production historique armoricaine et constitue la plus grande mine d'antimoine française (42000 t Sb et 8.4 t Au, Serment 1978). Comme de nombreux indices et d'autres mines de plus petites dimensions, elle est située dans le domaine centre

armoricain (DCA). Contrairement au domaine sud armoricain (DSA) et au MCF qui font partie du domaine interne de la chaine varique et où les minéralisations à Au-Sb sont nombreuses, le DCA appartient au domaine externe de la chaine varisque. Bien que limité de part et d'autre par deux zones de cisaillement majeures, ce domaine reste peu déformé et n'a jamais subi d'épaississement crustal. De plus, les intrusions granitiques varisques, y restent très limitées, hormis le long des zones de cisaillement bordières.

Se posent alors des questions majeures :

Comment peut-on expliquer les processus hydrothermaux à l'origine des nombreuses minéralisations Sb ± Au au sein d'un domaine où la thermicité et la déformation, nécessaire à la mobilisation des fluides minéralisateurs, sont d'apparence très faibles ?

Quel est le moteur thermique qui permet la circulation des fluides ?

Quels sont les paramètres qui peuvent contrôler la présence importante d'antimoine dans ce domaine et son absence dans d'autres domaines géodynamiques similaires ?

Quels sont les processus tectoniques capable de générer des circulations de fluides à grande échelle ?

L'objectif de cette thèse est donc d'apporter de nouveaux éléments sur la compréhension des gisements Sb ± Au et d'apporter de nouvelles contraintes temporelles, géochimiques et structurales afin d'établir un modèle métallogénique des minéralisations Au-Sb au sein du domaine centre armoricain et de les replacer au sein de l'orogenèse varisque. Pour ce faire, nous nous sommes majoritairement focalisés sur l'ancienne mine du Semnon et de manière plus ponctuelle nous nous sommes intéressés à la mine de La Lucette et à d'autres petits indices aurifères et antimonifères. En effet, contrairement à la mine de classe mondiale de La Lucette qui est fermée et ennoyée depuis les années 1970, la mine du Semnon est encore accessible. De plus, ce gisement est situé au cœur du Domaine Centre Armoricain et constitue par conséquent une zone d'étude idéale pour répondre aux questions scientifiques posées dans cette thèse.

Ce manuscrit s'organise en cinq parties subdivisées en chapitres avec une introduction générale ainsi qu'une conclusion générale. Il contient principalement des articles scientifiques rédigés en anglais soit publiés, soit soumis et soit en préparation. Certains chapitres originaux ou discussions complémentaires sont tout de même rédigés en français, tout comme le sont l'introduction et la conclusion. Les articles scientifiques sont précédés d'un bref résumé en français.

La première partie constitue une vue d'ensemble sur les minéralisations aurifères et antimonifères dans le monde et au sein de la chaîne varisque ouest-européenne et du Massif Armoricain. Elle a pour but de présenter un état de l'art sur les minéralisations à antimoine et or, et notamment sur leur affinité géochimique, qui est fondamentale pour appréhender la source, le transport et le dépôt de ces métaux. Un bref aperçu des types de gisements Au-Sb que l'on rencontre dans le monde et dans la chaine varisque ainsi que leurs caractéristiques principales sont présentés. Enfin, la place du Massif Armoricain au sein de la chaîne varisque ouest-européenne ainsi que son évolution sont résumées afin d'illustrer le cadre géodynamique dans lequel se mettent en place les gisements Au-Sb au sein du Massif Armoricain.

La deuxième partie est axée sur la réévaluation des facteurs géologiques pouvant contrôler la localisation des gisements au sein du Massif Armoricain et constitue un article publié en 2016 dans la revue ***Terra Nova***. Cet article est principalement basé sur des données existantes, appartenant au BRGM, notamment sur les cartes géologiques et les levés géophysiques (gravimétrie et magnétisme) utilisés dans cette étude. La méthode d'analyse statistique spatiale utilisée est détaillée dans l'article. Nous avons montré que **plus de la moitié des indices antimonifères du Massif Armoricain étaient situé à l'aplomb de zones à forte densité et relativement magnétique**. De plus, les districts antimonifères majeurs, représentant 99% de la ressource connue en antimoine au sein du Massif Armoricain, sont également situés à l'aplomb de ces zones. Ces zones à forte densité et relativement magnétique sont **interprétés comme liées à la présence de corps mafiques à ultramafiques en profondeur**, une analyse étayée par les nombreuses intrusions de dykes de dolérites à travers toute la région. Ajouté à cette forte corrélation spatiale, nous avons montré que les indices antimonifères qui n'étaient pas spatialement associés avec ces corps mafiques/ultramafiques en profondeur, étaient spatialement associés aux zones de cisaillement et leurs satellites.

La troisième partie se consacre à l'étude du magmatisme mafique du Massif Armoricain et fait suite aux résultats de l'analyse spatiale de la partie précédente qui nous a orientés vers la caractérisation et la datation de ce magmatisme. Cette partie se trouve exclusivement sous la forme d'un article publié en 2016 dans la revue ***American Mineralogist***. Dans cet article, **la datation de plusieurs dykes et sills de dolérite**, au sein des domaines nord et centre armoricain, **a révélé un épisode magmatique mafique majeur à ca. 360 Ma**. Ce magmatisme généralisé, qui a une composition géochimique très homogène et qui ne montre aucune contribution crustale significative, a une signature d'épanchement basaltique alcalin d'intraplaque. **Ces magmas mafiques sont contemporains d'un changement drastique de la dynamique varisque**. En effet, ils se mettent en place lors de la subduction continentale et au début du fonctionnement des zones

de cisaillements majeurs au niveau du Massif Armoricain et peut-être dans une plus grande partie de la chaine varisque, **ce qui pose la question du rôle de ce magmatisme dans la mobilité des métaux et la circulation de fluides au sein du Massif Armoricain**. Cette question majeure constitue le cœur de cette thèse et est abordée en détails dans la partie suivante. Au-delà du résultat de l'âge de ce magmatisme, l'article est également orienté sur la méthode U-Pb sur apatite par LA-ICP-MS nouvellement développée par D. Chew à Trinity College en Irlande et qui permet de dater des apatites en les corrigeant du Pb commun. Cet article est donc également un cas d'étude démontrant l'applicabilité de cette méthode concernant les roches mafiques.

La quatrième partie est consacrée à la compréhension des minéralisations Au-Sb du Domaine Centre Armoricain depuis la source de la circulation de fluides jusqu'à la formation des gisements. Il est divisé en deux chapitres et d'un complément de discussion. **Le chapitre 1** porte sur la métallogénie de l'or et de l'antimoine dans le district du Semnon et les travaux réalisés sont présentés sous la forme d'un article sous presse dans la revue ***Ore Geology Reviews*** et d'un autre article en préparation pour la revue ***Mineralium Deposita.*** Le premier article est axé sur **la mobilité des métaux durant la déstabilisation des oxydes de fer-titane (Fe-Ti) du dyke de dolérite encaissant la minéralisation Au-Sb pendant l'altération hydrothermale au niveau de la mine du Semnon**. Nous avons montré, par l'analyse des éléments traces par LA-ICP-MS et par un calcul de balance de masse, que **les fluides responsables de la transformation de l'ilménite magmatique en rutile hydrothermal étaient enrichis en antimoine**. Ceci est un résultat majeur puisque la cristallisation du rutile est considérée comme précoce dans l'évolution paragénétique de la minéralisation et semble être sub-synchrone de la mise en place du dyke de dolérite. Cela semble indiquer que **les fluides hydrothermaux précoces enrichis en Sb altèrent très rapidement la dolérite et qu'ils ne sont pas totalement déconnectés de la mise en place du magmatisme mafique**. Le deuxième article est consacré à l'histoire hydrothermale du district du Semnon via la caractérisation texturale et minéralogique de la minéralisation, l'analyse de la déformation, l'étude des inclusions fluides, l'étude isotopique des carbonates et la datation des évènements minéralisateurs. A travers cette étude multi-méthodes, le résultat majeur qui en découle est **la mise en place précoce de la minéralisation Au-Sb du Semnon** dans l'histoire varisque du Massif Armoricain. Ceci va à l'encontre d'un évènement hydrothermal tardi-varisque unique et généralisé à travers toute la chaine varisque ouest-européenne, comme il est communément admis. Enfin, cette partie se termine avec une discussion complémentaire sur les données d'inclusions fluides du gisement de La Lucette et la comparaison avec les fluides du gisement du Semnon.

La cinquième partie est une discussion synthétique des possibles modèles d'intégration des minéralisations Sb-Au vis-à-vis des processus tectoniques à grande échelle qui caractérisent le

segment de la chaîne varisque armoricaine. Elle se compose d'un premier chapitre portant sur les apports géochronologique de la célèbre occurrence polymétallique à Au et Sb de Saint-Aubin-des-Châteaux. Les résultats sont présentés sous la forme d'un article en préparation en vue d'une soumission simultanée avec l'article #4 pour la revue ***Mineralium Deposita***. Dans cet article, nous mettons en évidence **la circulation de fluides minéralisateurs associés au stade aurifère et antimonifère à *ca.* 360 Ma à l'échelle du Domaine Centre Armoricain**. De plus, nous proposons que **le magmatisme mafique constitue un paramètre clé dans la mobilisation de fluides hydrothermaux** à l'échelle régionale. Cet article est suivi de données complémentaires sur l'évidence d'un évènement hydrothermal aurifère, dépourvu de Sb, localisé le long de la branche nord du cisaillement sud armoricain et plus jeune que les minéralisations Au-Sb du domaine Centre Armoricain. Des données complémentaires en isotopes radiogéniques (Sr-Nd) sur le magmatisme mafique du Massif Armoricain sont également présentées afin de contraindre l'origine de ce magmatisme. Enfin, cette partie se termine sur l'intégration des données à grande échelle et sur la compréhension des mécanismes permettant la mise en place d'un tel magmatisme mafique et la mobilisation des fluides à l'échelle d'un cycle orogénique.

Partie 1

Antimoine, Or et Massif Armoricain

1. Généralités sur l'antimoine

Cette partie a pour objectifs principaux de présenter les nombreux travaux effectués sur l'antimoine dans le monde, notamment sur la géochimie de l'antimoine. Cette dernière est effectivement fondamentale et nécessaire pour comprendre les processus de transport, de concentration et de piégeage des gîtes métallifères. Contrairement à l'or, l'antimoine est un métal peu connu du grand public mais largement utilisé dans la vie quotidienne et plus particulièrement dans le monde industriel. Il est principalement employé comme retardateur de flammes pour ses propriétés stabilisatrices et ignifuge, dans les batteries plomb-acide et également dans les alliages de plomb et d'étain pour sa résistance à la corrosion (e.g. Audion 2012). En plus d'être relativement précieux, l'antimoine est considéré comme un métal critique par l'Union Européenne. Il présente en effet un grand risque d'approvisionnement dans les années à venir puisque l'UE est dépendante à 100 % des importations. Le principal producteur mondial et fournisseur européen est la Chine qui a produit entre 2010 et 2014 près de 87 % de la production mondiale et fournit environ 90 % des importations totale de l'UE pour ce métal (COM 490 European Commission 2017). En ce qui concerne l'or, bien que n'étant pas une substance critique, ce métal précieux reste actuellement très recherché dans le domaine de la joaillerie et de l'électronique. L'UE ne fournit effectivement que 0.6 % de la production mondiale d'or comparativement au premier producteur qu'est la Chine (14.7 %, European Commission 2017). En raison des besoins d'approvisionnement en antimoine et du monopole de la Chine, cette thèse se situe ainsi dans un contexte socio-économique particulier, nécessitant de comprendre la genèse des minéralisations antimonifères et aurifères pour mieux affiner les critères de recherche pour l'exploration future et ainsi permettre de promouvoir le sous-sol européen qui possède un bon potentiel de nouvelles ressources. Nous présentons ici les connaissances et les caractéristiques principales des différents types de gisements d'antimoine connus dans le monde et surtout dans la chaîne varisque ouest-européenne. Cette dernière contient en effet la majorité des gisements d'antimoine en Europe. C'est pour cette raison que nous avons étudié le Massif Armoricain, segment de la chaîne varisque connus pour sa richesse en antimoine et or, afin d'y préciser et d'y contraindre les processus permettant la formation de gisements d'antimoine et or.

1.1 La géochimie de l'antimoine

L'abondance de l'antimoine varie de 0.02 à 0.8 ppm au sein de la croûte océanique (Jochum et Hoffmann 1997) et est estimée entre 0.2 et 0.45 ppm au sein de la croûte continentale supérieure (Rudnick et Gao 2003), ce qui en fait un métal relativement peu abondant. Par exemple, la teneur d'un gisement d'antimoine économiquement rentable est généralement 150000 fois supérieur à la

teneur de la croûte moyenne ce qui nécessite des facteurs de concentrations très élevés (Robb 2005; Schwarz-Schampera 2014). L'antimoine (Sb) est un élément chalcophile (i.e. un élément ayant une forte affinité avec le soufre) appartenant au groupe des métalloïdes à l'instar du silicium (Si), de l'arsenic (As) ou du germanium (Ge) dans la classification périodique des éléments. On le trouve sous plusieurs états d'oxydation (i.e. Sb^{5+}, Sb^{3+}, Sb^{0}) mais la forme la plus fréquente est Sb^{3+}. Le pH, la température, la fugacité en oxygène (fO_2) et l'activité en soufre sont des facteurs majeurs contrôlant la solubilité de l'antimoine (Williams et Normand 1997). Au sein d'une solution, il est principalement transporté sous la forme d'hydroxyle ($Sb(OH)_3^0$, Wood et al. 1987; Shikina et Zotov 1991; Obolensky et al. 2007) lorsque le pH est neutre et de bisulfure et d'hydroxyle de soufre ($HSb_2S_4^-$ (< 180°C) et $Sb_2S_2(OH)_2^0$ (180 et 280°C), Krupp 1988 ; Spycher et Reed 1989) lorsque fO_2 est intermédiaire. Il s'agit également d'un élément très volatile appartenant à ce que l'on considère comme les éléments traces facilement mobilisables par les fluides ou « Fluid-mobile elements » en anglais (e.g. B, Li, Cl, As, Sb, Pb, U, Cs, Sr, Ba). Ces derniers sont particulièrement enrichis au sein des fluides provenant de la déshydratation du panneau plongeant ou du coin mantellique des zones de subduction (Bonatti et al. 1984; Deschamps et al. 2010, 2011, 2012; Hattori and Guillot 2003, 2007; Kodolányi et al. 2012; Lafay et al. 2013; Scambelluri et al. 2001a, 2001b, 2004a, 2004b; Tenthorey et Hermann 2004; Vils et al. 2008, 2011). Comme son étymologie grecque l'indique (« anti » et « monos » signifie « pas seul »), Sb possède une forte affinité géochimique avec de nombreux éléments, notamment avec As et Hg, et se trouve fréquemment en étroite association minéralogique avec Au et Ag. En effet, dans le monde, rares sont les gisements où Sb est le seul métal économiquement valorisable. Il est très fréquemment associé à des minéralisations à Au, à Ag ou en métaux de base (e.g. Pb, Zn), ce qui en fait un très bon indicateur (i.e. métallotecte) pour ces types de gisements. Il existe également une très grande variété de minéraux porteurs de Sb : sous la forme de sulfure (stibine - Sb_2S_3), de sulfosels complexes (e.g. berthiérite – $FeSb_2S_4$, boulangérite – $Pb_5Sb_4S_{11}$, tétraédrite – $PbCuSbS_3$, gudmundite – FeSbS) ou d'oxydes (kermésite –Sb_2S_2O, valentinite/sénarmontite – Sb_2O_3). Le principal minerai exploité reste, sans conteste, la stibine.

1.2 Un aperçu des gisements d'antimoine dans le monde

Les minéralisations à Sb sont présentes dans divers types de gisements de l'actuel à l'Archéen, comme par exemple dans les précipités de fumerolles des volcans actifs (e.g. le district géothermal de Wai-O-Tapu en Nouvelle-Zélande) ou encore les gisements au sein des ceintures de roches vertes (e.g. l'« Antimony Line » au sein de la « Murchison belt » en Afrique du Sud). La plupart des gisements à Sb sont d'origine hydrothermale et épigénétique (Obolensky et al. 2007). A

l'instar des gisements à Au, la classification des gisements est relativement variée et peut être fonction : (1) du type d'encaissant qui contient la minéralisation (e.g. intrusion, turbidite, schistes noirs), (2) de la température/profondeur de mise en place (e.g. épi-, mésothermal), (3) du style de minéralisation (e.g. remplacement, stockwerk), (4) de leurs associations métallique et minéralogique (e.g. Hg-Sb, Sb-Au, Pb-Zn-Sb) ou (5) d'une combinaison de tous ces éléments (Poulsen et al. 2000; Robert et al. 2007; Schwarz-Schampera 2014). Les principales caractéristiques de ces gisements sont succinctement décrites ci-dessous tant la diversité est grande au sein des gisements épigénétiques. Les minéralisations à Sb sont très fréquentes au sein des gisements d'or orogéniques et souvent considérées comme telles. Pour cette raison, ce type de gisement sera beaucoup évoqué dans la suite de ce chapitre.

Contexte géologique. Les gisements de Sb se mettent en place à diverses époques géologiques et présentent des caractéristiques communes quel que soit leur âge, permettant de les distinguer d'autres types de gisements (Gebre-Mariam et al. 1995; Goldfarb et Groves 2015 ; Goldfarb et al. 2001, 2005; Groves et al. 1998), comme l'illustre la Figure 1.1 basée sur des gisements d'or orogéniques d'âge Archéen mais applicable à la plupart des gisements Au-Sb d'âge Protérozoïque à Phanérozoïque. Ils sont présents au sein de divers terrains métamorphiques et variablement déformés, incluant des séries volcano-plutoniques et sédimentaires clastiques. Les roches métamorphiques encaissantes appartiennent majoritairement au faciès schistes verts et plus rarement au faciès amphibolite ou granulite. Ces gisements se trouvent généralement sur ou à proximité de grandes zones de déformations d'échelle crustale, principalement en contexte compressif ou décrochant (e.g. Goldfarb et Groves 2015).

Morphologie et contrôle structural. Il y a un contrôle structural très fort sur la mise en place et la morphologie des minéralisations à toute échelle. La morphologie est très variée, incluant des failles fragiles et des zones de cisaillement ductiles, des fractures, des stockwerks, des brèches ou des charnières de pli (Hodgson 1989; Robert 1996). Le corps minéralisé peut se présenter sous la forme de dissémination au sein de la roche encaissante ou en remplissage de failles ou de fractures sous formes de veines. Les gisements ont parfois une grande extension verticale (1 km en moyenne) à l'instar des gisements d'or orogéniques (Fig. 1.1). La minéralisation est classiquement syn- à post-tectonique et discordante sur la stratigraphie de la roche encaissante bien qu'il existe des veines parallèles au plan de stratification ou parallèles au contact de roches intrusives. Cependant, les gisements qui constituent les plus grosses réserves et ressources en Sb du monde, sont de type stratiforme (Schwarz-Schampera 2014), comme par exemple le gisement géant de Xikuangshan dans la province du Hunan en Chine contenant à lui seul environ 2110 kt (Fan et al. 2004; Laznicka

2010). Ce gisement est constitué d'une minéralisation relativement simple, composée uniquement de stibine, associée à une intense silicification et carbonatisation, et encaissée au sein de calcaires dévoniens (Fig. 1.2a), où la calcite synchrone de la stibine a été datée entre le Jurassique supérieur et le Crétacé inférieur (Peng et al. 2003). Il existe également des systèmes minéralisés associés à l'auréole et à la « carapace » fragile située à l'aplomb d'intrusions plutoniques (Fig. 1.2b; Hart et al. 2002). Ces gisements sont caractérisés par une grande variété de styles de minéralisations (e.g. skarns, gîtes de remplacement et gîtes filoniens) et une forte zonalité minéralogique avec une association métallifère proximale à Au-W-As, intermédiaire à As-Sb-Au et distale à Ag-Pb-Zn. Dans ce système, les minéralisations à Sb sont principalement trouvées au sein de réseaux filoniens similaires aux gisements d'or orogéniques et parfois difficile à discriminer (Goldfard et Groves 2015). La grande variabilité de ces gisements reflète leurs caractères épigénétiques et l'influence de la rhéologie sur leurs géométries.

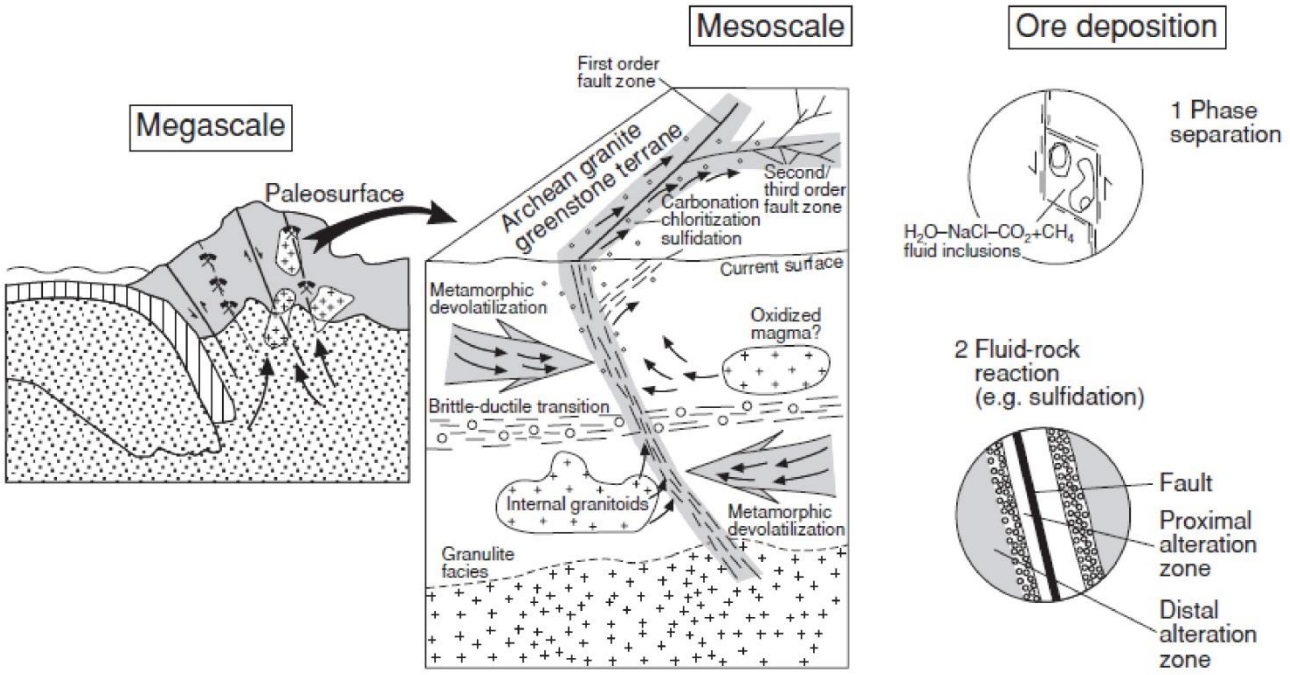

Figure 1.1 Schéma multi-échelle illustrant les principales caractéristiques des gisements d'or orogéniques Archéen applicable pour la majorité des gisements Protérozoïque et Phanérozoïque. A l'échelle lithosphérique, les gisements sont localisés aux frontières de plaques convergentes où le métamorphisme expulse des fluides vers la surface à travers de grandes discontinuités structurales majeures. A l'échelle crustale, les zones de cisaillement majeures et leurs failles associées représentent les principales structures encaissant les minéralisations. Ces structures majeures sont marquées par d'intenses zones d'altération. Le dépôt de la minéralisation est fonction de l'interaction fluides-roches et/ou de la séparation de phase entre H2O et CO2 d'après Hagemann et Cassidy (2000) et Robb (2005).

Minéralogie et altération hydrothermale. La gangue des veines est largement dominée par le quartz bien que les carbonates peuvent être localement abondants. La minéralogie de la minéralisation est généralement monominérale, sous forme de stibine massive. En revanche, lorsqu'elle est associée avec d'autres métaux (e.g. Pb-Zn ou Au), la minéralisation peut être très complexe et former une grande variété de sulfosels (e.g. boulangérite, tétraédrite, aurostibite).

Lorsqu'elle est associé à une minéralisation à Au, la stibine est quasi-systématiquement tardive dans l'évolution paragénétique. En effet, les domaines de stabilité de la stibine et de l'or natif diffèrent par leur gamme de température de précipitation ; la stibine est généralement considérée comme un minéral de basse température alors que l'or cristallise à relativement plus haute température.

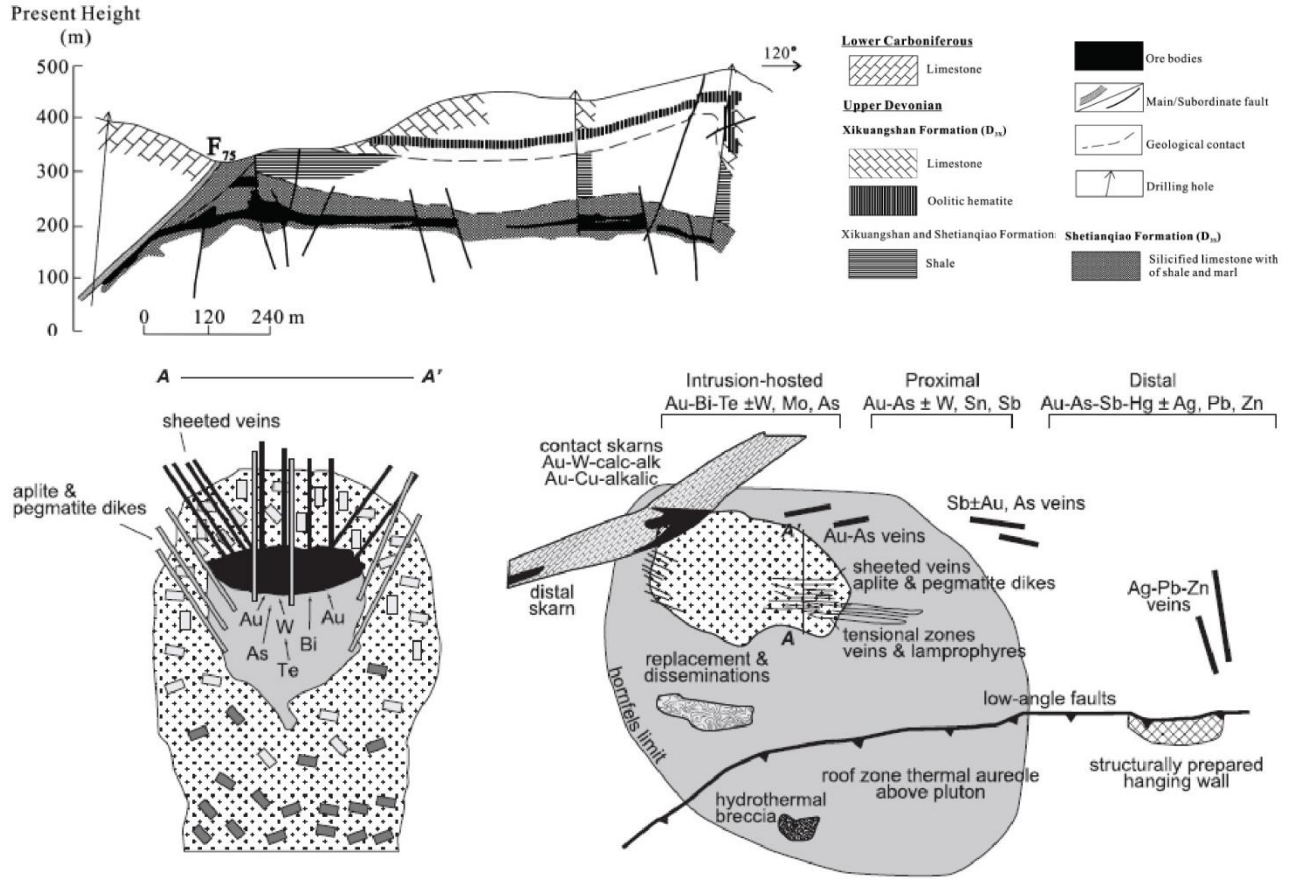

Figure 1.2 A Coupe géologique d'un corps minéralisé en antimoine stratiforme en remplacement dans une roche carbonatée au sein du gisement de Xikuangshan (Yang et al. 2006). **B** Modèle d'un système aurifère associée à une intrusion réduite d'après Hart et al. 2002 tel que le gisement de Fort Knox en Alaska. Dans un tel système, on y observe plusieurs styles de minéralisation et une zonalité minéralogique. En effet, ce type de gisement peut générer des skarns à Au, des disséminations ou des stockwerks directement encaissés dans le pluton

L'altération hydrothermale est progressive et diminue drastiquement en s'éloignant des corps minéralisés. L'échelle, l'intensité et la minéralogie est fonction de la composition de l'encaissant de la minéralisation et du niveau structural de sa mise en place (e.g. McCuaig et Kerrich 1998) mais elle est principalement représentée par une forte carbonatisation (calcite, dolomite, ankerite, sidérite, magnésite), un enrichissement en sulfure (pyrite, pyrrhotite et/ou arsénopyrite) et un métasomatisme alcalin (e.g. séricite, albite).

Contraintes isotopiques et physico-chimiques des fluides. Afin de contraindre la source des métaux et l'origine des fluides responsables du dépôt de Sb et des métaux associés comme Au, de nombreuses études isotopiques stables (et radiogéniques) et d'inclusions fluides ont été effectuées. Les données sont extrêmement variables et parfois indépendante de l'âge et de la localisation

géographique. Les larges gammes de valeurs de $\delta^{18}O$, $\delta^{13}C$ ou encore de $\delta^{34}S$ fréquemment observées à travers de nombreux gisements (et même parfois au sein d'un même gisement) reflètent certainement des interactions fluides/roches hétérogènes entre des roches de composition variées (Goldfarb et Groves 2015) et des fluides minéralisateurs depuis leur source vers le site de dépôt des minéralisations. Néanmoins, malgré de multiples sources isotopiques des fluides au sein d'un même gisement, il peut parfois exister une grande homogénéité isotopique au sein d'une portion de chaîne. Par exemple, au sein de la cordillère Canadienne, les valeurs de $\delta^{18}O$ des veines de quartz minéralisées en Au-Ag-Hg-Sb sont d'une grande homogénéité, les valeurs variant seulement de 5 ‰ à travers toute la cordillère (Nesbitt et al. 1989). Cela témoigne probablement d'une source de fluides commune pour tous les gisements de la Cordillère Canadienne, en l'occurrence l'infiltration profonde d'un fluide météorique acquérant une signature crustale. A l'inverse, les valeurs de $\delta^{13}C$ oscillent entre -10 et +2 ‰ et reflètent ainsi une hétérogénéité de la signature isotopique du carbone au sein de la cordillère.

Les interprétations des données d'inclusions fluides divergent également en raison de (i) la possible rééquilibration des fluides due à la déformation et à la lente exhumation de ces gisements ou (2) la circulation de fluides postérieurs et déconnectés de l'histoire de la minéralisation (e.g. Kerrich 1976). En dépit de ces problèmes, quelques types majeurs de fluides récurrents ont été mis en évidence dans la genèse des minéralisations Sb-Au par de nombreux auteurs (e.g. Boiron et al. 2003; Garofalo et al. 2014; Ridley et Diamond 2000) : (1) des fluides aqua-carboniques (H_2O-CO_2) biphasées ou triphasées avec une quantité variable de CH_4, N_2 et sels dissous, (2) des fluides carboniques (CO_2) avec des teneurs variables en CH_4, N_2 et H_2S et des teneurs en H_2O très faible voire indétectable, et (3) des fluides aqueux biphasées avec une salinité (NaCl) faible à intermédiaire et avec ou sans CO_2. La présence de CO_2 au sein des fluides est cohérente avec la forte carbonatisation observée dans les roches encaissantes de ces gisements Sb-Au. Cependant, il est difficile de différencier clairement l'origine des fluides à l'instar des gisements d'or orogéniques. En effet, la présence de CO_2 dans un fluide peut être interprétée comme la preuve d'une origine profonde via la granulitisation de la croûte inférieure (Fyon et al. 1984, 1989) ou la libération progressive de fluides sous des conditions du faciès amphibolite (Phillips et Powell 1993). D'autres auteurs ont également montré que des intrusions magmatiques peuvent générer des fluides carboniques (McCoy et al. 1997 ; Sillitoe et Thompson 1998). Néanmoins, la combinaison de toutes les données disponibles sur les gisements Sb-Au suggère une gamme de P-T moyenne comprise entre 100 MPa et 300 MPa et 250-450°C pour le dépôt de Au, bien qu'il existe des gisements proches de la surface enregistrant des conditions P-T beaucoup plus basse et des gisements beaucoup plus profonds avec des conditions P-T plus élevées (0.5 kbar et 150 °C et 5 kbar et 700°C, respectivement ; Hagemann et Brown 1996). La stibine se forme à des températures

généralement plus basses que les alliages d'or (e.g. electrum, maldonite), de l'ordre de 150-200°C (e.g. Kay et Strong 1983; Boiron et al. 2003). Sa précipitation reflète dans la majorité des cas une baisse de température qui est souvent identifié comme le facteur responsable de la formation de stibine (Hagemann et Lüders 2003; Williams-Jones et Normand 1997). Bien que les avis divergent et qu'une controverse majeure persiste sur l'origine des fluides (i.e. l'oxygène, le carbone ou le soufre), la source des métaux, notamment Sb et Au, fait également débat. En effet, il est extrêmement difficile de tracer la source de Sb et Au, en raison du nombre de lithologies traversées par les fluides avant d'atteindre le piège de ces métaux. Les travaux les plus récents, en termes de sources des métaux, semblent impliquer une source par réaction de déshydratation lors du métamorphisme prograde (Beaudoin and Pitre 2005; Goldfarb et al. 2005; Groves and Bierlein 2007; Phillips and Powell 2010; Tomkins 2010, 2013; Mortensen et al. 2010; Gaboury 2013). Cela implique soit (1) une dévolatilisation à grande échelle de large volume de roches métasédimentaires (Pitcairn et al. 2006a, 2010, 2014a, 2014b) ou métabasaltiques (Henley et al. 1976; Glasson and Keays 1978; Bierlein and Craw 2008; Bierlein and Pisarevsky 2008; Willman et al. 2010) ou (2) un lessivage plus local de roches fertiles métasédimentaires (Large et al. 2007, 2011; Thomas et al. 2011).

Un modèle génétique controversé. Parce qu'il est difficile de définir une source unique de Sb et Au et des fluides minéralisateurs de nombreux modèles génétiques ont été proposés pour justifier leur genèse: (1) la granulitisation de la croûte inférieure due à des fluides mantelliques riche en CO_2, et accompagné de magmatisme felsique (Fyon et al. 1989; Hodgson et Hamilton 1989), (2) des fluides magmatiques exsolvés des intrusions de type TTG (Burrows et Spooner 1987), (3) des fluides produit par des processus métamorphiques (e.g. Kerrich et Cassidy 1994; Kontak et al. 1990; Phillips et Powell 1993) ou encore (4) des circulations profondes de fluides météoriques (Boiron et al. 2003; Nesbitt et al. 1986). Plus récemment, Goldfarb et Groves (2015) ont proposé un modèle en faveur d'une origine commune des fluides de tous les gisements d'or orogénique. En effet, les fluides seraient tous d'origines profondes et métamorphiques et résulteraient de divers processus de mobilisation en fonction du contexte géodynamique : désintégration radioactive lors d'un épaississement crustal, la remontée asthénosphérique lors d'un retrait de panneau plongeant (« slab rollback »), la subduction d'une ride océanique ou encore la présence d'un point chaud (Fig. 1.3).

La majorité des gisements Sb-Au étudiés dans le monde sont d'âge Archéen à Paléoprotérozoïque mais d'autres périodes géologiques sont fertiles en ces métaux, à l'instar de la chaîne varisque européenne, qui fait l'objet de cette thèse et est abordée en détail dans le chapitre suivant.

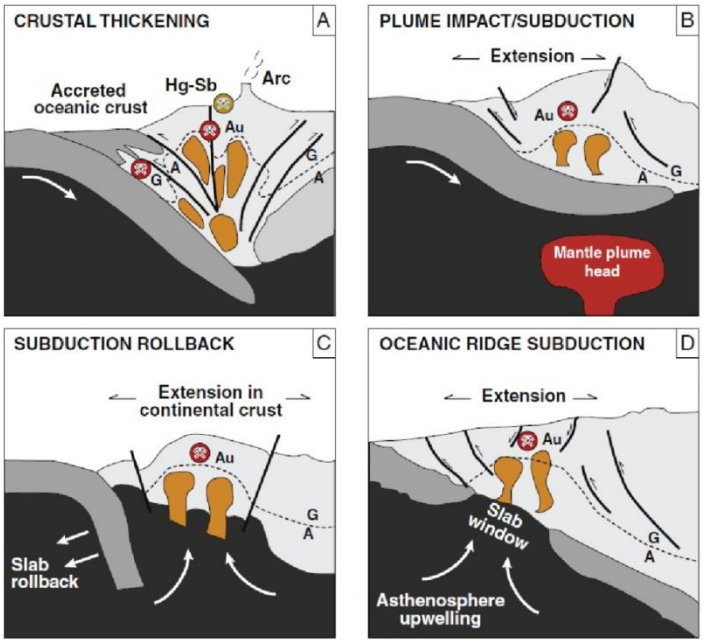

Figure 1.3 Scénarios possibles de mise en place de gisement Au-Sb liés à la subduction qui pourrait conduire à la dévolatilisation de croûte océanique accrétée le long d'une marge continentale active d'après Goldfarb et Groves (2015). (a) inversion d'une séquence métamorphique barrovienne lors d'un épaississement crustal. (b) interactions entre une subduction et un point chaud (c) extension de la plaque supérieure et/ou « metamorphic core complex » résultant d'un retrait du panneau plongeant (« slab rollback ») et par conséquent d'une remontée asthénosphérique. (d) subduction d'une ride océanique permettant la formation d'une fenêtre asthénosphérique.

2. Les minéralisations antimonifères et aurifères au sein de la chaîne Varisque

Il existe, au sein de la chaîne varisque européenne, de nombreux gisements Sb-Au, principalement épigénétiques, notamment dans le Massif Ibérique (e.g. Gumiel et Arribas 1987; Couto et al. 1990; Neiva et al. 2008), dans le Massif Central français (e.g. Bellot et al. 2003; Bouchot et al. 2005), dans le Massif Armoricain (e.g. Bailly et al. 2000; Chauris et Marcoux 1994), en Cornouailles (Clayton 1993; Clayton et Spiro 2000; Stanley et al. 1990), dans la Zone Saxo-Thuringienne (Dill 1985; Němec et Zachariáš 2017) ou encore dans les Carpates (Chovan et al. 1995). A l'instar des gisements connus dans le monde, les minéralisations varisque à Sb sont de styles variés mais présentent également de nombreuses similitudes à travers toute la chaîne. Pour des raisons d'exhaustivité, seules les caractéristiques principales des gisements Au-Sb varisque sont mentionnées et résumées dans la Table 1.1 modifiée d'après Wagner et Cook (2000).

Les gisements Sb-Au de la chaîne varisque sont majoritairement contrôlées par des failles ou des zones de cisaillement d'échelle régionale et/ou des failles/zones de cisaillement secondaires associées (Bellot et al 2003; Bouchot et al. 2005; Ortega et Vindel 1995) et se mettent en place postérieurement au pic du métamorphisme régional (Bouchot et al. 1997, 2005). Les gisements sont encaissés au sein de nombreuses lithologies allant de métasédiments peu métamorphiques d'âge Néoprotérozoïque à Carbonifère, comme dans la Zone Centrale Ibérique (Gumiel et Arribas 1987) ou dans le domaine Saxo-Thuringien (Dill 1985; Wagner et Cook 2000), à des gneiss métamorphiques comme dans le Massif Central français (Périchaud 1980) ou encore à des granites tardi-varisque (Dill 1985). La localisation du système filonien au sein de charnières anticlinales semble être un contrôle structural majeur au sein de la chaîne varisque européenne (Table 1.1). Des

relations génétiques ont été proposées entre les minéralisations et la mise en place de granites peralumineux tardi-orogéniques dans certaines zones de la chaîne, notamment dans le Massif Ibérique en Espagne (Ortega et al. 1996). La minéralisation est principalement dominée par la stibine, bien que la berthiérite puisse être localement abondante (Neiva et al. 2008). L'évolution paragénétique débute classiquement par un stade Fe-As-Au constitué d'arsénopyrite, pyrite et pyrrhotite suivi par un stade intermédiaire à métaux de base (Zn-Pb-Cu) et sulfosels de Sb (e.g. Massif Central français, Bouchot et al. 2005; Munoz et al. 1992 ; Massif Ibérique, Couto et al. 1990; Neiva et al. 2008). Le stade Sb principal (stibine) est toujours tardif dans la paragenèse et peut également être associé à des sulfosels. Les nombreuses études d'inclusions fluides à travers différents endroits de la chaîne ont permis de préciser les conditions physico-chimiques responsables du dépôt de la phase à Sb. Elles montrent que plusieurs types de fluides sont impliqués dans les minéralisations Sb-Au : des fluides aqua-carboniques (avec le CO_2 comme principal constituant) et relativement chauds (e.g. 160-410°C, Table 1.1), des fluides aqua-carboniques, dont la contribution aqueuse est plus grande, enregistrent des températures légèrement plus faibles (e.g. 180-390°C, Table 1.1) et des fluides aqueux généralement peu salins et de faible température (e.g. 100-280°C, Table 1.1). Les processus favorisant la précipitation de la stibine sont due soit à (1) un refroidissement de fluides convectifs (Bril et Beaufort 1989; Munoz et al. 1992), (2) une ébullition des fluides par décompression (Ortega et al. 1996; Boiron et al. 2003) ou (3) une dilution de fluides métamorphiques riche en CO_2 par des fluides météoriques à H_2O-NaCl durant l'exhumation post-orogénique (Boiron et al. 2003; Couto et al. 1990; Wagner et Cook 2000). La période de mise en place des minéralisations Au-Sb semble être également similaire au sein des différents segments de la chaîne varisque et semble être synchrone d'évènements tectoniques tardi-orogéniques résultant d'un changement de régime tectonique majeur, à savoir le passage d'un régime compressif à un régime décrochant dominant (Arthaud et Matte 1987; Malavieille et al. 1990) et/ou à un régime d'extension post-effondrement de la chaîne (Bouchot et al. 2005).

Dans le Massif Central français (MCF), les gisements Sb-Au sont interprétés comme résultant d'un seul évènement hydrothermal majeur autour de 300 Ma dans un laps de temps relativement court de l'ordre de 10 à 20 Ma, appelé communément « or 300 » (Bouchot et al. 1997, 2005). Cette période est considérée comme une période favorable au piégeage de Au et Sb et des métaux associés dans la croûte continentale. De nombreux arguments de chronologie relative, tels que les relations géométriques avec des granites tardi-carbonifère ou des lamprophyres permiens, ont permis le calage temporel de certains gisements. L'âge absolu des minéralisations reste néanmoins difficile à déterminer, en raison du peu de minéraux datables et des complexités liées à la perturbation fréquente des systèmes U-Pb et Ar-Ar par la circulation de fluides et la déformation

Table 1.1 : Synthèse des caractéristiques minéralogiques, structurales et des données d'inclusions fluides des minéralisations Sb-(Au) tardi-orogénique de la Chaine Varisque européenne

	District de Dúrico–Beirã (Portugal)	**Massif Central (France)**	**Cornouailles (Angleterre)**
Encaissant	Ordovicien à Silurien	Néoprotérozoique à Silurien	Dévonien moyen à Carbonifère supérieur
Position structurale	Anticlinal varisque	Anticlinal et nappe de charriage varisque	Anticlinal varisque
Structures minéralisées	Fractures sub-verticales N-NE	Réseaux filoniens, zone de cisaillement secondaires	Systèmes de veines dilatantes
Evolution paragénétique	Stade 1 : asp + py + Au ± cass ± wol + qz	Stade 1 : asp + py + Au + qz + carb	Stade 1 : asp + py
	Stade 2 : sp ± cp ± po ± py ± tet + qz	Stade 2 : sp + ga + cp + qz + sulfosels	Stade 2 : cp + sp
	Stade 3 : jam ± sp ± bou ± ga + qz + carb	Stade 3 : st + qz ± sulfosels	Stade 3 : ga + st + jam + bnn + bou + tet
	Stade 4 : brt + st ± asp ± py + carb	Stade 4 : remobilisation	
	Stade 5 : remobilisation		
Composition des fluides	Type 1: H_2O-NaCl(2%)-CO_2	Type 1: CO_2-H_2O-NaCl(0-6%)	Type 1: CO_2-H_2O-NaCl(4%)
	Type 2: H_2O-NaCl(2%)-(CO_2)	Type 2: H_2O-NaCl(0-8%)-(CO_2)	Type 2: H_2O-NaCl(4%)-(CO_2)
	Type 3: H_2O-NaCl(<2%)	Type 3: H_2O-NaCl(<5%)	Type 3: H_2O-NaCl(0-6%)
Température d'homogénéisation des inclusions fluides	Type 1: 290-340°C Type 2: 230-320°C Type 3: 128-225°C	Type 1: 280-410°C Type 2: 260-390°C Type 3: 100-280°C	Type 1: 250-350°C Type 2: 270-290°C Type 3: 170-230°C
Pression		10-40 Mpa	70-160 Mpa
Mécanisme de précipitation	Mélange, dilution et refroidissement de fluides	Simple refroidissement et dilution de fluides	Refroidissement et démixtion de fluides
Magmatisme	Granites Stéphanien à post-Stéphanien	Granites peralumineux tardi-varisque	Aucune relation avec des granites

	Mari Rosa (Espagne)	**Rheinisches Schiefergebirge (Allemagne)**	**Zone Saxo-Thuringienne (Allemagne)**
Encaissant	Néoprotérozoique	Dévonien inférieur à Carbonifère inférieur	Ordovicien à Carbonifère
Position structurale	Cœur d'anticlinal varisque	Anticlinal varisque	Anticlinal varisque
Structures minéralisées	Systèmes de veines dilatantes	Fentes de tension parallèles au litage	Systèmes de veines dilatantes parallèle à la schistosité
Evolution paragénétique	Stade 1 : asp ± py + qz	Stade 1 : py + qz ± chl	Stade 1 : py + asp ± Au
	Stade 2 : st + Au + qz	Stade 2 : st + zin ± plg ± sem + sp	Stade 2 : st + qz
	Stade 3 : py ± po ± sp ± sulfosels + qz		Stade 3 : sulfosels ± sp ± ga + carb
Composition des fluides	Type 1: H_2O-NaCl-CO_2-CH_4-(N_2)	Type 1: H_2O-NaCl(1-11%)	
	Type 2: H_2O-NaCl(<9%)-N_2-(CO_2-CH_4)	Type 2: H_2O-NaCl(3-5%)	
	Type 3: H_2O-NaCl(<9%)-N_2-(CH_4)		
Température d'homogénéisation des inclusions fluides	Type 1: 270-390°C Type 2: 180-330°C Type 3: 150-270°C	Type 1: 160-390°C Type 2: 110-180°C	
Pression	90-100 Mpa	20-120 Mpa	
Mécanisme de précipitation	Démixtion de fluides	Refroidissement de fluides, (ébullition)	
Magmatisme	Granite tardi-varisque de Albuquerque	Aucune relation avec des roches magmatiques	Granites tardi-varisque

Données d'après Boiron et al. (1990), Bril (1982), Bril et Beaufort (1989), Clayton (1993), Clayton et al. (1990), Couto et al. (1990), Dill (1985, 1993), Munoz et Shepherd (1987), Munoz et al. (1992), Ortega et Vindel (1995), Ortega et al. (1991a), Ortega et al. (1996), Wagner et Cook (2000)

postérieures à la mise en place des systèmes minéralisés. Par conséquent, seules quelques rares datations sont disponibles dans la littérature et tendent à confirmer un âge tardi-varisque (Bouchot et al. 2005; 313 ± 5 Ma par la méthode K/Ar sur phengite, Marcoux et al. 1988; 317-306 Ma par la méthode $^{40}Ar/^{39}Ar$ sur phengite, Monié et al. 2000). L'hypothèse d'un événement aurifère unique repose donc majoritairement sur l'analyse de la déformation, des champs de contraintes et de la chronologie des structures. En effet, une grande majorité des structures porteuses de la minéralisation à Sb-Au ont fonctionné lors du Carbonifère supérieur dans un régime décrochant et/ou d'extension généralisée (Mattauer et al. 1988; Malavielle et al. 1990; Gapais et al. 1993; Burg et al. 1994; Faure 1989, 1995).

La synthèse des études pétrographiques, minéralogiques et géochimiques de ces districts Sb-Au du MCF a permis de distinguer deux types de gisements en fonction de leurs conditions de mises en places dans la croûte. Les gisements dits « profonds » formés sous des conditions de pression lithostatiques et Les gisements dits « peu profonds » plutôt formés sous des conditions de pression hydrostatiques (Bouchot et al. 2005). La limite de ces deux domaines se situe approximativement entre 5 et 7 km de profondeur (Hagemann et Brown 1996).

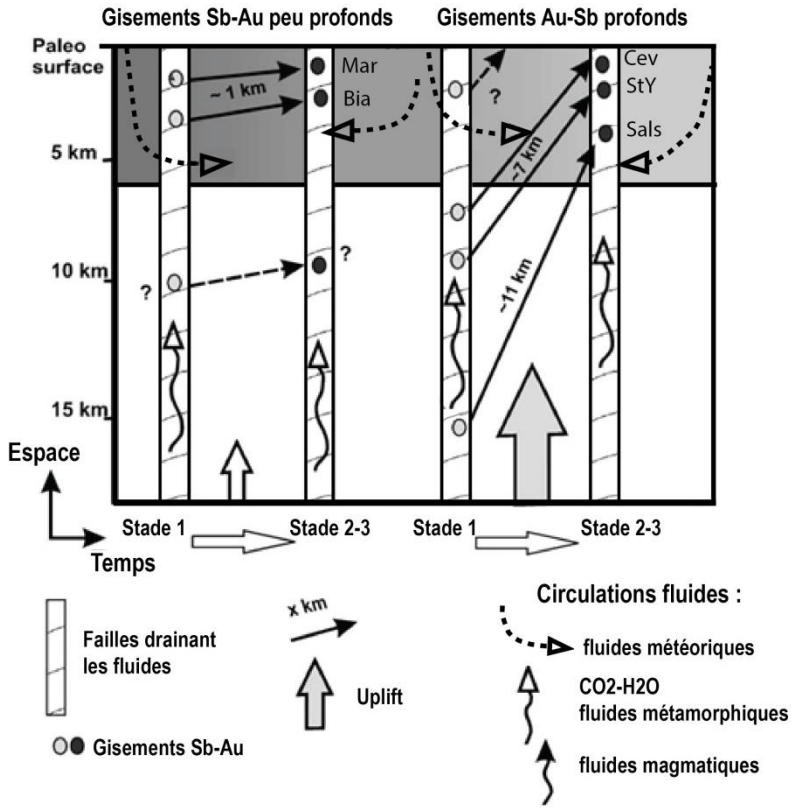

Figure 1.4 Coupe schématique de la croûte continentale montrant les deux stades de mises en place des gisements Au-Sb profonds et Sb-Au peu profonds affectés par une remontée différentielle de la croûte. Bia = Les Biards; Cev = Cévennes; Mar = La Marche; Sals = Salsigne; StY = Saint-Yrieix. Modifiée d'après Bouchot et al. (2005)

Ces gisements présentent une évolution paragénétique en trois principaux stades, similaire aux gisements Sb-Au de la chaîne varisque européenne (Table 1.1). Hormis leur profondeur de mise en place dans la croûte, le caractère majeur qui les distingue est la place de Au dans la paragenèse. En effet, dans les gisements dits « peu profonds », Au est associé au stade précoce (stade 1) et piégé

dans le réseau cristallin de l'arsénopyrite et de la pyrrhotite (Johan et al. 1989; Picot et al. 1987), ou en inclusions dans ceux-ci ; tandis que dans les gisements dits « profonds », Au se trouve sous sa forme native dans la gangue ou en remplissage de fractures et plutôt associé au stade intermédiaire (stade 2; Bouchot et al. 2005). Néanmoins, dans les deux systèmes, le dépôt de l'or est associé à la rencontre de fluides métamorphiques et de fluides météoriques lors de la remontée des blocs continentaux (Boiron et al. 2003; Bouchot et al. 2005; Fig. 1.4). Quelle que soit la profondeur de mise en place des stades précoces, le stade à Sb est toujours tardif et composé de stibine massive plus ou moins associée avec la berthiérite, des sulfosels à Sb et remobilisation de Au.

Comme l'illustre la Table 1.1, les données sur le Massif Armoricain sont absentes et bien trop parcellaires pour être synthétisées. Il existe néanmoins quelques travaux sur les minéralisations Sb-Au armoricaines qui seront présentés dans le chapitre suivant après la présentation du contexte géologique armoricain.

3. Le Massif Armoricain : contexte géologique et métallogénique

Le Massif Armoricain, situé dans la partie ouest de la France, est un segment de l'orogène varisque qui résulte de la collision entre deux plaques lithosphériques majeures au cours du Paléozoïque : Gondwana au Sud et Laurussia au Nord. Cette collision résulte de la fermeture de l'océan Iapetus engendrant la collision de Laurentia et Baltica (e.g. Matte 2001; Ballèvre et al. 2009, 2013, 2014; Kroner et Romer 2013; Franke et al. 2017). La chaîne varisque ouest-européenne s'étend sur près de 5000 km de long et affleure aujourd'hui, entre autres, dans le Massif Ibérique, le Massif Armoricain, la Cornouaille, le Massif Central, le bloc Corso-Sarde, les Ardennes, le Nord de l'Allemagne et le Massif de Bohême (Fig. 1.5). Au Paléozoïque inférieur, ces deux plaques lithosphériques sont séparées par l'océan Rhéique, formé au Cambro-ordovicien. Selon des études paléontologiques et paléomagnétiques (Cocks et Fortey 1982; Van der Voo 1983; Perroud 1985; Paris et Robardet 1990, 1994), des blocs continentaux de faible extension sont soupçonnés entre ces deux plaques. Ces blocs sont principalement rattachés à la marge Nord du Gondwana au début du Paléozoïque mais sont par la suite détachés du Gondwana et largement impliqués dans la formation de la chaîne. La plaque « Armorica » qui couvre une grande partie du Massif Armoricain constitue un de ces blocs (e.g. Matte 2001; Kroner et Romer 2013; Ballèvre et al. 2014; Franke et al. 2017).

La structuration de cet orogène varisque reste encore largement débattue à l'heure actuelle en raison des difficultés à corréler différentes portions de chaîne qui n'offrent pas de continuité longitudinale entre elles (e.g. le Massif Ibérique est actuellement séparé du Massif Armoricain par le Golfe de Gascogne). Cependant, la naissance de la chaîne varisque pourrait résulter de deux

zones de subduction de deux domaines océaniques à vergences opposées (e.g. Matte 1986 ; Ballèvre et al. 2013) ou d'une seule zone de subduction majeure liée à la fermeture de l'océan rhéique et dont la vergence est toujours discutée et dépasse de loin les objectifs de cette thèse (e.g. .Kroner et Romer 2013).

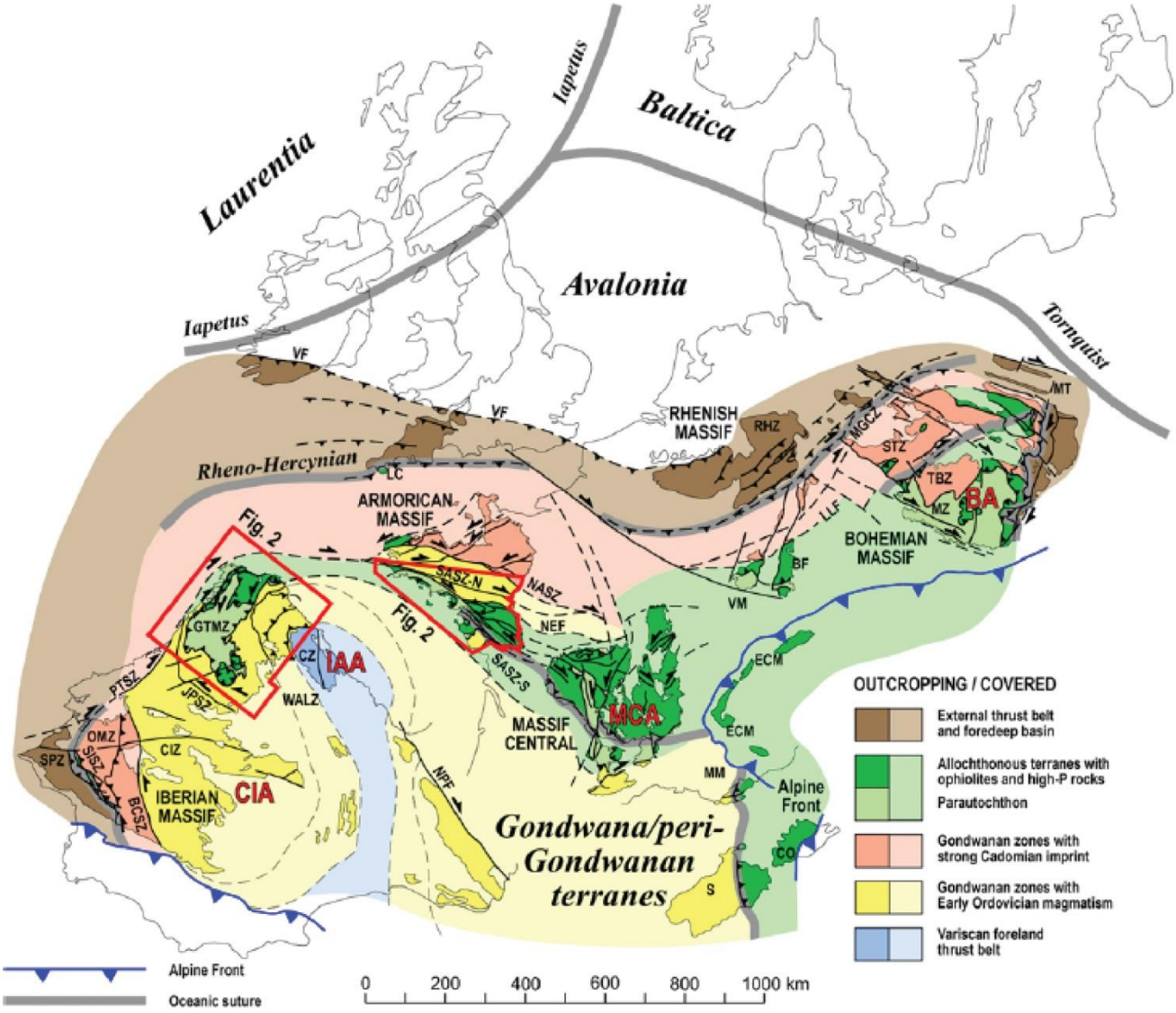

Figure 1.5 Carte synthétique représentant la place du Massif Armoricain au sein de la chaîne varisque ouest-européenne avant l'ouverture du Golfe de Gascogne. Les différentes teintes représentent les possibles corrélations des différents domaines continentaux reconnus au sein de la chaîne (Ballèvre et al. 2014).

3.1 Structuration du Massif Armoricain

Dans le Massif Armoricain, trois domaines principaux sont reconnus, les domaines Nord (NAD), Centre (CAD) et Sud (SAD) armoricain (Fig. 1.6). Ils sont séparés par deux zones de cisaillements majeures d'échelle crustale : le cisaillement Nord Armoricain (NASZ) et le cisaillement Sud Armoricain (SASZ, Goré et Le Corre 1987; Gumiaux et al. 2004 a, 2004b; Jégouzo 1980; Watts et Williams 1979;). Ces zones de cisaillement, orientés E-W à NW-SE, sont des décrochements

dextres jalonnés de granites syn-cinématiques fixant l'âge de la déformation au Carbonifère (e.g. Berthé et al. 1979a, 1979b; Bernard-Griffiths et al. 1985a).

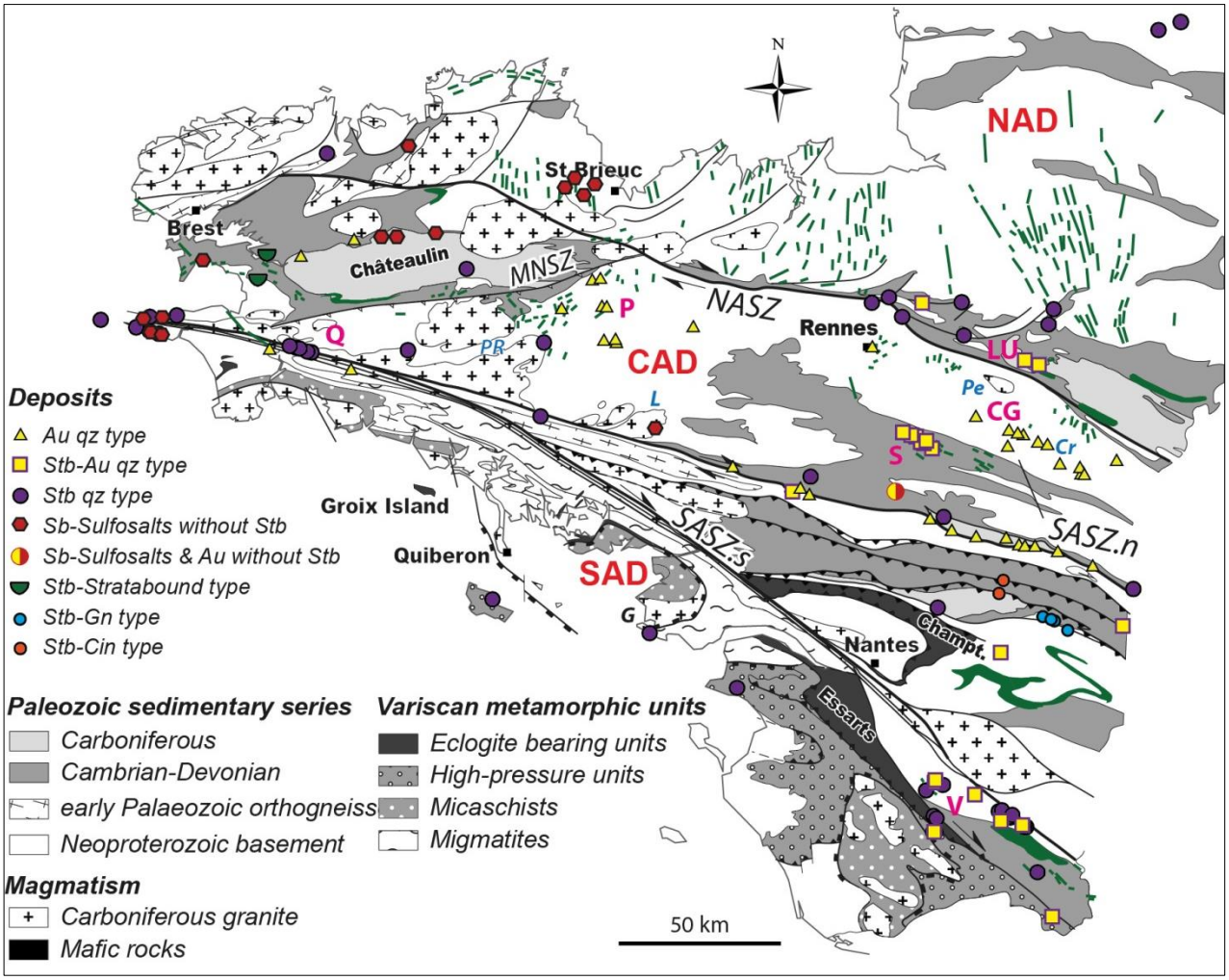

Figure 1.6 Carte synthétique représentant la place du Massif Armoricain au sein de la chaîne varisque ouest-européenne avant l'ouverture du Golfe de Gascogne. Les différentes teintes représentent les possibles corrélations des différents domaines continentaux reconnus au sein de la chaîne (Ballèvre et al. 2014). LU : district Sb-Au de La Lucette, S : district Sb-Au du Semnon-La Coëfferie, V : district Sb-(Au) de Vendée, Q : district Sb de Quimper-Cap Sizun CG : district Au de Château-Gontier, P : district Au de Pontivy-Loudéac, L : granite de Lizio, PR : complexe de Pontivy-Rostrenen, Pe : granite du Pertre et Cr : granite de Craon.

Le NAD est composé d'un socle néoprotérozoïque affecté d'une déformation ductile cadomienne (620-530 Ma) et seule une légère déformation fragile, concentrée le long de structures héritées, affecte ce domaine durant la collision varisque (Brun et al. 2001; Gumiaux et al. 2004b). Le SAD constitue une portion des zones internes de la chaîne varisque et se compose essentiellement de roches fortement métamorphiques (e.g. éclogites, schistes bleus, migmatites) présentant une intense déformation ductile. L'épaississement de ce domaine est suivi ensuite par une extension à partir de 310-300 Ma (Gapais et al. 1993, 2015; Gumiaux et al. 2004b). Trois unités tectono-métamorphiques peuvent distinguées au sein du SAD : (1) des unités à haut grade métamorphique

(HP-BT et HP-HT) comprenant notamment les schistes bleus de l'île de Groix enregistrant des conditions P-T comprises entre 1.4-1.8 GPa et 500-550°C (Bosse et al. 2002) ; (2) des unités intermédiaires composées de micaschistes au faciès schistes vert à amphibolite (Bossiere 1988; Triboulet et Audren 1988) et (3) des unités de haute température composées de migmatites, de gneiss et de granitoïdes (0.8 GPa et 700-750°C, Jones et Brown 1990). La présence de complexes ophiolitiques (e.g. complexes d'Audierne et de Champtoceaux, Figs. 1.5 et 1.6) et d'unités de HP-BT (e.g. schistes bleus de Vendée et éclogites du Cellier et des Essarts, Figs. 1.5 et 1.6) suggèrent la présence d'une ou plusieurs sutures océaniques et d'au moins une zone de subduction (Ballèvre et al. 2009, 2013, 2014). De plus, un vestige de panneau plongeant (à pendage NE) a été mis en évidence par tomographie sismique sous le CAD (Gumiaux et al. 2004c). Le métamorphisme de HP-BT enregistré est daté à environ 360 Ma (Bosse et al. 2000, 2005), et témoigne d'une subduction continentale. Un épisode d'extension d'âge Carbonifère supérieur, marqué par un métamorphisme barrovien de type HT-MP, suit l'épaississement crustal dans le SAD (Gapais et al. 1993, 2015).

3.2 Le domaine Centre Armoricain (CAD)

Le CAD, qui constitue notre principale zone d'étude, est décrit ci-dessous.

Caractéristiques lithologiques et stratigraphiques. La séquence stratigraphique commence au Néoprotérozoïque, avec une série sédimentaire appelée « Briovérien ». Bien que les âges de dépôts soient particulièrement délicats à déterminer, ils s'étalent de la fin de l'Ediacarien : 635 Ma au début du Cambrien : 540 Ma (Guerrot et al. 1992; Chantraine et al. 1994). Le Briovérien couvre une grande majorité du domaine (Fig 1.6) et est constitué essentiellement d'une épaisse série sédimentaire monotone d'origine détritique terrigène (Chantraine et al. 1983). Cette série est organisée en séquences alternantes, entières ou tronquées, de pélites, de grès, et de conglomérats. Elle est interprétée comme le produit d'érosion de la chaîne cadomienne plus au Nord (Le Corre 1977; Chantraine et al. 1994). Le Cambrien semble absent au sein du CAD, mais a sans doute été plus probablement intégré au Briovérien (Guerrot et al. 1992). L'histoire de la sédimentation paléozoïque débute par le dépôt en discordance d'une série détritique discontinue, la Formation des schistes de Montfort, attribuée à des dépôts associés à des structures extensives de types blocs basculés. Suit un dépôt d'échelle régionale d'alternances de grès et pélites ordoviciennes (majoritairement représenté par la formation appelée « Grès Armoricain » de l'Ordovicien inférieur). La sédimentation marine se poursuit durant le Silurien avec une abondance de sédiments argileux/silteux noirs riches en matière organique (ampélites). La sédimentation marine est continue jusqu'au milieu du Dévonien avec des faciès arénacés puis argilo-calcaires. Elle se caractérise

ensuite durant le Dévonien supérieur par une légère régression (e.g. absence totale de dépôt de cette période dans la région de Laval), par des variations verticales et horizontales rapides avec une érosion locale et par le début de l'individualisation de bassins d'extension plus locale et indépendants (principalement bassins carbonifères de Laval et de Châteaulin) contenant en outre des dépôts carbonatés et continentaux. La sédimentation se restreint finalement à ces bassins, durant tout le Carbonifère.

Plusieurs granitoïdes syn-tectoniques sont localisés le long de la branche nord du SASZ et datés à *ca.* 315 Ma comme par exemple le granite de Lizio (316 ± 1.3 Ma, Tartèse et al. 2011) et le complexe de Pontivy-Rostrenen (310.3 ± 4.7 Ma et 316.7 ± 2.5 Ma, Ballouard et al. 2017). Dans la partie orientale du CAD, l'activité magmatique felsique semble plus réduite que dans sa partie occidentale puisque seuls deux granites affleurent (Fig. 3) : le granite peralumineux du Pertre (340 ± 2 Ma, Cocherie 2007) et le petit granite de Craon (320 Ma, Leutwein 1968). Ce dernier est un monzogranite sub-leucocrate modérément alumineux avec des teneurs relativement élevées en Li, Be et Sn (Chèvremont, 1983) et est situé au cœur d'un district aurifère (Château-Gontier). Vers l'Est, un granite non-affleurant est reconnu au niveau de Nozay, le long de la branche nord du SASZ au nord de Nantes via la présence d'un métamorphisme de contact à andalousite dans les schistes sus-jacents (Le Corre, 1978). A l'instar du NAD, le CAD est marqué par de nombreux réseaux de dykes et sills de dolérites, intrusifs dans toutes les lithologies jusqu'au Dévonien supérieur (Le Gall 1999).

Caractéristiques géométriques et structurales. Le CAD est délimité au sud par la branche nord du SASZ et au nord par le NASZ (Fig. 1.6). La déformation du domaine est principalement d'âge Viséen et contemporaine du jeu dextre le long du SASZ (Gapais et Le Corre 1980; Choukroune et al. 1983; Gumiaux et al. 2004a). Elle se caractérise essentiellement par des plis droits avec des axes subhorizontaux d'orientation N90 à N120°. La flexure et la longueur d'onde de ces plis (d'ordre plurikilométrique) sont contrôlées par la formation du « Grès Armoricain » (Gumiaux et al. 2004a; Le Corre 1978; Le Corre et al. 1991). Une schistosité de plan axial est associée à ces plis et les marqueurs de la déformation (les clastes dans les conglomérats par exemple) indiquent une linéation d'étirement subhorizontale et parallèle à l'axe de ces plis (Le Théoff 1977; Le Corre 1978). Une augmentation de l'intensité de la déformation est observée vers le Sud à proximité de la branche nord du CSA (Gapais et Le Corre 1980). Les plis droits sont également accompagnés d'une fracturation en système de petits décrochements dextres orientés N150-N160° avec un décalage horizontal atteignant parfois 1000 m, et en système de décrochements sénestres orientés N20-30° avec un décalage horizontal moindre de 100 à 200 m

(Herrouin et al. 1989). A l'échelle crustale et régionale, un modèle de déformation du CAD a été proposé à partir d'une analyse géostatistique des données de direction de schistosité et d'une modélisation cinématique de la déformation finie (Gumiaux et al. 2004a, 2004b; Fig. 1.7). Dans ce modèle de cisaillement simple régional, la globalité du CAD est affectée par un cisaillement dextre orienté N123°E compatible avec les rotations des axes de plis, de la schistosité et de grandes structures héritées (e.g. Montagnes Noires ou branche Nord du CSA). Ces structures héritées de l'orogenèse cadomienne (e.g. Montagnes Noires) ou de l'extension ordovicienne (e.g. branche nord du SASZ; Gumiaux et al. 2004b) jouent également un rôle important au cours de la déformation régionale en facilitant la localisation de la déformation (Gumiaux et al. 2004b).

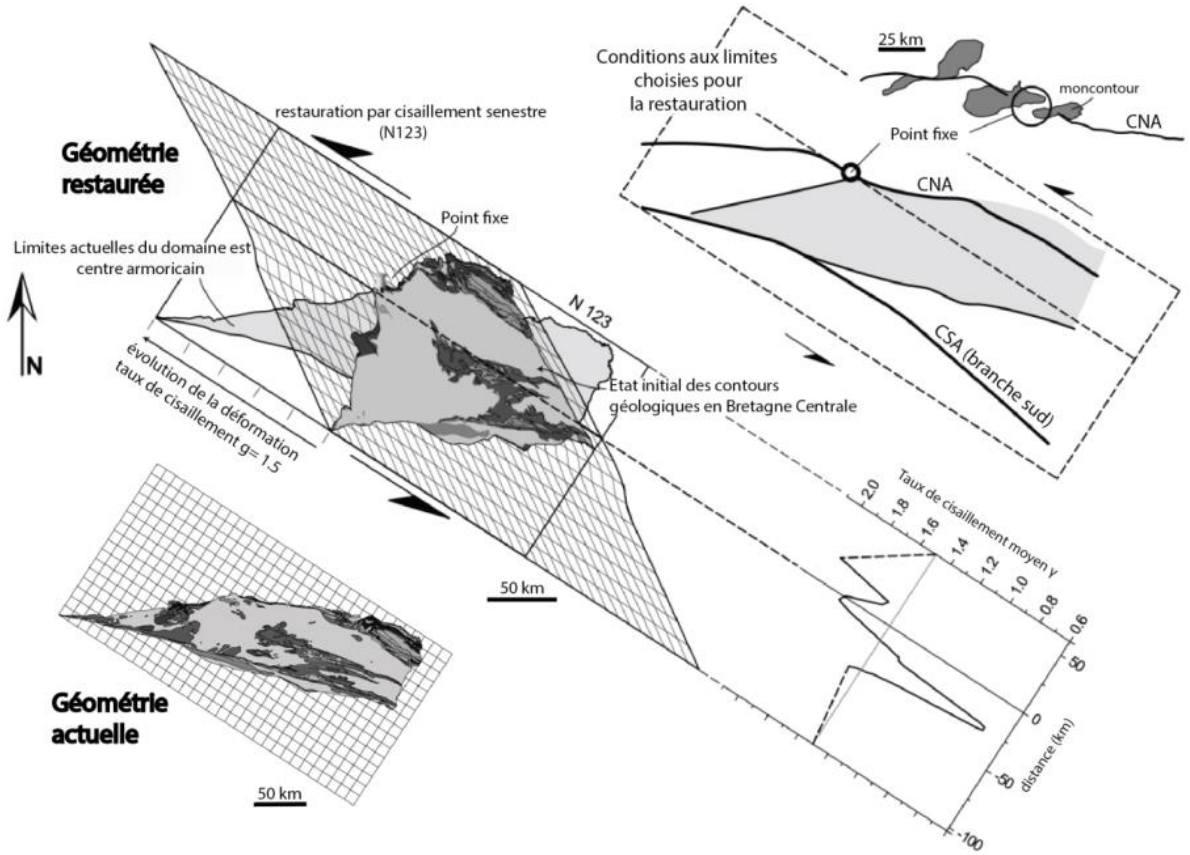

Figure 1.7 Restauration de la déformation de la partie orientale du CAD par un cisaillement simple senestre orienté N123° (modifié d'après Gumiaux et al. 2004a).

3.3 Minéralisations Sb-Au du Massif Armoricain

Au sein du Massif Armoricain, de nombreux indices et gisements Sb-Au sont connus et principalement répartis dans quatre districts principaux (Chauris et Marcoux 1994 ; Gloaguen et al 2016a) : le district de la Lucette (42 kt de Sb et 8.2 t de Au extraits, Guiollard 2009; Moyroud et al. 1979; Serment 1978), le district vendéen (18,8 kt de Sb extraits et ~ 11 kt de réserves estimées, Blouin 1991; BRGM 1988; Marcoux et al. 1984; Moyroud et al. 1979), le district du Semnon-La Coëfferie (500 t de Sb et ~ 45 kt de réserves estimées, BRGM 1987; Chauris et al. 1985; Gloaguen

et al. 2016b; Moyroud et al. 1979), et le district de Quimper-Cap Sizun (890 t de Sb et ~ 5.2 kt de réserves estimées, BRGM 1990; Fouquet 1980; Gorichon et Kerjean 1979; Moyroud et al. 1979). Les deux plus gros districts en termes de ressources et de réserves en Sb sont localisés dans le CAD (Fig. 1.6). Il existe également deux districts Au de dimensions moindres, également localisés dans le CAD, qui sont les districts de Pontivy-Loudéac et de Château-Gontier (Fig. 1.6) et qui ont seulement été exploités à l'époque gallo-romaine (Vasquez-Lopez et al. 1985a, 1985b). Les minéralisations Sb armoricaines se trouvent principalement au sein de structures filoniennes bien qu'il existe une occurrence unique et stratiforme au sein du Massif Armoricain: le petit gisement (1000 t) de Rosnoën situé dans le bassin de Châteaulin. Le district de la Lucette est localisé au sein du bassin de Laval et est majoritairement représenté par un seul gisement de classe mondiale, la mine éponyme de la Lucette (Laznicka 2010). Ce gisement est constitué d'un essaim de filons centimétrique à pluri-métrique orientés N30°E, localisé au cœur d'un anticlinal orienté N120°E, et encaissé au sein de grès et métapélites ordoviciens à siluriens (Chauris and Marcoux 1994; Serment 1978). Les veines quartzo-carbonatées contiennent principalement de la stibine, de l'arsénopyrite, de la pyrite, de l'or natif et de nombreux sulfosels. Le district de Vendée est constitué d'une vingtaine de filons de taille et d'extension variable exploité jusqu'en 1992 (e.g. mine des Brouzils). La minéralisation est majoritairement constituée de stibine et de quartz en remplissage de fentes de tensions et de failles, encaissés au sein de schistes Briovérien à Cambrien (Marcoux et al. 1984). Le district du Semnon-La Coëfferie est caractérisé par une minéralisation à berthiérite, stibine et or natif dans des veines quartzo-carbonatées encaissés au contact entre des dykes de dolérites et des schistes Ordovicien inférieur (Chauris et al. 1985). Ce district fait l'objet de 3 articles publiés et soumis dans ce présent manuscrit, et sera détaillé et discuté de nombreuses fois dans les parties suivantes. Enfin, le district de Quimper-Cap Sizun est le seul district situé dans la partie occidentale du Massif Armoricain. Il consiste en des veines de quartz et de stibine, avec localement des sulfosels, encaissées au sein de granitoïdes Ordovicien et Carbonifères (Fouquet 1980). Les minéralisations sont spatialement proches de zones de cisaillements majeurs (Chauris et al. 1977; Chauris et Marcoux 1994). Une position externe des filons à stibine par rapport aux granites varisques a été suggérée dans le district de Quimper-Cap Sizun (Chauris et Guigues 1969; Fouquet 1980; Chauris et Marcoux 1994) ainsi qu'un lien avec le volcanisme cambro-trémadocien dans le district vendéen (Marcoux et al. 1984). Ceci peut suggérer une pré-concentration de l'antimoine anté-varisque ainsi qu'une remobilisation par les évènements magmatiques et hydrothermaux tardi-varisques (Chauris et Marcoux 1994). De plus, Chauris (1977) et Chauris et Marcoux (1994) évoquent une forte concentration des indices à Sb à l'est du Massif Armoricain. Cette dissymétrie pourrait être liée à un niveau d'érosion moins prononcé à l'est qu'à l'ouest (e.g. Fouquet 1980). L'érosion serait alors responsable de la rareté des gisements d'antimoine à l'ouest (Chauris et

Marcoux 1994). Les principales caractéristiques de tous les indices antimonifères du Massif Armoricain ainsi que leur localisation sont référencées au sein de l'Annexe 1 à la fin de ce manuscrit.

Partie 2

Analyse spatiale : réexamen des facteurs géologiques contrôlant la localisation des gisements à Sb-Au

Résumé en français de l'article #1

Le Massif Armoricain était l'un des plus grands producteurs mondiaux de l'antimoine au début du 20ème siècle. Cependant, les facteurs géologiques qui contrôlent la localisation de ces gisements à travers le Massif Armoricain restent, aujourd'hui, encore mal contraints. Dans cet article, nous présentons des données de terrain au sein de notre cas d'étude, le district à or-antimoine du Semnon, et nous avons effectué une analyse statistique spatiale en utilisant un logiciel de Système d'Information Géographique, des données géologiques et cartographiques ainsi que des données géophysiques. L'analyse spatiale montre que les gisements d'antimoine sont spatialement corrélés avec des zones à forte densité et relativement magnétiques. Cela pourrait indiquer la présence de corps mafique à ultra-mafique en profondeur, ce qui est suggéré par les nombreuses occurrences de dykes et sills doléritiques à travers la région. La future prospection minière pour l'antimoine devrait se focaliser sur ces zones denses et magnétiques qui couvrent environ 18 % de la surface du Massif Armoricain. Les liens entre les gisements d'antimoine et les intrusions mafiques ont déjà été reconnu ailleurs dans la chaine varisque ouest-européenne, ce qui pourrait être un métallotecte dans la prospection de l'antimoine au sein d'orogènes.

Antimony deposits in the Variscan Armorican belt, a link with mafic intrusives?

Anthony Pochon[1], Denis Gapais[1], Eric Gloaguen[2, 3], Charles Gumiaux[2, 3], Yannick Branquet[1, 2, 3], Florence Cagnard[2, 3], Guillaume Martelet[2, 3]

[1] *Géosciences Rennes, UMR 6118, Université de Rennes 1, Campus de Beaulieu, 35042 Rennes Cedex*

[2] *Institut des Sciences de la Terre d'Orléans, UMR 7327, Université d'Orléans, Campus Géosciences, 1A rue de la Férollerie, 45071 Orléans Cedex 2*

[3] *Bureau de Recherche Géologique et Minière (BRGM), UMR 7327, 3 avenue Claude-Guillemin, BP 36009, 45060 Orléans Cedex 02*

Publié à *Terra Nova*, vol. 28, pp 138-145 (2016)

Terra Nova

doi: 10.1111/ter.12201

Antimony deposits in the Variscan Armorican belt, a link with mafic intrusives?

Anthony Pochon,[1] Denis Gapais,[1] Eric Gloaguen,[2,3] Charles Gumiaux,[2,3] Yannick Branquet,[1,2,3] Florence Cagnard[2,3] and Guillaume Martelet[2,3]

[1]*Géosciences Rennes, UMR 6118, Université de Rennes 1, Campus de Beaulieu, Rennes Cedex 35042, France;* [2]*Institut des Sciences de la Terre d'Orléans, UMR 7327, Université d'Orléans, Campus Géosciences, 1A rue de la Férollerie, Orléans Cedex 2 45071, France;* [3]*Bureau de Recherche Géologique et Minière (BRGM), UMR 7327, 3 avenue Claude-Guillemin, BP 36009, Orléans Cedex 02 45060, France*

ABSTRACT

The Variscan Armorican belt was the World leading producer of antimony at the beginning of the twentieth century. However, geological controls on the deposits remain unconstrained. Here, we illustrate the field setting of mineralisations and perform a statistical analysis using Geographical Information System software, geophysical and geological data. The analysis shows that Sb deposits are spatially correlated with high-density and magnetic zones. This may reflect the presence of mafic/ultramafic bodies at depth – a suggestion that is further supported by numerous occurrences of doleritic dykes throughout the region. Future antimony prospecting should focus on the high-density and high-magnetic zones which comprise about 18% of the Armorican massif. Links between Sb deposits and mafic intrusions are recognised elsewhere in the West European Variscan belt, emphasising that these may be key for antimony prospecting in deformation belts.

Terra Nova, 28: 138–145, 2016

Introduction

Antimony is considered to be a critical metal by the European commission (2010) and is classically associated with other metals such as gold or mercury. Antimony occurrences are widespread throughout the European Variscan belt (e.g. French Massif Central, Périchaud, 1980; Cornwall, Stanley *et al*., 1990; Ossa Morena, Tornos *et al*., 2005).

The Armorican Massif (western France) constitutes the most important past (61 kt of Sb extracted) and present (>32 kt) resource of antimony known in the French Variscan belt. It was the world leading producer of Sb at the beginning of the twentieth century (La Lucette mine, 42 kt Sb metal, Fig. 1; Guiollard, 2009; Laznicka, 2010) and has been subject to a recent relaunching of mining exploration.

Sb deposits are hosted by late Proterozoic to Palaeozoic lithologies and are related to a large-scale late Variscan hydrothermal mineralising event (Marcoux *et al*., 1984, 1988; Munoz *et al*., 1992; Chauris and Marcoux, 1994; Bouchot *et al*., 2005). In spite of numerous studies, the mineralisation history remains unconstrained. To date, hypotheses for sources and reworking of antimony have invoked magmatic events ranging from Cambrian to Variscan in age, late Variscan hydrothermalism and the activity of Variscan shear zones (Chauris and Marcoux 1994 and references therein).

Here, we reappraise the geological environment of mineralisation using (i) a field example in the Le Semnon district, the only ancient Sb mining zone that crops out in Central Brittany, and (ii) a regional-scale statistical approach using a Geographical Information System and geophysical and mapping data. Our results reveal useful first-order geological and geophysical features related to mineralisation, provide tools to locate zones of high potential for mining exploration and better constrain their geological significance (Bonham-Carter, 2002; Cassard *et al*., 2008; Carranza, 2009; Deveaud *et al*., 2013).

Correspondence: Anthony Pochon, Géosciences Rennes, UMR 6118, Université de Rennes 1, Campus de Beaulieu, Rennes 35042, France. Tel.: +33(6)28200871; e-mail: anthony.pochon@univ-rennes1.fr

Geological setting

The Armorican Massif

The Armorican Massif is part of the Ibero-Armorican Arc in the Western European Variscan belt. It comprises three main domains with different tectonic and metamorphic histories separated by two major dextral wrench zones, the North and South Armorican Shear Zones (NASZ and SASZ) (Fig. 1).

Deformation in the northern domain (NAD) mainly occurred in the late Neoproterozoic; this domain was part of the upper brittle crust during the Variscan orogeny (Brun *et al*., 2001).

The southern domain (SAD) corresponds to the internal metamorphic zones of the belt (Ballèvre *et al*., 2013). It is marked by late-Devonian to Carboniferous crustal thickening and by late-Carboniferous extension, which was accompanied by numerous intrusions of leucogranites coeval with strike-slip along the SASZ (Gapais *et al*., 2015 and references therein).

The central domain (CAD), where mineralisation is widespread, consists mainly of Late Neoproterozoic to upper Palaeozoic sediments affected by greenschist facies metamorphism. During the Variscan orogeny, the CAD underwent N120–125-striking dextral wrenching that produced upright folds with E–W sub-horizontal axes and sub-vertical axial planes (Gapais and Le Corre, 1980; Gumiaux *et al*., 2004). Folds are associated with a sub-vertical slaty cleavage bearing a sub-horizontal stretching lineation.

© 2016 John Wiley & Sons Ltd

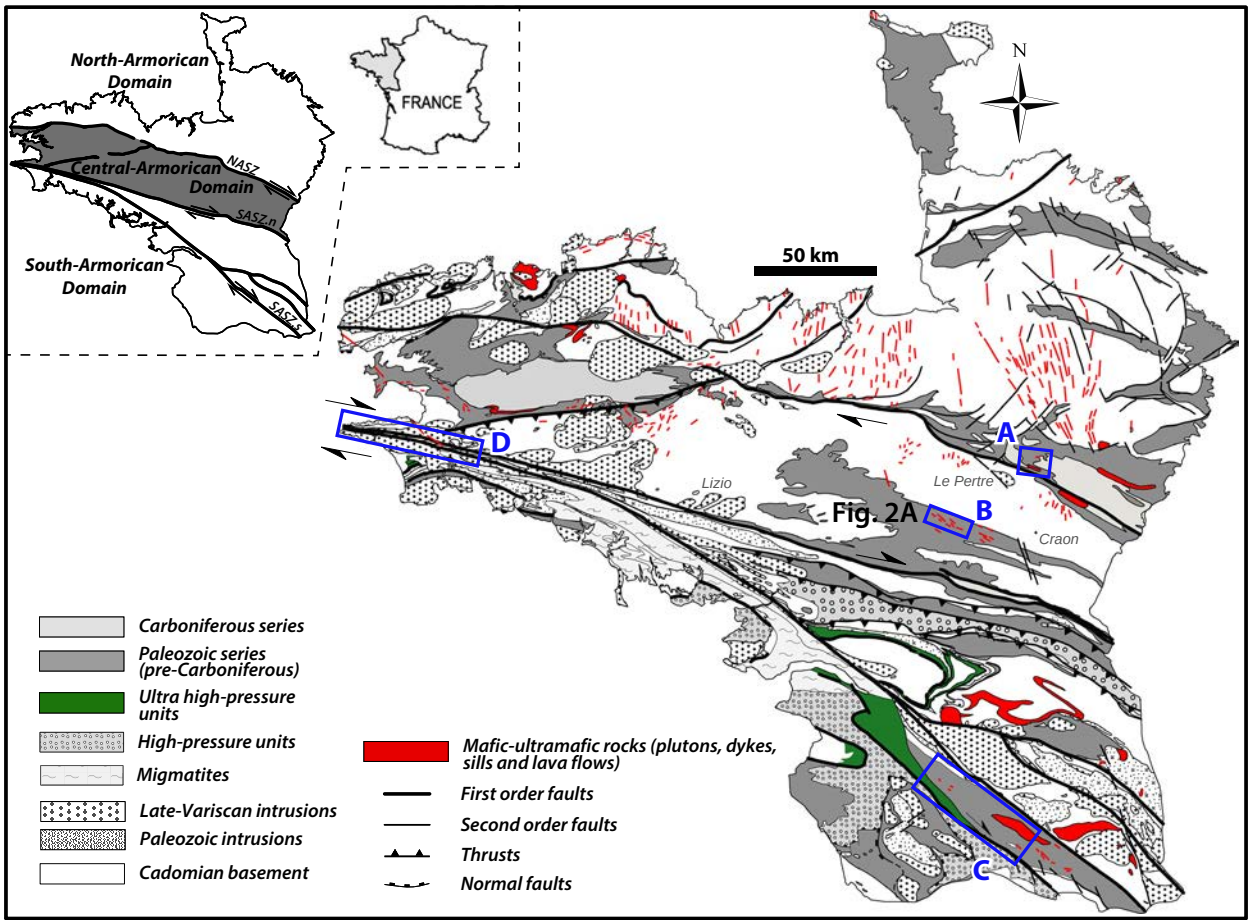

Fig. 1 Simplified geological map of the Armorican Massif; the main domains are indicated within the upper left corner inset (modified after Chantraine *et al.*, 1996). A = La Lucette district, B = Le Semnon district, C = Vendée district and D = Quimper-Cap Sizun district.

The NAD and CAD are marked by widespread swarms of doleritic dykes and sills (Fig. 1). Some scarce granitic intrusions also occur in the CAD (Fig. 1). Poorly constrained dates exist for the granitic bodies of the CAD: Craon (320 Ma, Rb–Sr; Leutwein *et al.*, 1968); Le Pertre (377.6 ± 9.2 Ma, Pb–Pb evaporation on zircons, Trautmann *et al.*, 2002; 343 ±3 Ma, U–Pb on zircons and 387 ± 13 Ma, U–Th–Pb on monazites; Vernhet *et al.*, 2009); Lizio (316 ± 6 Ma, U–Pb on zircons, Tartèse *et al.*, 2011). The ages of the dolerites are also poorly constrained. Lower Carboniferous ages have been reported (K–Ar dates of 330 ± 10 Ma and palaeomagnetic interpretations; Perroud *et al.*, 1986). On the other hand, because post-Devonian dykes are not observed, an emplacement age around 360 Ma has been suggested (Le Gall, 1999).

Sb mineralisation

In the Armorican belt, antimony occurrences consist mainly of stibnite-bearing quartz lodes. Sb was mined in four districts (Chauris and Marcoux, 1994) (Fig. 1): La Lucette (42 kt), Le Semnon (~15.4 kt), Vendée (~28 kt) and Quimper-Cap Sizun (~3.89 kt).

The Le Semnon district is characterised by berthierite–stibnite–arsenopyrite and gold-bearing quartz–carbonate veins (Chauris *et al.*, 1985), which are hosted by dolerite dykes within metapelites of lower Ordovician age.

The La Lucette deposit consists of a swarm of metre-thick, N030°E-trending quartz–carbonate veins hosted by Ordovician to upper Silurian metapelites and sandstones (Chauris and Marcoux, 1994). The paragenesis mainly consists of stibnite, arsenopyrite and native gold. The geological map shows doleritic dykes around the district (Le Gall *et al.*, 2011). Furthermore, Œhlert *et al.* (1906) report close relationships between mafic dykes and mineralisations, and a mining shaft near La Lucette has cut across a mafic dyke (Le Gall *et al.*, 2011).

The Vendée district, where more than 20 lodes were recognised and mined up to 1992, shows mineralisation marked by stibnite and quartz that fills tension gashes and shear fractures mainly hosted by Cambrian and Brioverian slates (Marcoux *et al.*, 1984).

The Quimper-Cap Sizun district is the only one located in the western part of the Armorican Massif. There,

© 2016 John Wiley & Sons Ltd

Sb deposits consist of stibnite-bearing quartz veins with locally Sb-sulfosalts, hosted by Ordovician and Variscan granitoids.

Many Sb deposits are located in the vicinity of shear zones (Chauris, 1977; Chauris and Marcoux, 1994). Various hypotheses have been proposed for their genesis, including granitic sources (Chauris and Marcoux, 1994), or a link with late Cambrian to early Ordovician volcanism (Marcoux *et al.*, 1984). This latter hypothesis suggests that antimony was pre-concentrated before the Variscan orogeny and remobilised during late-Variscan magmatic and hydrothermal events.

A field example: the Le Semnon district

The Le Semnon district (Figs 1 and 2) is well suited for examining relationships between mineralisation and geological structures, because it is the only area where outcropping Sb was exploited. There, excellent outcrops highlight the relationships between Sb-bearing veins and the country rocks. In this district, as well as in the La Lucette district, antimony is associated with gold (Bouchot *et al.*, 1997).

The area contains doleritic dykes up to 20–25 m thick (Fig. 2A,B). They strike NW–SE and are steeply dipping. They are mainly intrusive within lower Ordovician slates (Fig. 2B). In map view, the dykes are spatially associated with mineralisations (Fig. 2A). In the field, quartz–carbonate veins containing berthierite–stibnite–arsenopyrite± gold cut across dolerites affected by an overall E–W trending sub-vertical cleavage (Fig. 2C) and contain fragments of hydrothermalised dolerite (Chauris *et al.*, 1985). The location of Sb-bearing quartz veins within dolerite dykes may be related to the rheological contrast between competent intrusives and weaker country rocks. However, other extensively faulted competent layers in the area (Armorican quartzite or middle Ordovician sandstones) do not contain Sb-bearing veins. Geological maps of other districts also suggest links between mineralisation and mafic intrusives (Le Gall *et al.*, 2011).

Spatial statistical analysis

We used statistical analyses to quantify spatial relationships between Sb deposits, gravimetric and magnetic anomalies, and geological structures. We also compared the distribution of geophysical anomalies near deposits with that of the Armorican Massif

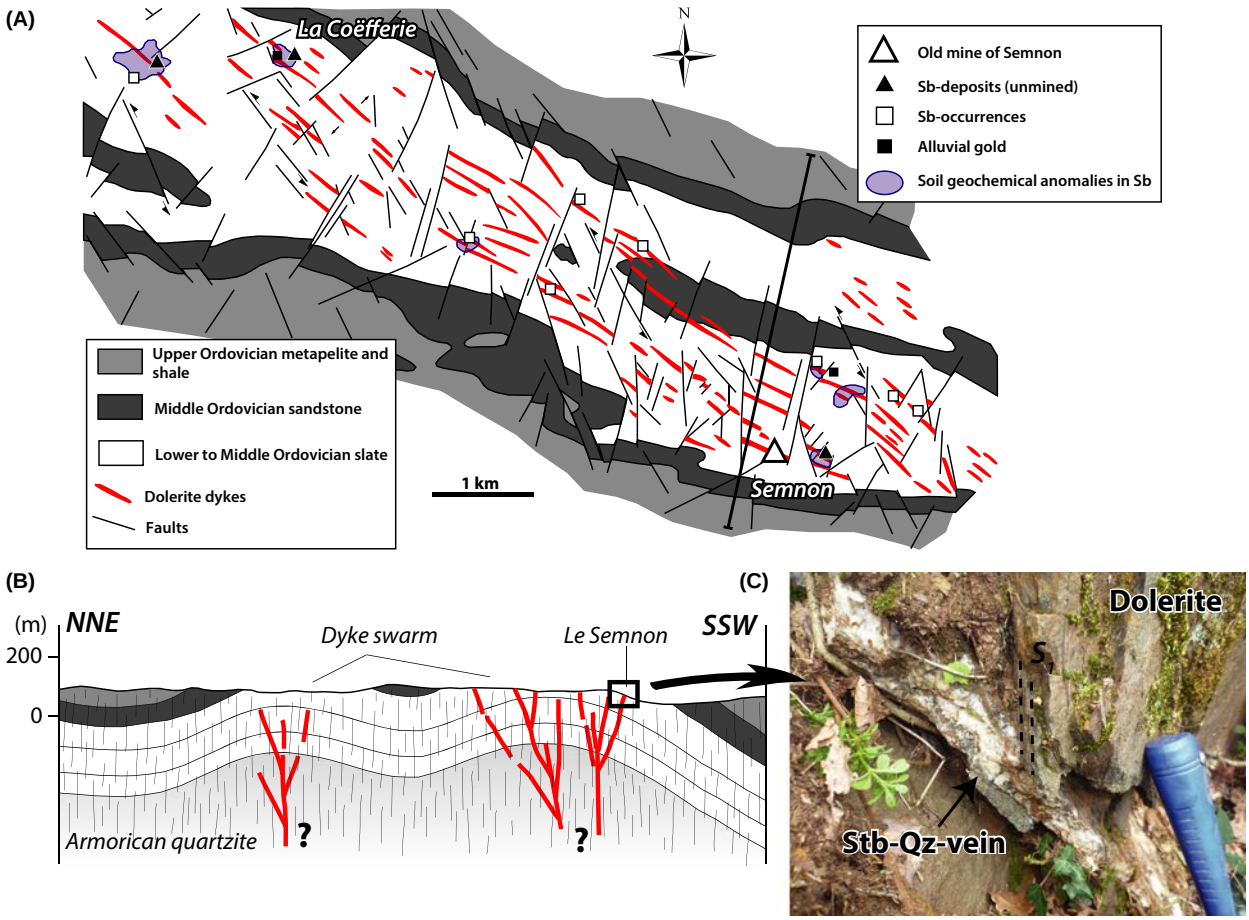

Fig. 2 (A) Detailed map of the Le Semnon district with the locations of old mines and Sb occurrences (modified after Chauris *et al.*, 1985). (B) Cross-section through the Le Semnon district. (C) An altered stibnite-bearing quartz vein crosscutting a dolerite dyke with a slight cleavage in the hangingwall.

© 2016 John Wiley & Sons Ltd

considered as a regional reference (see methodology in Deveaud *et al.*, 2013).

Statistical analysis of geophysical data

The data we used are (i) gravity data from the "Banque Gravimétrique de la France" (Martelet *et al.*, 2009), including the Bouguer anomaly and its vertical gradient continued upward to 2.5 km (with a mesh grid of 1 × 1 km) covering a 62101 km² area, (ii) an airborne magnetic anomaly reduced to the pole with a mesh grid of 1 × 1 km (sub-sampled from a high-resolution survey; Bonijoly *et al.*, 1999; Truffert *et al.*, 2001) covering a 54 461 km² area and (iii) mining databases (ProMine Mineral Deposit Database, Cassard *et al.*, 2015, complemented by BRGM unpublished data on other minor occurrences).

For the magnetic and gravity dataset, the frequency distribution of the anomaly value at Sb occurrence locations (Fig. 3, dark) was compared with the respective overall anomaly map (Fig. 3, light grey). The Bouguer anomaly displays high frequency values for the range]−6.077 – 1.784] mGal (Fig. 3A). This range represents 37% of the Armorican gravity cover and contains 60% of the Sb deposits. The frequency distribution of the vertical gradient of the Bouguer anomaly displays higher values for Sb locations than for the entire map (see the shift in the histogram, Fig. 3A). This range of]0.000527–0.001818] mGal m^{-1} covers only 18% of the Armorican gravity cover but contains 50% of the Sb deposits. The frequency distribution of the magnetic field values shows anomalously high values for the range]8.4681–108.6458] nT (Fig. 3B). This range contains 49% of the Sb occurrences and covers 28% of the aeromagnetic survey.

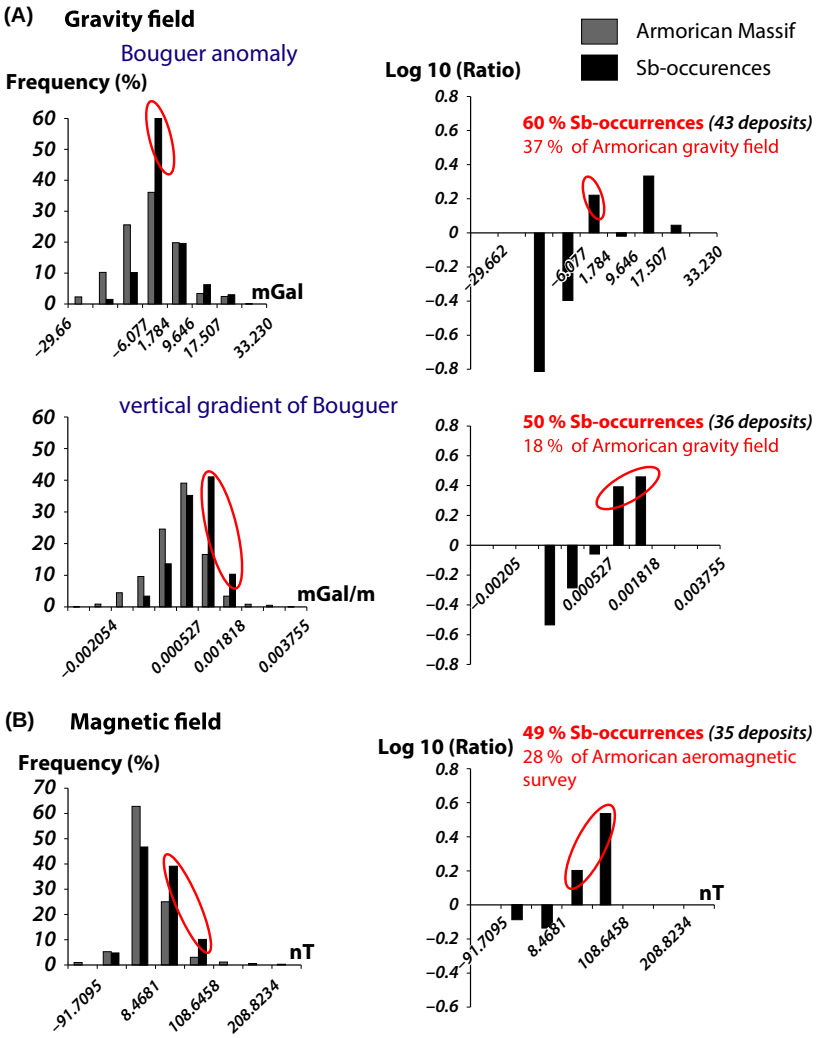

Fig. 3 Frequency distributions of (A) gravity anomaly data and (B) magnetic anomaly data. The histograms on the left-hand-side show the relative frequency values for Sb occurrences (dark) and those for the corresponding overall geophysical grid map (light grey). The distribution of the anomalies is further highlighted in the Log 10 histograms (right-hand side). The total coverage of the geophysical anomaly maps is 62 101 km² for the gravity data (A) and 54 461 km² for the magnetic data (B). 72 Sb occurrences were used in the statistical analysis.

Analysis of the Sb spatial distribution

Zones corresponding to the high frequency contrasts identified above are delineated on Figure 4 as high-density (HDZ) and high-magnetic (HMZ) zones. The map underlines the spatial links between these zones and Sb occurrences. However, HDZ and HMZ relate to different types of objects, such as outcropping eclogites (Champtoceaux and Essarts areas) and mafic intrusions (e.g. Trégor area), and non-outcropping geophysical bodies (e.g. Le Semnon area).

A spatial analysis was further performed to examine the spatial relationships between Sb deposits and several objects, such as major faults, granitoids, mafic intrusives, and HDZ and HMZ. The frequency distribution of the measured shortest distance between deposits and relevant objects was compared with that of a reference set of points representing "any given location" in the study area. For the reference set, calculations were done using two different techniques to avoid any bias: (i) points were defined as nodes of a regular 500 m spaced grid covering the entire study area, and (ii) points were randomly distributed; this was performed through 10 computing runs to have a minimum–maximum possible envelope for the reference frequency values. The results show a close spatial relationship between HDZ, HMZ and Sb-deposit locations.

© 2016 John Wiley & Sons Ltd

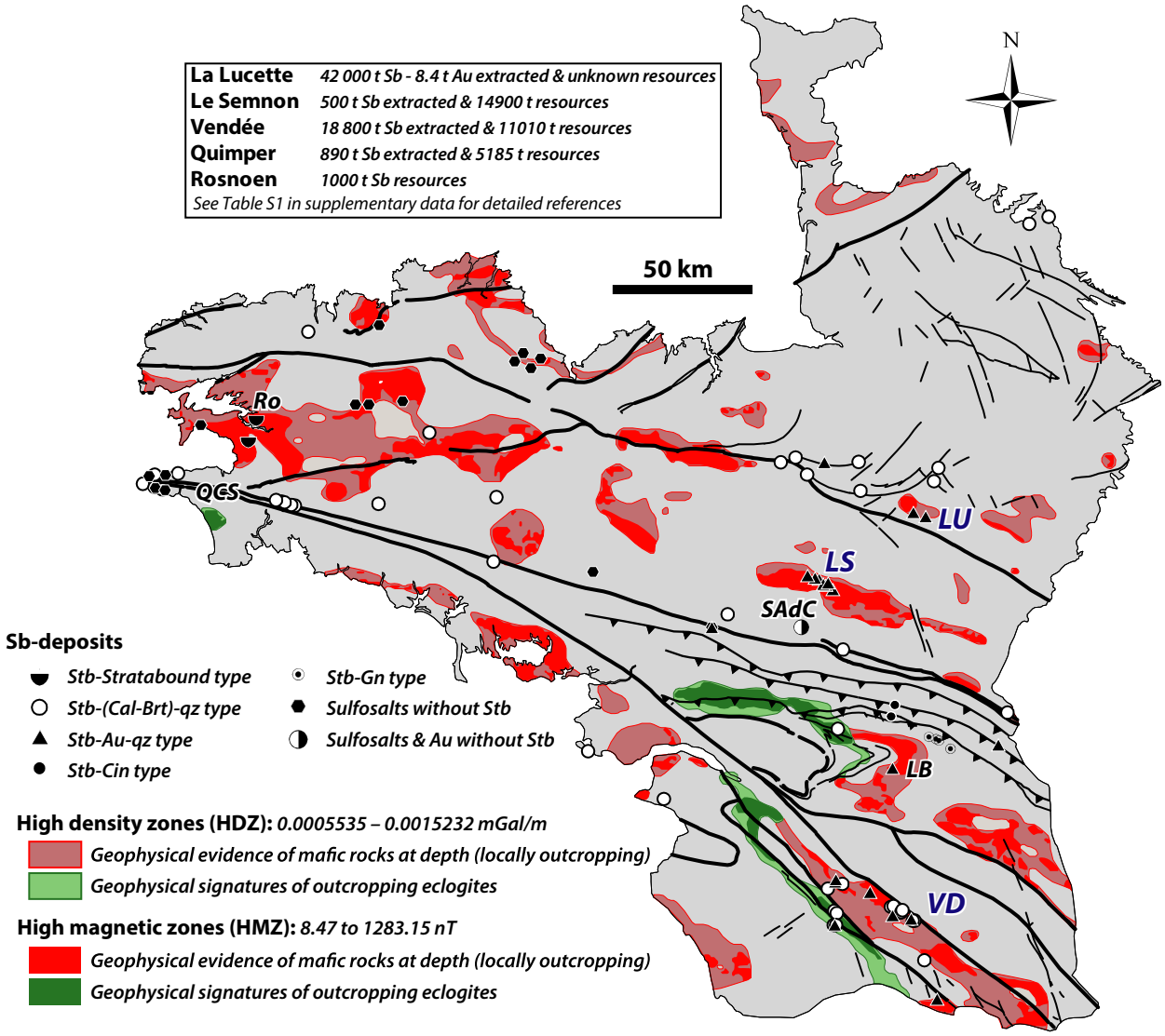

Fig. 4 Map displaying the spatial relationships between Sb deposits and high-density and high-magnetic zones throughout the Armorican massif. HMZ have the same range of gravimetric values as HDZ. Sulfosalts-bearing mineralisations are shown on the map but they were not considered in the statistical analysis. The insert shows productions and reserve estimates for the main Sb districts (see Table S1 for detailed references). LU, La Lucette district; LS, Le Semnon district; VD, Vendée district; QCS, Quimper-Cap Sizun district; Ro, Rosnoën deposit; SAdC, Saint-Aubin-des-Châteaux deposit; LB, La Bellière deposit; Stb, stibnite; Cal, calcite; Brt, barite; Au, gold; Cin, cinnabar; Gn, galena.

Thus, cumulative frequency distributions for short distances (0–5 km) show higher values for the deposits than for the reference datasets. Approximately 50% of the Sb deposits are located less than 2 km from a HMZ, whereas only 20–30% of the various reference points are less than 2 km from these zones (Fig. 5A,B). A close spatial link is also observed between outcropping mafic intrusions and Sb deposits, with distinct cumulative frequency distributions (Fig. 5C): 80% of the mineralisations are located within less than 5 km of mafic rocks. In contrast, Sb deposits do not show a strong spatial link with granitic intrusions (Fig. 5D). The analysis also confirms links between Sb deposits and major faults, although these links do not look strong for very short distances (Fig. 5E).

Discussion

When comparing anomalous geophysical zones with Sb-deposit locations (Fig. 4), we found that three of the four main antimony districts are localised within HMZ. The small Quimper-Cap Sizun district is not localised near a HDZ/HMZ but it is the only one strictly located along the SASZ. Statistics show that 99% of the known antimony resources in the Armorican Massif are localised above HMZ. Furthermore, the deposit of Rosnoën (Stb-Stratabound type) is located above the wider HMZ and has potential antimony reserves of at least 1000 t (Table S1).

© 2016 John Wiley & Sons Ltd

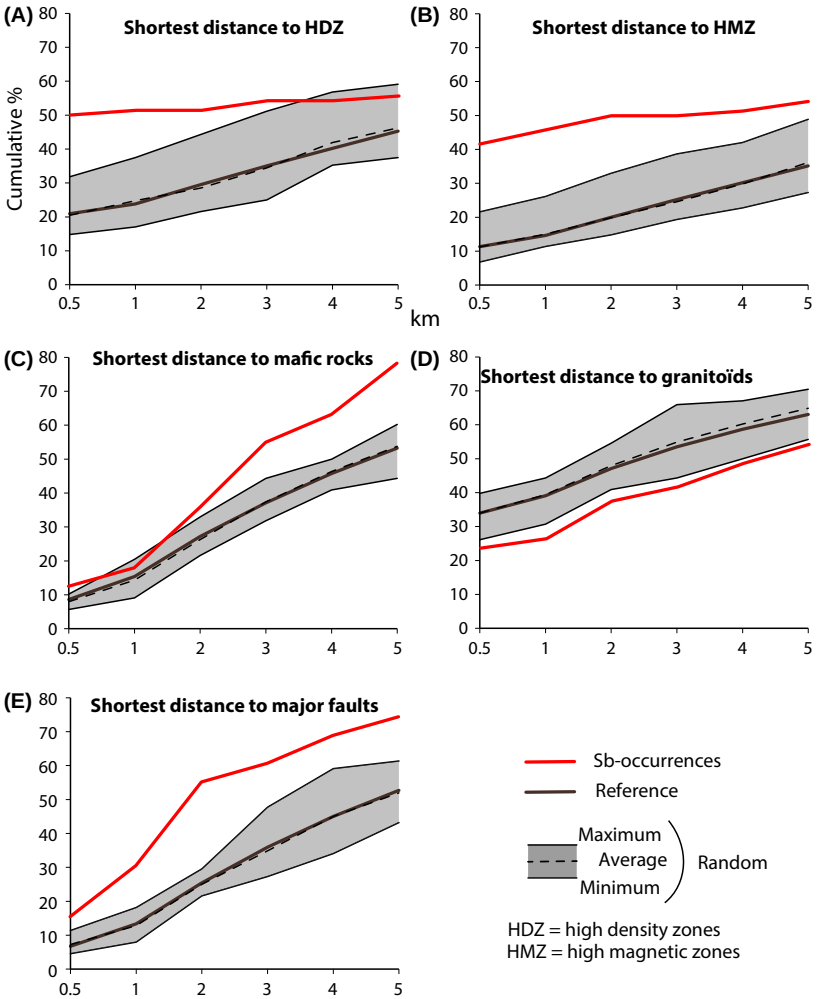

Fig. 5 Spatial proximity analyses calculated from the locations of Sb deposits, random sets of points (ten random layers), all map points and: (A) the shortest distance to high-density gravimetric zones (HDZ), (B) the shortest distance to high-density magnetic zones (HMZ), (C) the shortest distance to mafic rocks, (D) the shortest distance to granitoids, and (E) the shortest distance to major faults.

Mafic/ultramafic rocks or iron-mineral deposits (such as pyrrhotite-bearing VMS) are good candidates to account for the geophysical anomalies observed in the belt. Scarce pyrrhotite-bearing VMS are known in the Armorican Massif. Palaeozoic oolitic ironstones are also known in the region, and are associated with Sb mineralisation with sulfosalts (e.g. Saint-Aubin-des-Châteaux area, Gloaguen *et al.*, 2007). However, magnetic anomalies corresponding to such candidates appear to be too narrow, and the associated sources are not deep enough, to generate the observed geophysical signals linked to Sb deposits. Furthermore, they are quite poorly associated with the particular gravimetric anomalies highlighted in this study that combine high density with high-magnetic values (Fig. 4). The HDZ/HMZ anomalies outlined here are therefore more likely to be related to concentrations of mafic dykes and to their magmatic source at depth, as argued in the NAD (Aïfa and Lefort, 2001).

Field evidence and statistical analyses definitely suggest strong links between mineralisations and mafic/ultramafic intrusions. Sb mineralisations in the Le Semnon district are hosted by dolerite dykes (Fig. 2). In the La Lucette district, they are hosted by Upper Silurian black shales intruded by dolerites. Such spatial links between mafic rocks and Sb–Au mineralisation have already been reported in the French Massif Central (Périchaud, 1980; Floc'h *et al.*, 1984), the Ossa Morena Zone in Spain (Tornos *et al.*, 2005), the Mid-European Saxothuringian Zone (Dill, 1985) and the Loddiswell gold–antimony prospect in Devon, UK (Stanley *et al.*, 1990).

Genetic relationships between mafic bodies and mineralisation remain to be further examined. Sb-rich zones are spatially correlated with HDZ and HMZ but post-date the doleritic intrusions (Fig. 2C). However, the spatial correlation implies that mafic bodies have played a role in the history of antimony mineralisation. The presently unknown time gap between mafic intrusion and mineralisation may reflect magmatism-induced Sb pre-concentration, which is later reworked by hydrothermal events (Marcoux *et al.*, 1984). The age of the magmatic event is currently only constrained at ca. 360 Ma by field observations (Le Gall, 1999). Additional studies of the geochemistry and geochronology of the dolerites may better constrain their source at depth.

Concluding remarks

- There is a strong geometrical link between Sb occurrences and high-density and high-magnetic zones. Local correlations occur with mafic rocks, a feature also reported in other parts of the west European Variscan belt.
- 99% of known antimony resources are located within these geophysical anomalies. These zones cover about 18% of the Armorican Massif, which limits potential research areas for antimony prospecting.
- The best candidates to account for the outcropping doleritic intrusions and for the observed combined density and magnetic anomalies are mafic/ultramafic bodies at depth.
- Our results imply that mafic bodies have played some role in the subsequent evolution of antimony mineralisation in the Armorican Variscan belt. The importance of

© 2016 John Wiley & Sons Ltd

later hydrothermalism remains to be studied.
- Our results provide a new frame for exploration strategies of antimony–gold mineralisations in the Variscan belt of Western Europe.

Acknowledgements

This research was carried out in the frame of A.P.'s PhD Thesis. It was supported by the "Région Bretagne", the BRGM, the CNRS-INSU, and the OSUR. The reviewers and Editor are acknowledged for their constructive remarks.

References

Aïfa, T. and Lefort, J.P., 2001. Relationship between dip and magma flow in the Saint-Malo dolerite dyke swarm (Brittany, France). *Tectonophysics*, **331**, 169–180.

Ballèvre, M., Bosse, V., Dabard, M.-P., Ducassou, C., Fourcade, S., Paquette, J.-L., Peucat, J.-J. and Pitra, P., 2013. Histoire géologique du Massif armoricain : actualité de la recherche. *Bull. Soc. Géol. Minéral. Bretagne*, **10–11**, 5–96.

Bonham-Carter, G.F., 2002. *Geographic Information System From Geoscientists: Modeling With GIS*. Pergamon, Oxford.

Bonijoly, D., Perrin, J., Truffert, C. and Asfirane, F., 1999. Couverture géophysique aéroportée du Massif Armoricain. Magnétisme et radiométrie spectrale. Public BRGM report, RR-40471-FR, BRGM, Orléans, 75 pp.

Bouchot, V., Milési, J.-P., Lescuyer, J.-L. and Ledru, P., 1997. Les minéralisations aurifères de la France dans leur cadre géologique autour de 300 Ma. *Chron. Min. Rech. Min.*, **528**, 13–62.

Bouchot, V., Ledru, P., Lerouge, C., Lescuyer, J.L. and Milesi, J.P., 2005. 5: Late Variscan mineralizing systems related to orogenic processes: the French Massif Central. *Ore Geol. Rev.*, **27**, 169–197.

Brun, J.-P., Guennoc, P., Truffert, C. and Vairon, J., 2001. Cadomian tectonics in northern Brittany: a contribution of 3-D crustal-scale modelling. *Tectonophysics*, **331**, 229–246.

Carranza, E.J.M., 2009. Controls on mineral deposit occurrence inferred from analysis of their spatial pattern and spatial association with geological features. *Ore Geol. Rev.*, **35**, 383–400.

Cassard, D., Billa, M., Lambert, A., Picot, J.C., Husson, Y., Lassere, J.L. and Delor, C., 2008. Gold prospectivity mapping in French Guiana using an expert-guided data-driven approach based on a regional-scale GIS. *Ore Geol. Rev.*, **34**, 471–500.

Cassard, D., Bertrand, G., Billa, M., Serrano, J.J., Tourlière, B., Angel, J.M. and Gaál, G., 2015. ProMine Mineral Databases: new tools to assess primary and secondary mineral resources in Europe. In: *3D, 4D and Predictive Modelling of Major Mineral Belts in Europe, Mineral Resources Reviews* (P. Weihed, ed), pp. 9–58. Springer International Publishing, Switzerland.

Chantraine, J., Autran, A. and Cavelier, C. 1996. *Geological map of France, 1/1 000 000*. BRGM, Orléans.

Chauris, L., 1977. Les associations paragénétiques dans la metallogénie varisque du massif armoricain. *Miner. Deposita*, **12**, 353–371.

Chauris, L. and Marcoux, E., 1994. Metallogeny of the Armorican Massif. In: *Pre-Mesozoic Geology in France and Related Areas, IGCP-Project 233* (J. Chantraine, J. Rolet, D.S. Santallier, A. Piqué and J.D. Keppie, eds), pp. 243–264. Springer, Berlin Heidelberg.

Chauris, L., Houlgatte, E., Laforêt, C. and Picot, P., 1985. Un district antimono-aurifère à gangue quartzo-carbonatée : Le Semnon (Ille-et-Vilaine, Massif Armoricain, France). *Hercynica*, **1**, 111–119.

Deveaud, S., Gumiaux, C., Gloaguen, E. and Branquet, Y., 2013. Spatial statistical analysis applied to rare-element LCT-type pegmatite fields: an original approach to constrain faults-pegmatites-granites relationships. *J. Geosci.*, **58**, 163–182.

Dill, D.H., 1985. Antimoniferous mineralization from the Mid-European Saxothuringian Zone: mineralogy, geology, geochemistry and ensialic origin. *Geol. Rundsch.*, **74**, 447–466.

European Commission, 2010. Critical raw materials for the EU: Report of the Ad-hoc Working Group on defining critical raw materials, Raw Materials Supply Group chaired by the European Commission, 85 pp.

Floc'h, J.-P., Santallier, D. and Henry, B., 1984. La série limousine: réflexion axée sur une synthèse géologique régionale et son utilisation pour la prospection de l'or. *Chron. Min. Rech. Min.*, **474**, 5–10.

Gapais, D. and Le Corre, C., 1980. Is the Hercynian belt of Brittany a major shear zone. *Nature*, **288**, 574–576.

Gapais, D., Brun, J.-P., Gumiaux, C., Cagnard, F., Ruffet, G., Carlier, Le and de Veslud, C., 2015. Extensional tectonics in the Hercynian Armorican belt (France). An overview. *Bull. Soc. Geol. Fr.*, **186**, 17–129.

Gloaguen, E., Branquet, Y., Boulvais, P., Moelo, Y., Chauvel, J.J., Chiappero, P.J. and Marcoux, E., 2007. Palaeozoic oolitic ironstone of the French Armorican Massif: a chemical and structural trap for orogenic base metal–As–Sb–Au mineralisation during Hercynian strike-slip deformation. *Miner. Deposita*, **42**, 399–422.

Guiollard, P.C., 2009. L'industrie minière de l'Antimoine et du Tungstène. Emergence, prospérité et disparition des exploitations de France métropolitaine aux XIXe et XXe siècles. Doctoral dissertation (in French), Université de Haute-Alsace Mulhouse-Colmar, Atlantica editions, Biarritz, 400 pp.

Gumiaux, C., Brun, J.P. and Gapais, D., 2004. Strain removal within the Hercynian Shear Belt of Central Brittany (western France): methodology and tectonic implications. In: *Flow Processes in Faults and Shear Zones* (G.I. Alsop, R.E. Holdsworth, K.J.W. McCaffrey and M. Hand, eds), *Geol. Soc. Spec. Publ.*, **224**, 287–305.

Laznicka, P., 2010. *Giant Metallic Deposits*, 2nd edn. Springer-Verlag, Berlin Heidelberg. 950 pp.

Le Gall, J., 1999. Les dolérites et basaltes tholéiitiques varisques du domaine nord-est armoricain. *Géol. Fr.*, **4**, 3–26.

Le Gall, J., Gigot, P., Savaton, P., Lacquement, F., Poprawsky, Y. and Vernhet, Y., 2011. *Geological map of France (1/50000), Laval Sheet (319)*. BRGM, Orléans.

Leutwein, F., Sonet, J. and Zimmermann, J.L., 1968. Géochronologie et évolution orogénique précambrienne et hercynienne de la partie nord-est du Massif Armoricain. Dissertation in Earth Sciences (in French), 11, 84 pp.

Marcoux, E., Serment, R. and Allon, A., 1984. Les gîtes d'antimoine de Vendée (Massif Armoricain, France). Historique des recherches et synthèse métallogénique. *Chron. Min. Rech. Min.*, **476**, 3–30.

Marcoux, E., Moëlo, Y., Picot, P. and Baubron, J.C., 1988. Evolution minéralogique et isotopique (Pb) du filon sulfuré complexe des Borderies (Massif Central francais) - Implications métallogéniques. *Miner. Deposita*, **23**, 58–70.

Martelet, G., Pajot, G. and Debeglia, N., 2009. Nouvelle carte gravimétrique de la France; RCGF09 – Réseau et Carte Gravimétrique de la France, 2009. Public BRGM report, RP-57908-FR, BRGM, Orléans, pp 26.

Munoz, M., Courjault-Radé, P. and Tollon, F., 1992. The massive stibnite veins of the French Palaeozoic basement: a metallogenic marker of Late Variscan brittle extension. *Terra Nova*, **4**, 171–177.

Œhlert, D.-P., Bigot, A. and Matte, H., 1906. *Carte Géologique Détaillée de la France au 80 000e*. Feuille de Laval (octobre 1906). Service de la Carte géologique de la France, Paris.

 © 2016 John Wiley & Sons Ltd

Périchaud, J.-J., 1980. L'antimoine, ses minérais et ses gisements. Synthèse gîtologique sur les gisements du Massif Central français. *Chron. Min. Rech. Min.*, **456**, 5–64.

Perroud, H., Auvray, B., Bonhommet, N., Macé, J. and Van der Voo, R., 1986. Palaeomagnetism and K-Ar dating of Lower Carboniferous dolerite dykes from northern Brittany. *Geophys. J. Roy. Astron. Soc.*, **87**, 143–154.

Stanley, C.J., Halls, C., Camm, G.S. and James, J., 1990. Gold-antimony mineralization at Loddiswell, Devon, UK. *Terra Nova*, **2**, 226–233.

Tartèse, R., Poujol, M., Ruffet, G., Boulvais, P., Yamato, P. and Košler, J., 2011. New U-Pb zircon and $^{40}Ar/^{39}Ar$ muscovite age constraints on the emplacement of the Lizio syn-tectonic granite (Armorican Massif, France). *CR Geosci.*, **343**, 443–453.

Tornos, F., Casquet, C. and Relvas, J.M.R.S., 2005. 4: Transpressional tectonics, lower crust decoupling and intrusion of deep mafic sills: a model for the unusual metallogenesis of SW Iberia. *Ore Geol. Rev.*, **27**, 133–163.

Trautmann, F., Becq-giraudon, J.-F., Chèvremont, P., Guerrot, C. and Thiéblemont, D., 2002. Dating the Pertre Massif at 378 Ma: a Middle to Late Devonian peraluminous leucogranite in Central Brittany. *Géol. Fr.*, **1**, 65–80.

Truffert, C., Gumiaux, C., Chantraine, J., Perrin, J., Galdeano, A., Gapais, D., Ballèvre, M., Asfirane, F., Guennoc, P. and Brun, J.P., 2001. A detailed airborne geophysical survey in southeast Armorican massif (Geo-France3D programme). Magnetism and spectral radiometry. *CR Acad. Sci. II A*, **333**, 263–270.

Vernhet, Y., Plaine, J., Trautmann, F. and Pivette, B., 2009. *Geological map of France (1/50000), Notice of the Cossé-le-Vivien Sheet (355)*. BRGM, Orléans, France. 222 pp.

Received 31 July 2015; revised version accepted 18 January 2016

Supporting Information

Additional Supporting Information may be found in the online version of this article:

Table S1. Supplementary data.

© 2016 John Wiley & Sons Ltd

Supporting Information: Table S1

District	Deposit	Production (t Sb)	Production date	Measured resources (t Sb)	Indicated resources	Total Resources	Production + resources	References
La Lucette	La Lucette	42000	1899-1913; 1916-1934				42000	Moyroud et al., 1979
	Port Brillet	insignificant	1899-1910					Guiollard, 2009
		42000					**42000**	
Vendée	Rochetréjoux	16500	1907-1925		100	100	16600	Moyroud et al., 1979
	Les Brouzils	1100	1988-1992	4465	5640	10310	11205	Blouin, 1991
	La Véronnière	250	1881-1889				250	Moyroud et al., 1979
	La Ramée	850	1882-1884; 1903-1906; 1915; 1917; 1926-1932				850	Moyroud et al., 1979
	Sainte-Marie	100	1924-1927				100	Moyroud et al., 1979
	La Baussonnière				600	600	600	BRGM 1988b; Gentilhomme et al., 2001
		18800		**4465**	**6340**	**11010**	**29605**	
Le Semnon	Le Semnon	500	1913-1918		5000	5000	5500	Moyroud et al., 1979
	La Coëfferie			9900		9900	9900	BRGM 1987
		500		**9900**	**5000**	**14900**	**15400**	
Quimper	Kerdévot	325	1913-1916; 1927-1928				325	Moyroud et al., 1979
	Ty Gardien	565	1981-1982	2885	900	3785	4350	Gorichon and Kerjean, 1979
	Kerveady			400	1000	1400	1400	Gorichon and Kerjean, 1979; BRGM, 1990
		890		**3285**	**1900**	**5185**	**6075**	
Châteaulin	Rosnoën			**500**	**500**	**1000**	**1000**	BRGM 1988; Gentilhomme et al., 2001
Total		**62190**		**18150**	**13740**	**32095**	**94080**	

References

Blouin, J.P., 1991. District antimonifère de Vendée.Rappel sur les réserves démontrées à l'intérieur des divers P.E.R. Rapport BRGM DMM/DL/NANTES RVL/FD92-04

BRGM, 1987. Plan minier breton, exercice 1985, rapport de fin de travaux, les recherches minières. BRGM report 87-DAM-018-OP4, 12 p.

BRGM, 1988. Plan minier breton, exercice 1986, rapport de fin de travaux, les recherches minières. BRGM report 88-DAM-019-OP4, 11p.

BRGM, 1988b. Inventaire du Territoire Métropolitain. Les minéralisations Sb de La Baussonnière (Vendée). BRGM report DAM/DL/NANTES. RVL/FD 91-01., 6 p.

BRGM, 1990. Plan minier breton, convention 1988, rapport de fin de travaux, les recherches minières. BRGM Report RR-30413-FR, 10p.

Gentilhomme, P., Deschamps, Y., Mroz, J.P. and Vadala, P., 2001. Synthèse et bilan de l'Inventaire minier métropolitain, volet de réévaluation économique. BRGM report RP-51422-FR, 62p.

Gorichon, A. and Kerjean, M. 1979., Reconnaissance par travaux miniers des indices d'antimoine de Quimper (PER de l'Odet). Résultats au 31 mai 1979. BRGM report 79-RDM-035-FE, 13 p.

Guiollard, P.C., 2009. L'industrie minière de l'Antimoine et du Tungstène. Emergence, prospérité et disparition des exploitations de France métropolitaine aux XIXe et XXe siècles. Doctoral dissertation (in French), Université de Haute-Alsace Mulhouse-Colmar, Atlantica editions, Biarritz, 400 pp.

Moyroud, B., Féraud, J., Bornuat, M. and Ziserman, A., 1979. Ressources minières françaises. Tome 6, les gisements d'Antimoine (Situation en 1979). BRGM report RR-41430-FR-06, 121 p.

Partie 3

Le magmatisme mafique du Massif Armoricain : contraintes temporelles et signification

Résumé en français de l'article #2

L'apatite est un minéral accessoire ubiquiste au sein de la plupart des roches magmatiques. Ce minéral est souvent la seule phase disponible à retenir de l'uranium dans son réseau cristallin pour dater les roches mafiques puisque le zircon et/ou la baddeleyite sont rarement présent. Dans cette étude, la datation U-Pb de l'apatite par LA-ICP-MS a été effectuée sur 7 dykes et sills de dolérites distincts au sein du Massif Armoricain (France). Ces dolérites, caractérisées par une signature géochimique tholéiitique intra-plaque, sont organisées en plusieurs essaims relativement denses à travers le Massif Armoricain. Leurs compositions géochimiques sont relativement homogènes bien qu'ils traversent une vaste zone subdivisés en plusieurs domaines caractérisés par différentes histoires tectono-métamorphiques. Leurs âges de mise en place sont très peu contraints due à la difficulté de dater ces roches mafiques en utilisant des méthodes classiques de datation ^{40}Ar / ^{39}Ar et U-Pb sur des minéraux comme le mica, plagioclase ou zircon. Bien que la température de fermeture du système isotopique U-Pb de l'apatite soit inférieure à la température de mise en place du magma, les modèles physiques montrent que le temps nécessaire pour solidifier et refroidir ces dykes et sills mafiques en dessous de la température de fermeture de l'apatite est de l'ordre de la centaine d'années voire moins. Par conséquent, les dates U-Pb obtenues sur l'apatite peuvent être interprétées comme l'âge de mise en place de ces intrusions mafiques. Nos résultats ont démontré, dans tous les cas, que les grains d'apatite contiennent assez de Pb radiogénique pour être datés par des analyses U-Pb in-situ et donnent un âge moyen corrigé par le ^{207}Pb de 363,4 ± 5,8 Ma. Ces résultats révèlent l'existence d'un évènement magmatique majeur et de courte durée à travers une grande partie du Massif Armoricain à la limite Dévono-Carbonifère. Au-delà des implications géologiques de ces résultats, la datation U-Pb sur apatite par LA-ICP-MS semble représenter un outil puissant pour dater des petites intrusions mafiques.

U-Pb LA-ICP-MS dating of apatite in mafic rocks: evidence for a major magmatic event at the Devonian-Carboniferous boundary in the Armorican Massif (France)

Anthony Pochon[1], Marc Poujol[1], Eric Gloaguen[2, 3], Yannick Branquet[1, 2], Florence Cagnard[2,3], Charles Gumiaux[2], Denis Gapais[1]

[1] *Géosciences Rennes, UMR 6118, Université de Rennes 1, Campus de Beaulieu, 35042 Rennes Cedex*

[2] *Institut des Sciences de la Terre d'Orléans, UMR 7327, Université d'Orléans, Campus Géosciences, 1A rue de la Férollerie, 45071 Orléans Cedex 2*

[3] *Bureau de Recherche Géologique et Minière (BRGM), UMR 7327, 3 avenue Claude-Guillemin, BP 36009, 45060 Orléans Cedex 02*

Publié à *American Mineralogist*, vol. 101, pp 2430-2442 (2016)

American Mineralogist, Volume 101, pages 2430–2442, 2016

SPECIAL COLLECTION: APATITE: A COMMON MINERAL, UNCOMMONLY VERSATILE

U-Pb LA-ICP-MS dating of apatite in mafic rocks: Evidence for a major magmatic event at the Devonian-Carboniferous boundary in the Armorican Massif (France)

Anthony Pochon[1,*], Marc Poujol[1], Eric Gloaguen[2], Yannick Branquet[1,2], Florence Cagnard[2], Charles Gumiaux[2], and Denis Gapais[1]

[1]Géosciences Rennes, UMR CNRS 6118, Université de Rennes 1, OSUR, Campus de Beaulieu, 35042 Rennes Cedex, France
[2]Université d'Orléans-CNRS/INSU-BRGM, UMR 7327 Institut des Sciences de la Terre d'Orléans, 45071 Orléans, France

Abstract

Apatite is a ubiquitous accessory mineral found in most magmatic rocks and is often the only U-bearing mineral available to date mafic rocks because primary zircon and/or baddeleyite are not present. In this paper, U-Pb LA-ICP-MS dating of apatite was applied to seven different dike and sill samples of dolerite from the Variscan belt of Brittany (Armorican Massif, western France). These dolerites, which are characterized by a within-plate tholeiite geochemical signature, are organized in several dense swarms across the belt. Their geochemical compositions are homogeneous although they intrude a large geographical area subdivided into several domains each characterized by different tectonic-metamorphic settings. Their emplacement ages were so far poorly constrained due to the difficulty to date these mafic rocks using either the $^{40}Ar/^{39}Ar$ or the U-Pb methods on classical minerals like mica, plagioclase, or zircon. Although the closure temperature of apatite is lower than the emplacement temperature of the magma, physical models show that the time needed to solidify and cool these mafic dikes and sills below the apatite closure temperature is basically of the order of 100 years or less. Consequently, the U-Pb dates obtained on apatite can be interpreted as the emplacement ages for these mafic intrusions. Our results demonstrate that, in all cases, the apatite grains do carry enough radiogenic Pb to be dated by in situ U-Pb analyses and yield a ^{207}Pb-corrected mean age of 363.4 ± 5.8 Ma. These results reveal the existence of a major and short-lived magmatic event in the Variscan belt of Brittany during the Devonian-Carboniferous transition, a feature further highlighted by field evidence. Beyond the geological implications of these results, U-Pb LA-ICP-MS dating of apatite appears to represent an ideal tool to date small size mafic intrusions.

Keywords: Apatite, LA-ICP-MS, U-Pb dating, mafic rocks, French Variscan belt

Introduction

Apatite is a common accessory mineral in metamorphic, sedimentary, mafic, and felsic igneous rocks (Watson 1979, 1980; Green and Watson 1982; Harrison and Watson 1984; Piccoli and Candela 2002; Spear and Pyle 2002; Webster and Piccoli 2015). The structure of apatite is very stable and can accommodate several substitutions including Pb (McConnell 1938) and U, which may substitute for Ca via a charge-coupled substitution involving a Ca-deficiency (Oosthuyzen and Burger 1973; Baumer et al. 1983; Hughes and Rakovan 2002). Furthermore, it is the most ubiquitous U-bearing mineral in mafic rocks, unlike zircon or baddeleyite, and can consequently represent a powerful tool for U-Pb geochronology. Empirical and experimental closure temperatures for Pb diffusion in apatite are between ca. 375 and 550 °C (Cherniak et al. 1991; Chamberlain and Bowring 2001; Harrison et al. 2002; Schoene and Bowring 2007; Cochrane et al. 2014), which is a range of temperatures that is lower than the U-Pb closure temperatures for zircon, baddeleyite, and titanite but higher than the one for Ar-Ar in biotite (Reiners et al. 2005 and references therein). Furthermore, in small-size mafic bodies (dikes, sills, and plugs), the K-Ar whole rock and $^{40}Ar/^{39}Ar$ on plagioclase methods are often hard to apply either because of the excess Ar acquired from the host-rock or because of the loss or excess of K resulting from chemical weathering and/or alteration (Ruffet et al. 1992; Kelley 2002; Faure and Mensing 2005). The $^{40}Ar/^{39}Ar$ dating of biotite and amphibole can be used but these minerals are rarely present in mafic dikes and sills. Because of its medium-range closure temperature, U-Pb dating of apatite may not appear to be the best choice to date the emplacement of hot and large, slowly cooling, mafic bodies. However, for mafic dikes or sills, objects that are limited in size with a fast cooling rate, it may represent a very pertinent mineral to use provided that these rocks have not experienced a reheating event above the closure temperature of apatite.

Apatite was first dated with the U-Pb method by Aldrich et al. (1955) and Tilton et al. (1955). However apatite accommodates significant amounts of common Pb in its crystal lattice (Chamberlain and Bowring 2000; Hugues and Rakovan 2002; Cochrane et al. 2014) and has typically low U and radiogenic Pb concentrations and, consequently, low radiogenic Pb/common Pb ratios. It is therefore necessary to perform a so-called common Pb correction to distinguish the radiogenic Pb from

* E-mail: anthony.pochon@univ-rennes1.fr
Special collection papers can be found online at http://www.minsocam.org/MSA/AmMin/special-collections.html.

0003-004X/16/0011–2430$05.00/DOI: http://dx.doi.org/10.2138/am-2016-5736

the common Pb. Although this problem can be easily resolved using the isotope dilution thermal ionization mass spectrometry (ID-TIMS) technique, it becomes more problematic for in situ analyses [secondary ion mass spectrometry (SIMS) or laser ablation-inductively coupled plasma-mass spectrometry (LA-ICP-MS)]. Indeed, in situ analysis requires the use of a standard (most often an external standard, i.e., a matrix-matching mineral with a known age) to correct the raw data for the analytical biases inherent to this technique, namely the downhole fractionation and the instrumental drift. Although it is easy to find high-quality natural and concordant standards for minerals that carry no common Pb (such as zircon, monazite, or baddeleyite), it is very difficult for common Pb bearing minerals such as apatite. Therefore, these standards, while potentially usable to correct the analyses for the instrumental biases, do often carry common Pb, which in turns means that they are not concordant. Thus, a common Pb correction also needs to be applied to the standards themselves. Recent developments using either MC-ICP-MS and/or new data treatment, as well as the discovery of age homogeneous apatite standards (Storey et al. 2007; Carrapa et al. 2009; Thomson et al. 2012; Chew et al. 2011, 2014) have considerably improved the applicability of U-Pb dating of apatite by in situ LA-ICP-MS analysis. In this study, we implemented a new approach developed by Chew et al. (2014) using apatite standards carrying variable common Pb.

This paper focuses on the application of U-Pb dating of apatite by in situ LA-ICP-MS to obtain the emplacement ages of various dikes and sills of dolerite from the Armorican Massif, which is located in the western part of French Variscan belt. These mafic rocks are widespread in the region and form several swarms of dikes crosscutting a Neoproterozoic to Paleozoic sedimentary series. Some dikes are spatially associated with Sb and Au mineralization, especially in the central part of the Armorican Massif (Chauris et al. 1985; Pochon et al. 2016). This magmatism, described as characteristic of within-plate tholéiite, is constrained by some previous studies (Le Gall and Mary 1983; Mary and Le Gall 1985; Houlgatte et al. 1988; Lahaye et al. 1995; Le Gall 1999; Aïfa et al. 1999), but the precise timing of the emplacement of these mafic rocks remains poorly constrained, in particular because of the scarcity of minerals suitable for dating. Apatite is present as an accessory mineral in all of these rocks and appears to represent the best candidate to date them. Petrography, whole-rock analyses, and apatite geochemical analyses have been performed on samples from these rocks to check for their degrees of alteration/weathering and to confirm a magmatic origin for the apatite grains before performing the LA-ICP-MS analyses.

Geological background

Main structural features

The Armorican Massif is located in western France and is part of the West European Variscan belt, which resulted from the continental collision between the Gondwana and Laurussia plates and the Armorica microplate (Ballèvre et al. 2009, 2014). This collision began during the Late Devonian and continued until the Early Carboniferous (Matte 1986; Ballèvre et al. 2014). The Armorican Massif comprises three main domains with contrasted structural styles and deformation histories: the North Armorican, Central Armorican, and South Armorican domains. These domains are bounded by two dextral crustal-scale shear zones, the North Armorican Shear Zone and the South Armorican Shear Zone (NASZ and SASZ, respectively, Fig. 1). The North Armorican domain was essentially affected by Neoproterozoic deformations and constituted a part of the upper brittle crust unmetamorphosed during the Variscan orogeny (Brun et al. 2001). The Central Armorican domain is made of Late Neoproterozoic to upper Paleozoic sediments affected by moderate deformations (Gumiaux et al. 2004a, 2004b) and a low-grade regional metamorphism during the Variscan orogeny. The maximum temperature reached is estimated to be close to 250–300 °C, based on vitrinite reflectance (Donnot et al. 1973), chloritoid-bearing slate occurrences (Le Corre 1969), the illite crystallinity (Le Corre 1975), and the chlorite geothermometer (Gloaguen et al. 2007). The South Armorican domain belongs to the internal metamorphic zones of the Variscan belt. It was affected by crustal thickening during Late Devonian to Carboniferous times, with a high-pressure–low-temperature event at ca. 360 Ma (Bosse et al. 2000, 2005), followed by Late Carboniferous extension (Gapais et al. 1993, 2015).

Magmatism in the Armorican Massif

Several magmatic events occurred during the Paleozoic in the Armorican Massif. These are first represented by bimodal magmatism and volcanism during the Late Cambrian-early Ordovician, featuring calc-alkaline and rare peraluminous series (Ballèvre et al. 2014 and references therein). The Late Cambrian event is best developed in the North Armorican domain, whereas the Early Ordovician event is best developed in the Central and South Armorican domains.

Numerous Variscan granitoids have been emplaced in the Armorican Massif and are characterized by different geochemical associations (Capdevila 2010; Tartèse and Boulvais 2010; Tartèse et al. 2011a, 2011b; Ballouard et al. 2015). According to Capdevila (2010), five main associations are currently recognized: (1) a ca. 370 Ma (U-Pb method on zircon; Cuney et al. 1993) calc-alkaline association containing orogenic biotite-hornblende granites resulting from the partial melting of an enriched mantle; (2) a ca. 330 Ma Mg-potassic metaluminous association that includes mafic to intermediate rocks and porphyroid biotite-hornblende monzogranites (e.g., Plouaret granite, 329 ± 5 Ma, whole-rock Rb-Sr, Peucat et al. 1984); (3) a Mg-potassic peraluminous association made up of monzodiorite with a mantle origin, monzogranite, and cordierite granite from partial melting of metasediments; and (4) a ca. 316–310 Ma two mica peraluminous leucogranites formed by the partial melting of a similar metasedimentary sources (Tartèse and Boulvais 2010), e.g., the Guérande leucogranite (309.7 ± 1.3 Ma by U-Pb method on zircon and monazite; Ballouard et al. 2015) and the Lizio granite (316 ± 1.3 Ma by U-Pb on zircons, Tartèse et al. 2011b); and (5) ca. 300 Ma red monzogranites and porphyroid syenogranites (e.g., the Ploumanac'h granite, 303 ± 15 Ma, whole-rock Rb-Sr, Vidal 1980).

The North and Central Armorican domains are also marked by a dense swarm of dikes and sills of dolerite that intrude the Late Proterozoic to Devonian sediments (Velde 1970; Ruffet et al. 1992; Lahaye et al. 1995; Aïfa et al. 1999; Le Gall 1999). They are spatially distributed in several groups (Fig. 1) defined

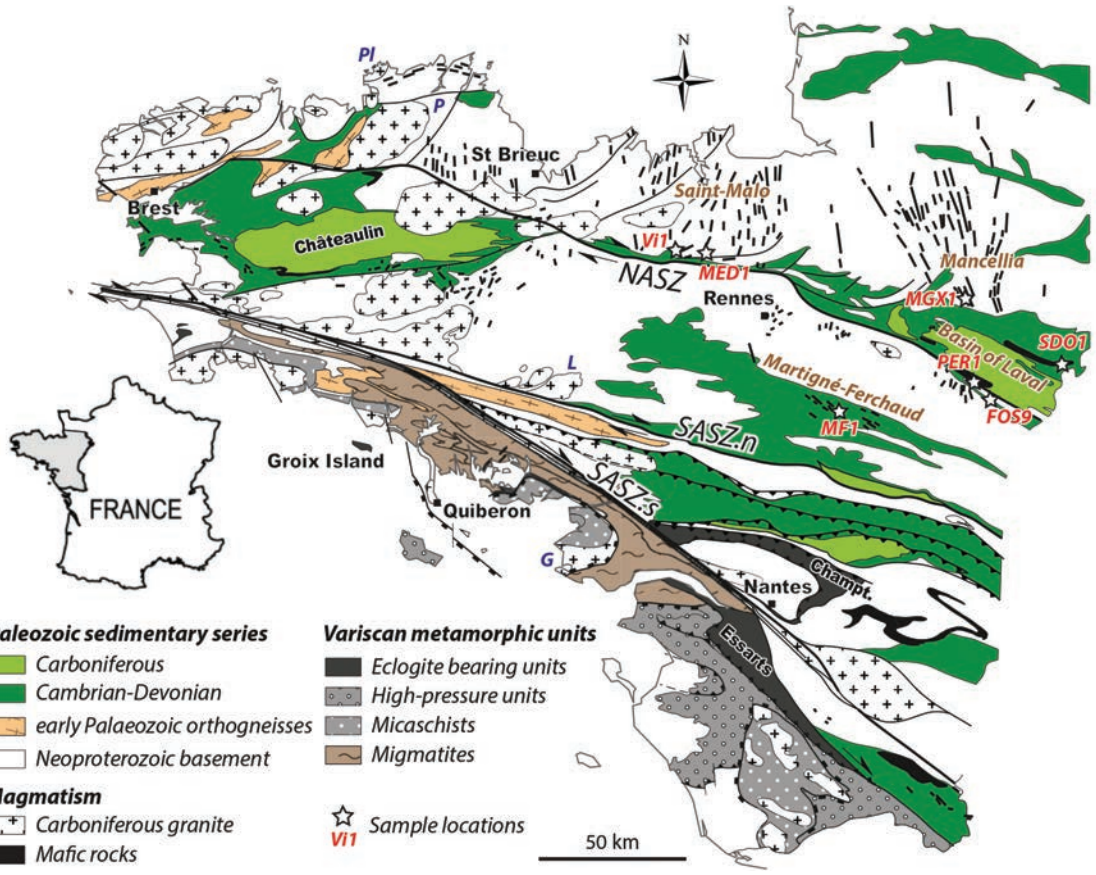

FIGURE 1. Simplified geological map of the Armorican Massif modified from Chantraine et al. (1996) and Le Gall (1999). P = Plouaret granite; G = Guérande granite; L = Lizio granite; Pl = Ploumanac'h granite. Sample names and locations are reported in the WGS84 geographic coordinate system: Vi1 (48°16′5.23″N, 1°45′20.03″W); MED1 (48°17′0.05″N, 1°40′1.67″W); MGX1 (48°12′52.26″N, 0°41′55.74″W); PER1 (47°59′22.98″N, 0°44′30.32″W); SDO1 (48°0′34.05″N, 0°17′53.39″W); FOS9 (47°56′17.62″N, 0°42′20.79″W); MF1 (47°50′26.83″N, 1°18′0.71″W). (Color online.)

by Le Gall (1999). The Mancellia and Saint-Malo group consists of wide and dense swarms of dolerite dikes oriented North-South. The Laval Basin group comprises dikes and sills of dolerite crosscutting Silurian and Devonian sediments and basaltic flows emplaced within Early Carboniferous series (Plaine 1976; Houlgatte et al. 1988; Pelhate 1994). The Martigné-Ferchaud group consists of dike swarms striking N140° and spatially associated with Sb mineralization (Chauris et al. 1985; Pochon et al. 2016). According to Le Gall (1999), the dolerites of these groups present homogeneous geochemical compositions and appear to be similar in composition to the thick mafic and felsic volcano sedimentary sequences of the Châteaulin Basin in the western part of the Armorican Massif (Pelhate 1994; Caroff et al. 1996). They are interpreted as within-plate tholeiites emplaced during a distensive/transtensive event or during a transpressive phase prior to the Late Carboniferous (Le Gall and Mary 1983; Mary and Le Gall 1985; Houlgatte et al. 1988; Lahaye et al. 1995; Le Gall 1999; Rolet et al. 1994). Although these dolerites are relatively common throughout the Armorican Massif (Fig. 1), their ages are poorly constrained, due in particular to the difficulty to date this type of rock (Ruffet et al. 1992). Only one doubtful whole-rock K-Ar age of 330 ± 10 Ma (Perroud et al. 1986) is so far available. Because post-Devonian dikes are not observed in the field and because doleritic fragments have been observed inside Early Carboniferous volcanic breccias and conglomerate (Plaine 1976), an age of around 360 Ma has been suggested for the emplacement of these mafic intrusions (Le Gall 1999).

DESCRIPTION OF THE SAMPLES

Samples were collected within the un-metamorphosed North Armorican domain and the low-grade Central Armorican domain (Fig. 1): two within the Saint Malo group (MED1 and Vi1); three within the Laval Basin group [two in the southern part (PER1 and FOS9) and one in the northern part (SDO1)]; one within the Mancellia group (MGX1); and one from the Martigné-Ferchaud group (MF1). Samples collected in the Saint Malo and Mancellia groups are very similar and consist of dolerite dikes intrusive within the Neoproterozoic basement (Figs. 1 and 2a). In the Laval Basin, two samples (PER1 and SDO1) consist of sills of dolerite intrusive within Silurian black shales (Fig. 2b), and a third sample (FOS 9) consists of an altered sill of dolerite found within Ordovician sandstones (Fig. 2c). In the Martigné-Ferchaud group, the sample belongs to a dolerite dike crosscutting Ordovician slates and sandstones and was subse-

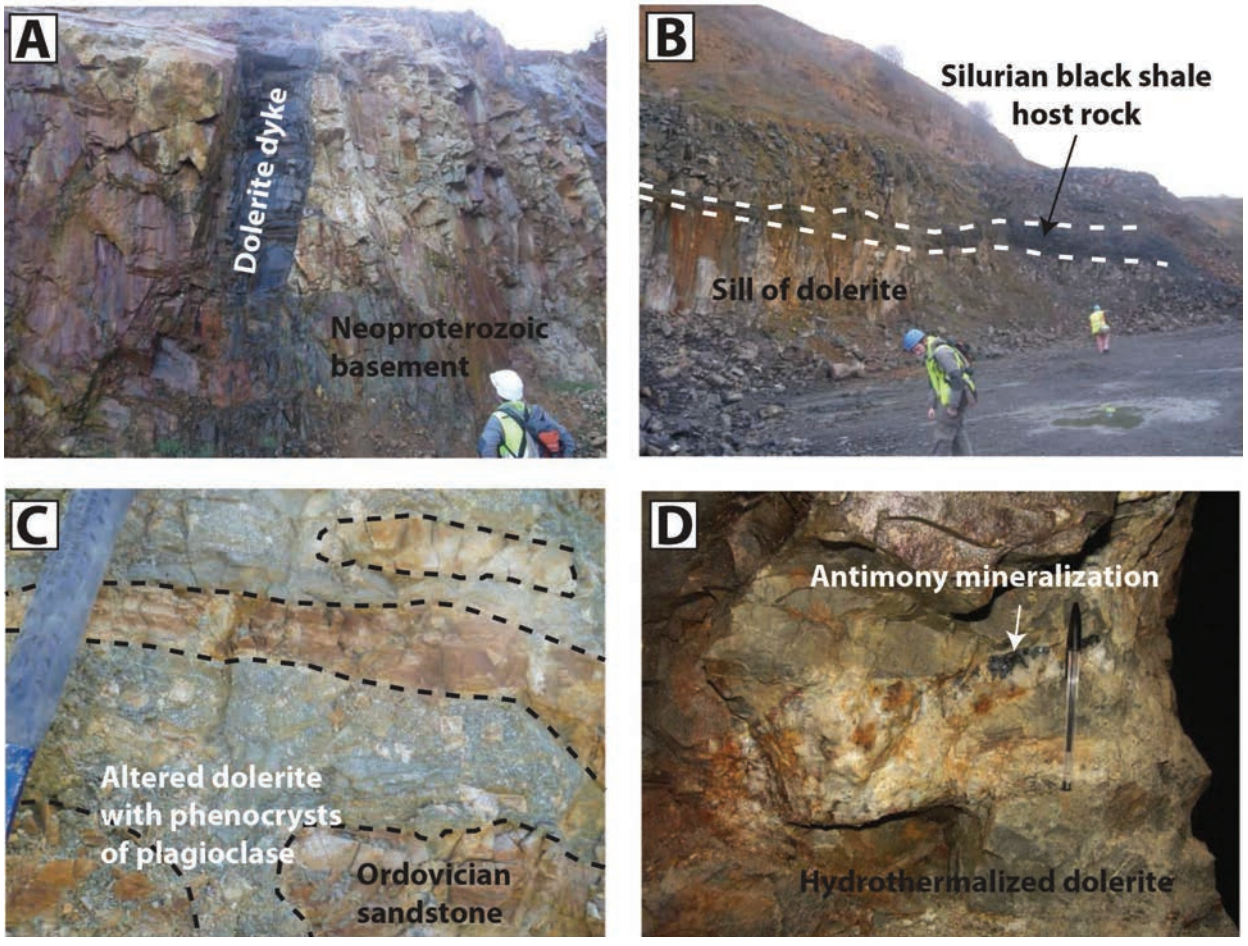

FIGURE 2. Representative field photographs showing: (**a**) A typical dolerite dike intruding Neoproterozoic basement from the Saint-Malo group in the North Armorican domain. (**b**) A sill of dolerite intruding Silurian black shales in the northern part of the Laval Basin. The white dashed line represents the contact between the sill and the host rock. (**c**) A mafic intrusive facies with phenocrysts of plagioclase within Ordovician sandstones in the southern part of the Laval Basin. (**d**) A hydrothermalized dolerite dike associated with Sb mineralization in Ordovician slates from the Martigné-Ferchaud group. (Color online.)

quently partially hydrothermalized during the formation of Sb mineralization (Fig. 2d).

Despite their relatively wide geographical distribution, dolerites show similar textures and mineralogy. Only the mafic sill FOS9 is different from the others because it contains centimeter-scale phenocrysts of plagioclase that are strongly saussuritized and because it is magmatic texture is not preserved. The textures of the other doleritic samples are mainly porphyritic and the principal mineral assemblages consist of elongate plagioclase laths, clinopyroxene (mainly augite), and Fe-Ti oxides such as ilmenite, rutile, and magnetite with exsolved ilmenite (Fig. 3a). Late-stage crystallization is represented by rare interstitial quartz (Figs. 3b, 3c, and 3d) and/or quartz and alkali-feldspar intergrowths (granophyric textures). The accessory mineral assemblage consists of apatite, rare primary biotite and titanite, pyrite, chalcopyrite, pyrrhotite, chlorite, green amphibole, and epidote (pistachite). Apatite is the most common of all the accessory minerals and occurs in the groundmass of primary plagioclases but also in the mesostasis or within other minerals such as quartz, amphibole, or clinopyroxene (Figs. 3a, 3b, 3c, and 3d). Apatite appears as euhedral and often acicular crystals up to 250 μm in length. Chemical weathering and hydrothermal alteration of these Armorican dolerites are common and may be locally strong. It is evidenced by the presence of sheets of silicates in interstitial glass, the destabilization of biotite into chlorite, and the replacement of clinopyroxene and plagioclase by a typical propylitic assemblage of chlorite, actinote, epidote, and carbonates.

MATERIALS AND METHODS

Major and trace element analyses

Seven samples were collected mainly in quarries providing relatively fresh outcrop conditions. Only the least-altered rocks were finally selected for analyses. These selected samples were crushed and powdered using agate mortars. Major and trace element analyses, including REE, were performed by the French analytical laboratory (SARM, CRPG-CNRS, Nancy) using an inductively coupled plasma optical emission spectrometry (ICP-OES) and mass spectrometry (ICP-MS), respectively, following the standard analytical procedures of Carignan et al. (2001).

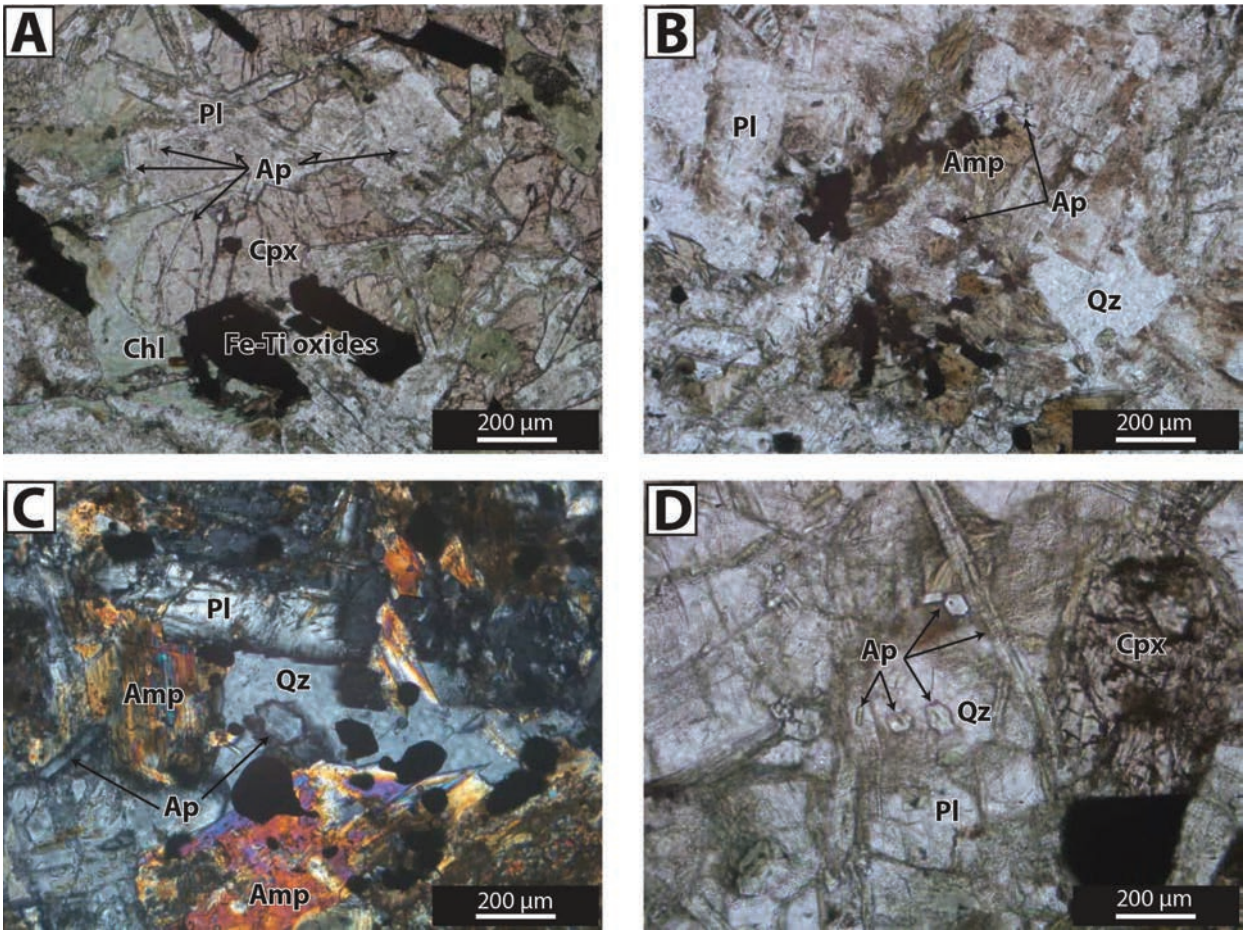

FIGURE 3. Selected thin section micro-photographs illustrating: (**a**) the typical texture of a dolerite dike with laths of plagioclase intergrown with clinopyroxene and apatite crystals occurrence in the groundmass of fresh and saussuritized plagioclase and acicular apatite in clinopyroxene. (**b**) Primary amphibole and interstitial anhedral quartz (<2%) in dolerite dike. (**c**) Apatite growing in primary amphibole and interstitial quartz. (**d**) Several apatite crystals in the groundmass of plagioclase, interstitial quartz, and clinopyroxene. See Whitney and Evans (2010) for mineral abbreviations. (Color online.)

Mineral compositions

Apatite crystals were examined in polished thin sections through a scanning electron microscope (SEM equipped with EDS), and analyzed using an electron microprobe (Cameca SXFive, common analytical laboratory, BRGM-CNRS-University, Orléans, France). The major elements Ca, P, and F as well as Cl, Fe, Mg, Si, Mn, Sr, Na, and S were analyzed in the apatite crystals. It has been demonstrated that the measured X-ray flux from apatite is affected by crystal orientation (Stormer et al. 1993), nevertheless, highly accurate analyses of F and Cl can be achieved using low electron beam densities, large beams, and by analyzing grains with the electron beam perpendicular to the apatite c axis (Goldoff et al. 2012). Analyses were performed using a 15 kV accelerating voltage, a counting time of 10 s, and a beam current of 6 nA for spot analyses, and 20 nA for elemental mapping purposes, using the following mineral standards: apatite (P$K\alpha$), topaz (F$K\alpha$), hematite (Fe$K\alpha$), andradite (Ca$K\alpha$, Mg$K\alpha$), $MnTiO_3$ (Ti$K\alpha$), celestite (Sr$K\alpha$, S$K\alpha$), albite (Na$K\alpha$, Si$K\alpha$), and vanadinite (Cl$K\alpha$). All the analyses were performed unambiguously with the electron beam perpendicular to the apatite c axis because of the strongly elongate shape of the grains. Several apatite grains were analyzed per sample. The OH contents of apatite have been estimated from EPMA measurements of F and Cl by charge balance, assuming that the halogen sites are full (Piccoli and Candela 2002).

U-Pb analyses

Mineral separation procedures were applied to concentrate the apatite crystals using the facilities available at Géosciences Rennes. Rocks were crushed and only the powder fraction with a diameter <250 µm has been kept. Heavy minerals were successively concentrated using the Wilfley table and heavy liquids. Magnetic minerals were then removed with an isodynamic Frantz separator. Apatite grains were carefully handpicked under a binocular microscope and embedded in epoxy mounts. The grains were then grounded and polished on a lap wheel with 6 and 1 µm diamond suspensions successively. Apatite grains were imaged by cathodoluminescence (CL) using a Reliotron CL system equipped with a digital color camera available in Géosciences Rennes.

U-Pb geochronology was conducted by in situ laser ablation-inductively coupled plasma-mass spectrometry (LA-ICP-MS) at Géosciences Rennes using a ESI NWR193UC excimer laser coupled to a quadripole Agilent 7700x ICP-MS equipped with a dual pumping system to enhance sensitivity (Paquette et al. 2014). The instrumental conditions are reported in Supplemental[1] Table 1.

The ablated material is carried by He, which is then mixed with N_2 and Ar, before injection into the plasma source. The alignment of the instrument and mass calibration was performed before each analytical session on the NIST SRM 612 reference glass, by inspecting the ^{238}U signal and by minimizing the ThO^+/Th^+ ratio (<0.5%). During the course of an analysis, the signals of ^{43}Ca, $^{204}(Pb+Hg)$, ^{206}Pb, ^{207}Pb, ^{208}Pb, and ^{238}U masses are acquired. The ^{235}U signal is calculated from ^{238}U on the basis of the ratio $^{238}U/^{235}U = 137.88$.

Single analyses consisted of 20 s background integration followed by 60 s integration with the laser firing and then a 10 s delay to wash out the previous

[1]Deposit item AM-16-115736, Supplemental Tables. Deposit items are free to all readers and found on the MSA web site, via the specific issue's Table of Contents (go to http://www.minsocam.org/msa/ammin/toc/2016/Nov2016_data/Nov2016_data.html).

sample. Ablation spot diameters of 50 μm with repetition rates of 5 Hz were used for most of the samples. In some samples, however, the apatite grains were acicular and could not therefore accommodate a 50 μm spot. The ESI NWR193UC laser is equipped with a rotational XY shutter allowing to perform rectangular ablations while ensuring an even "dosage" of the laser energy to the sample during the analyses. In these cases, we defined a rectangle that was suitable for most of the grains from a given sample. This ablation rectangle, which can rotate freely around its center, was then used for all the standards and the apatite crystals to use the same analytical conditions during the analyses.

For each sample (one analytical session of 43 measurements), we used the following standard bracketing procedure. Two analyses of the Madagascar apatite standard (ID-TIMS age of 473.5 ± 0.7 Ma; Cochrane et al. 2014) used as the primary apatite reference material, one analysis of the Durango apatite standard (31.44 ± 0.18 Ma; McDowell et al. 2005), one analysis of the McClure apatite standard (523.51 ± 2.09 Ma; Schoene and Bowring 2006), followed by six analyses of the apatite grains. This sequence was then repeated three times with one analysis of the Durango and two analyses of the Madagascar standards at the end of the session.

Data were corrected for U–Pb fractionation and for mass bias by the repeated measurements of the Madagascar apatite standard. The Durango and McClure apatite standards measurements were treated as unknowns and used to control the reproducibility and accuracy of the corrections. During the course of the analyses, they provided ^{207}Pb corrected ages of 32.22 ± 0.52 Ma (MSWD = 0.69; probability = 0.93) and 526.4 ± 3.3 Ma (MSWD = 0.57; probability = 0.98), respectively, (Figs. 4a and 4b, respectively).

Data reduction was carried out using the data reduction scheme VizualAge_UcomPbine, a set of Igor Pro procedures that work with Iolite (Chew et al. 2014). This data reduction scheme performs a common Pb correction using the ^{207}Pb method for the initial Pb isotope composition specified in the standard reference value file for the Madagascar apatite standard. Basically, a model downhole $^{207}Pb/^{235}U$ fractionation curve is fitted with a ^{207}Pb-based common Pb correction using an initial $^{207}Pb/^{206}Pb$ value of 0.8681 (Cochrane et al. 2014).

WHOLE-ROCK GEOCHEMISTRY

To account for the degree of alkali-element mobility during hydrothermal alteration or metasomatism, all the samples are plotted (Fig. 5a) in the K_2O+Na_2O vs. $K_2O/(K_2O+Na_2O)$ diagram of Hughes (1973). Most of the samples lie within the igneous spectrum field, with only two samples (FOS9) and a sample from the Mancellia group analyzed by Le Gall (1999) plotting outside of this field. This suggests that most of the mobile elements have not been significantly affected after the magma emplacement. For the Laval Basin group, samples are slightly altered with a loss of K_2O in some samples and almost a total loss of Na_2O in one sample (FOS9). According to the Zr/TiO_2 vs. Nb/Y plot (Fig. 5b), most of the samples display basaltic affinities ($Zr/TiO_2 < 0.02$) with sub-alkalic ratios for the Saint-Malo group and the Martigné-Ferchaud (MF1) dike ($Nb/Y < 0.8$) and with sub-alkali to alkali ratios for the Mancellia and the Laval Basin groups ($0.4 > Nb/Y < 1.6$). Only one sample from the Mancellia group (MGX1) displays an intermediate affinity. Most of the samples have a relatively low MgO content (MgO < 6 wt%) except for PER1 (Supplemental[1] Table 2).

Data from this study, as well as the available values for different group of dolerites (Lahaye et al. 1995; Le Gall 1999), have been plotted in a chondrite-normalized spider diagram (Fig. 5c). Most of the dolerites display similar REE contents and subparallel REE patterns with a slight to moderate fractionation of the light REE vs. the heavy REE [$(La/Lu)_N = 3.56–7.45$]. These patterns are similar to those reported for the Armorican dolerites by Le Gall (1999). Only sample FOS9 yields a moderate negative Eu anomaly. Although this sample is strongly altered (Fig. 5a), it shows a similar REE spectrum suggesting that the REE were not affected by hydrothermal alteration and/or chemical weathering. The mantle-normalized spider diagram (Fig. 5d) displays similar incompatible element contents and ratios for all the samples, with the exception of several elements such as Th, Hf-Zr, and Ti. Indeed, samples SDO1 and FOS9 show slightly positive anomalies in Th that may be linked to the fact that the dolerites have incorporated some country rocks during their emplacement. The Zr-Hf fractionations (Zr/Hf = 35.65–46.07) are very similar for all the samples. Their respective contents are relatively high in sample MGX1 because of the presence of zircon crystals inherited from the country rocks during emplacement. Three samples display negative anomalies in Ti ($Ti/Ti^* = [Ti]_N/([Sm]_N+[Gd]_N) = 0.11–0.30$) compared to the mean pattern for the Mancellia, Saint-Malo, and Laval Basin groups. The largest negative anomaly is recorded in the dike MGX1 (Ti = 1.87 wt%). Finally, the diagram also shows a light positive Y anomaly in sample PER1. According to mantle-normalized trace element patterns proposed by Li et al. (2015), most of the samples are similar to average compositions of alkaline continental flood basalts (CFB).

APATITE CHEMISTRY

We studied between 50 and 100 apatite grains for each of the 7 samples. In the MF1 and SDO1 samples, apatite

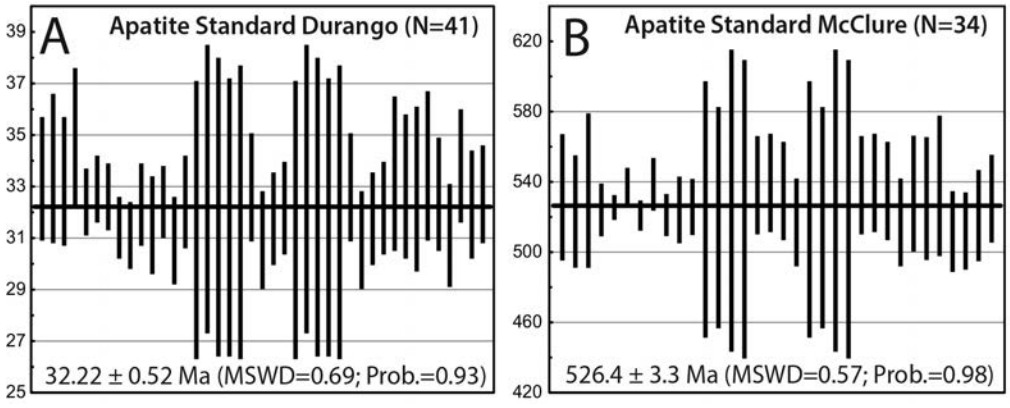

FIGURE 4. Diagrams representing the weighted average ^{207}Pb-corrected measured ages for the secondary apatite standards analyzed during this study: (**a**) Durango apatite and (**b**) McClure apatite. Prob. = Probability.

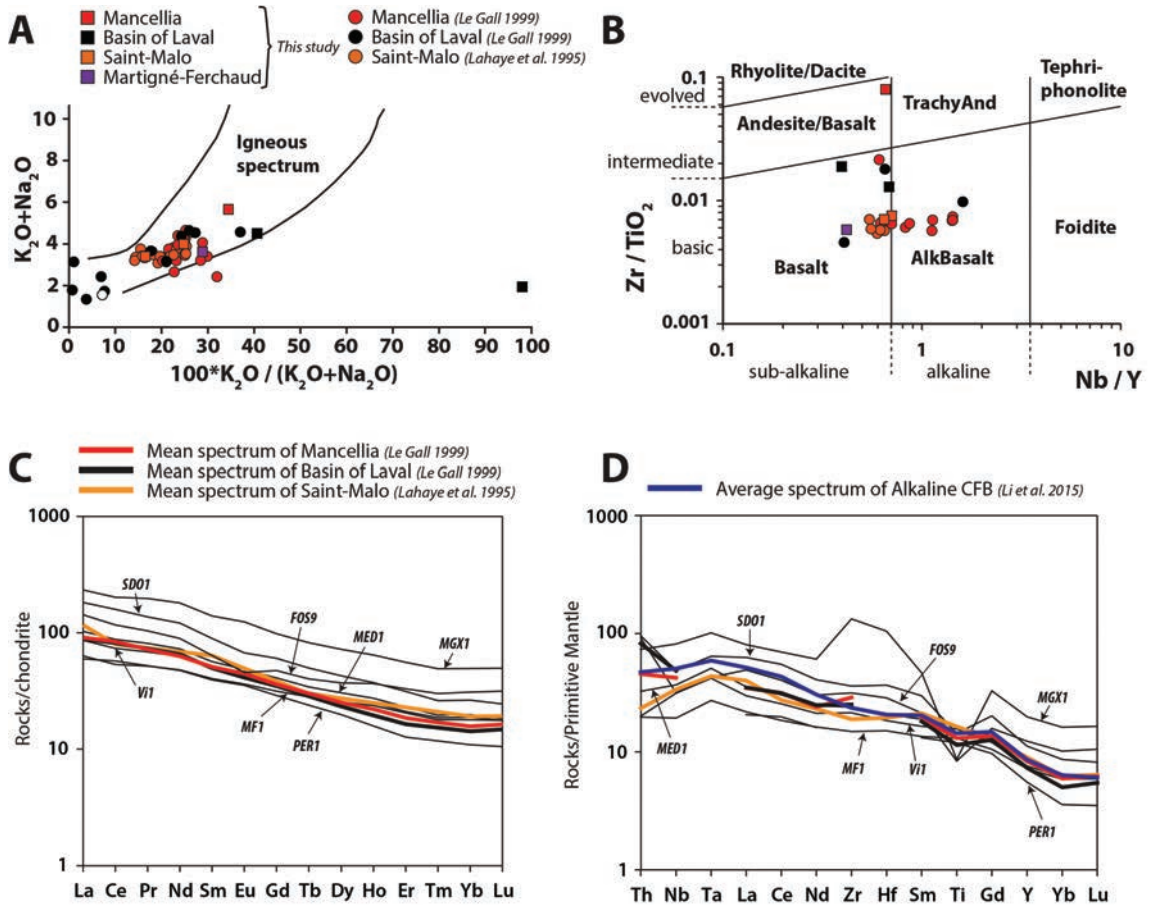

FIGURE 5. (**a**) Whole-rock composition in the chemical diagram of Hughes (1973) for the dolerite samples. (**b**) Zr/TiO_2 vs. Nb/Y diagram of Winchester and Floyd (1977) modified by Pearce (1996) with alkaline, subalkaline, basic, and intermediate rocks subdivision. (**c**) Chondrite normalized REE diagram and (**d**) mantle-normalized spider diagrams reporting the mean patterns for the Mancellia, Laval Basin and Saint-Malo groups of dolerite. Chondrite and primitive mantle normalizing values are taken from Sun and McDonough (1989). (Color online.)

grains appear as squat prisms up to 100 μm in length. In the PER1, MED1, and Vi1 samples, apatite crystals have an elongate acicular shape up to 150 μm in length and a width of ~25 μm. Finally, there are two types of apatite in samples MGX1 and FOS9: elongate crystals with an acicular shape up to 250 μm in length and squat grains up to 150 μm.

SEM examinations, X-ray maps (Figs. 6a, 6b, 6c, and 6d), and electron microprobe data show that F is always present in amounts above 0.62 apfu (Supplemental[1] Table 4), which indicates that all the apatite crystals are fluorapatite. These fluorapatite crystals are unzoned or sometimes poorly zoned around the rim. Oscillatory zoning has never been observed and, where present, the zoning is mainly marked by differences in the Mg (0–0.04 apfu), Mn (0–0.07 apfu), and Fe (0–0.07 apfu) contents. X-ray maps reveal that the edges are slightly enriched in Mg and Fe (Figs. 6b and 6d) but the reverse has also been observed (e.g., sample SDO1). Average composition, standard deviation, maximum, and minimum (Supplemental[1] Table 3) demonstrate that these fluorapatite grains have a narrow range of compositions and do not contain Sr despite the fact that Sr is available (between 48–455 ppm) in these rocks (Supplemental[1] Table 4). In the ternary OH-Cl-F diagram (Fig. 6e), most of the grains match the compositions of fluorapatite from typically ultramafic/mafic complexes. According to the data of Webster and Piccoli (2015), these compositions are the most frequently encountered independently from the host-rock origin (mafic, felsic, and hydrothermal systems).

FEASIBILITY OF U-PB DATING OF APATITE IN MAFIC DIKE/SILL

To evaluate the feasibility to use apatite U-Pb to date the emplacement age of mafic rocks, we performed some calculations and models dealing with the time necessary to crystallize and cool these mafic dikes and sills. First, we aim at estimating the time necessary to completely crystallize a mafic dike or sill according to its thickness (up to 200 m) and the host-rock temperatures (100, 200, and 300 °C). We used the 1D analytical solution of the Stefan problem transposed to dike and/or sill crystallization (see Turcotte and Schubert 1982 and Fig. 7a). For doleritic dikes and sills, we assumed that their rock parameters are close to basaltic ones. Noteworthy, the solution implies that solidified doleritic magma and host rocks have the same physi-

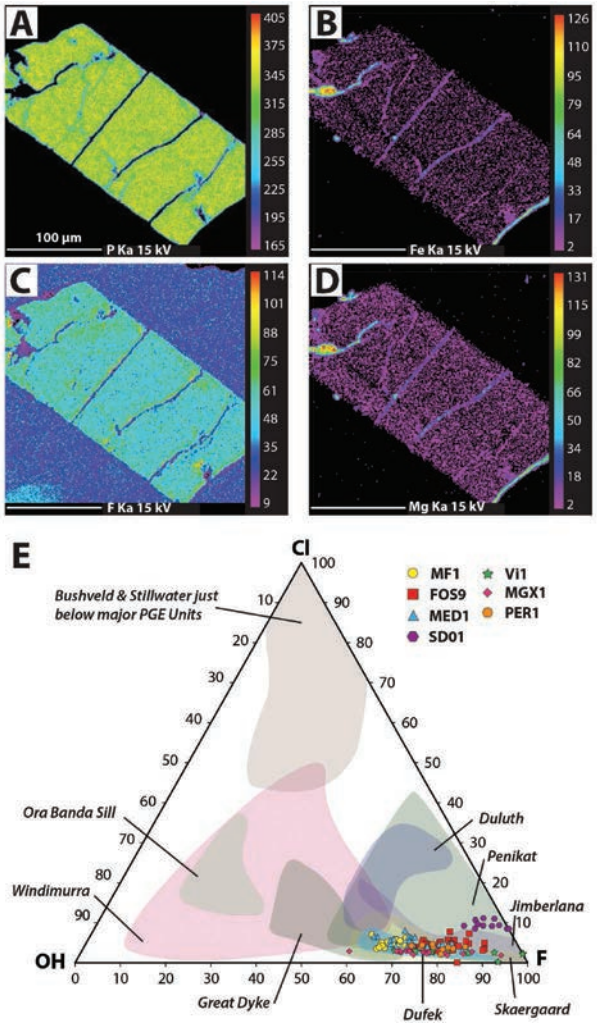

Figure 6. Chemistry of representative poorly zoned fluorapatite crystals using X-ray maps: (**a**) P*K*α, (**b**) Fe*K*α, (**c**) F*K*α, and (**d**) Mg*K*α. (**e**) Plot of the halogen contents (in molar proportions) with fields from various mafic layered intrusions modified after Boudreau (1995). (Color online.)

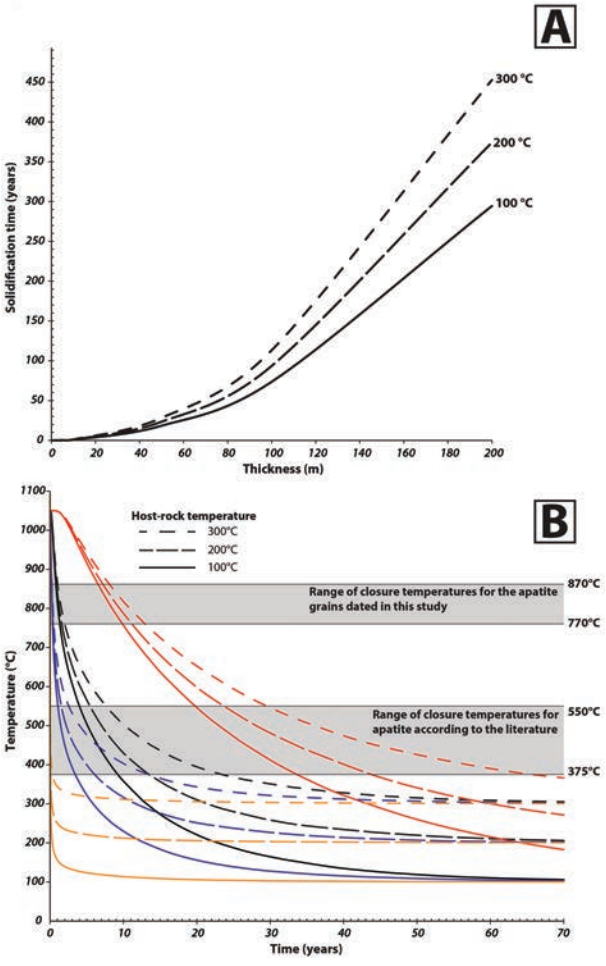

Figure 7. (**a**) Solidification time (time necessary for a complete crystallization of the magma) vs. thickness of doleritic dikes and/or sills for three different host-rock temperatures (100, 200, and 300 °C). Calculation was performed using a crystallization temperature of 1050 °C, a latent heat of 400 kJ/kg, a mean specific heat capacity of 1 kJ/kg/K and a mean thermal diffusivity of 7 $e^{-7}m^2s^{-1}$. (**b**) Cooling temperature of the center of a mafic dike/sill vs. time as a function of different thicknesses and host-rock temperatures. For a mafic rock density of 3000 kg/m^3, the specific heat capacity is 800 J/kg/K and the thermal conductivity is 3.5 $Wm^{-1}K^{-1}$. Host-rock properties correspond to averages for silico-clastic metasediments with a density of 2800 kg/m^3, specific heat capacity of 750 J/kg/K, and thermal conductivity of 2 $Wm^{-1}K^{-1}$. Colors used correspond to a dike or a sill with a thickness of 1 m (orange), 10 m (blue), 20 m (black), and 60 m (red). (Color online.)

cal properties (i.e., thermal diffusivity and specific heat capacity are similar for both lithologies). The models show that the solidification can be considered as instantaneous (<20 years) on the geological timescale for a thickness less than 40 m whatever the host-rock temperatures. When the mafic dikes or sills are thicker, the solidification times remain shorter than 450 years. Consequently, the time necessary for the crystallization of the mafic dikes and sills in this study is negligible.

Therefore, once solidified, we have to constrain the cooling temperature profile of a mafic dike or sill in host rocks for different temperatures (100, 200, and 300 °C). At the end of the solidification process, the temperature of the dolerite and its host rock has slightly changed when compared to the solidus temperature (e.g., 1050 °C) and the initial host-rock temperature. However, in the following model, we consider that those changes are not significant considering the thickness of the mafic dikes and sills sampled in this study. Therefore, we assume a temperature of 1050 °C at the center of the dike or sill for $t = 0$ (Fig. 7b). Models are built with a 2D finite element code using Comsol Multiphysics software to account for the different physical properties between the dolerites and their host rocks, which is not possible with the classical analytical 1D solution. We also calculated the apatite closure temperatures using the Dodson (1973)'s equation with data from Cherniak et al. (1991). We used a radius ranging from 10 to 50 µm and the slowest cooling rate estimated for these dikes (7 °C/yr, Fig. 7b) corresponding to a 60 m wide mafic sill or dike and a host rock temperature of 300 °C.

The closure temperature obtained following these calculations range from 770 to 870 °C, depending on the apatite radius. They are therefore well above the accepted closure range between 375 and 550 °C because of the very fast cooling rate experienced by our samples. Independent of the host-rock temperature, the models show that time range for solidification of a mafic dike or sill less than 60 m thick (maximum thickness of these intrusives) is very rapid (<40 yr). For a doleritic sill such as sample SDO1 (Fig. 1) with a thickness of ca. 60 m, the closure temperature of apatite during post-solidification cooling is reached in less than 20 years. Consequently, apatite appears to be a suitable mineral to date the emplacement age of such small-size mafic bodies that have not been reheated above the closure temperature of apatite.

Apatite dating

We present the results obtained by U-Pb LA-ICP-MS dating on some of the apatite grains described in the previous sections. For all the samples, the results are plotted in Tera-Wasserburg diagrams using Isoplot/Ex (Ludwig 2012). All errors, given in Supplementary[1] Table 5 and the final results in Figures 8 and 9, are provided at 2σ level. In all the diagrams, the red dashed-lines represent the unforced discordias, and the black lines represent the discordias calculated if the initial common Pb value is forced to a $^{207}Pb/^{206}Pb$ value of 0.860 calculated following the Pb evolution model of Stacey and Kramers (1975) for an age of 360 Ma.

In the Saint-Malo group, data obtained from samples MED1 (dolerite dike) and Vi1 (dolerite dike) are discordant with a relatively high proportion of common Pb ($^{207}Pb/^{206}Pb$ values between 0.17–0.37 and 0.25–0.49, respectively). For sample MED1, the data define a lower intercept date of 362 ± 13 Ma (MSWD = 1.4) with a $^{207}Pb/^{206}Pb$ initial value of 0.853 (Fig. 8a). If the discordia is forced to a value of 0.860, we obtain a similar date of 363.0 ± 4.9 Ma (MSWD = 1.3). For sample Vi1, the unforced lower intercept date is 353 ± 17 Ma (MSWD = 1.8, initial $^{207}Pb/^{206}Pb$ value = 0.81). If the discordia is forced to a $^{207}Pb/^{206}Pb$ value of 0.860 (Fig. 8b), the resulting lower intercept date is equivalent within error at 367.2 ± 5.6 Ma (MSWD = 2.1). The weighted average ^{207}Pb-corrected dates (calculated using Stacey and Kramers (1975) terrestrial Pb evolution model) are equivalent within error at 361.2 ± 6.3 Ma (MSWD = 0.62) for MED1 (Fig. 8c) and 363.9 ± 5.2 Ma (MSWD = 1.5) for Vi1 (Fig. 8d). The analyses of sample MF1 (dolerite dike in Martigné-Ferchaud locality) are also discordant with $^{207}Pb/^{206}Pb$ values between 0.25–0.32 (Fig. 8e). The unforced discordia date is 346 ± 17 Ma (MSWD = 2.2, initial $^{207}Pb/^{206}Pb$ value of 0.774). If we calculate the lower intercept date by forcing the discordia to a $^{207}Pb/^{206}Pb$ initial value of 0.860, we end up with a more precise date, comparable within error, at 363.3 ± 3.1 Ma (MSWD = 2.6). The weighted average ^{207}Pb-corrected date is 364 ± 14 Ma (MSWD = 0.041; Fig. 8f).

The analyses of MGX1 (dolerite dike from the Mancellia group) are discordant with various amounts of common Pb ($^{207}Pb/^{206}Pb$ values between 0.25–0.55). They provide a lower intercept date of 364.5 ± 9.7 Ma (MSWD = 0.39; $^{207}Pb/^{206}Pb$ = 0837; Fig. 8g). When the discordia is calculated with an initial $^{207}Pb/^{206}Pb$ value of 0.860, the resulting lower intercept date is similar within error at 361.9 ± 4.2 Ma (MSWD = 0.39). The weighted average ^{207}Pb-corrected date is equivalent within error at 369.7 ± 6.3 Ma (MSWD = 0.101; Fig. 8h).

In the Laval Basin group, the analyses of FOS9 (intermediate volcanic rock), SDO1 (sill of dolerite), and PER1 (sill of dolerite) are also discordant with variable amounts of common Pb. For samples FOS9 and SDO1, the amount of common Pb is high ($^{207}Pb/^{206}Pb$ values between 0.50–0.77 and 0.48–0.57). The lower intercept dates are constrained at 376 ± 12 Ma (MSWD = 2.0; $^{207}Pb/^{206}Pb$ initial value of 0.877) and 344 ± 44 Ma (MSWD = 3.0; $^{207}Pb/^{206}Pb$ initial value of 0.83), respectively, (Figs. 9a and 9b). If the discordias are forced to a $^{207}Pb/^{206}Pb$ initial value of 0.860, the resulting lower intercept dates are 362.0 ± 3.9 (MSWD = 2.5) and 367.1 ± 6.7 Ma (MSWD = 3.1), respectively, while the weighted average ^{207}Pb-corrected dates are similar at 362.6 ± 8.5 Ma (MSWD = 0.21; Fig. 9c) for FOS9 and 363.1 ± 6.7 Ma (MSWD = 1.3; Fig. 9d) for SDO1. LA-ICPMS analyses of apatite grains from sample PER1 show the highest amount of radiogenic Pb ($^{207}Pb/^{206}Pb$ = 0.14–0.29). The lower intercept date is at 354 ± 11 Ma (MSWD = 0.38; $^{207}Pb/^{206}Pb$ initial value of 0.81; Fig. 9e). If we calculate the lower intercept date by forcing the discordia to a value of 0.860, we end up with a date comparable within error of 360.2 ± 3.8 Ma (MSWD = 0.44). The weighted average ^{207}Pb-corrected date is 359.8 ± 4.3 Ma (MSWD = 0.27; Fig. 9f).

Interpretation and discussion

In the Northern and Central domains of the Armorican Massif, especially in the eastern part, the regional metamorphism is of very low grade with maximum temperatures close to 250–300 °C (Donnot et al. 1973; Le Corre 1969, 1975; Gloaguen et al. 2007). Consequently, we can assume that the isotopic systems of the dated apatite grains were not reset after the emplacement of the dikes. In all the samples, the crystals are not hydrothermal but primary and magmatic in origin because they are mainly found within magmatic plagioclase crystals.

In this study, the dolerite dikes are relatively thin with a maximum thickness of 10 m, whereas the dolerite sill is up to ~60 m thick in the Laval Basin. Because of their small thicknesses, numerical models show that the solidification and cooling of these mafic rocks were very fast (Figs. 7a and 7b). Therefore, although the apatite closure temperature is far cooler than the magma temperature, we can safely assume that the dates we obtain in this study can be interpreted as the emplacement ages for the mafic intrusives.

Furthermore, the apatite U-Pb dates obtained for the seven samples are similar within error. In the case of the unforced discordias, the weighted average of the lower intercept dates is 360.3 ± 8.7 Ma (MSWD = 1.9), the ^{207}Pb-corrected mean date is 363.4 ± 5.8 Ma, and the weighted average of the lower intercept dates forced to a $^{207}Pb/^{206}Pb$ initial value of 0.860 is 363.0 ± 1.7 Ma (MSWD = 1.05). Even the most altered samples collected in the Laval Basin (PER1 and FOS9, Fig. 5a) yield a comparable age suggesting that the apatite U-Pb system is not necessarily disturbed when the rocks suffered some degree of hydrothermal alteration and weathering. Therefore, we conclude that all these samples were emplaced ca. 360 Ma ago. The $^{40}Ar/^{39}Ar$ dating of saussuritized plagioclase in a doleritic dike from the North Armorican domain give anomalous dates (330 ± 10 Ma) because of the presence of excess argon (Ruffet et al. 1992). Whereas apatite grains extracted from saussuritized plagioclase were not affected. This demonstrates that apatite should be considered as

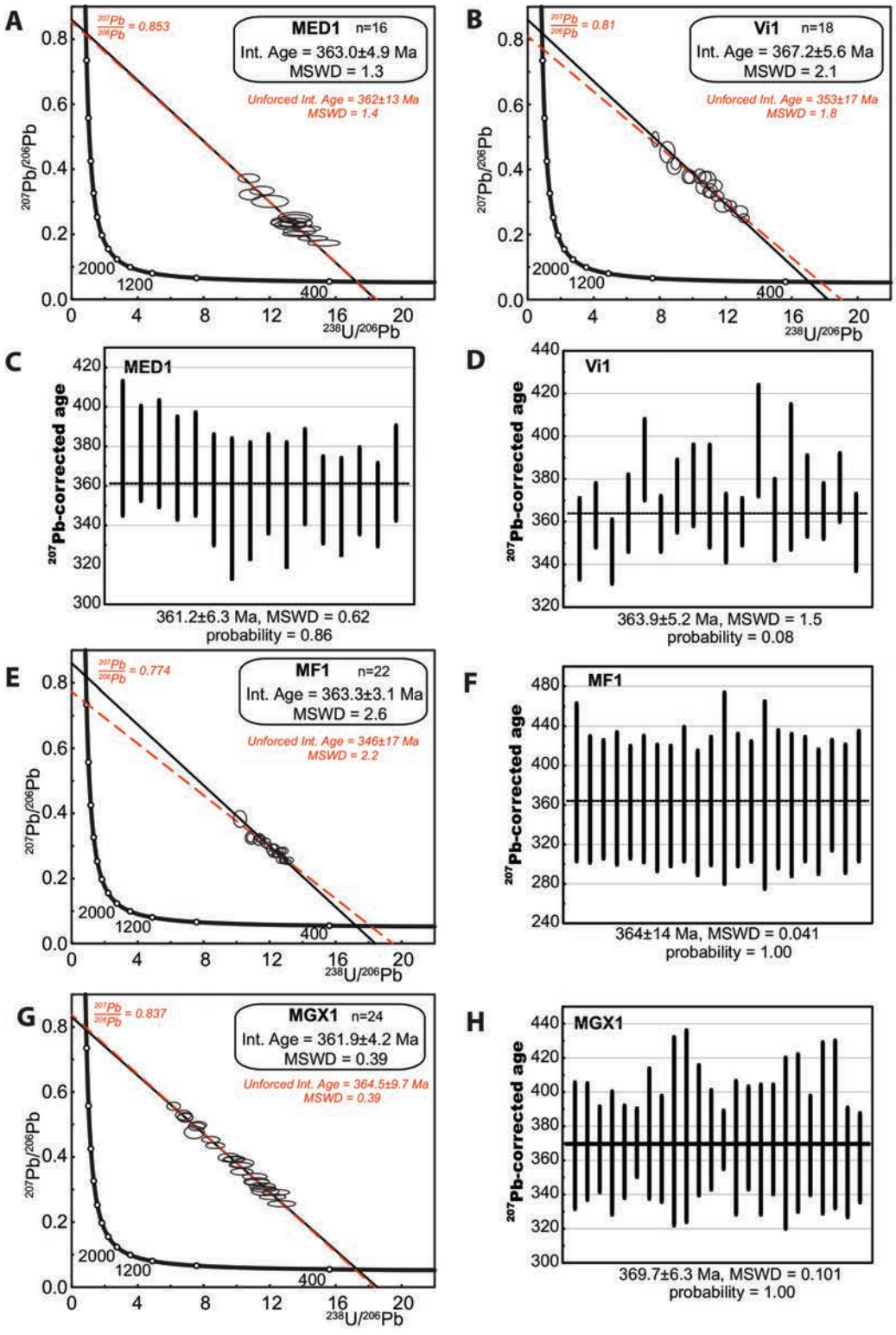

FIGURE 8. Tera-Wasserburg concordia diagram with the corresponding ^{207}Pb-corrected average dates for the dolerites from the Saint-Malo group with samples MED1 and Vi1 (**a**, **b**, **c**, and **d**), the Martigné-Ferchaud group with sample MF1 (**e** and **f**) and the Mancellia group with sample MGX1 (**g** and **h**). The red dashed-lines represent the unforced discordias and the black lines represent the discordias calculated if the initial common Pb value is forced to a $^{207}Pb/^{206}Pb$ value of 0.860 calculated following the Pb evolution model of Stacey and Kramers (1975) for an age of 360 Ma. N corresponds to the number of apatite grains that have been analyzed per sample. Ellipses and errors are reported at 2σ. (Color online.)

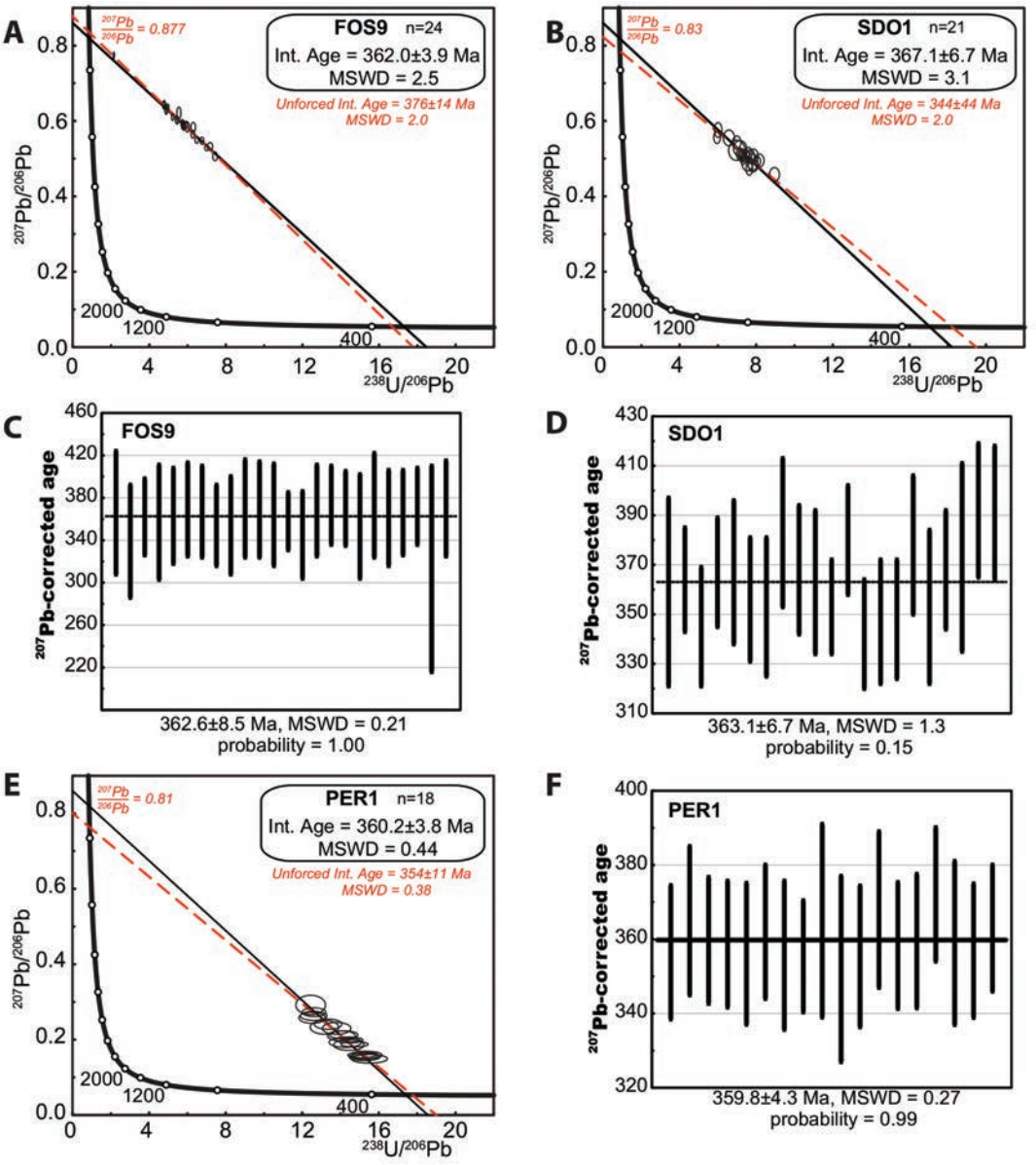

FIGURE 9. Tera-Wasserburg concordia diagram and the corresponding ^{207}Pb-corrected average dates for dolerites from the Basin Laval for samples FOS9, SDO1 (**a**, **b**, **c**, and **d**), and PER1 (**e** and **f**). See legend in the Figure 8. (Color online.)

the best mineral to date mafic dike and sill emplacements even though they underwent propylitic alteration and very low-grade metamorphism. Nevertheless, further studies are necessary to unravel precisely the action of hydrothermal alteration and corrosive hot fluids on the apatite U-Pb geochronometer.

On the scale of our studied area (~160 × 200 km), within the Armorican Massif, we demonstrate that a major mafic magmatic event took place ca. 360 Ma ago, at least in the eastern part of the area. This age is confirmed by field evidence as doleritic fragments of the same nature are found within Early Carboniferous volcanic breccias and conglomerates (Plaine 1976), and because dikes in post-Devonian rocks have never been observed (Le Gall 1999). This mafic magmatic event, characterized by geochemically homogeneous compositions with no significant crustal input, is interpreted as a within-plate type like alkaline continental flood basalts (Fig. 5d). It occurred on a regional scale during a brief episode and appears to be equivalent to the mafic and felsic volcano sedimentary sequences of the Châteaulin Basin in the western part of the Armorican Massif (Pelhate 1994; Caroff et al. 1996). This similarity seems to indicate that this major magmatic event can be generalized to the entire North and Central Armorican domains (ca. 40–45 000 km^2). This event appears coeval with a drastic change in the tectono-sedimentary regime. Indeed, it coincides with the paroxysm of high-pressure/low-temperature metamorphism recorded in the South Armorican domain (eclogite-facies in Champtoceaux complex, Bosse et al.

2000; blueschist-facies in the Groix Island, Bosse et al. 2005) that marks the maximum depth of the presently exposed rocks from the north Gondwanian margin. At the same time, the distributed marine sedimentation becomes localized in the narrow Carboniferous basins (Fig. 1), such as the Laval or Châteaulin Basins, where continental sedimentary deposits occur locally. This period corresponds to the initiation of the collision sensu stricto of the Variscan orogeny in the Armorican Massif (Ballèvre et al. 2014). The origin of this magmatism may result from a melting of enriched lithospheric mantle (see the enrichment of LREE vs. HREE, Fig. 5c). However, additional geochemical investigations (e.g., radiogenic isotopes) are necessary to identify and characterize the geodynamical context and the deep sources responsible for this major mafic magmatic event.

IMPLICATIONS

Mafic rocks are generally difficult to date due to a lack of suitable minerals. Consequently, the dating of apatite by U-Pb LA-ICP-MS appears to be a very useful, quick, and pertinent method to date mafic rocks, which were emplaced in a single injection as dikes or sills. Furthermore, it is now evident that in situ LA-ICP-MS dating, which is a fast and relatively inexpensive technique, can be successfully applied. We can, however, consider that this dating approach may not be suitable to date the emplacement age of large-scale layered mafic/ultramafic complexes or intrusions characterized by repeated injection of magma. However, it might be convenient to perform modeling of other examples of solidification and cooling to check the range of sizes and emplacement contexts for mafic intrusions that could be successfully dated using the U-Pb geochronometer on apatite. Prior to applying this dating technique, it is necessary to study the regional geology, especially the metamorphic, hydrothermal alteration, and/or weathering events that may have modified the chemistry and mineralogy of the studied rocks after their emplacement. Because of the relatively good precision (ca. 5 Ma) obtained in the age determination of the Variscan mafic rocks in this study, U-Pb LA-ICPMS geochronometry of apatite appears to be a key mineral in unraveling the history of mafic magmatism.

ACKNOWLEDGMENTS

This work was supported by the French Geological Survey (BRGM), the region of Brittany, the OSUR, the CNRS-INSU and CESSUR program, and the Ulysses program (PHC). The authors thank the following groups and chief-geologists for allowing access to their granulate quarries: Y. Lemaitre and R. Le Droff from the "Pigeon Carrière" group, L. Seguin from the Eurovia group, the employees from the Hervé group, and the Nivet group. G. Wille (BRGM) is acknowledged for the microprobe analytical analyses. We particularly thank X. Le Coz and Y. Lepagnot from Géosciences Rennes laboratory for the thin sections and rock crushing preparations, respectively. We also address our thanks to the SARM (Nancy) for the whole-rock geochemistry. Constructive reviews by D. Chew, D. Harlov, and an anonymous reviewer have greatly improved the manuscript.

REFERENCES CITED

Aïfa, T., Lefort, J.-P., and Guennoc, P. (1999) Anisotropy of magnetic susceptibility investigations of the St Malo dyke swarm (Brittany, France): emplacement mechanism of doleritic intrusions. Geophysical Journal International, 139, 573–582.

Aldrich, L.T., Tilton, G.R., Davis, G.L., Nicolaysen, L.O., and Patterson, C.C. (1955) Comparison of U–Pb, Pb–Pb, and Rb–Sr ages of Precambrian minerals. In D.R. Derry, Ed., Symposium on Precambrian Correlation and Dating 7, p. 7–13. Geological Association of Canada Proceedings.

Ballèvre, M., Bosse, V., Ducassou, C., and Pitra, P. (2009) Paleozoic history of the Armorican Massif: Models for the tectonic evolution of the suture zones. Comptes Rendus Geosciences, 341, 174–201.

Ballèvre, M., Catalán, J.R.M., López-Carmona, A., Pitra, P., Abati, J., Fernández, R.D., Ducassou, C., Arenas, R., Bosse, V., Castiñeiras, P., and others (2014) Correlation of the nappe stack in the Ibero-Armorican arc across the Bay of Biscay: a joint French–Spanish project. Geological Society, London, Special Publications, 405, 77–113.

Ballouard, C., Boulvais, P., Poujol, M., Gapais, D., Yamato, P., Tartèse, R., and Cuney, M. (2015) Tectonic record, magmatic history and hydrothermal alteration in the Hercynian Guérande leucogranite, Armorican Massif, France. Lithos, 220–223, 1–22.

Baumer, A., Caruba, R., Bizouard, H., and Peckett, A. (1983) Chlorapatite de synthese; substitution et inclusions de Mn, Ce, U et Th en traces. Canadian Mineralogist, 21, 567–573.

Bosse, V., Féraud, G., Ballèvre, M., Peucat, J.-J., and Corsini, M. (2005) Rb–Sr and $^{40}Ar/^{39}Ar$ ages in blueschists from the Ile de Groix (Armorican Massif, France): Implications for closure mechanisms in isotopic systems. Chemical Geology, 220, 21–45.

Bosse, V., Féraud, G., Ruffet, G., Ballèvre, M., Peucat, J.-J., and De Jong, K. (2000) Late Devonian subduction and early-orogenic exhumation of eclogite-facies rocks from the Champtoceaux Complex (Variscan belt, France). Geological Journal, 35, 297–325.

Boudreau, A. (1995) Fluid evolution in layered intrusions: evidence from the chemistry of the halogen-bearing minerals. In J.F.H. Thompson, Ed., Magmas, Fluids and Ore Deposits, 23, pp. 25–46. Geological Society of Canada Short Course.

Brun, J.-P., Guennoc, P., Truffert, C., and Vairon, J. (2001) Cadomian tectonics in northern Brittany: a contribution of 3-D crustal-scale modelling. Tectonophysics, 331, 229–246.

Capdevila, R. (2010) Les granites variques du Massif Armoricain. Bulletin de la Société géologique et minéralogique de Bretagne, (D) 7, 1–52.

Carignan, J., Hild, P., Mevelle, G., Morel, J., and Yeghicheyan, D. (2001) Routine analyses of trace elements in geological samples using flow injection and low pressure on-line liquid chromatography coupled to ICP-MS: A study of Geochemical Reference Materials BR, DR-N, UB-N, AN-G and GH. Geostandards Newsletter, 25, 187–198.

Caroff, M., Le Gal, X., Rolet, J., Cotten, J., and Thonon, P. (1996) Magmatisme tholeiitique continental en contexte orogénique hercynien: l'exemple du volcanisme viséen de Kerroc'h, Massif Armoricain (France). Comptes rendus de l'Académie des sciences de Paris, II, 322, 269–275.

Carrapa, B., DeCelles, P.G., Reiners, P.W., Gehrels, G.E., and Sudo, M. (2009) Apatite triple dating and white mica $^{40}Ar/^{39}Ar$ thermochronology of syntectonic detritus in the Central Andes: A multiphase tectonothermal history. Geology, 37, 407–410.

Chamberlain, K.R., and Bowring, S.A. (2001) Apatite–feldspar U–Pb thermochronometer: a reliable, mid-range (~450°C), diffusion-controlled system. Chemical Geology, 172, 173–200.

Chantraine, J., Autran, A., Cavelier, C., and others. (1996) Geological map of France, 1/1 000 000. BRGM, Orléans.

Chauris, L., Houlgatte, E., Laforêt, C., and Picot, P. (1985) Un district antimonoaurifère à gangue quartzo-carbonatée: Le Semnon (Ille-et-Vilaine, Massif Armoricain, France). Hercynica, 1, 111–119.

Cherniak, D.J., Lanford, W.A., and Ryerson, F.J. (1991) Lead diffusion in apatite and zircon using ion implantation and Rutherford backscattering techniques. Geochimica et Cosmochimica Acta, 55, 1663–1673.

Chew, D.M., Sylvester, P.J., and Tubrett, M.N. (2011) U–Pb and Th–Pb dating of apatite by LA-ICPMS. Chemical Geology, 280, 200–216.

Chew, D.M., Petrus, J.A., and Kamber, B.S. (2014) U–Pb LA-ICPMS dating using accessory mineral standards with variable common Pb. Chemical Geology, 363, 185–199.

Cochrane, R., Spikings, R.A., Chew, D., Wotzlaw, J.-F., Chiaradia, M., Tyrrell, S., Schaltegger, U., and Van der Lelij, R. (2014) High temperature (>350 °C) thermochronology and mechanisms of Pb loss in apatite. Geochimica et Cosmochimica Acta, 127, 39–56.

Cuney, M., Stussi, J.-M., Brouand, M., Dautel, D., Michard, A., Gros, Y., Poncet, D., Bouton, P., Colchen, M., and Vervialle, J.-P. (1993) Géochimie et géochronologie U/Pb des diorites quartziques du Tallud et de Moncoutant: nouveaux arguments pour une extension de la "Ligne Tonalitique Limousine" en Vendée. Comptes Rendus de l'Académie des Sciences de Paris, II, 316, 1383–1390.

Dodson, M.H. (1973) Closure temperature in cooling geochronological and petrological systems. Contributions to Mineralogy and Petrology, 40, 259–274.

Donnot, M., Guigues, J., Lulzac, Y., Magnien, A., Parfenoff, A., and Picot, P. (1973) Un nouveau type de gisement d'europium: la monazite grise à europium en nodules dans les schistes paléozoïques de Bretagne. Mineralium Deposita, 8, 7–18.

Faure, G., and Mensing, T.M. (2005) Isotopes: Principles and applications, xxvii+897 p. Wiley, Hoboken, New Jersey.

Gapais, D., Lagarde, J.L., Le Corre, C., Audren, C., Jégouzo, P., Casas Sainz, A., and Van Den Driessche, J. (1993) La zone de cisaillement de Quiberon: témoin d'extension de la chaine varisque en Bretagne méridionale au Carbonifère. Comptes Rendus de l'Académie des Sciences de Paris, II, 316, 1123–1129.

Gapais, D., Brun, J.-P., Gumiaux, C., Cagnard, F., Ruffet, G., and Veslud, C.L.C.D. (2015) Extensional tectonics in the Hercynian Armorican belt (France). An overview. Bulletin de la Société Géologique de France, 186, 117–129.

Gloaguen, E., Branquet, Y., Boulvais, P., Moelo, Y., Chauvel, J.-J., Chiappero, P.-J., and Marcoux, E. (2007) Palaeozoic oolitic ironstone of the French Armorican Massif: a chemical and structural trap for orogenic base metal–As–Sb–Au mineralisation during Hercynian strike-slip deformation. Mineralium Deposita, 42, 399–422.

Goldoff, B., Webster, J.D., and Harlov, D.E. (2012) Characterization of fluor-chlorapatites by electron probe microanalysis with a focus on time-dependent intensity variation of halogens. American Mineralogist, 97, 1103–1115.

Green, T.H., and Watson, E.B. (1982) Crystallization of apatite in natural magmas under high pressure, hydrous conditions, with particular reference to "Orogenic" rock series. Contributions to Mineralogy and Petrology, 79, 96–105.

Gumiaux, C., Brun, J.P., and Gapais, D. (2004a) Strain removal within the Hercynian Shear Belt of Central Brittany (western France): methodology and tectonic implications. Geological Society, London, Special Publications, 224, 287–305.

Gumiaux, C., Gapais, D., Brun, J.P., Chantraine, J., and Ruffet, G. (2004b) Tectonic history of the Hercynian Armorican Shear belt (Brittany, France). Geodinamica Acta, 17, 289–307.

Harrison, T.M., and Watson, E.B. (1984) The behavior of apatite during crustal anatexis: Equilibrium and kinetic considerations. Geochimica et Cosmochimica Acta, 48, 1467–1477.

Harrison, T.M., Catlos, E.J., and Montel, J.-M. (2002) U-Th-Pb dating of phosphate minerals. Reviews in Mineralogy and Geochemistry, 48, 524–558.

Houlgatte, E., Le Hérissé, A., Pelhate, A., and Rolet, J. (1988) Evolution géodynamique du bassin carbonifère de Laval (Massif Armoricain). Géologie de la France, no. 1, 27–46.

Hughes, C.J. (1973) Spilites, keratophyres and the igneous spectrum. Geological Magazine, 503–527.

Hughes, J.M., and Rakovan, J. (2002) The crystal structure of apatite, $Ca_5(PO_4)_3(F, OH, Cl)$. Reviews in Mineralogy and Geochemistry, 48, 1–12.

Kelley, S. (2002) Excess argon in K–Ar and Ar–Ar geochronology. Chemical Geology, 188, 1–22.

Lahaye, Y., Blais, S., Auvray, B., and Ruffet, G. (1995) Le Volcanisme fissural paleozoique du domaine nord-armoricain. Bulletin de la Societe Geologique de France, 166, 601–612.

Le Corre, C. (1969) Sur une paragenèse à chloritoïde dans les schistes de l'Ordovicien moyen des synclinaux du Sud de Rennes (Massif Armoricain). Bulletin de la Société Géologique Minéralogique de Bretagne, C, 33–44.

——— (1975) Analyse comparee de la cristallinite des micas dans le Brioverien et le Paleozoique centre-armoricains; zoneographie et structure d'un domaine epizonal. Bulletin de la Societe Geologique de France, 7, XVII, 547–553.

Le Gall, J. (1999) Les dolérites et basaltes tholéiitiques varisques du domaine nord-est armoricain. Géologie de la France, 4, 3–26.

Le Gall, J., and Mary, G. (1983) Place et signification du complexe basique de Brée et des autres venues gabbroïques et doléritiques dans l'histoire cadomo-varisque de l'Est du Massif Armoricain. Bulletin de la Société géologique et minéralogique de Bretagne, C-15, 169–180.

Li, C., Arndt, N.T., Tang, Q., and Ripley, E.M. (2015) Trace element indiscrimination diagrams. Lithos, 232, 76–83.

Ludwig, K.R. (2012) User's Manual for Isoplot 3.75. A geochronological toolkit for Microsoft Excel. Berkeley Geochronological Center, 1–75.

Mary, G., and Le Gall, J. (1985) Le Dinantien basal du flanc Nord du Bassin de Laval à Argentré: volcanites basiques et formations volcano-sédimentaires. Hercynica, 1, 155–163.

Matte, P. (1986) La chaîne Varisque parmi les chaînes Paléozoïques péri atlantiques, modèle d'évolution et position des grands blocs continentaux au Permo-Carbonifère. Bulletin de la Société Géologique de France, 8, II, 9–24.

McConnell, D. (1938) A structural investigation of the isomorphism of the apatite group. American Mineralogist, 23, 1–19.

McDowell, F.W., McIntosh, W.C., and Farley, K.A. (2005) A precise ^{40}Ar–^{39}Ar reference age for the Durango apatite (U–Th)/He and fission-track dating standard. Chemical Geology, 214, 249–263.

Oosthuyzen, E.J., and Burger, A.J. (1973) The suitability of apatite as an age indicator by the uranium-lead isotope method. Earth and Planetary Science Letters, 18, 29–36.

Paquette, J.-L., Piro, J.L., Devidal, J.L., Bosse, V., Didier, A., Sanac, S., and Abdelnour, Y. (2014) Sensitivity enhancement in LA-ICP-MS by N_2 addition to carrier gas: Application to radiometric dating of U-Th-bearing minerals. Agilent ICP-MS Journal, 58, 4–5.

Paton, C., Woodhead, J.D., Hellstrom, J.C., Hergt, J.M., Greig, A., and Maas, R. (2010) Improved laser ablation U-Pb zircon geochronology through robust downhole fractionation correction. Geochemistry, Geophysics, Geosystems, 11, Q0AA06.

Pearce, J.A. (1996) A user's guide to basalt discrimination diagrams. In D.A. Wyman, Ed., Trace Element Geochemistry of Volcanic Rocks: Applications for massive sulphide exploration, 12, p. 79–113. Geological Association of Canada, Short Course Notes.

Pelhate, A. (1994) Carboniferous of the Armorican Massif. In J. Chantraine, J. Rolet, D.S. Santallier, A. Piqué, and J.D. Keppie, Eds., Pre-Mesozoic Geology in France and Related Areas, p. 162–168. Springer.

Perroud, H., Auvray, B., Bonhommet, N., Mace, J., and Van Der Voo, R. (1986) Palaeomagnetism and K-Ar dating of lower carboniferous dolerite dykes from northern Brittany. Geophysical Journal of the Royal Astronomical Society, 87, 143–154.

Peucat, J.-J., Auvray, B., Hirbec, Y., and Calvez, J.-Y. (1984) Granites et cisaillements hercyniens dans le Nord du Massif Armoricain; geochronologie Rb-Sr. Bulletin de la Societe Geologique de France, 7, XXVI, 1365–1373.

Piccoli, P.M., and Candela, P.A. (2002) Apatite in igneous systems. Reviews in Mineralogy and Geochemistry, 48, 255–292.

Plaine, J. (1976) La bordure sud du synclinorium Paléozoïque de Laval (Massif armoricain): stratigraphie, volcanisme, structure. Université de Rennes, France.

Pochon, A., Gapais, D., Gloaguen, E., Gumiaux, C., Branquet, Y., Cagnard, F., and Martelet, G. (2016) Antimony deposits in the Variscan Armorican belt, a link with mafic intrusives? Terra Nova, 28, 138–145.

Reiners, P.W., Ehlers, T.A., and Zeitler, P.K. (2005) Past, present, and future of thermochronology. Reviews in Mineralogy and Geochemistry, 58, 1–18.

Rolet, J., Gresselin, F., Jegouzo, P., Ledru, P., and Wyns, R. (1994) Intracontinental Hercynian Events in the Armorican Massif. In J. Chantraine, J. Rolet, D.S. Santallier, A. Piqué, and J.D. Keppie, Eds., Pre-Mesozoic Geology in France and Related Areas, pp. 195–219. Springer.

Ruffet, G., Perroud, H., and Féraud, G. (1992) Palaeomagnetism and $^{40}Ar/^{39}Ar$ dating of the Trégor dolerites (Armorican Massif, France). Tectonophysics, 201, 121–140.

Schoene, B., and Bowring, S.A. (2006) U–Pb systematics of the McClure Mountain syenite: Thermochronological constraints on the age of the $^{40}Ar/^{39}Ar$ standard MMhb. Contributions to Mineralogy and Petrology, 151, 615–630.

——— (2007) Determining accurate temperature–time paths from U–Pb thermochronology: An example from the Kaapvaal craton, southern Africa. Geochimica et Cosmochimica Acta, 71, 165–185.

Spear, F.S., and Pyle, J.M. (2002) Apatite, monazite, and xenotime in metamorphic rocks. Reviews in Mineralogy and Geochemistry, 48, 293–335.

Stacey, J.S., and Kramers, J.D. (1975) Approximation of terrestrial lead isotope evolution by a two-stage model. Earth and Planetary Science Letters, 26, 207–221.

Storey, C.D., Smith, M.P., and Jeffries, T.E. (2007) In situ LA-ICP-MS U–Pb dating of metavolcanics of Norrbotten, Sweden: Records of extended geological histories in complex titanite grains. Chemical Geology, 240, 163–181.

Stormer, J.C., Pierson, M.L., and Tacker, R.C. (1993) Variation of F and Cl X-ray intensity due to anisotropic diffusion in apatite during electron microprobe analysis. American Mineralogist, 78, 641–648.

Sun, S.S., and McDonough, W.F. (1989) Chemical and isotopic systematics of oceanic basalts: implications for mantle composition and processes. Geological Society, London, Special Publications, 42, 313–345.

Tartèse, R., and Boulvais, P. (2010) Differentiation of peraluminous leucogranites "en route" to the surface. Lithos, 114, 353–368.

Tartèse, R., Boulvais, P., Poujol, M., and Vigneresse, J.-L. (2011a) Granite petrogenesis revealed by combined gravimetric and radiometric imaging. Tectonophysics, 501, 98–103.

Tartèse, R., Poujol, M., Ruffet, G., Boulvais, P., Yamato, P., and Košler, J. (2011b) New U-Pb zircon and $^{40}Ar/^{39}Ar$ muscovite age constraints on the emplacement of the Lizio syn-tectonic granite (Armorican Massif, France). Comptes Rendus Geoscience, 343, 443–453.

Thomson, S.N., Gehrels, G.E., Ruiz, J., and Buchwaldt, R. (2012) Routine low-damage apatite U-Pb dating using laser ablation–multicollector–ICPMS. Geochemistry, Geophysics, Geosystems, 13, Q0AA21.

Tilton, G.R., Patterson, C., Brown, H., Inghram, M., Hayden, R., Hess, D., and Larsen, E. (1955) Isotopic composition and distribution of lead, uranium, and thorium in a Precambrian Granite. Geological Society of America Bulletin, 66, 1131–1148.

Turcotte, D.L., and Schubert, G. (1982) Geodynamics: Applications of continuum physics to geological problems, 450 p. Wiley, New York.

Velde, D. (1970) Les filons doleritiques du Nord de la Bretagne. Bulletin de la Societe Geologique de France, 7, XII, 843–855.

Vidal, P. (1980) L'évolution polyorogénique du Massif armoricain; apport de la géochimie isotopique du strontium. Mémoires de la Société Géologique et Minéralogique de Bretagne, 21, 162 p.

Watson, E.B. (1979) Apatite saturation in basic to intermediate magmas. Geophysical Research Letters, 6, 937–940.

——— (1980) Apatite and phosphorus in mantle source regions: An experimental study of apatite/melt equilibria at pressures to 25 kbar. Earth and Planetary Science Letters, 51, 322–335.

Webster, J.D., and Piccoli, P.M. (2015) Magmatic Apatite: A powerful, yet deceptive, mineral. Elements, 11, 177–182.

Whitney, D.L., and Evans, B.W. (2010) Abbreviations for names of rock-forming minerals. American Mineralogist, 95, 185–187.

Winchester, J.A., and Floyd, P.A. (1977) Geochemical discrimination of different magma series and their differentiation products using immobile elements. Chemical Geology, 20, 325–343.

MANUSCRIPT RECEIVED FEBRUARY 25, 2016
MANUSCRIPT ACCEPTED JUNE 27, 2016
MANUSCRIPT HANDLED BY DANIEL HARLOV

Supporting information for:

U-Pb LA-ICP-MS dating of apatite in mafic rocks: evidence for a major magmatic event at the Devonian-Carboniferous boundary in the Armorican Massif (France)

Anthony Pochon[1], Marc Poujol[1], Eric Gloaguen[2, 3], Yannick Branquet[1, 2], Florence Cagnard[2,3], Charles Gumiaux[2], Denis Gapais[1]

[1] *Géosciences Rennes, UMR 6118, Université de Rennes 1, Campus de Beaulieu, 35042 Rennes Cedex*

[2] *Institut des Sciences de la Terre d'Orléans, UMR 7327, Université d'Orléans, Campus Géosciences, 1A rue de la Férollerie, 45071 Orléans Cedex 2*

[3] *Bureau de Recherche Géologique et Minière (BRGM), UMR 7327, 3 avenue Claude-Guillemin, BP 36009, 45060 Orléans Cedex 02*

Supporting Information

Table 1. Operating conditions for the LA-ICP-MS equipment

	U-Pb apatite analyses
Laboratory & Sample Preparation	
Laboratory name	Géosciences Rennes, UMR CNRS 6118, Rennes, France
Sample type/mineral	Magmatic apatite
Sample preparation	Conventional mineral separation, 1 inch resin mount, 1µm polish to finish
Imaging	CL: RELION CL instrument, Olympus Microscope BX51WI, Leica Color Camera DFC 420C
Laser ablation system	
Make, Model & type	ESI NWR193UC, Excimer
Ablation cell	ESI NWR TwoVol2
Laser wavelength	193 nm
Pulse width	< 5 ns
Fluence	6.5 J/cm-2
Repetition rate	5 Hz
Spot size	50 µm (round spot) or 70x30 µm (rotational XY shutter)
Sampling mode / pattern	Single spot
Carrier gas	100% He, Ar make-up gas and N2 (3 ml/mn) combined using in-house smoothing device
Background collection	20 seconds
Ablation duration	60 seconds
Wash-out delay	15 seconds
Cell carrier gas flow (He)	0.75 l/min
ICP-MS Instrument	
Make, Model & type	Agilent 7700x, Q-ICP-MS
Sample introduction	Via conventional tubing
RF power	1350W
Sampler, skimmer cones	Ni
Extraction lenses	X type
Make-up gas flow (Ar)	0.87 l/min
Detection system	Single collector secondary electron multiplier
Data acquisition protocol	Time-resolved analysis
Scanning mode	Peak hopping, one point per peak
Detector mode	Pulse counting, dead time correction applied, and analog mode when signal intensity > ~ 10^6 cps
Masses measured	^{43}Ca, ^{204}(Hg + Pb), ^{206}Pb, ^{207}Pb, ^{208}Pb, ^{232}Th, ^{238}U
Integration time per peak	10-30 ms
Sensitivity / Efficiency	28000 cps/ppm Pb (50µm, 10Hz)
Dwell time per isotope	5-70 ms depending on the masses
Data Processing	
Gas blank	20 seconds on-peak
Calibration strategy	Madagascar apatite used as primary reference material, Durango and McClure apatites used as secondary reference material (quality control)
Reference Material info	Madagascar (Thomson et al. 2012) Durango (McDowell et al. 2005) McClure (Schoene and Bowring 2006)
Data processing package used	Iolite (Paton et al. 2010), VizualAge_UcomPbine (Chew et al. 2014)
Quality control / Validation	Durango: Weighted average ^{207}Pb corrected age = 32.22 ± 0.52 Ma (MSWD = 0.69; probability=0.93) McClure: Weighted average ^{207}Pb corrected age = 526.4 ± 3.3 Ma (MSWD = 0.57; probability = 0.98)

Table 2. Major elements from studied rock samples.

Sample	**MED1**	**Vi1**	**SDO1**	**PER1**[a]	**FOS9**	**MF1**	**MGX1**
Facies	**Dolerite**	**Dolerite**	**Dolerite**	**Dolerite**	**Andesite**	**Dolerite**	**Dolerite**
SiO2	47.43	43.96	50.91	42.32	51.82	46.30	54.74
Al2O3	13.26	15.19	13.92	11.75	20.23	15.58	12.42
Fe2O3	14.413	15	12.707	12.86	12.40	14.24	14.05
MnO	0.20	0.20	0.15	0.11	0.18	0.19	0.26
MgO	5.51	5.95	3.43	11.15	3.53	5.99	2.00
CaO	9.22	7.53	6.63	6.04	0.64	7.58	5.31
Na2O	2.84	2.99	2.67	1.45	0.04	2.46	3.61
K2O	0.56	0.99	1.83	0.1	1.94	0.99	1.85
TiO2	3.56	3.38	3.10	2.58	1.81	2.81	1.87
P2O5	0.46	0.43	0.74	0.38	0.47	0.28	0.90
PF	1.35	3.50	2.95	11.6	8.22	2.84	2.05
Total	98.79	99.11	99.03	100.34	101.26	99.27	99.05

Notes: [a] The chemical composition of PER1 sample were performed by Le Gall (1999)

Table 3. Trace elements and REE from studied rock samples.

Sample	MED1	Vi1	SDO1	PER1	FOS9	MF1	MGX1
As	bdl	2.369	bdl	-	36.39	bdl	bdl
Ba	123.4	254.6	479.1	47	442.9	457.7	413.4
Be	1.54	1.609	2.326	-	6.587	1.169	3.339
Bi	bdl	bdl	bdl	-	bdl	bdl	bdl
Cd	0.286	0.233	0.421	-	0.411	0.296	1.499
Co	41.34	44.03	28.92	69	27.01	47.04	15.36
Cr	118.2	69.54	19.45	384	55.5	50	bdl
Cs	1.572	3.426	0.676	-	3.294	8.876	4.24
Cu	48.65	26.85	18.53	57	30.12	31.3	22.12
Ga	23.74	22.34	27.48	-	29.19	23.2	31.66
Ge	1.766	1.634	1.534	-	1.309	1.512	2.08
Hf	6.43	5.673	11.31	-	8.844	4.644	32.32
In	0.139	0.13	0.153	-	bdl	0.14	0.228
Mo	1.364	1.543	2.142	-	1.917	bdl	3.85
Nb	26.27	22.29	34.69	0	22.56	13.73	58.18
Ni	60.46	54.86	23.19	345	52.99	65.33	bdl
Pb	2.2269	1.9958	9.0967	-	9.4729	2.4961	8.926
Rb	13	43.54	41.94	bdl	58.25	56.89	42.94
Sc	32.34	24.09	21.03	0	23.48	28.24	28.8
Sb	bdl	0.251	bdl	-	4.723	bdl	bdl
Sn	2.96	2.536	3.331	-	3.446	2.302	6.048
Sr	307.9	318.6	281.1	222	48.66	455.1	234.1
Ta	2.087	1.716	2.638	-	1.746	1.114	4.166
Th	2.759	1.701	8.165	bdl	7.839	1.673	6.246
U	0.708	0.475	1.812	-	3.808	0.406	2.084
V	343.1	215.1	176.7	226	134.5	220.9	38.43
W	0.6	0.474	0.746	-	16.67	bdl	0.993
Y	37.32	34.47	50.66	25.17	55.81	32.81	89.84
Zn	142.4	132.7	165.9	bdl	195.8	161.9	251.4
Zr	267.6	239.4	403.2	bdl	351.6	166	1489
La	24.42	20.41	43.2	14.17	33.86	14.97	55.23
Ce	53.73	45.1	97.35	35.05	71.49	32.7	123.8
Pr	7.519	6.354	12.71	-	9.641	4.796	18.26
Nd	33.25	28.6	55.22	21.71	40.88	21.94	82.27
Sm	8.377	7.289	13.21	5.84	9.448	5.973	20.66
Eu	2.73	2.611	3.788	1.99	2.571	2.036	6.989
Gd	8.138	7.158	12	5.75	9.412	6.256	19.55
Tb	1.235	1.113	1.801	-	1.451	1.017	2.965
Dy	7.506	6.875	10.51	4.87	9.139	6.252	17.7
Ho	1.495	1.355	2.031	-	1.999	1.292	3.518
Er	3.682	3.364	5.012	2.03	5.272	3.282	8.922
Tm	0.484	0.46	0.646	-	0.742	0.442	1.216
Yb	3.191	3.014	4.245	1.76	4.982	2.886	7.943
Lu	0.451	0.435	0.602	0.26	0.776	0.436	1.217

Notes: bdl = below detection limit

Table 4. Average electron microprobe analyses and corresponding structural formulas of apatite

	APATITE													
Sample	MF1 (n=20)	σ	FOS9 (n=43)	σ	SDO1 (n=11)	σ	MED1 (n=23)	σ	Vi1 (n=10)	σ	MGX1 (n=17)	σ	PER1 (n=12)	σ
CaO	54.35	0.24	54.26	0.28	54.82	0.33	54.34	0.36	54.20	0.33	54.63	0.97	54.33	0.36
SrO	0.00	0.00	0.00	0.02	0.00	0.00	0.00	0.00	0.00	0.00	0.04	0.02	0.09	0.04
MgO	0.21	0.04	0.19	0.07	0.01	0.03	0.11	0.10	0.07	0.08	0.28	0.12	0.24	0.04
MnO	0.01	0.06	0.01	0.05	0.00	0.00	0.00	0.00	0.00	0.00	0.09	0.03	0.05	0.04
FeO	0.43	0.20	0.55	0.26	0.00	0.00	0.20	0.25	0.12	0.20	0.75	0.66	0.35	0.12
Na_2O	0.00	0.00	0.03	0.07	0.06	0.09	0.06	0.10	0.15	0.08	0.05	0.03	0.02	0.02
P_2O_5	40.96	0.25	41.62	0.24	41.32	0.27	41.37	0.37	41.34	0.14	41.63	0.79	40.86	0.44
SiO_2	0.63	0.12	0.14	0.07	0.23	0.05	0.47	0.21	0.33	0.11	0.31	0.39	0.58	0.14
SO_3	0.00	0.00	0.00	0.01	0.00	0.00	0.00	0.02	0.00	0.00	0.00	0.00	0.00	0.00
F	2.48	0.09	2.94	0.17	3.34	0.14	2.71	0.21	3.12	0.41	2.84	0.29	2.91	0.15
Cl	0.18	0.04	0.16	0.05	0.37	0.04	0.18	0.05	0.09	0.03	0.17	0.03	0.25	0.04
Total	99.25	0.28	99.91	0.38	100.15	0.50	99.45	0.41	99.42	0.39	100.78	0.81	99.68	0.62
O=F	1.04	0.04	1.24	0.07	1.40	0.06	1.14	0.09	1.32	0.17	1.20	0.12	1.23	0.06
O=Cl	0.04	0.01	0.04	0.01	0.08	0.01	0.04	0.01	0.02	0.01	0.04	0.01	0.06	0.01
Total*	98.16	0.29	98.64	0.36	98.67	0.49	98.26	0.39	98.09	0.29	99.54	0.78	98.40	0.59
Structural formula on the basis of a 12.5 oxygen equivalent														
Ca	4.95	0.02	4.93	0.03	5.00	0.02	4.95	0.04	4.95	0.03	4.92	0.05	4.96	0.03
Sr	0.00	0.00	0.00	0.00	0.00	0.00	0.00	0.00	0.00	0.00	0.00	0.00	0.00	0.00
Mg	0.03	0.01	0.02	0.01	0.00	0.00	0.01	0.01	0.01	0.01	0.04	0.02	0.03	0.00
Mn	0.00	0.02	0.04	0.00	0.00	0.00	0.00	0.00	0.00	0.00	0.02	0.01	0.01	0.01
Fe	0.03	0.01	0.04	0.02	0.00	0.00	0.01	0.02	0.01	0.01	0.05	0.05	0.02	0.01
Na	0.00	0.00	0.00	0.01	0.01	0.01	0.01	0.02	0.03	0.01	0.01	0.01	0.00	0.00
P	2.95	0.01	2.99	0.01	2.98	0.01	2.98	0.02	2.98	0.01	2.96	0.03	2.95	0.01
Si	0.05	0.01	0.01	0.01	0.02	0.00	0.04	0.02	0.03	0.01	0.03	0.03	0.05	0.01
S	0.00	0.00	0.00	0.00	0.00	0.00	0.00	0.00	0.00	0.00	0.00	0.00	0.00	0.00
F	0.67	0.02	0.79	0.05	0.90	0.04	0.73	0.06	0.84	0.11	0.76	0.08	0.78	0.04
Cl	0.03	0.01	0.02	0.01	0.05	0.01	0.03	0.01	0.01	0.00	0.02	0.00	0.04	0.01
OH^a	0.30	0.03	0.19	0.05	0.05	0.04	0.24	0.05	0.15	0.11	0.22	0.08	0.18	0.04

Notes: Oxide contents in wt.%, cationic contents in apfu and σ: standard deviation

Table S1. Representative LA-ICP-MS U-Pb apatite data for studied samples

Sample	U (ppm)	Pb (ppm)	$^{238}U/^{206}Pb$	Error (2σ)	$^{207}Pb/^{206}Pb$	Error (2σ)	Final ^{207}Age	Error (2σ)
FOS9								
FOS9_1	2,8	2,0	4,883	0,062	0,6310	0,0110	366	58
FOS9_2	2,8	1,8	5,543	0,085	0,6210	0,0130	339	53
FOS9_3	4,8	2,3	6,748	0,084	0,5478	0,0077	362	36
FOS9_4	4,1	3,0	4,755	0,044	0,6425	0,0075	357	54
FOS9_5	3,6	2,0	5,804	0,059	0,5909	0,0075	363	45
FOS9_6	3,4	2,1	5,438	0,060	0,6031	0,0087	369	44
FOS9_7	3,5	1,8	6,266	0,070	0,5647	0,0087	367	43
FOS9_8	3,9	2,1	5,924	0,061	0,5905	0,0072	354	38
FOS9_9	3,0	2,2	4,773	0,064	0,6431	0,0092	354	46
FOS9_10	2,8	1,6	5,790	0,068	0,5865	0,0089	370	46
FOS9_11	2,9	1,8	5,461	0,060	0,6024	0,0084	369	45
FOS9_12	3,5	2,0	5,727	0,060	0,5937	0,0083	364	48
FOS9_13	4,3	1,9	7,174	0,110	0,5325	0,0085	358	27
FOS9_14	4,5	2,4	6,293	0,094	0,5830	0,0110	345	41
FOS9_15	3,1	1,8	5,754	0,063	0,5873	0,0078	368	43
FOS9_16	3,7	1,9	6,477	0,071	0,5494	0,0072	373	37
FOS9_17	4,3	1,9	6,993	0,077	0,5293	0,0068	370	35
FOS9_18	3,7	2,6	4,968	0,049	0,6357	0,0074	353	49
FOS9_19	3,8	2,4	5,219	0,051	0,6106	0,0075	373	49
FOS9_20	3,4	1,9	5,984	0,090	0,5840	0,0110	361	45
FOS9_21	3,8	2,1	5,770	0,074	0,5904	0,0085	366	40
FOS9_22	3,0	1,2	7,435	0,098	0,5061	0,0097	372	36
FOS9_23	3,4	6,2	2,150	0,023	0,7740	0,0075	313	97
FOS9_24	5,2	3,5	4,888	0,048	0,6284	0,0064	370	45
MED1								
MED1_1	2,7	0,7	10,834	0,552	0,3220	0,0130	379	34
MED1_2	5,1	1,1	13,587	0,646	0,2013	0,0062	376,5	24
MED1_3	5,5	1,2	12,903	0,683	0,2348	0,0099	376,3	27
MED1_4	7,2	1,5	12,887	0,648	0,2380	0,0120	369	26
MED1_5	5,6	1,1	13,228	0,770	0,2281	0,0110	371,1	26
MED1_6	6,0	1,4	12,019	0,910	0,3010	0,0150	358	28
MED1_7	3,7	1,0	10,741	0,531	0,3720	0,0110	348	36
MED1_8	4,0	0,9	13,532	0,732	0,2470	0,0110	352	30
MED1_9	5,2	1,3	13,550	0,845	0,2347	0,0120	361	25
MED1_10	4,1	1,0	11,534	0,599	0,3340	0,0110	350	32
MED1_11	5,7	1,4	13,441	0,650	0,2321	0,0071	364,7	24
MED1_12	8,8	1,8	14,253	0,691	0,2175	0,0067	352,9	22
MED1_13	5,7	1,2	13,550	0,845	0,2520	0,0130	349	25
MED1_14	8,4	1,7	14,620	0,727	0,1878	0,0064	357,5	22
MED1_15	8,2	1,6	15,291	0,795	0,1732	0,0076	350,5	21
MED1_16	5,3	1,1	13,812	0,801	0,2110	0,0120	366,5	24
MF1								
MF1_1	6,1	2,0	10,858	0,190	0,3250	0,0110	383	80
MF1_2	9,2	2,8	12,469	0,200	0,2742	0,0080	365,7	64
MF1_3	7,8	2,4	12,887	0,200	0,2539	0,0067	365,8	60
MF1_4	10,5	3,0	12,821	0,190	0,2573	0,0086	366,7	67
MF1_5	5,6	1,8	11,751	0,240	0,3100	0,0120	362,8	57
MF1_6	4,6	1,4	11,507	0,210	0,3194	0,0094	366	64
MF1_7	6,8	2,0	13,193	0,200	0,2556	0,0076	357	64
MF1_8	6,0	1,9	12,165	0,280	0,2890	0,0140	359	61
MF1_9	5,7	1,7	11,351	0,280	0,3180	0,0130	371	68

MF1_10	7,0	2,0	12,788	0,270	0,2848	0,0091	352	63
MF1_11	4,8	1,5	11,377	0,210	0,3260	0,0100	364	65
MF1_12	6,8	2,2	10,881	0,290	0,3250	0,0160	377	97
MF1_13	8,8	2,6	12,903	0,180	0,2551	0,0072	365	67
MF1_14	7,3	2,1	13,055	0,190	0,2509	0,0064	363,7	61
MF1_15	4,8	1,7	10,204	0,320	0,3830	0,0210	370	95
MF1_16	5,7	1,7	11,891	0,190	0,3007	0,0086	365,8	70
MF1_17	6,2	1,9	12,300	0,230	0,2930	0,0100	360	72
MF1_18	10,1	2,9	12,453	0,260	0,2749	0,0089	366	63
MF1_19	7,1	2,1	12,723	0,210	0,2853	0,0075	353,1	63
MF1_20	7,3	2,2	12,270	0,280	0,2770	0,0100	370	56
MF1_21	8,8	2,6	12,579	0,200	0,2836	0,0082	356,2	65
MF1_22	8,0	2,2	12,723	0,260	0,2590	0,0110	369	66
SDO1								
SDO1_1	3,1	1,4	7,158	0,280	0,5270	0,0170	359	38
SDO1_2	3,2	1,5	7,310	0,150	0,5080	0,0120	364	21
SDO1_3	3,4	1,6	6,983	0,180	0,5430	0,0140	345	24
SDO1_4	3,4	1,5	7,257	0,160	0,5110	0,0120	367	22
SDO1_5	3,1	1,8	6,010	0,160	0,5760	0,0160	367	29
SDO1_6	3,4	1,5	7,704	0,170	0,5060	0,0150	356	25
SDO1_7	3,2	1,4	7,587	0,160	0,5130	0,0140	353	28
SDO1_8	3,8	1,6	7,541	0,230	0,4870	0,0160	383	30
SDO1_9	3,5	1,5	7,440	0,170	0,5070	0,0140	368	26
SDO1_10	3,4	1,4	7,813	0,220	0,4910	0,0180	363	29
SDO1_11	5,5	2,1	8,078	0,120	0,4930	0,0100	353	19
SDO1_12	3,3	1,5	7,326	0,130	0,4990	0,0120	380	22
SDO1_13	4,0	1,6	7,868	0,190	0,5070	0,0150	342	22
SDO1_14	3,4	1,2	8,953	0,210	0,4580	0,0150	347	25
SDO1_15	3,6	1,5	8,163	0,200	0,4950	0,0140	348	24
SDO1_16	3,4	1,6	7,153	0,150	0,5120	0,0130	378	28
SDO1_17	3,2	1,6	6,575	0,240	0,5550	0,0170	353	31
SDO1_18	3,1	1,2	7,837	0,210	0,4820	0,0140	368	24
SDO1_19	2,6	1,2	6,988	0,35	0,5220	0,0220	373	38
SDO1_20	3,0	1,2	7,639	0,14	0,4730	0,0140	392	27
SDO1_21	4,0	2,3	5,952	0,14	0,5560	0,0130	391	27
Vi1								
Vi1_1	3,1	0,9	10,905	0,404	0,3680	0,0210	352	19
Vi1_2	3,7	1,0	10,977	0,301	0,3300	0,0130	363	15
Vi1_3	4,8	1,5	10,730	0,322	0,3760	0,0150	346	15
Vi1_4	3,1	1,0	10,428	0,294	0,3790	0,0180	364	18
Vi1_5	2,8	1,0	8,961	0,217	0,4180	0,0150	389	19
Vi1_6	3,2	0,8	11,494	0,317	0,3180	0,0130	359	13
Vi1_7	3,4	1,4	9,728	0,303	0,3790	0,0180	372	17
Vi1_8	3,4	1,0	9,862	0,321	0,3770	0,0160	377	19
Vi1_9	3,8	2,1	7,734	0,179	0,4930	0,0190	372	24
Vi1_10	4,4	1,0	12,837	0,412	0,2700	0,0150	357	16
Vi1_11	4,5	1,0	13,106	0,258	0,2500	0,0110	360	11
Vi1_12	3,4	1,3	8,873	0,354	0,4110	0,0210	398	26
Vi1_13	4,1	1,1	11,086	0,320	0,3340	0,0180	361	19
Vi1_14	3,5	1,4	8,460	0,372	0,4530	0,0270	381	34
Vi1_15	5,5	1,4	11,834	0,420	0,2900	0,0170	372	19
Vi1_16	3,0	0,7	12,285	0,302	0,2880	0,0130	365	13
Vi1_17	5,1	1,5	10,560	0,290	0,3460	0,0170	376	16
Vi1_18	6,7	2,2	11,312	0,384	0,3500	0,0150	355	18
PER 1								

PER1_1	5,7	1,6	14,164	0,602	0,2128	0,0087	357	18
PER1_2	6,9	2,7	13,158	0,606	0,2330	0,0150	365	20
PER1_3	7,0	1,5	15,106	0,593	0,1590	0,0056	360	17
PER1_4	7,7	1,7	15,244	0,651	0,1535	0,0073	359	17
PER1_5	7,4	1,7	15,385	0,639	0,1588	0,0082	356	19
PER1_6	6,4	1,4	14,430	0,645	0,1860	0,0120	362	18
PER1_7	6,3	1,5	14,728	0,586	0,1878	0,0057	356	20
PER1_8	6,3	2,1	13,793	0,609	0,2300	0,0130	355	15
PER1_9	3,9	1,2	12,610	0,509	0,2730	0,0094	365	26
PER1_10	5,1	1,4	12,438	0,634	0,2920	0,0210	352	25
PER1_11	4,3	0,9	14,451	0,585	0,1991	0,0064	355	19
PER1_12	5,3	2,1	12,594	0,571	0,2630	0,0098	368	21
PER1_13	6,7	1,4	15,198	0,624	0,1583	0,0084	358	17
PER1_14	5,9	2,6	13,351	0,588	0,2410	0,0110	360	18
PER1_15	5,0	1,5	12,516	0,564	0,2580	0,0120	372	18
PER1_16	5,1	1,3	14,045	0,592	0,2100	0,0110	359	22
PER1_17	8,1	1,8	15,504	0,769	0,1493	0,0094	357	18
PER1_18	5,3	1,5	14,245	0,690	0,1930	0,0110	363	17
MGX1								
MGX1_1	3,4	0,8	9,814	0,530	0,3921	0,0071	369	37
MGX1_2	2,4	1,0	6,770	0,394	0,5290	0,0120	371	34
MGX1_3	4,4	0,9	11,198	0,627	0,3240	0,0099	366	25
MGX1_4	4,1	1,0	10,225	0,554	0,3750	0,0068	364	36
MGX1_5	4,9	1,0	11,236	0,606	0,3230	0,0074	365	27
MGX1_6	4,0	0,7	11,723	0,687	0,2940	0,0100	370	20
MGX1_7	2,8	0,6	10,309	0,553	0,3548	0,0082	376	38
MGX1_8	4,2	0,7	12,180	0,653	0,2774	0,0070	367	31
MGX1_9	2,4	1,2	6,180	0,336	0,5560	0,0100	377	55
MGX1_10	2,2	0,9	6,887	0,375	0,5220	0,0100	380	56
MGX1_11	4,1	1,3	8,703	0,470	0,4352	0,0074	378	38
MGX1_12	2,8	0,7	9,542	0,537	0,3980	0,0110	372	29
MGX1_13	3,6	1,3	7,429	0,491	0,4760	0,0160	372	17
MGX1_14	4,3	1,0	9,872	0,526	0,3938	0,0072	367	39
MGX1_15	4,7	0,8	11,628	0,635	0,3016	0,0074	373	30
MGX1_16	3,2	0,6	11,099	0,604	0,3397	0,0080	366	38
MGX1_17	2,8	0,5	11,547	0,640	0,3103	0,0083	372	32
MGX1_18	2,9	1,1	7,669	0,412	0,4984	0,0087	370	50
MGX1_19	2,8	1,0	8,432	0,455	0,4533	0,0077	376	46
MGX1_20	3,4	0,5	12,723	0,696	0,2563	0,0075	369	29
MGX1_21	2,2	0,8	7,576	0,413	0,4936	0,0099	379	50
MGX1_22	2,0	0,9	6,887	0,379	0,5220	0,0120	381	49
MGX1_23	3,5	0,5	12,376	0,674	0,2913	0,0074	359	32
MGX1_24	3,8	0,9	10,320	0,586	0,3810	0,0110	362	26

Données complémentaires : Datation U-Pb sur zircon et apatite d'un magmatisme anté-varisque

Lors de l'échantillonnage du magmatisme mafique du Massif Armoricain, nous nous sommes intéressés à d'autres objets magmatiques afin de vérifier s'il y avait d'autres évidences de magmatisme à 360 Ma. Ainsi, hormis les dykes de dolérites, nous avons également échantillonnés l'intrusion de diorite de Louvigné-de-Bais, le granite de Craon et le complexe de basaltique de La Meilleraie (Fig. 3.1). La diorite quartzique de Louvigné-de-Bais est exploitée par le groupe Pigeon Carrières pour les granulats et a fait l'objet d'un stage de Master 2 réalisé par Victorien Bastien, et encadré par Yannick Branquet, Philippe Boulvais et moi-même. L'objectif principal de ce stage était la réalisation d'une carte géologique précise de la carrière, la caractérisation du magmatisme et l'altération associée. La diorite de Louvigné-de-Bais, située dans le domaine Centre Armoricain, est constituée de petits corps intrusifs de faible extension (500 m) au sein du Briovérien. Ces corps sont fréquemment recoupés par un réseau de dykes de dolérite dont l'âge est toujours inconnu, en raison d'un manque de minéraux datables au sein de ces dykes. Cependant, comme proposé dans l'article #2, il est possible d'envisager un âge similaire au magmatisme mafique à 360 Ma. Cette diorite fait donc l'objet d'une étude géochronologique afin de vérifier si un magmatisme dit « acide » a également eu lieu à 360 Ma.

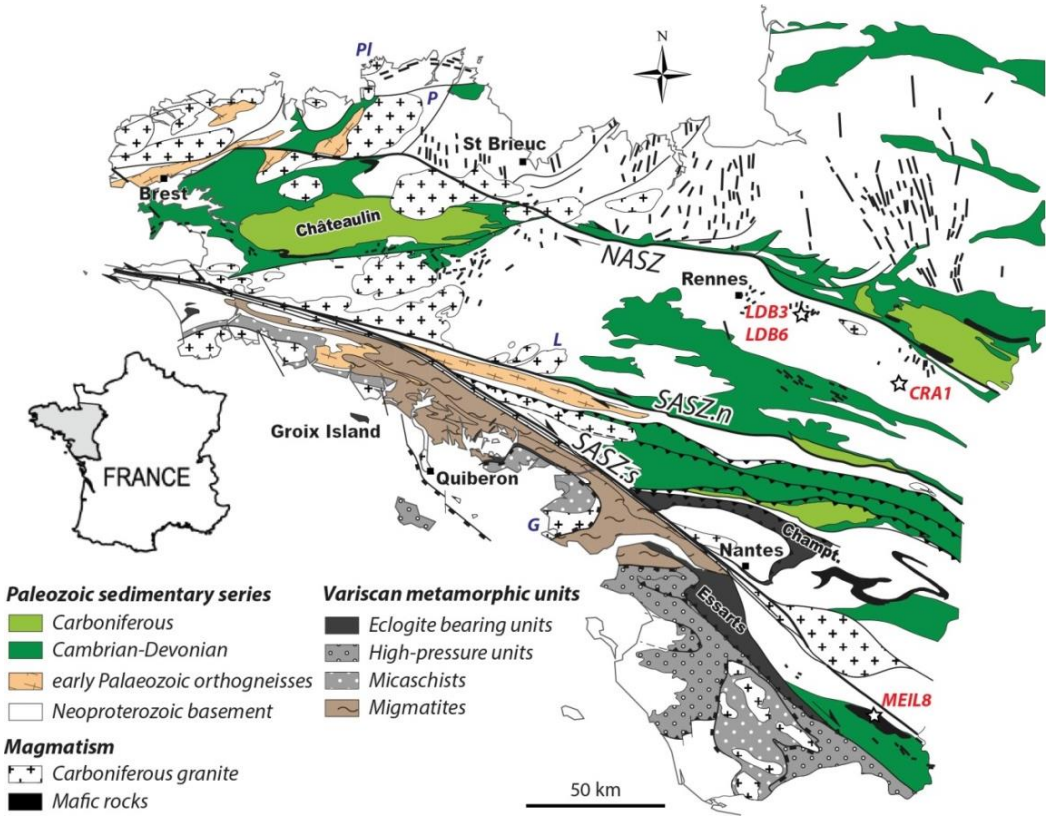

Figure 3.1 Carte géologique simplifiée du Massif Armoricain représentant la localisation des échantillons prélevés pour analyses U-Pb.

Le granite de Craon est situé dans le domaine Centre Armoricain au cœur du petit district aurifère de Château-Gontier, exploité à l'époque gallo-romaine (Vasquez-Lopez 1985a, 1985b). Il a été principalement mis en évidence par une étude gravimétrique et par l'observation d'un métamorphisme de contact, même si ce dernier est relativement limité (Chèvremont 1983; Guerangé et al. 1984). La présence de cette intrusion, dont le toit est estimé au moins à 400 m de profondeur, est attestée par une apophyse de ce granite affleurant (Vernhet 2010). Cette apophyse est constituée d'un monzogranite subleucocrate modérément alumineux présentant des teneurs relativement élevées en Li, Be et Sn (Chèvremont 1983). Deux autres intrusions de granites subaffleurantes ont également été mises en évidence dans ce secteur à travers la reconnaissance (i) d'anomalies gravimétriques légères (Guérangé et al. 1984), (ii) de valeurs anomales de l'indice de cristallinité de l'illite dans l'encaissant (Chèvremont et al. 1983) et (iii) d'anomalies alluvionnaires et géochimiques (B, Be, K, As, W, Au) (Guigues 1984). Le fait qu'il soit situé à l'aplomb d'un district aurifère et qu'il ait été daté par la méthode Rb-Sr à 320 Ma (Leutwein 1968), nous a conduits à dater de nouveau cette apophyse de granite par une méthode plus récente (U-Pb par LA-ICP-MS). Enfin, le complexe basaltique de la Meilleraie constitue l'épanchement volcanique mafique affleurant le plus important (1 km d'épaisseur) du Massif Armoricain. Il est situé au sein du domaine Sud Armoricain et fait donc partie de la plaque Gondwana en opposition au domaine Centre Armoricain qui appartient à la micro-plaque Armorica (e.g. Ballèvre et al. 2014). Ce complexe apparait donc comme une cible de choix pour vérifier si le magmatisme mafique à 360 Ma, qui affecte les domaines Nord et Centre Armoricain, est également généralisé au sud du cisaillement Sud-Armoricain (CSA). Nous avons ainsi sélectionné un faciès gabbroïque intrusif au sein du complexe basaltique (MEIL8).

Des datations U-Pb sur grains séparés de zircon ont été réalisées pour la diorite quartzique de Louvigné-de-Bais et le granite de Craon, et sur grains d'apatite pour le gabbro de la Meilleraie. Les conditions analytiques utilisées pour la méthode U-Pb sur zircon par LA-ICP-MS sont identiques à celles décrites par Ballouard et al. (2015) et celles utilisées pour l'apatite sont décrites au sein de l'article #2. Les résultats sont reportés dans la Table 3.1, la Table 3.2 et la Figure 3.2.

Concernant la diorite quartzique de Louvigné-de-Bais, les dates $^{207}Pb/^{206}Pb$ similaires de l'échantillon LDB3 varient entre 2409 ± 19 Ma et 466 ± 25 Ma. Un groupe d'analyses (n = 9) en position concordantes à sub-concordantes permet de calculer une date concordia à 469.5 ± 3.6 Ma (MSWD = 1.5), interprétée comme l'âge de cristallisation de cet échantillon de diorite quartzique. Les dates $^{207}Pb/^{206}Pb$ de l'échantillon LDB6 sont relativement similaire à celles de l'échantillon LDB3 (hormis la date archéenne) et varient entre 738 ± 24 Ma et 468 ± 25 Ma. Un groupe de 16 analyses concordantes à sub-concordantes permet le calcul d'une date concordia à 472.8 ± 2.6 Ma

(MSWD = 1.08), interprétée comme l'âge de cristallisation de cet échantillon. Les analyses donnant un âge plus jeune sont probablement liées à des pertes en Pb et/ou dues à une contamination en Pb commun tandis que les analyses affichant un âge plus vieux sont interprétées comme de l'héritage. Ainsi, dans la marge d'erreur, ces deux échantillons présentent le même âge et indiquent donc que la diorite quartzique de Louvigné-de-Bais se met en place au sein du Briovérien à *ca*. 470 Ma au cours de l'Ordovicien moyen. Elle est donc totalement déconnectées du magmatisme mafique à 360 Ma.

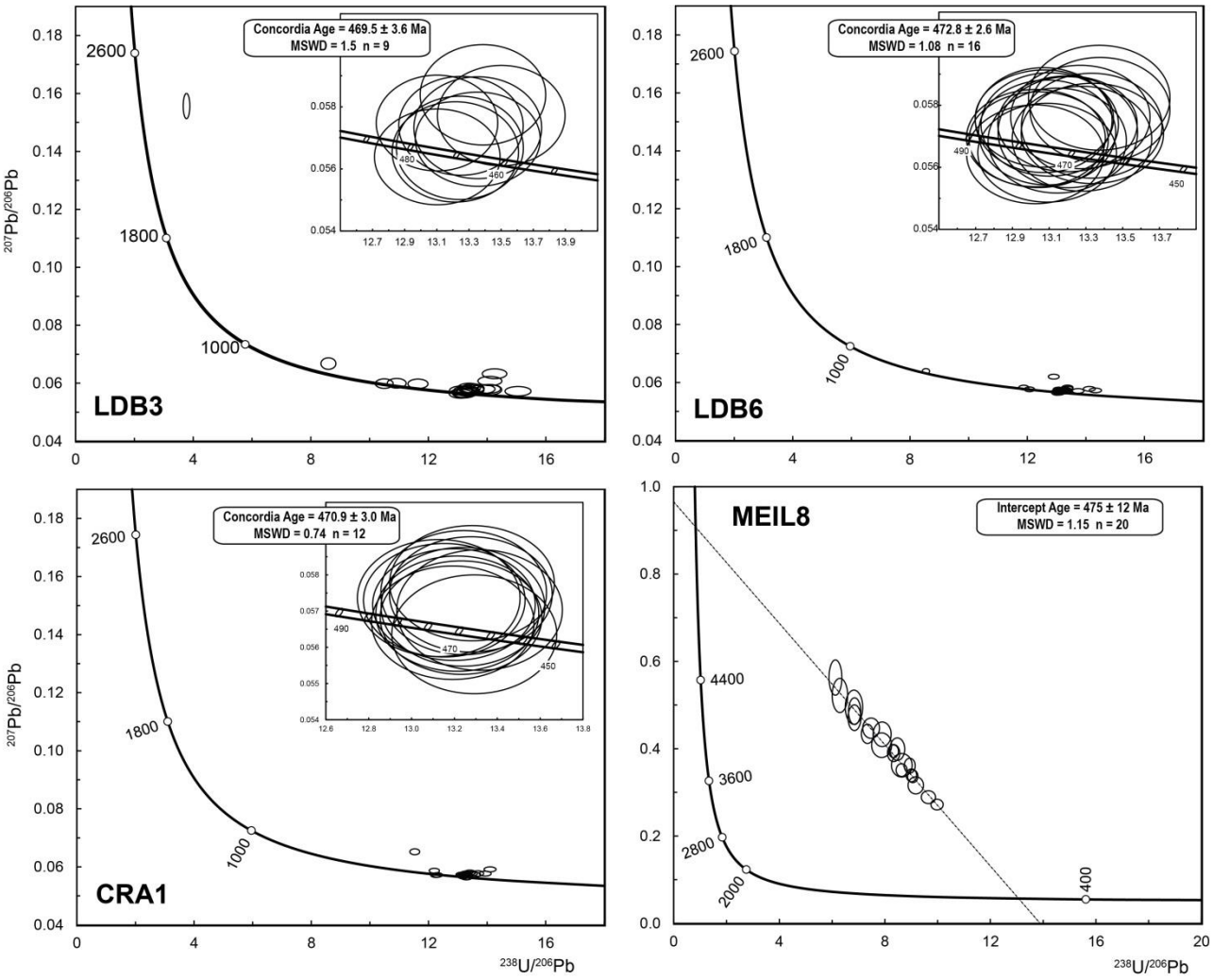

Figure 3.2 Diagrammes Tera-Wasserburg reportant les analyses U-Pb réalisées sur les grains de zircon des échantillons LDB3 et LDB6 (Louvigné-de-Bais), CRA1 (Craon) et les grains d'apatite de l'échantillon MEIL8 (La Melleraie). Les ellipses sont reportées à 2σ.

Les dates $^{207}Pb/^{206}Pb$ de l'échantillon du granite de Craon (CRA1) sont très similaires aux échantillons LDB3 et LDB6 et varient entre 781 ± 27 Ma et 466 ± 26 Ma. Un groupe d'analyses (n = 12) en position concordantes à sub-concordantes permet de calculer une date concordia à 470.9 ± 3.0 Ma (MSWD = 0.74), interprétée comme l'âge de cristallisation de cet échantillon d'apophyse de granite. Comme décrit précédemment, les ellipses présentant un âge apparent plus jeune sont interprétées comme liées à des pertes en Pb et/ou dues à une contamination en Pb commun, tandis

que les ellipses affichant un âge plus vieux sont interprétées comme étant de l'héritage. Ainsi, l'apophyse du granite de Craon, interprétée comme l'âge du granite sub-affleurant, présente le même âge Ordovicien moyen que la diorite quartzique de Louvigné-de-Bais, soit notablement plus vieux que l'âge obtenu précédemment par méthode Rb-Sr par (Leutwein 1968). Aucune minéralisation aurifère n'est connue au sein du Massif Armoricain à l'Ordovicien. Par conséquent, bien que l'âge des minéralisations aurifères du district de Château-Gontier soit inconnu, il est probable que la mise en place de ce granite soit également totalement déconnectée de l'histoire hydrothermale liée à ces minéralisations. Il serait donc intéressant par la suite de s'intéresser à la datation de ces minéralisations afin de confirmer ou d'infirmer cette hypothèse. Ce district ne constituant pas une cible prioritaire au cours de cette thèse, et puisqu'aucuns minéraux datables n'ont été observés au sein du quartz aurifère, ce travail n'a donc pas pu être effectué.

Le gabbro de la Meilleraie a été daté par la méthode U-Pb sur apatite puisqu'il ne contenait pas de zircons, ce qui est relativement fréquent au sein des roches mafiques très pauvres en SiO_2. Les analyses de l'échantillon MEIL8 sont relativement discordantes avec une quantité variable de Pb commun. Les valeurs $^{207}Pb/^{206}Pb$ s'étalent entre 0.289 et 0.563 et permettent de tracer une discordia et de calculer une date « Intercept » inférieur à 475 ± 12 Ma, interprétée comme l'âge de cristallisation de l'apatite et par conséquent l'âge de cristallisation du gabbro. Bien que la marge d'erreur soit relativement grande, cet âge semble être également en accord avec les âges (Ordovicien moyen) obtenus à Louvigné-de-Bais et à Craon. Le gabbro étant intrusif au sein des coulées basaltiques, cet âge est donc interprété comme l'âge maximum du complexe basaltique de La Meilleraie. Cependant, les coulées basaltiques se trouvent au cœur d'un synforme (appelé synclinorium de Chantonnay) d'âge indifférencié entre l'Ordovicien et le Dévonien. L'âge des différentes séries est difficile à déterminer dans cette région, mais des fossiles dévoniens ont été observés sur le flanc Nord du synforme (Wyns et al. 1988), soit en dessous des coulées volcaniques ordoviciennes. Ainsi, le complexe de La Meilleraie repose sur des sédiments dévoniens, au moins 150 Ma plus jeunes. Ceci questionne sur la géométrie de ce synforme et nécessite donc son réexamen stratigraphique et structural.

Enfin, il apparait à travers l'acquisition de nouvelles données géochronologiques qu'il existe un magmatisme mafique à intermédiaire d'âge Ordovicien moyen au sein du domaine Centre Armoricain et un volcanisme important au sein du domaine Sud Armoricain. Cette histoire est antérieure à l'histoire magmatique dévonienne. Nous préciserons que ce magmatisme est totalement déconnecté de l'histoire hydrothermale à Sb-Au et ne sera donc pas évoqué dans la suite de ce manuscrit Néanmoins il serait intéressant de poursuivre les investigations de ce magmatisme ordovicien : il était effectivement jusqu'alors insoupçonnés au sein du domaine Centre Armoricain

Son étude permettrait d'apporter de nouveaux éléments de compréhension sur l'évolution géodynamique du Massif Armoricain.

Table 3.1 Données U-Pb par LA-ICP-MS sur zircon pour la diorite quartzique de Louvigné-de-Bais et le granite de Craon

Sample	$^{207}Pb/^{206}Pb$	Error (1σ)	$^{207}Pb/^{235}U$	Error (1σ)	$^{206}Pb/^{238}U$	Error (1σ)	rho	$^{207}Pb/^{206}Pb$	Error (1σ)	$^{206}Pb/^{238}U$	Error (1σ)	$^{207}Pb/^{235}U$	Error (1σ)	Pb (ppm)	U (ppm)	Th/U
LDB3 (Diorite)																
LDB3_5	0.05987	0.00067	0.78615	0.00996	0.09524	0.00112	0.93	599	24.03	586.4	6.61	589	5.66	31.0	331.1	0.19
LDB3_7	0.05804	0.00061	0.56932	0.0069	0.07115	0.00084	0.97	530.7	23.24	443.1	5.04	457.6	4.47	188.0	2793.1	0.05
LDB3_8	**0.05748**	**0.00063**	**0.60493**	**0.00753**	**0.07633**	**0.0009**	**0.95**	**509.6**	**23.63**	**474.2**	**5.4**	**480.4**	**4.77**	**70.1**	**915.7**	**0.27**
LDB3_9	0.06078	0.00065	0.59439	0.00735	0.07094	0.00084	0.96	631.3	22.98	441.8	5.04	473.7	4.68	67.6	960.3	0.19
LDB3_11	0.05822	0.00064	0.59408	0.00748	0.07402	0.00088	0.94	537.3	24.47	460.3	5.26	473.5	4.76	51.8	709.0	0.22
LDB3_16	**0.05696**	**0.00062**	**0.58795**	**0.00742**	**0.07488**	**0.00089**	**0.94**	**489.2**	**24.31**	**465.5**	**5.35**	**469.6**	**4.75**	**61.2**	**852.7**	**0.15**
LDB3_17	**0.05839**	**0.00066**	**0.60138**	**0.00777**	**0.0747**	**0.00089**	**0.92**	**544.6**	**24.53**	**464.4**	**5.35**	**478.1**	**4.93**	**42.0**	**564.1**	**0.27**
LDB3_18	**0.05739**	**0.00065**	**0.59709**	**0.00775**	**0.07547**	**0.0009**	**0.92**	**506.1**	**24.8**	**469**	**5.41**	**475.4**	**4.93**	**61.3**	**825.7**	**0.24**
LDB3_19	0.06328	0.00069	0.61196	0.00768	0.07015	0.00084	0.95	717.5	22.85	437.1	5.05	484.8	4.84	101.8	1531.4	0.06
LDB3_20	0.06	0.00068	0.75713	0.00988	0.09154	0.0011	0.92	603.4	24.5	564.6	6.48	572.4	5.71	37.0	397.0	0.35
LDB3_21	0.0598	0.00067	0.70773	0.0091	0.08585	0.00103	0.93	596.3	24	530.9	6.11	543.4	5.41	56.3	697.2	0.09
LDB3_22	0.05799	0.00062	0.57659	0.00723	0.07212	0.00086	0.95	528.9	23.79	448.9	5.19	462.3	4.66	417.4	6310.0	0.01
LDB3_23	0.05725	0.00066	0.52438	0.0069	0.06643	0.0008	0.92	500.8	25.34	414.6	4.83	428.1	4.6	57.9	914.2	0.14
LDB3_27	0.06679	0.00081	1.07058	0.01469	0.11627	0.00141	0.88	831.3	25.08	709	8.14	739	7.2	25.2	214.5	0.32
LDB3_28	**0.05772**	**0.00066**	**0.58945**	**0.00772**	**0.07407**	**0.00089**	**0.92**	**519**	**24.98**	**460.6**	**5.37**	**470.5**	**4.93**	**63.8**	**887.8**	**0.22**
LDB3_29	0.05778	0.00073	0.56564	0.00805	0.07101	0.00086	0.85	521.2	27.82	442.2	5.2	455.2	5.22	33.2	468.1	0.31
LDB3_30	**0.05655**	**0.00066**	**0.58991**	**0.00787**	**0.07567**	**0.00092**	**0.91**	**473.2**	**25.69**	**470.2**	**5.5**	**470.8**	**5.03**	**44.2**	**616.2**	**0.15**
LDB3_31	**0.05668**	**0.00068**	**0.59008**	**0.00805**	**0.07551**	**0.00092**	**0.89**	**478.5**	**26.45**	**469.3**	**5.5**	**470.9**	**5.14**	**62.0**	**856.9**	**0.19**
LDB3_32	**0.05733**	**0.00067**	**0.59181**	**0.00796**	**0.07488**	**0.00091**	**0.90**	**503.8**	**25.61**	**465.5**	**5.46**	**472**	**5.07**	**44.1**	**616.4**	**0.19**
LDB3_33	**0.05639**	**0.00063**	**0.59327**	**0.00776**	**0.07632**	**0.00093**	**0.93**	**466.9**	**24.85**	**474.1**	**5.55**	**473**	**4.95**	**376.1**	**5333.1**	**0.09**
LDB3_34	0.15567	0.00178	5.69086	0.07526	0.26517	0.00323	0.92	2409.2	19.23	1516.2	16.46	1930	11.42	64.4	224.6	0.26
LDB6 (Diorite)																
LDB6_5	**0.05709**	**0.00066**	**0.59015**	**0.0077**	**0.07499**	**0.00089**	**0.91**	**494.3**	**25.55**	**466.1**	**5.35**	**471**	**4.91**	**39.8**	**544.5**	**0.24**
LDB6_6	0.05728	0.00064	0.55128	0.00705	0.06981	0.00083	0.93	502	24.7	435	4.99	445.8	4.61	60.3	923.1	0.10
LDB6_7	0.05782	0.00065	0.56457	0.00722	0.07083	0.00084	0.93	522.7	24.69	441.1	5.05	454.5	4.68	28.2	420.3	0.15
LDB6_8	**0.05694**	**0.00064**	**0.60259**	**0.00774**	**0.07676**	**0.00091**	**0.92**	**488.6**	**25.07**	**476.8**	**5.45**	**478.9**	**4.9**	**29.6**	**398.5**	**0.21**
LDB6_9	0.06391	0.00074	1.03121	0.01342	0.11704	0.00139	0.91	738.5	24.23	713.5	8.01	719.5	6.71	19.7	171.4	0.23
LDB6_10	**0.05689**	**0.00063**	**0.60133**	**0.00763**	**0.07667**	**0.00091**	**0.94**	**486.6**	**24.72**	**476.2**	**5.43**	**478.1**	**4.84**	**41.2**	**547.8**	**0.24**
LDB6_11	**0.0574**	**0.00063**	**0.59955**	**0.00749**	**0.07576**	**0.00089**	**0.94**	**506.5**	**23.87**	**470.8**	**5.36**	**476.9**	**4.75**	**57.5**	**786.2**	**0.18**
LDB6_12	**0.05647**	**0.00065**	**0.59478**	**0.00771**	**0.0764**	**0.0009**	**0.91**	**470.1**	**25.44**	**474.6**	**5.41**	**473.9**	**4.91**	**30.7**	**419.5**	**0.16**
LDB6_16	0.05826	0.00065	0.67597	0.00858	0.08416	0.00099	0.93	539	24.97	520.9	5.89	524.3	5.2	40.1	491.2	0.18
LDB6_17	0.06202	0.00069	0.6626	0.00835	0.07749	0.00091	0.93	674.9	23.59	481.1	5.45	516.2	5.1	45.2	586.0	0.22
LDB6_18	**0.05757**	**0.00064**	**0.60709**	**0.00765**	**0.07649**	**0.0009**	**0.93**	**513**	**24.02**	**475.1**	**5.38**	**481.7**	**4.84**	**45.2**	**616.6**	**0.13**
LDB6_19	**0.05642**	**0.00065**	**0.59731**	**0.00773**	**0.07678**	**0.0009**	**0.91**	**468.3**	**25.5**	**476.9**	**5.41**	**475.5**	**4.91**	**39.3**	**533.4**	**0.15**
LDB6_20	0.05765	0.00066	0.65812	0.00847	0.0828	0.00097	0.91	516.2	24.59	512.8	5.79	513.5	5.19	35.1	440.8	0.15
LDB6_21	0.0571	0.00066	0.57312	0.00739	0.07281	0.00086	0.92	494.7	25.49	453	5.14	460	4.77	30.9	438.3	0.18
LDB6_22	**0.05734**	**0.00069**	**0.59294**	**0.00787**	**0.07501**	**0.00088**	**0.88**	**504.1**	**26.15**	**466.2**	**5.29**	**472.7**	**5.02**	**36.0**	**497.4**	**0.16**
LDB6_23	**0.05824**	**0.00069**	**0.6004**	**0.00787**	**0.07478**	**0.00088**	**0.90**	**538.1**	**26.14**	**464.9**	**5.27**	**477.5**	**4.99**	**32.3**	**442.9**	**0.18**
LDB6_27	**0.05738**	**0.00068**	**0.60382**	**0.00794**	**0.07632**	**0.00089**	**0.89**	**505.9**	**25.85**	**474.1**	**5.35**	**479.7**	**5.03**	**39.9**	**535.5**	**0.18**
LDB6_28	**0.05762**	**0.00068**	**0.59867**	**0.00787**	**0.07536**	**0.00088**	**0.89**	**515.1**	**25.49**	**468.4**	**5.29**	**476.4**	**5**	**32.9**	**450.1**	**0.16**
LDB6_29	**0.05692**	**0.00069**	**0.59104**	**0.00785**	**0.07531**	**0.00088**	**0.88**	**487.9**	**26.66**	**468.1**	**5.28**	**471.5**	**5.01**	**36.6**	**499.5**	**0.17**
LDB6_30	**0.05752**	**0.00069**	**0.60675**	**0.00802**	**0.07651**	**0.00089**	**0.88**	**511.2**	**25.87**	**475.3**	**5.36**	**481.5**	**5.07**	**32.3**	**435.8**	**0.15**
LDB6_31	**0.05686**	**0.00069**	**0.59642**	**0.008**	**0.07608**	**0.00089**	**0.87**	**485.5**	**27**	**472.7**	**5.33**	**475**	**5.09**	**25.6**	**346.9**	**0.15**
LDB6_32	**0.05785**	**0.00069**	**0.59622**	**0.00782**	**0.07476**	**0.00087**	**0.89**	**523.8**	**26.05**	**464.8**	**5.23**	**474.8**	**4.97**	**48.2**	**667.2**	**0.14**
LDB6_33	**0.05713**	**0.00073**	**0.59665**	**0.00827**	**0.07575**	**0.00089**	**0.85**	**496.1**	**28.13**	**470.7**	**5.32**	**475.1**	**5.26**	**33.9**	**460.9**	**0.15**
LDB6_34	**0.05712**	**0.00069**	**0.60169**	**0.00802**	**0.0764**	**0.00089**	**0.87**	**495.7**	**26.86**	**474.6**	**5.34**	**478.3**	**5.08**	**34.9**	**464.6**	**0.2**

Table 3.1 (suite)

Sample	$^{207}Pb/^{206}Pb$	Error (1σ)	$^{207}Pb/^{235}U$	Error (1σ)	$^{206}Pb/^{238}U$	Error (1σ)	rho	$^{207}Pb/^{206}Pb$	Error (1σ)	$^{206}Pb/^{238}U$	Error (1σ)	$^{207}Pb/^{235}U$	Error (1σ)	Pb (ppm)	U (ppm)	Th/U
CRA1 (Granite)																
CRA1_5	**0.05718**	**0.00063**	**0.59736**	**0.00746**	**0.07577**	**0.00089**	**0.94**	**498.1**	**24.53**	**470.8**	**5.31**	**475.6**	**4.74**	**33.2**	**452.1**	**0.16**
CRA1_6	**0.05682**	**0.00064**	**0.59207**	**0.00748**	**0.07558**	**0.00088**	**0.92**	**484**	**24.88**	**469.7**	**5.3**	**472.2**	**4.77**	**47.6**	**647.8**	**0.18**
CRA1_7	0.05722	0.00063	0.64122	0.00799	0.08129	0.00095	0.94	499.3	24.39	503.8	5.67	503.1	4.95	39.3	491.2	0.22
CRA1_9	0.05868	0.00069	0.66314	0.00869	0.08198	0.00096	0.89	555.1	25.46	507.9	5.74	516.5	5.3	28.6	357.1	0.20
CRA1_10	0.05769	0.00065	0.59025	0.00748	0.07421	0.00087	0.93	517.9	24.78	461.5	5.22	471	4.78	31.0	434.4	0.15
CRA1_11	**0.0573**	**0.00064**	**0.60057**	**0.00754**	**0.07603**	**0.00089**	**0.93**	**502.5**	**24.44**	**472.4**	**5.34**	**477.6**	**4.79**	**33.4**	**455.3**	**0.15**
CRA1_12	**0.05746**	**0.00065**	**0.59668**	**0.00756**	**0.07532**	**0.00088**	**0.92**	**508.9**	**24.41**	**468.1**	**5.3**	**475.1**	**4.81**	**32.7**	**443.2**	**0.21**
CRA1_16	**0.05668**	**0.00064**	**0.59225**	**0.00753**	**0.0758**	**0.00089**	**0.92**	**478.4**	**24.93**	**471**	**5.34**	**472.3**	**4.8**	**36.8**	**500.6**	**0.19**
CRA1_17	**0.05777**	**0.00065**	**0.59958**	**0.00764**	**0.07529**	**0.00089**	**0.93**	**520.7**	**24.8**	**467.9**	**5.31**	**477**	**4.85**	**35.5**	**489.9**	**0.16**
CRA1_18	**0.05693**	**0.00065**	**0.59399**	**0.00763**	**0.07568**	**0.00089**	**0.92**	**488.2**	**25.25**	**470.3**	**5.34**	**473.4**	**4.86**	**32.5**	**443.5**	**0.19**
CRA1_19	**0.05712**	**0.00067**	**0.59479**	**0.00782**	**0.07553**	**0.00089**	**0.90**	**495.6**	**26.05**	**469.4**	**5.34**	**473.9**	**4.98**	**38.2**	**520.8**	**0.19**
CRA1_20	**0.05736**	**0.00066**	**0.60238**	**0.00781**	**0.07618**	**0.0009**	**0.91**	**504.9**	**25.23**	**473.3**	**5.38**	**478.7**	**4.95**	**39.1**	**527.6**	**0.20**
CRA1_21	**0.05636**	**0.00067**	**0.58454**	**0.00778**	**0.07523**	**0.00089**	**0.89**	**466**	**26.35**	**467.6**	**5.33**	**467.4**	**4.98**	**42.1**	**579.0**	**0.19**
CRA1_22	0.05715	0.00063	0.64309	0.00807	0.08163	0.00096	0.94	496.6	24.45	505.8	5.73	504.2	4.99	100.3	1319.2	0.07
CRA1_23	0.05773	0.00078	0.58169	0.00852	0.07309	0.00087	0.81	519.3	29.52	454.7	5.23	465.5	5.47	38.6	534.0	0.24
CRA1_27	**0.05751**	**0.0007**	**0.59864**	**0.00809**	**0.07551**	**0.0009**	**0.88**	**510.8**	**26.21**	**469.2**	**5.37**	**476.4**	**5.14**	**22.1**	**305.0**	**0.16**
CRA1_28	0.0573	0.00068	0.58158	0.00776	0.07362	0.00087	0.89	502.6	26.13	457.9	5.24	465.5	4.98	33.5	470.5	0.19
CRA1_29	0.05806	0.00069	0.59683	0.00795	0.07457	0.00088	0.89	531.5	26.29	463.6	5.3	475.2	5.06	42.3	585.3	0.20
CRA1_31	0.06521	0.00084	0.77971	0.01108	0.08672	0.00104	0.84	781.3	26.93	536.1	6.14	585.3	6.32	18.2	183.5	0.17
CRA1_32	**0.05703**	**0.00068**	**0.59033**	**0.00786**	**0.07509**	**0.00089**	**0.89**	**491.9**	**26.29**	**466.7**	**5.34**	**471.1**	**5.02**	**43.9**	**610.7**	**0.16**
CRA1_33	0.05915	0.0007	0.57835	0.00771	0.07092	0.00084	0.89	572.7	25.61	441.7	5.07	463.4	4.96	45.3	667.6	0.13
CRA1_34	0.05768	0.00069	0.57066	0.00764	0.07176	0.00085	0.88	517.5	26.26	446.7	5.13	458.4	4.94	36	516.9	0.21

Table 3.2 Données U-Pb par LA-ICP-MS sur ite pour le gabbro de La Meilleraie

Sample FOS9	**U (ppm)**	**Pb (ppm)**	**$^{238}U/^{206}Pb$**	**Error (2σ)**	**$^{207}Pb/^{206}Pb$**	**Error (2σ)**
MEIL8_1	2.3	0.6	8.475	0.230	0.399	0.021
MEIL8_2	2.5	0.7	8.333	0.190	0.390	0.016
MEIL8_3	2.0	0.7	7.342	0.190	0.434	0.018
MEIL8_4	4.66	1.29	8.636	0.170	0.351	0.012
MEIL8_5	3.06	0.97	8.333	0.150	0.394	0.012
MEIL8_6	2.3	0.57	8.643	0.320	0.362	0.022
MEIL8_7	3.49	0.94	9.058	0.160	0.337	0.012
MEIL8_8	2.23	0.88	6.849	0.200	0.471	0.024
MEIL8_9	2.73	0.7	9.174	0.240	0.316	0.016
MEIL8_10	2.39	0.73	7.899	0.280	0.433	0.023
MEIL8_11	2.36	0.87	6.854	0.190	0.486	0.025
MEIL8_12	1.97	0.68	7.479	0.260	0.447	0.019
MEIL8_13	3.59	0.82	9.653	0.220	0.289	0.012
MEIL8_14	2.21	1.07	6.297	0.240	0.522	0.032
MEIL8_15	3.49	0.77	9.980	0.190	0.272	0.010
MEIL8_16	2.17	0.99	6.127	0.200	0.563	0.033
MEIL8_17	2.16	0.71	7.880	0.310	0.408	0.023
MEIL8_18	3.7	1.06	9.009	0.160	0.339	0.012
MEIL8_19	2.59	0.86	8.945	0.170	0.361	0.014
MEIL8_20	1.96	0.83	6.831	0.270	0.495	0.032

Partie 4

Les minéralisations Sb-Au de Bretagne Centrale : implications métallogéniques et tectoniques

Résumé en français de l'article #3

L'altération hydrothermale associée aux minéralisations Sb-Au est répandue au sein du Massif Armoricain, mais les réactions de pseudomorphose ne sont pas toujours bien caractérisées, en particulier la déstabilisation hydrothermale de l'assemblage ilménite-titanohématite. Basés sur une analyse pétrographique et une analyse des éléments traces par microsonde et par spectromètre de masse par ablation laser, nous documentons les changements minéralogiques à l'échelle de la roche et à l'échelle du minéral, et la redistribution de Sb et autres éléments traces pendant la recristallisation de rutile hydrothermal. L'altération hydrothermale est principalement potassique avec une carbonatation associée. Le processus de remplacement est interprété comme une réaction de dissolution-reprécipitation. Les résultats montrent que Mn, Zn, Co, Ni, Sn, Mo et U sont libérés pendant l'altération hydrothermale alors que Sb et W sont incorporés au sein du rutile hydrothermal néoformé à partir des fluides hydrothermaux. De plus, la concentration en Sb évolue à travers le temps suggérant un changement de la composition du fluide probablement dû à un enrichissement en Sb pendant la cristallisation du rutile. Considérant que la déstabilisation des oxydes de Fe-Ti est relativement fréquente au sein des systèmes Sb-Au épithermaux et orogéniques, nos résultats apportent de nouvelles contraintes quant à la mobilité des métaux dans les systèmes hydrothermaux aurifères et antimonifères.

Metal mobility during hydrothermal breakdown of Fe-Ti oxides: insights from Sb-Au mineralizing event (Variscan Armorican Massif, France)

Anthony Pochon[1*], Georges Beaudoin[2], Yannick Branquet[1, 3], Philippe Boulvais[1], Eric Gloaguen[3, 4], Denis Gapais[1]

[1] *Géosciences Rennes, UMR 6118, Université de Rennes 1, OSUR, Campus de Beaulieu, 35042 Rennes Cedex, France*

[2] *Département de géologie et de génie géologique, Université Laval, Québec (QC) G1V 0A6, Canada*

[3] *Institut des Sciences de la Terre d'Orléans, UMR 7327, Université d'Orléans, Campus Géosciences, 1A rue de la Férollerie, 45071 Orléans Cedex 2, France*

[4] *Bureau de Recherche Géologique et Minière (BRGM), UMR 7327, 3 avenue Claude-Guillemin, BP 36009, 45060 Orléans Cedex 02, France*

Accepté pour publication le 23 octobre 2017 à *Ore Geology Reviews*

Abstract

Hydrothermal alteration related to Sb-Au mineralization is widespread in the Variscan Armorican Massif, but mineral replacement reactions are not well characterized, in particular the hydrothermal breakdown of ilmenite-titanohematite. Based on petrography, electron probe micro-analyzer and laser ablation-inductively coupled plasma-mass spectrometer analyses, we document mineralogical change at rock- and mineral-scale and the redistribution of Sb and others trace elements during the recrystallization of ilmenite-titanohematite to hydrothermal rutile. Hydrothermal alteration is mainly potassic with associated carbonation. The replacement mechanism is interpreted to be an interface-coupled dissolution-reprecipitation process. Results show that Mn, Zn, Co, Ni, Sn, Mo and U are released during hydrothermal alteration, whereas Sb and W are incorporated in newly-formed hydrothermal rutile from the hydrothermal fluid. Furthermore, the concentration of Sb evolves through time suggesting a change in fluid composition likely related to an enrichment of fluid in Sb during rutile crystallization. Considering that Fe-Ti oxides breakdown during hydrothermal alteration is common within epithermal and mesothermal/orogenic Au-Sb mineralizing systems, results report in this study yield important constraints about metal mobility and exchanges in hydrothermal gold systems.

Keywords: Ilmenite-titanohematite hydrothermal breakdown, Sb mineralization, EPMA, LA-ICP-MS, Redistribution of trace elements, Hydrothermal alteration, Rutile

1. Introduction

Understanding trace element behavior and redistribution processes is a fundamental step with respect to large-scale transport of heat and chemical elements in the crust. Consequently, it is a critical process in the formation of various types of mineral deposits. Fluid-assisted mineral replacement reactions can release chemical elements into the fluid, or incorporate some elements in the fluid into the newly-formed phase, such that it is possible to trace some specific mineral reactions from which metals are released from crustal rocks (Zack and John, 2007; Putnis and Fernandez-Diaz, 2010; Pitcairn et al., 2014, 2015; Cave et al., 2015). For example, rutile is used as an indicator of deposit types (Meinhold, 2010). One reason for this is that rutile is common in many rock types, especially those that have undergone metasomatic alteration (Williams and Cesbron, 1977). Rutile incorporates significant amount of trace elements into its lattice, such as high field strength elements (HFSE), Al, V, Cr, Fe, Sn, U, Sb and W (Smith and Perseil, 1997; Rice et al.,

1998; Zack et al., 2002, 2004; Bromiley and Hilairet, 2005; Scott, 2005; Carruzzo et al., 2006; Scott and Radford, 2007; Tomkins et al., 2007; Triebold et al., 2007; Meinhold 2010). Enrichments in Sb, W and V are commonly considered characteristic of rutile associated with orogenic gold deposits (Urban et al., 1992; Clark and Williams-Jones, 2004; Scott and Radford, 2007), whereas the incorporation of Cu and Mo in rutile is assumed to be characteristic of porphyry deposits (Scott, 2005; Rabbia et al., 2009). On the other hand, the breakdown of detrital rutile to titanite during prograde metamorphism (Otago Province, New Zealand) has been shown to release significant amounts of W (Cave et al., 2015), later incorporated in scheelite disseminated in Otago Schist and in orogenic gold veins (Cave et al., 2016). More generally, breakdown of Fe-Ti oxides is common during diagenetic, metamorphic and hydrothermal reactions (Morad and Aldahan, 1986; Luvizotto et al., 2009; Rabbia et al., 2009), a process that can redistribute metals at a regional scale.

The Variscan Armorican Massif (France) is a metallogenic province characterized by several types of mineral deposits (Chauris and Marcoux, 1994), including orogenic gold and antimony deposits. Fe-Ti oxide breakdown associated with Sb mineralization has been recognized at the Le Semnon Sb-Au deposit (Chauris et al., 1985; Gloaguen et al., 2016). In this paper, we present the textural, mineralogical and geochemical characteristics of the Fe-Ti oxide breakdown reaction, and discuss its implications in terms of metal mobility and potential metal source.

2. Geological framework

A significant part of French Sb-deposits are located in the Armorican Massif, in western France (Fig. 1), which belongs to the Ibero-Armorican Arc of the western European Variscan belt. The Armorican Massif is divided in several domains separated by two dextral crustal-scale shear zones, the North (NASZ) and South (SASZ) Armorican Shear Zones that were active during the Carboniferous (Gumiaux et al., 2004). The main Sb districts are located in the Central Armorican Domain (CAD) and in the South Armorican Domain (SAD). Antimony deposits (e.g., Le Semnon deposit in the CAD) are commonly associated with gold mineralization and spatially coexist with gold-sulfosalts deposits (e.g., Saint-Aubin-des-Châteaux deposit, Gloaguen et al., 2007). The CAD consists of Late Neoproterozoic to Late Paleozoic sedimentary rocks affected by low-grade regional metamorphism and moderate deformation. Deformation consists of upright folds with sub-vertical axial planes and E–W sub-horizontal axes produced by a N120-125-striking dextral wrenching of the CAD (Gapais and Le Corre, 1980; Gumiaux et al., 2004). Folding is associated with a sub-vertical cleavage (S1 on Fig. 1b) bearing a sub-horizontal stretching lineation. Several magmatic events occurred during the Variscan orogeny in the Armorican Massif, notably the emplacement of syntectonic granites (around 316-300 Ma) along the SASZ (Tartèse and Boulvais, 2010; Tartèse et al., 2011a, 2011b) or in association with crustal detachments (Gapais et al., 1993; Ballouard et al.,

2015). In the eastern part of the CAD, the main magmatic event is characterized by a swarm of gabbro dykes and sills, locally called dolerite (Lahaye et al., 1995; Aïfa et al., 1999; Le Gall, 1999). This gabbroic event has been dated by the U-Pb method with LA-ICP-MS on magmatic apatite at 363 ± 6 Ma (Pochon et al., 2016b).

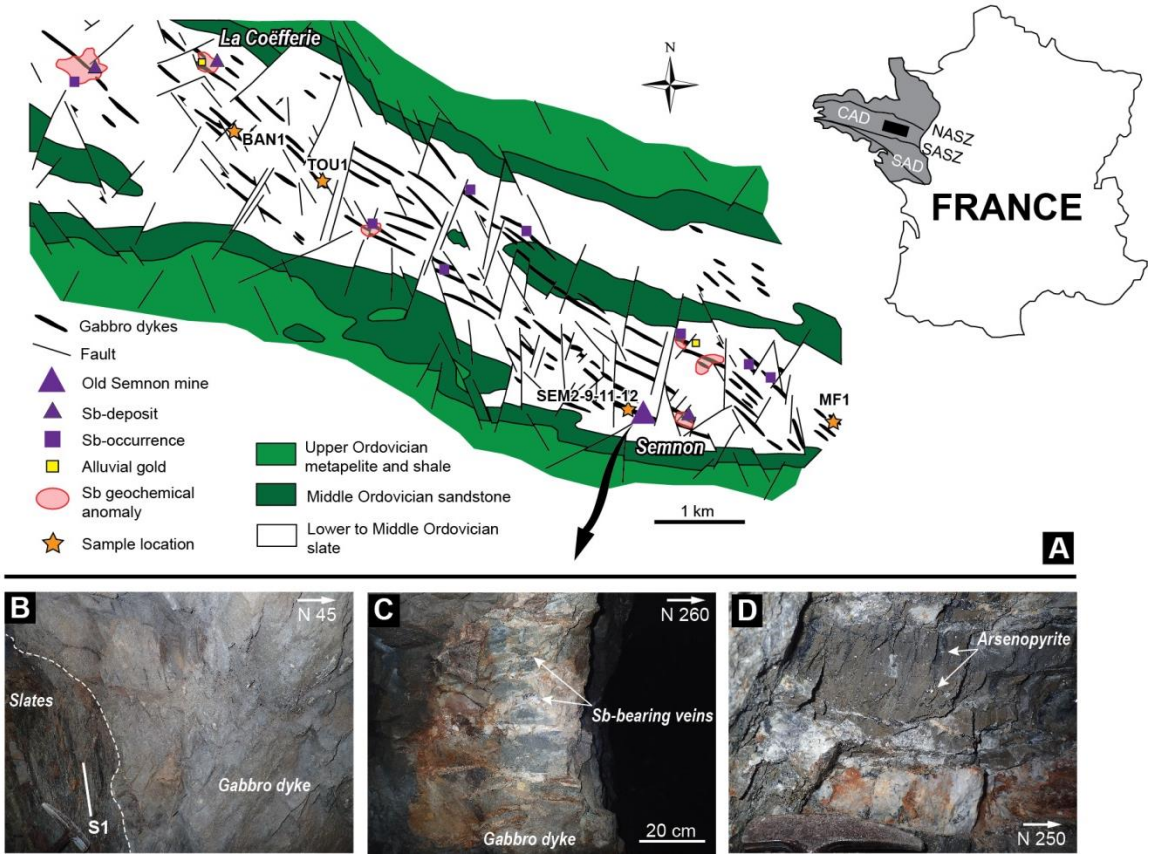

Fig. 1 a Geological map of the Semnon Sb-Au district with the location of the old Semnon mine and other Sb occurrences (modified from Pochon et al. 2016a). See text for abbreviation. Photographs of outcrops showing at the Semnon deposit: (**b**) relation between Ordovician slates, gabbro dyke, and regional cleavage (S1), (**c**) the location and geometry of flat stibnite-bearing veins cutting the gabbro and (**d**) alteration zone of the vein wallrock (Ordovician slates) with disseminated arsenopyrite

The stibnite-gold quartz veins are generally considered to belong to a late Variscan hydrothermal event (Bouchot et al., 2005) that postdate Devonian hydrothermal fluid flow (Tartèse et al., 2015), although there is no geochronological data to support this hypothesis. Chauris and Marcoux (1994) suggest that the Sb-Au mineralization is sourced from various felsic magmatic events spanning the Cambrian-Carboniferous period, and deposited within Late Variscan shear zones. However, a strong spatial correlation between Sb (± Au) occurrences and relatively high density and magnetic zones has been demonstrated (Pochon et al., 2016a). These high density and magnetic zones are suggested to correspond to mafic/ultramafic bodies at depth, and are likely the parent magmatic intrusions of the numerous gabbroic dyke swarms outcropping in the area (Pochon et al., 2016a). These interpreted deep mafic/ultramafic bodies may represent an important source of metals for these mineralizing systems.

The Le Semnon Sb-Au district (Fig. 1) consists of a NW-SE striking, near vertical, gabbro dyke swarm intruded in the lower to middle Ordovician slates at *ca.* 363 Ma (Pochon et al., 2016b). These slates have been affected by regional deformation during the Variscan orogeny. The walls of the gabbro dykes are affected by a weak E-W trending, sub-vertical cleavage (Fig. 1b). Mineralization is spatially associated with gabbro dykes and consists of Sb- and Au-bearing quartz-carbonate flat veins (Fig. 1b). These mineralised veins crosscut the contact between the gabbro and the slate, and the regional cleavage. Some veins are folded and are affected by a weak regional cleavage. Mineralization consists of three main stages (Chauris et al., 1985): (1) an early Fe-As-(Au) stage consisting of arsenopyrite, pyrite and pyrrhotite, commonly replaced by pyrite and marcasite, (2) an intermediate Fe-Sb stage characterized by berthierite, and (3) a final Sb stage with massive stibnite and rare native antimony. Sphalerite and native gold occur with the Sb-mineralization, but their paragenetic position is unclear. Indeed, the sphalerite is in rare association with stibnite, whereas native gold is interpreted to be remobilized during the final stage (Chauris et al., 1985). The mineralization gangue is composed of quartz and carbonate (70 and 30 %, respectively). Arsenopyrite is rare inside the veins, but abundant disseminated in hydrothermally altered gabbro and slate wall rocks. Hydrothermal alteration is characterized by potassic metasomatism, highlighted by hydrothermal illite and sericitized plagioclase, accompanied by carbonation and a weak silicification. Within the altered gabbro dykes, the magmatic ilmenite is totally replaced by rutile, used in this paper in the general sense of "TiO_2-polymorph", and by an alteration product called leucoxene by Chauris et al. (1985).

3. Sampling

Five gabbro samples have been selected for characterizing the trace element geochemistry of Fe-Ti oxides: three unaltered gabbro samples were collected from the same dyke swarm (BAN1, TOU1, and MF1; Fig. 1) and two hydrothermally altered gabbro samples from the dyke hosting the Le Semnon deposit (SEM9 and SEM11). These five samples from four dykes are representative of the textural and compositional variety recognized in the area.

To investigate the geochemical variations and to quantify the metasomatic change of whole rock, we collected two additional samples of the hydrothermally altered gabbro from the Le Semnon mine to address primary magmatic heterogeneity. Both samples represent the core (SEM2) and the rim (SEM12) of the least and the more altered gabbro dyke, respectively. The sedimentary host rocks were not studied because of the difficulty establishing the protolith composition of the detrital host rocks.

The least altered gabbro dyke samples (BAN1, TOU1, and MF1) have a porphyritic and doleritic texture in which the principal mineral assemblage (Fig. 2a and b) consist of elongate plagioclase laths, clinopyroxene (mainly augite) and Fe-Ti oxides reaching up to 12 % in mineral proportion. The grain size of the Fe-Ti oxides ranges between 50 and 500 µm. Late stage crystallization is represented by rare interstitial quartz. The accessory minerals consist of apatite, rare primary biotite and titanite, pyrite, chalcopyrite, pyrrhotite, chlorite, green amphibole and epidote.

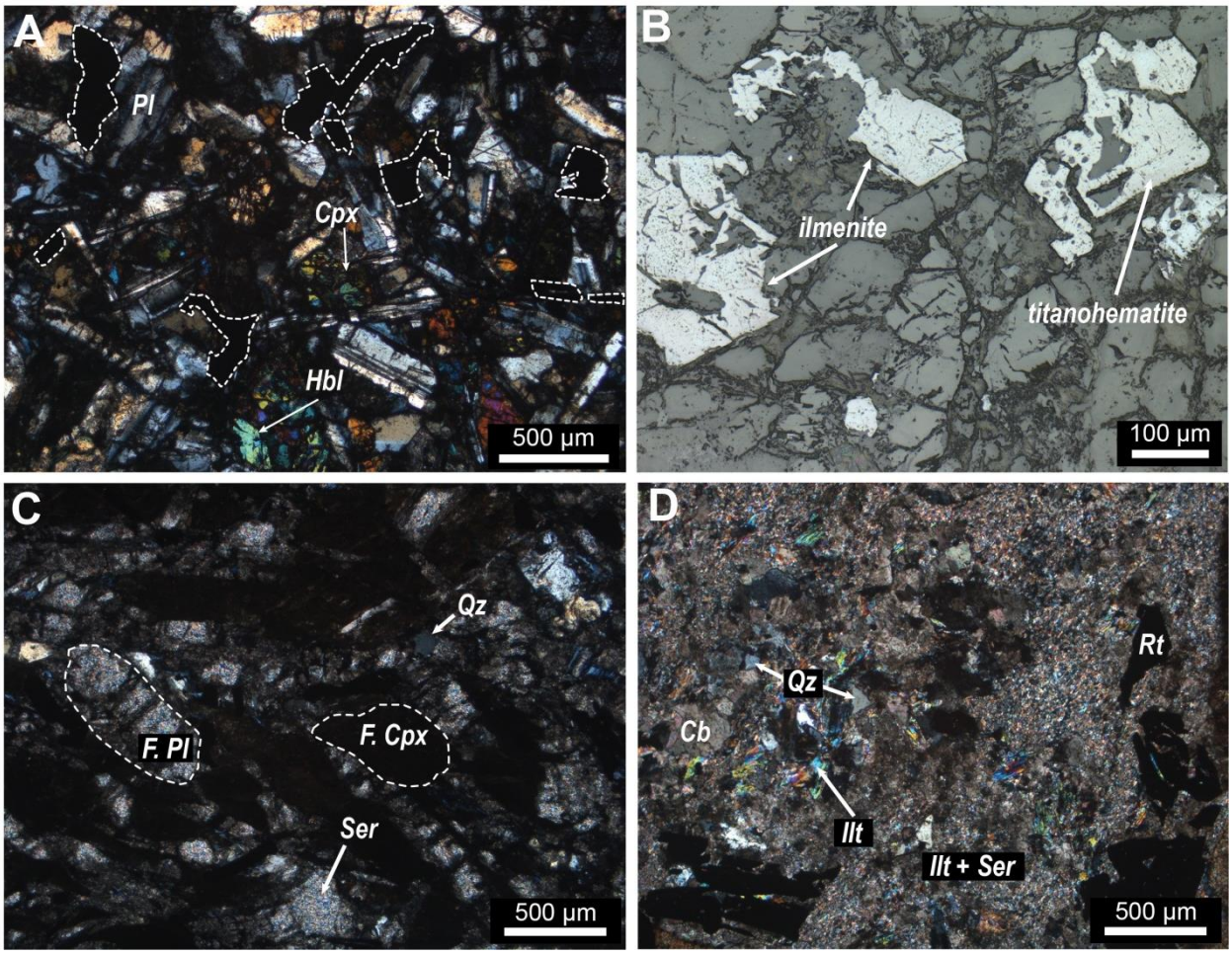

Fig. 2 Photomicrographs showing the initial magmatic texture of an unaltered gabbro from the dyke swarm (**a** and **b**) and the hydrothermally altered gabbro from the Le Semnon deposit (c and d). **a** Typical texture of gabbro dyke (BAN1) with laths of plagioclase intergrown with clinopyroxene. Areas delineated by white dashed lines correspond to Fe-Ti oxides. **b** Fe-Ti oxides in the groundmass of TOU1 sample. **c** Typical texture of altered gabbro (SEM12) with replaced phenocrysts of sericitized plagioclase (F. Pl), clinopyroxene (F. Cpx) and interstitial quartz. **d** Strong hydrothermal alteration of gabbro (SEM12) with illite, sericite, carbonates, quartz and rutile. Abbreviation from Whitney and Evans (2010).

In contrast, the primary magmatic texture is not preserved in hydrothermally altered gabbro. The alteration variably affects gabbro along, and across, dykes. Plagioclase and clinopyroxene are totally altered into sericite, chlorite, carbonate and quartz and the initial shape of the phenocrysts is hardly recognizable (Fig. 2c) or destroyed (Fig. 2d). Carbonate (ankerite and calcite) is heterogeneously distributed forming clusters inside altered gabbro, in place associated with illite,

sulfides and/or quartz (Fig. 2d). K-micas are relatively common in the altered gabbro groundmass, with typical grain size of 5-10 μm, but less commonly up to 200-250 μm. Altered gabbro contains disseminated arsenopyrite, pyrite, and less commonly stibnite and berthierite.

4. Analytical methods

4.1. Whole rock composition

Samples were crushed and powdered in an agate mortar. Major and trace elements analyses were performed using by inductively coupled plasma optical emission spectrometry (ICP-OES) and mass spectrometry (ICP-MS) by the SARM (CRPG-CNRS, Nancy) and following standard analytical procedures (Carignan et al., 2001).

4.2. Mineral chemistry

Fe-Ti oxides and pyrite from hydrothermally altered gabbro were examined in polished thin-sections using reflected-light optical and scanning electron microscopes. Minerals were analyzed using Cameca SX-100 electron probe micro-analyzers at IFREMER (Brest, France) and at Université Laval (Québec, Canada). The major and minor elements analyzed are Fe, Mg, Mn, Ti, V, Cr, Ca, Al, Ni, Si for Fe-Ti oxides and Fe, S, As, Sb, Au, Zn, Cu, Ni, Co for pyrite and arsenopyrite. Analyses were performed using a 3 μm diameter beam, a 15 kV accelerating voltage, a beam current of 20 nA and a counting time of 20s on peak. Analytical conditions and calibration are detailed in Appendix A.1.

4.3. Trace elements in minerals

Trace and selected major element concentrations were determined by laser ablation-inductively coupled plasma-mass spectrometer (LA-ICP-MS) at LabMaTer in the Université du Québec à Chicoutimi (UQAC, Canada). Selected elements and isotopes for Fe-Ti oxides and pyrite analyses are listed in Appendices. Sulfur (34S) was monitored to avoid signal interference of sulfides inclusions inside Fe-Ti oxides. Silicon, Ca and Ti were monitored to avoid signal interference from silicate and Fe-Ti oxides inclusions.

The LA-ICP-MS system used at UQAC consists of a RESOlution (ASI) 193nm excimer laser equipped with a S155 ablation cell (Laurin Technic) and coupled to a quadrupole Agilent 7900 ICP-MS. Ablation is carried out using a He carrier gas, mixed with Ar and N2 before entering the ICP-MS. Alignment of the instrument and mass calibration was performed before each analytical session on the GSE-1g reference glass. Single analysis consists of 30 s of gas blank followed by 60 s of ablation. The beam size was dependent on the grain size of the analyzed mineral and ranged between 25 and 55 μm. A repetition rate of 17 Hz, and a laser beam energy of 3 J/cm² (Fe-Ti

oxides) and 2 J/cm² (pyrite) were used during analyses. Analytical conditions and calibration are detailed in Appendix A.2.

Iron (57Fe) was used as the internal standard for Fe-oxides and pyrite, whereas 47Ti was used for rutile because of the low concentration of Fe in rutile. Following the approaches of Dare et al., (2014) calibration for Fe-Ti oxide minerals was performed on GSE-1g. To monitor the quality of analyses, we used the certified reference materials GSD-1g (synthetic basalt glass), and Gprob6 (matrix artificial basalt glass) and an in-house monitor BC28 which consists of a natural Ti-rich magnetite from the Bushveld complex (Barnes et al., 2004; Dare et al., 2012). Analyses of GSD-1g and Gprob6 show good accuracy and precision, with a relative differences (RD) and relative standard deviations (RSD) for all elements < 10 % (Appendix A.3). The accuracy and precision for the in-house monitor BC28 are < 15 % for RD and RSD for most elements. This in-house monitor is a natural magnetite, hence some elements are heterogeneously distributed within crystal lattice, such as Cu that is underestimated by 65 %. The accuracy and precision of rutile analyses are less good because of the low content of Ti (450 ppm) in the external standard GSE-1g. All elements of GSD-1g are underestimated by 20 % with a RSD < 10 % whereas the RD and RSD are < 15 % for Gprob6 (Appendix A.4). Isobaric interferences were checked following Dare et al. (2012, 2014). This revealed that 90Zr is constantly and slightly underestimated compared to 91Zr and the certified values for GSD-1g and Gprob6. Zirconium (91Zr) values are close to those reported for GSD-1g and Gprob6, hence 91Zr values were used when reporting Zr concentrations.

For pyrite, calibration of PGE and Au was performed using reference material po-727 (a synthetic FeS doped in PGE and Au, provided by Memorial University of Newfoundland). For the remaining elements, MASS-1 (a ZnFeCuS pressed pellet doped in trace elements, provided by the USGS) was used for calibration. The calibration was monitored using JBMSS-5 (synthetic FeS sulfide doped in trace elements, provided by Prof. James Brenan). Analyses are in good agreement within the analytical error with a RD and RSD < 10 % for GSE-1g except for Cd, Sn, Ir and Tl. For the in-house monitor JB-MSS5, the accuracy of analyses are relatively good with a RD < 15 % and a RSD < 10 %, except for Co and Re (Appendix A.5).

5. Results

5.1. Major element composition of Fe-Ti oxides

5.1.1. Least altered dyke

The magmatic Fe-Ti oxides mainly consist of ilmenite and titanohematite (Appendix A.6; Table 1; Fig. 3a-d) plotting along the true solid solution between the ilmenite and hematite end-

members (Fig. 4). Although hematite exsolutions are observed in both ilmenite and titanohematite, selected areas for analyses have been carefully checked using scanning electron microscope in order to avoid exsolutions.

These two types of Fe-Ti oxides are frequently in a closely associated mineral assemblage of ilmenite and titanohematite (Fig. 3c-d). Ilmenite contains approximately 49 % TiO2, whereas titanohematite contains close to 20 % TiO2. Using the equations of Droop (1987), an estimate of Fe2+/Fe3+ yields approximatively 42 % FeO and 6 % Fe2O3 for ilmenite, and 17 % FeO and 61 % Fe2O3 for titanohematite. Titanohematite contains mainly lamellar exsolutions (<2 μm) of ilmenite, hematite and possibly magnetite. Lamellae are often composite as they can contain at least ilmenite and hematite in exsolution (Fig. 3a). Other types of exsolution include "fish-bone" and mosaic textures. The "fish-bone" exsolution consists of nm-scale exsolution of ilmenite and hematite oriented parallel and perpendicularly to the c-axis of titanohematite crystals (Fig. 3b and c). The mosaic texture is characterized by a μm-scale disordered patchwork of phase exsolution of ilmenite and hematite with the presence of some micropores (Fig. 3b-d).

5.1.2. Hydrothermally altered dyke

One of the main textural characteristics of altered dykes is the replacement of primary ilmenite-titanohematite by rutile. According to its grain size, rutile can be divided in two types: coarse grained (CG) rutile and fine grained (FG) rutile (Figs. 3e, f and h), and both types appear to be contemporaneous. Coarse grained rutile is characterized by 99 % TiO2 (Table 1; Fig. 4). It crystallizes with an irregular habit within the preserved shape of the parent crystal (Fig. 3g). Its grain size is variable and ranges between 10 and 80 μm. It is frequently cracked and the preserved shape contains interconnected micron-scale pores between CG rutile (Fig. 3e-f). Some Sb-sulfosalts are found filling micro-pores and micro-fractures (Fig. 3e). Fine grained rutile consists of intergrowths of rutile with others silicates and it is always associated with CG rutile. Because of its very small grain size (< 2μm) and the porosity between grains, TiO2 is under-estimated in electron microprobe analyses (Table 1; Fig. 4). It consists of 76 % TiO2 and 8 % Fe2O3 total. Fine grained rutile is restricted to fractures and to the external rim of preserved shape of the parent mineral (Fig. 3e, f and h). Selected X-ray chemical maps of the two types of rutile are displayed in Figure 5.

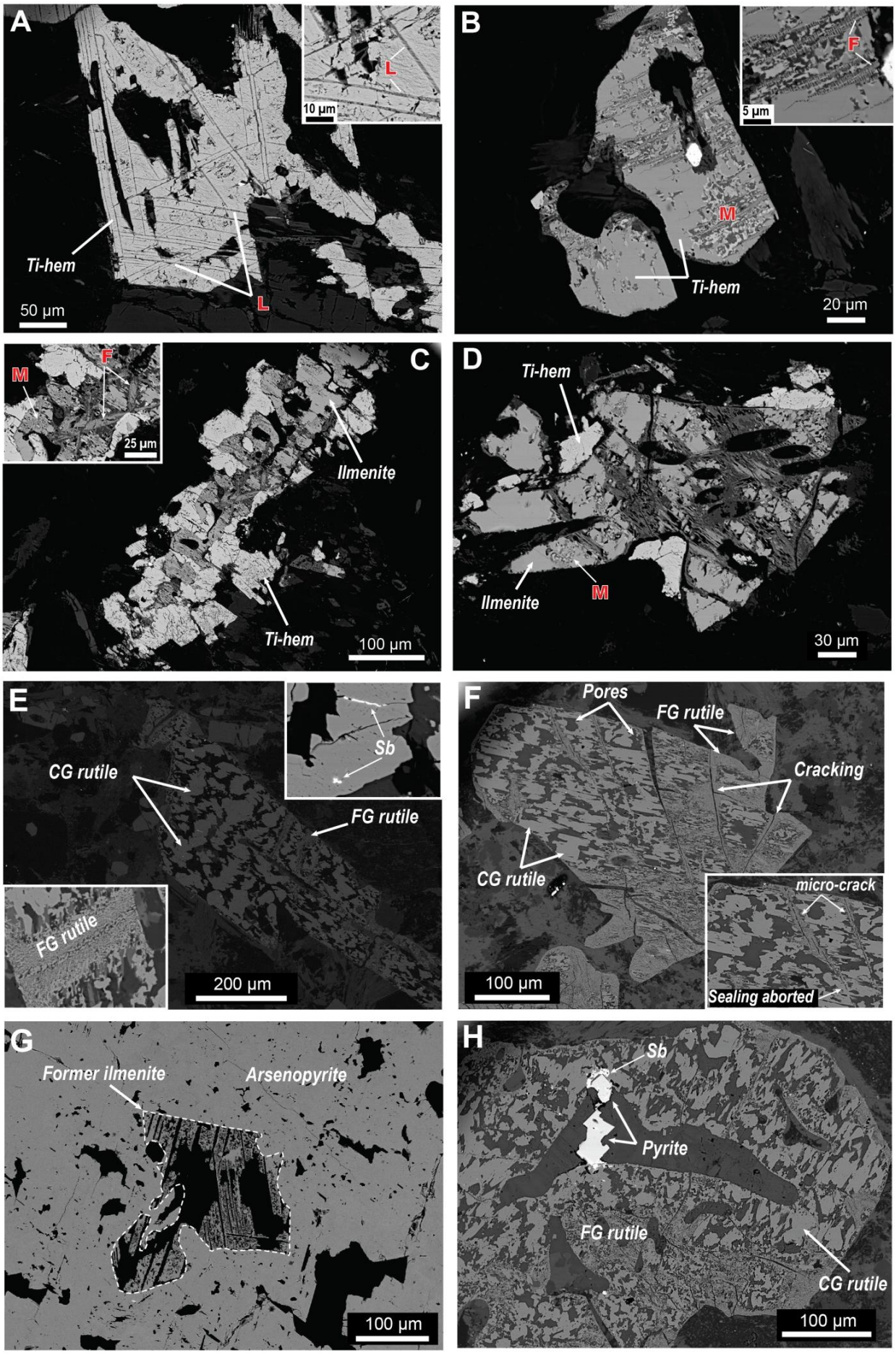
A
L
10 µm
Ti-hem
L
50 µm
B
F
5 µm
M
Ti-hem
20 µm
M
F
25 µm
C
Ilmenite
Ti-hem
100 µm
D
Ti-hem
Ilmenite
M
30 µm
E
Sb
CG rutile
FG rutile
FG rutile
200 µm
F
Pores
FG rutile
Cracking
CG rutile
micro-crack
100 µm
Sealing aborted
G
Former ilmenite
Arsenopyrite
100 µm
H
Sb
Pyrite
FG rutile
CG rutile
100 µm

Fig. 3 SEM photomicrographs showing the texture of Fe-Ti oxides in the unaltered gabbro BAN1 (**a-d**) and the hydrothermally altered gabbro SEM9 and SEM11 (**e-h**). **a** Crystal of titanohematite (Ti-Hem) with typical lamellar exsolutions. Insert in the upper right corner represents zoom of the lamellar exsolutions. **b** Crystal of titanohematite with the mosaic (M) and the "fish-bone" (F) textures. Insert in the upper right corner represents zoom of the "fish-bone" texture. **c** Mineral assemblage composed of a core of ilmenite and a rim of titanohematite. Insert in the upper left corner shows occurrences of mosaic and "fish-bone" textures in ilmenite. **d** Ilmenite crystal displaying altered areas with overgrowth of Ilm-Hem ss crystals. **e** Ghost of ilmenite-titanohematite assemblage of SEM9 sample, with its preserved external shape, replace by coarse grained rutile (CG rutile) crystals. These crystals exhibit a strong porosity and they are frequently cracked. Insert, in the lower left corner, shows very fine grain of rutile mainly located in micro-crack and defined as fine grained rutile (FG rutile). The insert in the upper right corner shows a Sb-sulphide inclusion within CG rutile and a micro-crack filled by Sb-sulphide. **f** Ghost of ilmenite-titanohematite assemblage of SEM11 sample replace by CG and FG rutile. Crystals are cracked and some of these cracks are partially sealed as shown in the insert in the upper right corner. **g** Ghost of ilmenite invades and includes inside arsenopyrite. **h** Overgrowth of pyrite and Sb-sulfides inside invagination of rutile. Abbreviation from Whitney and Evans (2010).

They show that Ti and V are exclusively incorporated in both rutile and that these elements appear to be immobile during alteration and restricted inside the preserved shape of the parent mineral (Fig. 5a and b). Micro-pores between CG and FG rutile crystals are filled by illite, ankerite, calcite and rare quartz (Fig. 5c-f).

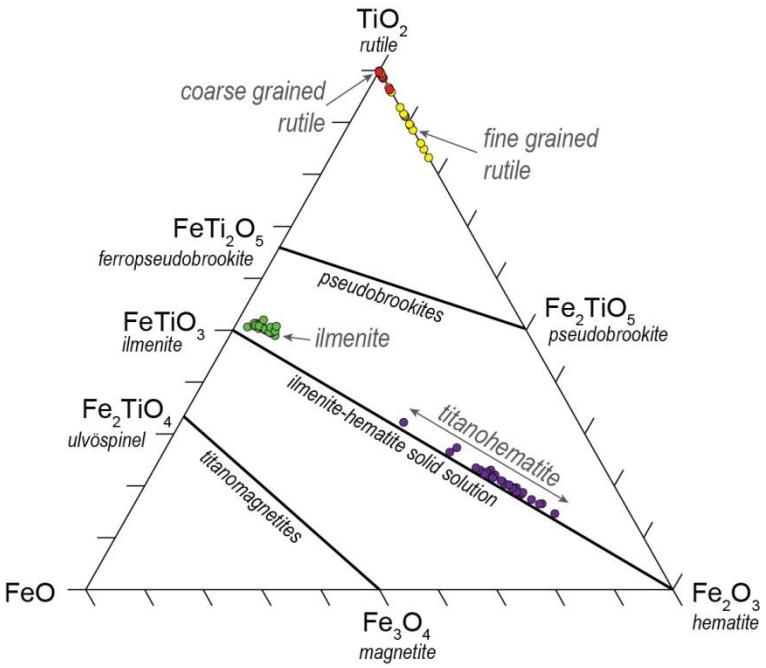

Fig. 4 Ternary system FeO-Fe2O3-TiO2 showing the high-temperature solid solution series magnetite-ulvöspinel, hematite-ilmenite, pseudobrookite-ferropseudobrookite (modified from Buddington and Lindsley, 1964)

Compositions of arsenopyrite and pyrite show that they contain Sb in minor and trace proportions, respectively (Appendix A.7 and A.8). Moreover, pyrite contains significant traces of arsenic and gold. Arsenopyrite and pyrite are texturally synchronous and/or slightly subsequent to breakdown of ilmenite-titanohematite assemblage, because they frequently encompass (Fig. 3g) or cut them (Fig. 3h). They may also replace primary ilmenite exsolutions (Fig. 3g).

5.2. Trace element composition of Fe-Ti oxides

Distribution of trace elements in ilmenite, titanohematite, CG and FG rutile are summarized in Table 2 (complete analyses in Appendix A.9), and plotted on multi-element variation diagrams

(Fig. 6) and bivariate diagrams (Fig. 7). Ilmenite crystals are moderately homogeneous between individual grains (Fig. 6a). Moderately compatible elements (Mn, V, Cr, Co, Ni) and HFSE show small variations, whereas the sum of total HFSE is more variable (Fig. 7). Molybdenum, Sb, W, Pb and U, considered as incompatible elements into ilmenite (Klemme et al., 2006), exhibit strong variations up to 2 orders of magnitude (Fig. 6, 7a and b). Mean concentrations of trace elements show that ilmenite grains are characterized by high concentrations of Mn, V, Cr, Zn and Zr (140-14500 ppm), moderate concentrations of Co, Ni, Cu, Sc, Hf, Nb and Ta (5-90 ppm), and low concentrations of As, Sn, Mo, Sb, W, Pb and U (< 2 ppm).

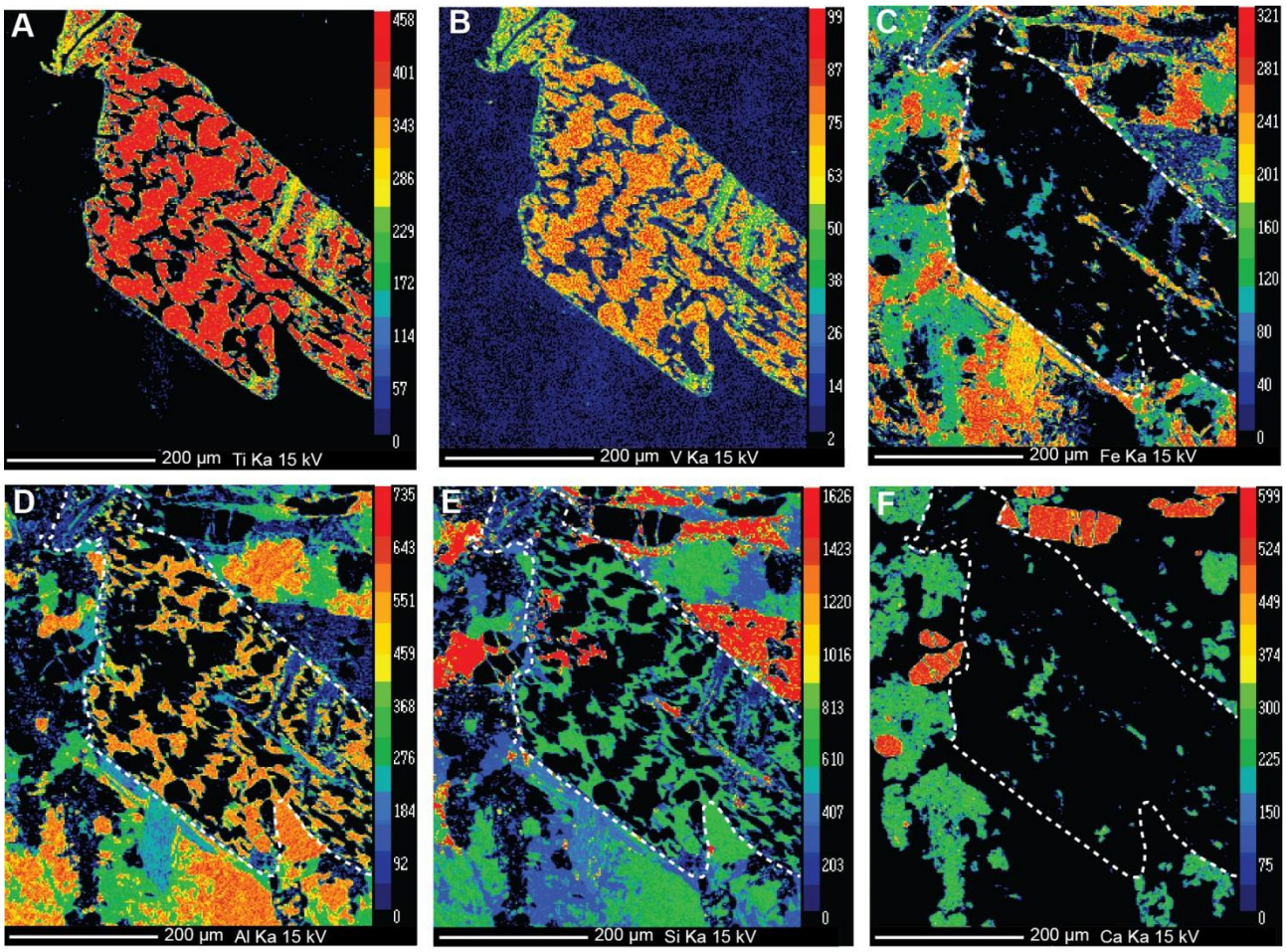

Fig. 5 X-ray chemical map of the distribution of the major elements of rutile grains displayed in the Fig. 3c. **a** Ti Kα, **b** V Kα, **c** Fe Kα, **d** Al Kα, **e** Si Kα and **f** Ca Kα

Compositionally, titanohematite is less homogeneous between individual crystals than ilmenite grains (Fig. 6b). For example, Cr shows significant variation with a range of values between 2 and 11000 ppm and a mean of 1100 ppm. This variation can be explained by numerous nm-scale exsolutions in various proportions in different grains. However, other elements (HFSE, V, Mn and Co) show small or no significant variations (Fig 6b and 7). In titanohematite, there is a significant decrease of Sc (7.3 ppm) and an increase of As (4.9 ppm) compared to ilmenite grains.

Antimony is more enriched in titanohematite (Fig. 6b). Zinc has a high concentration (75-1660 ppm) likely related to its compatible behavior in Fe-Ti oxides (Klemme et al., 2006).

Coarse grained rutile displays a homogeneous trace element composition with the exception of Mn, Co, Ni, As, Sb and W, which show variations in composition between individual grains. Compared to ilmenite and titanohematite, Mn, Co and Ni are depleted, and Sb and W are enriched (Fig. 6c). The Zn concentration (< 15 ppm) is much lower than in ilmenite and titanohematite (Fig. 7a), whereas the V concentration is similar (Fig. 7b). With respect to Sb, there is a sharp limit in concentration in CG rutile defining two distributions (Fig. 7c): some rutile has a relatively low concentration of Sb (< 10 ppm), whereas others have high concentrations of Sb (> 100 ppm). This suggests that CG rutile with low Sb concentration has a Sb concentration relatively close to its precursor mineral, and likely to preserve the signature of the precursor mineral, in contrast with CG rutile with high Sb concentration. The trace element composition of FG rutile is homogeneous with no significant variation (Fig. 6d). Its trace element composition is similar to that of coexisting CG rutile, except for the enrichment in Co and Ni.

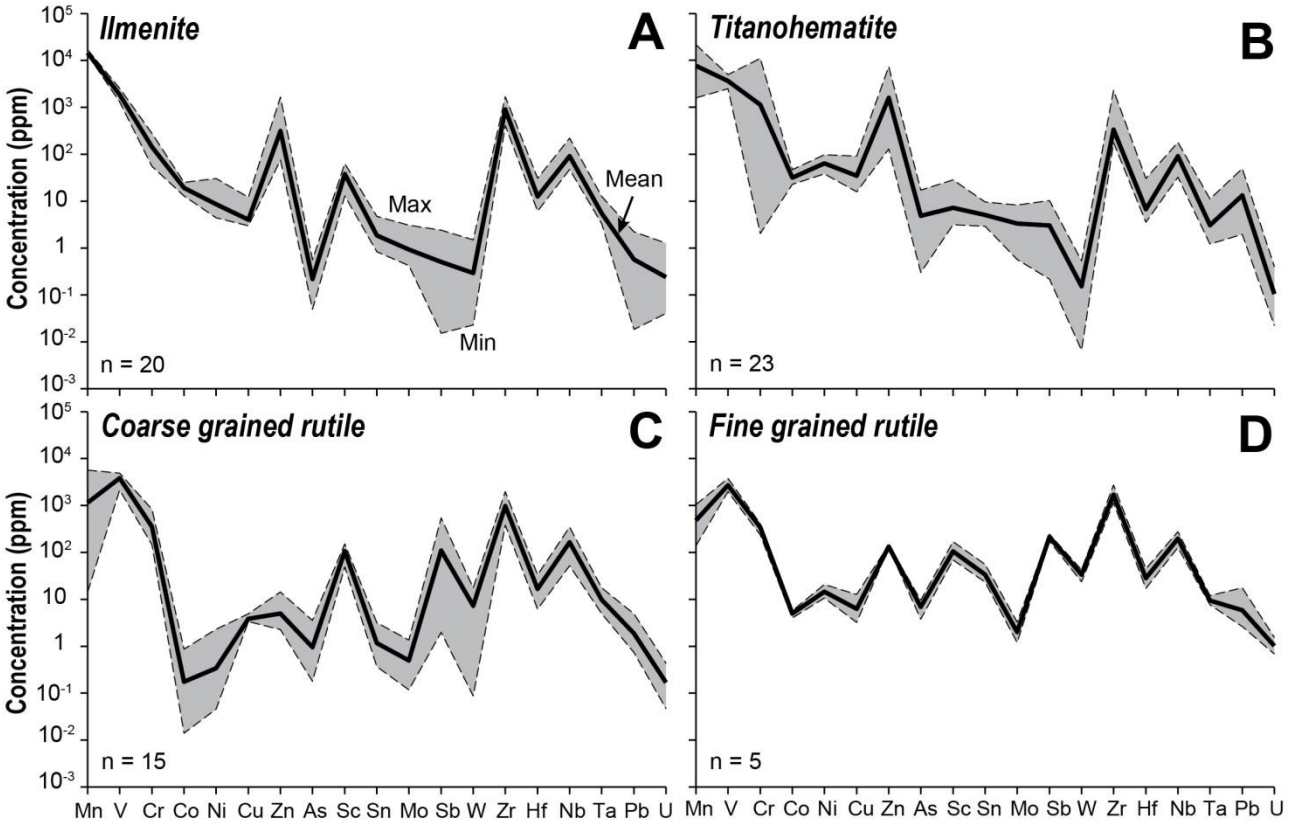

Fig. 6 Multi-element variation diagrams of trace elements composition of Fe-Ti oxides. **a** Trace element concentration of ilmenite, and **b** titanohematite from unaltered gabbro. **c** Trace element concentration of coarse grained rutile, and **d** fine grained rutile from the hydrothermally altered gabbro

6. Discussion

The trace element patterns reveal that the main changes in composition between ilmenite-hematite and rutile are the depletion in Zn, and the enrichment in Sb and W in rutile. High field strength elements (HFSE) appear to be immobile through the transformation. Partitioning behavior of several trace elements between ilmenite and melt (Klemme et al., 2006), between rutile and melt (Foley et al., 2000; Klemme et al., 2005) and between rutile and fluid (Brenan et al., 1994; Stalder et al., 1998) provide a framework to investigate the trace element composition of these minerals during the breakdown of Fe-Ti oxides under hydrothermal conditions. The partitioning of trace elements during the breakdown of ilmenite in the presence of fluids, and the Sb behavior between rutile and fluid, however, is less well constrained.

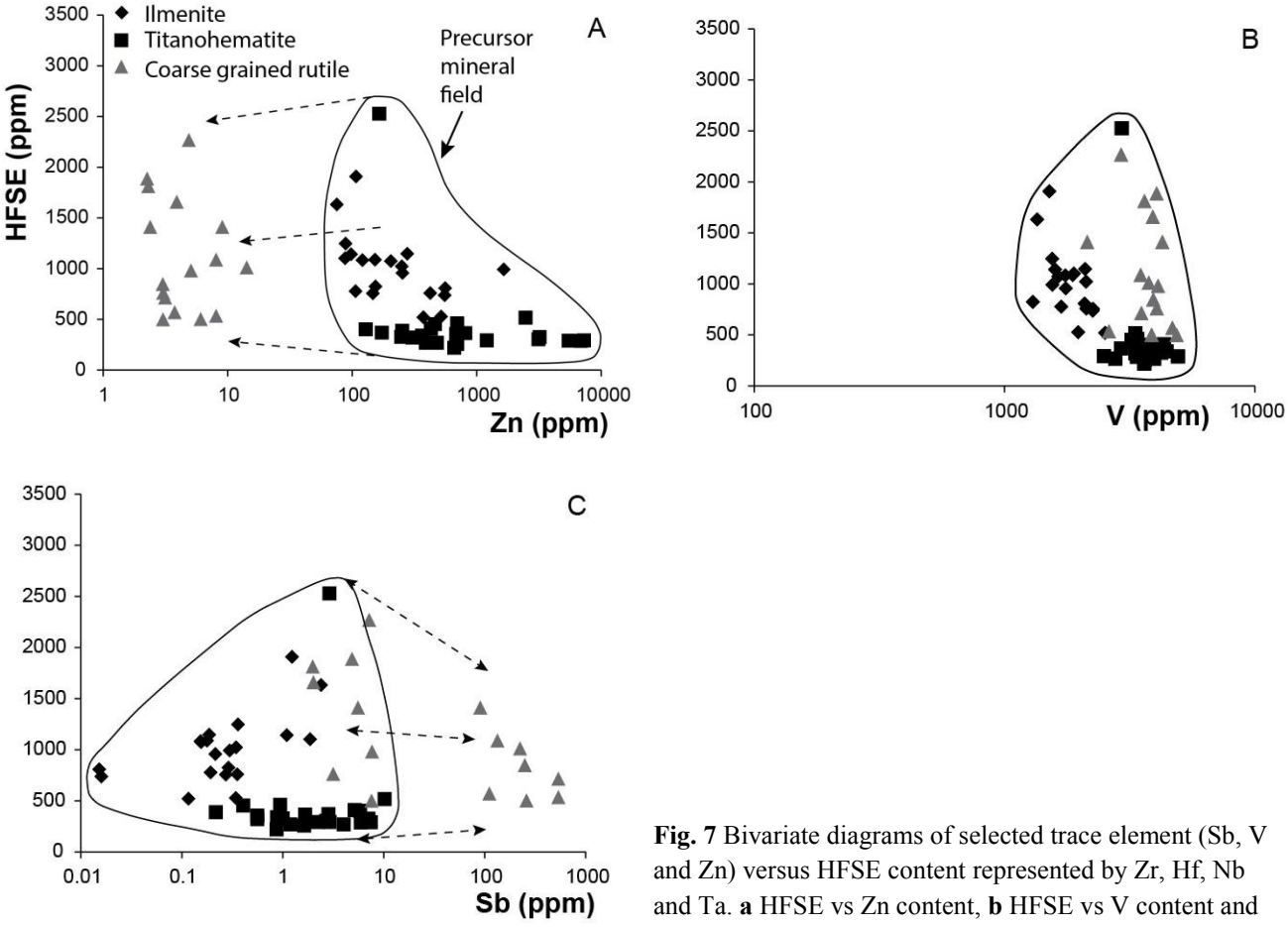

Fig. 7 Bivariate diagrams of selected trace element (Sb, V and Zn) versus HFSE content represented by Zr, Hf, Nb and Ta. **a** HFSE vs Zn content, **b** HFSE vs V content and **c** HFSE vs Sb content

6.1. Metasomatic change of gabbro dyke

Hydrothermal alteration associated with Sb mineralization causes metasomatic change of the gabbro dyke composition consistent with the mineralogical transformations previously described. These geochemical variations are displayed in Table 3 and in the isocon diagram (Fig. 8; Grant, 1986, 2005). Based on lowest loss on ignition (LOI) values, the least altered sample (SEM2) was selected to represent the protolith gabbro composition. However, as hydrothermal alteration is pervasive throughout the area, a degree of alteration was unavoidable. We define our isocon, using

the following elements that are considered immobile, Al2O3, TiO2, P2O5, Hf, Zr, Nb, Ta, Sc, Th, Y and some REE. Figure 8 shows that alteration is associated with significant mass gains in K and Ca, accompanied by Rb, Cs and As, and a significant mass loss in Na. This is consistent with the destruction of plagioclase and growth of illite during potassic alteration. Leaching of plagioclase will release Na into the fluids, whereas the formation of illite accounts for the enrichment of K, Rb and Ba. Plagioclase dissolution should release Ca, however carbonate precipitation causes an overall mass gain in Ca. The isocon diagram shows that As (mainly contained in arsenopyrite) correlates with potassic alteration and carbonation (Fig. 8). In contrast to As, Sb shows no significant mass change. Even if some dissemination of Sb-sulfides (stibnite and berthierite) with carbonates is observed in altered gabbro, this can be easily explained because arsenopyrite is more abundant in altered gabbro, whereas Sb-sulfides are mainly found inside veins. Furthermore, this may also indicate that our least altered sample (SEM2) was anomalous in Sb, and consequently that Sb was concentrated either during magmatic processes within the gabbroic dyke or was enriched during early pervasive alteration of the dyke. Silica shows no mobility despite quartz neo-crystallization. Iron also shows no mobility and may indicate that all Fe in the altered gabbroic rocks comes from the protolith, likely from the breakdown of ilmenite-titanohematite assemblage and clinopyroxene. Alteration is characterized by a small overall mass gain of 10 % (Fig. 8).

6.2. Growth of hydrothermal rutile

From petrographic observations, we infer that rutile grew during hydrothermal alteration of the dykes, concomitant with breakdown of ilmenite. Numerous natural and experimental studies show that the recrystallization of ilmenite to rutile typically occurs via pseudomorphic replacement (van Dyk et al., 2002; El-Hazek et al., 2007; Janssen et al., 2010; Janssen and Putnis, 2011). This mineral reaction process can be explained by two main models. First, the classical solid-state model involves a two-stage alteration mechanism (Grey and Reid, 1975; Mücke and Bhadra Chaudhuri, 1991; Ignatiev, 1999; Schroeder et al., 2002; Grey and Li, 2003): (i) a first stage of solid-state diffusion of iron and oxidation of Fe 2+ to form a transitional phase, pseudorutile, and (ii) a second stage where iron is leached from pseudorutile, causing concentration of Ti and subsequent precipitation of rutile.

The other model proposed as an alternative to the classical solid-state transformation, consists of the direct transformation of ilmenite to rutile via an interface-coupled dissolution-precipitation process (Janssen et al., 2010). The general principle of this mechanism is that an aqueous fluid causes dissolution of the parent mineral, producing an interfacial supersaturated fluid relative to the more stable product phase(s). These phases may nucleate at the surface of the parent mineral in epitaxial

relation and initiate an autocatalytic reaction that couples dissolution and precipitation (Putnis, 2002, 2009; Janssen et al., 2010; Ruiz-Agudo et al., 2014).

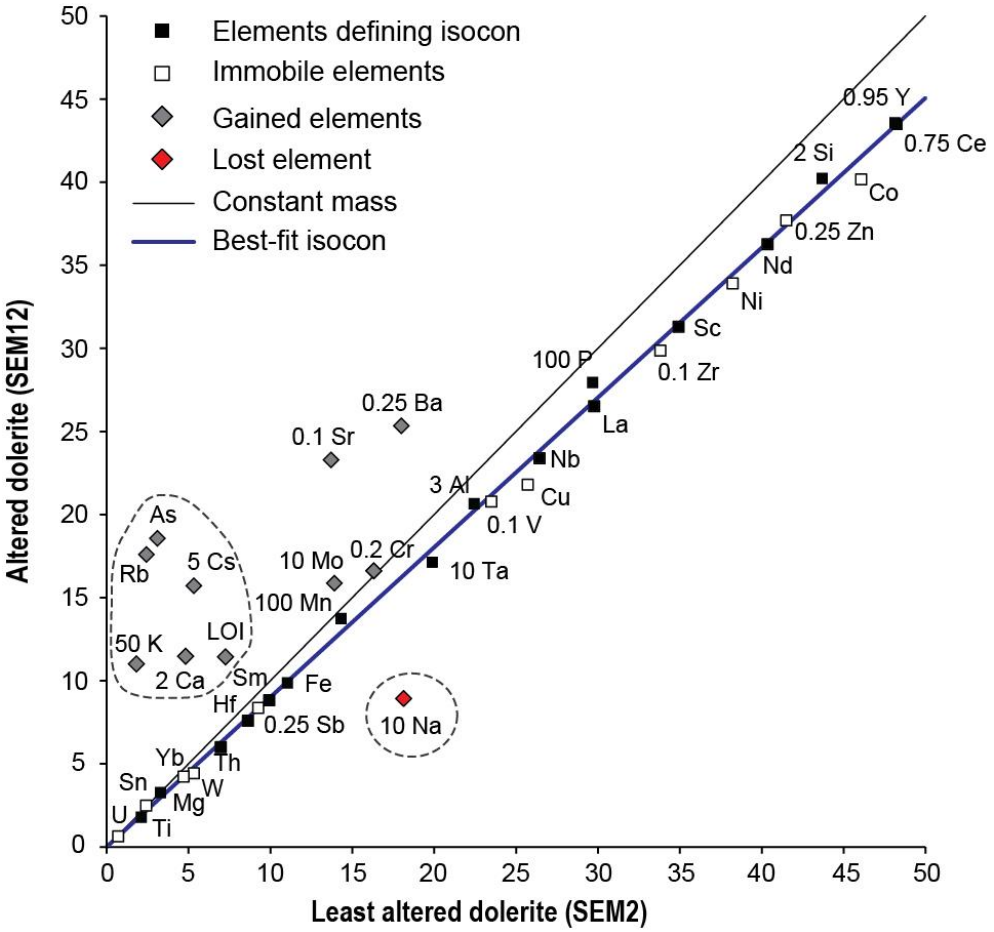

Fig. 8 Isocon diagram comparing the least altered with altered samples from the same gabbro dyke from the Semnon Sb-Au deposit. Major and trace elements values are scaled in order to compare the data to the best advantage but the scaling does not affect the results

Our textural observations and chemical analyses are consistent with the breakdown of ilmenite-titanohematite being via interface-coupled dissolution-reprecipitation process. For example, direct recrystallization of ilmenite to rutile is strongly suggested by associated porosity, and by lack of intermediate products (pseudorutile).

The newly formed rutile (i.e. CG and FG rutile) contains a strong interconnected network of µm-scale porosity. These pores are filled with later ankerite, calcite, quartz or illite (Fig. 3c-f and 5). CG rutile also contains numerous cracks mainly filled by FG rutile. Some cracks appear to have formed prior to the pseudomorphic replacement reaction (Fig. 3d). Infiltration of the fluid toward the core of the precursor mineral to generate fresh reaction surfaces is critical to the interface-coupled dissolution-reprecipitation process (Putnis and Austrheim, 2010, Putnis et al. 2005). Cracks and pores would have provided effective pathways for fluid infiltration, and provide further evidence that these mineral reactions occurred via interface-coupled dissolution-reprecipitation processes.

The occurrence of FG rutile around the preserved shape of precursor mineral and inside fractures (Fig. 3e and f) may represent paleo-reaction fronts.

Volume reduction associated with the recrystallization of ilmenite to rutile has previously been calculated at 40 % (Mücke and Bhadra Chaudhuri, 1991). In our samples, as the ratio ilmenite / titanohematite is not precisely known, we have estimated the volume change using the area of rutile in the preserved external shape of the precursor mineral parent by image analysis (e.g., Fig. 3c-f). Using this method, the volume reduction in our sample is estimated at 45 %. The small difference in volume change between ours and Mücke and Bhadra Chaudhuri (1991) values, is likely related to fact that the Le Semnon precursor mineral is not pure ilmenite, but an assemblage of ilmenite and titanohematite. Such volume reduction, combined with slight mass increase in the whole rock implicate a density increase probably related to the precipitation of sulfides, a process able to increase the rock density.

6.3. Redistribution of trace elements

A mineral replacement process may facilitate incorporation of elements from an external source and/or release of some elements to others phases or fluids, and hence contribute to the redistribution of elements in the Earth's crust and to mineralization processes (Rabbia et al., 2009; Lucassen et al., 2010; Putnis and Fernandez-Diaz, 2010; Pitcairn et al., 2014, 2015; Cave et al., 2015). An assessment of what elements are retained, released, or incorporated during coupled dissolution-reprecipitation mechanism can provide information about the mobility of trace elements, especially metals, during hydrothermal alteration. Thus, the geochemistry of ilmenite, titanohematite and rutile can be used to constrain the mass balance of the reaction and to quantify the mobility of trace elements during hydrothermal breakdown of Fe-Ti oxides related to Sb-mineralizing hydrothermal event.

The mineral assemblage composed of ilmenite and titanohematite is considered the precursor mineral because these two minerals are rarely found alone (Fig. 3c-d), which does not exclude the fact that the breakdown of ilmenite (or titanohematite) alone can also lead to rutile precipitation. Because of lesser quality microprobe analyses of FG rutile compared to CG rutile, we only consider CG rutile as the product mineral of the reaction. Assuming direct transformation, the overall mineral reaction can be written as:

$$Fe^{2+}TiO_3 + \left(Fe_x^{2+}, Fe_{2-2x}^{3+}\right)Ti_xO_3 + \downarrow fluid \uparrow \rightharpoonup (1+x)TiO_2 + [(1+x)Fe^{2+} + (2-2x)Fe^{3+}]_{solution} + \downarrow fluid \uparrow$$

Because the fluid composition is unknown, this theoretical mineral reaction cannot be balanced, but it illustrates that the destabilization of the mineral assemblage of ilmenite and

titanohematite leads to rutile precipitation and a release of iron in fluids. The mass balance of this reaction has been calculated following the approach of Gresens (1967). The density calculation follows Rabbia and Hernández (2012) and the required unit cell parameters are taken from Mücke and Bhadra Chaudhuri (1991) and Brown et al. (1993). The volume factor corresponds to the volume reduction between the precursor mineral and its product, estimated at ~ 45 % at the Le Semnon mine. Assuming that (1) Ti is completely incorporated in rutile and consequently it is immobile during the reaction and (2) trace elements from the precursor mineral are conservatively incorporated in rutile, the mass balance of the reaction indicates that, for a complete transformation, it requires 100 g of ilmenite and 2.9 g titanohematite to nucleate 50.1 g rutile which implies a release of 42.5 g FeO + 7.65 g Fe2O3 + 2.07 g MnO. As predicted by the mineral reaction, most elements, iron in particular, are released into the fluid phase during the reaction. Considering, the low TiO2 concentration in titanohematite, it is likely that titanohematite contributes to a small proportion of titanium in the nucleation of rutile, and a large proportion of iron into the fluid. Taking into account the stoichiometry of the reaction, 102.9 g of precursor minerals is necessary to produce 50.1 g of product mineral, such that a concentration factor of ~ 2.1 is calculated. This factor can be used to investigate what element will be incorporated into the newly formed mineral or released into the fluid (Gresens, 1967; Lucassen et al., 2010; Cave et al., 2015).

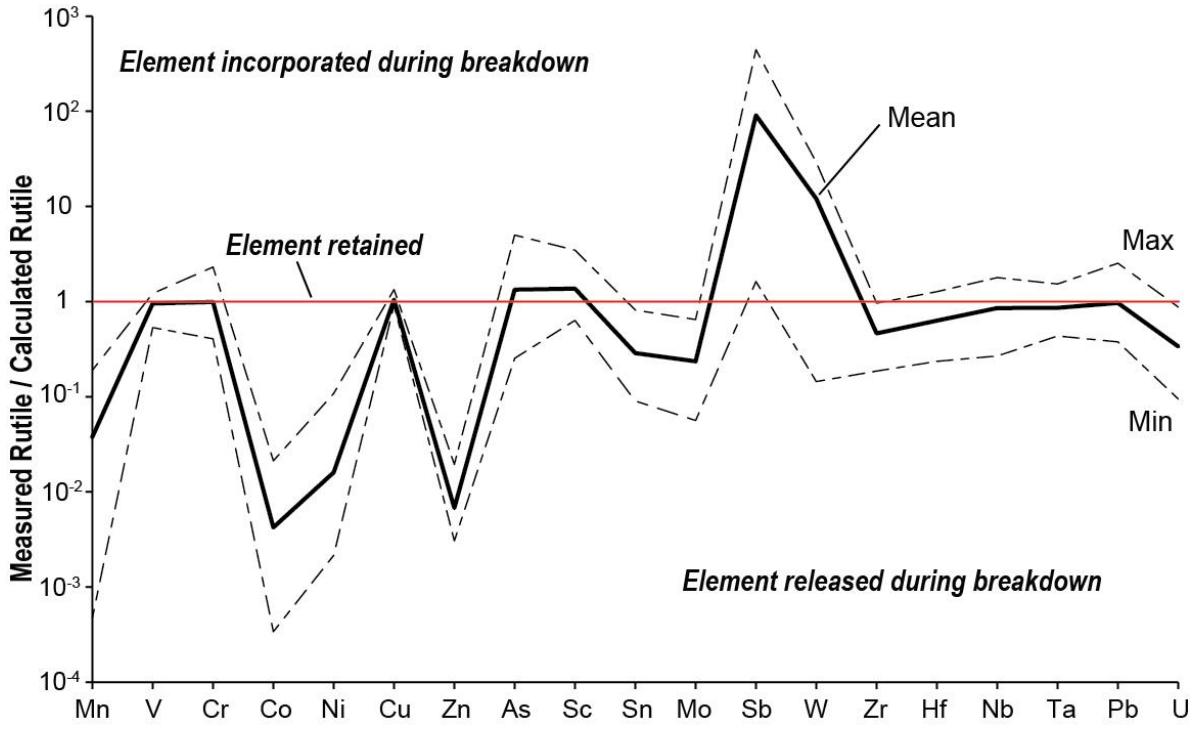

Fig. 9 Trace element profile for the average composition of hydrothermal CG rutile normalized to CG rutile composition calculated after Gresens (1967) for the Le Semnon gabbro dyke. See text for methodology

Using this concentration factor, we calculated the trace element composition of hydrothermal rutile using the average measured trace elements concentrations of precursor minerals, ilmenite and

titanohematite (Table 4). The mean of hydrothermal rutile trace element concentrations was normalized using calculated hydrothermal rutile trace element values (Fig.9).

Values < 1 indicate an element concentration lower than predicted by the calculation, therefore suggesting that this element was released into the fluid and/or incorporated into another mineral phase. Values ≈ 1 and > 1 correspond to retention from precursor minerals, or addition from an external source (such as a reactive fluid phase), respectively. In Figure 8, a comparison between calculated and measured values for hydrothermal rutile shows that most elements (HFSE, V, Cr, Cu, As, Sc, and Pb) have values ~ 1 indicating that they are sequestered by rutile precipitation, likely attesting to their compatible behavior in rutile, in particular the HFSE (Foley et al., 2000; Zack et al., 2002; Klemme et al., 2005). The remaining elements identified as being released into fluid phase and/or partitioned into other mineral phases are Mn, Co, Ni, Sn, Mo, U and Zn. Antimony and W have values above 1, suggesting incorporation into rutile from an external fluid phase. This is consistent with the data displayed in Fig. 7a, which shows that Zn is depleted in rutile compared to ilmenite-hematite, and which indicates that the precursor mineral signature is not completely preserved. In contrast, the concentration of V is quite similar between rutile and ilmenite-hematite (Fig. 7b). This suggests that part of precursor signature is preserved in the reaction product, and that this element is immobile in the hydrothermal fluids. Antimony behaves differently from the other elements, forming CG rutile with the precursor trace element signature (i.e., low Sb concentration) and with a hydrothermal fingerprint (i.e., high Sb concentration, Fig. 7c). This may be explained by two hypotheses: (1) either the first rutile is Sb-poor and Sb becomes enriched in fluids during the replacement reaction; consequently, the last-formed rutile is Sb-rich or (2) the first rutile is Sb-rich followed by an input of sulfur in the system, which causes precipitation of sulfides (e.g., arsenopyrite, pyrite, berthierite and stibnite), leading to rutile with low Sb concentration later. Unfortunately, lack of textural criteria to constrain the time relationships between the two subtypes of rutile prevents assessment of the two hypotheses.

The release of trace elements into fluids during the breakdown of ilmenite-titanohematite may constitute a potential, local source of elements for newly-formed phases, such as Zn for the sphalerite in mineralized veins, Co and Ni for pyrite and arsenopyrite, and Mn for ankerite in hydrothermally altered gabbro. In contrast, Sb cannot come from this mineral replacement reaction, as Sb has been largely added by an external source (Fig. 9). The identification of the external source(s) for Sb is relatively complex as Sb is strongly mobile in fluids (Noll et al., 1996; Deschamps et al., 2015). Sb could have been leached from another mineral reaction in the gabbro or sedimentary country rocks, or a deep-seated source, possibly related to the parent magma intrusions of gabbroic dyke swarms.

Although quantitative mass balance was not performed on FG rutile, it is important to note that most elements are enriched compared to CG rutile, particularly metals such as Zn, As, Sb, and W (Fig. 6 and Table 3). In the previous section, FG rutile is interpreted as a "fossilized" replacement reaction front. The enrichment of metals (Sb in particular) is in agreement with this assumption. This suggests that sealed fractures in pseudomorphically replaced minerals might be useful in investigating element mobility during coupled dissolution-precipitation reactions. Thus, the concentration of Sb in both FG and CG rutile types suggests that percolating hydrothermal fluids were rich in Sb, during the replacement process.

7. Hydrothermal Sb alteration model

A model for the alteration process, and redistribution of elements in Fe-Ti oxides at the Le Semnon mine, is proposed for the early hydrothermal event prior to the main stage of Sb mineralization (Fig. 10a-c). First, petrography of unaltered and altered gabbro documents several mineral transformations as a result of pervasive hydrothermal alteration, particularly the breakdown of magmatic ilmenite-titanohematite into hydrothermal rutile. This breakdown was accompanied by a significant increase in K and Ca, and a significant decrease in Na in the whole rock gabbro, consistent with pervasive illite and carbonate precipitation in gabbro. Part of the Ca was likely recycled from the destruction of plagioclase and clinopyroxene. The mineral replacement resulted from an interface-coupled dissolution-reprecipitation process. This autocatalytic reaction gradually generated porosity and micro fractures as a consequence of volume reduction which accelerated propagation of reaction fronts. This volume-change fracturing may have been coupled with tectonically-induced fracturing which would increase the progression of the reaction, but no evidence for tectonic fractures are recorded. These fluid pathways acted as the vector for redistribution of major and trace elements as illustrated in Fig. 10b. The mass balance indicates a release of Fe^{2+}, Fe^{3+}, Mn and Zn to the fluid phase, in a large part likely being sequestered by ankerite, Fe-sulfides and sphalerite precipitation. HFSE and Ti were retained by rutile precipitation, whereas Sb and W were carried by hydrothermal fluids and incorporated in the structure of rutile. Rutile recorded a sharp change in Sb concentration, likely corresponding to change in fluids composition and/or an input of sulfur in the hydrothermal system that resulted in sulfide precipitation, particularly arsenopyrite, pyrite, berthierite and stibnite (Fig. 10c).

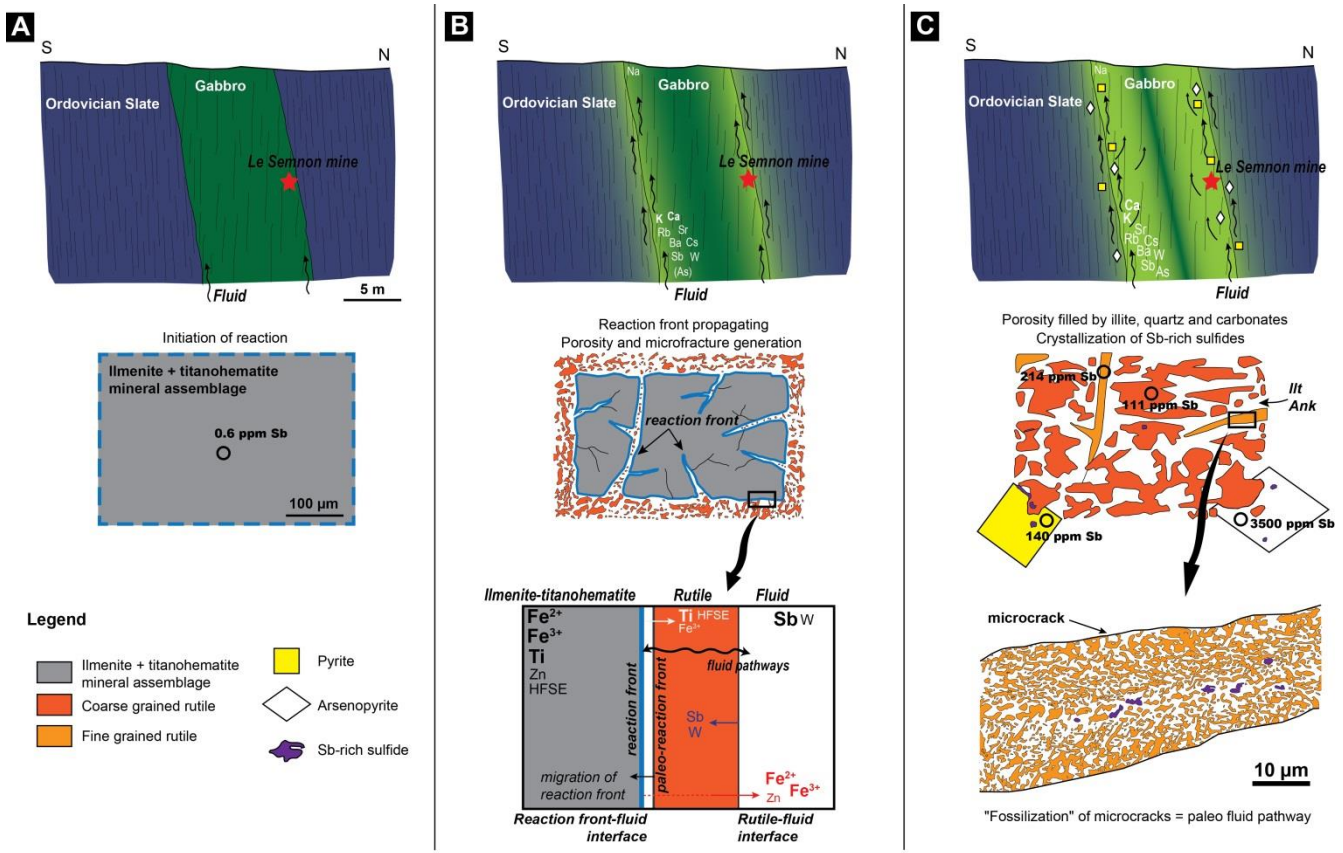

Fig. 10 Model of alteration process for the early hydrothermal event. **a** Stage 1: initiation of mineral replacement with progressive infiltration of fluids. Magmatic texture is preserved and Sb concentration is low in the precursor mineral assemblage composed of ilmenite and titanohematite. **b** Stage 2: progression of the reaction with the increase of hydrothermal alteration of gabbro and rutile precipitation. The altered dyke is enriched in K, Ca, Rb, Sr, Ba, Cs, Sb and W, and depleted in Na. Volume reduction associated with the mineral replacement reaction generates porosity and fractures inside the parent crystal and, consequently, promote the reaction front propagation. During the cementation of fluid pathways, the reaction principally releases iron, retains Ti, and incorporates external Sb. **c** The final stage ends the reaction by filling of the porosity by illite, quartz, carbonates and sulfide precipitation.

8. Conclusion

The breakdown of magmatic ilmenite-titanohematite to hydrothermal rutile is associated with a redistribution of trace elements. This reaction is mainly characterized by a release of Fe, Mg, Mn and Zn into hydrothermal fluids, and the incorporation of Sb and W into hydrothermal rutile. The mineral replacement reaction is not a potential source for the Sb mineralization, but likely contributes to the precipitation of sphalerite and ankerite. The hydrothermal fingerprint of rutile indicates a change of fluid composition during mineral replacement. Because rutile is a common accessory mineral in hydrothermal alteration and Sb is commonly associated with orogenic and subduction-related gold and base metal deposits, it appears fundamental to improve the knowledge of the behavior of Sb during fluid/rock interactions in order to characterize alteration, especially the partitioning between ilmenite-titanohematite assemblage, rutile, sulfides and hydrothermal fluids. New experimental data are necessary in order to better constrain the partitioning of Sb between these minerals, particularly at temperatures lower than 400°C. This would provide quantitative information about the parameters which controls HFSE and chalcophile behavior of Sb in Ti-bearing hydrothermal systems.

Acknowledgement

This work was funded by the BRGM, the region of Brittany, the OSUR and the doctoral school SDLM, with contributions from the Natural Sciences and Engineering Research Council of Canada, Agnico Eagle Mines and the Ministère de l'Énergie et des Ressouces naturelles of Québec. The author thanks Xavier Le Coz for thin sections, Jessica Langlade (UBO) and Marc Choquette (Laval) for EPMA analyses, and Dany Savard and Philippe Pagé (UQAC) for their assistance with LA-ICP-MS analyses. Constructive reviews by Pr. Dave Craw and an anonymous reviewer have greatly improved the manuscript.

References

Aïfa, T., Lefort, J.P., Guennoc, P., 1999. Anisotropy of magnetic susceptibility investigations of the St Malo dyke swarm (Brittany, France): emplacement mechanism of doleritic intrusions. Geophys. J. Int. 139, 573–582.

Ballouard, C., Boulvais, P., Poujol, M., Gapais, D., Yamato, P., Tartèse, R., Cuney, M., 2015. Tectonic record, magmatic history and hydrothermal alteration in the Hercynian Guérande leucogranite, Armorican Massif, France. Lithos 220–223, 1–22.

Barnes, S-.J., Maier, W.D., Ashwal, L.D., 2004. Platinum-group element distribution in the Main Zone and Upper Zone of the Bushveld Complex, South Africa. Chem. Geol. 208, 293–317.

Bouchot, V., Ledru, P., Lerouge, C., Lescuyer, J.L., Milesi, J.P., 2005. 5: Late Variscan mineralizing systems related to orogenic processes: The French Massif Central. Ore Geol. Rev. 27, 169–197.

Brenan, J.M., Shaw, H.F., Phinney, D.L., Ryerson, F.J., 1994. Rutile-aqueous fluid partitioning of Nb, Ta, Hf, Zr, U and Th: implications for high field strength element depletions in island-arc basalts. Earth Planet. Sc. Lett. 128, 327–339.

Bromiley, G.D., Hilairet, N., 2005. Hydrogen and minor element incorporation in synthetic rutile. Mineral. Mag. 69, 345–358.

Brown, N.E., Navrotsky, A., Nord, G.L., Banerjee, S.K., 1993. Hematite-ilmenite (Fe2O3-FeTiO3) solid solutions: Determinations of Fe-Ti order from magnetic properties. Am. Mineral. 78, 941–951.

Buddington, A.F., Lindsley, D.H., 1964. Iron–titanium oxide minerals and synthetic equivalents. J. Petrol. 5, 310–357.

Carignan, J., Hild, P., Mevelle, G., Morel, J., Yeghicheyan, D., 2001. Routine Analyses of Trace Elements in Geological Samples using Flow Injection and Low Pressure On-Line Liquid Chromatography Coupled to ICP-MS: A Study of Geochemical Reference Materials BR, DR-N, UB-N, AN-G and GH. Geostandards Newslett 25, 187–198.

Carruzzo, S., Clarke, D.B., Pelrine, K.M., MacDonald, M.A., 2006. Texture, composition, and origin of rutile in the South Mountain Batholith, Nova Scotia. Can. Mineral. 44, 715–729.

Cave, B.J., Stepanov, A.S., Craw, D., Large, R.R., Halpin, J.A., Thompson, J., 2015. Release of Trace Elements Through the Sub-Greenschist Facies Breakdown of Detrital Rutile to Metamorphic Titanite in the Otago Schist, New Zealand. Can. Mineral. 53, 379–400.

Chauris, L., Houlgatte, E., Laforêt, C., Picot, P., 1985. Un district antimono-aurifère à gangue quartzo-carbonatée : Le Semnon (Ille-et-Vilaine, Massif Armoricain, France). Hercynica 1, 111–119.

Chauris, L., Marcoux, E., 1994. Metallogeny of the Armorican Massif. In: Chantraine, J., Rolet, J., Santallier, D.S., Piqué, A., Keppie, J.D. (Eds.), Pre-Mesozoic Geology in France and Related Areas. Springer, Berlin Heidelberg, pp 243–264.

Clark, J.R., Williams-Jones, A.E., 2004. Rutile as a potential indicator mineral for metamorphosed metallic ore deposits. Rapport Final de DIVEX, Sous-projet SC2, Montréal, Canada. 17 pp.

Dare, S.A.S., Barnes, S-.J., Beaudoin, G., Méric, J., Boutroy, E., Potvin-Doucet, C., 2014. Trace elements in magnetite as petrogenetic indicators. Miner. Deposita 49, 785–796.

Dare, S.A.S., Barnes, S-.J., Beaudoin, G., 2012. Variation in trace element content of magnetite crystallized from a fractionating sulfide liquid, Sudbury, Canada: Implications for provenance discrimination. Geochim. Cosmochim. Ac. 88, 27–50.

Deschamps, F., Godard, M., Guillot, S., Hattori, K., 2013. Geochemistry of subduction zone serpentinites: A review. Lithos 178, 96-127.

Droop, G., 1987. A general equation for estimating Fe 3+ concentrations in ferromagnesian silicates and oxides from microprobe analyses, using stoichiometric criteria. Mineral. Mag. 51, 431–5.

El-Hazek, N., Lasheen, T.A., El-Sheikh, R., Zaki, S.A., 2007. Hydrometallurgical criteria for TiO2 leaching from Rosetta ilmenite by hydrochloric acid. Hydrometallurgy 87, 45–50.

Foley, S.F., Barth, M.G., Jenner, G.A., 2000. Rutile/melt partition coefficients for trace elements and an assessment of the influence of rutile on the trace element characteristics of subduction zone magmas. Geochim. Cosmochim. Ac. 64, 933–938.

Gapais, D., Le Corre, C., 1980. Is the Hercynian belt of Brittany a major shear zone. Nature 288, 574–576.

Gapais, D., Lagarde, J.L., Le Corre, C., Audren, C., Jégouzo, P., Casas Sainz, A., Van Den Driessche, J., 1993. La zone de cisaillement de Quiberon : témoin d'extension de la chaine varisque en Bretagne méridionale au Carbonifère. Cr. Acad. Sci. II 316, 1123–1129.

Gloaguen, E., Branquet, Y., Boulvais, P., Moelo, Y., Chauvel, J.J., Chiappero, P.J., Marcoux, E., 2007. Palaeozoic oolitic ironstone of the French Armorican Massif: a chemical and structural trap for orogenic base metal–As–Sb–Au mineralisation during Hercynian strike-slip deformation. Miner. Deposita 42, 399–422.

Gloaguen, E., Tourlière, B., Angel, J.M. 2016. Revalorisation du potentiel minier français : le district antimonifère du Semnon (Ille-et-Vilaine, France). BRGM report. BRGM/RP-66200-FR 71 pp.

Grant, J.A., 1986. The isocon diagram; a simple solution to Gresens' equation for metasomatic alteration. Econ. Geol. 81, 1976–1982.

Grant, J.A., 2005. Isocon analysis: A brief review of the method and applications. Phys. Chem. Earth Pt A/B/C 30, 997–1004.

Gresens, R.L., 1967. Composition-volume relationships of metasomatism. Chem. Geol. 2, 47-65.

Grey, I.E., Li, C., 2003. Hydroxylian pseudorutile derived from picroilmenite in the Murray Basin, southeastern Australia. Mineral. Mag. 67, 733-747.

Grey, I.E., Reid, A.F., 1975. The structure of pseudorutile and its role in the natural alteration of ilmenite. Am. Mineral. 60, 898–906.

Gumiaux, C., Gapais, D., Brun, J.P., Chantraine, J., Ruffet, G., 2004. Tectonic history of the Hercynian Armorican Shear belt (Brittany, France). Geodinamica Acta 17, 289–307.

Ignatiev, V.D., 1999. Solid phase mechanism of the ilmenite leucoxenisation. Lithol. Miner. Resour. 34, 184-189.

Jamtveit B, CV, Malthe-Sørenssen A (2009) Reaction induced fracturing during replacement processes. Contrib Mineral Petr 157:127-133.

Janssen, A., Putnis, A., 2011. Processes of oxidation and HCl-leaching of Tellnes ilmenite. Hydrometallurgy 109, 194–201.

Janssen, A., Putnis, A., Geisler, T., Putnis, C.V., 2010. The experimental replacement of ilmenite by rutile in HCl solutions. Mineral. Mag. 74, 633–644.

Klemme, S., Günther, D., Hametner, K., Prowatke, S., Zack, T., 2006. The partitioning of trace elements between ilmenite, ulvospinel, armalcolite and silicate melts with implications for the early differentiation of the moon. Chem. Geol. 234, 251–263.

Klemme, S., Prowatke, S., Hametner, K., Günther, D., 2005. Partitioning of trace elements between rutile and silicate melts: Implications for subduction zones. Geochim. Cosmochim. Ac. 69, 2361-2371.

Lahaye, Y., Blais, S., Auvray, B., Ruffet, G., 1995. Le Volcanisme fissural paleozoique du domaine nord-armoricain. B. Soc. Geol. Fr. 166, 601-612.

Le Gall, J., 1999. Les dolérites et basaltes tholéiitiques varisques du domaine nord-est armoricain. Géologie de la France 4, 3-26.

Lucassen, F., Dulski, P., Abart, R., Franz, G., Rhede, D., Romer, R.L., 2010. Redistribution of HFSE elements during rutile replacement by titanite. Contrib. Mineral. Petr. 160, 279 – 295

Luvizotto, G.L., Zack, T., Triebold, S., von Eynatten, H., 2009. Rutile occurrence and trace element behavior in medium-grade metasedimentary rocks: example from the Erzgebirge, Germany. Miner. Petrol. 97, 233-249.

Malthe-Sørenssen, A., Jamtveit, B., Meakin, P., 2006. Fracture patterns generated by diffusion controlled volume changing reactions. Phys. Rev. Lett. 96, 245-501.

Meinhold, G., 2010. Rutile and its applications in earth sciences. Earth Sci. Rev. 102, 1-28.

Mücke, A., Bhadra Chaudhuri, J.N., 1991. The continuous alteration of ilmenite through pseudorutile to leucoxene. Ore Geol. Rev. 6, 25-44.

Morad, S., Aldahan, A.D., 1986. Alteration of detrital Fe-Ti oxides in sedimentary rocks. Geol. Soc. Am. Bull. 97, 567-578.

Noll, P.D., Newsom, H.E., Leeman, W.P., Ryan, J.G., 1996. The role of hydrothermal fluids in the production of subduction zone magmas: Evidence from siderophile and chalcophile trace elements and boron. Geochim. Cosmochim. Ac. 60, 587-611.

Pitcairn, I.K., Craw, D., Teagle, D.A.H., 2014. The gold conveyor belt: Large-scale gold mobility in an active orogeny. Ore Geol. Rev. 62, 129-142.

Pitcairn, I.K., Craw, D., Teagle, D.A.H., 2015. Metabasalts as sources of metals in orogenic gold deposits. Miner. Deposita 50, 373-390.

Pochon, A., Gapais, D., Gloaguen, E., Gumiaux, C., Branquet, Y., Cagnard, F., Martelet, G., 2016a. Antimony deposits in the Variscan Armorican belt, a link with mafic intrusives? Terra Nova 28, 138–145.

Pochon, A., Poujol, M., Gloaguen, E., Branquet, Y., Cagnard, F., Gumiaux, C., Gapais, D., 2016b. U-Pb LA-ICP-MS dating of apatite in mafic rocks: Evidence for a major magmatic event at the Devonian-Carboniferous boundary in the Armorican Massif (France). Am. Mineral. 101, 2430–2442.

Putnis, A., 2002. Mineral replacement reactions: from macroscopic observations to microscopic mechanisms. Mineral. Mag. 66, 689–708.

Putnis, A., 2009. Mineral Replacement Reactions. Reviews in Mineralogy and Geochemistry 70, 87–124.

Putnis, A., Austrheim H., 2010. Fluid-induced processes: metasomatism and metamorphism. Geofluids 10, 254–269.

Putnis, C.V., Fernandez-Diaz, L., 2010. Ion Partitioning and Element Mobilization During Mineral Replacement Reactions in Natural and Experimental Systems. EMU Notes in Mineralogy: Ion Partitioning in Ambient Temperature Aqueous Systems, 10, 189–226.

Rabbia, O.M., Hernández, L.B., French, D.H., King, R.W., Ayers, J.C., 2009. The El Teniente porphyry Cu–Mo deposit from a hydrothermal rutile perspective. Miner. Deposita 44, 849–866.

Rabbia, O.M., Hernández, L.B., 2012. Mineral chemistry and potential applications of natural-multi-doped hydrothermal rutile from porphyry copper deposits. In: It-Meng (Jim) Low (Ed.), Rutile: Properties, Synthesis and Application. Nova Science Publishers, Inc., pp 209-228.

Rice, C., Darke, K., Still, J., 1998. Tungsten-bearing rutile from the Kori Kollo gold mine

Bolívia. Mineral. Mag. 62, 421–429.

Ruiz-Agudo, E., Putnis, C.V., Putnis, A., 2014. Coupled dissolution and precipitation at mineral–fluid interfaces. Chem. Geol. 383, 132–146.

Schroeder, P., Le Golvan, J., Roden, M., 2002. Weathering of ilmenite from granite and chlorite schist in the Georgia Piedmont. Am. Mineral. 87, 1616-1625.

Scott, K.M., 2005. Rutile geochemistry as a guide to porphyry Cu–Au mineralization, Northparkes, New South Wales, Australia. Geochem. Explor. Env. A 5, 247–253.

Scott, K.M., Radford, N.W., 2007. Rutile compositions at the Big Bell Au deposit as a

guide for exploration. Geochem. Explor. Env. A 7, 353–361.

Smith, D.C., Perseil, E.A., 1997. Sb-rich rutile in the manganese concentrations at St. Marcel-Praborna, Aosta Valley, Italy; petrology and crystal-chemistry. Mineral. Mag. 61, 655–669.

Stalder, R., Foley, S.F., Brey, G.P., Horn, I., 1998. Mineral–aqueous fluid partitioning of trace elements at 900 °C–1200 °C and 3.0 GPa to 5.7 GPa: new experimental data set for garnet, clinopyroxene and rutile and implications for mantle metasomatism. Geochim. Cosmochim. Ac. 62, 1781–1801.

Tartèse, R., Boulvais, P., 2010. Differentiation of peraluminous leucogranites “en route” to the surface. Lithos 114, 353–368.

Tartèse, R., Poujol, M., Ruffet, G., Boulvais, P., Yamato, P., Košler, J., 2011a. New U-Pb zircon and 40Ar/39Ar muscovite age constraints on the emplacement of the Lizio syn-tectonic granite (Armorican Massif, France). C. R. Geosci. 343, 443–453.

Tartèse, R., Ruffet, G., Poujol, M., Boulvais, P., 2011b. Simultaneous resetting of the muscovite K-Ar and monazite U-Pb geochronometers: a story of fluids. Terra Nova 23, 390–398.

Tartèse, R., Poujol, M., Gloaguen, E., Boulvais, P., Drost, K., Košler, J., Ntaflos, T., 2015. Hydrothermal activity during tectonic building of the Variscan orogen recorded by U-Pb systematics of xenotime in the Grès Armoricain formation, Massif Armoricain, France. Miner. Petrol. 109, 485–500.

Tomkins, H.S., Powell, R., Ellis, D.J., 2007. The pressure dependence of the zirconium-in-rutile thermometer. J. Metamorph. Geol. 25, 703–713.

Triebold, S., von Eynatten, H., Luvizotto, G.L., Zack, T., 2007. Deducing source rock lithology from detrital rutile geochemistry: an example from the Erzgebirge, Germany. Chem. Geol. 244, 421–436.

Urban, A.J., Hoskins, B.F., Grey, I.E., 1992. Characterization of V–Sb–W-bearing rutile from the Hemlo gold deposit, Ontario. Can. Mineral. 30, 319–326.

van Dyk, J.P., Vegter, N.M., Pistorius, P.C., 2002. Kinetics of ilmenite dissolution in hydrochloric acid. Hydrometallurgy 65, 31–36.

Whitney, D.L., Evans, B.W., 2010. Abbreviations for names of rock-forming minerals. Am. Mineral. 95, 185-187.

Williams, S.A., Cesbron, F.P., 1977. Rutile and apatite: useful prospecting guides for porphyry copper deposits. Mineral. Mag. 41, 288-292.

Zack, T., John, T., 2007. An evaluation of reactive fluid flow and trace element mobility in subducting slabs. Chem. Geol. 239, 199-216.

Zack, T., Kronz, A., Foley, S.F., Rivers, T., 2002. Trace element abundances in rutiles from eclogites and associated garnet mica schists. Chem. Geol. 184, 97–122.

Zack, T., von Eynatten, H., Kronz, A., 2004. Rutile geochemistry and its potential use in quantitative provenance studies. Sediment. Geol. 171, 37-58.

Résumé en français de l'article #4

De nombreux gisements à Sb-Au sont connus au sein de la chaîne Varisque ouest-européenne. Ces minéralisations sont souvent considérées comme appartenant à des évènements hydrothermaux tardi-varisque associés à l'extension post-orogénique et à des systèmes décrochant à travers toute la chaîne. Le domaine central du Massif Armoricain (Bretagne Centrale) contient de nombreux indices Sb-Au, dont le gisement du Semnon. Cependant, peu de données ont été apportées quant à la compréhension de sa formation, tels que les contrôles structuraux ou l'histoire hydrothermale dans son ensemble. Afin d'apporter de nouvelles contraintes sur les minéralisations Varisque à Sb-Au du Massif Armoricain, des données structurales, géochronologique et géochimique ont été acquises sur le gisement Sb-Au du Semnon. Premièrement, nous mettons en lumière que la minéralisation Sb-Au se compose de fentes de tension et de veines à remplissage de failles et résulte d'un mécanisme de valve sismique à faible profondeur et contrôlé par des surpressions de fluides cycliques. En effet, ce gisement est caractérisé par la présence de dykes de dolérites qui jouent le rôle d'un système de plomberie pour les fluides au sein d'une couche de schistes imperméable permettant d'atteindre une pression de fluides supralithostatique dans un régime hydrostatique dominant. Couplées avec de nouvelles données structurales, minéralogique et physico-chimique, les analyses ^{40}Ar / ^{39}Ar et U-Pb par LA-ICP-MS révèlent que la minéralisation Sb-Au du Semnon se met en place vers 360 Ma et est précoce dans l'hydrothermalisme varisque du Massif Armoricain. Il apparait également que la mise en place de cette minéralisation est sub-synchrone de la mise en place de la dolérite encaissante. De plus, les fortes températures enregistrées au sein des inclusions fluides et l'évolution paragénétique suggèrent une anomalie thermique élevée au sein du Domaine Centre Armoricain. Ainsi, nous proposons que la mise en place d'un magmatisme mafique généralisé à 360 Ma joue un rôle majeur dans la mobilisation des fluides et dans la redistribution des métaux au sein de la croûte armoricaine.

Hydrothermal history of Variscan Sb-Au mineralization in Central Brittany (France)

Anthony Pochon[1*], Eric Gloaguen[2, 3], Yannick Branquet[1, 2], Marc Poujol[1], Gilles Ruffet[1], Philippe Boulvais[1], Marie-Christine Boiron[4], Charles Gumiaux[2], Florence Cagnard[3], Fanny Gouazou[4], Denis Gapais[1]

[1] *Géosciences Rennes, UMR 6118, Université de Rennes 1, OSUR, Campus de Beaulieu, 35042 Rennes Cedex, France*

[2] *Institut des Sciences de la Terre d'Orléans, UMR 7327, Université d'Orléans, Campus Géosciences, 1A rue de la Férollerie, 45071 Orléans Cedex 2, France*

[3] *Bureau de Recherche Géologique et Minière (BRGM), UMR 7327, 3 avenue Claude-Guillemin, BP 36009, 45060 Orléans Cedex 02, France*

[4] *GeoRessources, CNRS, Université de Lorraine, CREGU, Faculté des Sciences et Technologies, Campus des Aiguillettes, B.P. 70239, F-54506, Vandœuvre-lès-Nancy cedex, France*

Article en préparation en vue d'une soumission simultanée avec l'article #5 (« compagnon papers ») pour la revue *Mineralium Deposita*

Abstract

Numerous Sb-Au deposits are known in the European Variscan belt. These mineralization are often considered as belonging to the late Variscan hydrothermal events associated with postorogenic extension and strike-slip faults, through the whole belt. The central part of the Armorican Massif (Central Brittany) hosts several Sb-Au deposits, such as the Le Semnon deposit. However, little is known about its formation, such as the structural control or hydrothermal history. In order to provide new constraints on the Sb-Au mineralization framework of the Variscan Armorican belt, structural, geochronological and chemical analyses have been performed on the Le Semnon Sb-Au deposit. First, we highlighted that Sb-Au mineralization consists of fault-fill and flat extensional vein systems resulting from small-scale fault-valve controlled by fluid overpressure at shallow depth. Indeed, this deposit is characterized by the presence of dolerite dykes which acted as the plumbing system for fluids within impermeable slates allowing for supralithostatic fluid pressure in a predominantly hydrostatic regime. Coupled with new (micro-)structural evidences, a reappraisal of the paragenetic evolution and new physico-chemical data, ^{40}Ar / ^{39}Ar and LA-ICP-MS U-Pb analyses show that the Le Semnon Sb-Au mineralization was emplaced around 360 Ma and therefore corresponds to an early hydrothermal event in the Variscan history of the Armorican Massif. It also appears that the emplacement of the Sb-Au mineralization is coeval with the emplacement of the host rock doleritic dyke. Furthermore, the high temperature recorded in fluid inclusions and by the paragenetic evolution suggests an elevated thermal anomaly in Central Brittany. Thus, we propose that the emplacement of the widespread mafic magmatism at *ca.* 360 Ma played a major role in the mobilization of fluid flows and the redistribution of metals in the Armorican crust.

Keywords: Sb-Au mineralization, Early Carboniferous hydrothermal event, Spatiotemporal link with mafic rocks, Fluid overpressure.

1. Introduction

Antimony deposits are frequently associated with other metals such as gold. Sb-Au mineralization mainly forms at shallow depths and belongs to orogenic gold deposit type (e.g. Groves et al. 1998, 2003, Bierlein and Crowe 2000, Goldfard et al. 2001, 2005, 2015). Although most orogenic Au ± Sb deposits are mainly Archean or Proterozoic in age, some are known in Phanerozoic belts, such as the European Variscan belt. Indeed, Sb-Au deposits are widespread in the Iberian Massif in Spain and Portugal (e.g. Gumiel and Arribas 1987, Couto et al. 1990; Neiva et al. 2008), in the French Massif Central (FMC) and Armorican Massif in France (e.g. Périchaud 1980, Boiron et al. 1990, Chauris and Marcoux 1994, Bouchot et al. 2005), in the Saxo-Thuringian zone in Germany (Dill et al. 1985, Wagner and Cook 2000), in the Bohemian Massif (e.g. Němec and Zachariáš 2017) and in the Slovakian Western Carpathians (e.g. Chovan et al. 1995). Variscan Sb-Au hydrothermal deposits share many features such as (1) spatial relationships with regional-scale faults and shear zones (e.g. Bellot et al. 2003), (2) localization of Sb-Au quartz veins within anticlinal hinge or (3) relation with late-Variscan tectonic processes (e.g. post-thickening collapse, Bouchot et al. 2005). Sb-Au deposits from the FMC are considered to be formed during a short-time and large-scale hydrothermal event around 300 Ma resulting from thermal events related to post-thickening collapse of the Variscan orogen (Costa and Rey 1995, Bouchot et al. 2005). During this period, Sb-Au deposits results from the exhumation of lower continental crust and the mixing between deep metamorphic fluids and cold meteoric fluids (Boiron et al. 2003).

Although the Armorican Massif contains the largest part of Sb resources in France (Gloaguen et al. 2016a), Sb-Au deposits are not very well documented in contrast to those in the FMC. In particular in Central Brittany, the hydrothermal history of Sb-Au mineralization remains unconstrained. It is commonly assumed that regional-scale shear zones control the localization of the deposits. Chauris and Marcoux (1994) suggested that the Sb could be sourced from various felsic magmatic rocks emplaced during the Cambrian-Carboniferous period, and deposited within Late Variscan shear zones. However, in Central Britany, a significant part of the Sb-Au deposits, including the Le Semnon Sb-Au deposit, is located away from shear zones (Fig. 1). In addition, Pochon et al. (2016a) highlighted the strong spatial relationship between Sb-Au mineralization and high density and magnetic zones, which have been interpreted as mafic/ultramafic bodies at depth. In this paper, we focus on the Le Semnon Sb-Au deposit, which hosts the largest potential in Sb in the Armorican Massif (Gloaguen et al. 2016b). We present evidences for structural control, geochemical data on mafic rocks associated with mineralization, geochronological, isotopic and fluid inclusions data that help constraining hydrothermal event. We reveal that Sb-Au mineralization formed from shallow fluid flow associated with mafic magmatism. Mineralization

was early in the Variscan history of the Armorican Massif (near 360 Ma), significantly older than the Late Variscan assumed age for other Sb-Au deposits from the West-European Variscan belt.

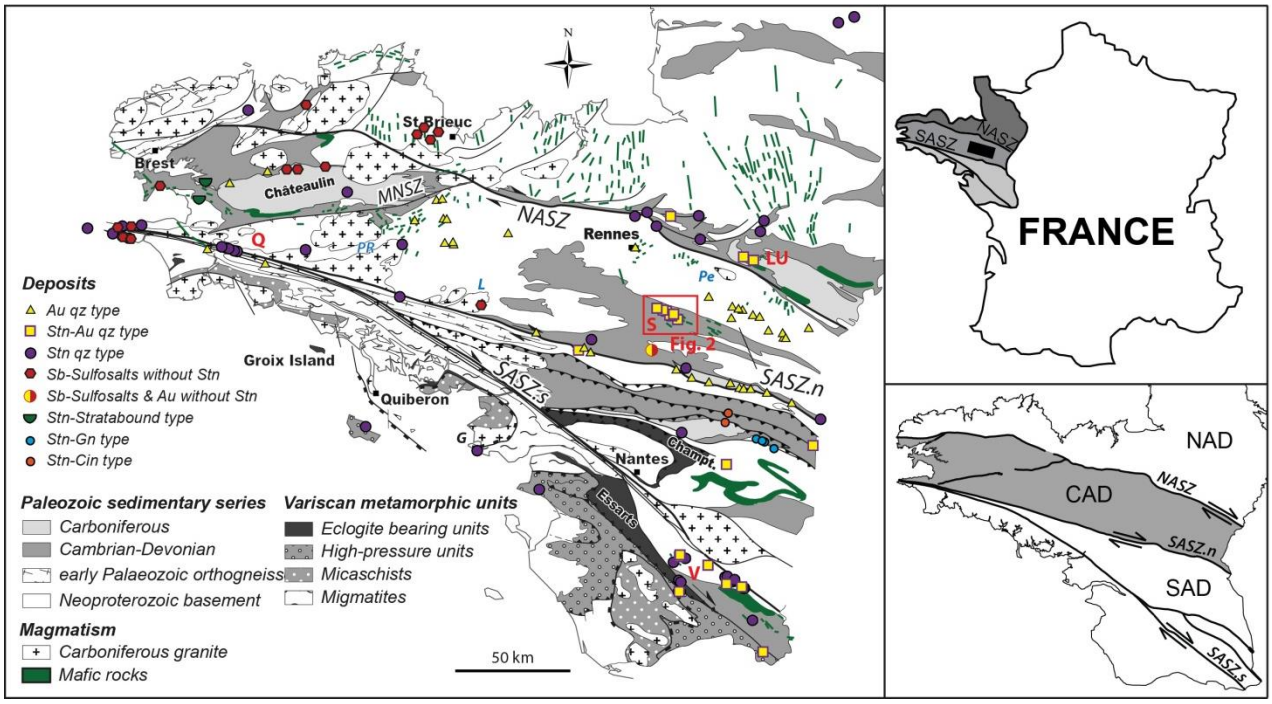

Figure 1 Simplified geological map of the Armorican Massif modified from Chantraine et al. (1996) with the geographic position of the Armorican Massif in France and the localization of the three main domains: North Armorican domain (NAD), Central Armorican domain (CAD), and South Armorican domain (SAD). Typology of Sb-Au occurrences is from Pochon et al. (2016a). NASZ = North Armorican Shear Zone; SASZ.n and SASZ.s = northern and southern branch of the South Armorican Shear Zone, respectively; MNSZ = Montagnes Noires Shear Zone; PR = Pontivy-Rostrenen magmatic complex; L = Lizio granite; Pe = Le Pertre granite; LU = world-class La Lucette Sb-Au mine; S = Le Semnon Sb-Au district; V = Vendée Sb-(Au) district; Q = Quimper-Cap Sizun Sb district; Stb = stibnite; Gn = galena; Cin= cinnabar

2. Geological background

2.1 Central Brittany

Central Brittany, the central part of the Armorican Massif, belongs to the external domain of the West-European Variscan belt, which resulted from the continental collision between the Gondwana and Laurussia plates and the Armorica microplate (Ballèvre et al. 2009, 2014). This collision began during the late Devonian, highlighted by the record of continental subduction at c. 360 Ma (Bosse et al. 2000, 2005), and ended in the late Carboniferous around 300 Ma (Matte 1986, Gumiaux et al. 2004b, Ballèvre et al. 2014). This domain is bounded by two dextral crustal-scale shear zones (Fig. 1), the North Armorican Shear Zone (NASZ) and the northern branch of the South Armorican Shear Zone (SASZ). Another shear zone, the Montagnes Noires Shear Zone (MNSZ), separates two distinct sub-domains with contrasted structural styles and magmatic history, the Western and Eastern Central Brittany (Gumiaux et al. 2004b). Eastern Central Brittany mainly shows a continuous Carboniferous deformation that affected the Late Neoproterozoic to upper

Paleozoic sediments, compatible with the N125°E-trending dextral simple shear of the entire Central Brittany (Gumiaux et al. 2004a, 2004b). Deformation is characterized by upright folds with E-W striking and horizontal axes and wavelength-controlled by the competent unit of the lower Ordovician Armorican sandstone. Folds are associated with a sub-vertical axial-plane cleavage bearing a sub-horizontal lineation parallel to folds axes (Gapais and Le Corre, 1980). During the Variscan orogeny, Eastern Central Brittany underwent a very low-grade metamorphism with an estimated maximum temperature reaching up to 250-300°C, based on vitrinite reflectance (Donnot et al. 1973), chloritoid-bearing slate occurrences (Le Corre 1969), the illite crystallinity (Le Corre 1975) and the chlorite geothermometer (Gloaguen et al. 2007). Contrary to the western and southern part of the Armorican Massif, granitic intrusions are relatively scarce in Eastern Central Brittany (Fig. 1) with (1) some late Carboniferous intrusions emplaced at *ca.* 315 Ma, such as the Lizio granite (Tartèse et al. 2011) and the Pontivy-Rostrenen magmatic complex (Ballouard et al. 2017), and (2) the Le Pertre granite with an emplacement poorly constrained at *ca.* 340 Ma (Vernhet et al. 2009). Central Brittany is also marked by a widespread swarm of dolerite dykes and sills dated at 363.4 ± 5.8 Ma (U-Pb on apatite, Pochon et al. 2016b). These mafic rocks are characterized by geochemically homogeneous compositions with no significant crustal input, interpreted as a within-plate type like alkaline continental basalts (Pochon et al. 2016b). Antimony and gold mineralization, such as the Le Semnon Sb-Au district (Chauris et al. 1985, Pochon et al. 2016a, Gloaguen et al. 2016b), are geometrically associated with these mafic rocks.

Most of Sb-Au occurrences – with the exception of the Vendée district – are localized within Central Brittany and along the northern branch of SASZ (Fig. 1). Sb-Au ore deposits generally consist of stibnite-gold bearing quartz lodes, such as the world-class La Lucette mine (42 kt Sb and 8.4 t Au) or the Le Semnon district with an estimated reserve of 45 kt Sb and 3.3 t Au (Gloaguen et al. 2016b). According to Chauris and Marcoux (1994), in the Armorican Massif, the source of antimony could be pre-Variscan, probably from various felsic magmatic events spanning the Cambrian-Carboniferous period (Marcoux et al. 1984), remobilized by late Variscan magmatic and hydrothermal events and deposited within Late Variscan shear zones at shallow depths around 300 Ma such as those of the French Massif Central (Boiron et al. 1989, 2003, Bouchot et al. 2005). This short-time and large-scale fluid flow is contemporaneous with granites emplacement and associated W ± Sn deposits, which results from thermal events related to post-thickening collapse of the Variscan Orogen (Costa and Rey 1995, Bouchot et al. 2005). More recently, a strong statistical and spatial correlation between Sb (± Au) occurrences and relatively high density and magnetic zones has been demonstrated (Pochon et al. 2016a). These high density and magnetic zones might correspond to the occurrence at depth of mafic/ultramafic bodies, which have been interpreted as magma chambers responsible for the numerous dolerite dyke and sill swarms observed close to the

paleo-surface in Central Brittany and dated at *ca.* 360 Ma (Pochon et al. 2016b), such as the Le Semnon area (Fig. 1).

2.2 The Le Semnon Sb-Au district

The Le Semnon Sb-Au district is located in the center of Central Brittany, far away from NASZ and the northern branch of SASZ (Fig. 1). The district consists of a N120°E striking, near vertical, dolerite dyke swarm intruded in the Lower to Middle Ordovician slates (Fig. 2), locally called "Formation d'Angers-Traveusot".

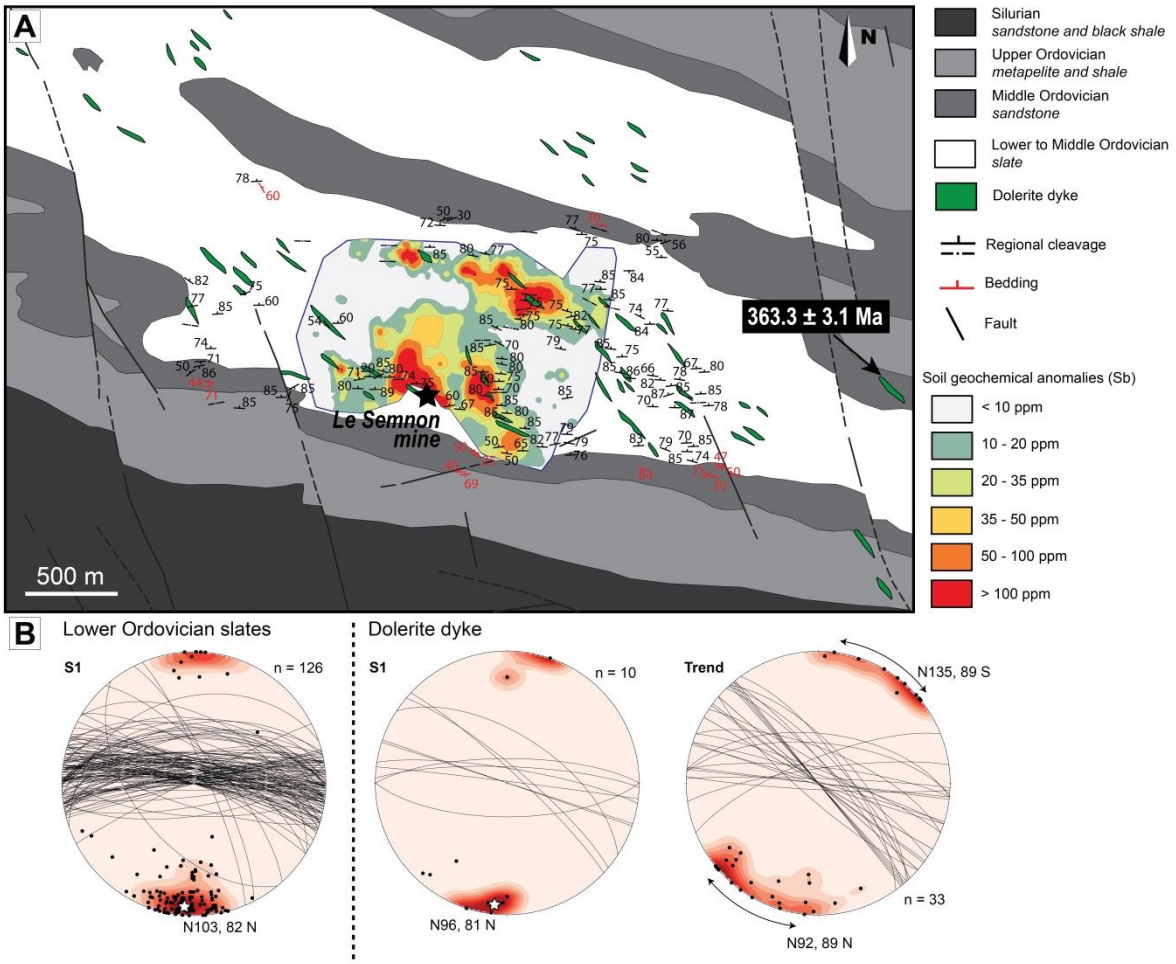

Figure 2 a Geological and structural map of the Semnon Sb-Au district with the location of the old Semnon mine and the soil geochemical Sb anomalies compiled by Gloaguen et al. (2016b). Dolerite dyke in the eastern part of the map comes from the Martigné-Ferchaud quarry and it has been dated at 363.3 ± 3.1 Ma by Pochon et al. (2016). **b** Stereograms showing the density, great circles and poles of regional cleavage of the Lower Ordovician slates and dolerite dykes and the trending of dolerite dykes modified from Marot (1984). Stereograms are projected in equal area and in the lower hemisphere

These slates are mainly composed of quartz, sericite and chlorite and they have been affected, as above mentioned, by upright folds and by a E-W trending sub-vertical cleavage. The dolerite dyke swarm is about 17 km in length, 3 km in width (Gloaguen et al. 2016b). The thickness

of dolerites is variable from 1 to 25 m and their extension is about 500 m. The dolerite dyke from the historical Le Semnon mine is about 10 m in width with a minimal extension of 350 m and steeply dips (85°) to the north. All of the dolerite dykes are folded and heterogeneously affected by the regional cleavage depending of their size; small dykes are strongly affected by cleavage whereas only the walls of large dykes are affected. The district is also marked by a network of N160-170°E trending dextral strike-slip fault with normal component (Fig. 2). According to Chauris et al. (1985), the trending of dolerite dykes and faults seems to be compatible with the regional-scale and dextral simple shear of Central Brittany.

Sb-Au occurrences and deposits are spatially associated with dolerite dykes as shown by numerous mining exploration works and by the high Sb content (> 100 ppm) close to dolerite dykes (Fig. 2). Sb-Au mineralization consists of a network of irregular quartz-carbonate veins, up to 80 cm thick, crosscutting the contact between the dolerite dyke and slates. Three main stages have been identified in the paragenetic sequence (Chauris et al. 1985): (1) an early Fe-As-(Au) stage made of arsenopyrite, pyrite and pyrrhotite commonly replaced by pyrite and marcasite, (2) an intermediate Fe-Sb stage characterized by berthierite and (3) a final Sb stage with massive stibnite and rare native antimony. One of the major characteristic of this deposit is the strong dissemination of arsenopyrite at the contact between the dolerite dyke and slates, which consequently underline a strong As-bearing hydrothermal alteration zone in the country rocks. Gold can be found: (1) in the crystal lattice of arsenopyrite, with a mean content of about 200 ppm (Gloaguen et al. 2016b), (2) in native form in quartz veins, arsenopyrite and stibnite or (3) in aurostibite within stibnite (Chauris et al. 1985). Hydrothermal alteration is characterized by carbonation, as revealed by the destruction of calcic plagioclase and clinopyroxene and the presence of ankerite and calcite in the groundmass, by potassic metasomatism, as highlighted by sericitized plagioclase and hydrothermal illite in the groundmass of hydrothermally altered dyke, and by a weak silicification (Pochon et al. in press). All the magmatic Fe-Ti oxides, represented by ilmenite and ilmenite-hematite solid solution, are totally replaced by rutile and leucoxene at the beginning of hydrothermal event (Chauris et al. 1985, Pochon et al. in press). During the breakdown of ilmenite-hematite assemblage into rutile, rutile incorporated Sb (~ 100 ppm) suggesting that the fluid was already enriched in Sb at the early stage of hydrothermal alteration (Pochon et al. in press). Sb-Au mineralization is considered syn- to post-kinematic by Marot (1984) because some Sb-veins are affected by regional cleavage, cleavage planes can contain “rosette”-type stibnite or crosscut by massive stibnite, and pressure shadows of arsenopyrite can contain native antimony and acicular stibnite.

3. Material and Methods

3.1 Mineral chemistry

Arsenopyrite from hydrothermally altered slates was examined in polished thin-sections using reflected-light optical microscope and scanning electron microscope (SEM) equipped with energy dispersive X-ray spectrometer (EDS), and analyzed using Cameca SX-100 electron probe micro-analyzers at IFREMER (Brest, France) and Cameca SX-50 at BRGM (Orléans, France). Analyses were mainly performed in order to check the Au and Sb content and to estimate the crystallization temperature of arsenopyrite according to experimental data of Sharp et al. (1985). The major and minor elements analyzed are Fe, S, As, Sb, Bi, Au, Zn, Cu, Ni, Co, Ag, Se. Analyses were performed using a 3 µm diameter beam, a 15-20 kV accelerating voltage, a beam current of 20 nA and a counting time of 20s on peak. Concerning phyllosilicates and carbonates from hydrothermally altered dolerite, slates, and veins, they were also examined in polished thin-sections using SEM equipped with EDS. Minerals were analyzed using Cameca SX-100 electron probe micro-analyzers at IFREMER (Brest, France). Elements analyzed are Si, Al, Ti, Fe, Mg, Mn, Ca, Ba, Na, K, V, Cr. Analyses were performed using a 3 µm diameter beam, a 15 kV accelerating voltage, a beam current of 20 nA and a counting time of 20s on peak.

3.2 Fluid inclusion

Fluid inclusions from 150 µm-thick doubly polished wafers have been carefully investigated and related to the paragenetic sequence of mineral crystallization within the mineralized veins to constrain the conditions of fluid flow and Sb-Au deposition. In order to check the chronology of fluid events, typology and petrography of fluid inclusions from representative samples have been studied looking at relationships between fluid inclusions, quartz and the location of ore minerals.

Microthermometric characterization of fluid inclusions was carried out using an Olympus BX 51 transmitted optical microscope equipped with a heating-freezing Linkam THMS 600 at GeoResources laboratory in Nancy (France) in order to measure temperatures for H2O melting ($Tm(H_2O)$), CO_2 melting ($Tm(CO_2)$), clathrate melting (Tm(Cl)), CO_2 homogenization ($Th(CO_2)$) and total homogenization (Th). The standards used for calibration were natural or synthetic fluid inclusions, including a CO_2-H_2O fluid inclusion with a $Tm(CO_2)$ at -56.6°C and a pure H_2O fluid inclusion with $Tm(H_2O)$ at 0°C. Typology of fluid inclusions (aqueous – carbonic and aqueous inclusions) is determined following the nomenclature of Boiron et al. (1992).

Molar fractions of gas species (CO_2, CH_4, H_2S and N_2) were determined in aqueous carbonic representative inclusions, previously studied by microthermometry, with a Raman microspectrometer at GeoResources laboratory. The bulk composition, molar volume, volatile/water ratio and salinity were calculated from the *P-V-T-X* properties of individual aqueous carbonic inclusions in the C-O-H-S system (Dubessy 1984; Dubessy et al. 1989; Thiery et al. 1994;

Bakker 1999). Isochores were calculated using the program ISOC from the computer package FLUIDS-1 (Bakker 2003) based on data from Bowers and Helgeson (1983).

3.3 Stable isotopes

Calcite samples, except for SEM62 sample, come from the collection of the museum of Géosciences Rennes (France) because calcite crystals are relatively rare within current outcrops at the Le Semnon mine. Ankerite crystals are relatively abundant and were collected from fresh outcrops. Samples were crushed in agate mortar or reduced in powder with microdrilling, depending of their size. A minimum of about 12 mg of powder was collected for each sample. Powders were reacted with anhydrous H_3PO_4, at 50°C. Reaction times were a few hours for calcite and about 36 hours for ankerite. The O and C isotope compositions were measured using a VF Delta Isoprime triple-collector mass spectrometer at the University of Rennes 1. Repeated measurements of international and in-house standards allow estimating uncertainties at ±0.1‰ and ±0.2‰ for C and O isotope values. Results are reported using the delta notation, with PDB and SMOW as references for the C and O isotope systems, respectively.

3.4 Geochronology

3.4.1 U-Pb dating

Apatite and rutile crystals, from the hydrothermally altered dolerite dyke of the Le Semnon mine, were carefully examined in polished thin-sections using reflected-light optical microscope and apatite were imaged by cathodoluminescence (CL) using a Reliotron CL system equipped with a digital color camera available in Géosciences Rennes (Université de Rennes 1, France).

U-Pb dating of apatite and rutile was performed by in-situ laser ablation inductively coupled plasma mass spectrometry (LA-ICP-MS) at Géosciences Rennes using a ESI NWR193UC excimer laser coupled to a quadripole Agilent 7700x ICP-MS equipped with a dual pumping system to enhance sensitivity (Paquette et al. 2014). The instrumental conditions and analytical procedure are reported in ESM 1. Further information about the apatite and rutile method dating can be found in Pochon et al. (2016b) and Boutin et al. (2015), respectively.

An ablation rectangle corresponding to a spot of 50 and 40 µm was defined for ablation laser of the apatite and rutile grains, respectively. Data were corrected for U–Pb fractionation and for mass bias by the repeated measurements of the Madagascar apatite standard (473.5 ± 0.7 Ma; Cochrane et al. 2014) and the R10 rutile standard (Zack et al. 2011) for apatite and rutile, respectively. The apatite

standards McClure (523.51 ± 2.09 Ma; Schoene and Bowring 2007) and Durango (31.44 ± 0.18 Ma; McDowell et al. 2005) and the rutile standard R19 (489.5 ± 0.9 Ma; Zack et al. 2011) were treated as unknowns and used to monitor precision and accuracy of the analyses. They provided 207Pb corrected ages of 529.7 ± 5.7 Ma (N=8, MSWD=3.1), 31.47 ± 0.87 Ma (N=9, MSWD=2.7) and 476 ± 30 Ma (N=5, MSWD=1.6), respectively.

Data reduction was carried out with the data reduction scheme VizualAge_UcomPbine, a set of Iolite procedures that work with Igor Pro (Chew et al. 2014) for apatite and with the GLITTER® software package developed by the Macquarie Research Ltd. (Van Achterbergh et al. 2001) for rutile. Apatite and rutile ages were calculated and plotted in Tera-Wasserburg diagram using Isoplot/Ex software (Ludwig 2012) and errors are provided at 2σ level.

3.4.2 ^{39}Ar-^{40}Ar dating

Euhedral to subeuhedral illite crystals, selected for ^{40}Ar / ^{39}Ar dating, were carefully handpicked under a binocular microscope from the 0.25-1.0 mm fractions and analyzed by step-heating with an ^{40}Ar / ^{39}Ar laser probe at Géosciences Rennes, following the analytical procedure described in Ruffet et al. (1991, 1995). Details on the method and analytical data are given in ESM 2. The samples were wrapped in Al foil to form small packets (11 x 11 mm) that were stacked up to form a pile, within which packets of fluence monitors were inserted every 8 samples. The stack, placed in an irradiation can, was irradiated for c. 195 hours at the McMaster reactor (Hamilton, Canada) with a J/h of c. 5.4 x 10-5 h-1. Analyses were performed on a Map215® mass spectrometer. To define a plateau age, a minimum of three consecutive steps are required, corresponding to a minimum of 70% of the total 39ArK released, and the individual fraction ages should agree to within 1σ or 2σ of the integrated age of the plateau segment. Pseudo-plateau ages, with less than 70% of 39ArK released, can also be defined. Errors are provided at the 1σ level.

4. Results

4.1 Sb-Au mineralization of the Le Semnon deposit

4.1.1 Vein geometry and microstructures

In agreement with previous study (Marot 1984, Chauris et al. 1985, Gloaguen et al. 2016b), two types of Sb-Au veins have been distinguished. They consist of cm-scale fault-fill veins and mm to cm-scale extensional veins (Figs. 3a-c). Sb-Au veins are preferentially localized at the contact between slates and dolerite dyke and become rare away from the contact (~ 1 m). The first type

occurs along reverse faults and consists of an average of N84°E-striking veins with a dip of 49° to the north (Fig. 4a). These veins typically have a banded texture where quartz ribbons are separated by slivers of altered wall rock (slates or dolerite) impregnated with stibnite and contain clasts of quartz (Fig. 3b). The second type is contemporaneous with fault-fill vein and corresponds to a network of N91°E-striking flat veins with a mean dip of 11° to the south (Fig. 4a). Extensional veins are filled by elongate blocky and fibrous quartz and carbonates mainly growing from the vein wall toward the center of the vein indicating the extension component of the veins. At microscopic scale, quartz and carbonate crystals host frequently solid and fluid inclusions bands and trails (Fig. 3d), which is the main feature of the crack-seal mechanism indicating a process of repeated cracking and intermittent sealing (Ramsay 1980). These veins cut across the sub-vertical regional cleavage and reciprocally (Figs. 3c, 3e). In the extensional veinlets hosted by slates, where regional deformation is well-expressed compared to the large dyke of the Le Semnon mine, cleavage frequently crosscut them showing mm-scale offsets (Fig. 3e). Veinlets are also affected by pressure-solution mechanism accompanied by a neo-crystallization of illite at the pressure-solution joint (Fig. 3f).Within the slates, disseminated arsenopyrite and pyrite crystals show also kinematic criteria because they were generally surrounded by cleavage (Fig. 3g) and numerous pressure shadows can be observed around them (Figs. 3g, h). The vein geometry and microstructures observed in the Le Semnon deposit are summarized in Fig. 4.

4.1.2 Mineralogy of the Le Semnon Sb-Au deposit

Quartz is the main filling constituent (~ 70 vol %) of the Sb-Au veins and typically contains numerous inclusion trails of carbonates and illite (Figs. 3d and 5a), suggesting synchronous and repeated deposition of these three minerals. In fault-fill vein, quartz is banded (Fig. 3b) and commonly white whereas it is typically elongate blocky and grey translucent in extensional veins. In these latter veins, quartz may be deformed as shown by undulose extinction and sub-grains formation. These sub-grains are frequently accompanied by neo-crystallization of carbonates and illite (Fig. 5c). Carbonates constitute an average volume of 25 to 30 vol % in the vein gangue but they may reach up to 80 vol % in veinlets and they also constitute the main minerals markers of hydrothermal alteration within host rocks. Although calcite can be abundant, carbonates are mostly represented by ankerite (ESM 3.1) with an average composition of 51.9 % $CaCO_3$, 27.5 % $MgCO_3$, 19.5 % $FeCO_3$ and 1 % $MnCO_3$.

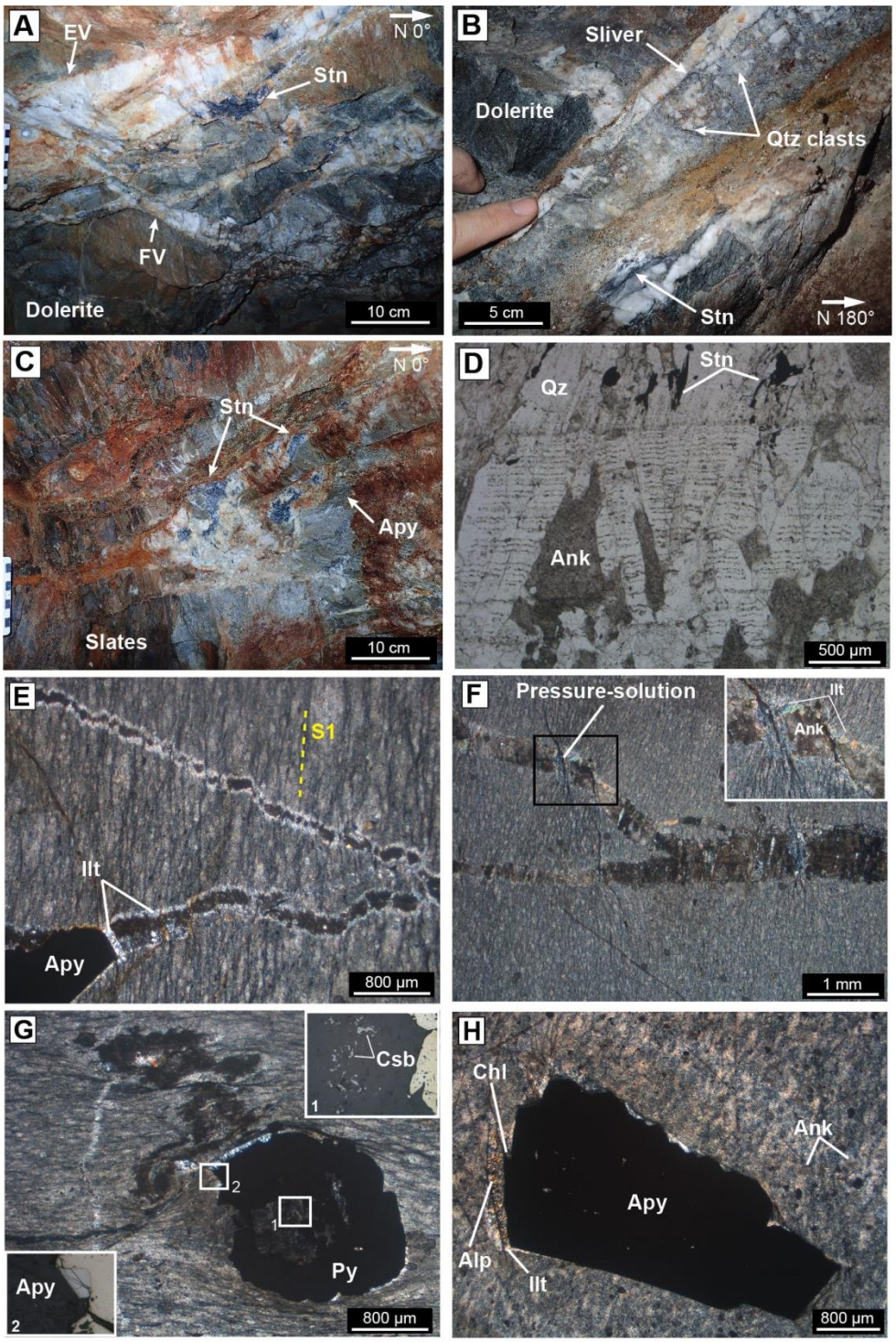

Figure 3 a Contemporaneous system of fault-fill and extensional veins at the contact between dolerite dyke and slates. **b** Typical fault-fill vein with parallel quartz ribbons, quartz clasts, wall rock sliver and stibnite. **c** Folded extensional vein crosscutting the regional cleavage of the slates with a typical As-bearing hydrothermal alteration zone in the vein wall rock. **d** Texture of extensional vein of quartz-ankerite-stibnite with classical inclusions bands. **e** Veinlets mainly composed of ankerite and illite clearly affected by the regional cleavage S1. **f** Ankerite-illite-quartz veinlets showing pressure-solution joint filled by illite. **g** Pyrite synkinematic surrounded by the cleavage and with pressure shadows. Insert in the upper right corner shows the presence of chalcostibite and insert in the lower left corner shows the presence of arsenopyrite. **h** Pressure shadows of arsenopyrite filled by chlorite, allophane and illite in the slates. EV = extensional vein; FV = fault-fill vein; Alp = allophane; Ank = ankerite; Apy = arsenopyrite; Chl = chlorite; Csb = chalcostibite; Ilt = illite; Py = pyrite; Qz = quartz; Stn = Stibnite. Mineral abbreviations from Whitney and Evans (2010)

Carbonate (ankerite and calcite) is characterized by euhedral crystals up to 500 µm in size. It hosts numerous solid inclusion bands such as quartz crystals. It is typically related to the main mineralization of Sb (berthierite and stibnite) because it contains numerous inclusions of them (Fig. 5b), and may be locally associated with pyrite, pyrrhotite and sphalerite. White mica is represented by illite in composition ($(K_{0.63}Na_{0.07}Ca_{0.01})$ $(Al_{2.01}Fe_{0.02}Mg_{0.03})$ $(Si_{3.12}Al_{0.88}O_{10})$ $(OH)_2 \cdot 2H_2O$, ESM 3.2) and it is present in veins and in the wall rock alteration. Illite is characterized by aggregate of poly-grains up to 250 µm in size. It may form mm-scale veinlets alone, form clusters at the boundary of quartz and carbonates grains (Fig. 5c) and precipitate at the selvages of the veins (Fig. 3e). Illite may contain acicular stibnite and berthierite between its sheets (Fig. 5d). Illite is also found in the pressure shadows around arsenopyrite and pyrite (Fig. 3g), locally with chlorite and allophane (Fig. 3h). Chlorite and allophane are relatively scarce in the deposit and they are closely associated with illite.

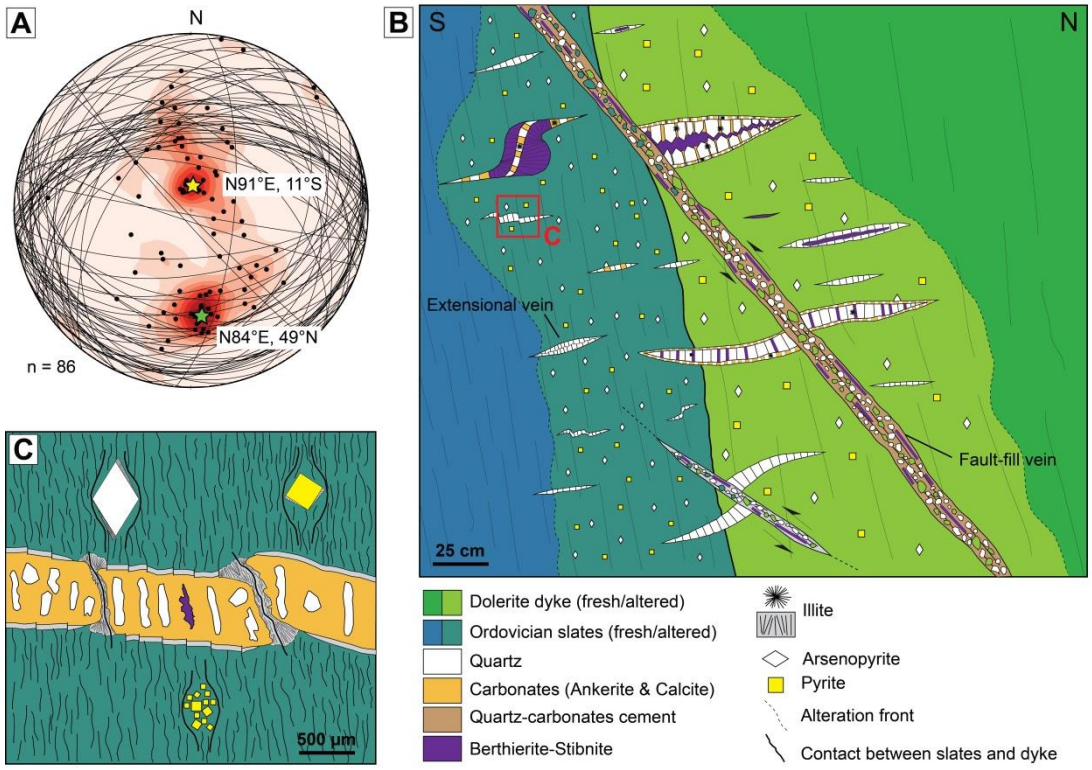

Figure 4 a Stereogram of the veins from the Le Semnon mine. Yellow star represent the mean pole of the trending of extensional veins and green star represent mean pole of the trending of fault-fill veins. Stereogram is projected in equal area and in the lower hemisphere. **b** Sketch representing the main features of vein geometry in the Le Semnon deposit and the As-bearing hydrothermal alteration zone. **c** Zoom of an extensional veinlet showing the main microstructures observed in the Le Semnon Sb-Au deposit

Arsenopyrite is the most dominant sulfide in the hydrothermally altered dolerite dyke and slates, almost absent in veins and appears as the earliest sulfide in the mineralization. It forms euhedral grains up to 1 cm in size with rhomb shape. It is frequently associated with pyrite and hosts numerous inclusions of rutile, pyrite, chalcostibite and sphalerite (Fig. 5e).

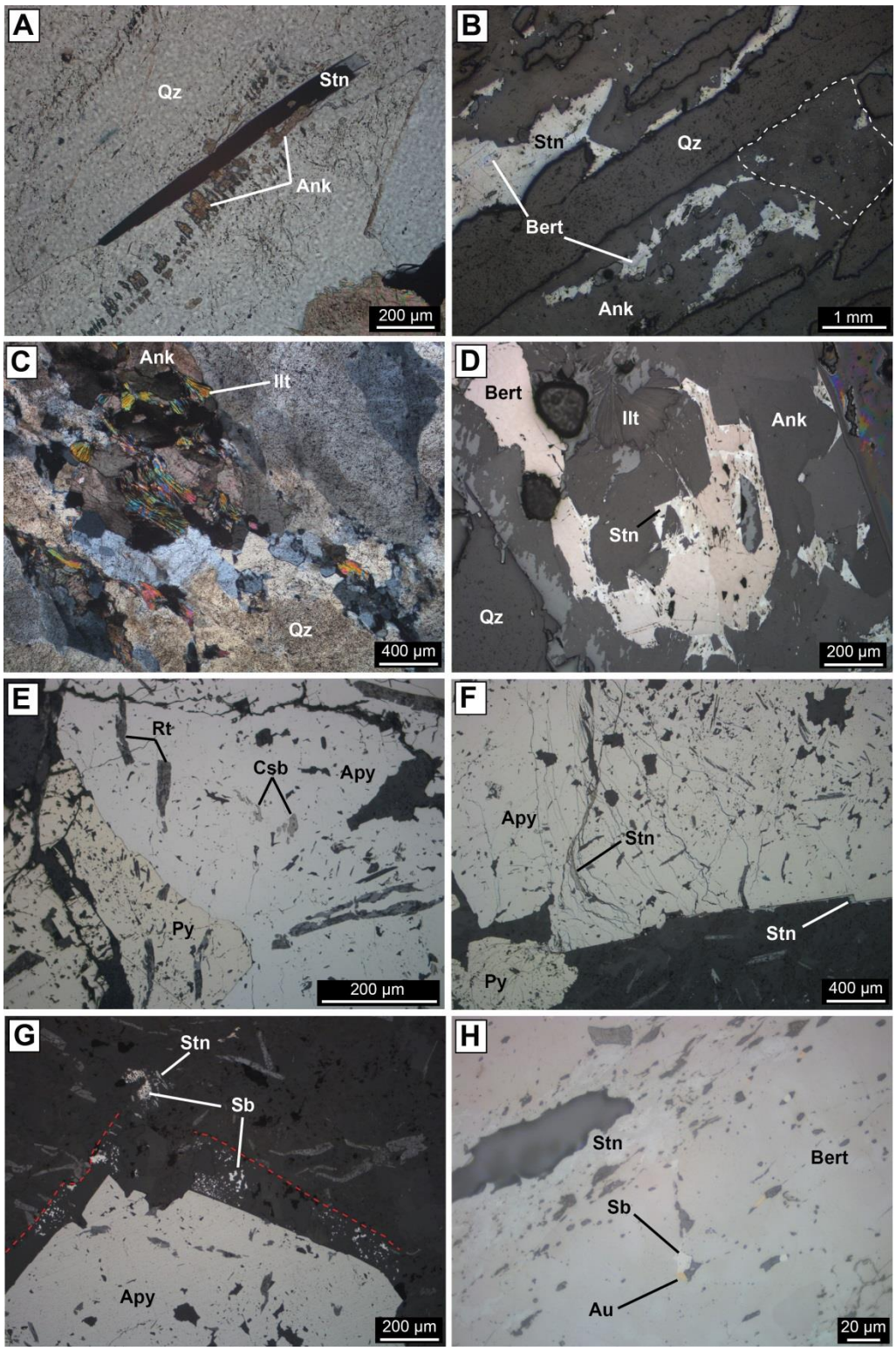

Fig. 5 a Inclusions trail of ankerite within quartz crystal and stibnite needle at the boundary between two quartz crystals. **b** Typical relationships between elongate blocky quartz, ankerite, berthierite and stibnite. White dashed line shows the numerous micro-inclusions of stibnite hosted by ankerite. **c** Sub-grains of quartz with the neocrystallization of illite and ankerite at the boundary of sub-grains. **d** Common replacement of berthierite by stibnite within ankerite. Stibnite also crystallizes between sheets of illite. **e** Arsenopyrite and pyrite association with many inclusions of chalcostibite and rutile. **f** Fracture and pressure shadow filled by stibnite in arsenopyrite. **g** Native antimony and stibnite within pressure shadow of arsenopyrite. **h** Inclusions of native gold and antimony within berthierite partially replaced by stibnite. Ank = ankerite; Apy = arsenopyrite; Bert = berthierite; Csb = chalcostibite; Ilt = illite; Py = pyrite; Qz = quartz; Rt = rutile; Sb = native antimony; Stn = Stibnite. Mineral abbreviations from Whitney and Evans (2010)

Arsenopyrite (n = 122) have an average chemical composition of 30.7 at. % As, 33.3 at. % Fe and 0.2 at. % Sb (ESM 3.3). Using the arsenopyrite geothermometer of Kretschmar and Scott (1976) modified by Sharp et al. (1985) and assuming that crystallization began at the pyrite-pyrrhotite buffer because pyrrhotite is decomposed into pyrite and arsenopyrite is in textural equilibrium with pyrite , a temperature of crystallization can be estimate at about 360°C (ESM 4). Like arsenopyrite, pyrite is scarce in the veins and rather disseminated in the hydrothermally altered country rocks. It forms frequently aggregates of euhedral to sub-euhedral crystals with a millimetric grain size. Pyrite is associated with arsenopyrite and hosts many inclusions of chalcostibite, sphalerite and rutile. Pyrrhotite is relatively rare in the deposit forming irregular anhedral porous grains up to 1 mm in size. It is commonly decomposed into pyrite and stibnite.

Berthierite is rather abundant in both fault-fill and extensional vein types and also in dissemination in the vein wall rock. It is associated with intergrowth carbonates and its precipitation was prior to stibnite deposition. Berthierite contains inclusions of native antimony and native gold and it is always found partially replaced by stibnite (Fig. 5d), likely due to its narrow stability range of oxygen and sulfur fugacity compared to stibnite (Williams-Jones and Normand 1997). Stibnite is the most abundant sulfide in both types of veins and appears to be the last sulfide in the paragenetic evolution. Consequently, it can be found in various textural positions. Two types of stibnite were distinguished: fine- to coarse-grained stibnite replacing berthierite (Fig. 5d) and stibnite associated with carbonates. The latter type of stibnite is mainly massive and coarse-grained and overgrows quartz and illite, fills micro-cracks in arsenopyrite (Fig. 5f) or sphalerite, intergranular spaces, pressure shadows (Figs. 5f-g) or geodic cavities. The two types of stibnite may also be found in dissemination or replacing disseminated berthierite within hydrothermally altered dolerite dyke and slates. Stibnite contains rare inclusions of chalcopyrite and native antimony (only in stibnite replacing berthierite). Some massive stibnite aggregates show pressure deformation twining resulting from a slight intracrystalline deformation.

Chalcostibite and tetrahedrite are the most abundant Sb-sulfosalt in the deposit although they are very scarce and forms millimeter irregular grains. They are associated with ullmannite and bournonite (Chauris et al. 1985) and can be found in inclusions in arsenopyrite, pyrite (Fig. 5e) and stibnite, in contact with sphalerite or in thin dissemination in the vein wall rock (Fig. 3g). Native antimony is relatively small in size up to 20 μm and found in inclusions in stibnite and berthierite and in the pressure shadows of arsenopyrite (Fig. 5g). Native gold is relatively rare and has been observed within a quartz-carbonates veinlet in close association with ankerite and chalcostibite and especially in inclusions within berthierite in textural equilibrium with native antimony (Fig. 5h). Native gold has been already described in a previous study (Chauris et al. 1985) and it may be

found in the crystal lattice of arsenopyrite (Gloaguen et al. 2016b), in inclusions within arsenopyrite, ullmannite and stibnite and forms aurostibite into stibnite.

On the basis of mineralogical and textural description and previous studies (Chauris et al. 1985, Gloaguen et al. 2016b), the paragenetic evolution has been reassessed and three main stages of ore deposition can be distinguished: an early stage of pervasive alteration without sulfides deposition followed by a second As-Au pervasive alteration stage and by a Sb-Fe fracturing stage. The paragenetic evolution of Sb-Au mineralization of the Le Semnon mine is summarized in Fig. 6

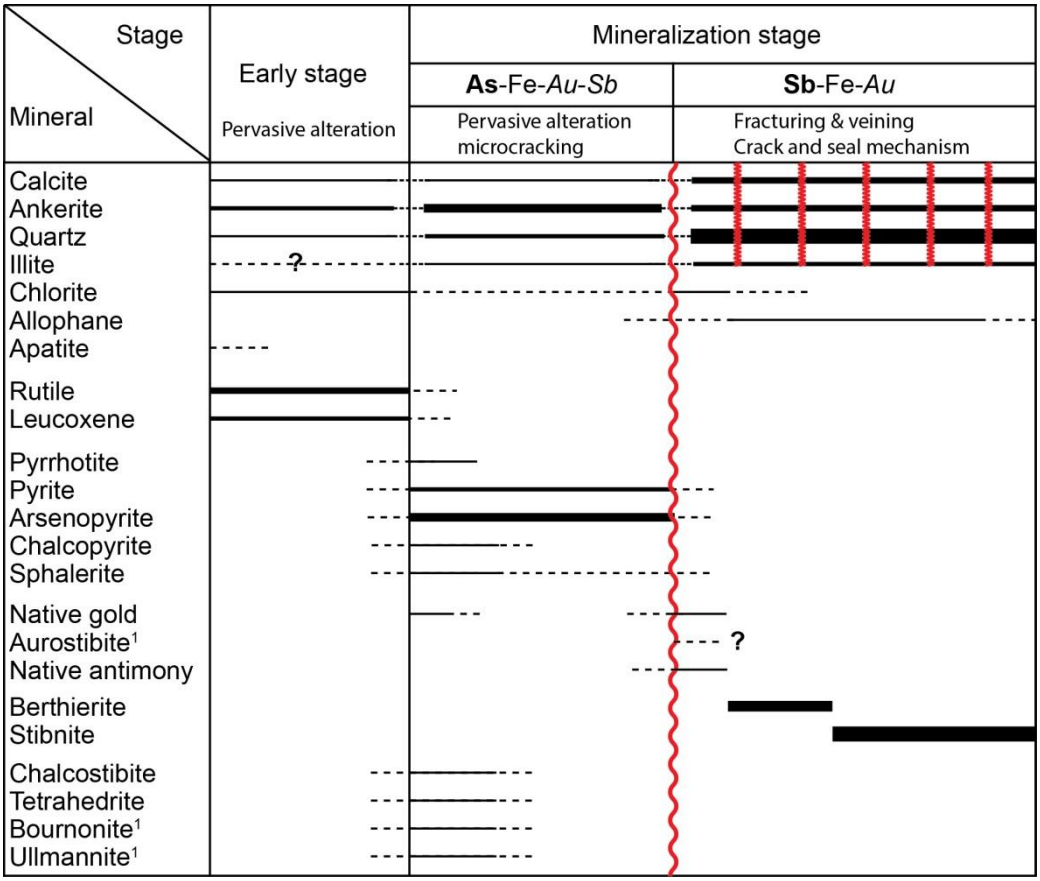

Figure 6 Paragenetic sequence of the Le Semnon Sb-Au mineralization. [1] = these minerals was not observed during this study but they are mentioned by Chauris et al. (1985). The red line represents the beginning of main fracturing and events by crack-seal mechanisms.

4.2 Fluid characterization

Fluid inclusions (FIs) were studied in 6 samples of quartz. Unfortunately, only one sample was suitable for a FIs study because FIs from the Le Semnon Sb-Au deposit are relatively rare with a relative small size (~ 10 µm) and quartz is generally too dark, and consequently, few data were acquired (n = 30). FIs study has revealed two types of FIs in the same quartz generation from extensional veins associated with stibnite: aqueous-carbonic and aqueous inclusions (Fig. 7). First, aqueous-carbonic FIs are primary and secondary inclusions, relatively abundant with commonly irregular shape and variable liquid/vapor (L/V) ratios. Aqueous-carbonic FIs consists of Lc-w type

inclusions with a vapor phase ranging from 20 to 60 % in total volume of FI and Lw-c type inclusions with a vapor phase ranging from 10 to 40 vol % (Table 1).

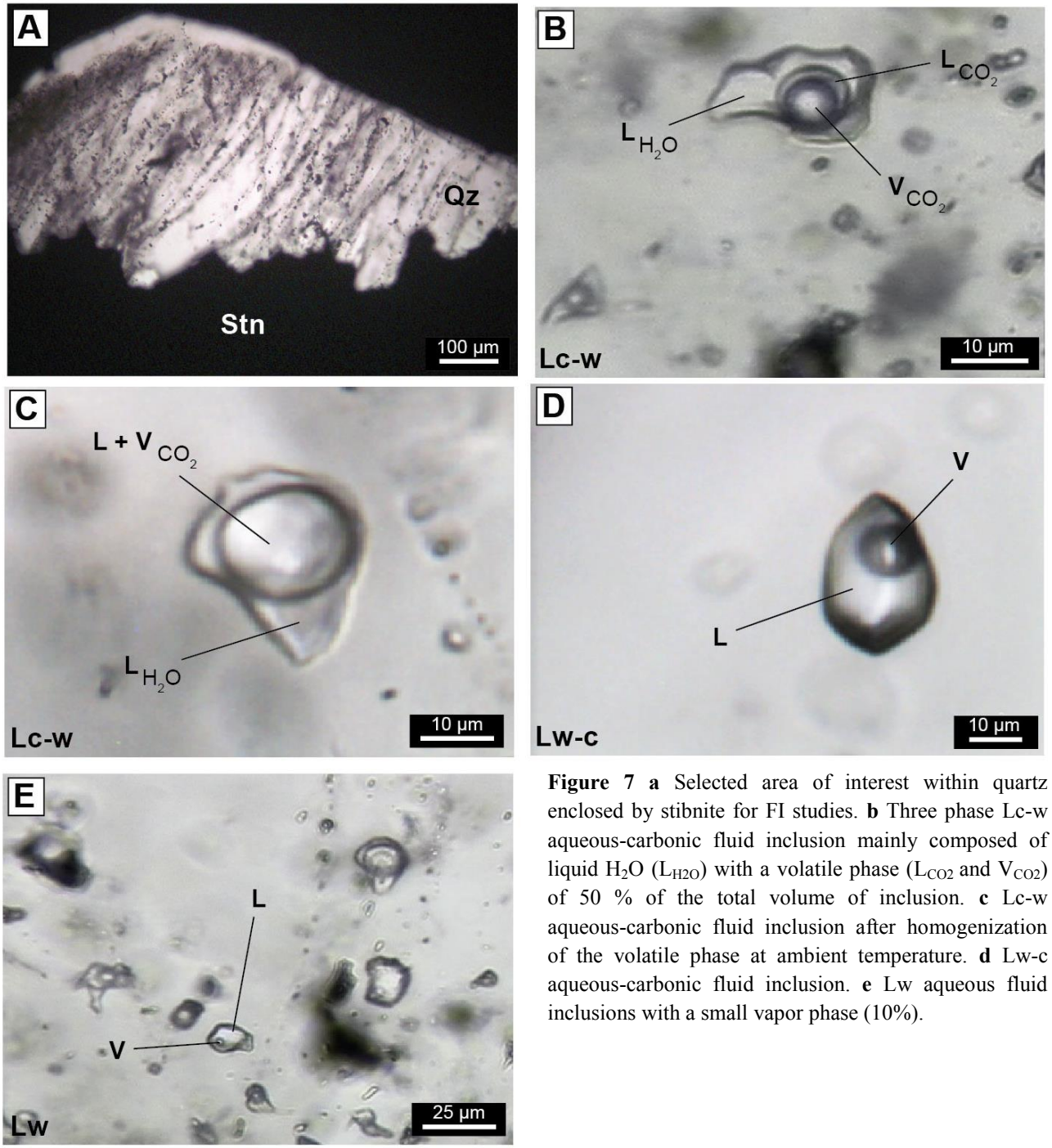

Figure 7 a Selected area of interest within quartz enclosed by stibnite for FI studies. **b** Three phase Lc-w aqueous-carbonic fluid inclusion mainly composed of liquid H_2O (L_{H2O}) with a volatile phase (L_{CO2} and V_{CO2}) of 50 % of the total volume of inclusion. **c** Lc-w aqueous-carbonic fluid inclusion after homogenization of the volatile phase at ambient temperature. **d** Lw-c aqueous-carbonic fluid inclusion. **e** Lw aqueous fluid inclusions with a small vapor phase (10%).

Aqueous-carbonic FIs have a narrow range of Tm (CO_2) from -57.8 to -56.9 °C with a mode of -57.7 °C for the Lc-w type and from -57.8 to -57.4 °C for the Lw-c type. Melting of ice Tm (H_2O) has been measured on five inclusions only ranging from -4.4 to -3.5 °C with a mode of -4.1 °C for the Lc-w type and on nine inclusions ranging from -4.2 to -2.7 °C for the Lw-c type. Clathrate melting temperature Th (Cl) of the Lc-w and Lw-c types range from 9.4 to 9.9 °C and 9.4 to 10 °C, respectively. Homogenization temperatures of CO2 to liquid (Th CO_2) range from 15.7 to 22.1 °C for the Lc-w type. The liquid phase homogenized into liquid (Th) between 293 and 314 °C

but almost all inclusions decrepitated between 245 and 320°C for the Lc-w type (Fig. 8a, Table 1, ESM 5). For the FIs Lw-c type, global homogenization temperatures are comprised between 137 and 310 °C. Aqueous FIs are very rare, smaller than aqueous-carbonic FIs (< 10 µm), and have relatively low homogenization temperatures ranging between 115 and 154 °C.

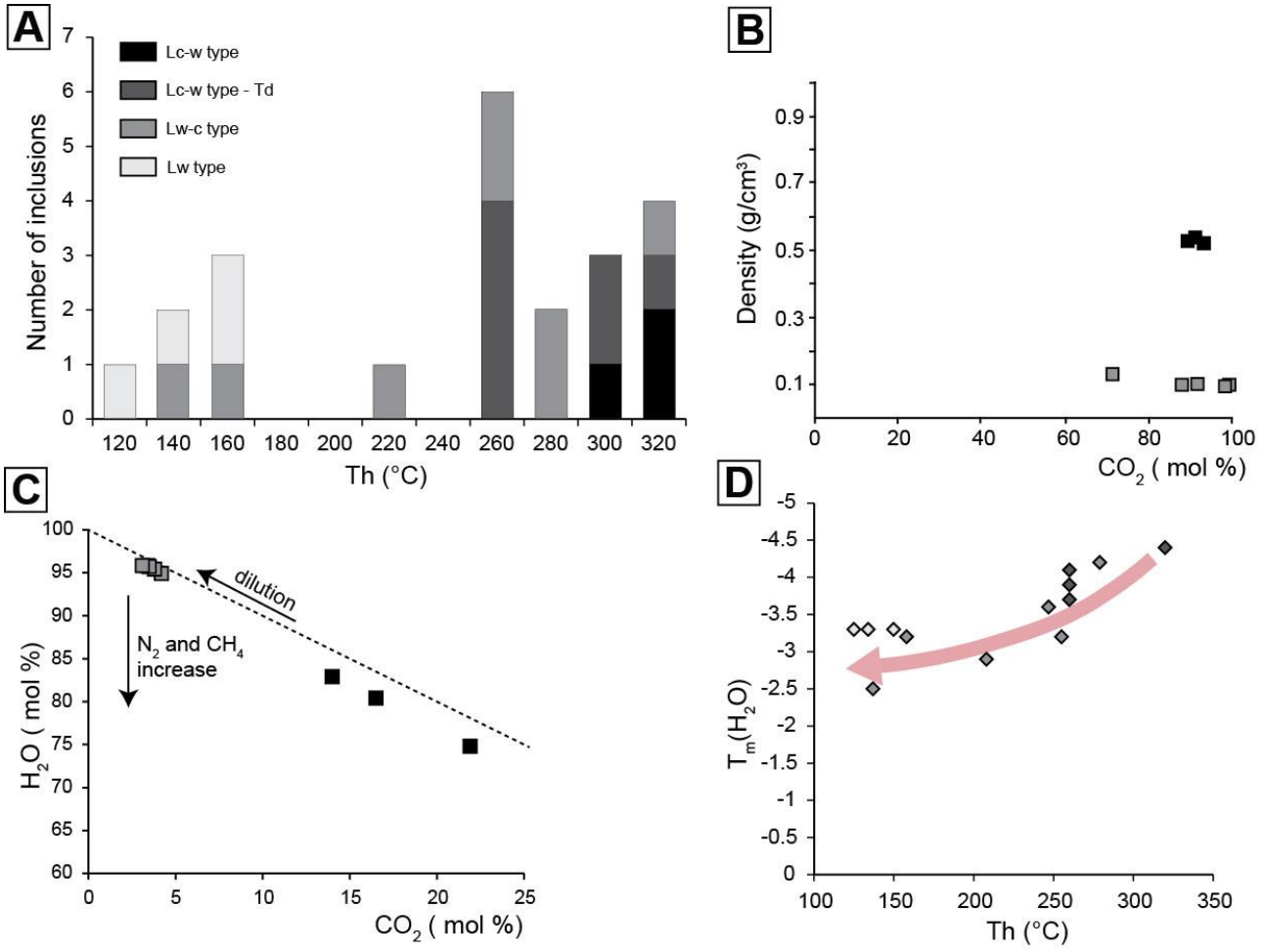

Figure 8 a Histogram of final homogenization to the liquid phase (Th) and decrepitation (Td) temperatures (°C) of fluid inclusions. **b** Diagram showing the evolution of density of volatile phase depending of composition of CO_2. **c** Diagram illustrating the evolution of the global composition of H_2O versus CO_2. **d** Ice melting temperatures ($T_m(H_2O)$) versus final homogenization to the liquid phase (Th) and decrepitation (Td) temperatures

Composition of the volatile phase of aqueous-carbonic FIs is mostly dominated by CO_2, containing very low CH_4 content, but locally enriched in N_2 (up to 28.8 mol %, ESM5). Compositional change in the volatile phase is related to a decrease in its density (Fig. 8b). Values of Lc-w inclusion type are about 0.55 g/cm3, whereas Lw-c inclusions values are around 0.12 g/cm3. FIs with the lowest densities are characterized by the highest water contents (~ 95 mol% H_2O), a decrease of the CO_2 content and enrichment in CH_4, N_2 (Figs. 8b, c). All these features define a characteristic and continuous time evolution (Boiron et al. 2003). Figure 8d shows that fluids of the Le Semnon deposit have an evolution trend from hot aqueous-carbonic fluids evolving toward cooler aqueous-carbonic and aqueous fluids.

4.3 Stable isotopes

Carbonates from extensional veins were analyzed for oxygen and carbon isotopes (Table 3, Fig. 9). The three samples of ankerite (LS1, SEM33 and SEM43) arise from different stibnite-bearing quartz-ankerite-illite veins collected at the same level. Five samples of calcite were analyzed: two samples (15-17681 and 15-17683) of white calcite without stibnite from similar calcite veins but at distinct level, two samples (87-14132 and SEM32) of white calcite containing stibnite needles from different veins and one sample (15-17675) of black calcite rich in stibnite inclusions and in close association with stibnite. Ankerite displays minor variations in $\delta^{13}C$ (from -13.6 to -12.6 ‰) and in $\delta^{18}O$ (from 13.9 to 14.7 ‰). Calcite display similar $\delta^{18}O$ values from 13.6 to 14.4 ‰ and different $\delta^{13}C$ values compared to ankerite with minor variations from -9.8 to -9.5 ‰, except for SEM62 sample ($\delta^{13}C$ = -12.5 ‰) and 15-17675 sample ($\delta^{18}O$ = 22.5 ‰).

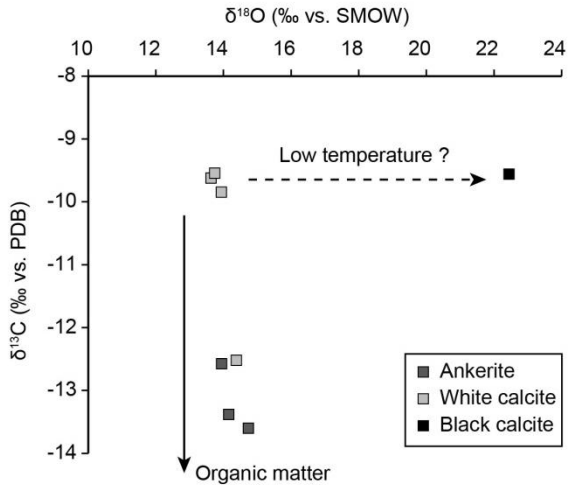

Figure 9 $\delta^{18}O$ (‰ vs. SMOW) versus $\delta^{13}C$ (‰ vs. PDB) diagram with ankerite and calcite isotopic values plotted.

4.4 Geochronology

4.4.1 U-Pb dating

Apatite and rutile from the hydrothermally altered dolerite dyke of the Le Semnon mine have been investigated in order to characterize their textural relationships. Apatite consists of euhedral to sub-euhedral grains and commonly has an elongate acicular shape up to 800 µm in length and 50 µm in width. Apatite exhibit blue purplish luminescence, systematic zoning from rim (light blue purple) toward core (dark blue purple) and frequent patchy zoning. Cathodoluminescence reveals overgrowths of recrystallized apatite at the rims and micro-cracks (Figs. 10a, b). Apatite crystals of the Le Semnon dyke are almost systematically cracked and the µm-scale cracks, generally filled by carbonates or illite (Figs. 10a, b, c), delimit micro-blocks of apatite which can be tilted such as a fracture boudinage of a brittle layer embedded in much more ductile matrix (Fig. 10b). Apatite can be found in the groundmass or enclosed within quartz and carbonates and in very frequent association with rutile suggesting a textural equilibrium (Figs. 10c,

d). Rare apatite grains have been observed inside Sb-bearing quartz veins close to the wall and perpendicular to blocky elongate quartz. Rutile comes from the breakdown of magmatic ilmenite-hematite assemblage during a deuteric and/or hydrothermal event (Chauris et al. 1985, Pochon et al. in press) and mainly consists of irregular-grained shape up to 10-80 µm in size within the external preserved shape of its parent mineral (Fig. 10e).

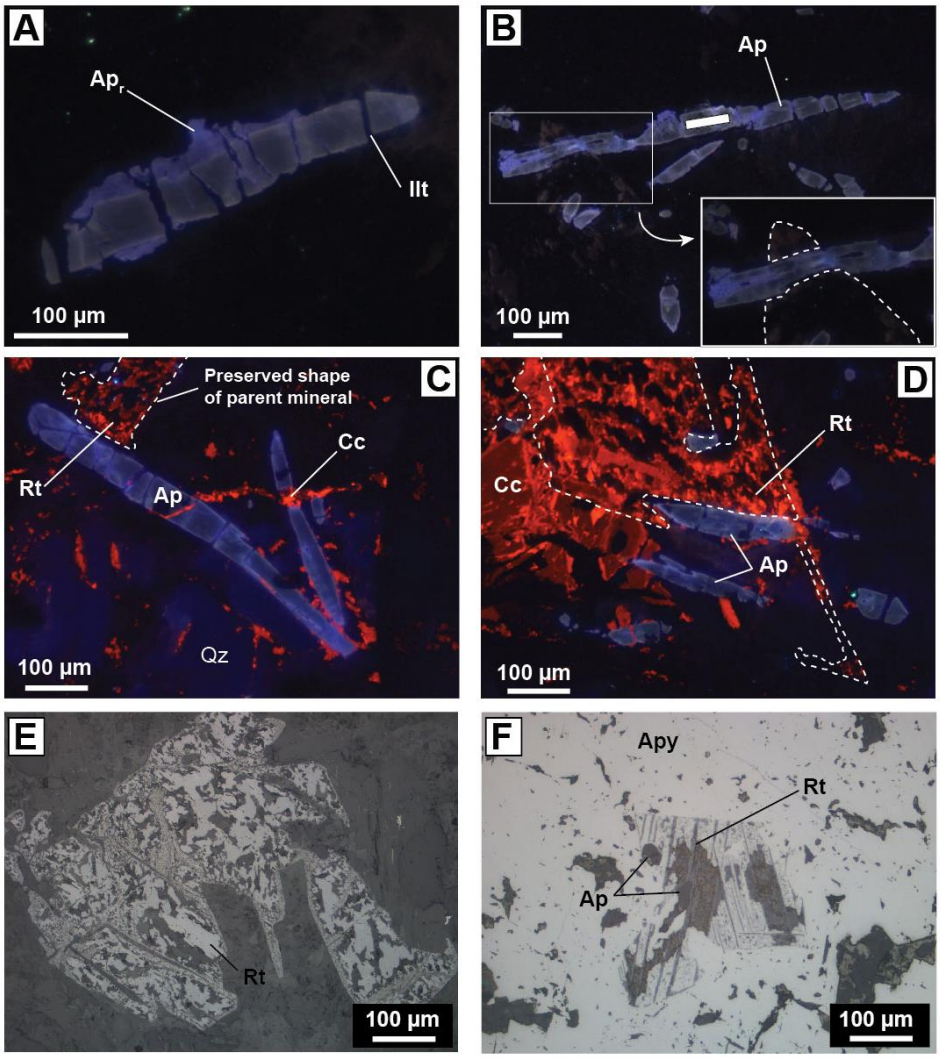

Figure 10 a-d Cold-stage cathodoluminescence photomicrographs of apatite. **a** Magmatic apatite with typical elongate acicular shape showing multiple micro-cracks and an overgrowth of hydrothermal apatite at the rim. **b** Elongated apatite crystal cracked crosscutting rutile and showing tilted micro-blocks and overgrowth within cracks. The insert in the lower right corner shows patchy zoning and the preserved external shape (white dashed line) of ilmenite-hematite assemblage replaced by rutile. White rectangle represents the laser ablation spot. **c** Apatite crystals cross cut by a veinlet of calcite. **d** Frequent association between apatite and rutile suggesting a textural equilibrium. **e-f** Typical ghost of ilmenite-hematite assemblage replaced by rutile crystals in reflected light (**e**) and transmitted light (**f**). These crystals exhibit a strong porosity, within the preserved external shape of ilmenite-hematite assemblage, filled by carbonates and illite

Rutile is frequently encompassed by arsenopyrite (Figs. 5e and 10f) and it belongs to the early stage of the paragenetic sequence (Fig. 6). It incorporates large content of Sb (mean value of 111 ppm) during its crystallization and fluids responsible to its precipitation are enriched in Sb according to Pochon et al. (in press). Consequently, dating of inferred magmatic apatite and hydrothermal rutile,

in textural equilibrium, may give constraints about the timing of hydrothermal event associated with Sb mineralization.

Apatite U-Pb results obtained are reported in Tera-Wasserburg diagrams (Fig. 11) and analytical data of apatite are given in the ESM 6. In the diagrams, the red dashed-lines represent the unforced discordias whereas the black lines represent the discordias calculated with the initial common Pb value forced to a $^{207}Pb/^{206}Pb$ value of 0.860 calculated following the Pb evolution model of Stacey and Kramers (1975) for an age of 360 Ma, representing the age of mafic magmatism in the area (Pochon et al. 2016b). The $^{207}Pb/^{206}Pb$ value is in agreement with the lead isotopes values measured ($^{206}Pb/^{204}Pb$ = 18.200, $^{207}Pb/^{204}Pb$ = 15.661, $^{207}Pb/^{206}Pb$ = 0.860495) by Marcoux (1987) on berthierite from the Le Semnon mine.

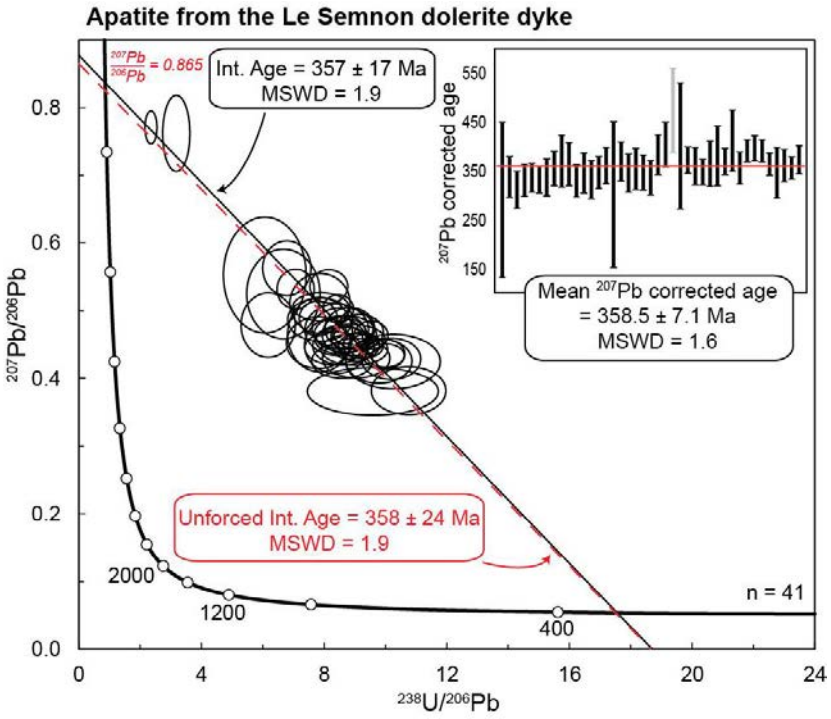

Figure 11 Tera-Wasserburg concordia diagram with the corresponding mean ^{207}Pb-corrected age for the apatite from the dolerite dyke of the Le Semnon mine. The red dashed-line represents the unforced discordia and the black line represents the forced discordia with $^{207}Pb/^{206}Pb$ value of 0.860 calculated following the Pb evolution model of Stacey and Kramers (1975) for an age of 360 Ma. Errors are provided at 2σ level

Data obtained from apatite of the dolerite dyke are discordant with a relatively high proportion of common Pb ranging from 0.38 to 0.77 (ESM 6) and form a cluster around the $^{207}Pb/^{206}Pb$ value of 0.48. The data define a lower intercept date of 358 ± 24 Ma (MSWD=1.9) with a $^{207}Pb/^{206}Pb$ initial value of 0.865 (Fig. 11). If the discordia is forced to a value of 0.860, we obtain a similar date of 357 ± 17 Ma (MSWD=1.9). The weighted average ^{207}Pb-corrected date (calculated using Stacey and Kramers (1975) terrestrial Pb evolution model) are equivalent within error at 358.5 ± 7.1 Ma (MSWD = 1.6). Unfortunately, data obtained from U-Pb analyses of rutile are of poor quality and extremely discordant with $^{207}Pb/^{206}Pb$ values close to the common Pb, ranging

from 0.78 to 0.87 (ESM 6), which makes it difficult to give a geological meaningful date. Although the $^{207}Pb/^{206}Pb$ initial value is identical to apatite (~ 0.865), this value reflects probably an assimilation of common Pb from ilmenite-hematite assemblage during its breakdown into rutile.

4.4.2 ^{39}Ar-^{40}Ar dating

Illite ^{40}Ar / ^{39}Ar data from quartz-carbonates-stibnite vein are displayed in Fig. 12. Illite analyses from the selvage of the mineralized vein display disturbed saddle-shaped spectra with no plateau date, indicating that illite grains underwent at least one hydrothermal disturbing event. However, the spectra display a ^{40}Ar / ^{39}Ar pseudo-plateau date of 339.0 ± 0.9 Ma with 70.8 % of $^{39}Ar_K$ released and ^{40}Ar / ^{39}Ar pseudo-plateau date of 338.7 ± 1.0 Ma with 42.3 % of $^{39}Ar_K$ released (Fig. 12). These pseudo-plateau dates are identical within errors and seem to indicate that illite crystallization age are older than ~ 339 Ma and give a maximum age for the late disturbing event at least ~ 339 Ma. Analyses of illite grains, found at the contact of massive stibnite, also display disturbing spectra with no plateau date. One ^{40}Ar / ^{39}Ar pseudo-plateau date of 335.5 ± 0.9 Ma with 32 % of $^{39}Ar_K$ released has been calculated (Fig. 12) which is slightly younger than pseudo-plateau dates of illite grains from the selvage of the vein. Then, saddle shapes of spectra clearly indicate that illite underwent at least a partial resetting and that the crystallization age of illite is necessarily older than *ca.* 339 Ma.

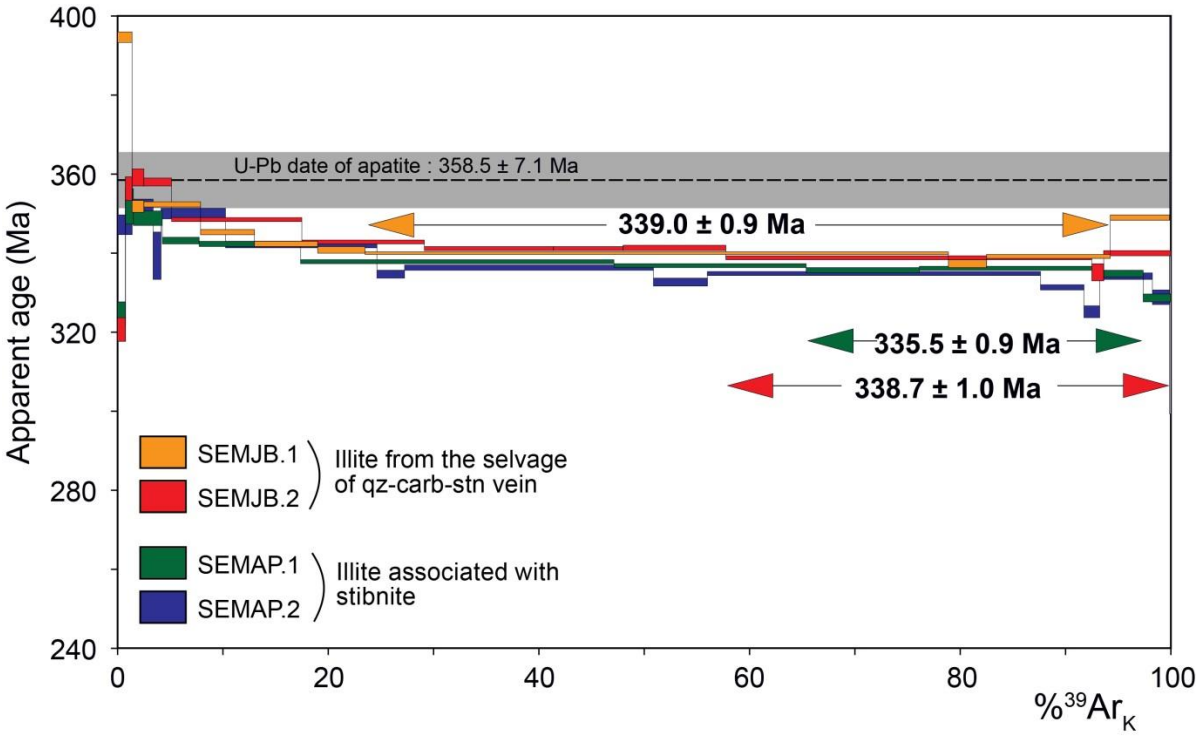

Figure 12 ^{40}Ar / ^{39}Ar age spectra (1σ relative uncertainties) of illite samples from quartz-carbonates-stibnite veins

5. Discussion

5.1 Formation of Sb-Au vein systems: evidence of fluid overpressure and "small-scale fault-valve mechanism"

Fault-valve behavior is known in fault-systems that are unfavorably oriented for typical frictional reactivation (Boullier and Robert 1992, Cox 1995, Henderson and MacCaig 1996, Robert et al. 1995, Sibson 2001, Sibson et al. 1988) although this process has been described for fault systems favorably oriented for fault reactivation (Faleiros et al. 2007, Kolb et al. 2004, Nguyen et al. 1998). Many orogenic gold deposits result from this process in high flux regimes associated with high-angle reverse faults and opening hydraulic fractures (e.g. Boullier and Robert 1992, Henderson and MacCaig 1996, Robert et al. 1995, Sibson et al. 1988). Sub-horizontal extensional veins resulting from hydraulic fracturing are formed within dilatant zones during pre-failure stages and indicate that fluid pressure reaches or exceeds the minimum principal stress (σ3) (i.e. lithostatic load, Cox et al. 1991, 1995, Robert et al. 1995, Sibson et al. 1988). Then, when fluid pressure in the fault becomes higher than fluid pressure in the country rocks, the shear failure occurs along the reactivated fault, promoting fracture permeability and a substantial drop of fluid pressure toward hydrostatic values. During the immediate post-failure stage, fluids migrate into the opened fault from the dilatant zones forming fault-fill veins and sealing fractures (Sibson et al. 1988). Hydrothermal sealing decreases the fault-permeability and allows repetition of cycle of fluid pressure from (supra)-lithostatic to hydrostatic pressure, the so-called fault-valve action by fluid-overpressure cycling (Sibson et al. 1988).

At the Le Semnon Sb-Au deposit, fault-fill and associated extensional veins are preferentially localized at the contact between the dolerite dyke and the lower Ordovician slates (Fig. 4b) suggesting a first-order rheological control of the localization of Sb-Au ore deposition. Slates act as an impermeable barrier whereas dolerite dyke may act as a plumbing system for fluids. The scarcity of veins away from the contact could indicate that: (1) the interface between slates and dolerite dyke constitutes a discontinuity enhancing permeability and promoting upward fluid flow and fluid pressure increase, and/or (2) the strong viscosity contrast between the competent dyke and the incompetent slates promotes fracturing at the interface. The vein geometric arrangement (Fig. 4) suggests sub-horizontal maximum principal stress (σ1) and sub-vertical minimum principal stress (σv = σ3), typical for a compressional regime. Fault-fill veins have an angle of about 60° compared to σ1, indicating that reverse faults are misoriented (i.e. an optimum angle between σ1 and a fault should be around 30° for a typical coefficient of rock friction, Sibson 1985) and probably activated at high fluid pressure conditions (Sibson et al. 1988, Cox et al. 2001, Micklethwaite 2008). This may suggest either a reactivation of preexisting misoriented discontinuity or either a continuous reactivation of an initially well-oriented thrust that steepens progressively as the wall rocks absorb

some of the regional shortening strain (Sibson et al. 1988). The latter is the most probable scenario because of the anisotropy that exists between dyke and slates and because the contact accommodates a part of the regional strain (e.g. cleavage more develop at the contact). This contact is extremely misoriented and shows no displacement or slip events along it. Sub-horizontal extensional veins with elongated blocky and fibrous growth perpendicularly to vein wall-rock (Figs. 3d, 4b, c and 5b) suggest, at least locally and intermittently, a lithostatic to supralithostatic fluid pressure. Furthermore, crack-seal textures in extensional veins (Figs. 3d and 5a) indicate fluid pressure fluctuations associated with repeated crack events (Ramsay 1980, Cox 1987, 1995, Cox et al. 1991).

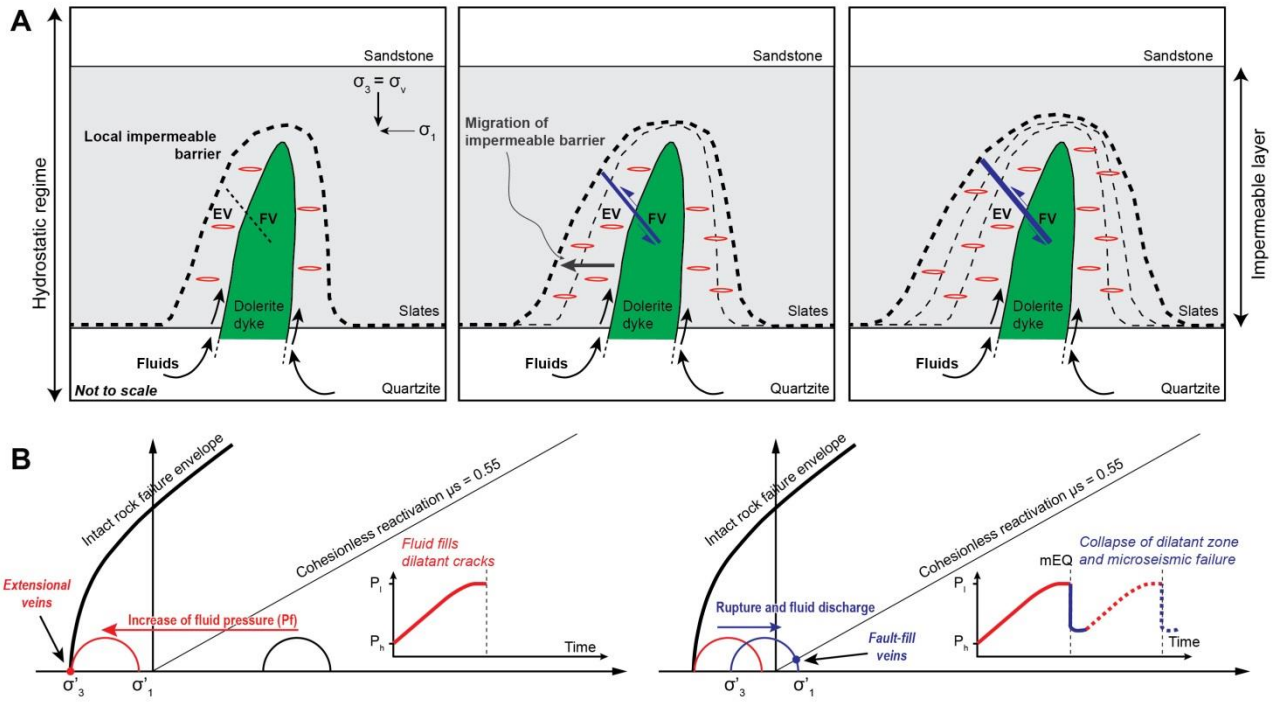

Figure 13 a Schematic evolution of local tectonic setting of formation of fault-fill (FV) and extensional veins (EV) of the Le Semnon Sb-Au deposit. Dolerite dyke injection into impermeable slates creates a local impermeable barrier around dyke promoting upward fluid flow and the substantial increase of fluid pressure at the contact. Fluid overpressure reaches (supra)-lithostatic values leading to dilatant cracks filled by fluids. When fluid overpressure is too high, misoriented fault is reactivated promoting micro-earthquake rupture, fluids discharge and a migration of the local impermeable barrier. Sketch is not to scale and consequently, the thickness of the local impermeable barrier and its migration is overestimated in order to illustrate the mechanism. **b** Mohr diagrams with composite envelopes failure for intact rock and for frictional reactivation of an existing cohesionless fault, illustrating stress and fluid pressure conditions at the Le Semnon deposit for hydraulic extension fracturing and misoriented fault reactivation. Mohr diagrams are also related to the fluid pressure fluctuations induced by fault-valve action in relation to micro-earthquake rupturing cycle (mEQ). Extensional veins occur during pre-rupture dilatation stage whereas fault-fill veins occur just after the rupture.

The veins geometry of the Le Semnon deposit, described above, is very similar to many natural case studies of gold orogenic deposit associated with high-angle reverse faults (e.g. Boullier and Robert 1992, Henderson and MacCaig 1996, Robert et al. 1995, Sibson et al. 1988) and seems fulfill all of the expected conditions for a fault-valve mechanism. However, the small-scale of the

extensional and fault-fill veins from the Le Semnon deposit are hardly comparable with the conditions prevailing for crustal-scale Archean shear zone-hosted gold deposits (e.g. Sigma mine, Val d'or, Quebec, Robert and Brown 1986). Furthermore, the formation of the Le Semnon Sb-Au deposit occurred close to the surface at predominant hydrostatic regime (see below), and because dolerite dyke injection into impermeable slates locally breaches the impermeable barrier of slates, fluid overpressure may have occurred. The schematic model of the "small-scale fault valve mechanism" is illustrated in Figure 13. Magma injection into impermeable slates created a newly-formed and local impermeable barrier around the dolerite dyke and allowed upward fluid flow at the contact (Fig. 13a). However, fluids were restricted to the breached contact between dyke and slates, and fluid pressure substantially increased because fluids cannot have passed through the local impermeable barrier. Fluid pressure reached (supra)-lithostatic values and fluid-filled dilatant cracks (i.e. extensional veins) formed as illustrated by the shift to the left of Mohr circle (Fig. 13b). In order to tend to stability, fluid overpressure was always followed by rock failure or by faults reactivation (Fig. 13a). In this case study, it is believed that fault rupture induced micro-earthquake, breaking through the local impermeable barrier and allowing a fluids discharge along the fault (Fig. 13b). Sealing of the fault by veins acted as a plug and promoted to a re-accumulation of fluids leading to a new fluid overpressure cycling up to the end of hydrothermal system life.

5.2 Sb evolution in the hydrothermal system: record of a progressive cooling

There is abundant evidence that Sb was present and relatively enriched in the fluids from the early to the last stage in the paragenetic evolution. In the early stage, rutile resulting from the hydrothermal breakdown of ilmenite-titanohematite mineral assemblage has relatively high concentration of Sb (~ 100 ppm) in its crystal lattice (Pochon et al. in press). Although the crystallization temperature of rutile is not known, it is assumed that this stage is relatively hot (> 400°C?) in so far as the mineral replacement seems to be a deuteric coupled hydrothermal alteration. Formed in the following stage, disseminated arsenopyrite displays an average content of 0.37 % of Sb (ESM 3) and contains numerous inclusions of Sb-sulfosalts (e.g. tetrahedrite and chalcostibite), like associated pyrite (Fig. 5e). Using the arsenopyrite geothermometer of Kretschmar and Scott (1976) modified by Sharp et al. (1985), the temperature of crystallization is estimated at about 360°C (ESM 4). Finally, the last stage consists of the main Sb mineralization with precipitation of native antimony and native gold following by berthierite and by final stibnite (Figs. 5b, d, g, h and 6).

The major factors controlling antimony solubility are temperature, oxygen fugacity (fO2), pH and the total sulfur activity (William-Jones and Normand 1997). Within hydrothermal solution,

it is known that antimony is mainly transported by $Sb(OH)_3^0$ (Wood et al. 1987, Shikina and Zotov 1991), $HSb_2Sb_4^-$ (which predominates at intermediate pH, Krupp 1988, Spycher and Reed 1989) and $Sb_2S_2(OH)_2^0$ (which is important at low pH, Krupp 1988). In solution at neutral pH, the predominant Sb species are $Sb(OH)_3^0$, except at intermediate fO2 where $Sb_2S_2(OH)_2^0$ and $HSb_2Sb_4^-$ are predominant at 180-280°C and <180°C, respectively (William-Jones and Normand 1997). A decrease of temperature is the simplest way to explain the precipitation of native antimony followed by the deposition of berthierite and by later stibnite (Fig. 14) from the last stage (e.g. Barton 1971, Barton and Skinner 1979, William-Jones and Normand 1997). Thus, the multistage paragenetic evolution can reflect a progressive cooling of the hydrothermal system from early Sb-rich rutile to late stibnite rather than a contrasted mineralizing event developing at different times. This single mineralizing event is consistent with the early saturation of the fluid in Sb and by the compositionally single potassic (ESM3) hydrothermal assemblage during the paragenetic evolution.

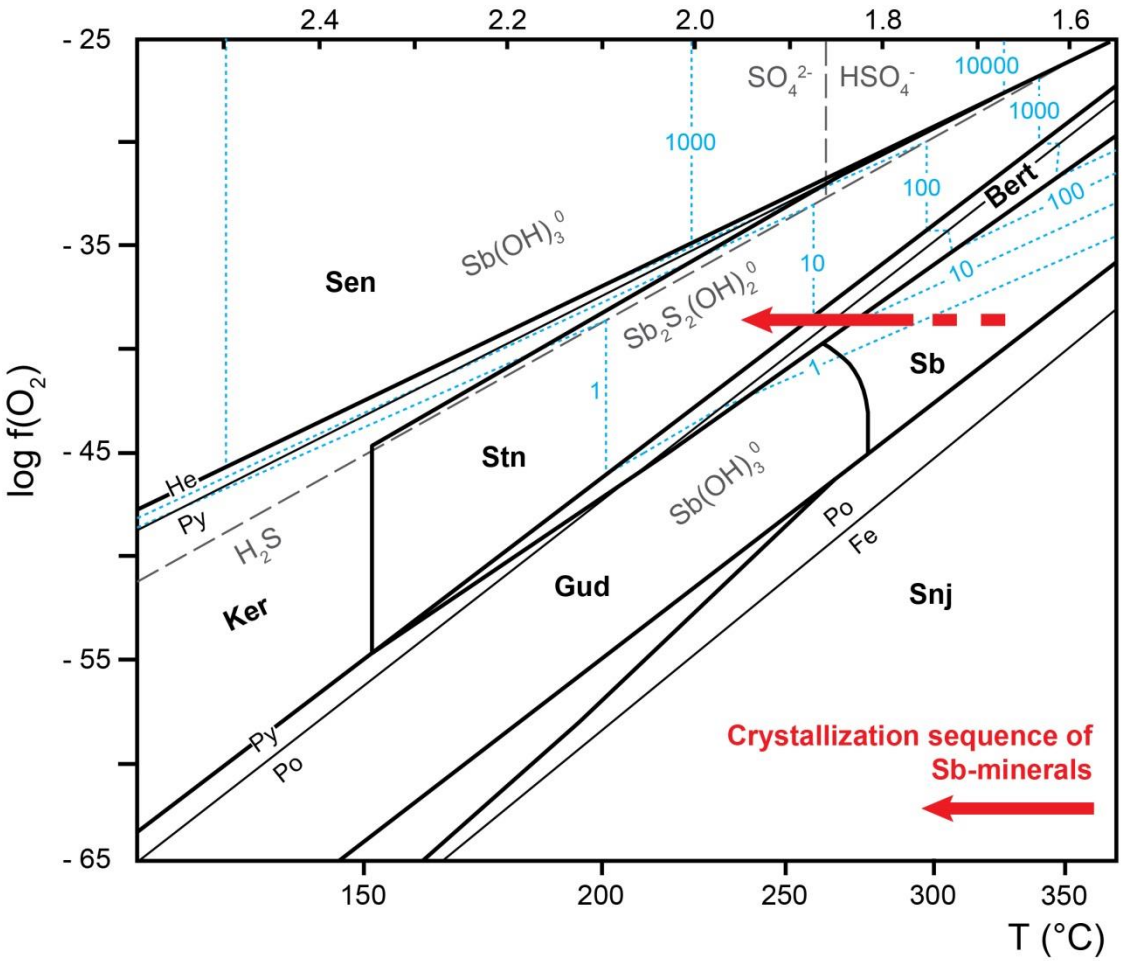

Figure 14 Log fO_2 – 1000/T (K) diagram at neutral pH and $\Sigma a_s = 0.01$, showing stability relationships in the system Fe-Sb-S-O and contours of antimony mineral solubility in ppm in light blue dashed lines (after Williams-Jones and Normand 1997). The heavy dashed gray lines show the predominance boundaries of species in the system H-S-O. Bert = berthierite, gud = gudmundite, hem = hematite, po = pyrrhotite, py = pyrite, sb = native antimony, sen = senarmontite, snj = seinajokite, stn = stibnite. Mineral abbreviations from Whitney and Evans (2010)

5.3 Nature and fluid evolution of the hydrothermal system

Except for one sample with a high δ 18O value likely recording low-temperature formation, the $\delta^{18}O$ values of carbonates are homogeneous (Table 2, Fig. 9). This observation suggests that the conditions of precipitation ($\delta^{18}O$ value of fluid, fluid temperature and fluid/rock ratio) were similar for calcite and ankerite. In contrast, the $\delta^{13}C$ values are more dispersed and tend toward organic matter reservoir (Fig. 9). This suggests an interaction with country rocks, probably the lower Ordovician slates enriched in organic matter (Herrouin et al. 1990). It comes then that the oxygen isotope signature is likely resulting from equilibration of fluids with local crustal rocks, leading to homogeneous, unspecific crustal signatures.

Results of fluid inclusions study suggest the presence of two types of fluids: (1) hot aqueous-carbonic fluids (Lc-w and Lw-c type) with minor N_2 and CH_4 and relatively low salinity (~ 6 wt% eq. NaCl), (2) cold aqueous fluids. It is difficult to establish a chronology of FIs entrapment because crack-seal evidenced in quartz records fluid pressure cycling associated with repeated crack events and because all types of FIs are found inside a single quartz sample. However, the lower volatile phase density, the lower salinity, and the lower CO_2 proportion correlated to the increase of H_2O Lw-c inclusions seems to show that these fluids could come from the dilution of the fluids trapped in Lc-w inclusions. This dilution can be illustrated by the evolution trend showing fluids trapped at relatively high temperature conditions which evolved toward fluids trapped at lower temperature (Fig. 8d). Fluids composition is similar to fluids encountered in many orogenic gold deposits from the West-European Variscan belt (Clayton et al. 1990, Couto et al. 1990, Ortega and Vindel 1995, Ortega et al. 1996, Essaraj et al. 2001, Boiron et al. 2003) and these fluids are characteristic of crustal fluids probably metamorphic in origin.

Figure 15 illustrates the possible P-T conditions of fluids entrapment of the Le Semnon mineralization. In order to constrain P-T ranges of entrapment, the maximum lithostatic and hydrostatic loads were calculated from tectonic and stratigraphic considerations known in the area. Central Brittany never undergone crustal thickening during the Variscan orogeny (Gumiaux et al. 2004a) and sedimentation stopped at the end of Devonian (Ballèvre et al. 2014; Herrouin et al. 1990), except in the Carboniferous basin localized along major shear zones (Chateaulin Basin and East of La Lucette in Fig. 1). Consequently, the stratigraphic sequence in the Le Semnon area is considered as continuous series from lower Ordovician to Upper Devonian and has a maximum thickness of 2.5 km (Herrouin et al. 1990). Considering reasonable free seawater column (1 km), this depth correspond to a maximum pressure of 75 MPa under a lithostatic regime and 35 MPa under a hydrostatic regime (Fig. 15). Three aqueous-carbonic isochores have a minimum pressure of entrapment higher than this lithostatic load. The highest pressure record by aqueous-carbonic

isochores corresponds to a 5 km depth under lithostatic regime. Record of entrapment pressure higher than the lithostatic pressure suggests a supralithostatic fluid overpressure consistent with flat extensional veins associated with crack-seal mechanism and small-scale fault-valve behavior (Figs. 3a-d, 4b and 13). Considering that the maximum lithostatic pressure (i.e. 75 MPa) is the minimum necessary condition to generate sub-horizontal extensional veins, almost aqueous-carbonic fluids are interpreted to have a minimum entrapment temperature ranging between 240 and 330°C (Fig. 15). This range of temperature is consistent with the temperature decrease highlighted by the crystallization of native gold and Sb followed by berthierite and stibnite (Fig. 14), observed inside extensional veins. Consequently, aqueous FIs, interpreted as meteoric fluids, were likely trapped under hydrostatic regime at a minimum temperature range comprised between 130 and 160°C (Fig. 15).

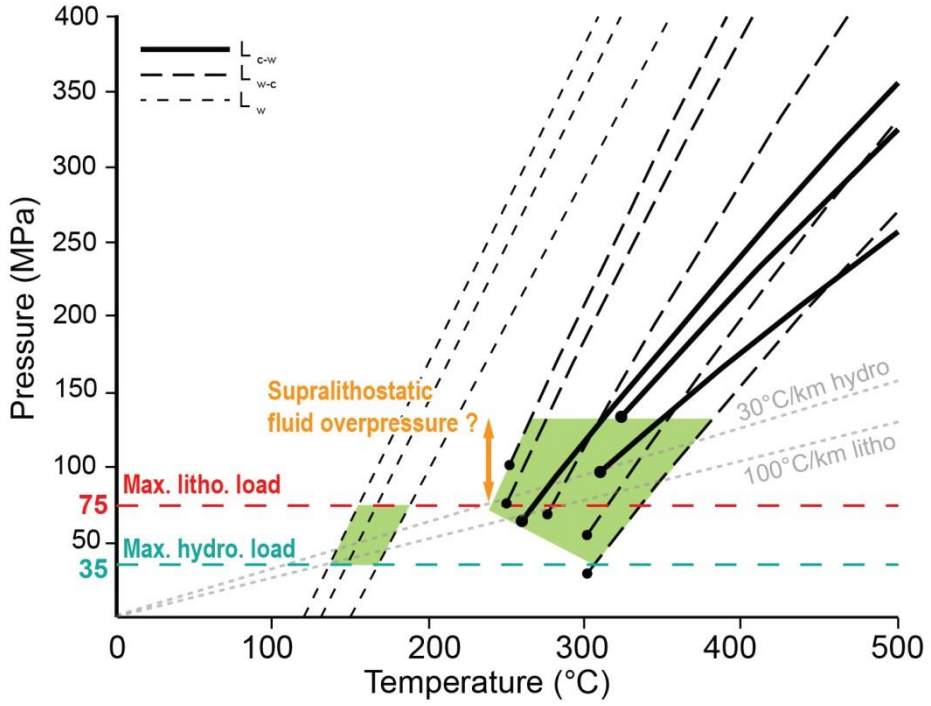

Figure 15 Estimated P-T conditions for the formation of the Sb-Au extensional veins from calculated isochores. The most likely P-T fields are represented by color shades. See text for more details about estimation of the maximum lithostatic load (max. litho. load) and hydrostatic load (max. hydro. load)

Considering the shallow depth emplacement of the Le Semnon deposit, it requires an anormal geothermal gradient (here 100°C/km in lithostatic regime) to explain such elevated temperature near the surface. Such elevated geothermal gradient is inconsistent with the low-grade regional metamorphism and rather involves a thermal source in disequilibrium, such as magmatic component or heat brought by fluids. However, geothermal gradient (30°C/km in lithostatic regime) appears ordinary for meteoric aqueous fluids trapped in hydrostatic regime, likely suggesting that these fluids are disconnected with the high thermal event related to Sb-Au mineralization.

5.4 Timing of Sb-Au mineralization

The paragenetic sequence of Sb-Au mineralization of the Le Semnon mine (Fig. 6) seems to reveal a three-stage model evolution. The early stage, described in details in Pochon et al. (in press), is best expressed in dolerite dyke and probably results of a hot deuteric/hydrothermal and pervasive alteration because it is characterized by the complete breakdown of magmatic ilmenite-hematite assemblage into rutile, and the destruction of calcic plagioclase and clinopyroxene. This stage is following by an As-Fe-Sb-Au pervasive hydrothermal alteration characterized by arsenopyrite dissemination and by the main Sb-Fe mineralization event characterized by hydraulic fracturing at the contact between dolerite and slates.

U-Pb analyses of apatite from the dolerite dyke of Le Semnon deposit provide a weighted average ^{207}Pb-corrected date at 358.5 ± 7.1 Ma (MSWD = 1.6), consistent with the unforced and forced lower intercept dates of 358 ± 24 Ma (MSWD = 1.9) and 357 ± 17 Ma (MSWD=1.9), respectively (Fig. 11). Although uncertainty is relatively high, this date is quite similar to the emplacement age of mafic magmatism in the Armorican Massif, dated at *ca.* 360 Ma (Pochon et al. 2016b). Furthermore, this date is also similar to the age of another dolerite dyke (363.3 ± 3.1 Ma, N=22, MSWD=2.6; Pochon et al. 2016b), belonging to the same dyke swarm and located at 4 km to the east (Fig. 2), suggesting that all dykes from this swarm have the same emplacement age. However, the other dolerite dykes from the Armorican massif that have been selected for dating were not affected by hydrothermal alteration (Pochon et al 2016b). In the Le Semnon case study, the dolerite dyke is completely deeply altered and modified by a pervasive and mineralizing hydrothermal event. Magmatic apatite seems to be in textural equilibrium with hydrothermal rutile replacing all magmatic Fe-Ti oxides (Figs. 10b-e) and formed at the early stage of paragenetic evolution (Fig. 6). In addition to this, the patchy zoning (Figs. 10b and d), the zoning around the rim and micro-cracks of apatite (Figs. 10a-d), calcite-fill micro-cracks (Figs. 10c-d) and overgrowths around apatite (Fig. 10a) reveal that apatite was affected. Taking this into account, two assumptions can be proposed as to the U-Pb apatite data significance: (1) either the U-Pb chronometer of apatite has not been sensitive to two pervasive hydrothermal events (early stage and As-Au stage, Fig. 6), which completely modify the dolerite dyke, and consequently, the U-Pb date reflects the emplacement age of the dolerite dyke, (2) or the U-Pb chronometer of apatite was reset by pervasive fluids and the uncertainties of the age are too high to clearly discriminate this event from the emplacement age of dyke, suggesting that it occurs almost immediately after the emplacement. The latter is more realistic because it is well known that phosphate minerals, such as apatite or monazite, are very sensitive to crustal fluid circulations on a wide range of temperatures (Budzyń et al. 2011, Harlov et al. 2005, 2007, 2011, Seydoux-Guillaume et al. 2012, Grand'Homme et al.

2016) and the interaction with pervasive hot fluid (360°C on arsenopyrite geothermometry) is the most effective way to reset chronometer (Harlov and Hetherington 2010, Harlov et al. 2011). For this reasons, we believe that the U-Pb date of apatite reflects a hydrothermal (and/or deuteric) event, already enriched in Sb (Pochon et al. in press), occurring shortly after the emplacement of dolerite dyke swarm.

$^{40}Ar/^{39}Ar$ pseudo-plateau dates (Fig. 12) indicate that the crystallization age of illite is older than *c.* 339 Ma. Indeed, $^{40}Ar/^{39}Ar$ chronometer of illite was partially reset by subsequent perturbing event, as evidenced by saddle-shaped spectra. $^{40}Ar/^{39}Ar$ spectra also display a "recoil" effect producing a fictitiously low age in the highest temperature degassing domain, supposed to reflect the early age of crystallization of illite, but the low temperature steps of SEMJB samples might suggest a least a crystallization age close to the emplacement age of dolerite dyke (*c.* 360 Ma). SEMAP samples spectra are more disturbed suggesting that illite grains from different veins were partially reset at various degrees thus providing a different maximum age for recrystallization. Two most probable scenarios may be suggested for the hydrothermal history recorded by illite samples: (1) a hydrothermal fluid pulse at *ca.* 339 Ma or younger which partially resetted all the different samples to various degrees, or (2) a more or less continuous fluid flow locally and partially affecting different samples at different times. In the Le Semnon hydrothermal context, we favor the second scenario especially because the veins geometric arrangement (Fig. 4b) indicates a fault-valve behavior with seismic cycles and the crack-seal textures in extensional veins (Figs. 3d and 5a) indicate fluid pressure fluctuations (e.g. Cox 1995). Furthermore, several evidences of early Sb-bearing phases have been documented. The incorporation of Sb inside the crystal lattice of hydrothermal rutile (~100 ppm in average and up to 500 ppm) has been demonstrated according to Pochon et al. (in press), suggesting that early fluids responsible to the breakdown of ilmenite-hematite assemblage into rutile was already enriched in Sb. The frequent inclusions of Sb-sulfosalts (e.g. chalcostibite and tetrahedrite) within arsenopyrite also indicate that Sb was already present before the main Sb deposition (e.g. berthierite and stibnite). Based on structural, petrological and geochronological data, it is reasonable to consider that paragenetic evolution, from early to final stage, reflects a continuous Sb-bearing fluid flow with a progressive evolution of its composition showing a decrease of temperature of ore deposition. Thus, timing of Sb ore deposition would be comprised between the early hydrothermal event, coinciding with the emplacement age of dolerite dyke near 360 Ma and the maximum age of alteration near 339 Ma. One cannot exclude that this maximum age of recrystallization may reflect a fluid event totally disconnected from the Sb history, as suggested by the meteoric fluid inclusions trapped in quartz from extensional veins.

5.5 Toward a genetic model for the Le Semnon Sb-Au deposit

The emplacement model for the Le Semnon Sb-Au deposit and the continuous evolution of the hydrothermal system are illustrated in Figure 16. U-Pb and $^{40}Ar/^{39}Ar$ results seem to show that Sb-Au mineralization is rather early in the Variscan history of the Central Brittany and it was not totally disconnected from the dolerite dyke emplacement occurring at *ca.* 360 Ma in the Armorican Massif. As discussed above, U-Pb date of apatite is interpreted as the age of pervasive alteration of the dyke. As this fluid event was already enriched in Sb (Pochon et al. in press), it is believed that dolerite dyke brought Sb-rich fluids during its ascent leading to breakdown of Fe-Ti oxides and U-Pb reset of magmatic apatite (Fig. 16a.1). Antimony-rich fluids may have been variable in origin, with magmatic and country rocks contributions. Following the dyke emplacement, upward fluid flow continued at the contact, which acted as a plumbing system (Fig. 16b), pervasively modifying the chemical composition of host rocks and led to dissemination of Sb-rich arsenopyrite, pyrite and Sb-sulfosalt. Growth of these minerals seems to have been contemporaneous with regional deformation as recorded by pressure shadows around arsenopyrite and pyrite. Then, as the fluid pressure increase was promoted by the impermeable barrier of slates, fracturing and veining event likely occurred, leading to the main Sb mineralization stage (Fig. 16c). Fracturing is clearly both contemporaneous and subsequent to regional cleavage and a part of Sb-minerals deposition occurred during regional deformation as highlighted by pressure shadows filled by Sb and stibnite (Fig. 16c) and by extensional veins affected by cleavage. Fluid overpressure cycling is recorded by extensional veins (Fig. 16d). Crack-seal evidence and reactivation of misoriented reverse fault were coupled with a temperature decrease as revealed by Sb-minerals evolution sequence (Fig. 16e). As discussed above, the Le Semnon Sb-Au hydrothermal event is interpreted as a progressive cooling of a single mineralizing event and consequently it is believed that U-Pb and $^{40}Ar/^{39}Ar$ results seem to show that Sb-Au mineralization is early in the Variscan history of the Central Brittany and probably very close to the emplacement age of dolerite dyke swarms at *ca.* 360 Ma in the Armorican Massif. Disturbing event(s), highlighted by $^{40}Ar/^{39}Ar$ spectra of illite grains, rather reflects a subsequent fluid flow disconnected from the mineralizing event, possibly of meteoric origin.

The Le Semnon Sb-Au deposit has a number of key features typical of orogenic gold deposits worldwide (Groves et al. 1998, McCuaig and Kerrich 1998, Ridley and Diamond 2000, Bierlein and Maher 2001, Goldfarb et al. 2001, 2005, 2015, Groves et al. 2003, Bierlein at al. 2006) including the strong structural control on Sb-Au mineralization, a compressional regime, predominant aqueous-carbonic fluids and an Au-As-Sb mineral association. The deposit emplaced at very shallow level (< 2.5 km depth) and could have corresponded to a so-called epizonal Sb-Au

(≤ 5 km, 150-300°C) mineralisation in the proposed classification of orogenic gold deposits by Groves et al. (1998). This is near-consistent with the estimated temperatures reveal by mineral association (e.g. arsenopyrite, native gold and native antimony), arsenopyrite geothermometry (~360°C) and the fluid inclusions microthermometry (240-330°C). However, the recorded temperatures are far too high for fluids in thermal equilibrium with country rocks because this would imply a geothermal gradient of about 100°C/km. According to Obolensky et al. (2009), such disequilibrium with host rocks could indicate deep-level circulation solutions in the ore-forming fluids. A thermal source is needed to promote upward deep fluids flow to the surface.

The Le Semnon Sb-Au deposit is located in a part of the orogen (i.e. the Central Brittany) that never underwent crustal thickening (Gumiaux et al. 2004b). Variscan granitic plutons are only localized at the limit of the domain along the major shear zones (Fig. 1) and are younger than Sb-Au mineralization. Possible assumptions about thermal source could be either deep metamorphic dehydration processes involving a very fast upward fluid flow unable to equilibrate with country rocks or either a magmatic source which is able to mobilize fluids in the surrounding rocks. In regards to regional geology of the Central Brittany, it appears that only the mafic magmatism could be able to induce such thermal effect in this domain. Consequently, the Le Semnon Sb-Au deposit is likely the result from the large-scale fluids mobilization induced by the shallow emplacement of mafic magmas at *ca.* 360 Ma throughout the area (Pochon et al. 2016b).

Table 1 Summary of the microthermometric data from the different groups of fluid inclusions of the Le Semnon Sb-Au deposit and range of compositions for the volatile phase obtained by Raman spectroscopy

Fluid Type	n	% volatile phase	Tm CO_2	Tm H_2O	Tm Cl	Th CO_2	Th	Mode	Composition of the volatile phase (% mol)		
									CO_2	N_2	CH_4
Lc-w : L_{H2O}-L_{CO2}-V_{CO2}	12	25 to 60 %	-57.8 to -56.8	-4.4 to -3.5	9.4 to 9.9	15.7 to 22.1	245* to 320*	L	89.4 to 92.2	6.6 to 9.9	0.5 to 0.8
mode			-57.7	-4.1	9.7	20.8 /20.9 (L)	-				
n			12	5	8	12	10		6		
Lw-c : L_{H2O}-L_{CO2}	13	10 to 40 %	-57.8 to -57.4	-4.2 to -2.7	9.4 to 10	-	137 to 310	L	70.1 to 99.7	0.3 to 28.8	0 to 1.4
mode			-57.4	-3.2	9.9		-				
n			5	9	4		8		8		
Lw : L_{H2O} _ V_{H2O}	5	<10%	-	-3.3	-	-	115 to 154	L			
n				1			4				

Abbreviations : n = number of inclusions ; Tm CO_2 = melting temperature of CO_2 solide ; Tm H_2O = melting temperature of H20; Tm Cl = melting temperature of clathrates ; Th CO_2 = Homogenization temperature of CO_2 ; Th = Homogenization temperature ; L = liquid ; * decrepitation temperature. Temperatures are given in °C

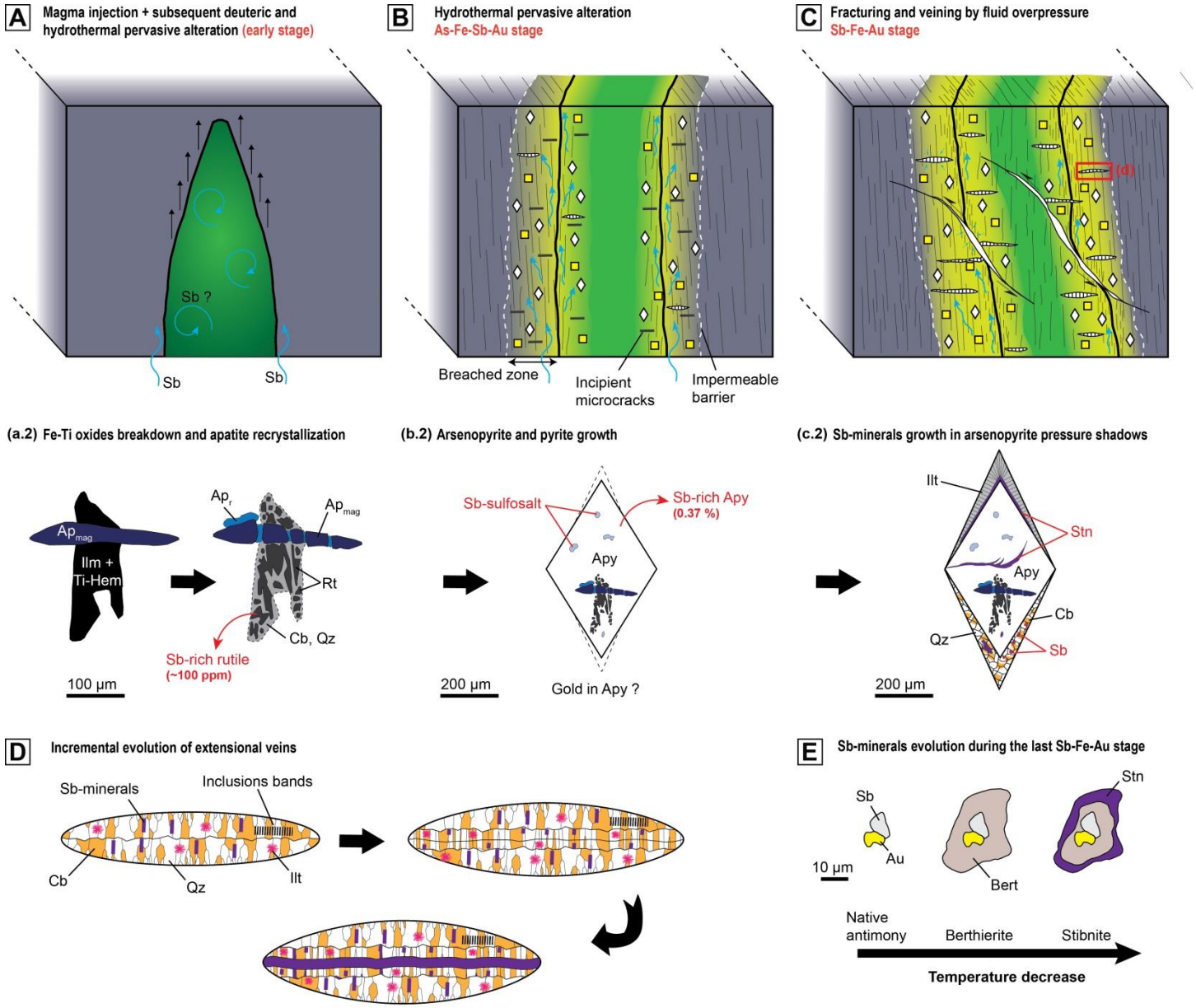

Fig. 16 Sketch illustrating the succession of the major deformation and Sb-minerals evolution events during the lifespan of the hydrothermal system at the Le Semnon Sb-Au deposit. **a** Early stage: dolerite dyke intrudes the Lower Ordovican slates at 360 Ma. It is following by a deuteric and/or hydrothermal pervasive alteration from fluids, which completely modified the dyke. At mineralogical scale, magmatic ilmenite-titanohematite assemblage is replaced by rutile and apatite is partially recrystallized suggesting that U-Pb system was likely reset. **b** As-Fe-Sb-Au stage: upward fluid flow continued at the contact between dolerite and slates (which act as an impermeable barrier for fluids). These hot fluids are responsible to dissemination of arsenopyrite, pyrite and Sb-sulfosalts in host rocks. **c** Sb-Fe-Au stage: Fluid overpressure cycling promote the development of extensional veins and fault-fill veins by small-scale fault-valve mechanism. During this stage, the main Sb-minerals (in association with illite and carbonates) mainly crystallize in the veins and pressure shadows of arsenopyrite and pyrite during the regional deformation. **d** Sketch illustrating the incremental evolution of extensional veins formed by successive cracks event evidenced by crack-seal textures. **e** Sketch illustrating the evolution of Sb-minerals (native antimony, berthierite and stibnite) by decrease of temperature during this last mineralizing stage

6. Conclusions

New structural constraints of the Le Semnon Sb-Au deposit indicate that at least a major part of the Sb-Au mineralization is contemporaneous with the regional shortening deformation. The local tectonic setting, the veins geometric arrangement and evidence of crack-seal mechanism have revealed that Sb-Au mineralisation occurred at shallow depth and supralithostatic fluid overpressure conditions associated with a small-scale fault valve mechanism. Mineralogical and geochronological results strongly suggest that the Le Semnon Sb-Au mineralization formed early during the Variscan orogeny and was coeval with the emplacement of mafic magmatism at *ca.* 360 Ma. Indeed, U-Pb dating has highlighted a pervasive Sb-rich hydrothermal alteration affecting the dolerite dyke just after its emplacement (358.5 ± 7.1 Ma) whereas 40Ar/39Ar dating has revealed that illite associated with stibnite were older than *ca.* 339 Ma. Furthermore, the paragenetic sequence indicates a gradually decrease of temperature from the early stage to the last Sb stage. In addition to Sb-minerals crystallization sequence, which reflects a decrease of temperature, fluid inclusions data also document cooling from 330 to 240°C for the Sb mineralization stage. Thus, mineralogical, geochronological and physicochemical data are consistent with a single mineralizing event rather than a contrasted style of mineralization at different time. Such hot temperature fluids (at least 330 °C) close to the surface (< 2.5km depth) imply a shallow thermal source. In the Armorican Massif, the most likely thermal source able to mobilize large-scale fluids is the widespread mafic magmatic event at 360 Ma. This proposed genetic link between mafic magmatism and Sb-Au mineralization has important implications on the understanding of the mobilization of metals in the Earth's crust and large-scale tectonic processes related to the emplacement of regional-scale mafic magma. Considering the significance of this mafic magmatism in the Armorican Massif, our results provide a new framework for future mining exploration of antimony and gold in the Western European Variscan belt.

Acknowledgements

This work was funded by the Bureau des Recherches Géologiques et Minières (BRGM), the region of Brittany, the Observatoire des Sciences de l'Univers de Rennes (OSUR), with contributions from INSU through the CESSUR Project. The author thanks Xavier Le Coz for thin sections and Jessica Langlade (UBO) for EPMA analyses.

References

Ballèvre M, Bosse V, Ducassou C, Pitra P (2009) Paleozoic history of the Armorican Massif: Models for the tectonic evolution of the suture zones. C R Geosci 341:174–201.

Ballèvre M, Catalán JRM, López-Carmona A, Pitra P, Abati J, Fernández RD, Ducassou C, Arenas R, Bosse V, Castiñeiras P, Fernández-Suárez J, Barreiro JG, Paquette JL, Peucat JJ, Poujol M, Ruffet G, Sánchez Martínez S (2014) Correlation of the nappe stack in the Ibero-Armorican arc across the Bay of Biscay: a joint French–Spanish project. Geol Soc Spec Publ 405:77–113.

Bakker RJ (1999) Adaptation of the Bowers and Helgeson (1983) equation of state to the H2O-CO2-CH4-N2-NaCl system. Chem Geol 154:225–236.

Bakker RJ, Package FLUIDS 1 (2003) Computer programs for analysis of fluid inclusion data and for modelling bulk fluid properties. Chem Geol 194:3–23.

Ballouard C, Poujol M, Boulvais P, Zeh A (2017) Crustal recycling and juvenile addition during lithospheric wrenching: The Pontivy-Rostrenen magmatic complex, Armorican Massif (France), Variscan belt. Gondwana Res 49:222–247.

Barton PB (1971) The Fe-Sb-S system. Econ Geol 66:121–132.

Barton PB, Skinner BJ (1979) Sulfide mineral stabilities. In: Barnes HL (ed) Geochemistry of hydrothermal ore deposits, New York, John Wiley, pp. 278–403.

Bellot JP, Lerouge C, Bailly L, Bouchot V (2003) The Biards Sb–Au-bearing shear zone (Massif Central, France): an indicator of crustal-scale transcurrent tectonics guiding Late Variscan collapse. Econ Geol 98:1427–1447.

Bierlein FP, Crowe DE (2000) Phanerozoic orogenic lode gold deposits. Rev Econ Geol 13:103–139.

Bierlein FP, Maher S (2001) Orogenic disseminated gold in Phanerozoic fold belts—examples from Victoria, Australia and elsewhere. Ore Geol Rev 18:113–148.

Bierlein FP, Groves DI, Goldfarb RJ, Dubé B (2006) Lithospheric controls on the formation of provinces hosting giant orogenic gold deposits. Miner Deposita 40:874–886.

Boiron MC, Cathelineau M, Trescases JJ (1989) Conditions of gold-bearing arsenopyrite crystallization in the Villeranges Basin, Marche-Combrailles shear zone, France; a mineralogical and fluid inclusion study. Econ Geol 84:1340–1362.

Boiron MC, Cathelineau M, Dubessy J, Bastoul AM (1990) Fluids in Hercynian Au veins from the French Variscan belt. Mineral Mag 54:231–243.

Boiron MC, Cathelineau M, Essarraj S, Lespinasse M, Sellier E, Poty B (1992) Identification of fluid inclusions in relation to their host microstructural domains in quartz by cathodoluminescence. Geochim Cosmochim Acta 56:175–185.

Boiron MC, Cathelineau M, Banks DA, Fourcade S, Vallance J (2003) Mixing of metamorphic and surficial fluids during the uplift of the Hercynian upper crust: consequences for gold deposition. Chem Geol 194:119–141.

Bosse V, Féraud G, Ruffet G, Ballèvre M, Peucat J-J, De Jong K (2000) Late Devonian subduction and early-orogenic exhumation of eclogite-facies rocks from the Champtoceaux Complex (Variscan belt, France). Geological Journal 35:297–325.

Bosse V, Féraud G, Ballèvre M, Peucat J-J, Corsini M (2005) Rb–Sr and 40Ar/39Ar ages in blueschists from the Ile de Groix (Armorican Massif, France): Implications for closure mechanisms in isotopic systems. Chem Geol 220:21–45.

Bouchot V, Ledru P, Lerouge C, Lescuyer JL, Milesi JP (2005) 5: Late Variscan mineralizing systems related to orogenic processes: The French Massif Central. Ore Geol Rev 27:169–197. Boullier AM, Robert F (1992) Palaeoseismic events recorded in Archaean gold–quartz vein networks, Val d'Or, Abitibi, Quebec. Canada J Struct Geol 14:164–179.

Boutin A, de Saint Blanquat M, Poujol M, Boulvais P, de Parseval P, Rouleau C, Robert JF (2015) Succession of Permian and Mesozoic metasomatic events in the eastern Pyrenees with emphasis on the Trimouns talc–chlorite deposit. Int J Earth Sci 105:747–770.

Bowers TS, Helgeson HC (1983) Calculation of the thermodynamic and geochemical consequences of nonideal mixing in the system H2O-CO2-NaCl on phase relations in geologic systems: Equation of state for H2O-CO2-NaCl fluids at high pressures and temperatures. Geochim Cosmochim Ac, 47:1247–1275.

Budzyń B, Harlov DE, Williams ML, Jercinovic MJ (2011) Experimental determination of stability relations between monazite, fluorapatite, allanite, and REE-epidote as a function of pressure, temperature, and fluid composition. Am Mineral 96:1547–1567.

Chantraine J, Atran A, Cavelier C (1996) Geological map of France, 1/ 1 000 000. BRGM, Orléans.

Chauris L, Houlgatte E, Laforêt C, Picot P (1985) Un district antimono-aurifère à gangue quartzo-carbonatée : Le Semnon (Ille-et-Vilaine, Massif Armoricain, France). Hercynica 1:111–119.

Chauris L, Marcoux E (1994) Metallogeny of the Armorican Massif. In: Chantraine J, Rolet J, Santallier DS, et al. (eds) Pre-Mesozoic Geology in France and Related Areas. Springer Berlin Heidelberg, pp 243–264.

Chew DM, Petrus JA, Kamber BS (2014) U–Pb LA–ICPMS dating using accessory mineral standards with variable common Pb. Chem Geol 363:185–199.

Chovan M, Hurai V, Sachan HK, Kantor J (1995) Origin of the fluids associated with granodiorite-hosted Sb-As-Au-W mineralization at Dúbrava (Nízke-Tatry Mts,Western Carpathians). Miner Deposita 30:48–54.

Clayton RE, Scrivener RC, Stanley CJ (1990) Mineralogical and preliminary fluid inclusion studies of lead-antimony mineralisation in north Cornwall. Proceedings of the Ussher Society 7, 258–262.

Cochrane R, Spikings RA, Chew D, Wotzlaw J-F, Chiaradia M, Tyrrell S, Schaltegger U, Van der Lelij R (2014) High temperature (>350 °C) thermochronology and mechanisms of Pb loss in apatite. Geochim Cosmochim Acta 127:39–56.

Costa S, Rey P (1995) Lower crustal rejuvenation and growth during post-thickening collapse: insights from a crustal cross section through a Variscan core complex. Geology 23:905–908.

Couto H, Roger G, Moëlo Y, Bril H (1990) Le district à antimoine-or Dúrico–Beirão (Portugal): évolution paragénétique et géochimique; implications méttalogéniques. Miner Deposita 25:569–581.

Cox SF (1987) Antitaxial crack-seal vein microstructures and their relationships to displacement paths. J Struct Geol 9:79–787.

Cox SF (1995) Faulting processes at high fluid pressures: an example of fault valve behavior from the Wattle Gully Fault, Victoria, Australia. J Geophys Res 100:12841–12859.

Cox SF, Wall VJ, Etheridge MA, Potter TF (1991) Deformation and metamorphic processes in the formation of mesothermal vein-hosted gold deposits — examples from the Lachlan Fold Belt in central Victoria, Australia. Ore Geol Rev 6:391–423.

Cox SF, Knackstedt MA, Braun J (2001) Principles of structural control on permeability and fluid flow in hydrothermal systems. Rev Econ Geol 14:1–24.

Dill HG (1985) Antimoniferous mineralization from the Mid-European Saxothuringian Zone: mineralogy, geology, geochemistry and ensialic origin. Geologische Rundschau 74:447–466.

Donnot M, Guigues J, Lulzac Y, Magnien A, Parfenoff A, Picot P (1973) Un nouveau type de gisement d'europium: la monazite grise à europium en nodules dans les schistes paléozoïques de Bretagne. Miner Deposita 8:7–18.

Dubessy J (1984) Simulation des équilibres chimiques dans le système COH. Conséquences méthodologiques pour les inclusions fluides. B Mineral 107:155–168.

Dubessy J, Poty B, Ramboz C (1989) Advances in COHNS fluid geochemistry based on micro-Raman spectrometric analysis of fluid inclusions. Eur J Mineral, 517–534.

Essarraj S, Boiron MC, Cathelineau M, Fourcade S (2001) Multistage deformation of Au-quartz veins (Laurieras, French Massif Central): evidence for late gold introduction from microstructural, isotopic and fluid inclusion studies. Tectonophysics 336:79-99.

Faleiros FM, Campanha GAC, Bello RMS, Fuzikawa K (2007) Fault–valve action and vein development during strike–slip faulting: an example from the Ribeira Shear Zone, southeastern Brazil. Tectonophysics 438:1–32.

Gapais D, Le Corre C (1980) Is the Hercynian belt of Brittany a major shear zone. Nature 288:574–576.

Gloaguen E, Branquet Y, Boulvais P, Moelo Y, Chauvel J-J, Chiappero P-J, Marcoux E (2007) Palaeozoic oolitic ironstone of the French Armorican Massif: a chemical and structural trap for orogenic base metal–As–Sb–Au mineralization during Hercynian strike-slip deformation. Miner Deposita 42:399–422.

Gloaguen E, Tourlière B, Angel JM (2016a) Revalorisation du potentiel minier français Méthodes prédictives appliquées à la province à antimoine du Massif armoricain. BRGM report. BRGM/ RP-65534-FR 71 pp.

Gloaguen E, Tourlière B, Angel JM (2016b) Revalorisation du potentiel minier français : le district antimonifère du Semnon (Ille-et-Vilaine, France). BRGM report. BRGM/RP-66200-FR 71 pp.

Goldfarb RJ, Groves DI, Gardoll S (2001) Orogenic gold and geologic time; a global synthesis. Ore Geol Rev 18:1–75. http://infoterre.brgm.fr/rapports/RP-66200-FR.pdf

Goldfarb RJ, Baker T, Dubé B, Groves DI, Hart CJR, Gosselin P (2005) Distribution, character, and genesis of gold deposits in metamorphic terranes. Econ Geol 100th Anniversary, 407–450.

Goldfarb RJ, Groves DI (2015) Orogenic gold: Common or evolving fluid and metal sources through time. Lithos 233:2–26.

Grand'Homme A, Janots E, Seydoux-Guillaume AM, Guillaume D, Bosse, V, Magnin V (2016) Partial resetting of the U-Th-Pb systems in experimentally altered monazite: Nanoscale evidence of incomplete replacement. Geology 44:431–434.

Groves DI, Goldfarb RJ, Gebre-Mariam M, Hagemann SG, Robert F (1998) Orogenic gold deposits—a proposed classification in the context of their crustal distribution and relationship to other gold deposit types. Ore Geol Rev 13:7–27.

Groves DI, Goldfarb RJ, Robert F, Hart CJR (2003) Gold deposits in metamorphic belts: overview of current understanding, outstanding problems, future research, and exploration significance. Econ Geol 98:1–29.

Gumiaux C, Brun JP, Gapais D (2004a). Strain removal within the Hercynian Shear Belt of Central Brittany (western France): methodology and tectonic implications. In: Alsop GI, Holdsworth RE, McCaffrey KJW, Hand M (eds) Flow processes in faults and shear zones. Geol Soc Spec Publ 224:287–305.

Gumiaux C, Gapais D, Brun JP, Chantraine J, Ruffet G (2004b) Tectonic history of the Hercynian Armorican Shear belt (Brittany, France). Geodin Acta 17:289–307.

Gumiel P, Arribas A (1987) Antimony deposits in the Iberian Peninsula. Econ Geol 82:1453–1463.

Harlov DE, Hetherington CJ (2010) Partial high-grade alteration of monazite using alkali-bearing fluids: Experiment and nature. Am Mineral 95:1105–1108.

Harlov DE, Wirth R, Förster HJ (2005) An experimental study of dissolution–reprecipitation in fluorapatite: fluid infiltration and the formation of monazite. Contrib Mineral Petr 150:268–286.

Harlov DE, Wirth R, Hetherington CJ (2007) The relative stability of monazite and huttonite at 300-900 C and 200-1000 MPa: metasomatism and the propagation of metastable mineral phases. Am Mineral 92:1652–1664.

Harlov DE, Wirth R, Hetherington CJ (2011) Fluid-mediated partial alteration in monazite: the role of coupled dissolution–reprecipitation in element redistribution and mass transfer. Contrib Mineral Petr 162:329–348.

Henderson IHC, MacCaig AM (1996) Fluid pressure and salinity variations in shear zone-related veins, central Pyrenees, France: implications for the fault–valve model. Tectonophysics 262:321–348.

Herrouin Y, Rabu D, Chantraine J, Chauvel JJ, Etienne H (1990) Geological map of France (1/50000), notice of the Châteaubriand sheet (389), BRGM, Orléans, France 53 pp.

Kolb J, Rogers A, Meyer FM, Vennemann TW (2004) Development of fluid conduits in the auriferous shear zones of the Hutti Gold Mine, India: evidence for spatially and temporally heterogeneous fluid flow. Tectonophysics 378:65–84.

Kretschmar U, Scott SD (1976) Phase relations involving arsenopyrite in the system Fe–As–S and their application. Can Miner 14:364–386.

Krupp RE (1988) Solubility of stibnite in hydrogen sulfide solutions, speciation, and equilibrium constants, from 25 to 350°C. Geochim Cosmochim Ac 52:3005–3015.

Le Corre C (1969) Sur une paragenèse à chloritoïde dans les schistes de l'Ordovicien moyen des synclinaux du Sud de Rennes (Massif Armoricain). Bulletin de la Société Géologique Minéralogique de Bretagne C 33–44.

Le Corre C (1975) Analyse comparee de la cristallinite des micas dans le Brioverien et le Paleozoique centre-armoricains; zoneographie et structure d'un domaine epizonal. B Soc Geol Fr 7:547–553.

Ludwig KR (2012) User's Manual for Isoplot 3.75. A geochronological toolkit for Microsoft Excel. Berkeley Geochronological Cent, 1–75.

Marcoux E (1987) Isotopes du plomb et paragenèses métalliques, traceurs de l'histoire des gîtes minéraux. Doc BRGM 117, Orléans.

Marcoux E, Serment R, Allon A (1984) Les gîtes d'antimoine de Vendée (Massif Armoricain, France). Historique des recherches et synthèse métallogénique. Chron Rech Min 476:3–30.

Marot A (1984) Etude géologique de la concession du Semnon. BRGM report. AGI/OST/84.02 MA 56 pp.

Matte P (1986) La chaîne Varisque parmi les chaînes Paléozoïques péri atlantiques, modèle d'évolution et position des grands blocs continentaux au Permo-Carbonifère. B Soc Geol Fr 2:9–24.

McCuaig TC, Kerrich R (1998) P–T–t–deformation-fluid characteristics of lode gold deposits: evidence from alteration systematics. Ore Geol Rev 12:381–454.

McDowell FW, McIntosh WC, Farley KA (2005) A precise 40Ar–39Ar reference age for the Durango apatite (U–Th)/He and fission-track dating standard. Chem Geol 214:249–263.

Micklethwaite S (2008) Optimally oriented 'faultvalve' thrusts: Evidence for aftershock-related fluid pressure pulses? Geochem Geophy Geosy 9, Q04012, doi: 10.1029/2007GC001916.

Neiva AMR, Andras P, Ramos JMF (2008) Antimony quartz and antimony–gold quartz veins from northern Portugal. Ore Geol Rev 34:533–546.

Němec M, Zachariáš J (2017) The Krásná Hora, Milešov, and Příčovy Sb-Au ore deposits, Bohemian Massif: mineralogy, fluid inclusions, and stable isotope constraints on the deposit formation. Miner Deposita doi: 10.1007/s0012.

Nguyen PT, Cox SF, Harris LB, Powell CM (1998) Fault–valve behaviour in optimally oriented shear zones: an example at the Revenge gold mine, Kambalda, Western Australia. J Struct Geol 20:1625–1640.

Obolensky AA, Gushchina LV, Borisenko AS, Borovikov AA, Nevol'ko PA (2009) Computer thermodynamic modeling of the transport and deposition of Sb and Au during the formation of Au-Sb deposits: Russ Geol Geophys+ 50:950–965.

Ortega L, Vindel E (1995) Evolution of ore-forming fluids associated with late Hercynian antimony deposits in central/western Spain: case study of Mari Rosa and El Juncalón. Eur J Mineral 7:655–673.

Ortega L, Oyarzun R, Gallego M (1996) The Mari Rosa late Hercynian Sb–Au deposit, western Spain. Miner Deposita 31:172–187.

Paquette JL, Piro JL, Devidal JL, Bosse V, Didier A, Sanac S, Abdelnour Y (2014) Sensitivity enhancement in LA-ICP-MS by N2 addition to carrier gas: Application to radiometric dating of U-Th-bearing minerals. Agilent ICP-MS Journal 58:4–5.

Périchaud JJ (1980) L'antimoine, ses minérais et ses gisements. Synthèse gîtologique sur les gisements du Massif Central français. Ch Rech Min 456:5–64.

Pochon A, Gapais D, Gloaguen E, Gumiaux C, Branquet Y, Cagnard F, Martelet G (2016a) Antimony deposits in the Variscan Armorican belt, a link with mafic intrusives? Terra Nova 28:138–145.

Pochon A, Poujol M, Gloaguen E, Branquet Y, Cagnard F, Gumiaux C, Gapais D (2016b) U-Pb LA-ICP-MS dating of apatite in mafic rocks: Evidence for a major magmatic event at the Devonian-Carboniferous boundary in the Armorican Massif (France). Am Mineral 101:2430–2442.

Pochon A, Beaudoin G, Branquet Y, Boulvais P, Gloaguen E, Gapais D (in press) Metal mobility during hydrothermal breakdown of Fe-Ti oxides: insights from Sb-Au mineralizing event (Variscan Armorican Massif, France). Ore Geol Rev doi: 10.1016/j.oregeorev.2017.10.021.

Ramsay JG (1980) The crack-seal mechanism of rock deformation. Nature 284: 135–139.

Ridley JR, Diamond LW (2000) Fluid chemistry of orogenic lode gold deposits and implications for genetic models. Rev Econ Geol 13:141–162.

Robert F, Brown AC (1986) Archean gold-bearing quartz veins at the Sigma Mine, Abitibi greenstone belt, Quebec, I. Geologic relations and formation of the vein system. Econ Geol 81: 578–592.

Robert F, Boullier AM, Firdaous K (1995) Gold–quartz veins in metamorphic terranes and their bearing on the role of fluids in fauting. J Geophys Res 100:12841–12859.

Ruffet G, Féraud G, Amouric M (1991) Comparison of 40Ar/39Ar conventional and laser dating of biotites from the North Tregor batholith. Geochim Cosmochim Acta 55:1675–1688.

Ruffet G, Féraud G, Ballèvre M, Kiénast JR (1995) Plateau ages and excess argon in phengites: A 40Ar-39Ar laser probe study of Alpine micas (Sesia Zone, Western Alps, northern Italy). Chem Geol (Isotopic Geoscience Section) 121:327–343.

Seydoux-Guillaume AM, Montel JM, Bingen B, Bosse V, De Parseval P, Paquette JL, Janots E, Wirth R (2012) Low-temperature alteration of monazite: Fluid mediated coupled dissolution–precipitation, irradiation damage, and disturbance of the U–Pb and Th–Pb chronometers. Chem Geol 330:140–158.

Schoene B, Bowring SA (2007) U–Pb systematics of the McClure Mountain syenite: thermochronological constraints on the age of the 40Ar/39Ar standard MMhb. Contrib Mineral Petr 151:615–630.

Sharp ZD, Essene EJ, Kelly WC (1985) A re-examination of the arsenopyrite geothermometer: pressure considerations and applications to natural assemblages. Can Miner 23:517–534.

Shikina ND, Zotov AV (1991) Thermodynamics parameters of Sb(OH)03(sol) up to 723.15 K and 1000 bar. Geochem Int+ 28:97–103.

Sibson RH (1985) A note on fault reactivation. J Struct Geol 7:751–754.

Sibson RH (2001) Seismogenic framework for hydrothermal transport and ore deposition. Rev. Econ Geol 14:25–50.

Sibson RH, Robert F, Poulsen KH (1988) High-angle reverse faults, fluid pressure cycling, and mesothermal gold–quartz deposits. Geology 16:551–555.

Spycher NF, Reed MH (1989) As(III) and Sb(III) sulfide complexes: An evaluation of stoichiometry and stability from existing experimental data. Geochim Cosmochim Ac 53:2185–2194.

Stacey JS, Kramers JD (1975) Approximation of terrestrial lead isotope evolution by a two-stage model. Earth Planet Sc Lett 26:207–221.

Tartèse R, Poujol M, Ruffet G, Boulvais P, Yamato P, Košler J (2011) New U-Pb zircon and 40Ar/39Ar muscovite age constraints on the emplacement of the Lizio syn-tectonic granite (Armorican Massif, France). C R Geosci 343:443–453.

Thiéry R, Van Den Kerkhof AM, Dubessy J (1994). vX properties of CH 4-CO 2 and CO 2-N 2 fluid inclusions: Modelling for T< 31 C and P< 400 bars. European Journal of Mineralogy, 6(6), 753–771.

Van Achterbergh E, Ryan CG, Jackson SE, Griffin WL (2001) Data reduction software for LA–ICP–MS: appendix. In: Sylvester PJ (ed) Laser ablation-ICP-mass spectrometry in the earth sciences: principles and applications. Mineralogical Association of Canada, Ottawa, pp 239–243.

Vernhet Y, Plaine J, Trautmann F, Pivette B (2009) Geological map of France (1/50000), notice of the Cossé-le-Vivien sheet (355), BRGM, Orléans, France 222 pp.

Wagner T, Cook NJ (2000) Late-Variscan antimony mineralization in the Rheinisches Schiefergebirge, NW: evidence for stibnite precipitation by drastic cooling of high temperature fluid systems. Miner Deposita 35:206–222.

Whitney DL, Evans BW (2010) Abbreviations for names of rock-forming minerals. Am Mineral 95:185–187.

Williams-Jones AE, Normand C (1997) Controls of mineral parageneses in the System Fe-Sb-S-O. Econ Geol 92: 308–324.

Wood SA, Crerar DA, Borcsik MP (1987) Solubility of the assemblage pyrite-pyrrhotite-magnetite-galena-gold-stibnite-bismuthinite-argentite-molybdeniitne H2O-NaC1-CO2 solutions from 200 to 350°C. Econ Geol 82:1864–1887.

Zack T, Stockli DF, Luvizotto GL, Barth MG, Belousova H, Wolfe MR, Hinton RW (2011) In situ U–Pb rutile dating by LA–ICP–MS: 208Pb correction and prospects for geological applications. Contrib Miner Petr 162:515–530.

Données complémentaires : étude des inclusions fluides du gisement Sb-Au de la Lucette

La mine Sb-Au de la Lucette est localisée au sein du bassin de Laval et constitue un gisement de classe mondiale (Laznicka 2010). Malheureusement, l'accès y est aujourd'hui complétement impossible et par conséquent nous n'avons pas de contrôle structural à l'instar du gisement du Semnon. Cependant, nous avons pu caractériser l'évolution paragénétique de la minéralisation et acquérir des données d'inclusions fluides grâce à des échantillons de collection fournis par le BRGM. Les données d'inclusions fluides de la Lucette (comme celle du Semnon) ont été réalisées par Fanny Gouazou lors de son stage de Master 2 à l'université de Lorraine (Gouazou 2016). Ce stage a été encadré par Marie-Christine Boiron, Denis Gapais et moi-même. Les échantillons de ce district, 10 au total, proviennent du filon Georges, qui fut le filon le plus important et économique de la mine de la Lucette (Guiollard 1995).

Caractérisation de la paragenèse

Ce gisement est constitué d'un essaim de filons centimétrique à pluri-métrique orientés N30°E, localisé au cœur d'un anticlinal orienté N120°E, et encaissé au sein de grès et métapélites ordoviciens à siluriens (Chauris and Marcoux 1994; Serment 1978). Les veines quartzo-carbonatées contiennent principalement de la stibine, de l'arsénopyrite, de la pyrite, de l'or natif et de nombreux sulfosels. A l'échelle macroscopique, la plupart des échantillons montre une zonalité avec, de la bordure au cœur, (1) un encaissant gréseux et quartzitique fracturé par une première génération de quartz nommé Q0, (2) une zone riche en asrsénopyrite dans une gangue constituée de quartz (Q1), (3) une autre génération de quartz Q3 géodique remplie ensuite par de la stibine massive. Le quartz Q2 n'est pas visible sur la Figure 15 car il est relativement rare et associé aux carbonates qui ne sont pas représentés ici. De l'or visible s'observe également sur certains échantillons au sein d'un quartz de génération indéterminée.

A l'échelle microscopique, l'arsénopyrite, automorphe et parfois zonée (Fig. 4.1h), est fréquemment en contact avec la sphalérite et contient des inclusions de pyrrhotite et d'électrum I (Figs. 4.1a, d). Elle se trouve aux joints de grains du quartz Q1. Une deuxième génération de quartz (Q2) contient des inclusions fréquentes de jamesonite (sulfosel de Pb-Fe) et de sphalérite avec lesquelles il semble cogénétique (Figs. 4.1b, f). Hormis ces deux premières générations de quartz, la sphalérite se trouve exclusivement en contact avec l'arsénopyrite et les sulfosels. La zinkénite est intimement associé à la jamesonite. La famatinite et la tétraédrite se trouvent fréquemment en inclusions au sein de la chalcostibite et sont toujours associés l'un avec l'autre (Fig. 4.1c).

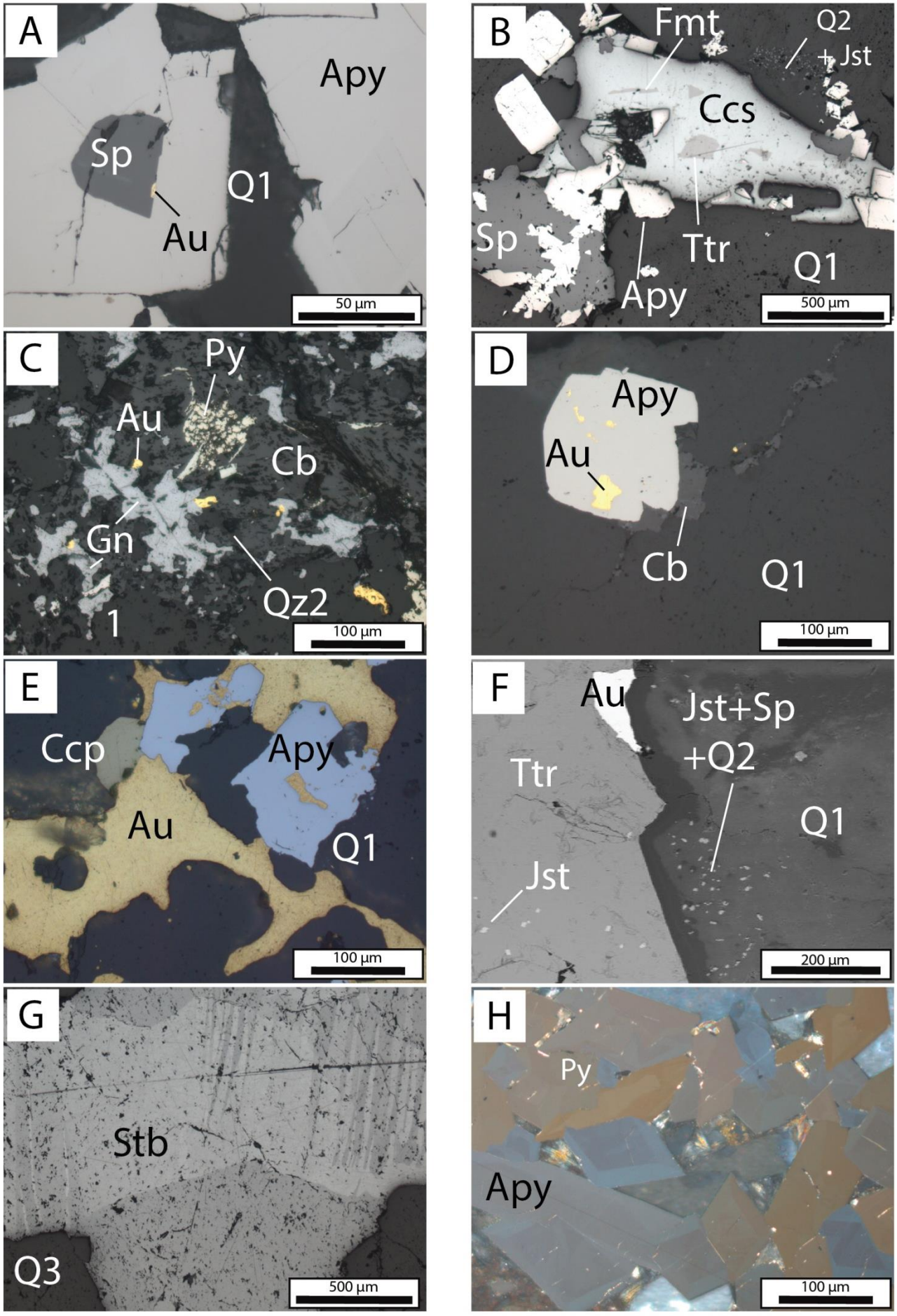
A
Apy
Sp
Q1
Au
50 µm
B
Fmt
Q2
+ Jst
Ccs
Sp
Ttr
Apy
Q1
500 µm
C
Py
Au
Cb
Gn
Qz2
1
100 µm
D
Apy
Au
Cb
Q1
100 µm
E
Ccp
Apy
Au
Q1
100 µm
F
Au
Jst+Sp
+Q2
Ttr
Q1
Jst
200 µm
G
Stb
Q3
500 µm
H
Py
Apy
100 µm

Figure 4.1 a Inclusion d'or et de sphalérite au sein d'un cristal d'arsénopyrite. **b** Remplissage de chalcostibite xénomorphe avec inclusions de tétraédrite, famatinite, arsénopyrite, jamesonite et sphalérite. **c** Veinule de sidérite associée à un quartz de 2ème génération, à la pyrite secondaire, à la galène et à l'or et recoupant la génération de quartz (Q1). L'or est associé à la galène et se trouve en inclusions avec celle-ci. **d** Inclusions d'or au sein d'un cristal d'arsénopyrite étroitement associé à une micro-veinule de sidérite aux joints de grains du quartz Q1. **e** Grains d'or englobant des cristaux d'arsénopyrite et également en remplissage de vide et de fractures au sein de ces dernières. A noter la présence de chalcopyrite au contact avec de l'or et une arsénopyrite. **f** Cristal de tétraédrite avec inclusions de micro grains de jamesonite et grain d'or entouré premièrement par la génération de quartz 1b associé à de la jamesonite et sphalérite puis par la génération de quartz 1a dépourvu de sulfures. **g** Remplissage de stibine au sein des géodes du quartz 3. **h** Plage d'arsénopyrite automorphe zonée avec rares cristaux de pyrite. Abréviations d'après Whitney et Evans (2010).

Parfois la tétraédrite est en contact avec de l'or natif et contient fréquemment des inclusions de jamesonite automorphe (Fig 4.1f). Quant à la chalcostibite, elle englobe parfois l'arsénopyrite et la sphalérite et présente également de fines inclusions de jamesonite (Fig. 4.1b)

Quant à la galène, la pyrite et la chalcopyrite, elles sont souvent en association avec les carbonates. Ces derniers, constitués essentiellement de sidérite, recoupent parfois le Q1 et sont associés à une autre génération de quartz (Q2). De l'électrum se trouve assez fréquemment (1) à l'état libre au sein des carbonates (Fig. 4.1d), (2) intimement associés à la galène (Fig. 4.1c) et parfois (3) en remplissage de fractures de pyrite et d'arsénopyrite (Fig. 4.1e), à proximité des carbonates. Enfin une dernière génération de quartz géodique (Q3) est postérieure à toutes les phases minérales hormis la stibine qui vient en remplissage finale de celui-ci (Fig. 4.1g).

La succession paragénétique est résumée au sein de la Figure 4.2 et se traduit par : (1) un stade 1, constituant la première venue de fluide aurifère à As, Zn, Au et de Sb, est composé de quartz, d'arsénopyrite, de sphalérite, de sulfosels, d'or natif ; (2) une deuxième venue (stade 2) aurifère composée essentiellement de carbonates, de métaux de bases (Pb-Cu-Fe) et d'or natif ; et (3) un dernier stade (stade 3) constituant la dernière venue de fluide minéralisé et représente la minéralisation en stibine, avec une légère remobilisation de l'or.

Résultats des données d'inclusions fluides

Pétrographie des inclusions fluides

La plupart des inclusions fluides étudiées au sein de la minéralisation de la Lucette mesurent environ 10µm et peuvent atteindre parfois 20 µm. La méthode est identique à celle décrite dans l'article #4. A travers l'étude de 8 lames épaisses (150 µm), deux lames représentatives ont été choisies pour analyses. Quatre types d'inclusions de fluides ont été observés :

- Des inclusions triphasées en fonction de la température ambiante dont le volume de la phase volatile est généralement compris entre 15 et 40% du volume total de l'inclusion (Figure 4.3a). Elles semblent principalement primaires (sans orientation particulière) ou secondaires

(alignées dans des plans), dans le quartz Q1 associé à l'arsénopyrite, le quartz Q3 en contact avec la stibine ou dans le quartz Q3b en inclusion dans la stibine.

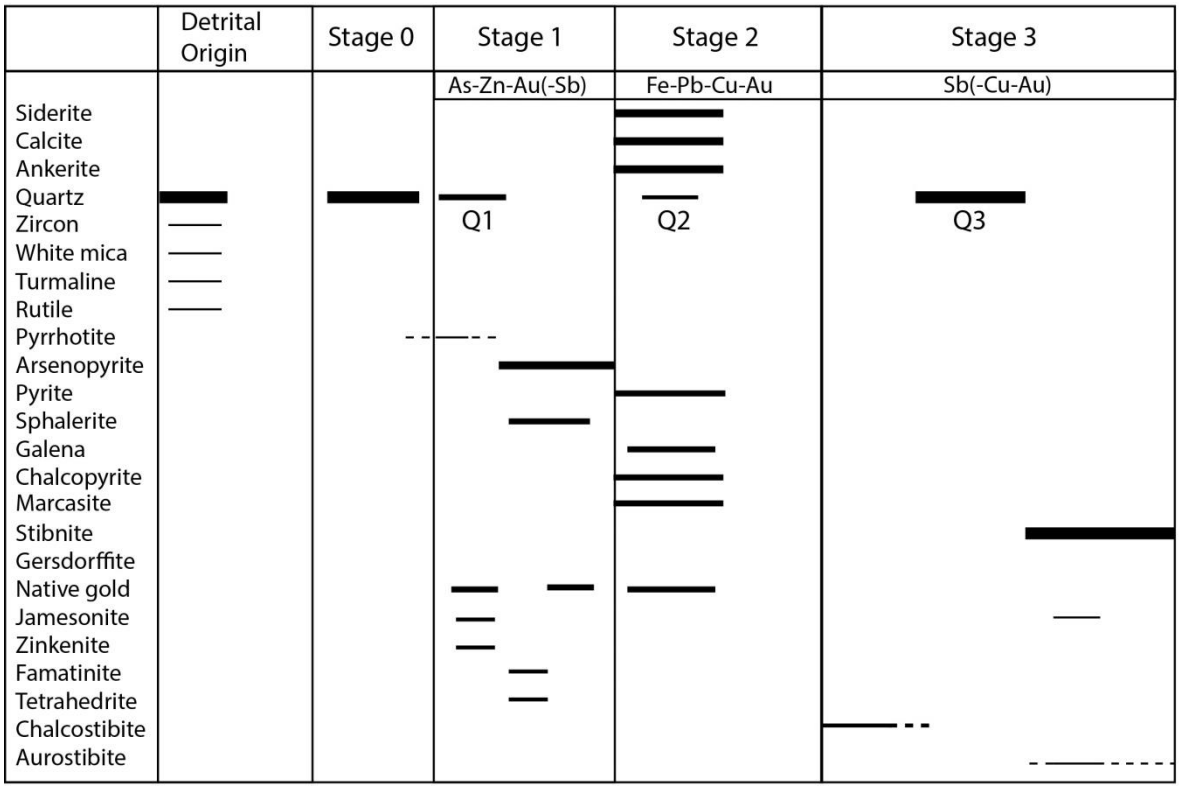

Figure 4.2 Séquence paragénétique du gisement de la Lucette. La scheelite est présente au sein de la séquence paragénétique de la Lucette. Cependant, elle n'est pas représentée dans ce tableau car nous ne disposons d'aucunes relations directes ou indirectes avec les autres minéraux de la paragenèse.

- Des inclusions biphasées dont le volume de la phase volatile varie entre 10% et 50% du volume total de l'inclusion avec une moyenne de 20-30% (Figure 4.3b). Il s'agit des inclusions les plus nombreuses et elles sont observées de manière dispersée ou bien sont secondaires, aussi bien dans le quartz Q1, Q3 et Q3b.

- Des inclusions biphasées de taille inférieure à 10 μm (Figure 4.3c), contenues dans des plans d'inclusions et comprenant une phase volatile inférieure à 10% du volume total de l'inclusion et très mobile à température ambiante. Elles sont observées dans le quartz Q3 en bordure de stibine. Celles-ci sont très peu abondantes et n'ont pas été observées au stade 1 à arsénopyrite.

- Des inclusions monophasées plus ou moins sombres, au sein de plan d'inclusions alignées dans le quartz Q1 pour les sombres (I) (Figure 4.3d) ou dans le quartz géodique Q3 pour les plus claires (II) (Figure 4.3e). Quelques inclusions très sombres plus rares et plus dispersées sont également présentes.

Microthermométrie et spectroscopie Raman des inclusions fluides

Au total 97 inclusions fluides appartenant aux quatre types d'inclusions ont été analysées. Les résultats sont reportés au sein des Table 4.1 et 4.2 et ont permis d'identifier trois types de fluides : des fluides aquo-carboniques, carboniques et aqueux.

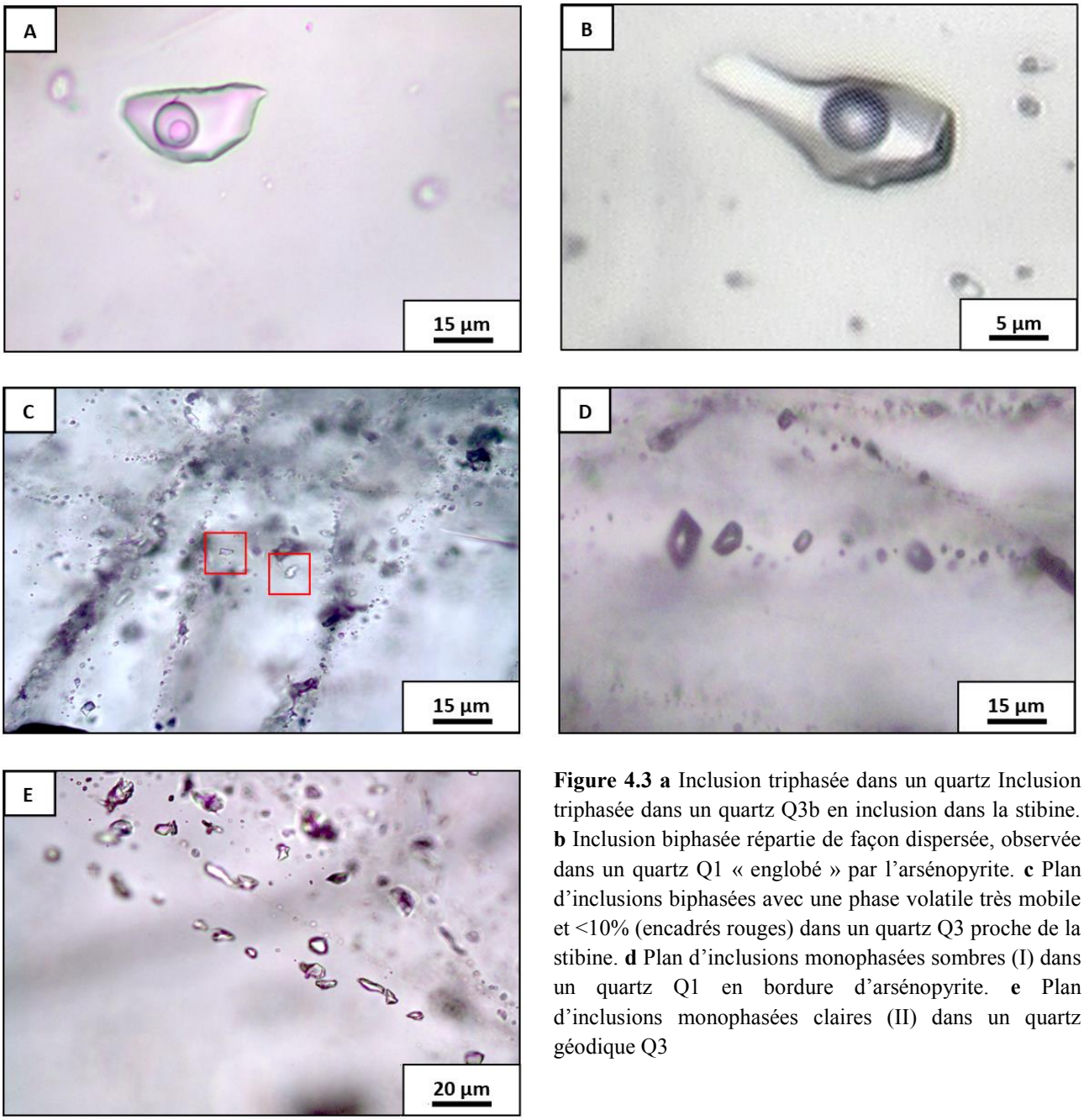

Figure 4.3 a Inclusion triphasée dans un quartz Inclusion triphasée dans un quartz Q3b en inclusion dans la stibine. **b** Inclusion biphasée répartie de façon dispersée, observée dans un quartz Q1 « englobé » par l'arsénopyrite. **c** Plan d'inclusions biphasées avec une phase volatile très mobile et <10% (encadrés rouges) dans un quartz Q3 proche de la stibine. **d** Plan d'inclusions monophasées sombres (I) dans un quartz Q1 en bordure d'arsénopyrite. **e** Plan d'inclusions monophasées claires (II) dans un quartz géodique Q3

Les résultats microthermométriques et données Raman des inclusions triphasées aquo-carboniques de type L_{H2O}-L_{CO2}-V_{CO2} présentent peu de différence entre les inclusions du stade 1 à arsénopyrite et du stade 3 à stibine, et sont donc regroupées au sein d'un même type d'inclusion. Les Tf CO_2 sont comprises entre -60.3 à -56.9°C avec un mode à -57.5°C. La fusion de la glace n'a pas été observée sur toutes les inclusions mais la gamme de température est assez restreinte (-4.1 et -3°C) avec un mode à -3.2. Les valeurs de Tf Cl ne varient pas beaucoup et sont comprises entre 9,8

et 10,2°C avec un mode à 9.9°C. Ces inclusions présentent des Th CO_2 relativement variables entre 17.1 et 24.8°C, évoluant en phase liquide. Les valeurs de Th sont assez dispersées et comprises entre 225 à 330°C où les valeurs les plus élevées correspondent au stade 1 à arsénopyrite et les valeurs les plus basses au stade 3 à stibine. Elles homogénéisent toutes en phase liquide. De nombreuses inclusions enregistrent des températures de décrépitation vers 250°C. Les données Raman montrent une composition en CO_2 de la phase volatile très élevée (entre 96 et 99.7 mol %) aussi bien pour les inclusions du stade 1 que celles du stade 3, hormis une inclusion du stade 3 affichant une valeur en CO_2 plus basse (79.9 mol %). Ces valeurs sont cohérentes avec des Tf Cl proches ou égales à 10°C (Collins 1979; Hollister et Burrus 1976).

Pour les inclusions biphasées aquo-carboniques de type L_{H2O}-L_{CO2}, la fusion du CO_2 solide a difficilement été observée, soit en raison d'une phase gazeuse trop petite soit parce qu'elle n'était pas assez dense, mais les températures mesurées sont comparables au premier type, à savoir une gamme comprise entre -57.8 et -56.9°C avec un mode à -57.5°C. Les Tf H_2O sont également très proche et comprises entre -4.2 à -2.4°C avec un mode à -3°C. Les Tf Cl sont comprises entre 10 et 11.2°C avec un mode à 10.1°C. Pour les Th, les valeurs sont très variables, entre 204 et 279°C avec un mode compris entre 204 et 210°C. Pour le quartz Q1, les valeurs sont comprises entre 254 et 278°C (n=4) avec des températures de décrépitation autour de 250°C. Pour le quartz géodique Q3 et Q3b, les valeurs sont plus basses (204 à 279°C, n=15). Les inclusions homogénéisent toutes en phase liquide. Concernant la phase volatile, les compositions sont beaucoup plus variables que le type précédent (i.e. L_{H2O}-L_{CO2}-V_{CO2}). Elles sont comprises entre 67.7 et 97.5 mol % pour le CO_2 et sont corrélées les valeurs en N_2 et CH_4. Les valeurs les plus élevées en CO_2 (92-97.1 mol %) ont été mesurées au sein du quartz Q1 tandis que les valeurs les plus faibles correspondent au quartz géodique Q3.

Les inclusions monophasées carboniques de type L_{CO2} I et II sont principalement observées au sein du stade 1 à arsénopyrite. Elles sont composées d'une seule phase purement carbonique et peuvent se différencier en deux catégories du fait de leur localisation et de leur Th CO_2 : (1) les sombres (I) dans le quartz Q1 au contact de l'arsénopyrite avec des Tf CO_2 entre -61.1 et -59°C et des Th CO_2 entre -4.8 et -0.1°C en phase liquide et (2) les plus claires (II) dans le quartz géodique Q3 avec une gamme de Th CO_2 plus large : entre -23 à -4.7°C (en phase liquide). Cependant, ces deux types d'inclusions contiennent des proportions en gaz équivalentes: $70 < CO_2 < 79$ mol % pour les L_{CO2} (I) et $73 < CO_2 < 83$ mol % pour les L_{CO2} (II) avec une augmentation en N_2 et CH_4.

Les inclusions biphasées avec une phase volatile <10%, de type L_{H2O} sont peu nombreuses et seulement observées dans le quartz Q3 en bordure de stibine. Elles présentent des caractéristiques différentes du type des inclusions biphasées précédentes. En effet, aucune transition de phase

caractéristique du CO_2 n'est observée en dessous de -40°C. La Tf H_2O n'a pu être mesurée que sur une seule inclusion (-3°C) en raison de leur petite taille et des glaçons très difficilement visibles. Toutefois, la fusion de la glace est estimée entre -5 et 0 °C. La Th reste relativement basse et est comprise entre 132 et 172°C (n=4). La phase volatile n'a pu être analysée au Raman car celle-ci était trop petite et trop mobile mais la phase liquide contient quelques traces de CO_2 et N_2.

L'évolution de la densité de la phase volatile en fonction de sa composition en CO_2 est présentée dans la Figure 4.4a. Les données montrent un lien entre le changement de la composition de cette phase et une diminution de sa densité: (1) les densités moyennes (0.45-0.61 g/cm3) du type L_{H2O}-L_{CO2}-V_{CO2} sont associées aux teneurs en CO_2 les plus élevées, (2) les inclusions L_{CO2} sont légèrement plus denses (0.67-0.7 g/cm^3) mais ont des teneurs en CO_2 plus faibles (75.7-78.5 mol %) et (3) les inclusions L_{H2O}-L_{CO2} sont beaucoup moins denses (0.11-0.17 g/cm^3) associées à des compositions en CO_2 plus faibles. Les données les plus représentatives pour le calcul des isochores sont reportés au sein de la Table 4.2. Les résultats révèlent des fluides peu salins compris entre 0,54 et 1.76 mol % pour les fluides aquo-carboniques. Les densités globales s'étalent entre 0.67 et 0.94 g/cm3. Les valeurs les plus élevées (0.91-0.94 g/cm^3) correspondent principalement aux inclusions L_{H2O}-L_{CO2}-V_{CO2} (excepté l'inclusion L8-3.7 à 0.65 g/cm^3). Les valeurs intermédiaires (0.74-0.93 g/cm^3) correspondent aux inclusions L_{H2O}-L_{CO2}, et les valeurs les plus faibles (0,67-0.88 g/cm^3) représentent les inclusions L_{CO2}. L'évolution de la composition globale des inclusions en H_2O en fonction de CO_2 (Figure 4.4b) montre que le type L_{H2O}-L_{CO2}, moins dense, est caractérisé par des teneurs en H_2O les plus élevées (94.2-95,7 mol %), et une diminution du CO_2 corrélée par une augmentation en N_2-CH_4. Les inclusions L_{H2O}-L_{CO2}-V_{CO2} moyennement denses, quant à elles ont une teneur en CO_2 qui diminue au profit de H_2O.

Nature des fluides

Les données du gisement de la Lucette semblent montrer un premier fluide (fluide 1) caractérisé par les inclusions triphasées L_{H2O}-L_{CO2}-V_{CO2} observées dans le quartz Q1 associé à l'arsénopyrite et dans le quartz Q3 associé à la stibine. Ce fluide est aquo-carbonique, assez dense, généralement supérieur à 0.9 g/cm3, et peu salin, entre 0.6 et 1.7 mol % (2 à 7.4 % poids NaCl). La composition de la phase volatile des inclusions est largement dominée par le CO2 qui peut atteindre 99.7 mol % et contient des traces de N_2 et CH_4 mais la composition globale reste dominée par H_2O.

Un deuxième fluide (fluide 2) peut être déterminé à partir des inclusions biphasées L_{H2O}-L_{CO2} localisées dans le quartz Q1 et Q3. Celui-ci est également du type aquo-carbonique mais légèrement moins dense (0,74 à 0,93 g/cm^3) et moins salin que le fluide 1 (0,54 à 1 mol % correspondant à 1,8 à 3,3 % poids NaCl). La phase volatile est beaucoup moins dense et est liée à une augmentation de H_2O dans les inclusions, tout comme le N_2 et CH_4, au détriment du CO_2

(Figure 4.4, Table 4.2). Enfin, quelques Th sont légèrement plus basses que celles obtenues pour les inclusions triphasées (mode à 204-210°C). Ces données traduisent une évolution continue dans le temps de la composition des inclusions et suggère que le fluide 2 pourrait provenir d'une dilution du fluide 1 (aquo-carbonique). Quant aux inclusions monophasées L_{CO2}, elles semblent avoir la même composition que la phase volatile du fluide dilué. Elles pourraient résulter d'un phénomène de démixtion entre la phase liquide et la phase volatile de ce fluide puisqu'elles contiennent les mêmes proportions en gaz que les inclusions L_{H2O}-L_{CO2}.

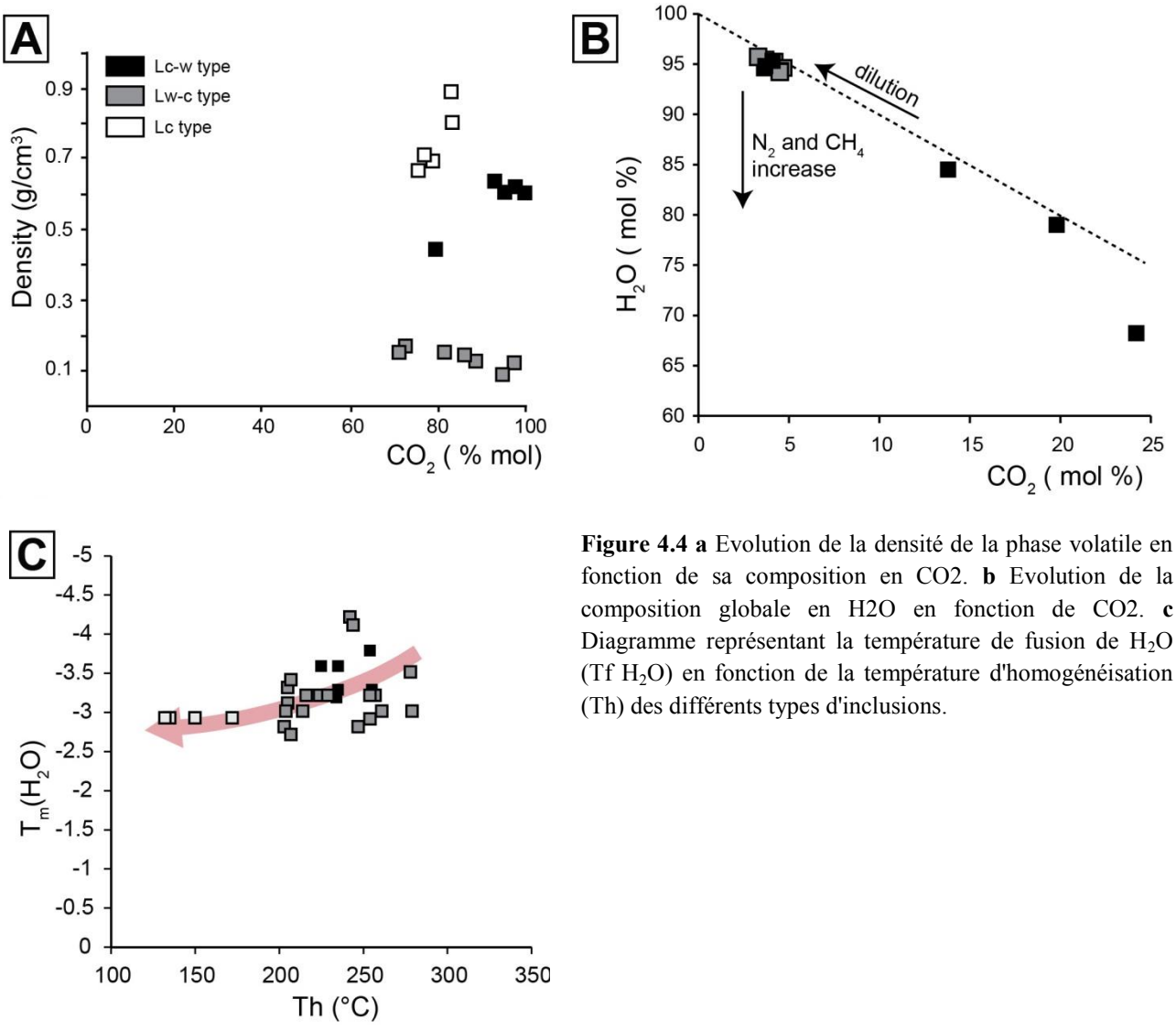

Figure 4.4 a Evolution de la densité de la phase volatile en fonction de sa composition en CO2. **b** Evolution de la composition globale en H2O en fonction de CO2. **c** Diagramme représentant la température de fusion de H_2O (Tf H_2O) en fonction de la température d'homogénéisation (Th) des différents types d'inclusions.

Enfin un troisième fluide (fluide 3), peu abondant, a été observé au sein de plans d'inclusions au sein du quartz Q3. Il est considéré comme principalement aqueux, très peu salin mais contient des traces de CO_2 et N_2. Les Th entre 132°C et 172°C témoignent de conditions minimales de piégeage plus faibles que les deux premiers fluides aquo-carboniques. Ce type de fluide est caractéristique d'un fluide superficiel, probablement météorique.

Les valeurs de Tf H_2O en fonction de Th ont été reportées dans la Figure 4.4c et montre que des fluides 1 et 2 peu salins et chauds (280°C) associés aux Tf H_2O les plus basses (-3,5 à -4,5°C)

évoluent vers des Th plus basses et des Tf H_2O plus hautes. Enfin le fluide 3, encore moins salin et probablement météorique, est piégé dans des conditions de températures plus basses (entre 125 et 170°C) avec des Tf H_2O entre -3 et -3,3°C.

Comparaison de l'évolution des fluides entre les gisements Sb-Au de la Lucette et du Semnon

Contrairement au gisement du Semnon, nous disposons de moins de contraintes stratigraphiques au niveau du gisement de la Lucette. Les différences majeures qui les distinguent sont que :

- le gisement du Semnon est situé au cœur du domaine Centre Armoricain. Ce domaine est très faiblement déformé et n'a jamais subi d'épaississement crustal (e.g. Gumiaux et al 2004a). De plus, le Carbonifère ne s'est jamais déposé au sein de ce domaine (e.g. Herrouin et al. 1990 ; Ballèvre et al. 2013). Par conséquent, la séquence stratigraphique se trouvant au-dessus du gisement du Semnon est relativement continue jusqu'au Dévonien supérieur et peut être estimée aux alentours de 2.5 km d'épaisseur maximum (Herrouin et al. 1990).

- le gisement de la Lucette est situé au sein du bassin Carbonifère de Laval qui a une histoire tectonique et volcano-sédimentaire plus complexe (e.g. chevauchement de Changé, Houlgatte et al. 1988). En effet, ce bassin est plus déformé que la série paléozoïque du domaine Centre Armoricain. Le Carbonifère y est abondant et relativement épais mais l'épaisseur de cette série complète n'est pas connue. De plus, un volcanisme bimodal avec des coulées de basaltes et de rhyolites y est très important et l'épaisseur totale est également difficile à évaluer. Ainsi il est difficile d'estimer l'épaisseur totale des séries volcano-sédimentaires qui se trouvait au-dessus du gisement de la Lucette lors de sa formation. Cependant, nous pouvons donner une épaisseur minimale aux alentours de 2.4 km (Le Gall et al. 2011), ce qui suggère au premier ordre que le gisement de la Lucette s'est formé à relativement plus grande profondeur que celui du Semnon.

Bien que les inclusions fluides localisées dans le quartz Q1 associé à l'arsénopyrite présentent les mêmes caractéristiques que celles du quartz Q3 associé à la stibine, il est tout de même possible de proposer une évolution P-T des fluides grâce au calcul des isochores des inclusions qui figurent dans la Table 4.2. Le diagramme P-T est représenté dans la Figure 4.5. Il révèle que 5 isochores de fluides aquo-carboniques ont une pression minimum de piégeage supérieure au poids lithostatique minimum. En considérant que (1) nous n'avons aucune évidence de surpression de fluides comme mécanisme de formation du système de veines (à l'inverse du Semnon) et (2) les fluides aquo-caboniques 1 et 2 sont contemporains (i.e. fluide 2 provient de la dilution du fluide 1), il semble raisonnable de proposer des conditions minimales de piégeage de la minéralisation entre 225 et 380°C pour une pression lithostatique d'environ 100 MPa, soit ~ 3 km de profondeur, en comptant une tranche d'eau de mer raisonnable de 2 km. Le phénomène de

démixtion identifié localement et associé au fluide 2 résulterait alors d'un changement de pression entre les fluides 1 et 2. Le fluide 3 purement aqueux a probablement été piégé dans des conditions de pression hydrostatique, entre 150 et 190°C. Il peut être considéré comme météorique, en raison de sa faible salinité et peut être associé à une circulation de fluide plus tardive et potentiellement déconnecté des minéralisations. Au regard de la profondeur minimale de formation de la minéralisation Sb-Au, il apparait que le gradient géothermal le plus approprié en condition lithostatique (~ 70°C/km) reste anormalement élevé mais il est beaucoup moins élevé que celui du Semnon (~ 100°C/km). Les conditions de piégeage des fluides météoriques semblent être régies par un gradient géothermal classique (30°C/km), suggérant par conséquent que l'anomalie thermique, présente lors du piégeage des fluides aquo-carboniques, n'existait plus. Si l'on considère le gisement de la Lucette comme synchrone de celui du Semnon (bien que nous ne disposons d'aucune contrainte géochronologique) et du magmatisme mafique, il se peut que les fluides météoriques soient déconnectés de l'histoire hydrothermale minéralisatrice. Pour cela, il est nécessaire, à l'avenir, de dater la minéralisation de la Lucette (e.g. la scheelite observée mais non calée dans la paragenèse pourrait être un bon candidat pour dater au moins la minéralisation à W) et d'apporter de nouvelles contraintes quant à la profondeur de mise en place de ce gisement.

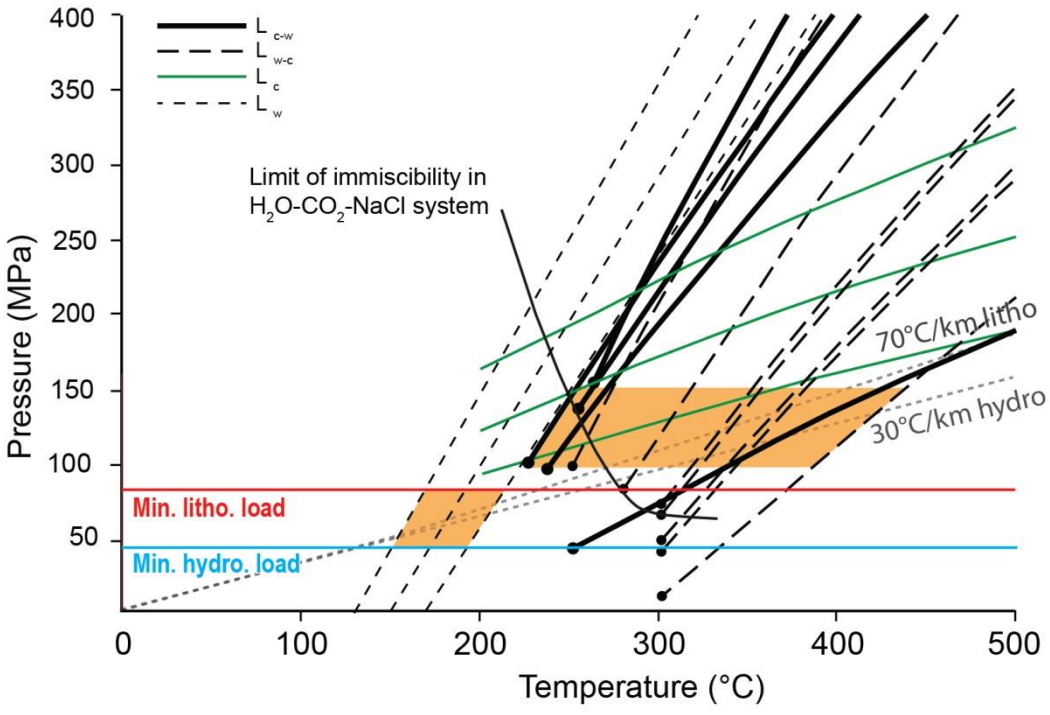

Figure 4.5 Diagramme P-T des inclusions fluides observées au sein du gisement de la Lucette

Table 4.1 Summary of the microthermometric data from the different groups of fluid inclusions of the La Lucette deposit and range of compositions for the volatile phase obtained by Raman spectroscopy

Fluid Type	n	% volatile phase	Tm CO_2	Tm H_2O	Tm Cl	Th CO_2	Th	Mode	Volatile phase composition (% mol)		
									CO_2	N_2	CH_4
Lc-w : L_{H2O}-L_{CO2}-V_{CO2}	26	15 to 40 %	-60.3 to -56.8	-4.1 to -3	9.8 to 10.2	17.1 to 24.8	225 to 330 (250*)	L	79.9 to 99.7	0.3 to 19.3	0 to 1.2
mode			-57.5	-3.2	9.9	21.4 (L)	-				
n			25	15	8	25	10		10		
Lw-c : L_{H2O}-L_{CO2}	44	10 to 50 %	-57.8 to -56.9	-4.2 to -2.4	10 to 11.2	-	204 to 279 (254*)	L	67.7 to 97.5	2.1 to 27.7	0.1 to 4.6
mode			-57.5	-3	10.1		204-210				
n			9	39	12		19		27		
Lc: L_{CO2} (I)	14		-61.1 to -59			-4.8 to -0.1		L	70 to 79.2	17.9 to 26.4	2.8 to 3.6
mode			-59.4			-4.5 (L)					
n			13			12			5		
Lc: L_{CO2} (II)	13		-60.4 to -59.5			-23 to -4.7		L	73.3 to 83.4	15.8 to 23	0.8 to 3.6
mode			-59.5			-4/-13 (L)					
n			13			10			7		
Lw : L_{H2O} _ V_{H2O}	5	<10%	-	-3.1	-	-	132 to 154	L			
n				1			4				

Abbreviations : n = number of inclusions ; Tm CO_2 = melting temperature of CO_2 solide ; Tm H_2O = melting temperature of H20; Tm Cl = melting temperature of clathrates ; Th CO_2 = Homogenization temperature of CO_2 ; Th = Homogenisation temperature ; L = liquid ; * decrepitation temperature. Temperatures are given in °C

Table 4.2 Chemical composition of representative aqueous-carbonic inclusions of the La Lucette Sb-Au deposit obtained by Raman spectroscopy and corresponding microthermometric data

	Tm CO2	Tm H2O	TmCl	Th CO2	Th	Composition of the volatile phase (% mol)				Bulk composition (% mol)				Density (g/cm^3)
Sample						**CO_2**	**N_2**	**CH_4**	**H_2O**	**CO_2**	**N_2**	**CH_4**	**NaCl**	
Lc- w aqueous carbonic inclusions, L_{H2O}-L_{CO2}-V_{CO2} :														
L1-2.2.7	-57.5	-3.8	10	24.3	254*	92.2	4.5	0.3	84.5	13.8	0.6	<0.1	1.1	0.93
L8-1.2	-59.5	-3.4	9.8	21		99.7	0.3	n.d.	95.3	4.1	<0.01	n.d.	0.6	0.94
L8-1.9	-60.3	-3.6	9.8	19.4	225	93	6.5	0.5	94.8	3.7	0.5	~0.01	1	0.94
L8-2.1.4	-57.3	-3.2	10	21.3	234	97.5	2.4	0.1	79	19.8	0.4	~0.02	0.8	0.91
L8-3.7	-57.2	n.o.	10	17.1		79.5	19.3	1.2	68.2	24.2	5.6	0.3	1.7	0.65
Lw-c aqueous carbonic inclusions, L_{H2O}-L_{CO2} :														
L1-1.1.1	-57.7	-3	10.7			97.1	2.1	0.8	95.2	4.2	<0.1	~0.01	0.6	0.83
L1-2.2.11	-57.3	-3.2	10.1		254*	95.6	4.2	0.2	94.6	4.7	0.1	<0.01	0.6	0.74
L1-6.1.5	n.o.	-3.4	10.8	-	207	81.3	16.8	1.9	94.3	4.5	0.4	<0.1	0.7	0.8
L1-6.1.7	n.o.	-3	10	-	204	70.7	25.7	3.6	94.7	3.7	0.5	<0.1	1	0.84
L8-2.2.9	n.o.	-3	10.2	-	279	86.4	12.9	0.7	95.4	3.7	0.2	~0.01	0.7	0.88
L8-2.2.27	n.o.	-2.6	11.2		n.o.	72.5	26.2	1.3	94.2	4.5	0.7	<0.1	0.5	0.8
L8-2.2.28	n.o.	-3.2	10	-	214	87.9	11.6	0.5	95.7	3.3	0.1	<0.01	0.9	0.93
Lc carbonic inclusions, L_{CO2} :														
L1-3.1	-60.8			-4.6		78.5	18.7	2.8	0	78.5	18.7	2.8	0	0.69
L1-3.4	-61			-4.8		75.7	21	3.3	0	75.7	21	3.3	0	0.67
L1-6.2.1	-60.5			-15.3		77.5	19.8	2.7	0	77.5	19.8	2.7	0	0.7
L1-3b2	-59.5			-23		83	16.1	0.9	0	83	16.1	0.9	0	0.88
L1-3b9	-59.5			-4.7		83.4	15.8	0.8	0	83.4	15.8	0.8	0	0.8

Abbreviations: n = number of inclusions; Tm CO_2 = melting temperature of CO_2 solide; Tm H_2O = melting temperature of H20; Tm Cl = melting temperature of clathrates; Th CO_2 = Homogenisation temperature of CO_2; Th = Homogenisation temperature; L = liquid; * decrepitation temperature; n.o. = not observed. Temperatures are given in °C

Partie 5

Intégration des minéralisations Sb-Au dans l'évolution géodynamique du Massif Armoricain

1. Minéralisations Sb-Au : témoins de circulations de fluides à l'échelle régionale

Résumé en français de l'article #5

Les analyses ^{40}Ar / ^{39}Ar sur des grains séparés de tobelite et les analyses U-Pb par LA-ICP-MS sur des grains séparés d'apatite ont été réalisées afin de dater la minéralisation Sb-Au et l'hydrothermalisme de l'occurrence polymétallique de Saint-Aubin-des-Châteaux (Loire-Atlantique, Domaine Centre Armoricain, France). Les résultats montrent que le dépôt de Sb-Au est d'âge Carbonifère inférieur (*ca.* 360 Ma). Couplé avec les résultats récents obtenus dans la région voisine (gisement Sb-Au du Semnon), nous avons identifié un pic minéralisateur à or et antimoine, d'importance économique, dans la partie sud-est du Domaine Centre Armoricain, précoce dans l'histoire Carbonifère. La mise en place contemporaine d'un magmatisme mafique généralisé au sein du Domaine Centre Armoricain semble jouer un rôle majeur dans la mobilisation des circulations de fluides associées aux systèmes minéralisés à faible profondeur (moins de 3 km). Ce magmatisme mafique à 360 Ma doit maintenant être pris en considération dans la genèse des systèmes minéralisés au sein de la chaîne Varisque. Enfin, les différentes générations de phosphates des niveaux de minerais de fer oolithique intercalés au sein du Grès Armoricain permettent d'établir une histoire hydrothermale de longue durée du Carbonifère inférieur jusqu'au début du Permien au sein du Domaine Centre Armoricain.

Note : Au sein de l'article #5, Pochon et al. (in prep) fait référence à l'article #4 de ce présent manuscrit

An Early Carboniferous Sb-Au mineralizing peak in a long-lived hydrothermal history: major tectono-magmatic implications for the Armorican Massif (France)

Anthony Pochon[1], Yannick Branquet[1, 2], Gilles Ruffet[1], Marc Poujol[1], Eric Gloaguen[2, 3], Philippe Boulvais[1], Charles Gumiaux[2], Florence Cagnard[2, 3], Denis Gapais[1], Jean-Marc Baele[4], Inoussa Kéré[1]

[1] *Géosciences Rennes, UMR 6118, Université de Rennes 1, OSUR, Campus de Beaulieu, 35042 Rennes Cedex, France*

[2] *Institut des Sciences de la Terre d'Orléans, UMR 7327, Université d'Orléans, Campus Géosciences, 1A rue de la Férollerie, 45071 Orléans Cedex 2, France*

[3] *Bureau de Recherche Géologique et Minière (BRGM), UMR 7327, 3 avenue Claude-Guillemin, BP 36009, 45060 Orléans Cedex 02, France*

[4.] *Géologie Fondamentale et Appliquée, Université de Mons, Rue de Houdain, 9, 7000 Mons, Belgium*

Article en préparation en vue d'une soumission simultanée avec l'article #4 (« compagnon papers ») pour la revue *Mineralium Deposita*

Abstract

^{40}Ar / ^{39}Ar and LA-ICP-MS U-Pb absolute dating on tobelite (an ammonium-rich white mica) and apatite, respectively, have been performed in order to provide some geochronological constraints on the Sb-Au mineralization and hydrothermalism at the Saint-Aubin-des-Châteaux base metal-Sb-Au occurrence (Loire Atlantique, Central Armorican Domain, France). The results show that the Sb-Au deposition is Early Carboniferous in age (ca. 360 Ma). Coupled with recent results obtained in the neighboring area, we identify an Early Carboniferous economic Sb-Au mineralizing peak in the southeastern part of the Central Armorican Domain. Furthermore, the emplacement of a coeval widespread mafic magmatism in the region appears to represent a major trigger for this mineralizing system at shallow depths (less than 3 km). In the light of these new data, this Early Carboniferous mafic magmatism has to be taken into account for the understanding of the genesis of mineralizing systems at the scale of whole Variscan belt. Finally, phosphates generations from the oolithic ironstone horizons intercalated within Ordovician sandstones allow establishing a long-lived Carboniferous-Early Permian history in this part of Armorican domain.

1. Introduction

Dating of hydrothermal events remains a major challenge for geochronologists. This can be due to the lack of datable minerals within the mineralization paragenetic sequence itself. But also, if such suitable minerals are present, to either their low parent isotopes contents (low-uranium content in apatite for example) or to their incapacity to retain sufficient amounts of daughter isotopes (e.g. Ar loss in mica). In addition, overprints due to thermal input and/or fluid circulations frequently disturb the isotopic system of the chronometers which might yield meaningless dates (e.g. Tartèse et al. 2011, 2015). For these main reasons, the exact timing of the emplacement of the Sb ± Au mineralization from the Central Armorican Domain (CAD, Fig. 1) remains poorly constrained. Based on relative chronology and "analogy" with Au ± Sb mineralization of the Variscan thickened internal zones (e.g. French Massif Central and Brittany southern domain), most of the Variscan Sb ± Au deposits including those of the CAD (i.e. the giant La Lucette or Le Semnon deposits Fig. 1a) are generally considered to be late Carboniferous in age (Chauris and Marcoux 1994; Bouchot et al. 2005). Indeed, these works identify a unique Au ± Sb mineralizing peak (the so-called "Or 300 Ma" event) along the French Variscan belt, involving large-scale fluid flow related to thermal events during the post-thickening collapse of the orogen. In this scenario, this mineralizing peak is associated with the coeval emplacement of leucogranites related to W ± Sn deposits and rare-metal granite emplacement (Costa and Rey 1995; Bouchot et al. 2005).

However, several lines of evidence argue against the validity of such model for the Au ± Sb mineralization in the CAD. Indeed, the CAD represents the external zone of the orogeny and did not experience important thickening (i.e. no metamorphic nappe stacking, e.g. Gumiaux et al. 2004). Then, subsequent fluid flows driven by thermal effect of post-orogenic collapse are totally missing and make the late Carboniferous fluid flows scenario difficult. Furthermore, recent works of Pochon et al. (2016a, 2016b, in press and in prep) highlighted a strong spatial and temporal relationship between a widespread mafic magmatism at ca. 360 Ma (Fig. 1a) and the Le Semnon Au ± Sb mineralization. Indeed, the Le Semnon Sb-Au deposit was formed before 340 Ma with an unequivocal contribution of a 360-350 Ma event revealed by ^{40}Ar / ^{39}Ar and U-Pb ages on hydrothermal illite and apatite respectively (see details in Pochon et al. in prep).

In order to evaluate the local vs. regional signification of those new magmatic and hydrothermal ages, we attempt to date other Sb ± Au hydrothermal occurrences within the CAD. In this paper, we focussed on the base metal-Sb ± Au occurrence of Saint-Aubin-des-Châteaux (SADC, Figs. 1a, b). This occurrence is a famous locality for mineralogists dealing with Sc-Sr-REE –rich phosphates and consequently presents the advantage to have a well-constrained hydrothermal paragenetic sequence updated through many studies (Léone et al. 2000; Moëlo et al. 2000, 2002,

2008; Gloaguen et al. 2007, Mesto et al. 2012; Frost et al. 2014; Tartèse et al. 2015; Capitani et al. 2016).

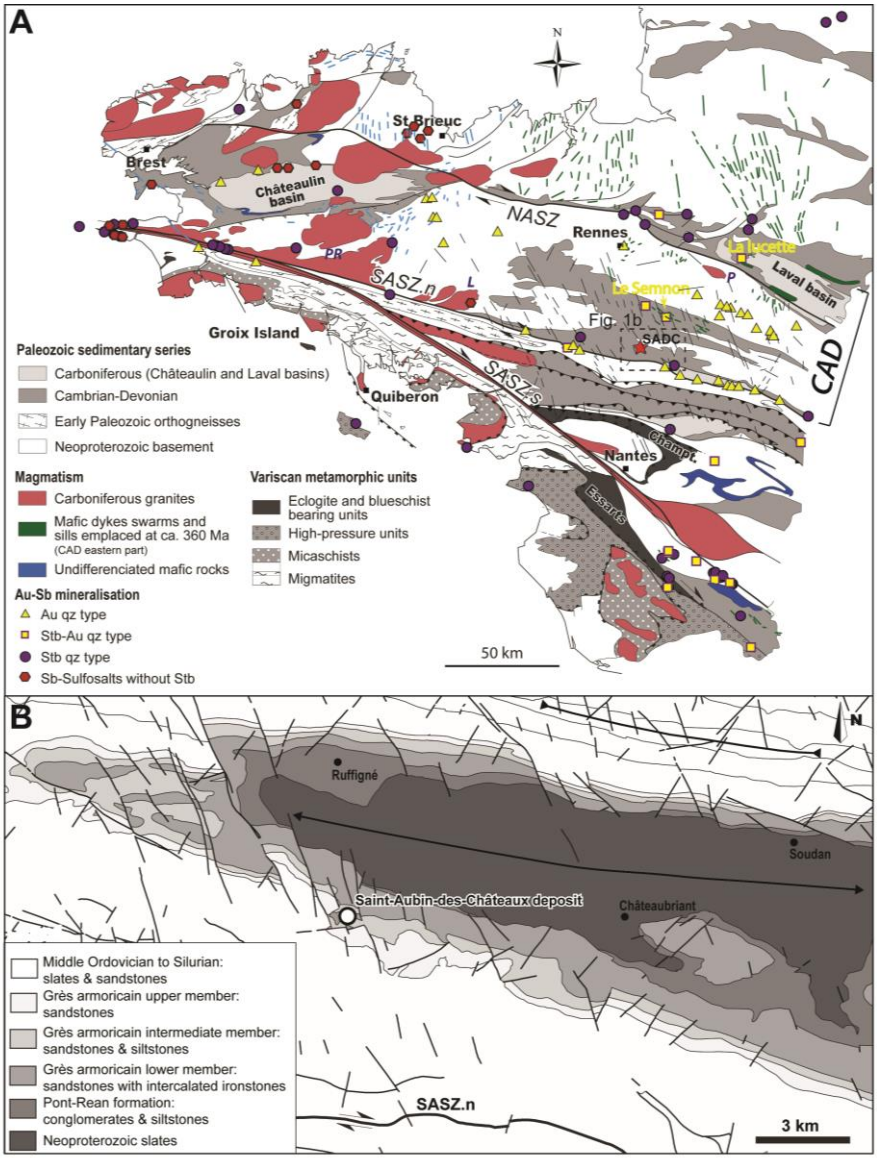

Figure 1 a Geological map of the Armorican Massif with location of the different Sb-Au mineralization types. The eastern parts of both the Central Armorican Domain (CAD) and the Cadomian northern domain suffered important basic magmatism attested by numerous dolerite dyke swarms and sills (in green) at ca. 360 Ma (Pochon et al., 2016b). South of Rennes city, the CAD is affected by a high density network of kilometre-scale NNW-SSE-trending vertical faults. NASZ: North Armorican Shear Zone; SASZ.n,.s: South Armorican Shear Zone, northern and southern branches respectively; Champt.: Champtoceaux metamorphic complex; PR, L, P: Pontivy-Rostrenen, Lizio and Le Pertre granites respectively; SADC: Saint-Aubin-Des-Châteaux (red star). **b** Geological map of the area around the SADC base metal-Sb-Au occurrence located in the very low dipping anticline southern flank. The SADC quarry is located within an important N160-150-E-trending fault corridor.

We report new $^{40}Ar/^{39}Ar$ and U/Pb ages on this Sb ± Au hydrothermal system performed on tobelite (an uncommon ammonium-rich white mica, $(NH_4,K)Al_2(Si_3Al)O_{10}(OH)_2$) and apatite, respectively. Then, we discuss the meaning of these ages with respect to regional tectonics, deformations, magmatism and hydrothermalism.

2. Geological background

2.1 Regional geology

The Saint-Aubin-des-Châteaux (SADC) occurrence is located in the CAD, a part of the Variscan Armorican belt bounded by two dextral crustal-scale shear zones (Gumiaux et al. 2004 and references therein): the North Armorican Shear Zone (NASZ) and the South Armorican Shear Zone (SASZ) (Fig. 1a). The CAD is mostly composed of a Late Neoproterozoic to Cambrian pelitic basement with its Ordovician to Devonian sedimentary cover, both affected by a low greenschist facies metamorphism. During the Carboniferous, the whole CAD underwent a N123°E trending regional-scale dextral shearing that produced upright folds with N110°E trending sub-horizontal axes and sub-vertical axial planes (Gapais and Le Corre 1980; Gumiaux et al. 2004). Large-scale wavelength folds are mechanically controlled by the thick and competent "Grès Armoricain" formation (Fig. 1b) and they are associated with a weakly developed sub-vertical cleavage bearing a sub-horizontal stretching lineation (Choukroune et al. 1983; Gumiaux et al. 2004). Strain intensity increases from North to South reaching its maximum near the northern branch of the SASZ (Gapais and Le Corre 1980). The dominant N160°E trending regional faulting (Fig. 1b) is compatible with the regional dextral simple shear (Choukroune et al. 1983).

Contrary to the western part of the CAD, the eastern part experienced little granitic intrusions. Some synkinematic granite intrusions were emplaced near 316 Ma along the northern branch of the SASZ, such as the Lizio granite (Tartèse et al. 2011) and an older granitic intrusion occurs near the NASZ, the Le Pertre granite (343 ± 3 Ma by U-Pb on zircons, Vernhet et al. 2009, Fig. 1a). The CAD is mainly marked by a widespread network of mafic dikes and sills (Fig. 1a) corresponding to a large-scale mafic magmatic event at ca. 360 Ma (Pochon et al. 2016b). This magmatism is therefore coeval with the high-pressure metamorphic event in the South Armorican Domain (Bosse et al. 2000, 2005) and with the beginning of the bulk dextral wrenching of the CAD (Gumiaux et al. 2004). As mentioned in introduction, this mafic magmatic event has strong spatio-temporal and likely genetic relationships with Sb-Au deposits (Pochon et al. 2016a, in press and in prep) which are widespread in the CAD (Fig. 1a).

2.2 The Saint-Aubin-des-Châteaux base metal-Sb ± Au occurrence

The SADC polymetallic deposit is mainly hosted by the lower member of Grès Armoricain formation, which consists of homogeneous dark grey massive sandstone beds intercalated with thin cm-scale dark pelitic beds. At a regional scale, four main oolitic ironstone horizons (Fig. 2a, OIH) intercalated within the lower part of the Grès Armoricain formation are recognized (Chauvel 1974). In the SADC deposit, only the uppermost OIH is currently cropping out. OIH were affected by diagenesis and by the regional low-grade metamorphism (Le Corre 1978), as indicated by the growth of a diagenetic and/or metamorphic Sr-bearing fluorapatite (Moëlo et al. 2008). Moreover,

four main stages of OIH epigenetic hydrothermal alteration have been distinguished (see Gloaguen et al. 2007 for detailed paragenetic sequence): (i) a massive sulphidation event along and laterally of cross-cutting vertical strike-slip faults (stage 1 Fe-As, Fig. 2a). The OIH is strongly replaced by a pyrite- pyrrhotite-arsenopyrite assemblage. The sulphidation front across the OIH front is marked by the growth of hydrothermal apatite and REE-phosphates (Möelo et al. 2002, 2008); (ii) a second base-metal stage characterized by extensional and shear veins, crosscutting the massive suphide lenses, and mainly filled with quartz, pyrite, chalcopyrite, sphalerite and galena (stage 2, Cu-Zn(-Pb), Fig. 2a); (iii) a subsequent Pb-Sb-Au stage 3, still related to vertical strike-slip faults activity (Fig. 2a) and characterized by veins filled with Sb-sulphosalts (bournonite, boulangerite, tetrahedrite, Fig. 2b) and associated electrum (Fig. 2c).

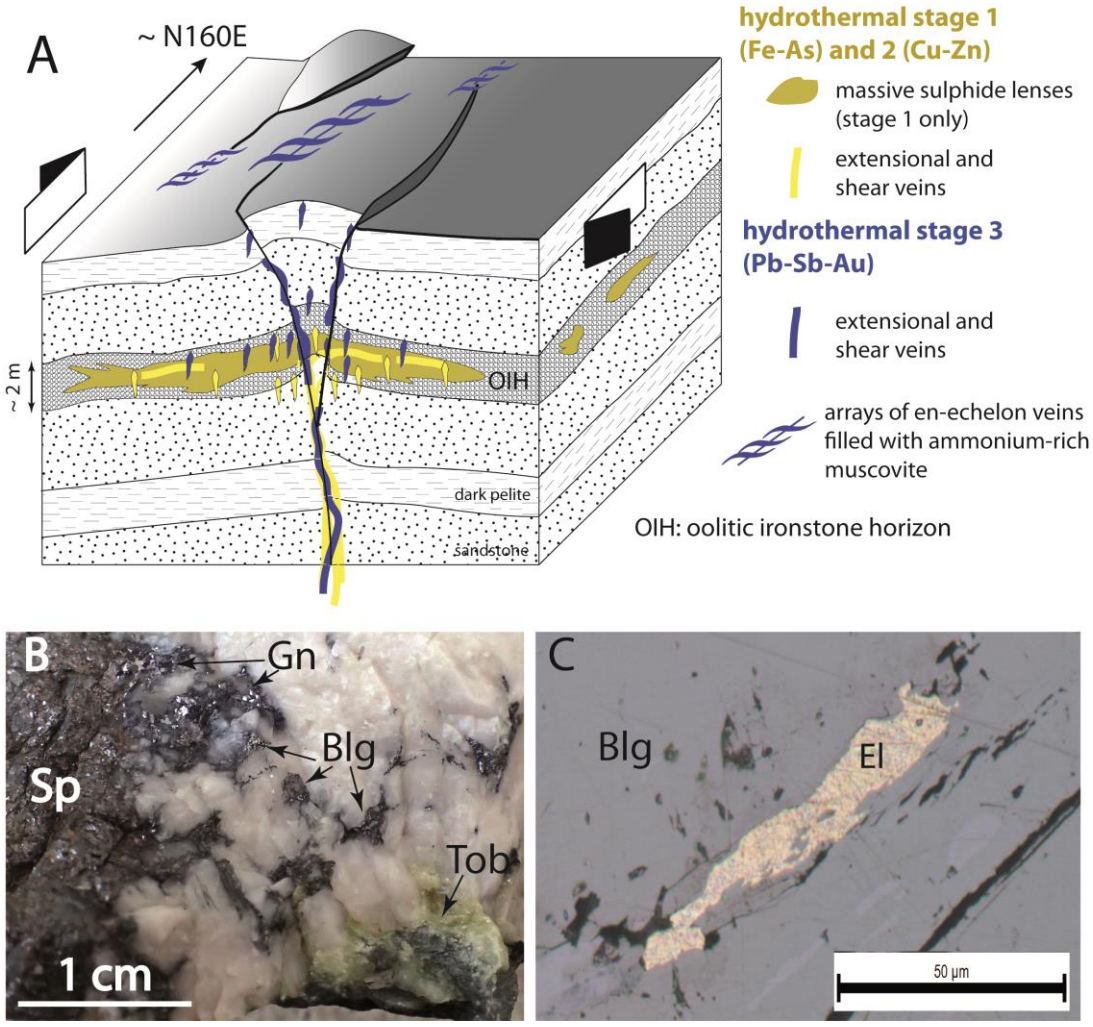

Figure 2 a Simplified and synthetic structural framework of the SADC mineralizing system. Second-order faults (e.g. Riedel shear) are not shown. All stages of hydrothermal fluid flows are channelized by vertical strike-slip faults. Some reverse component induces local flexure and associated interbedded slips in flower structures. Intersection of this fault system with OIH triggered the intense massive sulphidation of this reactive horizon. **b** Typical Pb-Sb-Au vein from SADC. Wall rocks (to the left) are rich in sphalerite (Sp) and galena (Gn) whereas vein centre (to the right) shows sulfosalts (here boulangerite, Blg) and tobelite (Tob) enclosed within a quartz gangue. **c** Polished thin section microphotograph (reflected polarized light) of boulangerite (Blg) and electrum (El) of the stage 3 assemblage at SADC.

En-echelon veins arrays and polymetallic veins of stage 3 are often filled with peculiar mm to cm ammonium-rich white micas (tobelite and $NH4^+$-rich muscovite) (Figs. 2a, b). These tobelite occurrences are controlled by organic matter enclosed in OIH and in dark pelites beds, and are therefore clearly associated with antimony and gold deposition ; (iv) a late carbonate deposition (stage 4).

The hydrothermal plumbing system of the SADC is fully controlled by right-lateral wrenching accommodated by N160E-trending sub-vertical strike-slip faults with some reverse component (e.g. positive flower structure, Fig. 2a). In detail, deformation analysis of shear and extensional veins shows that successive increments of non-coaxial dextral shearing are recorded by the different veins orientation and their respective hydrothermal mineral fillings (i.e. stage 1, 2 or 3, Gloaguen et al. 2007). Based on this structural analysis and coupled with the regional strain restoration of Gumiaux et al. (2004), Gloaguen et al. (2007) suggested a long-time span for the SADC hydrothermal system: the massive sulphidation stage 1 might initiated around 340-330 Ma and the final Pb-Sb-Au stage 3 formed lately around 300 Ma, i.e. coeval with the "Or 300" event (see supra). More recently, based on their REE characteristics, Tartèse et al. (2015) described three generations of epitaxial xenotime overgrowths, found around detrital zircon grains within the OIH. Their growths are attributed to successive hydrothermal events. Their U-Pb systematics were disturbed by these successive events returning apparent ages between~420 and~330 Ma. The younger dates cluster around ~340–330 Ma was interpreted as coeval with stages 1 and 2.

3. $^{40}Ar/^{39}Ar$ and U-Pb Geochronology

3.1 Tobelite $^{40}Ar / ^{39}Ar$ dating

Tobelite generally occurs within sedimentary terrains rich in organic components where NH_4-mica formation is attributed to N liberation during the thermal decomposition of organic matter (Bentabol and Ruiz Cruz 2016 and reference therein). Tobelite occurs generally as very fine grains (<1mm) although in SADC it was found as exceptionally large crystals up to 1 cm. This exceptional size allows a crystallographic characterisation of the tobelite species (Mesto et al. 2012; Capitani et al. 2016). As they are only found in deposition stage 3 in association with gold and antimony (Fig. 2, Gloaguen et al. 2007), tobelite aggregates were selected for $^{40}Ar/^{39}Ar$ dating. They were carefully handpicked under a binocular microscope from the 0.25-1.0 mm fractions and analysed by step-heating with an $^{40}Ar/^{39}Ar$ CO_2 laser probe, following the analytical procedure described in Ruffet et al. (1991, 1995). Details on the method, calculation parameters and analytical data are given in the Supplementary Materials 1 (SM1).

Duplicated tobelite experiments yielded two distinct but coherent age spectra. First one displayed a perfect plateau age (ca. 98.3 % of $^{39}Ar_K$ released) at 358.8 ± 0.9 Ma (1σ) when duplicate experiments produced a saddle-shaped age spectrum (Fig. 3). This shape probably expresses the mixing of two tobelite components coming from a partial recrystallization (Cheilletz et al. 1999; Alexandrov et al. 2002; Castonguay et al. 2007; Tartèse et al. 2011; Tremblay et al. 2011) of a primary tobelite during a subsequent disturbing event. According to interpretation proposed by Alexandrov et al. (2002), saddle sidewalls apparent ages yield a minimum estimate of the primary component age, in this case at least ca. 357.6 ± 1.5 Ma according to low to intermediate temperature steps. This age is perfectly coherent with plateau age previously obtained and suggests that part of the primary tobelite was preserved during recrystallization event and its radiogenic signal is fully isolated during degassing. However, this may not be the case with the component that crystallized during the disturbing event. Referring back to the model proposed by Alexandrov et al. (2002) and according to the degree of separation achieved during degassing experiment, the apparent age of the base of the saddle (ca. 340 Ma in the present case) yields a maximum age estimate of the secondary component, more or less close to the age of the subsequent disturbing event.

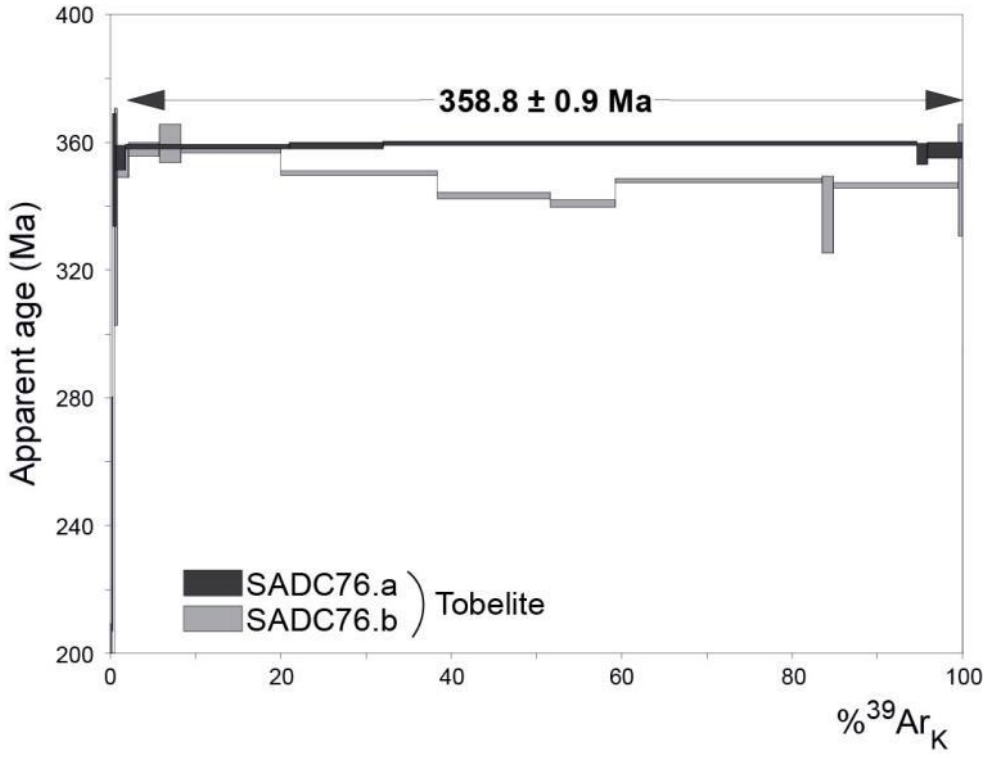

Figure 3 Single grain ^{40}Ar / ^{39}Ar datation of SADC tobelite from vein of the hydrothermal stage 3 (Pb-Sb-Au). The age error bars for each temperature steps and plateau age are given at the 1σ level.

These two results suggest that tobelite would have initially crystallized at or slightly before ca. 359 Ma which would be a minimum age estimate of the hydrothermal fluid flow responsible for the deposition of gold and antimony. These two results also suggest that tobelite partly

recrystallized during a subsequent hydrothermal and probably heterogeneous fluid pulse occurring after ca. 340 Ma

3.2 Apatite U-Pb dating

Four generations of fluorapatite (hereafter named I to IV from older to younger, Möelo et al. 2008) have been described in the paragenetic sequence of Saint-Aubin-des-Châteaux mineralization: (1) the fluorapatite I results of recrystallization process during a diagenetic/metamorphic event, (2) the fluorapatite II crystallized during the massive sulphidation of OIH (stage 2), (3) the fluorapatite III and IV postdate this main sulphidation stage within OIH and crystallized in lower temperature conditions (Moëlo et al. 2008). Furthermore, no mineralogical nor textural relationships allow establishing the precise timing of these last apatite generations with respect to the Pb-Sb-Au stage 3. LA-ICP-MS U-Pb analytical procedure followed the method described in Pochon et al. (2016b). Details and standards analyses are given in Supplementary Material 2 (SM2). All errors are provided at 2σ level.

Attempts to date the first three generations of apatite were unsuccessful because of the absence (or quasi absence) of radiogenic lead. Therefore, only the large fluorapatite IV crystal (Fig. 4a) studied by Moëlo et al. (2008) returned meaningful data. Plotted in a Tera-Wasserburg diagram (Fig. 4b), all data are discordant to very discordant.

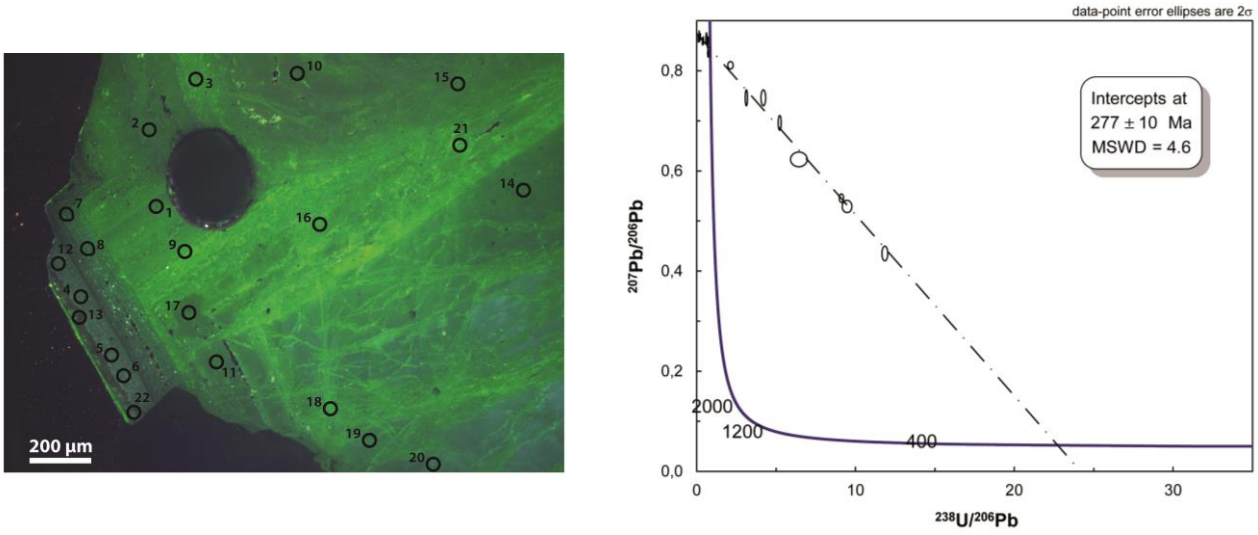

Figure 4 a CL image of a large fluoroapatite IV crystal from SADC(cold cathode type CITL Mk5, 15 kV, 500 µA, defocalized beam of 4 mm diameter, 20° incidence angle, Mons Polytechnique University, Belgium). The black circle is cylindrical hollow formed by laser ablation performed in Moëlo et al. (2008). The growth banding is due to Sr (green) ↔ Ca (blue) substitution. Labelled laser spots correspond to U-Pb analyses reported in SM2 (analysis 23 is outside the photo framework). **b** Tera-Wasserburg diagram and intercept age obtained on fluorapatite IV from SADC.

A first group of analyses corresponding to the inner parts of the crystal returned data that are almost radiogenic Pb free. Analyses performed on the outer rims of the crystal (Fig. 4a and b) yielded less discordant data allowing to draw a discordia which returns a lower intercept date of 277 ± 10 Ma

(MSWD=4.6) and an initial $^{207}Pb/^{206}Pb$ value of ca. 0.86 compatible with the common Pb value given by the Stacey and Kramers (1975) Pb evolution model. Therefore, growth banding of apatite IV within the OIH recorded a Lower Permian event. These data also show that uranium was available in the fluids only during the Lower Permian. Another explanation could be that all the available uranium was captured by xenotime and/or pretulite during the older fluid flow events.

4. Discussion

4.1 Timing of Sb-Au deposition in the Central Armorican Domain

The oldest ^{40}Ar / ^{39}Ar plateau date at *ca.* 360 Ma (Fig. 3) is interpreted as the crystallization age of tobelite. Because tobelite growth is contemporaneous with the deposition of Sb-sulfosalts and gold (Fig. 2, Gloaguen et al. 2007), this age is also that of the Pb-Sb-Au mineralizing event (stage 3). The oldest apparent age around 358 Ma of the disturbed saddle-shaped spectrum in Figure 3, also strengthens this interpretation. As, the Pb-Sb-Au hydrothermal stage is unequivocally the last metal bearing mineralizing event at SADC (Gloaguen et al. 2007), the massive sulphidation and base-metal stages (1 and 2) are probably Devonian in age. This result is inconsistent with the younger ages and the long mineralizing time span proposed by Gloaguen et al. (2007) who based their model on the deformation analysis of extensional and shear veins coupled with geostatistical restoration of deformation at the CAD scale. We suggest that some component of rigid rotation and flexural slip folding due to bulk regional dextral simple shear in CAD, might be responsible for re-orientation of extensional and shear veins, therefore introducing bias in their structural analysis. Moreover, stress refraction, commonly observed between stiff sandstone and less competent dark pelite beds at SADC, might also disturb finite strain analysis only based on brittle structures. This result, coupled with the Early Carboniferous ages recently obtained for the Le Semnon Sb-Au mineralization (Fig. 1, Pochon et al. in prep), clearly argues for a regional Sb-Au mineralizing event at the beginning of the Carboniferous in the CAD. This also suggests that other undated Sb-Au deposits from the CAD (e.g. the world-class La Lucette deposit) might have been formed around ca. 360 Ma. Consequently, in the CAD, most of Sb-Au mineralization are not related to the Late Carboniferous hydrothermal mineralizing event known as “Or 300 Ma”, identified in the Variscan southernmost internal zones and especially in the French Massif Central (Bouchot et al. 2005).

4.2 Depth and tectono-magmatic framework of Sb-Au deposition in the Central Armorican Domain

At the beginning of carboniferous times, the sedimentary thickness overlying the SADC Sb-Au active hydrothermal system did not exceed ca. 2800 meters (i.e. around 72 MPa without a potential free water column, cf. Pochon et al. in prep for detailed estimation). This strong constrain

induces a shallow formation depth for this Sb-Au rich hydrothermal systems which consequently involved channelized hot advective upward fluid flows along active fractures. At 360 Ma, with the exception of the CAD, an unthicken incipient fold belt subjected to the initiation of a regional-scale simple shear was present (Choukroune et al. 1983, Gumiaux et al. 2004). Our results demonstrate that most of the N160E-trending strike-slip faults of the CAD (Fig. 1) and associated flower structures (e.g. at SADC, Fig. 2a) were already active at the beginning of the Carboniferous and drained mineralizing fluids in thermal disequilibrum with the Paleozoic hosting sediments. At a larger scale, this incipient CAD fold belt was at ca. 360 Ma, in supra-continental subduction context as demonstrated by the Early Carboniferous ages of high-pressure/low-temperature metamorphism peak recorded in the South Armorican Variscan internal domain (Bosse et al. 2000, 2005; Ballèvre et al. 2014). In detail, this period corresponds to a plate dynamic shift from Gondwana-Armorica continental subduction to a collision with subsequent Middle-Late Carboniferous nappe stacking and exhumation in internal domains. This tectonic shift coincides with the large-scale mafic magmatism spreading over the Central and North Armorican external domains (Fig. 1a, Pochon et al. 2016b). Plate-scale boundary conditions are not clearly established yet, but the coeval occurrence of a HP-LT metamorphic event that produced eclogites in the internal part of the belt, south of the suture zone, and the widespread development of a mafic magmatism in the upper plate is rather remarkable. Furthermore, the Devonian-Carboniferous transition in the CAD is marked by a switch from a rather regional-scale marine sedimentation to a more localised and continental one in the Carboniferous (e.g. Chateaulin and Laval basins, Gumiaux et al. 2004). This means that a convergence-induced emersion occurred in the CAD in early Carboniferous times.

A most consistent hypothesis is therefore a slab rollback and/or breakoff coupled with a hot astenospheric upwelling below the upper plate. Such a process might have had two coeval effects: (1) local extension on top of the subducting margin to the south, allowing for the exhumation of the eclogitic units after 360 Ma (Bosse et al. 2000, 2005) and (2) intrusion and emplacement of hot mafic magmas inside the cold upper crust probably induced a thermal event at *c.* 360 Ma at the external domain scale and especially within the CAD (e.g. the dolerite dyke swarms outcropping close to the Le Semnon Sb-Au deposit, Fig. 1a).

This Early Carboniferous metallogenic event, mainly underline by volcanogenic massive sulphides located in Carboniferous basins, was well identified at the scale of the Variscan belt (e.g. Lescuyer et al., 1998) but these authors did not apprehend the extension of the phenomenon (outside basins) nor its direct link with a mantle magmatism responsible for a strong thermal anomaly as demonstrated by studies of Pochon et al. (2016a, 2016b, in press and in prep). Based on these recent works, we propose that this thermal event, induced by mafic magmatism, is responsible

for triggering highly advective mineralizing fluid flows in the CAD upper crust. These fluids were then channelized along vertical high-permeability zones as the SADC faults and flower structures (Fig. 2a) active at ca. 360 Ma.

4.3 A long-lived hydrothermalism during Carboniferous and Lower Permian

Gloaguen et al. (2007) pointed out that the Oolithic Ironstone Horizons (OIH) hosted within the "Grès Armorican" formation reacted as a chemical and physical "sponge" to external fluid flows (e.g. the epigenetic massive sulphidation, Fig. 2a). Owing to the high initial content in P and REE coupled with a high porosity, the different phosphate generations encountered within OIH might have recorded successive hydrothermal fluid flows. Indeed, Tartèse et al. (2015) have shown that the U-Pb system of xenotime from the OIH at Saint-Aubin-des-Châteaux were disturbed by one or several disturbing hydrothermal event, one of them occurring around of 340-330 Ma. Our U-Pb data on the fluoroapatite IV from the OIH (Fig. 4) attest that Early Permian fluid flows (ca. 280 Ma) were responsible the growth of a new generation of apatite. This hydrothermal Lower Permian event is well documented elsewhere in the Armorican Massif (see Ballouard et al. 2017, in press). Moreover, the saddle-shape ^{40}Ar / ^{39}Ar spectrum of tobelite (Fig. 3) together with the illite ^{40}Ar / ^{39}Ar spectra from the Le Semnon Sb-Au deposit (Pochon et al. in prep), also indicate a partially re-equilibration of the isotopic system after 360 Ma. Consequently, we infer that after the Sb-Au mineralization event around 360 Ma, several hydrothermal pulses affected the CAD during the Carboniferous and the Early Permian. During those successive hydrothermal events, metal-rich fluids did not appear to be trapped, at least in the south-eastern part of the CAD.

5. Conclusions

New ^{40}Ar / ^{39}Ar and U-Pb absolute dating of tobelite and apatite from the Saint-Aubin-des-Châteaux base metal-Sb-Au occurrence allow to discuss several points: (i) the Sb-Au deposition is Early Carboniferous in age. Coupled with recent results obtained on the Le Semnon northernmost Sb-Au district, an Early Carboniferous economic Sb-Au mineralizing peak is identified in the southeastern part of the Central Armorican Domain. There is consequently no relationship between this Early Carboniferous Sb-Au mineralization event and the Late Carboniferous mineralising events recognized over most of the Variscan orogen; (ii) that mineralizing hydrothermal event coincides with a widespread mafic magmatism which appears to be a major trigger for the mineralising systems and acted as a major driving force for hot advective fluid flows in shallow depths (less than 3 km). This Early Carboniferous mafic magmatism has to be (re-) considered in mineralising system genesis studies within the Variscan belt; (iii) The N160°E-trending fracturation affecting the whole Central Armorican domain is active at 360 Ma. This implies further structural studies (e.g. heritage, relation with folding) and especially in term of magma and fluid plumbing

systems; (iv) finally, phosphates generations from the oolitic ironstone horizons intercalated within Ordovician sandstones allow establishing a long-lived Carboniferous-Early Permian history of this Central Armorican Domain while southward internal zones thickened and melted

Acknowledgements

We are very grateful to Yves Moëlo who provided us the "historical" polished section of apatite grains from the Saint-Aubin-des-Châteaux deposit. We also thank Sylvain Janiec and Xavier Le Coz for thin section preparation. F. Grasset and C. Friot from the HERVE SA group have greatly facilitated access to the Saint-Aubin-Des-Châteaux quarries. This study has been granted by INSU through the CESSUR Project 2016, the BRGM and the Région Bretagne.

References

Alexandrov P, Ruffet G, Cheilletz A (2002) Muscovite recrystallization and saddle-shaped $^{40}Ar/^{39}Ar$ age spectra: Example from the Blond granite (Massif Central, France).Geochim Cosmochim Ac 66:1793–1807.

Ballèvre M, Catalán JRM, López-Carmona A, Pitra P, Abati J, Fernández RD, Ducassou C, Arenas R, Bosse V, Castiñeiras P, Fernández-Suárez J, Barreiro JG, Paquette JL, Peucat JJ, Poujol M, Ruffet G, Sánchez Martínez S (2014) Correlation of the nappe stack in the Ibero-Armorican arc across the Bay of Biscay: a joint French–Spanish project. Geol Soc Spec Publ 405:77–113.

Bentabol M, Cruz MDR (2016) Characterization of Tobelite Formed from Kaolinite under Hydrothermal Conditions (200 °C). Appl Clay Sci 126:160–172.

Bosse V, Féraud G, Ruffet G, Ballèvre M, Peucat J-J, De Jong K (2000) Late Devonian subduction and early-orogenic exhumation of eclogite-facies rocks from the Champtoceaux Complex (Variscan belt, France). Geological Journal 35:297–325.

Bosse V, Féraud G, Ballèvre M, Peucat J-J, Corsini M (2005) Rb–Sr and 40Ar/39Ar ages in blueschists from the Ile de Groix (Armorican Massif, France): Implications for closure mechanisms in isotopic systems. Chem Geol 220:21–45.

Bouchot V, Ledru P, Lerouge C, Lescuyer JL, Milesi JP (2005) 5: Late Variscan mineralizing systems related to orogenic processes: The French Massif Central. Ore Geol Rev 27:169–197.

Capitani GC, Schingaro E, Lacalamita M, Mesto E, Scordari F (2016) Structural anomalies in tobelite-2M2 explained by high resolution and analytical electron microscopy. Mineral Mag 80:143–156.

Castonguay S, Ruffet G, Tremblay A (2007) Dating polyphase deformation across low-grade metamorphic belts: An example based on $^{40}Ar/^{39}Ar$ muscovite age constraints from the southern Quebec Appalachians, Canada. Geol Soc Am Bull 119:978–992.

Chauris L, Marcoux E (1994) Metallogeny of the Armorican Massif. In: Chantraine J, Rolet J, Santallier DS, et al. (eds) Pre-Mesozoic Geology in France and Related Areas. Springer Berlin Heidelberg, pp 243–264.

Chauvel JJ (1974) Les minerais de fer de l'Ordovicien inférieur du bassin de Bretagne-Anjou, France. Sedimentology 21:127–147.

Cheilletz A, Ruffet G, Marignac C, Kolli O, Gasquet D, Féraud G, Bouillin JP (1999) $^{40}Ar/^{39}Ar$ dating of shear zones in the Variscan basement of Greater Kabilia (Algeria). Evidence of an Eo-Alpine event at 128 Ma (Hauterivian-Barremian boundary): Geodynamic consequences. Tectonophysics 306:97–116.

Choukroune P, Lopez-Munoz M, Ouali J (1983) Cisaillement ductile sud-armoricain et déformations discontinues associées: mise en évidence de la déformation régionale non coaxiale dextre. C R Acad Sci Paris 296:657–660.

Costa S, Rey P (1995) Lower crustal rejuvenation and growth during post-thickening collapse: insights from a crustal cross section through a Variscan core complex. Geology 23:905–908.

Frost RL, López A, Belotti FM, Xi Y, Scholz R (2014) A Vibrational Spectroscopic Study of the Phosphate Mineral Lulzacite $Sr_2Fe^{2+}(Fe^{2+},Mg)_2Al_4(PO_4)_4(OH)_{10}$. Spectrochim Acta A 127:243–247.

Gapais D, Le Corre C (1980) Is the Hercynian belt of Brittany a major shear zone. Nature 288:574–576.

Gloaguen E, Branquet Y, Boulvais P, Moelo Y, Chauvel J-J, Chiappero P-J, Marcoux E (2007) Palaeozoic oolitic ironstone of the French Armorican Massif: a chemical and structural trap for orogenic base metal–As–Sb–Au mineralization during Hercynian strike-slip deformation. Miner Deposita 42:399–422.

Gumiaux C, Gapais D, Brun JP, Chantraine J, Ruffet G (2004) Tectonic history of the Hercynian Armorican Shear belt (Brittany, France). Geodin Acta 17:289–307.

Le Corre C (1978) Approche quantitative des processus synschisteux. L'exemple du segment Hercynien de Bretagne Centrale. Unpubl. doctoral dissertation, Université de Rennes 1, Rennes, 382 pp.

Léone P, Palvadeau P, Moëlo Y (2000) Structure cristalline d'un nouveau phosphate de strontium naturel (lulzacite), $Sr_2Fe^{2+}(Fe^{2+},Mg)_2Al_4(PO_4)_4(OH)_{10}$. C R Acad Sci Paris, IIc, 3:301–308.

Mesto E, Scordari F, Lacalamita M, Schingaro E (2012) Tobelite and NH^{4+}-rich muscovite single crystals from Ordovician Armorican sandstones (Brittany, France): structure and crystal chemistry. Am Mineral 97:1460–1468.

Moëlo Y, Lasnier B, Palvadeau P, Léone P, Fontan F (2000) La Lulzacite, $Sr_2Fe^{2+}(Fe^{2+},Mg)_2Al_4(PO_4)_4(OH)_{10}$, un nouveau phosphate de strontium (Saint-Aubin-Des-Chateâux, Loire-Atlantique, France). C R Acad Sci Paris 330:314–324.

Moëlo Y, Lulzac Y, Rouer O, Palvadeau P, Gloaguen E, Léone P (2002) Scandium mineralogy: pretulite with scandian zircon and xenotime-(Y) within an apatite-rich oolitic ironstone from Saint-Aubin-Des-Châteaux, Armorican Massif, France. Can Miner 40:1657–1673.

Moëlo Y, Rouer O, Bouhnik-Le Coz M, (2008) From diagenesis to hydrothermal recrystallisation: polygenic Sr-rich fluorapatite from the oolitic ironstone of Saint-Aubin-des-Châteaux (Armorican Massif, France). Eur J Mineral 20:205–216.

Pochon A, Gapais D, Gloaguen E, Gumiaux C, Branquet Y, Cagnard F, Martelet G (2016a) Antimony deposits in the Variscan Armorican belt, a link with mafic intrusives? Terra Nova 28:138–145.

Pochon A, Poujol M, Gloaguen E, Branquet Y, Cagnard F, Gumiaux C, Gapais D (2016b) U-Pb LA-ICP-MS dating of apatite in mafic rocks: Evidence for a major magmatic event at the Devonian-Carboniferous boundary in the Armorican Massif (France). Am Mineral 101:2430–2442.

Pochon A, Beaudoin G, Branquet Y, Boulvais P, Gloaguen E, Gapais D (in press) Metal mobility during hydrothermal breakdown of Fe-Ti oxides: insights from Sb-Au mineralizing event (Variscan Armorican Massif, France). Ore Geol Rev, doi: 10.1016/j.oregeorev.2017.10.021.

Ruffet G, Féraud G, Amouric M (1991) Comparison of $^{40}Ar/^{39}Ar$ conventional and laser dating of biotites from the North Tregor batholith. Geochim Cosmochim Ac 55:1675–1688.

Ruffet G, Féraud G, Ballèvre M, Kiénast JR (1995) Plateau ages and excess argon in phengites: A ^{40}Ar-^{39}Ar laser probe study of Alpine micas (Sesia Zone, Western Alps, northern Italy). Chem Geol (Isotopic Geoscience Section) 121:327–343.

Tartèse R, Ruffet G, Poujol M, Boulvais P, Ireland TR (2011) Simultaneous resetting of the muscovite K-Ar and monazite U-Pb geochronometers: a story of fluids. Terra Nova 23:390–398.

Tartèse R, Poujol M, Gloaguen E, Boulvais P, Drost K, Košler J, Ntaflos T (2015) Hydrothermal activity during tectonic building of the Variscan orogen recorded by U-Pb systematics of xenotime in the GrèsArmoricain formation, Massif Armoricain, France. Miner Petrol 109:485–500.

Tremblay A, Ruffet G, Bédard JH (2011) Obduction of Tethyan-type ophiolites—A case-study from the Thetford-Mines ophiolitic Complex, Quebec Appalachians, Canada. Lithos 125:10–26.

Vernhet Y, Plaine J, Trautmann F, Pivette B (2009) Geological map of France (1/50000), notice of the Cossé-le-Vivien sheet (355), BRGM, Orléans, France, 222 pp.

2. Datation de l'indice aurifère de Beslé : témoin de circulation de fluides localisée le long de la branche Nord du CSA

L'indice aurifère de Beslé appartient à un axe aurifère discontinu sur plus de 100 km de longueur (appelé parfois l'axe de Beslé-Behelec) localisé le long de la branche Nord du CSA. Ces indices ont été exploités à l'époque gallo-romaine et ont fait l'objet de quelques travaux par le BRGM pendant l'Inventaire Minier du début des années 80. Cet indice est constitué d'un stockwerk de veines de quartz minéralisées encaissé dans des schistes ardoisiers (Kerforne 1910, 1921). La paragenèse est constituée d'un stade 1 à pyrite-arsénopyrite-pyrrhotite et d'un stade 2 à chalcopyrite-sphalérite±galène-or±stibine (Bouchot et al. 1997). Très peu de données structurales ont été acquises, ainsi les contrôles de ces minéralisations restent mal contraints. Malheureusement, nous n'avons pas pu établir de contrôles structuraux, en raison d'un manque d'affleurement notable dans le secteur. Cependant, nous avons pu effectuer une analyse géochronologique sur un échantillon de quartz aurifère contenant des muscovites aux épontes. Cet échantillon provient de la collection du Professeur Kerforne conservée au musée de Géosciences Rennes. Il a été prélevé au sein du puits de la Grenouillère et contient environ 8.5 ppm d'or (Kerforne 1921).

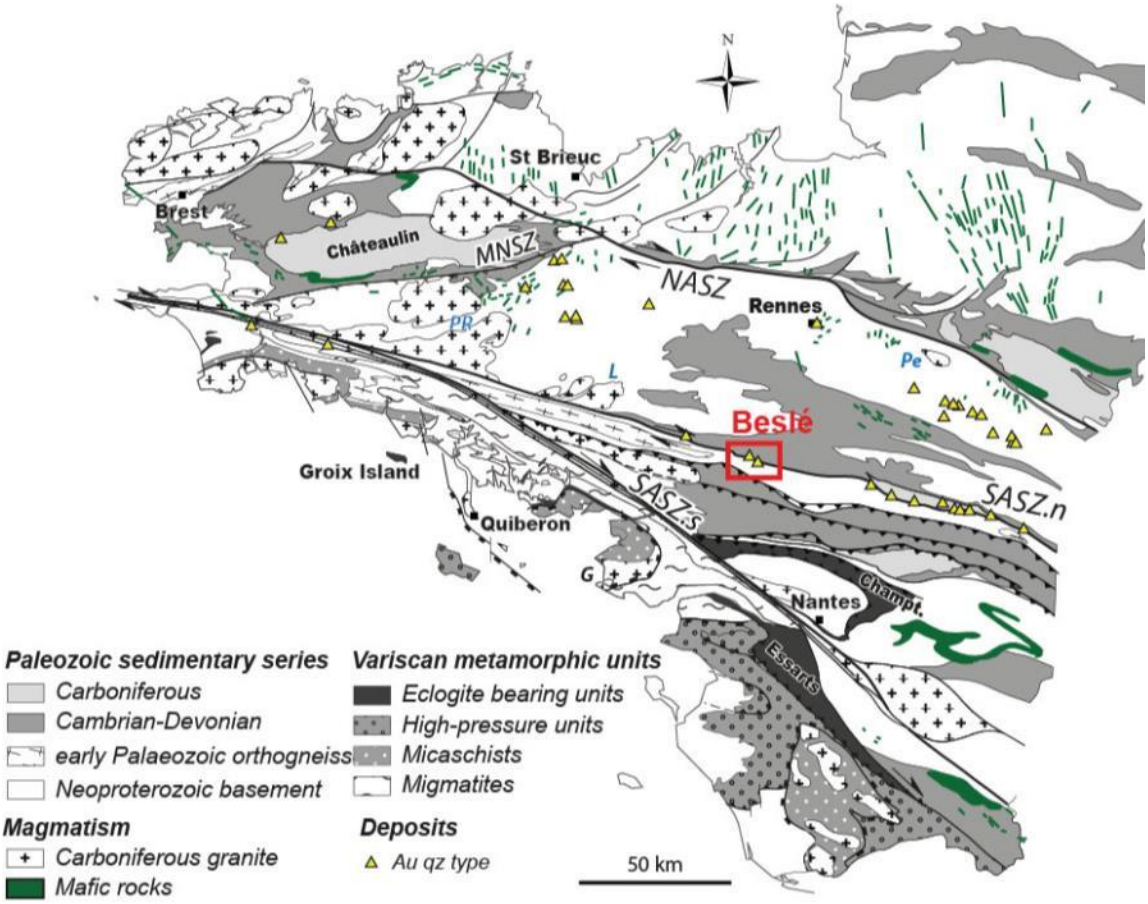

Figure 5.1 Carte géologique simplifiée du Massif Armoricain représentant la localisation de l'indice aurifère de Beslé

La minéralisation est encaissée au sein de schistes Ordovicien inférieur (i.e. la formation des « Schistes de Traveusot »). Elle est constituée d'un réseau de veines de quartz de puissance décimétrique à métrique et semble associée au fonctionnement du CSA. En effet, les veines contiennent fréquemment des fragments d'encaissant (i.e. « fault-fill vein » ou « shear veins » en anglais). La minéralisation se compose principalement de pyrite, arsénopyrite, chalcopyrite, sphalérite, galène et or natif. Les épontes des veines sont principalement soulignées par une dissémination de pyrite et de muscovites verdâtres.

La datation ^{40}Ar / ^{39}Ar sur grains séparés de muscovite a été réalisée par Gilles Ruffet et les conditions analytiques utilisées pour la méthode ^{40}Ar / ^{39}Ar sur muscovite sont identiques à celles décrites par Ruffet et al. (1991, 1995) et à celles décrites au sein de l'article #4 et #5. Les résultats sont reportés dans la Table 5.1 et la Figure 5.2.

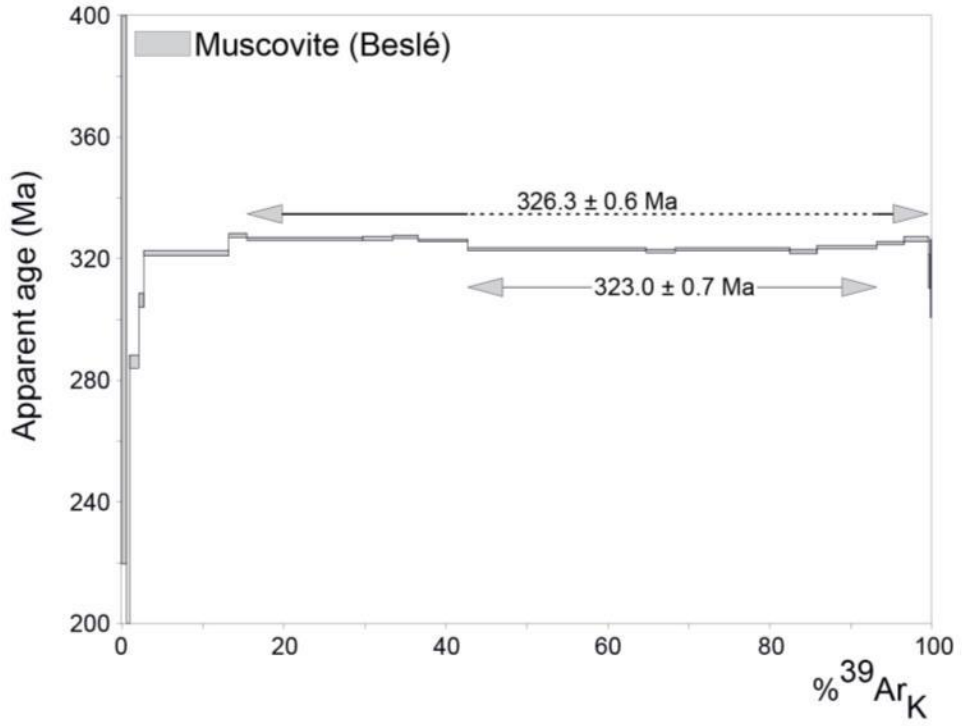

Figure 5.2 Spectre ^{40}Ar / ^{39}Ar d'un grain de muscovite provenant de l'éponte d'une veine de quartz aurifère de l'indice de Beslé

Le spectre de l'analyse de la muscovite de Beslé est caractérisé par une forme « en selle » et semble donc être légèrement perturbé (Fig. 5.2). En effet, ce type de spectre est considéré comme caractéristique d'événements perturbateurs ultérieurs affectant partiellement le chronomètre ^{40}Ar / ^{39}Ar du minéral. Par conséquent, la date pseudo-plateau de la forme « en selle » peut révéler l'âge maximum du dernier évènement perturbateur (Cheilletz et al. 1999; Alexandrov et al. 2002; Tremblay et al. 2011). Ce spectre est caractérisé par des domaines de basse et haute températures affichant un âge apparent identique à 326.3 ± 0.6 Ma et un domaine intermédiaire avec un âge apparent à 323.0 ± 0.7 Ma. L'âge le plus vieux est interprété comme l'âge minimum de

cristallisation de la muscovite alors que l'âge pseudo-plateau à 323.0 ± 0.7 Ma est interprété comme l'âge maximum de l'évènement de circulation de fluides perturbateurs. Cela indique donc que le grain de muscovite associé au quartz aurifère de Beslé a subi une réouverture partielle du système isotopique probablement. due à une circulation de fluides

En effet, cet indice aurifère est localisé sur la branche Nord du CSA, qui est connue pour être un drain crustal majeur responsable de la remontée de leucogranites tardi-varisques vers la surface (Tartèse et Boulvais 2010; Tartèse et al. 2011; Ballouard et al. 2017) et de circulations de fluides (Lemarchand et al. 2011; Tartèse et al. 2012). Ces leucogranites se mettent en place le long de la branche Nord du CSA aux alentours de 315 Ma : comme le granite de Lizio à 316 ± 6 Ma (Tartèse et al. 2011) et le complexe de Pontivy-Rostrenen à 316.7 ± 2.5 Ma (Ballouard et al. 2017). Le couplage entre l'étude de la déformation (i.e. mylonites) et les circulations de fluides associées ont révélé une circulation de fluides de longue durée et relativement continue sur une durée d'au moins 15 Ma (Tartèse et al. 2012) : depuis des évènements de haute température caractérisés par la mylonitisation (315 Ma) jusqu'à des évènements de plus basse température (cataclase et bréchification, 300 Ma). Cependant, les deux dates obtenues par analyse ^{40}Ar / ^{39}Ar sur la muscovite de Beslé (326.3 ± 0.6 Ma et 323.0 ± 0.7 Ma) montrent au moins deux évènements hydrothermaux plus vieux que la mise en place des granites. Bien qu'on ne soit pas certain que la muscovite soit réellement synchrone de l'or natif puisque la paragenèse est imprécise, il est raisonnable d'envisager que l'âge de la circulation de fluides responsables de la minéralisation aurifère soit aux alentours de 323 Ma. Ainsi, il apparait difficile de connecter cet indice à un évènement thermique associé à la mise en place des granites puisque la fusion partielle de la source de ces granites n'a pas encore eu lieu. Il est donc nécessaire de faire une caractérisation précise de l'évolution paragenétique et d'effectuer une série de datation de tous les indices aurifères localisés le long de la branche Nord du CSA afin de vérifier si l'évènement hydrothermal aurifère du CSA est unique et généralisé le long de cette structure majeure. De plus, l'âge le plus jeune (323.0 ± 0.7 Ma), interprété comme associé à l'évènement aurifère, révèle une fois de plus qu'il n'existe pas qu'un seul évènement hydrothermal à Sb-Au au sein du Massif Armoricain, et par conséquent sein de la chaîne varisque ouest-européenne.

Table 5.1 Muscovite $^{40}Ar/^{39}Ar$ analytical data

Laser power	$^{40}Ar_{Atm}$	Error ^{40}Ar	$^{39}Ar_K$	Error ^{39}Ar	^{38}Ar	Error ^{38}Ar	^{37}Ar	Error ^{37}Ar	^{36}Ar	Error ^{36}Ar	$^{40}Ar^*/^{39}ArK$	Error $^{40}Ar^*/^{39}ArK$	Apparent age (Ma)	Error Age (Ma)	Delay to irradiation (day)
SEMAP1															
260	74883.67	193.78	61.14	0.28	0.000001	0.021	0.000	0.030	256.251195	0.451101	19.61	7.47	336.5	116.9	124.17
280	496.18	0.25	25.17	0.04	0.006308	0.016	0.180	0.027	0.915768	0.013004	9.34	0.17	168.0	2.9	124.19
320	2712.42	2.94	114.73	0.13	0.000733	0.017	0.166	0.037	2.927905	0.042413	16.44	0.13	286.2	2.4	124.21
340	1230.59	0.65	52.60	0.14	0.000001	0.013	0.110	0.015	1.068651	0.022079	17.70	0.14	306.4	2.6	124.83
370	20722.56	6.15	967.73	0.62	0.001504	0.019	0.237	0.014	9.731191	0.061475	18.68	0.05	321.8	1.6	124.85
380	3993.77	1.97	204.99	0.18	0.000053	0.010	0.124	0.026	0.418074	0.014619	19.06	0.04	327.8	1.6	124.87
400	25199.17	8.42	1314.15	0.85	0.000001	0.010	0.304	0.032	1.598733	0.021101	18.99	0.03	326.6	1.5	124.89
410	6489.38	3.34	339.16	0.39	0.000001	0.017	0.076	0.026	0.355394	0.018040	18.99	0.04	326.7	1.6	124.93
425	5610.22	3.39	293.74	0.26	0.000001	0.018	0.022	0.017	0.249969	0.014010	19.01	0.04	327.1	1.6	124.95
450	10573.31	2.82	555.90	0.33	0.000001	0.012	0.066	0.031	0.452002	0.021858	18.95	0.03	326.0	1.5	124.96
480	38174.18	10.43	2026.94	1.03	0.000001	0.034	0.280	0.029	1.617167	0.038506	18.76	0.03	323.1	1.5	124.99
500	6465.71	2.91	341.41	0.32	0.000001	0.030	0.630	0.034	0.445075	0.023542	18.72	0.04	322.5	1.6	125.02
530	24366.23	22.96	1289.35	0.54	0.036937	0.019	0.832	0.038	1.325133	0.044034	18.76	0.03	323.1	1.6	125.04
550	6005.71	3.57	314.90	0.18	0.000001	0.013	0.647	0.024	0.567028	0.013438	18.71	0.03	322.3	1.5	125.06
600	12902.07	6.34	675.63	0.38	0.021098	0.020	0.699	0.032	1.047079	0.026651	18.81	0.03	323.9	1.5	125.08
670	5965.55	1.48	309.47	0.28	0.000001	0.021	0.170	0.030	0.582990	0.021239	18.89	0.04	325.2	1.6	125.12
800	5542.00	2.97	285.51	0.15	0.000001	0.023	0.153	0.033	0.597339	0.038969	18.97	0.05	326.4	1.7	125.14
1100	406.00	0.57	21.32	0.12	0.000001	0.019	0.162	0.026	0.067094	0.024132	18.30	0.35	315.8	5.7	125.16
Fusion	172.71	0.22	9.11	0.05	0.017575	0.017	0.077	0.028	0.030675	0.025191	18.15	0.81	313.4	12.9	125.18

J parameter	1.04E-02
error J	4.31E-05
Mass Discrimination (1+e)	1.009405
Err Discrimination	1.32E-03

Parameters

(36Ar/37Ar)Ca	0.000322	3	%	
(39Ar/37Ar)Ca	0.000788	4	%	
(38Ar/37Ar)Ca	0.000026	100	%	
(40Ar/37Ar)Ca	0.0006	100	%	
(40Ar/39Ar)K	0.00085	4	%	
(38A/39Ar)K	0.011	91	%	
(36Cli/38Cl)	316	5	%	[3]
(40Ar/36Ar)Atm	298.56	0.104	%	[1] and [1']
(38Ar/36Ar)Atm	0.1885	0.159	%	[1] and [1']
Lambda 40	5.53E-10	1.35E-12	y-1	[2]
Lambda 39	2.58E-03		y-1	
Lambda 37	1.98E-02		d-1	
Lambda 36Cl	2.26E-06		y-1	

[1] Lee, JY, Marti, K, Severinghaus, JP, Kawamura, K, Yoo, HS, Lee, JB, Kim, JS (2006). A redetermination of the isotopic abundances of atmospheric Ar. Geochimica Cosmochimica Acta, 70, 4507-4512.

[1'] Mark, DF, Stuart, FM, De Podesta, M (2011). New high-precision measurements of the isotopic composition of atmospheric argon. Geochimica Cosmochimica Acta, 75, 7494-7501.

[2] Renne, PR, Balco, G, Ludwig, RL, Mundil, R, Min, K, . (2011). Response to the comment by W.H. Schwarz et al. on "Joint determination of (40)K decay constants and (40)Ar*/(40)K for the Fish Canyon sanidine standard, and improved accuracy for (40)Ar/(39)Ar geochronology" by PR Renne et al. (2010). Geochimica Cosmochimica Acta, 75, 5097-5100.

[3] York, D, Personnal Communication - McMaster reactor

Regression method: York, D. (1969). Least-squares fitting of a straight line with correlated errors. Earth Planet. Sci. Lett. 5, 320-4.

Ages and errors of Hb3gr and TCs monitors refers to: Rennes, PR, Balco, G, Ludwig, Mundil, R, Min, K, . (2011). Response to the comment by W.H. Schwarz et al. on "Joint determination of (40)K decay constants and (40)Ar*/(40)K for the Fish Canyon sanidine standard, and improved accuracy for (40)Ar/(39)Ar geochronology" by PR Renne et al. (2010). Geochimica Cosmochimica Acta, 75, 5097-5100.

3. Apport des signatures isotopiques Sr-Nd sur la source du magmatisme mafique

Afin de proposer un modèle à grande échelle et de contraindre l'origine du magmatisme mafique à 360 Ma, des données complémentaires en isotopes radiogéniques Rb-Sr et Sm-Nd ont été effectuées sur plusieurs échantillons de dolérites localisés au sein des domaines Nord (DNA) et Centre (DCA) Armoricain : réseaux de dykes de Martigné-Ferchaud (dont fait partie le gisement du Semnon), de la Mancellia, de Saint-Malo, de Louvigné-de-Bais et les sills du Bassin de Laval (voir la Figure 5.3 pour la localisation).

Les analyses Sr-Nd ont été déterminées sur des échantillons de roches totales à Géosciences Rennes par spectromètre de masse multi-collecteur (Finnigan MAT-262). Les conditions analytiques sont identiques à celle décrites dans Ballouard et al. (2015). Le rapport initial $^{87}Sr/^{86}Sr$ et les valeurs en εNd (T) ont été recalculés pour un âge de 360 Ma pour être en cohérence avec l'âge du magmatisme mafique. Les résultats sont présentés dans la Table 5.2 et la Figure 5.4.

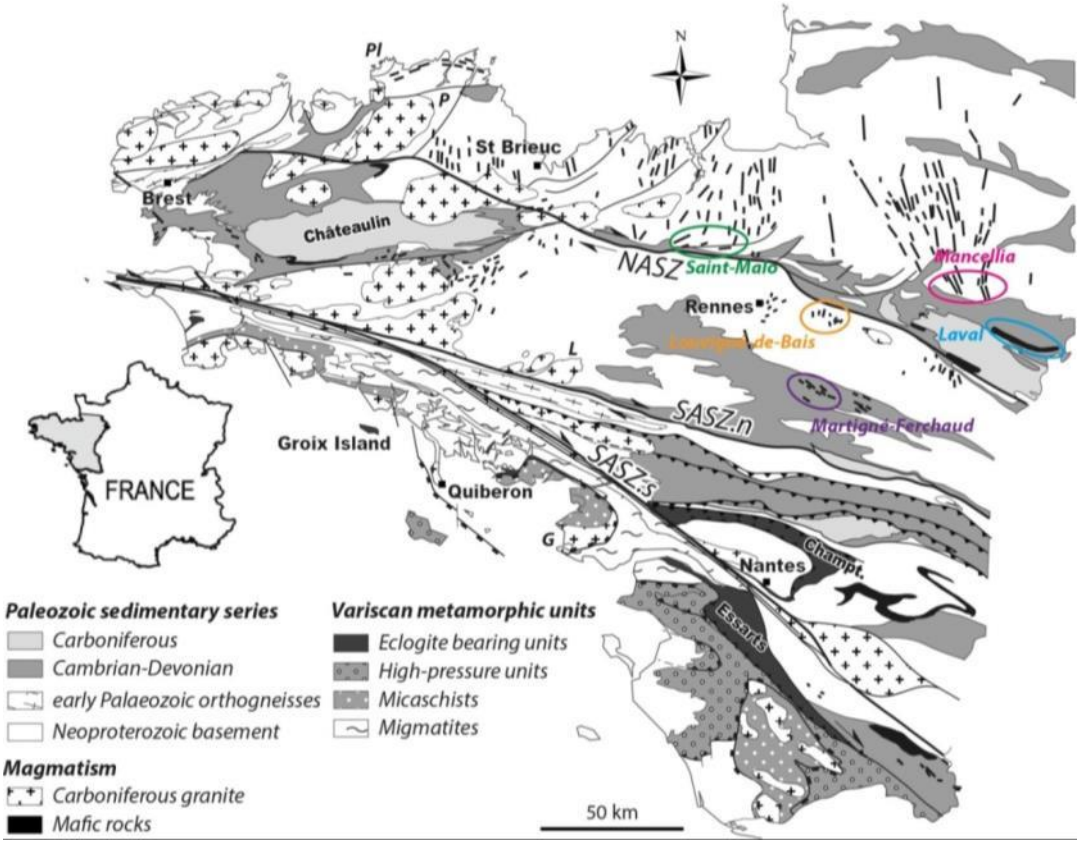

Figure 5.3 Carte géologique simplifiée du Massif Armoricain représentant la localisation des réseaux de dykes échantillonnés des domaines Nord et Centre Armoricain.

Les valeurs en εNd (T) montrent des valeurs relativement homogènes comprises entre 2.7 à 6.4, indépendamment de leur distribution géographique, hormis pour deux échantillons de l'essaim de dykes de la Mancellia (DNA) et de Louvigné-de-Bais (DCA). Alors que la majorité des échantillons

analysés montrent une contribution mantellique relativement appauvri, les deux échantillons (MGX1 et LDB15) ont probablement acquis une contribution crustale dans leur signature isotopique lors de leur mise en place.

Comparativement aux valeurs en εNd (T), les valeurs en $^{87}Sr/^{86}Sr$ sont extrêmement variables et comprises entre 0.7029 et 0.7126. Cette dichotomie entre des valeurs très variables en $^{87}Sr/^{86}Sr$ et des valeurs homogènes en εNd suggère une altération par des fluides plutôt qu'une interaction avec l'encaissant. En effet, s'il s'agissait d'une interaction avec un encaissant quelconque, les dolérites montrerait une signature crustale plus variable en εNd et corrélée avec les valeurs en $^{87}Sr/^{86}Sr$ en fonction des roches rencontrés (e.g. sédiments, granites) or ce n'est pas le cas ici, seul le rapport en $^{87}Sr/^{86}Sr$ est affecté. Le Nd étant très peu soluble au sein d'une solution, à l'inverse du Sr qui lui est très soluble, l'hypothèse d'une altération par des fluides semblent cohérentes.

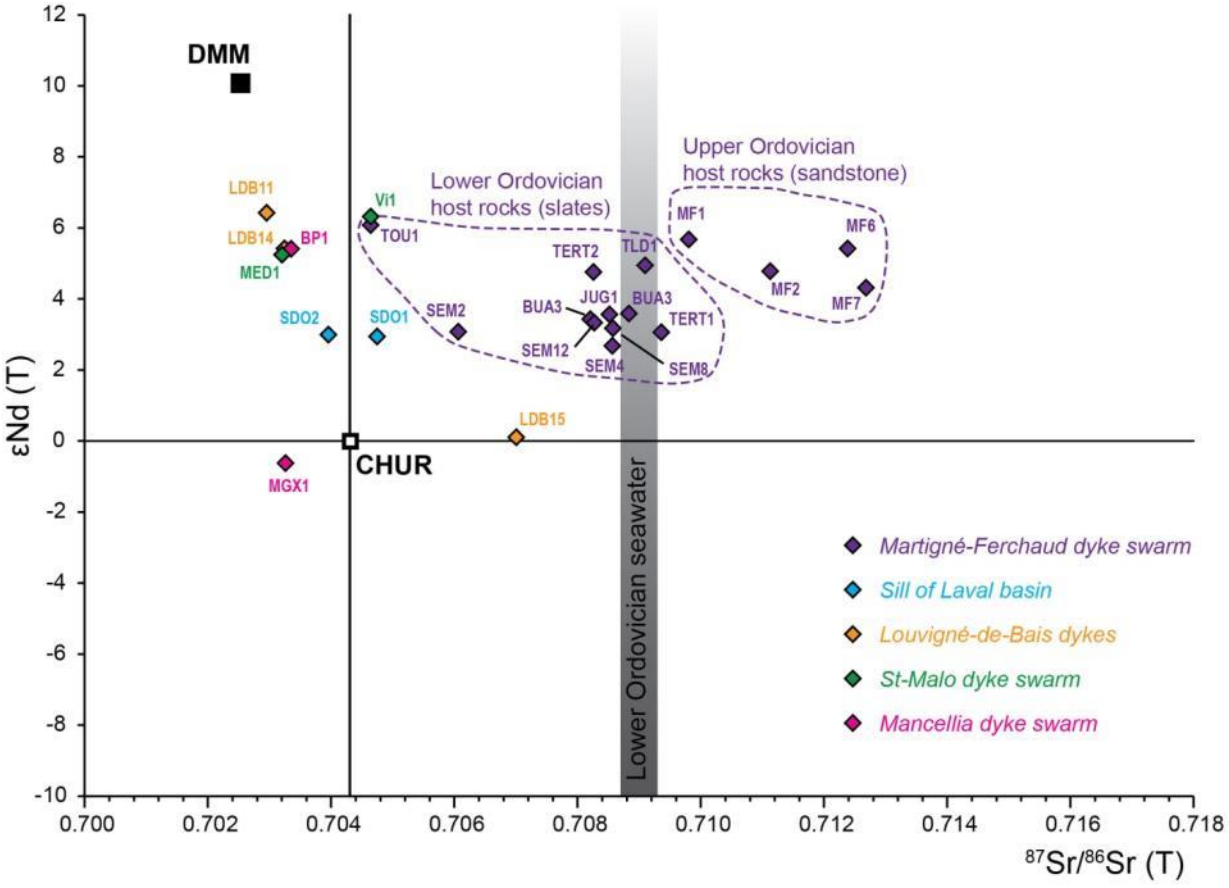

Figure 5.4 Compositions isotopiques en Sr et Nd des dykes de dolérite des domaines Nord et Centre Armoricain. Les valeurs en εNd (T) et en $^{87}Sr/^{86}Sr$ sont calculés pour un âge de 360 Ma, excepté la gamme de valeurs en $^{87}Sr/^{86}Sr$ de l'eau de mer ordovicienne inférieure.

Plus de la moitié des échantillons analysés du réseau de dykes de Martigné-Ferchaud forment un cluster proche de la composition isotopique en $^{87}Sr/^{86}Sr$ de l'eau de mer à l'Ordovicien inférieur. Cela indique qu'ils ont acquis une signature plus ou moins prononcé d'une eau de mer plus vieille d'environ 100 Ma. Parce que ces dykes sont majoritairement encaissés au sein des

schistes d'Angers-Traveusot (Ordovicien inférieur), il est donc possible d'envisager une altération de ces dykes par des fluides ayant acquis une signature isotopique en $^{87}Sr/^{86}Sr$ proche de celle de l'eau de mer ordovicienne par interactions fluides-dolérites-schistes. La signature plus ou moins forte au sein des dykes d'un même faisceau reflète probablement une variabilité des rapports fluide-roche lors de l'interaction. Par exemple, l'échantillon TOU1, qui représente l'un des dykes les moins altérés du secteur, montre la plus faible contribution hydrothermale en $^{87}Sr/^{86}Sr$. La Figure 5.4 nous révèle également que 4 échantillons de dykes du faisceau du Semnon ont un rapport $^{87}Sr/^{86}Sr$ plus élevé que tous les autres, appartenant au même faisceau. Comparativement aux autres dykes, ces échantillons sont encaissés au sein de la formation marine et gréseuse du Châtellier (Ordovicien supérieur), pourtant leurs signatures diffèrent de la composition isotopique de l'eau de mer ordovicienne supérieure (< 0.708). Cela suggère que les fluides qui ont interagi avec les dykes proviennent soit d'autre réservoir inconnu ou soit qu'ils ont acquis la signature d'un réservoir inconnu.

Pour résumer, nous avons donc un magmatisme mafique avec des valeurs en εNd typique de magmas provenant du manteau sans contribution crustale majeure. Cependant la signature isotopique en $^{87}Sr/^{86}Sr$ n'indique aucune informations quant à la source de ces magmas mais révèlent plutôt une altération par des fluides hydrothermaux.

Table 5.2 Rb–Sr and Sm–Nd whole-rock data for the dolerite dykes. Rb concentrations have been obtained by ICP-MS, other concentrations by isotopic dilution

Sample	Rb (ppm)	Sr (ppm)	$^{87}Rb/^{86}Sr$	$^{87}Sr/^{86}Sr$	Error	$^{87}Sr/^{86}Sr$ (360 Ma)	Sm (ppm)	Nd (ppm)	$^{147}Sm/^{144}Nd$	$^{143}Nd/^{144}Nd$	Error	$^{143}Nd/^{144}Nd$ (360 Ma)	εNd (360Ma)
LDB11	9.2	214.5	0.124	0.703595	0.000009	0.702957	4.6	18.0	0.155790	0.512870	0.000005	0.512503	6.4
LDB14	18.3	249.1	0.213	0.704339	0.000010	0.703248	4.7	18.1	0.156013	0.512819	0.000005	0.512452	5.4
MF1	56.9	462.9	0.356	0.711632	0.000010	0.709809	5.9	22.9	0.156318	0.512833	0.000005	0.512465	5.7
MF2	20.1	343.3	0.169	0.712001	0.000010	0.711133	5.7	21.9	0.157644	0.512790	0.000005	0.512419	4.8
MF6	6.3	123.2	0.147	0.713144	0.000012	0.712390	5.1	20.0	0.155136	0.512817	0.000005	0.512452	5.4
MF7	12.0	139.6	0.249	0.713965	0.000010	0.712688	5.1	20.3	0.151261	0.512751	0.000004	0.512395	4.3
MGX1	42.9	235.9	0.526	0.705966	0.000013	0.703268	20.1	83.6	0.145415	0.512485	0.000004	0.512142	-0.6
BP1	1.1	879.3	0.004	0.703376	0.000010	0.703358	10.1	40.8	0.150366	0.512805	0.000004	0.512451	5.4
LDB15	42.5	24.7	4.984	0.732552	0.000009	0.707010	3.8	16.5	0.138518	0.512506	0.000005	0.512179	0.1
SDO2	91.9	92.1	2.891	0.718779	0.000010	0.703962	15.3	71.9	0.129074	0.512631	0.000005	0.512327	3.0
MED1	13.0	324.2	0.116	0.703804	0.000011	0.703209	8.3	35.0	0.143412	0.512781	0.000005	0.512443	5.2
Vi1	43.5	339.6	0.371	0.706550	0.000010	0.704649	7.3	30.2	0.146426	0.512843	0.000005	0.512498	6.3
SDO1	41.9	269.0	0.451	0.707063	0.000010	0.704750	11.9	52.6	0.136855	0.512647	0.000005	0.512324	2.9
SEM2	2.4	141.9	0.050	0.706325	0.000010	0.706070	9.8	42.6	0.139555	0.512661	0.000005	0.512332	3.1
SEM4	43.4	59.6	2.107	0.719369	0.000010	0.708570	12.7	53.5	0.143460	0.512649	0.000005	0.512311	2.7
SEM8	35.8	121.1	0.856	0.712968	0.000011	0.708579	9.2	39.5	0.141026	0.512669	0.000005	0.512337	3.2
SEM12	17.6	237.5	0.214	0.709310	0.000010	0.708212	8.9	38.2	0.141467	0.512683	0.000005	0.512350	3.4
BUA2	53.5	243.3	0.637	0.711538	0.000010	0.708275	4.9	20.5	0.144182	0.512684	0.000006	0.512345	3.3
BUA3	41.3	135.0	0.887	0.713384	0.000009	0.708841	8.0	34.3	0.141950	0.512692	0.000006	0.512358	3.6
JUG1	3.9	278.6	0.041	0.708732	0.000010	0.708523	8.4	35.3	0.143891	0.512696	0.000005	0.512356	3.6
TOU1	3.3	296.9	0.032	0.704812	0.000009	0.704649	5.6	21.3	0.160075	0.512863	0.000005	0.512485	6.1
TLD1	1.0	52.0	0.056	0.709386	0.000010	0.709101	9.0	37.0	0.147888	0.512776	0.000005	0.512427	4.9
TERT1	24.4	37.5	1.888	0.719042	0.000012	0.709366	7.8	28.7	0.163961	0.512717	0.000005	0.512331	3.1
TERT2	25.8	84.0	0.890	0.712824	0.000010	0.708262	7.4	28.4	0.158149	0.512790	0.000005	0.512418	4.7

4. Intégration des données dans l'évolution géodynamique du Massif Armoricain à 360 Ma

A minima à l'échelle du Massif Armoricain, cette thèse a contribué à démontrer que les gisements Sb-Au de la chaîne varisque ne sont pas uniquement tardi-orogéniques et qu'il peut exister des circulations de fluides tout au long de l'évolution de la chaîne Varisque notamment durant le début du Carbonifère. Les circulations de fluides associées aux minéralisations Sb-Au, d'échelle régionale, apparaissent donc synchrones de la mise en place d'un magmatisme mafique important, lui-même contemporain d'un changement drastique de la dynamique de subduction varisque (article #2). Il se pose alors la question des processus tectoniques profonds capables de générer la mise en place d'un magmatisme mafique lors de la subduction continentale à 360 Ma.

4.1 Magmatisme mafique du Domaine Centre Armoricain : témoin d'une remontée asthénosphérique par slab rollback ?

Le magmatisme mafique est relativement homogène au sein des domaines Nord et Centre Armoricain et montre une signature isotopique mantellique unique à l'échelle régionale. Par conséquent, les dolérites armoricaines proviennent directement de la fusion partielle du manteau sans contamination crustale significative, comme également suggéré par de nombreux auteurs au sein du Massif Armoricain (Saint-Malo, Lahaye et al. 1985; Bassin de Châteaulin, Caroff et al. 1996; Bassin de Laval et domaine Nord Armoricain, Le Gall 1999). Les basaltes du volcanisme bimodal du Bassin de Châteaulin et les dolérites de Saint-Malo sont interprétés comme des tholéiites océaniques de type intraplaque (Caroff et al. 1996), directement remontés vers la surface depuis la base de la lithosphère. Ils sont considérés comme dérivant de sous-plaquage de corps magmatiques mafiques à la limite asthénosphère-manteau lithosphérique dû à la fusion partielle de l'asthénosphère (Caroff et al. 2016). Néanmoins, les processus tectoniques responsables d'un tel sous-plaquage magmatique mafique, à la base de la lithosphère, ne sont pas discutés par ces auteurs.

La fusion partielle du manteau asthénosphérique et/ou lithosphérique peut se produire soit par hydratation, par décompression adiabatique ou soit par apport de chaleur. En considérant la signature géochimique des dykes de dolérite (magmas basaltique alcalins de type intraplaque), il est peu probable qu'ils proviennent d'une fusion du manteau par hydratation. En effet, une telle fusion de manteau hydraté (et métasomatisé) impliquerait probablement une signature géochimique de composition calco-alcaline, caractéristique d'arc volcanique. Cependant, à 360 Ma, en contexte de subduction continentale, le panneau plongeant s'est déjà déshydraté durant les stades antérieurs (subduction de la croûte océanique). Par conséquent, les fluides dérivés de ce panneau plongeant,

classiquement responsables de la fusion du coin de manteau, se trouvent déjà au sein de l'arc volcanique (e.g. Richards 2011). De plus, une décompression adiabatique est inenvisageable dans un contexte de convergence, d'autant plus que les domaines Nord et Centre Armoricain n'ont jamais été amincis. Il est donc raisonnable d'envisager que seul un apport de chaleur soit à l'origine de la fusion partielle du manteau. Etant donné qu'il est très difficile de faire fondre le manteau asthénosphérique, sans l'hydrater ou sans faire intervenir un point chaud, il est plus raisonnable de considérer une fusion du manteau lithosphérique sous continental (SCLM) par remontée asthénosphérique à l'aplomb d'un manteau déjà hydraté.

En contexte de subduction continentale, plusieurs hypothèses peuvent être proposées pour faire fondre le SCLM par remontée asthénosphérique: (1) soit une délamination lithosphérique suite à un épaississement crustal, (2) soit un retrait du panneau plongeant (slab rollback) ou (3) soit un déchirement du panneau plongeant (slab break-off). La deuxième hypothèse semble la plus approprié dans le cas de la subduction varisque armoricaine. En effet, le domaine Nord et Centre Armoricain n'ont jamais été épaissi durant l'orogenèse varisque, rendant difficile la délamination du manteau lithosphérique en dessous de ces domaines. Des images tomographiques du manteau révèlent une anomalie de vélocité, en-dessous du Domaine Centre Armoricain, qui sont interprétées comme un vestige du panneau plongeant de la lithosphère océanique Galice-Massif Central (GMC) à fort pendage NE (Gumiaux et al. 2004c). Il apparait peu probable qu'un panneau plongeant de lithosphère océanique, déchiré à 360 Ma de la marge rentrée en subduction continentale, soit encore visible à l'heure actuelle en tomographie. Nous proposons donc que la remontée asthénosphérique, initiée par un retrait du panneau plongeant, soit responsable de la fusion partielle du SCLM. En effet, la subduction continentale permet l'arrêt de l'enfouissement du panneau plongeant dans le manteau et donc le retrait du panneau. Ce retrait du panneau permet ainsi la remontée du manteau asthénosphérique profond et chaud au contact du SCLM plus « froid » conduisant à la fusion partielle de ce dernier. Cependant, le SCLM est déjà probablement modifié par les stades antérieurs de subduction ou même par son histoire cadomienne, il n'est donc pas impossible que ce manteau soit légèrement métasomatisé. Le résultat de la fusion partielle du SCLM peut donc se traduire par un sous-plaquage de magmas mafiques en base de lithosphère (ou en base de croûte) et une remontée très rapide de magmas mafiques vers la surface.

La Figure 5.5 illustre le mécanisme du retrait du panneau plongeant conduisant à la mise en place du magmatisme mafique à ~360 Ma au sein des domaines Nord et Centre Armoricain. Comme décrit précédemment, la subduction continentale (enregistrée par les éclogites du Cellier et les schistes bleus de l'île de Groix, Bosse et al. 2000, 2005) permet le retrait du panneau plongeant et induit une large remontée asthénosphérique du bas vers le haut, mais également par un input

d'asthénosphère latéralement au panneau. Il est fréquent qu'un retrait du panneau plongeant se traduise par une extension généralisée de la plaque supérieure. Cependant, la subduction continentale indique clairement que le Massif Armoricain est dans une dynamique de convergence à l'échelle lithosphérique et soumis à un raccourcissement horizontal. De plus, la branche Nord du CSA et le CNA, interprétées comme des structures héritées anté-varisque (Gumiaux et al. 2004b), sont réactivées à partir de 360 Ma et peuvent jouer un rôle de faille de transfert avortant tout amincissement ou épaississement au sein des domaines Nord et Centre Armoricain. Ceci n'est pas le cas du domaine Sud Armoricain qui constitue la zone interne et métamorphique de la future chaîne varisque et qui accommode la majeure partie de la déformation varisque (e.g. Gumiaux et al. 2004b; Ballèvre et al. 2013, 2014). Ainsi le magmatisme à l'origine des dolérites se met en place dans un laps de temps relativement court au sein des domaines Nord et Centre Armoricain. Les magmas à l'origine des dolérites peuvent être guidés par des discontinuités majeures comme le CNA au sein du Bassin de Laval (Fig. 5.5) mais également par des structures héritées mineures anté-varisque (Cambro-Ordovicien ou Cadomien).

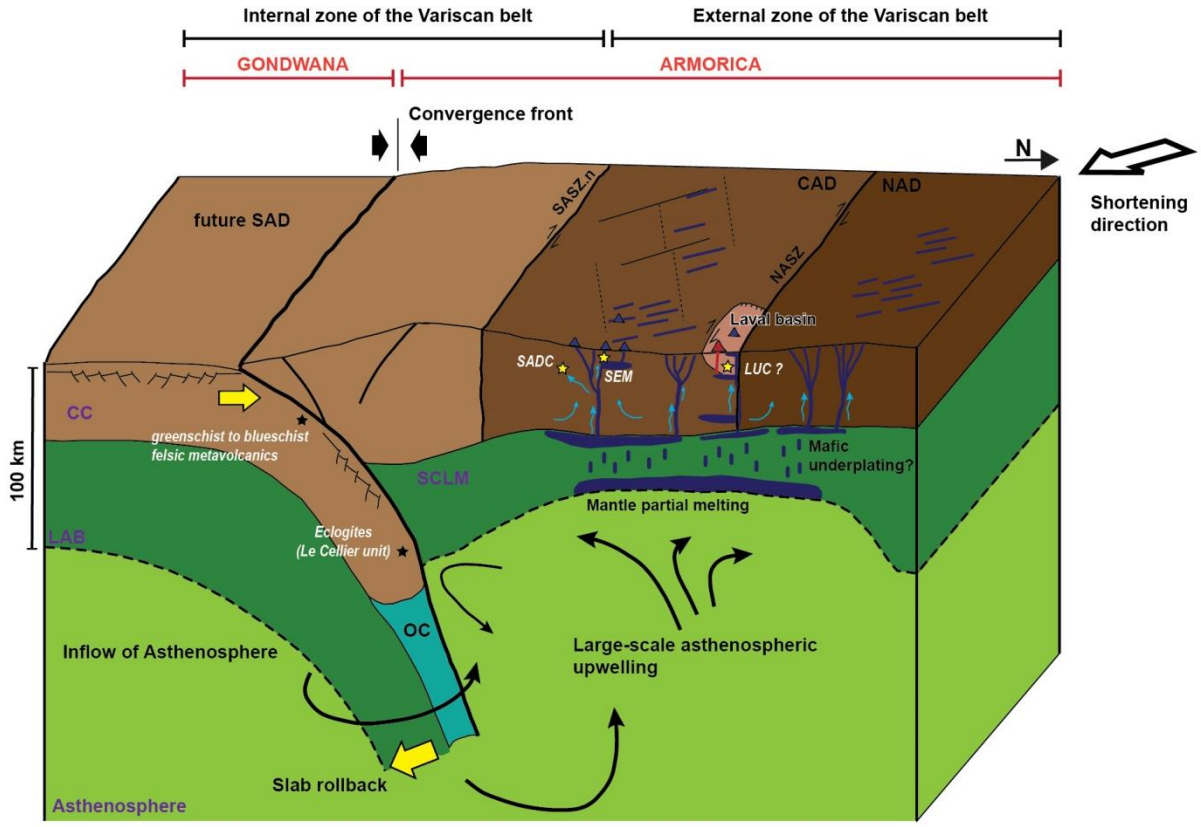

Figure 5.5 Bloc diagramme illustrant le processus de remontée asthénosphérique par un retrait du panneau plongeant à 360-355 Ma au niveau du domaine Centre Armoricain. Cette remontée asthénosphérique provoque la fusion partielle du manteau lithosphérique sous-continental (SCLM) et l'ascension du magmatisme mafique vers la surface avec potentiellement un sous-plaquage mafique à la base de la croûte. Les flèches bleues claires représentant la potentielle mobilisation de fluides crustaux par l'anomalie thermique générée par la mise en place du magmatisme mafique. Les flèches jaunes symbolisent le fait que la fosse continue d'avancer pendant le retrait du panneau plongeant.

Par exemple, les réseaux de dykes de Martigné-Ferchaud (domaine Centre Armoricain) et de la Mancellia (domaine Nord Armoricain) ne semblent pas contrôlés par des discontinuités apparentes en surface et pourraient s'être mis en place à la faveur de structures héritées du socle anté-varisque. Il n'est pas non plus à exclure qu'il y ait des corps gabbroïques se mettant en place à des niveaux intermédiaires au sein de la croûte. En effet, le sill doléritique, encaissé dans le silurien du Bassin de Laval, comporte des « rubans » de faciès différenciés dioritiques ce qui renforce l'existence probable de corps plutoniques différenciés de profondeur à faible profondeur. Au regard de la grande distribution géographique des réseaux de dykes et de sills au sein de la zone externe de la chaîne varisque (domaines Nord et Centre Armoricain), un important volume de magmas s'est mis en place à 360 Ma.

4.2 Remontée asthénosphérique : un processus tectonique profond ubiquiste dans la genèse des minéralisations en contexte de convergence ?

Les processus tectoniques évoqués dans la circulation des fluides responsables de la genèse des minéralisations à Au ± Sb phanérozoïques sont nombreux. En effet, Goldfarb et al. 1998 ont montré en Alaska que l'épaississement crustal (ceinture aurifère de Juneau), la subduction d'une ride océanique (prisme d'accrétion de Chugach) ou le retrait d'un panneau plongeant (Péninsule Seward) peuvent conduire à un métamorphisme régional et à une dévolatilisation des roches impliquées dans ces processus. Ces derniers impliquent donc une origine métamorphique des fluides, cependant la mise en place de magmas peut également conduire à la dévolatilisation de l'encaissant par métamorphisme de contact et générer des fluides métamorphiques bien que la source thermique soit magmatique (Kontak et al. 2011). Pour la plupart des gisements à Au ± Sb phanérozoïque, il apparait que les processus de subduction (ou du moins en convergence) joue un rôle important dans leurs genèses (e.g. Groves et al. 1998; Goldfarb et al. 1998; Goldfarb et Groves 2015). En effet, la dévolatilisation d'un panneau plongeant libère une grande quantité de fluides (e.g. « Fluid-mobile element », Deschamps et al. 2010, 2011, 2012, 2015) conduisant à la fusion partielle du manteau ce qui va permettre la remontée d'un cortège magmatique et hydrothermal au sein de la croûte continentale sus-jacente (e.g. Goldfarb et Santosh 2014). Un tel effet thermique peut également être provoqué par une remontée asthénosphérique lors d'un retrait du panneau plongeant ou lors de l'apparition d'une fenêtre asthénosphérique (e.g. subduction d'une ride océanique). Comme décrit précédemment, une telle remontée asthénosphérique conduit inévitablement à la fusion du coin de manteau et/ou du SCLM et par conséquent à la mise en place d'un magmatisme felsique et/ou mafique important au sein de la plaque supérieure. Le SCLM, lorsque fertile, est considéré comme un important réservoir à métaux (Hronsky et al. 2012; Griffin et al. 2013). La fusion partielle du SCLM fertile apparait donc comme un processus majeur à

l'origine d'anomalie thermique au sein de la croûte et par conséquent à la mobilisation de circulation de fluides à l'échelle lithosphérique et la formation de nombreuses provinces métallogéniques à Au ± Sb. Au sein de la chaine Varisque européenne et d'Asie centrale, De Boorder (2012) propose que les gisements Au ± Sb sont le résultat de la fusion de la croûte inférieure par le sous-plaquage de magma mafique à la base de la croûte. Enfin, il apparait à travers ces nombreux modèles qu'il est difficile d'établir un processus tectonique profond et unique pour tous les gisements à Au ± Sb, cependant dans tous les modèles à grande échelle, le facteur majeur et indispensable est la présence d'une forte anomalie thermique. Goldfarb et Groves (2015) montrent à travers un aperçu de nombreux gisements Au ± Sb (de type orogénique essentiellement) que le point commun de nombreux processus tectoniques comme la subduction d'une ride océanique, le retrait du panneau plongeant ou la délamination du SCLM est la remontée asthénosphérique. Ainsi, dans le cadre géologique varisque du Massif Armoricain, il semble approprié d'invoquer une remontée asthénosphérique par retrait du panneau plongeant comme le processus tectonique majeur responsable du magmatisme mafique régional (à 360 Ma) et des circulations de fluides associés aux minéralisations Sb-Au.

4.3 Modèle de circulations de fluides à l'échelle régionale : implications sur la localisation des minéralisations

Il est donc raisonnable d'envisager que la mise en place d'un tel volume magmatique mafique chaud au sein d'une zone externe non épaissie et relativement froide (i.e. métamorphisme régional de bas grade, Le Corre 1969, 1975; Donnot et al. 1973; Gumiaux et al. 2004b) implique une mobilisation de fluides à grande échelle (articles #4 et #5). Les granitoïdes de la zone externe sont localisés le long des zones de cisaillement et plus jeunes que les circulations de fluides associés aux minéralisations, et ne peuvent donc pas être considérés comme une source thermique. A 360 Ma, le seul moteur thermique capable de générer une telle circulation de fluides à l'échelle régionale est le magmatisme mafique. De plus, les âges obtenus sur les minéralisations Sb-Au du Semnon (358.5 ± 7.1 Ma sur apatite et > 339 Ma sur illite) et de Saint-Aubin-des-Châteaux (358.8 ± 0.9 Ma sur tobelite) révèlent une circulation de fluides minéralisateurs à Sb-Au d'échelle régionale. Bien qu'aucune roche mafique n'ait été identifiée aux alentours de la minéralisation de Saint-Aubin-des-Châteaux, l'âge identique entre la minéralisation et la mise en place du magmatisme renforce le fait que ce dernier est probablement à l'origine des circulations de fluides de grande échelle, au moins au sein du domaine Centre Armoricain. Nous proposons donc un modèle conceptuel de circulations de fluides responsable des minéralisations à Sb-Au et induit par la mise

en place du magmatisme mafique à l'échelle d'un segment de la zone externe de la chaîne varisque. Ce modèle est illustré par la Figure 5.6 et constitue un zoom de la Figure 5.5.

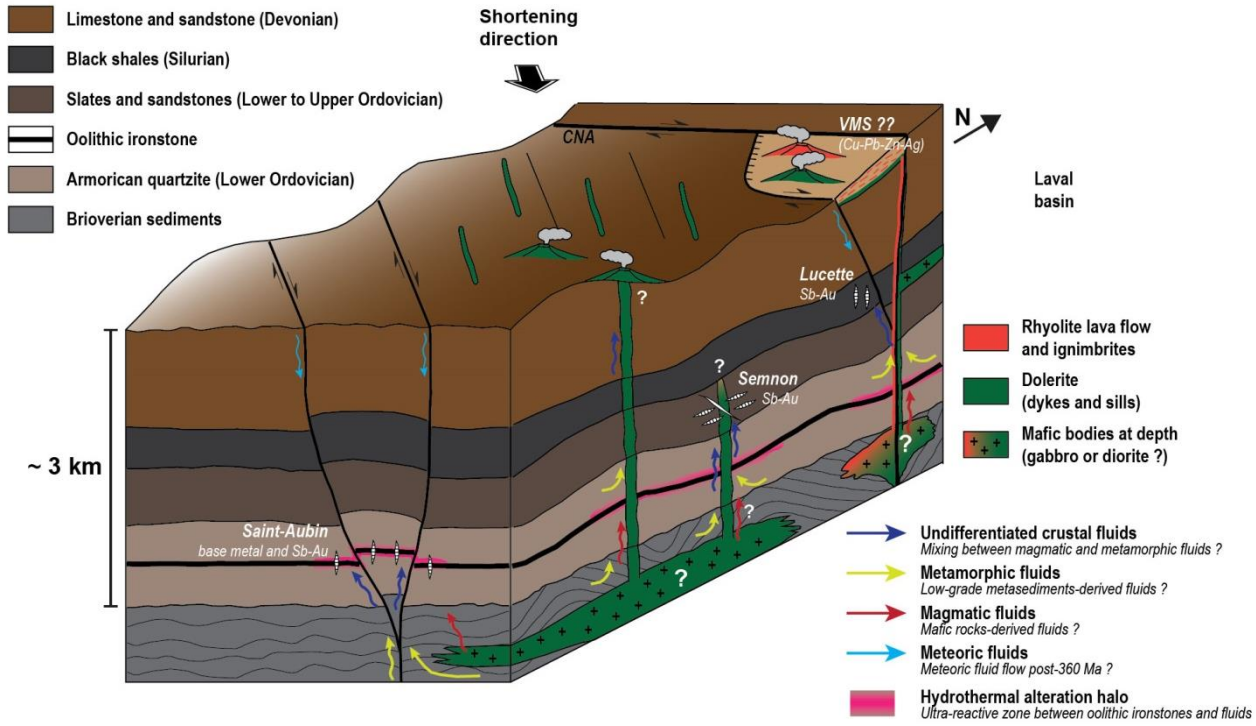

Figure 5.6 Bloc diagramme illustrant les circulations de fluides initiées par la mise en place du magmatisme mafique aux alentours de 360 Ma dans la partie superficielle du domaine Centre Armoricain.

En effet, alors que cette dernière illustre les processus tectoniques profonds responsable de la mise en place du magmatisme mafique, la Figure 5.6 illustre le rôle du magmatisme sur la mobilisation des fluides dans la partie superficielle de la croûte supérieure qui constitue le Massif Armoricain aux alentours de 360 Ma.

Dans ce modèle, nous proposons que les circulations de fluides soient générées par la mise en place de corps plutoniques et mafiques à faible profondeur (< 5km) associés aux dykes et sills de dolérite. Les anomalies denses et relativement magnétiques localisées en-dessous du gisement du Semnon et de La Lucette et les évidences de différenciation au sein du Bassin de Laval (e.g. diorite) nous suggèrent que des corps plutoniques et mafiques existent en profondeur. De plus, les fortes températures enregistrées au sein des inclusions fluides au sein des gisements du Semnon (240-330 °C) et de La Lucette (200-350°C) localisés à faible profondeur nécessitent une source thermique peu profonde. Le métamorphisme régional étant très faible au sein de cette zone externe, il est peu probable que le métamorphisme soit le moteur thermique de la circulation des fluides. Cependant, les compositions des fluides aquo-carboniques suggèrent une origine métamorphique. Bien qu'il existe des fluides magmatiques riches en CO_2 au sein de gisements Sb-Au orogéniques (e.g. McCoy et al. 1997; Sillitoe et Thompson 1998), nous proposons que l'apport de chaleur généré par la mise en place des magmas mafiques peut permettre la déshydratation des méta-sédiments briovériens et

paléozoïques et induire une circulation de fluides dit « métamorphiques » par une source magmatique. Ces méta-sédiments sont encore relativement hydratés et une source thermique telle qu'un magmatisme mafique peut facilement libérer les fluides contenus dans les minéraux hydratés (e.g. chlorite, chloritoïde) de ces méta-sédiments par un simple apport de chaleur. En effet, la majorité des phyllosilicates sont d'origine détritique au sein du domaine Centre Armoricain, (Le Corre 1969, 1975). Cependant, il n'est pas à exclure qu'il y ait également une contribution de fluides magmatiques mafiques ou à minima de fluides issus du métamorphisme de contact, et qu'ils puissent interagir avec les fluides métamorphiques, donnant ce qu'on pourrait appeler des fluides d'origine crustale indifférencié (Fig. 5.6). Les données d'inclusions fluides sur les gisements du Semnon et de La Lucette ont révélé qu'il existait également une circulation de fluides aqueux météoriques et froids. Ils ne sont pas dominant contrairement aux fluides chauds aquo-carboniques et sont probablement tardifs et vraisemblablement déconnectés de l'histoire hydrothermale des minéralisations à Sb-Au.

En effet, le mécanisme de surpression de fluides responsable de la formation du système minéralisé du Semnon indique qu'il s'est mis en place dans un régime supra-lithostatique (article #4) au sein de schistes. Par conséquent, il n'y avait probablement pas de connexion à la surface durant la majeure partie de l'évènement hydrothermal minéralisateur bien qu'on soit relativement à faible profondeur (< 2.5 km). La formation des schistes de Traveusot, encaissant les dykes de dolérites et les minéralisations Sb-Au du Semnon, est considérée comme une couche imperméable et les schistes noirs du Silurien situés au-dessus de cette formation (Fig. 5.6) peuvent également agir comme une deuxième barrière de d'imperméabilité. De plus, les séries sédimentaires commencent seulement à accommoder la déformation régionale par un début de plissement, ainsi la fracturation est relativement faible à 360 Ma dans la région du Semnon. Ceci n'est pas le cas des gisements de Saint-Aubin-des Châteaux et de La Lucette. En effet, le premier, situé à seulement 3 km de la branche nord du CSA, est en partie contrôlé par des failles décrochantes N160°E qui accommodent le plissement suggérant qu'elles sont précoces dans l'histoire tectonique Varisque. Le gisement de La Lucette est localisé au sein du Bassin de Laval, qui est le résultat d'un fonctionnement transtensif du CNA (Houlgatte et al. 1988; Gumiaux et al 2004b). Le CNA agit probablement comme un drain d'échelle crustale tout au long de la construction de la chaîne Varisque. Il n'est donc pas à exclure que des fluides météoriques aient interagi avec des fluides plus profonds au sein de ces deux régions. Bien que nous ne disposons d'aucune contrainte temporelle sur la mise en place du gisement de La Lucette, nous proposons que le dépôt de la minéralisation Sb-Au est contemporain de celui du Semnon et de Saint-Aubin-des-Châteaux pour plusieurs raisons : (1) le gisement de La Lucette est situé au sein du Bassin de Laval où ce magmatisme mafique est connu à 360 Ma, (2) la minéralisation est encaissé au sein du Silurien supérieur (Formation du Val) et

quelques dykes de dolérites se trouvent à proximité de la mine (< 3 km), (3) un dyke de dolérite a été recoupé lors de la construction de la descenderie de Port-Brillet (indice Sb-Au appartenant au district de La Lucette) et (4) un sill de dolérite (~ 60 m d'épaisseur) est encaissé au sein du Silurien inférieur (Formation de la Lande-Murée).

Une particularité notoire du domaine Centre Armoricain est la présence de niveaux de minerais de fer oolithiques au sein de l'Ordovicien inférieur (Chauvel 1974). Au niveau du gisement de Saint-Aubin-des-Châteaux, ce minerai de fer est fortement modifié par des fluides hydrothermaux (Moëlo et al. 2002, 2008; Gloaguen et al. 2007; Tartèse et al. 2015) et associé à des minéralisations Sb-Au (Gloaguen et al. 2007). Cette empreinte hydrothermale est marquée par un front d'altération, composée d'une grande multitude de phosphates, autour du minerai de fer riche en matière organique et considéré comme un niveau ultra-réactif aux circulations de fluides (Gloaguen et al. 2007). Ces niveaux de minerai de fer sont présents à travers tout le domaine Centre Armoricain et se trouvent à un niveau structural plus bas (Ordovicien inférieur) que les gisements du Semnon (Ordovicien inférieur à moyen) et de la Lucette (Silurien). Ils sont considérés comme un piège physique et chimique et jouent un rôle « d'éponge » à fluide. Etant donné la réactivité d'un tel minerai de fer en réponse à des circulations de fluides, il est donc probable que l'injection d'un magma mafique (et des fluides associés) dans ces niveaux de fer ait déclenché des modifications importantes de ce minerai de fer à l'échelle régionale. Cela laisse penser qu'il peut y avoir des équivalents du gisement de Saint-Aubin-des-Châteaux en profondeur au moins sous le Semnon ou à la base du Bassin de Laval où les circulations de fluides minéralisateurs sont connues. De plus, ces niveaux de minerais de fer très réactifs enregistrent (au moins dans le secteur de Saint-Aubin-des-Châteaux) des circulations de fluides allant du Silurien jusqu'au début du Permien, ce qui fait d'eux un excellent traceur de circulation de fluides au sein du Massif Armoricain. Bien qu'il ne soit pas à exclure une source magmatique et métamorphique des métaux, il se peut que l'interaction entre ces niveaux de fer et des fluides ait contribué à la redistribution des métaux au sein de la croûte armoricaine.

Enfin, un évènement métallifère situé à la limite Dévono-Carbonifère a déjà été identifié par Lescuyer et al. (1998) à l'échelle de la chaine Varisque, notamment par la présence de sulfures massifs volcanogéniques (VMS) au sein du bassin Carbonifère de Châteaulin du domaine Centre Armoricain (La Porte-aux-Moines, Bodennec), du Massif Central Français (Chessy et Chizeul), au sein de la ceinture pyriteuse ibérique (Rio Tinto, Neves Corvo) ou encore au sein du massif des Jebilet au Maroc (Draa Sfar). Au sein des VMS armoricains, il existe une paragenèse, certes mineures, à sulfosels d'antimoine (Lescuyer et al. 1998). Cet évènement métallifère type VMS est contemporain avec l'histoire hydrothermale Sb-Au du domaine Centre-Armoricain. Cela suggère,

qu'à l'instar de ces VMS, cet évènement hydrothermal Sb-Au pourrait potentiellement être généralisé dans plusieurs segments de la chaine Varisque ouest-européenne notamment dans le Massif Ibérique.

Références bibliographiques

Alexandrov P., Ruffet G., Cheilletz A. (2002). Muscovite recrystallization and saddle-shaped 40Ar/39Ar age spectra: Example from the Blond granite (Massif Central, France). *Geochimica Cosmochimica Acta* 66, 1793–1807.

Arthaud F., Matte P. (1977). Late Paleozoic strike slip faulting in southern Europe and northern Africa: result of a right lateral shear zone between the Appalachians and the Urals. *Geological Society of America Bulletin* 88, 1305– 1320.

Audion A.S. avec la collaboration extérieure de la Compagnie Européenne d'Intelligence Stratégique (CEIS) (2012). Panorama mondial 2011 du marché de l'antimoine. Rapport BRGM RP-61342-FR, BRGM, Orléans, 82 p.

Bailly L., Bouchot V., Bény C. Milési J.-P. (2000). Fluid inclusion study of stibnite using infrared microscopy: an example from the Brouzils antimony deposit (Vendee, Armorican Massif, France). *Economic Geology* 95, 221–226.

Ballèvre M., Bosse V., Ducassou C., Pitra P. (2009). Paleozoic history of the Armorican Massif: Models for the tectonic evolution of the suture zones. *Comptes Rendus Geoscience* 341, 174–201.

Ballèvre M., Bosse V., Dabard M.-P., Ducassou C., Fourcade S., Paquette J.-L., Peucat J.-J., Pitra P. (2013). Histoire géologique du Massif armoricain : actualité de la recherche. *Bulletin de la Société géologique et minéralogique de Bretagne* 10-11, 5–96.

Ballèvre M., Catalán J.R.M., López-Carmona A., Pitra P., Abati J., Fernández R.D., Ducassou C., Arenas R., Bosse V., Castiñeiras P., Fernández-Suárez J., Barreiro J.G., Paquette J.L., Peucat J.J., Poujol M., Ruffet G., Sánchez Martínez S. (2014). Correlation of the nappe stack in the Ibero-Armorican arc across the Bay of Biscay: a joint French–Spanish project. *Geological Society, London, Special Publications* 405, 77–113.

Ballouard C., Boulvais P., Poujol M., Gapais D., Yamato P., Tartèse R., Cuney M. (2015). Tectonic record, magmatic history and hydrothermal alteration in the Hercynian Guérande leucogranite, Armorican Massif, France. *Lithos* 220–223, 1–22.

Ballouard C., Poujol M., Boulvais P., Zeh A. (2017). Crustal recycling and juvenile addition during lithospheric wrenching: The Pontivy-Rostrenen magmatic complex, Armorican Massif (France), Variscan belt. *Gondwana Research* 49, 222–247.

Beach A. (1976). The Interrelations of Fluid Transport, Deformation, Geochemistry and Heat Flow in Early Proterozoic Shear Zones in the Lewisian Complex. *Philosophical Transactions of the Royal Society of London. Series A, Mathematical and Physical Sciences* 280, 569–604.

Beaudoin G., Pitre D. (2005). Stable isotope geochemistry of the Archean Val-d'Or (Canada) orogenic gold vein field. *Mineralium Deposita* 40, 59–75.

Bellot J-P., Lerouge C., Bailly L., Bouchot V. (2003). The Biards Sb–Au-bearing shear zone (Massif Central, France): an indicator of crustal-scale transcurrent tectonics guiding Late Variscan collapse. *Economic Geology* 98, 1427–1447.

Bernard-Griffiths J., Peucat J.-J., Sheppart S., Vidal P. (1985) Petrogenesis of Hercynian leucogranites from the southern Armorican Massif : contribution of REE and isotopic (Sr, Nb, Pb and O) geochemical data to the study of source rock characteristics and ages. *Earth and Planetary Science Letters* 74, 235–250.

Berthé D., Choukroune P., Gapais D. (1979a). Quartz Fabrics and Progressive Gneissification of Granites By Simple Shear - Example of the South Armorican Shear Zone. *Bulletin de Minéralogie* 102, 265–272.

Berthé D., Choukroune P., Jegouzo P. (1979b). Orthogneiss, mylonite and non coaxial deformation of granites: the example of the South Armorican Shear Zone. *Journal of Structural Geology* 1, 31–42.

Bierlein F.P., Crowe D.E. (2000). Phanerozoic orogenic lode gold deposits. *Reviews in Economic Geology* 13, 103–139.

Bierlein F.P., Craw D. (2008). Petrogenetic character and provenance of metabasalts in the aspiring and Torlesse Terranes, South Island, New Zealand: implications for the gold endowment of the Otago Schist? *Chemical Geology* 260, 301–315.

Bierlein F.P., Pisarevsky S. (2008). Plume-related oceanic plateaus as a potential source of gold mineralisation. *Economic Geology* 103, 425–430.

Boiron M.C., Cathelineau M., Dubessy J., Bastoul A.M. (1990). Fluids in Hercynian Au veins from the French Variscan belt. *Mineralogical Magazine* 54, 231–243

Boiron M.-C., Cathelineau M., Banks D.A., Fourcade S., Vallance J. (2003). Mixing of metamorphic and surficial fluids during the uplift of the Hercynian upper crust: consequences for gold deposition. *Chemical Geology* 194, 119–141.

Bonatti E., Lawrence J.R., Morandi N. (1984). Serpentinization of oceanic peridotites: temperature dependence of mineralogy and boron content. *Earth and Planetary Science Letters* 70, 88–94.

Bosse V., Féraud G., Ruffet G., Ballèvre M., Peucat J.-J., De Jong K. (2000). Late Devonian subduction and early-orogenic exhumation of eclogite-facies rocks from the Champtoceaux Complex (Variscan belt, France). *Geological Journal* 35, 297–325.

Bosse V., Ballevre M., Vidal O. (2002). Ductile thrusting recorded by the garnet isograd from blueschist-facies metapelites of the Ile de Groix, Armorican Massif, France. *Journal of Petrology* 43, 485–510.

Bosse V., Féraud G., Ballèvre M., Peucat J.-J., Corsini M. (2005). Rb–Sr and 40Ar/39Ar ages in blueschists from the Ile de Groix (Armorican Massif, France): Implications for closure mechanisms in isotopic systems. *Chemical Geology* 220, 21–45.

Bossière G. (1988). Evolutions chimico-minéralogiques du grenat et de la muscovite au voisinage de l'isograde biotite-staurotide dans un métamorphisme prograde de type barrovien: un exemple en Vendée littorale (Massif Armoricain). *Comptes rendus de l'Académie des sciences. Série 2, Mécanique, Physique, Chimie, Sciences de l'univers, Sciences de la Terre* 306, 135–140.

Bouchot V., Milesi J.-P., Lescuyer J-L., Ledru P. (1997). Les minéralisations aurifères de la France dans leur cadre géologique autour de 300 Ma. *Chronique de la Recherche Minière* 528,

13– 62

Bouchot V., Ledru P., Lerouge C., Lescuyer J.L., Milesi J.P. (2005) 5: Late Variscan mineralizing systems related to orogenic processes: The French Massif Central. *Ore Geology Review* 27, 169–197.

Bril H. (1982). Fluid Inclusions Study of Sn-W-Au, Sb- and Pb-Zn Mineralizations from the Brioude-Massiac District (French Massif Central). *Tschermaks Mineralogische und Petrographische Mlitteilungen* 30, 1–16.

Bril H., Beaufort D. (1989). Hydrothermal alteration and fluid circulation related to W, Au, and Sb vein mineralizations, Haut-Allier, Massif Central, France. *Economic Geology* 84, 2237–2251.

Brogi A., Fabbrini L., Liotta D. (2011) Sb–Hg ore deposit distribution controlled by brittle structures: The case of the Selvena mining district (Monte Amiata, Tuscany, Italy). *Ore Geology Reviews* 41, 35–48.

Brun J.P., Guennoc P., Truffert C., Vairon J., and Program T.A.W.G.O.T.G.-D. (2001). Cadomian tectonics in northern Brittany: a contribution of 3-D crustal-scale modeling. *Tectonophysics* 331, 229–246.

Burg J.P., Van Den Driessche J., Brun J.P. (1994). Syn- to post-thickening extension: mode and consequences. *Comptes Rendus de l'Académie des Sciences de Paris* 319, 1019–1032.

Caroff M., Le Gal X., Rolet J., Cotten J., Thonon P. (1996). Magmatisme tholeiitique continental en contexte orogénique hercynien: l'exemple du volcanisme viséen de Kerroc'h, Massif armoricain (France). *Comptes rendus de l'Académie des sciences. Série 2. Sciences de la terre et des planètes* 322, 269–275.

Caroff M., Le Gall B., Authemayou C., Bussien Grosjean D., Labry C., Guillong M. (2016). Relations between basalts and adakitic–felsic intrusive bodies in a soft-substrate environment: the South Ouessant Visean basin in the Variscan belt, Armorican Massif, France. *Canadian Journal of Earth Sciences* 53, 441–456.

Cathelineau M., Boiron M.C., Tuduri J. (2011). Fluides et genèse des concentrations minérales. *Geosciences* 13, 56–63.

Chantraine J., Chauvel J.-J., Dupret L., Gatinot F., Icart J.C., Le Corre C., Rabu D., Sauvan P., Villey M. (1983). Inventaire lithologique et structural du briovérien (protérozoïque) de la Bretagne Centrale et du Bocage Normand pour la recherche de guides métallogéniques. Documents du BRGM, v. 67, BRGM, Orléans, 306 p.

Chantraine J., Chauvel J.-J., Rabu D. (1994). Lithostratigraphy: In Chantraine, J., Rolet, J., Santallier, D.S., Piqué, A., and Keppie, J.D. (eds.), Pre-Mesozoic Geology in France and Related Areas, IGCP-Project 233, Springer Berlin Heidelberg, p. 81–95.

Chauris L. (1977). Les associations paragénétiques dans la métallogénie varisque du Massif Armoricain. *Mineralium Deposita* 12, 353–371.

Chauris L., Marcoux E. (1994). Metallogeny of the Armorican Massif. In: Chantraine J, Rolet J, Santallier DS, et al. (eds) Pre-Mesozoic Geology in France and Related Areas. Springer Berlin Heidelberg, pp 243–264.

Chauris L., Guigues J. (1969). Gîtes minéraux de la France, volume I, Massif Armoricain. Mémoires du BRGM 74, BRGM, Orléans.

Chauris L., Fouquet Y., Moëlo Y. (1977). Les occurrences antimonifères de l'île de Sein et du Cap Sizun (Finistère). Leur place dans la métallogénie armoricaine. *Bulletin de la Société française de Minéralogie et de Cristallographie* 100, 208–213.

Chauris L., Houlgatte E., Laforêt C., Picot P. (1985). Un district antimono-aurifère à gangue quartzo-carbonatée : Le Semnon (Ille-et-Vilaine, Massif Armoricain, France). *Hercynica* 1, 111–119.

Chauvel J.J. (1974). Les minerais de fer de l'Ordovicien inférieur du bassin de Bretagne-Anjou, France. *Sedimentology* 21, 127–147.

Cheilletz A., Ruffet G., Marignac C., Kolli O., Gasquet D., Féraud G., Bouillin J.P. (1999) $^{40}Ar/^{39}Ar$ dating of shear zones in the Variscan basement of Greater Kabilia (Algeria). Evidence of an Eo-Alpine event at 128 Ma (Hauterivian-Barremian boundary): Geodynamic consequences. *Tectonophysics* 306, 97–116.

Chèvremont P. (1983). Etude pétrologique des formations sédimentaires "briovériennes" et des roches éruptives de la région de Château-Gontier (Mayenne). Note technique BRGM 83 GEO EP 77, BRGM, Orléans, 46 p.

Choukroune P., Lopez-Munoz M., Ouali J. (1983). Cisaillement ductile sud-armoricain et déformations discontinues associées : mise en évidence de la déformation régionale non coaxiale dextre. *Comptes Rendus de l'Académie des Sciences de Paris* 296, 657–660.

Chovan M., Hurai V., Sachan H.K., Kantor J. (1995). Origin of the fluids associated with granodiorite-hosted Sb-As-Au-W mineralization at Dúbrava (Nízke-Tatry Mts,Western Carpathians). *Mineralium Deposita* 30, 48–54.

Clayton R.E. (1993). Basalt carbonatisation and its implications for antimony mineralisation in north Cornwall.

Clayton R.E., Spiro B. (2000). Sulphur, carbon and oxygen isotope studies of early Variscan mineralization and Pb–Sb vein deposits in the Cornubian orefield: implications for the scale of fluid movements during Variscan deformation. *Mineralium Deposita* 35, 315–331.

Clayton R.E., Scrivener R.C., Stanley C.J. (1990). Mineralogical and preliminary fluid inclusion studies of lead-antimony mineralisation in north Cornwall. *Proceedings of the Ussher Society* 7, 258–262.

Cocks L.R., Fortey R.A. (1982). Faunal evidence for oceanic separations in the Paleozoic of Britain. *Journal of Geology Society, London* 139, 465–478

Collins P.L.F. (1979) Gas hydrates in CO_2-bearing fluid inclusions and the use of freezing data for estimation of salinity. *Economic Geology* 74, 1435–1444.

Couto H., Roger G., Moëlo Y., Bril H. (1990). Le district à antimoine-or Dúrico–Beirão (Portugal): évolution paragénétique et géochimique; implications méttalogéniques. *Mineralium Deposita* 25, 569–581.

De Boorder H. (2012). Spatial and temporal distribution of the orogenic gold deposits in the Late Palaeozoic Variscides and Southern Tianshan: How orogenic are they? Ore Geology Reviews 46, 1–31.

de Ronde C.E.J., Faure K., Bray C.J., Whitford D.J. (2000). Round Hill shear zone-hosted gold deposit, Macraes Flat, Otago, New Zealand: evidence of a magmatic ore fluid. *Economic Geology* 95, 1025–1048.

Deschamps F., Guillot S., Godard M., Chauvel C., Andreani M., Hattori K. (2010). In situ characterization of serpentinites from forearc mantle wedges: timing of serpentinization and behavior of fluid-mobile elements in subduction zones. *Chemical Geology* 269, 262–277.

Deschamps F., Guillot S., Godard M., Andreani M., Hattori K. (2011). Serpentinites act as sponges for fluid-mobile elements in abyssal and subduction zone environments. *Terra Nova* 23, 171–178.

Deschamps F., Godard M., Guillot S., Chauvel C., Andreani M., Hattori K., Wunder B., France L. (2012). Behavior of fluid-mobile elements in serpentines from abyssal to subduction environments: examples from Cuba and Dominican Republic. *Chemical Geology* 312–313, 93–117.

Deschamps F., Godard M., Guillot S., Hattori K. (2015). Geochemistry of subduction zone serpentinites: A review. *Lithos* 178, 96–127.

Dill H.G. (1985). Antimoniferous mineralization from the Mid-European Saxothuringian Zone: mineralogy, geology, geochemistry and ensialic origin. *Geologische Rundschau* 74, 447–466.

Dill H.G. (1993). Die Antimonvorkommen der mitteleuropaischen Alpiden und Varisziden. *Zeitschrift der Deutschen Geologischen Gesellschaft* 144, 434–450.

Donnot M., Guigues J., Lulzac Y., Magnien A., Parfenoff A., Picot P. (1973). Un nouveau type de gisement d'europium: la monazite grise à europium en nodules dans les schistes paléozoïques de Bretagne. *Mineralium Deposita* 8, 7–18.

Etheridge M.A., Wall V.J., Vernon R.H. (1983). The role of the fluid phase during regional metamorphism and deformation. *Journal of Metamorphic Geology* 1, 205-226.

European Commission (2017). Study on the review of the list of Critical Raw Materials.

Fan D., Zhang T., Ye J. (2004). The Xikuangshan Sb deposit hosted by the Upper Devonian black shale series, Hunan, China. *Ore Geology Reviews* 24, 121–133.

Faure M. (1989). L'amincissement crustal dans la chaine varisque à partir de la déformation ductile des leucogranites du Limousin. *Comptes Rendus de l'Académie des Sciences de Paris* 309, 1839–1845.

Faure M. (1995). Late orogenic carboniferous extensions in the Variscan French Massif Central. *Tectonics* 14, 132–153.

Fouquet Y. (1980). Les districts antimonifères de Quimper et du Cap Sizun (Finistère): leur place dans la métallogénie de l'antimoine dans le massif armoricain (France). Thèse de troisième cycle Université de Clermont II, 191 p.

Franke W., Cocks L.R.M., Torsvik T.H. (2017). The Palaeozoic Variscan oceans revisited. *Gondwana Research* 48, 257–284.

Fyfe W.S, Price N.J., Thompson A.B. (1978). Fluids in the Earth's crust. Elsevier, New York.

Fyon J.A., Schwarcz H.P., Crocker J.H. (1984). Carbonatization and gold mineralization in the Timmins area, Abitibi greenstone belt—genetic links with Archean mantle CO2-degassing and lower crust granulitization [abs]. Geological Association of Canada Program With Abstracts vol. 9 p. 65.

Fyon J.A., Troop D.G., Marmont S., Macdonald, A.J. (1989). Introduction of gold into Archean crust, Superior Province, Ontario - Coupling between mantle-initiated magmatism and lower crustal thermal maturation. *Economic Geology Monograph* 9, 479–490.

Gaboury D. (2013). Does gold in orogenic deposits come from pyrite in deeply buried carbon-rich sediments? Insights from volatiles in fluid inclusions. *Geology* 41, 1207–1210.

Gapais D., Le Corre C. (1980). Is the Hercynian belt of Brittany a major shear zone. *Nature* 288:574–576.

Gapais D., Lagarde J.L., Le Corre C., Audren C., Jegouzo P., Casas Sainz A., Van Den Driessche J. (1993). La zone de cisaillement de Quiberon : témoin d'extension de la chaine varisque en Bretagne méridionale au Carbonifère. *Comptes Rendus de l'Académie des Sciences de Paris* 316, 1123–1129.

Gapais D., Brun J.P., Gumiaux C., Cagnard F., Ruffet G., De Veslud C.L.C. (2015). Extensional tectonics in the Hercynian Armorican belt (France). An overview. *Bulletin de la Société Géologique de France* 186, 117–129.

Garofalo P.S., Fricker P.S., Gunther M.B., Bersani D., Lotticci P.P. (2014). Physical–chemical properties andmetal budget of gold-transporting hydrothermal fluids in orogenic deposits. In: Garofalo, P.S., Ridley, J.R. (Eds.), Gold-transporting Hydrothermal Fluids in the Earth's Crust. *Geological Society Special Publication* 402, pp. 71–102.

Gebre-Mariam M., Hagemann S.G., Groves D.I. (1995). A classification scheme for epigenetic Archaean lode-gold deposits. *Mineralium Deposita* 30, 408–410.

Glasson M.J., Keays R.R. (1978). Gold mobilisation during cleavage development in sedimentary rocks fromthe auriferous slate belt of Central Victoria, Australia: some important boundary conditions. *Economic Geology* 73, 496–511.

Gloaguen E., Branquet Y., Boulvais P., Moelo Y., Chauvel J.-J., Chiappero P.-J., Marcoux, E. (2007). Palaeozoic oolitic ironstone of the French Armorican Massif: a chemical and structural trap for orogenic base metal–As–Sb–Au mineralisation during Hercynian strike-slip deformation. *Mineralium Deposita* 42, 399–422.

Gloaguen E., Tourlière B., Angel J.M. (2016a). Revalorisation du potentiel minier français Méthodes prédictives appliquées à la province à antimoine du Massif armoricain. BRGM report. BRGM/ RP-65534-FR 71 pp.

Gloaguen E., Tourlière B., Angel J.M. (2016b). Revalorisation du potentiel minier français : le district antimonifère du Semnon (Ille-et-Vilaine, France). BRGM report. BRGM/RP-66200-FR 71 pp.

Goldfarb R.J., Santosh M. (2014). The dilemma of the Jiaodong gold deposits: are they unique? *Geoscience Frontiers* 5, 139–153.

Goldfarb R.J., Phillips G.N., Nokleberg W.J. (1998). Tectonic setting of synorogenic gold deposits of the Pacific Rim. *Ore Geology Reviews* 13, 185–218.

Goldfarb R.J., Groves D.I., Gardoll S. (2001). Orogenic gold and geologic time; a global synthesis. *Ore Geology Reviews* 18, 1–75.

Goldfarb R.J., Baker T., Dubé B., Groves D.I., Hart C.J.R., Gosselin P. (2005). Distribution, character, and genesis of gold deposits in metamorphic terranes. *Economic Geology* 100th Anniversary, 407–450.

Goldfarb R.J., Groves D.I. (2015). Orogenic gold: Common or evolving fluid and metal sources through time. *Lithos* 233, 2–26.

Gore B., Le Corre C. (1987). Cinématique hercynienne du cisaillement nord-armoricain à la bordure du granite syntectonique de Saint Renan-Kersaint (Finistère). *Bulletin de la Société Géologique de France* 3, 811–819.

Gouazou F. (2016) Circulations de fluides associés aux minéralisations Sb ± Au de Bretagne Centrale. Mémoire de Master 2. Université de Lorraine, Nancy, pp. 42.

Griffin W.L., Begg G.C., O'Reilly Y. (2013). Continental-root control on the genesis of magmatic ore deposits. *Nature Geosciences* 6, 905–910.

Groves D.I., Bierlein F. (2007). Geodynamic settings of mineral deposit systems. *Journal of Geological Society of London* 164, 19–30.

Groves D.I., Goldfarb R.J., Gebre-Mariam M., Hagemann S.G., Robert F. (1998). Orogenic gold deposits—a proposed classification in the context of their crustal distribution and relationship to other gold deposit types. *Ore Geology Reviews* 13, 7–27.

Guérangé J., Guérangé B., Chèvremont P., Corpel J., Debeglia N., Martin P., Scanvic J.Y., Etienne H., Seguin J.J., Cottez S. (1984). Stockage de déchets radioactifs en formations géologiques. Région de Château-Gontier (Mayenne). Confirmation des caractéristiques favorables, 1ére phase, 1ère et 2ème parties. Rapport BRGM 84 SGN 067 GEO, BRGM, Orléans, 12 p.

Guerrot C., Calvez J.-Y., Bonjour J.-L., Chantraine J., Chauvel J.-J., Dupret L., Rabu D. (1992). Le Briovérien de Bretagne centrale et occidentale : nouvelles données radiométriques. *Comptes Rendus de l'Académie des Sciences de Paris* 315, 1741–1746.

Guigues J. (1984). Prospection stratégique et métallogénie : caractérisation d'auréoles autour des granites hercyniens dans l'Est du Massif Armoricain (France). *Chronique de la Recherche minière* 475, 19–34.

Guiollard P.C. (1995). La mine d'or et d'antimoine de la Lucette (Mayenne). P.C. Guiollard, Fichous, 116 p.

Gumiaux C., Brun J.P., Gapais D. (2004a). Strain removal within the Hercynian Shear Belt of Central Brittany (western France): methodology and tectonic implications. *Geological Society, London, Special Publications* 224, 287–305.

Gumiaux C., Gapais D., Brun J.P., Chantraine J., Ruffet G. (2004b). Tectonic history of the Hercynian Armorican Shear belt (Brittany, France). *Geodinamica Acta* 17, 289–307.

Gumiaux C., Judenherc S., Brun J.P., Gapais D., Granet M., Poupinet G. (2004c). Restoration of lithosphere-scale wrenching from integrated structural and tomographic data (Hercynian belt of western France). *Geology* 32, 333–336.

Gumiel P., Arribas A. (1987). Antimony deposits in the Iberian Peninsula. *Economic Geology* 82, 1453–1463.

Hagemann S.G., Brown P.E. (1996). Geobarometry in Archean lode-gold deposits. *European Journal of Mineralogy* 8, 937–960.

Hagemann S.G. and Cassidy K.F. (2000). Archean orogenic lode gold deposits. *Reviews in Economic Geology* 13, 9–68.

Hagemann S.G., Lüders V. (2003). P-T-X conditions of hydrothermal fluids and precipitation mechanism of stibnite-gold mineralization at the Wiluna lode-gold deposits, Western Australia: Conventional and infrared microthermometric constraints. *Mineralium Deposita* 38, 936–952.

Hart C.J.R., McCoy D., Goldfarb R.J., Smith M., Roberts P., Hulstein R., Bakke A.A., Bundtzen T.K. (2002). Geology, exploration and discovery in the Tintina gold province, Alaska and Yukon. *Society of Economic Geologists Special Publication* 9, 241–274.

Hattori K.H., Guillot S. (2003). Volcanic fronts form as a consequence of serpentinite dehydration in the forearc mantle wedge. *Geology* 31, 525–528.

Henley R.W., Norris R.J., Paterson C.J. (1976). Multistage ore genesis in the New Zealand geosyncline: a history of post-metamorphic lode emplacement. *Mineralium Deposita* 11, 180–196.

Herrouin Y., Dadet P., Guigues J., Laville P., Talbo H. (1989). Notice explicative, Carte géologique de la France (1:50000), feuille Bain-de-Bretagne (388), BRGM, Orléans, 83 p.

Herrouin Y., Rabu D., Chantraine J., Chauvel J.J., Etienne H. (1990). Geological map of France (1/50000), notice of the Châteaubriand sheet (389), BRGM, Orléans, France 53 pp.

Hodgson C.J. (1989). The structure of shear-related, vein-type gold deposits: a review. *Ore Geology Reviews* 4, 231–273.

Hodgson C.J., Hamilton J.V. (1989). Gold mineralization in the Abitibi greenstone belt: end-stage result of Archean collisional tectonics? *Economic Geology Monograph* 6, 86–100.

Hollister L.S., Burruss R.C. (1976). Phase equilibria in fluid inclusions from the Khtada Lake metamorphic complex. *Geochimica et Cosmochimica Acta* 40, 163–175.

Houlgatte E., Le Hérissé A., Pelhate A., Rolet J. (1988). Evolution géodynamique du bassin carbonifère de Laval (Massif Armoricain). *Géologie de la France* 1, 27–46.

Hronsky J.M.A., Groves D.I., Loucks R.R., Begg G.C. (2012). A unified model for gold mineralisation in accretionary orogens and implications for regional-scale exploration targeting methods. *Mineralium Deposita* 47, 339–358.

Jegouzo P. (1980). The South Armorican Shear Zone. *Journal of Structural Geology* 2, 39–47.

Jochum K.P., Hoffmann A.W. (1997). Constraints on earth evolution from antimony in mantle-derived rocks. *Chemical Geology* 139, 39–49.

Johan Z., Marcoux E., Bonnemaison M. (1989). Arsénopyrite aurifére: mode de substitution de Au dans la structure de FeAsS. *Comptes rendus de l'Académie des sciences* 308, p. 185–191.

Jones K.A., Brown M. (1990). High-temperature 'clockwise'P-T paths and melting in the development of regional migmatites: An example from southern Brittany, France. *Journal of Metamorphic Geology* 8, 551–578.

Kay A., Strong D.F. (1983). Geologic and fluid controls on As-Sb-Au mineralization in the Moretons Harbour area, Newfoundland. *Economic Geology* 78, 1590-1604.

Kerforne F. (1910). Note sur un filon aurifère situé à Beslé (Loire-Inférieure). *C.R. Acad. Sci.,* Paris, p. 224-225.

Kerforne F. (1921). Sur la mine d'or de Beslé (Loire-Inférieure). *Bull. Soc. géol. minéral. Bretagne,* t. II, spécial, p. 177-181.

Kerrich R. (1976). Some effects of tectonic recrystallization on fluid inclusions in vein quartz. *Contributions to Mineralogy and Petrology* 59, 195–202.

Kerrich R., Cassidy K.F. (1994). Temporal relationships of lode gold mineralization to accretion, magmatism, metamorphism and deformation – Archean to present: A review. *Ore Geology Reviews* 9, 263–310.

Kontak D.J., Smith P.K., Kerrich R., Williams P.F. (1990). Integrated model for Meguma Group lode gold deposits, Nova Scotia, Canada. *Geology* 18, 238–242.

Kontak D.J., Horne R.J., Kyser K. (2011). An oxygen isotope study of two contrasting orogenic vein gold systems in the Meguma Terrane, Nova Scotia, Canada, with implications for fluid sources and genetic models. *Mineralium Deposita* 46, 289–304.

Kodolányi J., Pettke T., Spandler C., Kamber B.S., Gméling K. (2012). Geochemistry of ocean floor and fore-arc serpentinites: constraints on the ultramafic input to subduction zones. *Journal of Petrology* 53, 235–270.

Kroner U., Romer R.L. (2013). Two plates—many subduction zones: the Variscan orogeny reconsidered. *Gondwana Research* 24, 298–329.

Krupp R.E. (1988). Solubility of stibnite in hydrogen sulfide solutions, speciation, and equilibrium constants, from 25 to 350°C. *Geochimica et Cosmochimica Acta* 52, 3005-3015.

Lafay R., Deschamps F., Schwartz S., Guillot S., Godard M., Debret B., Nicollet C. (2013). High-pressure serpentinites, a trap-and-release system controlled by metamorphic conditions: example from the Piedmont zone of the western Alps. *Chemical Geology* 343, 38–54.

Lahaye Y., Blais S., Auvray B., Ruffet G. (1995). Le Volcanisme fissural paléozoique du domaine nord-armoricain. *Bulletin de la Société Géologique de France* 166, 601–612.

Large R.R., Maslennikov V., Robert F., Danyushevsky L.V., Chang, Z, (2007) Multistage sedimentary and metamorphic origin of pyrite and gold in the giant Sukhoi Log deposit, Lena gold province, Russia. *Economic Geology* 102, 1232–1267.

Large R.R., Bull S.W., Maslennikov V.V. (2011). A carbonaceous sedimentary source rock model for Carlin-type and orogenic gold deposits. *Economic Geology* 106, 331–358.

Laznicka P. (2010). Giant Metallic Deposits, 2nd edition. Springer-Verlag, Berlin Heidelberg, 950 pp.

Le Corre C. (1969). Sur une paragenèse à chloritoïde dans les schistes de l'Ordovicien moyen des synclinaux du Sud de Rennes (Massif Armoricain). *Bulletin de la Société Géologique Minéralogique de Bretagne* C, 33–44.

Le Corre, C. (1975) Analyse comparee de la cristallinite des micas dans le Brioverien et le Paleozoique centre-armoricains; zoneographie et structure d'un domaine epizonal. *Bulletin de la Société Géologique de France* 7, 547–553.

Le Corre C. (1977). Le Briovérien de Bretagne Centrale : essai de synthèse lithologique et structurale. Bulletin du BRGM I, p. 219–254.

Le Corre C. (1978). Approche quantitative des processus synschisteux. L'exemple du segment Hercynien de Bretagne Centrale. Thèse d'état Université de Rennes 1, 382 p.

Le Corre C., Auvray B., Ballèvre M., Robardet M. (1991). Le Massif Armoricain. *Scientifical Geological Bulletin* 44, 31–103.

Le Gall J. (1999). Les dolérites et basaltes tholéiitiques varisques du domaine nord-est armoricain. *Géologie de la France* 4, 3–26.

Le Gall J., Gigot P., Savaton P., Lacquement F., Poprawsky Y., Vernhet Y. (2011). Geological map of France (1/50000), Laval sheet (319), BRGM, Orléans.

Lemarchand J., Boulvais P., Gaboriau M., Boiron M. C., Tartèse R., Cokkinos M., Bonnet S., Jégouzo P. (2012). Giant quartz vein formation and high-elevation meteoric fluid infiltration into the South Armorican Shear Zone: geological, fluid inclusion and stable isotope evidence. *Journal of the Geological Society* 169, 17–27.

Lescuyer J.L., Leistel J.M., Marcoux E., Milési J.P., Thiéblemont D. (1997). Late Devonian-early Carboniferous peak sulphide mineralization in the Western Hercynides. *Mineralium Deposita* 33, 208–220.

Le Théoff B. (1977). Marqueurs ellipsoïdaux et déformation finie. Thèse d'état Université de Rennes 1, 96 p.

Leutwein F., Sonet J., Zimmermann J.L. (1968). Géochronologie et évolution orogénique précambrienne et hercynienne de la partie nord-est du Massif Armoricain. Sciences de la Terre, mémoire v.11, 84 p.

Malavielle J., Guilhot S., Costa S., Lardeaux J.M., Gardien V. (1990). Collapse of the thickened Variscan crust in the French Massif Central: Mont du Pilat extensional shear zone and St.-Etienne carboniferous basin. *Tectonophysics* 177, 139–149.

Marcoux E., Serment R., Allon A. (1984). Les gîtes d'antimoine de Vendée (Massif Armoricain, France). Historique des recherches et synthèse métallogénique. *Chronique de la Recherche Minière* 476, 3–30.

Marcoux E., Moëlo Y., Picot P., Baubron J.C. (1988). Évolution minéralogique et isotopique (Pb) du filon sulfuré complexe des Borderies (Massif central français) — Implications métallogéniques. *Mineralium Deposita* 23, 58–70.

Mattauer M., Brunel M., Matte P. (1988). Failles normales ductiles et grands chevauchements. Une nouvelle analogie entre l'Himalaya et la chaîne hercynienne du Massif central français. *Comptes rendus de l'Académie des sciences. Série 2, Mécanique, Physique, Chimie, Sciences de l'univers, Sciences de la Terre* 306(10), 671–676.

Matte P. (1986). La chaîne Varisque parmi les chaînes Paléozoïques péri atlantiques, modèle d'évolution et position des grands blocs continentaux au Permo-Carbonifère. *Bulletin de la Société Géologique de France* 2, 9–24.

Matte P. (2001). The Variscan collage and orogeny (480–290 Ma) and the tectonic definition of the Armorica microplate: a review. *Terra nova* 13, 122–128.

McCoy D., Newberry R.J., Layer P., DiMarchi J.J., Bakke A., Masterman J.S., Minehane D.L. (1997) Plutonic-related gold deposits of Interior Alaska. *Economic Geology Monograph* 9, 191–241.

McCuaig T.C., Kerrich R. (1998). P-T-t-deformation-fluid characteristics of lode gold deposits: evidence from alteration systematics. *Ore Geology Reviews* 12, 381–453.

Menillet F., Plaine J., Manigault B., Le Hérissé A. (1988). Notice explicative, Carte géologique de la France (1:50000), feuille Meslay-du-Maine (356), BRGM, Orléans, 79 p.

Moëlo Y., Lulzac Y., Rouer O., Palvadeau P., Gloaguen E., Léone P. (2002). Scandium mineralogy: pretulite with scandian zircon and xenotime-(Y) within an apatite-rich oolitic ironstone from Saint-Aubin-Des-Châteaux, Armorican Massif, France. *Canadian Mineralogist* 40, 1657–1673.

Moëlo Y., Rouer O., Bouhnik-Le Coz M. (2008). From diagenesis to hydrothermal recrystallisation: polygenic Sr-rich fluorapatite from the oolitic ironstone of Saint-Aubin-des-Châteaux (Armorican Massif, France). *European Journal of Mineralogy* 20, 205–216.

Monié P., Respaut J.P., Brichaud S., Bouchot V., Faure M., Roig J.-Y. (2000). $^{40}Ar/^{39}Ar$ and U–Pb geochronology applied to Au–W–Sb metallogenesis in the Cévennes and Châtaigneraie districts (Southern Massif Central, France). In: Bouchot, V., Moritz, R. (Eds.), A Geode–GéoFrance 3D Workshop on Orogenic Gold Deposits in Europe with Emphasis on the Variscides; Extended Abstracts. Documents du BRGM 297, 77–79.

Mortensen J.K., Craw D., MacKenzie D.J., Gabites J.E., Ullrich T.E. (2010). Age and origin of orogenic gold mineralization in the Otago Schist Belt, South Island, New Zealand: constraints from lead isotope and 40Ar/39Ar dating studies. *Economic Geology* 105, 777–793.

Munoz M., Courjault-Radé P., Tollon F. (1992). The massive stibnite veins of the French Palaeozoic basement: a metallogenic marker of Late Variscan brittle extension. *Terra Nova* 4, 171–177.

Munoz M., Shepherd T.J. (1987). Fluid inclusion study of the Bournac polymetallic (Sb-As-Pb-Zn-Fe-Cu...) vein deposit (Montagne Noire, France). *Mineralium Deposita* 22, 11–17.

Neiva A.M.R., Andras P., Ramos J.M.F. (2008). Antimony quartz and antimony–gold quartz veins from northern Portugal. *Ore Geology Reviews* 34, 533–546.

Němec M., Zachariáš J. (2017). The Krásná Hora, Milešov, and Příčovy Sb-Au ore deposits, Bohemian Massif: mineralogy, fluid inclusions, and stable isotope constraints on the deposit formation. *Mineralium Deposita* doi: 10.1007/s0012.

Nesbitt B.E., Murowchick J.B., Muehlenbachs K. (1986). Dual origins of lode gold deposits in the Canadian Cordillera. *Geology* 14, 506-509.

Nesbitt B.E, Muehlenbachs K., Murowchick B. (1989). Genetic Implications of Stable Isotope Characteristics of Mesothermal Au Deposits and Related Sb and Hg Deposits in the Canadian Cordillera. *Economic Geology* 84, 1489-1506.

Obolensky A.A., Gushchina L.V., Borisenko A.S., Borovikov A.A., Pavlova G.G. (2007) Antimony in hydrothermal processes: solubility, conditions of transfer, and metal-bearing capacity of solutions. *Russian Geology and Geophysics* 48, 992–1001.

Ortega L., Vindel E. (1995). Evolution of ore-forming fluids associated with late Hercynian antimony deposits in central/western Spain: case study of Mari Rosa and El Juncalón. *European Journal of Mineralogy* 7, 655–673.

Ortega L., Vindel E., Beny C. (1991a). C-O-H-N fluid inclusions associated with gold-stibnite mineralization in low-grade metamorphic rocks, Mari Rosa mine, Caceres, Spain. Mineralogical Magazine 55, 235–247.

Ortega L., Oyarzun R., Gallego M. (1996). The Mari Rosa late Hercynian Sb–Au deposit, western Spain. *Mineralium Deposita* 31, 172–187.

Paris F., Robardet M. (1990). Early Paleozoic paleobiogeography of the Variscan regions. *Tectonophysics* 177, 192–213.

Paris F., Robardet M. (1994). Paleogeographic Synthesis. In: Chantraine, J., Rolet, J., Santallier, D.S., Piqué, A., and Keppie, J.D. (eds.), Pre-Mesozoic Geology in France and Related Areas, IGCP-Project 233, Springer Berlin Heidelberg, p. 172–176.

Peng J.-T., Hu R.-Z., Burnard P.G. (2003). Samarium–neodymium isotope systematics of hydrothermal calcites from the Xikuangshan antimony deposit (Hunan, China): the potential of calcite as a geochronometer. *Chemical Geology* 200, 129–136.

Périchaud J.J. (1980). L'antimoine, ses minérais et ses gisements. Synthèse gîtologique sur les gisements du Massif Central français. *Chronique de la Recherche Minière* 456, 5–64.

Perroud H. (1985) Synthèse des résultats paléomagnétiques sur le Massif Armoricain. *Hercynica* 1, 65–71.

Phillips G.N., Powell R. (1993). Link between gold provinces. *Economic Geology* 88, 1084–1098

Phillips G.N., Powell R. (2010). Formation of gold deposits: a metamorphic devolatilisation model. *Journal of Metamorphic Geology* 28, 689–718.

Picot P., Marcoux E., Guillemin C. (1987). Nouvelles données sur la métallogénie de l'or. *Comptes rendus de l'Académie des sciences* 304, 221–226.

Pitcairn I.K., Teagle D.A.H., Craw D., Olivo G.R., Kerrich R., Brewer T.S. (2006). Sources of metals in orogenic gold deposits: insights from the Otago and Alpine Schists, New Zealand. *Economic Geology* 101, 1525–1546.

Pitcairn I.K., Olivo G.R., Teagle D.A.H., Craw D. (2010). Sulfide evolution during prograde metamorphism of the Otago and Alpine Schists, New Zealand. *Canadian Mineralogist* 48, 1267–1296.

Pitcairn I.K., Craw D., Teagle D.A.H. (2014a). The gold conveyor belt: largescale gold mobility in an active orogen. *Ore Geology Reviews* 62, 129–142.

Pitcairn I.K., Craw D., Teagle D.A.H. (2014b). Metabasalts as sources of metals in orogenic gold deposits. *Mineralium Deposita* 62, 129–142.

Poulsen K.H., Robert F., Dubé B. (2000). Geological classification of Canadian gold deposits. Geological Survey of Canada Bulletin 540 (106 p).

Précigout J., Prigent C., Palasse L., Pochon A. (2017). Water pumping in mantle shear zones. *Nature Communications* 8, doi: 10.1038/ncomms15736.

Richards J.P. (2011). Magmatic to hydrothermal metal fluxes in convergent and collided margins. *Ore Geology reviews* 40, 1–26.

Ridley J.R., Diamond L.W. (2000). Fluid chemistry of orogenic lode gold deposits and implications for genetic models. *Reviews in Economic Geology* 13, 141–162.

Robb L. (2005). Introduction to ore-forming processes. Blackwell publishing, 373p.

Robert F. (1996). Quartz-carbonate vein gold. In: Eckstrand, O.R., Sinclair, W.D., Thorpe, R.I. (eds.), Geology of Canadian mineral deposit types, Geological Survey of Canada, Geology of Canada 8, 350–366.

Robert F., Brommecker R., Bourne B.T., Dobak P.J., McEwan C.J., Rowe R.R., Zhou X. (2007). Models and exploration methods for major gold deposit types. In: Milereit, B. (Ed.), Proceedings of Exploration '07: Fifth Decennial Conference onMineral Exploration, 691–711.

Rudnick R.L., Gao S. (2003). Composition of the continental crust. *Treatise on geochemistry* 3, 659 pp.

Ruffet G., Féraud G., Amouric M. (1991). Comparison of $^{40}Ar/^{39}Ar$ conventional and laser dating of biotites from the North Tregor batholith. *Geochimica Cosmochimica Acta* 55, 1675–1688.

Ruffet G., Féraud G., Ballèvre M., Kiénast J.R. (1995). Plateau ages and excess argon in phengites: A ^{40}Ar-^{39}Ar laser probe study of Alpine micas (Sesia Zone, Western Alps, northern Italy). *Chemical Geology (Isotopic Geoscience Section)* 121, 327–343.

Scambelluri M., Bottazzi P., Trommsdorff V., Vannucci R., Hermann J., Gòmez-Pugnaire M.T., Lòpez-Sànchez Vizcaìno V, (2001a). Incompatible element-rich fluids released by antigorite breakdown in deeply subducted mantle. *Earth and Planetary Science Letters* 192, 457–470.

Scambelluri M., Rampone E., Piccardo G.B. (2001b). Fluid and element cycling in subducted serpentinite: a trace-element study of the Erro–Tobbio high pressure ultramafites (Western Alps, NW Italy). *Journal of Petrology* 42 (1), 55–67.

Scambelluri M., Fiebig J., Malaspina N., Müntener O., Pettke T. (2004a). Serpentinite subduction: implications for fluid processes and trace-element recycling. *International Geology Review* 46, 595–613.

Scambelluri M., Müntener O., Ottolini L., Pettke T.T., Vannucci R. (2004b). The fate of B, Cl and Li in the subducted oceanic mantle and in the antigorite breakdown fluids. *Earth and Planetary Science Letters* 222, 217–234.

Schwarz-Schampera U. (2014). Antimony. In: Gunn, G. (Ed.), Critical Metals Handbook. John Wiley & Sons, pp. 70–98.

Serment R. (1978). La mine d'antimoine et or de la Lucette (Mayenne, France) : Historique - Etat des connaissances sur les travaux d'exploitation (1900-1934). *Chronique de la Recherche minière* 442, 35–52.

Shikina N.D., Zotov A.V. (1991). Thermodynamics parameters of $Sb(OH)^0_{3(sol)}$ up to 723.15 K and 1000 bar. *Geochemistry International* 28, 97–103.

Sibson R.H., Moore J.M., Rankin A.H. (1975). Seismic pumping: a hydrothermal fluid transport mechanism. *Journal of the Geological Society* 131, 653–659.

Sillitoe R.H., Thompson J.F.H. (1998). Intrusion-related vein gold deposits: types, tectono-magmatic settings and difficulties of distinction from orogenic gold deposits. *Resource Geology*, 48, 237–250.

So C.-S., Yun S.-Y. (1997). Jurassic mesothermal gold mineralization of the Samhwanghak Mine, Youngdong area, Republic of Korea; constraints on hydrothermal fluid geochemistry. *Economic Geology* 92, 60–80.

Spycher N.F., Reed M.H. (1989). As(III) and Sb(III) sulfide complexes: An evaluation of stoichiometry and stability from existing experimental data. *Geochimica et Cosmochimica Acta* 53, 2185–2194.

Stanley C.J., Halls C., Camm G.S., James J. (1990). Gold-antimony mineralization at Loddiswell, Devon, UK. Terra Nova 2, 224–231.

Tartèse R., Boulvais P. (2010). Differentiation of peraluminous leucogranites "en route" to the surface. *Lithos* 114, 353–368.

Tartèse R., Ruffet G., Poujol M., Boulvais P., Ireland T.R. (2011). Simultaneous resetting of the muscovite K-Ar and monazite U-Pb geochronometers: a story of fluids. *Terra Nova* 23, 390–398.

Tartèse R., Boulvais P., Poujol M., Chevalier T., Paquette J.L., Ireland T.R., Deloule E. (2012). Mylonites of the South Armorican Shear Zone: insights for crustal-scale fluid flow and water–rock interaction processes. *Journal of Geodynamics* 56, 86–107.

Tartèse R., Poujol M., Gloaguen E., Boulvais P., Drost K., Košler J., Ntaflos T. (2015). Hydrothermal activity during tectonic building of the Variscan orogen recorded by U-Pb systematics of xenotime in the GrèsArmoricain formation, Massif Armoricain, France. *Mineralogy and Petrology* 109, 485–500.

Tenthorey E., Hermann J. (2004). Composition of fluids during serpentinite breakdown in subduction zones: evidence for limited boron mobility. *Geology* 32, 865–868.

Thomas H.V., Large R.R., Bull S.W., Maslennikov V., Berry R.F., Fraser R., Froud S., Moye R. (2011). Pyrite and Pyrrhotite textures and composition in sediments, laminated quartz veins and reefs at Bendigo Gold Mine, Australia: insights into ore genesis. *Economic Geology* 106, 1–31.

Tomkins A.G. (2010). Windows of metamorphic sulfur liberation in the crust: implications for gold deposit genesis. *Geochimica Cosmochimica Acta* 74, 3246–3259.

Tomkins A.G. (2013). On the source of orogenic gold. *Geology* 41, 1255–1256.

Tremblay A., Ruffet G., Bédard J.H. (2011). Obduction of Tethyan-type ophiolites—A case-study from the Thetford-Mines ophiolitic Complex, Quebec Appalachians, Canada. *Lithos* 125, 10–26.

Triboulet C.L., Audren C. (1988). Controls on P–T–t deformation path from amphibole zonation during progressive metamorphism of basic rocks (estuary of the River Vilaine, South Brittany, France). *Journal of Metamorphic Geology* 6, 117–133

Van Der Voo R. (1983). Paleomagnetic constraints on the assembly of the old red continent. *Tectonophysics* 91, 273–283.

Vasquez-Lopez R., De Solere B., De Vaucorbeil H. (1985a). Les minéralisations aurifères de Vieuville (Mayenne). Rapport BRGM 85 RDM 011 FE, BRGM, Orléans, 55 p.

Vasquez-Lopez R., De Solere B., De Vaucorbeil H. (1985b). Les minéralisations aurifères du Coudreau (Mayenne). Rapport BRGM 85 RDM 012 FE, BRGM, Orléans, 49 p.

Vernhet Y. (2010) Carte géologique de la France (1/50000), feuille Craon (390), BRGM, Orléans.

Vils F., Pelletier L., Kalt A., Müntener O., Ludwig T. (2008). The lithium, boron and beryllium content of serpentinized peridotites from ODP Leg 209 (Sites 1272A and 1274A): implications for lithium and boron budgets of oceanic lithosphere. *Geochimica et Cosmochimica Acta* 72, 5475–5504.

Vils F., Müntener O., Kalt A., Ludwig T. (2011). Implications of the serpentine phase transition on the behaviour of beryllium and lithium-boron of subducted ultramafic rocks. *Geochimica et Cosmochimica Acta* 75, 1249–1271.

Wagner T., Cook N.J. (2000). Late-Variscan antimony mineralization in the Rheinisches Schiefergebirge, NW: evidence for stibnite precipitation by drastic cooling of high temperature fluid systems. *Mineralium Deposita* 35, 206–222.

Watts M.S., Williams G.D. (1979). Faults rocks as indicators of progressive shear deformation in the Guingamp region, Brittany. *Journal of Structural Geology* 1, 323–332

Whitney D.L., Evans B.W. (2010). Abbreviations for names of rock-forming minerals. *American Mineralogist* 95, 185–187.

Williams-Jones A.E., Normand C. (1997). Controls of mineral parageneses in the System Fe-Sb-S-O. *Economic Geology* 92, 308–324.

Willman C.E., Korsch R.J., Moore D.H., Cayley R.A., Lisitsin V.A., Rawling T.J., Morand V.J., OShea P.J. (2010). Crustal-scale fluid pathways and source rocks in the Victorian Gold Province, Australia: insights from deep seismic reflection profiles. *Economic Geology* 105, 895–915.

Wood S.A., Crerar D.A., Borcsik M.P. (1987). Solubility of the assemblage pyrite-pyrrhotite-magnetite-galena-gold-stibnite-bismuthinite-argentite-molybdeniitne H_2O-NaC1-CO_2 solutions from 200 to 350°C. *Economic Geology* 82, 1864–1887.

Wyns R., Lablanche G., Lefavrais-Raymond A. (1988). Notice explicative, Carte géologique de la France (1:50000), feuille Chantonnay (563), BRGM, Orléans, 81 p.

Yang D.S., Shimizu M., Shimazaki H., Li X.H., Xie Q.L. (2006). Sulfur isotope geochemistry of the supergiant Xikuangshan Sb deposit, central Hunan, China: Constraints on sources of ore constituents. *Resource Geology* 56, 385–396.

Annexes

Annexe 1

Typologie et référencement de tous les indices antimonifères connus du Massif Armoricain

Gisement	Couffé	Menez Hom	Rosnoen	Scubériou	Bois Roux	Chailland
Localisation	Bassin d'Ancenis	Bassin de Chateaulin	Bassin de Chateaulin	Bassin de Chateaulin	Bassin de Laval	Bassin de Laval
X (LII étendu, m)	326097.1355	112622.6554	115297.1269	178124.5907	310706.2568	360781.8757
Y (LII étendu, m)	2271894.873	2376328.385	2384140.593	2379256.342	2370254.718	2361601.266
Substances	Sb	Sb	Sb	Sb	Sb	Sb
Minéralogie principale	Stibine	Stibine	Stibine, pyrite	Stibine, stibiconite	Stibine	Stibine, pyrite
Minéralogie accessoire	/	/	/	Pyrite	Pyrite, sphalérite	/
Indications morphologiques	Filon ou veine (puissance > 50 cm), en champ ou isolé, discordant	Amas et lentille stratiformes (syn-encaissant) de minerai massif à sub-massif	Amas et lentille stratoïdes (stratabound) de minerai massif à sub-massif	Filon ou veine (puissance > 50 cm), en champ ou isolé, discordant	?	Filon ou veine (puissance > 50 cm), en champ ou isolé, discordant
Gangue			Graphite	Quartz	Quartz, calcite	?
Encaissant	Psammite	Grès	Schistes noir, schistes ampélitique	Schistes	Schistes, calcaires	Schistes et quartzites
Orientation (dir360)	?	?	?	?	?	?

Gisement	Bariteau	Chavagnes en Paillers	Grand Boireau	Grezaye	La Baussonnière	La Daudière
Localisation	District Vendéen	District Vendéen	District Vendéen	District Vendéen	District Vendéen	District Vendéen
X (LII étendu, m)	345278.6253	327704.2649	324762.8571	325672.0148	353900.9465	352499.3024
Y (LII étendu, m)	2207374.768	2215703.686	2205921.099	2205014.105	2202398.625	2203101.552
Substances	Sb	Sb	Sb	Sb	Sb	Sb, Au
Minéralogie principale	Stibine	Stibine	Stibine	Stibine	Stibine	Stibine
Minéralogie accessoire	/	/	Berthierite, melnicovite, stibiconite	Melnicovite, stibiconite	Pyrite, or natif, stibiconite	Or natif, covellite
Indications morphologiques	Filon	Filon	Filon avec une puissance allant de 1 à 8 m avec une extension de 900 m	Filon avec une extension de 80 m	Filon avec une puissance allant de 10 à 30 cm avec une extension de 25 m	Filon
Gangue	Quartz calcédonieux	Quartz	Quartz	Quartz	Quartz	Quartz calcedonieux
Encaissant	Schistes	Quartzites, phyllades	Gneiss à 2 micas, grenats, staurotide	Gneiss	Schistes	Schistes et grès
Orientation (dir360)	N270, 80	N135	N310, 70	N135	N275, 60	N270, 70

Gisement	Liffré	Port Brillet	Quénon	Taillis	Laize La Ville	Trois Monts
Localisation	Bassin de Laval	Bassin de Laval	Bassin de Laval	Bassin de Laval	Bocage Normand	Bocage Normand
X (LII étendu, m)	314972.4014	353400.2686	305362.85	334185.9306	402440.3825	395340.0542
Y (LII étendu, m)	2364014.873	2350287.557	2368480.366	2358153.92	2457510.126	2454896.926
Substances	Sb	Sb, Au	Sb	Sb	Sb, Ba	Sb
Minéralogie principale	Stibine, stibiconite	Stibine, chalcopyrite, cuivre gris	Stibine, marcassite, mélantérite	Stibine	Stibine, barytine	Stibine
Minéralogie accessoire	/	Or natif, pyrite, sphalérite, galène	Chalcopyrite, stibiconite	/	/	Pyrite
Indications morphologiques	Stockwerk (ou réseau) de filonnets ou veinules (puissance < 50 cm), discordant sur les strates	Stockwerk (ou réseau) de filonnets ou veinules (puissance < 50 cm), discordant sur les strates	Amas et lentille stratiformes (syn-encaissant) de minerai massif à sub-massif	Stockwerk (ou réseau) de filonnets ou veinules (puissance < 50 cm), discordant sur les strates	Stockwerk (ou réseau) de filonnets ou veinules (puissance < 50 cm), discordant sur les strates	Stockwerk (ou réseau) de filonnets ou veinules (puissance < 50 cm), discordant sur les strates
Gangue	Quartz	Quartz	Calcite, quartz	?	Calcite	?
Encaissant	grès schisteux	Schistes et quartzites	Calcaires	Schistes gréseux	Marbre, Cipolin	Schistes
Orientation (dir360)	?		?	?	?	

Gisement	Kerveady	Mez An Lez	Munuguic	Ty Gardien (Les Moulins)	Erbray	Chalonnes - 1
Localisation	CSA	CSA	CSA	CSA	CSA	Unité de Saint-Georges-sur-Loire
X (LII étendu, m)	124600.2204	128201.034	125796.2468	122598.6451	327999.5489	362599.6642
Y (LII étendu, m)	2354294.65	2352998.777	2353996.659	2354792.534	2300699.128	2267595.059
Substances	Sb	Sb	Sb	Sb	Sb	Pb, Sb
Minéralogie principale	Stibine, berthierite	Stibine	Stibine	Stibine	Stibine	Stibine, galène
Minéralogie accessoire	Melnicovite, pyrite, antimoine natif, arsenopyrite, zinkenite, plagionite	Arsenopyrite, melnicovite, kermésite, berthierite, argent natif, antimoine natif, pyritosphères, antimonocres	/	Sphalérite, arsénopyrite, berthierite, pyrite, pyrrhotite, antimoine natif, marcassite, zinkenite, plagionite, melnicovite	Kermesite, Valentinite, Stibiconite	Chalcopyrite
Indications morphologiques	Nombreux filonnets minéralisés (avec une puissance de 10 cm) disposés en stockwerk	Filon avec une puissance d'environ 50cm (avec des lentilles minéralisées de 15 à 20 cm)	?	Filon à puissance variable à lentilles métriques de stibine massive	Veinules ou amas disséminés au sin de l'encaissant	Amas et lentille stratiformes (syn-encaissant) de minerai massif à sub-massif
Gangue	Quartz	Quartz	Quartz	Quartz	Calcite	
Encaissant	Contact leucogranite-trondhjemite	Contact granite-micaschistes	Contact leucogranite-trondhjemite	Contact leucogranite-trondhjemite	Calcaire	Calcaire
Orientation (dir360)	N110, 80	N140	N0	N180, 75	?	?

Gisement	La Veronnière	Les Brouzils	Mervent	Mesnard-La-Barotière	Puits Ouvrard	Rochetréjoux
Localisation	District Vendéen	District Vendéen	District Vendéen	District Vendéen	District Vendéen	District Vendéen
X (LII étendu, m)	324891.7433	322502.4546	362000.7901	337716.3702	346230.889	345831.4176
Y (LII étendu, m)	2200910.154	2213930.307	2173995.311	2212797.605	2207583.458	2204285.049
Substances	Sb, Au	Sb	Sb, Au	Sb, Au	Sb	Sb, Au
Minéralogie principale	Stibine, berthierite	Stibine	Stibine	Stibine, arsenopyrite, berthierite	Stibine	Stibine
Minéralogie accessoire	Arsenopyrite, sphalérite, or natif, schwarzite, chalcopyrite, pyrite, marcassite, tétraédrite	Arsenopyrite, berthierite, pyrite, sphalérite, melnicovite, covellite, stibiconite	Or natif, galène	Or natif, chalcopyrite, galène, pyrite, pyrrhotite, sphalérite, tétraédrite	/	Pyrite, marcassite, berthierite, sphalérite, chalcostibite, or natif
Indications morphologiques	Filon avec une extension de 1300m en surface	Filon avec une puissance allant de 0,40 cm à 3 m avec une extension d'au moins 700 m	Filon ou veine (puissance > 50 cm), en champ ou isolé, discordant	Filon avec une puissance allant de 1 à 2 m avec une extension de 3200 m	Filon avec une puissance allant de 10 à 20 cm avec une extension de 100 m	Filon avec une puissance allant de 0,50 à 3 m avec une extension de 1100 m en surface et de 800 m en galerie
Gangue	Quartz	Quartz	Quartz	Quartz	Quartz	Quartz
Encaissant	Orthogneiss	Pelites et grès	Gneiss	Méta-siltite, schistes noirs et ampéliteux	Schistes	Grès schisteux
Orientation (dir360)	N320, 30	N35, 80	?	N125, 75	N90	N340-345 et N315-N325, 60-70

Gisement	Port de Roche	Belligné	La Rouxière	Mozé-sur-Louet	Montjean - 1	Montjean - 2
Localisation	Paléozoique de Bretagne Centrale (Synclinal de Martigné-Ferchaud)	Unité de Saint-Georges-sur-Loire	Unité de Saint-Georges-sur-Loire	Unité de Saint-Georges-sur-Loire	Unité de Saint-Georges-sur-Loire	Unité de Saint-Georges-sur-Loire
X (LII étendu, m)	286201.2622	346701.607	345303.0584	384176.739	358997.9646	361599.5721
Y (LII étendu, m)	2313296.737	2280503.696	2276401.996	2266070.087	2268997.519	2268102.447
Substances	Sb	Hg, Sb	Hg, Sb	Sb, Au	Pb, Sb	Pb, Sb
Minéralogie principale	Stibine, arsenopyrite	Stibine, cinabre	Stibine, cinabre	Stibine,	Stibine, galène	Stibine, galène
Minéralogie accessoire	/	Sphalérite, marcassite, pyrite	Sphalérite, marcassite, pyrite, tetraédrite, tennantite	Sphalérite, pyrite, or natif, chalcopyrite, arsenopyrite, berthierite, melnicovite	Chalcopyrite	Chalcopyrite
Indications morphologiques	Filon ou veine (puissance > 50 cm), en champ ou isolé, discordant	Filon ou veine (puissance > 50 cm), en champ ou isolé, discordant	Filon ou veine (puissance > 50 cm), en champ ou isolé, discordant	Stockwerk (ou réseau) de filonnets ou veinules (puissance < 50 cm), discordant sur les strates	Amas et lentille stratiformes (syn-encaissant) de minerai massif à sub-massif	Amas et lentille stratiformes (syn-encaissant) de minerai massif à sub-massif
Gangue	Quartz	Quartz	Quartz	Quartz, chlorite, sidérite		
Encaissant	Schistes pourpres	Schistes pyriteux et sériciteux	Psammites	Pélites et grès	Calcaire	Calcaire
Orientation (dir360)				?	?	?

Gisement	Le Chiron	La Saluade	Basse Combe	L'Eraudière	Le Reclus	Theolen
Localisation	District Vendéen	District Vendéen	District Vendéen	District Vendéen	District Vendéen	Cap Sizun
X (LII étendu, m)	325309.603	325394.5927	324674.9246	349544.4999	357414.5178	
Y (LII étendu, m)	2217206.287	2200762.026	2200772.609	2206244.446	2187976.763	
Substances	Sb, Au	Sb	Sb	Sb	Sb	Sb
Minéralogie principale	Stibine	Stibine	Stibine	Stibine	Stibine, berthierite	Stibine, sphalérite
Minéralogie accessoire	/	/	/		Limonite, barytine	/
Indications morphologiques	Filon	Filon	Filon	Minces filonnets de stibine massive (<10 cm) avec une puissance de 1,10 m	Filon d'une puissance allant de 1 à 10m sur une extension de 800m	?
Gangue	Quartz calcédonieux	Quartz	Quartz	Quartz	Quartz, barytine	Quartz
Encaissant	Schistes gréseux	Orthogneiss	Orthogneiss	Schistes	Schistes	Contact Micaschistes-Trondhjémites
Orientation (dir360)	N15	N140	N140	N255, 70	N150, 70	N340, 70

Gisement	Combourtillé	La Lucette	La Riottais	Les Gâches	La Ramée	La Télachère
Localisation	Bassin de Laval	Bassin de Laval	Bassin de Laval	Bassin de Laval	District Vendéen	District Vendéen
X (LII étendu, m)	333601.9235	357702.8551	362469.6854	321066.8045	348449.6052	325019.4761
Y (LII étendu, m)	2368632.31	2348894.542	2366507.868	2368519.301	2205726.783	2216496.898
Substances	Sb	Sb, Au	Sb	Sb, Au	Sb	Sb, Au, As, Cu, Zn
Minéralogie principale	Stibine, stibiconite	Stibine, arsenopyrite	Stibine, pyrite	Stibine, stibiconite	Stibine	Stibine, sphalérite
Minéralogie accessoire	Marcassite, pyrite, rutile	Or natif, pyrite, sphalérite, chalcostibite, tetrahedrite, scheelite, jamesonite, galène	/	Arsénopyrite, pyrite	Pyrite, marcassite, pyrrhotite, arsenopyrite, barytine, sphalérite, chalcopyrite, stibiconite	Tétraédrite, arsénpyrite, or natif, chalcopyrite, berthierite, pyrite, sphalérite, pentlandite, pyrrhotite, cobaltite, galène, melnicovite, kermésite, covellite, digénite, stibiconite
Indications morphologiques	Stockwerk (ou réseau) de filonnets ou veinules (puissance < 50 cm), discordant sur les strates	Filon ou veine (puissance > 50 cm), en champ ou isolé, discordant	Filon ou veine (puissance > 50 cm), en champ ou isolé, discordant	Stockwerk (ou réseau) de filonnets ou veinules (puissance < 50 cm), discordant sur les strates	Filon avec une puissance allant de 10 à 50 cm avec une extension de 375 m	Filon avec une puissance allant de 10 à 20 cm avec une extension de 10 à 40 m
Gangue	?	Quartz, calcite, ankérite	?	Quartz	Quartz calcedonieux, barytine	Quartz
Encaissant	Schistes ardoisiers (phyllades)	Schistes, grès	grès	grès	Schistes et grès	Schistes et micaschistes quartzo-chloriteux
Orientation (dir360)	?	N30, 90	?	?	N270, 65	N250, 25

Gisement	La Davière	La Poitière	Kerjulien	Angers	Bestrée	Kerdévot
Localisation	District Vendéen	District Vendéen	Briovérien de Bretagne Centrale	CSA	CSA	CSA
X (LII étendu, m)	348634.1945	353299.3396	159700.1955	387498.7309	74400.79235	129398.9427
Y (LII étendu, m)	2205339.028	2202300.976	2353396.942	2277797.46	2360794.779	2352701.407
Substances	Sb	Sb	Sb	Sb	Sb	Sb
Minéralogie principale	Stibine, pyrite	Stibine	Stibine, stibiconite	Stibine	Stibine	Stibine
Minéralogie accessoire	Sphalérite	/	Séricite, zinkénite, plagionite, antimoine natif, arsenopyrite, sphalérite	/	Arsénopyrite, pyrite, marcassite, antimoine natif, sphalérite, zinkénite, plagionite, melnicovite, semseyite, fülöppite, jamesonite, galène antimonifère	/
Indications morphologiques	Filon avec une puissance allant de 5 à 40 cm avec une extension de 540 m	Filon avec une puissance de 20 cm	Filon ou veine (puissance > 50 cm), en champ ou isolé, discordant	Amas et lentille stratiformes (syn-encaissant) de minerai massif à sub-massif	Filon avec une puissance de 20 cm (3 à 4cm de stibine massive)	Filon avec une puissance de 15 cm de stibine avec une extension de quelques centaines de mètres
Gangue	Quartz calcédonieux	Quartz	Quartz	Calcite	Quartz	Quartz
Encaissant	Schistes et grès	Schistes	Leucogranite de Scaër	Calcaires	Leucogranite	Contact leucogranite-micaschistes
Orientation (dir360)	N270, 70	N270,70			N30, 90	N320, 60

Gisement	Chalonnes - 2	Ber ar Galez	Pors Loubous	Pointe du Castel	Sainte Marie (85)	Batz-sur-Mer
Localisation	Unité de Saint-Georges-sur-Loire	Île de Sein	Pont Croix	Pont Croix	District Vendéen	Domaine interne : Sud du CSA
X (LII étendu, m)	366703.5533				349081.2094	235602.4107
Y (LII étendu, m)	2264695.415				2205389.608	2263793.139
Substances	Pb, Sb	Sb	Sb	Sb	Sb	Sb
Minéralogie principale	Stibine, galène	Stibine, sphalérite, kermésite	Stibine, berthierite	Stibine	Stibine	Stibine
Minéralogie accessoire	Chalcopyrite	Pyrite, arsénopyrite, marcassite, chalcopyrite, cuivre gris, zinkénite, semseyite, plagionite, antimoine natif	Arsénopyrite, melnicovite, sphalérite	Melnicovite	Pyrite	Kermesite, Stibiconite
Indications morphologiques	Amas et lentille stratiformes (syn-encaissant) de minerai massif à sub-massif	Stockwerk (ou réseau) de filonnets ou veinules (puissance < 50 cm), discordant sur les strates	Stockwerk (ou réseau) de filonnets ou veinules (puissance < 50 cm), discordant sur les strates	Stockwerk (ou réseau) de filonnets ou veinules (puissance < 50 cm), discordant sur les strates	Filon avec une puissance allant de 5 à 40 cm avec une extension de 540 m	Filon ou veine (puissance > 50 cm), en champ ou isolé, discordant
Gangue		Quartz	Quartz	Quartz	Quartz calcédonieux	Quartz
Encaissant	Calcaire	Leucogranite	Paragneiss	Migmatites	Schistes	Leucogranite
Orientation (dir360)	?	N60, 90	N30, 60	N170	N270, 70	?

Gisement	La Coëfferie	Le Semnon	La Chapelle Saint Melaine 1	Saint-Jean	Lesven	Leuriou Penhoat
Localisation	Paléozoique de Bretagne Centrale (Synclinal de Martigné-Ferchaud)	Paléozoique de Bretagne Centrale (Synclinal de Martigné-Ferchaud)	CSA	Pont Croix	Douarnenez	Quimper
X (LII étendu, m)	324101.9199	324099.6766	280401.5544			
Y (LII étendu, m)	2322296.094	2322296.2	2308698.249			
Substances	Sb, Au	Sb, Au	Sb, Au	Sb	Sb, As	Sb
Minéralogie principale	Stibine, berthierite	Stibine, berthierite, arsenopyrite	Stibine, jamesonite	Stibine	Stibine, melnicovite	Stibine
Minéralogie accessoire	Scheelite, or natif, antimoine natif, melnicovite, chalcopyrite, pyrite, galène, sphalérite, boulangérite, bournonite, ullmannite, chalcostibite	Or natif, pyrite, antimoine natif, ullmannite, sphalérite, aurostibite, chalcopyrite, bournonite, chalcostibite	Anglesite, bournonite, chalcopyrite, enargite, sphalérite, pyrite, arsénopyrite, covellite, malachite, stibiconite, cassitérite	/	Pyrite, pyrrhotite, arsénopyrite, antimoine natif, zinkénite, plagionite, sphalérite	/
Indications morphologiques	Champ de filons discordants (n*km2, n*ha)	Filon ou veine (puissance > 50 cm), en champ ou isolé, discordant	Filon croiseur puissant de 20 à 50 cm	Filon ou veine (puissance > 50 cm), en champ ou isolé, discordant	Stockwerk (ou réseau) de filonnets ou veinules (puissance < 50 cm), discordant sur les strates	Stockwerk (ou réseau) de filonnets ou veinules (puissance < 50 cm), discordant sur les strates
Gangue	Quartz, calcite	Quartz, calcite	Quartz	Quartz	Quartz	Quartz
Encaissant	Dolérite, diabase	Dolérite, diabase	Schistes	Migmatites	Trondhjémite	Contact leucogranite-gneiss
Orientation (dir360)	?	?	N20, 75 et N140	N150, 90	N350, 60	N135, 80

Annexe 2

Supporting information for:

Metal mobility during hydrothermal breakdown of Fe-Ti oxides: insights from Sb-Au mineralizing event (Variscan Armorican Massif, France)

Anthony Pochon[1*], Georges Beaudoin[2], Yannick Branquet[1, 3], Philippe Boulvais[1], Eric Gloaguen[3, 4], Denis Gapais[1]

[1] *Géosciences Rennes, UMR 6118, Université de Rennes 1, OSUR, Campus de Beaulieu, 35042 Rennes Cedex, France*

[2] *Département de géologie et de génie géologique, Université Laval, Québec (QC) G1V 0A6, Canada*

[3] *Institut des Sciences de la Terre d'Orléans, UMR 7327, Université d'Orléans, Campus Géosciences, 1A rue de la Férollerie, 45071 Orléans Cedex 2, France*

[4] *Bureau de Recherche Géologique et Minière (BRGM), UMR 7327, 3 avenue Claude-Guillemin, BP 36009, 45060 Orléans Cedex 02, France*

A.1 Analytical conditions of electron probe micro-analyzer of Fe-Ti oxides and sulfides

Fe-Ti oxides

X-ray lines and standards used: Mg Ka (forsterite), Si Ka (albite), Al Ka (Al_2O_3), Ca Ka (wollastonite), Ti Ka (synthetic MnTiO3), V Ka (V_SP055), Cr Ka (Cr_2O_3), Mn Ka (synthetic $MnTiO_3$), Fe Ka (andradite), Ni Ka (NiO)

Spectrometers conditions: Sp4 TAP, Sp1 TAP, Sp1 TAP, Sp5 LPET, Sp5 LPET, Sp5 LPET, Sp5 LPET, Sp3 LLIF, Sp3 LLIF, Sp3 LLIF, Sp3 LLIF, Sp4 TAP, Sp2 PET, Sp2 PET, Sp2 PET, Sp1 TAP, Sp3 LLIF, Sp2 PET, Sp5 LPET, Sp2 PET

Column conditions: 15keV 20nA

Overlap correction: Yes
- Measured element: Cr Ka
- Overlapping element: V Kb 1
- Used standard: V_SP055

Measured element: Hf Ma
- Overlapping element: Ti Kb 3
- Used standard: $MnTiO_3$

Analysis Parameters:

Sp	Elements	Xtal	Position	Bg+	Bg-	Slope	Bias	Gain	Dtime	Blin
	Wind Mode									
Sp4	Mg Ka Inte	TAP	38485		1200	1	1303	2359	3	560
Sp1	Si Ka Inte	TAP	27750		600	1.1	1313	2501	3	560
Sp1	Al Ka Inte	TAP	32470		600	1	1313	2501	3	560
Sp5	Ca Ka Inte	LPET	38388		600	1	1859	824	3	560
Sp5	Ti Ka Inte	LPET	31428		600	1.2	1859	824	3	560
Sp5	V Ka Inte	LPET	28633	-500	500		1854	803	1	560
Sp5	Cr Ka Inte	LPET	26191		500	1.1	1859	824	3	560
Sp3	Mn Ka Inte	LLIF	52194		600	1.2	1880	586	3	560
Sp3	Fe Ka Inte	LLIF	48083		950	1.05	1880	586	3	560
Sp3	Ni Ka Inte	LLIF	41181		500	1.1	1880	586	3	560

Standard composition:
Forsterite = O: 43.66%, Mg: 30.4%, Si: 19.%, Fe: 6.7%, Ni: 0.24%

Albite = Na: 8.52%, Mg: 0.09%, Al: 10.12%, Si: 31.94%, K: 0.18%, Ca: 0.45%, Fe: 0.05%, O: 48.65%
Al_2O_3 = Al: 52.93%, O: 47.07%
Wollastonite = Si: 23.98%, Ca: 34.4%, Mn: 0.12%, Fe: 0.35%, O: 41.15%
$MnTiO_3$ = Mn: 36.42%, Ti: 31.76%, O: 31.82%
V_SP055 = V: 100%
Cr_2O_3 = Cr: 68.42%, O: 31.58%
Andradite = Mg: 0.18%, Si: 16.36%, Ca: 23.84%, Fe: 21.89%, O: 37.73%
NiO = Ni: 78.58%, O: 21.42%

Beam size: 3 μm

Sulfides

X-ray lines and standards used: S Ka (pyrite), Au Ma (Au_SP055), Fe Ka (pyrite), Co Ka (cobalt metal), Ni Ka (nickel metal), Zn Ka (ZnS), As La (GaAs), Sb La (stibnite), Cu La (copper metal).

Spectrometers conditions: Sp2 PET, Sp5 LPET, Sp3 LLIF, Sp3 LLIF, Sp3 LLIF, Sp3 LLIF, Sp4 TAP, Sp2 PET, Sp1 PET, Sp5 LPET, Sp2 PET, Sp4 TAP, Sp1 PET

Column conditions: 15keV 20nA

Overlap correction: Yes
- Measured element: As La
- Overlapping element: Sb Lb 3
- Used standard: Sb_2S_3

Analysis parameters:

Sp	Elements	Xtal	Position	Bg+	Bg-	Slope	Bias	Gain		
Sp2	S Ka Inte	PET	61396	-500	500		1300	1011	3	560
Sp5	Au Ma Inte	LPET	66791	-800	800		1862	1058	3	560
Sp3	Fe Ka Inte	LLIF	48089	-950	950		1867	504	3	560
Sp3	Co Ka Inte	LLIF	44433		500	1.2	1867	504	3	560
Sp3	Ni Ka Inte	LLIF	41191		600	1.05	1867	504	3	560
Sp3	Zn Ka Inte	LLIF	35682	-500	500		1851	361	3	560
Sp4	As La Inte	TAP	37639	-500	500		1303	2359	3	560
Sp1	Sb La Inte	PET	39312		600	1	1304	790	3	560
Sp4	Cu La Inte	TAP	51871		600	1	1314	3057	3	560

Standard composition:
Pyrite = S: 53.4%, Fe : 46.6%
Au_SP055 = Au: 100%

Co metal = Co: 100%
Ni metal = Ni: 100%
ZnS = Zn: 67.1%, S: 32.9%
GaAs = Ga: 48.2%, As: 51.8%
Sb2S3_Sulf = Sb: 71.68%, S: 28.32%
Cu metal = Cu: 100%

Beam size: 3 μm

Table A.2 Operating conditions for the laser ablation ICP-MS analysis of Fe-Ti oxides and pyrite

Laser ablation system	RESOlution (ASI) 193nm excimer laser with a S155 ablation cell	
ICP-MS	Agilent 7900	
Laser frequency	17 Hz	
Fluence	3 J/cm² (Fe-Ti oxides) and 2 J/cm² (pyrite)	
Beam size	25-55 μm	
Dwell time	10ms/peak	
Sampling mode	Single spot	
Background collection	30 s	
Ablation duration	60 s	
Wash-out delay	15 s	
Gas flow	Helium (350 mL/min)	
	Argon (0.9-1.1 mL/min)	
	Nitrogen (2 mL/min)	
Calibration	**Fe-Ti oxides**	**Pyrite**
Internal Standard	Fe for ilmenite and titanohematite, and Ti for rutile (data from EPMA)	Fe (data from EPMA)
Reference material	GSE-1G (USGS-synthetic glass)	MASS-1 (USGS-sulfide pressed powder pellet) for Co, Ni, Cu, Zn, Ge, As, Se, Mo, Ag, Cd, In, Sn, Sb, Te, W, Tl, Pb, Bi po-727 (synthetic FeS) for PGE and Au
Monitoring	GSD-1G (USGS-synthetic glass) Gprob6 (USGS-matrix artificial basalt glass) natural magnetite BC28 (in-house monitor)	synthetic FeS JB-MSS5 (in-house monitor)
Monitor signal for inclusions	S, Si and Ca	Si, Ca and Ti
Data reduction	Iolite software (IGOR Pro 6.3)	

Table A.3 LA-ICP-MS analyses of reference material used for calibration and to monitor the data quality of ilmenite and titanohematite

Isotope	Calibration			Monitor (reference material)								In-house reference material for monitoring the data quality			
				GSD-1g (synthetic basalt glass)				Gprob6 (matrix glass)		artificial basalt		BC28 (natural Ti-rich magnetite from the Bushveld Complex)			
	Reference Material	Certificate value		Certificate value		**This study**		Working value		**This study**		Working value		**This study**	
		Ave	Stdev	Ave	Stdev	Ave (n=20)	Stdev	Ave	Stdev	Ave (n=4)	Stdev	Ave		Ave (n=20)	Stdev
^{24}Mg	GSE-1g	21106	181	21709	241	**22280**	430.14	51318	6935	**47538**	923	11618	INAA	**12412**	2071
^{25}Mg	GSE-1g	21106	181	21709	241	**22350**	481.01	51318	6935	**48710**	1385	11618	INAA	**12176**	2243
^{27}Al	GSE-1g	68804	2117	70922	1588	**71915**	2185.93	92145	12438	**81198**	2810	20787	INAA	**22300**	4293
^{29}Si	GSE-1g	250994	7011	248657	3739	**254590**	6465.61	224259	9418	**213575**	5811	220	EPMA	**668**	952.71
^{31}P	GSD-1g	70	20	860	160	Used in calibration		611	131	**509**	11	N.A.	N.A.	**bdl**	
^{44}Ca	GSE-1g	52858	2143	51429	714	**51283**	1994.40	86787	4643	**78008**	2637	<24	EPMA	**bdl**	
^{43}Ca	GSE-1g	52858	2143	51429	714	**52337**	2163.76	86787	4643	**80080**	1743	<24	EPMA	**bdl**	
^{45}Sc	GSE-1g	52	2	52	2	**48**	1.89	36.75	2.59	**31.95**	1.40	31	INAA	**26**	3
^{47}Ti	GSE-1g	450	42	7432	360	**8990**	755.52	7012	1319	**7144**	720	87615	INAA	**96739**	5134
^{49}Ti	GSE-1g	450	42	7432	360	**8984**	751.67	7012	1319	**7043**	654	87615	INAA	**97055**	5559
^{51}V	GSE-1g	440	20	44	2	**40**	2.94	238	27.1	**222**	10	9603	INAA	**9651**	716
^{52}Cr	GSE-1g	400	80	42	3	**40**	2.78	300	21.5	**319**	5	1172	INAA	**1363**	50
^{53}Cr	GSE-1g	400	80	42	3	**45**	0.71	300	21.5	**322**	7	1172	INAA	**1338**	69
^{55}Mn	GSE-1g	590	20	220	20	**216**	6.66	1255	93	**1264**	41	2125	INAA	**2159**	178
^{59}Co	GSE-1g	380	20	40	2	**36**	2.33	47	3.51	**43**	2.92	241	INAA	**260**	22.42
^{60}Ni	GSE-1g	58	4	58	4	**58**	1.32	146	18.9	**152**	5.09	573	INAA	**529**	40.36
^{63}Cu	GSE-1g	380	40	42	2	**40**	2.24	90	20.31	**71**	4.64	33	INAA	**11**	13.56
^{65}Cu	GSE-1g	380	40	42	2	**42**	1.14	90	20.31	**76**	5.30	33	INAA	**13**	14.76
^{66}Zn	GSE-1g	460	10	54	2	**52**	1.17	71	16.6	**74**	5.52	588	INAA	**560**	116.69
^{71}Ga	GSE-1g	490	70	54	7	**47**	2.63	16	2	**13**	0.37	41.1	LA (MASS-1)	**38**	1.80
^{72}Ge	GSE-1g	320	80	32	8	**32**	0.78	1.26	0.41	**1.27**	0.07	0.86	LA (MASS-1)	**1.59**	0.28
^{74}Ge	GSE-1g	320	80	32	8	**32**	0.79	1.26	0.41	**1.10**	0.03	0.86	LA (MASS-1)	**1.08**	0.16

^{75}As	GSE-1g	260	90	27	8	**26**	1.58	N.A.		**1.83**	0.06	N.A.	N.A.	**0.25**	0.68
^{88}Sr	GSE-1g	447	5	69	1	**62**	3.24	167	26.1	**138**	4.84	N.A.	N.A.	**0.22**	0.28
^{89}Y	GSE-1g	42	2	42	2	**36**	1.09	19	1.78	**15**	0.35	0.08	LA (BCR2g)	**0.04**	0.08
^{90}Zr	GSE-1g	42	2	42	2	**37**	1.83	55	2.4	**42**	1.87	27.50	LA (BCR2g)	**19.87**	3.87
^{91}Zr	GSE-1g	42	2	42	2	**43**	1.40	55	2.4	**48**	2.00	27.50	LA (BCR2g)	**23.08**	3.20
^{93}Nb	GSE-1g	42	3	42	3	**37**	1.85	4.16	0.41	**3.02**	0.18	1.72	LA (BCR2g)	**1.40**	0.13
^{95}Mo	GSE-1g	390	30	39	3	**39**	1.07	N.A.		**0.36**	0.04	0.76	LA (NIST361)	**0.39**	0.04
^{118}Sn	GSE-1g	29	6	29	6	**27**	0.73	1.33	0.71	**0.99**	0.10	2.20	LA (MASS-1)	**1.27**	0.15
^{121}Sb	GSE-1g	450	110	43	7	**40**	2.31	0.13	0.01	**0.12**	0.01	0.02	INAA	**0.02**	0.01
^{178}Hf	GSE-1g	395	7	39	2	**34**	1.30	1.52	0.15	**1.15**	0.04	0.58	INAA	**0.76**	0.11
^{181}Ta	GSE-1g	390	40	40	4	**34**	0.49	0.28	0.03	**0.18**	0.00	0.07	INAA	**0.12**	0.01
^{182}W	GSE-1g	430	50	43	4	**38**	2.18	N.A.		**0.22**	0.02	0.51	LA (NIST361)	**0.01**	0.01
^{208}Pb	GSE-1g	378	12	50	2	**43**	2.91	3.28	0.78	**3.05**	0.17	1.98	LA (MASS-1)	**0.05**	0.06

Abbreviations: Ave, average; Stdev, standard deviation; bdl, below detection limit; N.A., not analyzed
The internal standard used is the ^{57} Fe with the following values : 9.8 wt.% (GSE-1g), 10.3 wt.% (GSD-1g), 7.3 wt.% (Gprob6) and 57.2 wt.% (BC28)
Working values for BC28 are taken from Dare et al. (2012). INAA data have been recalculated to 100 % magnetite with a factor of 1.07 from values of Barnes et al. (2004)

Table A.4 LA-ICP-MS analyses of reference material used for calibration and to monitor the data quality of rutile

Isotope	Calibration			Monitor (reference material)								In-house reference material for monitoring the data quality			
				GSD-1g (synthetic basalt glass)				Gprob6 (matrix artificial basalt glass)				BC28 (natural Ti-rich magnetite from the Bushveld Complex)			
	Reference Material	Certificate value		Certificate value		This study		Working value		This study		Working value	This study		
		Ave	Stdev	Ave	Stdev	Ave (n=20)	Stdev	Ave	Stdev	Ave (n=4)	Stdev	Ave		Ave (n=20)	Stdev
^{24}Mg	GSE-1g	21106	181	21709	241	**18477**	1532	51318	6935	**46843**	4089	11618	INAA	**11197**	1720
^{25}Mg	GSE-1g	21106	181	21709	241	**18534**	1647	51318	6935	**48213**	6609	11618	INAA	**10988**	1874
^{27}Al	GSE-1g	68804	2117	70922	1588	**59505**	3623	92145	12438	**79960**	5720	20787	INAA	**19519**	5409
^{29}Si	GSE-1g	250994	7011	248657	3739	**211350**	17694	224259	9418	**211075**	18764	220	EPMA	**419**	1174
^{44}Ca	GSE-1g	52858	2143	51429	714	**42385**	2315	86787	4643	**76903**	5804	<24	EPMA	**bdl**	
^{43}Ca	GSE-1g	52858	2143	51429	714	**43262**	2691	86787	4643	**78928**	6768	<24	EPMA	**bdl**	
^{45}Sc	GSE-1g	52	2	52	2	**40**	5	37	2.59	**32**	5	31	INAA	**23**	2
^{51}V	GSE-1g	440	20	44	2	**34**	5	238	27.1	**219**	32	9603	INAA	**8731**	379
^{52}Cr	GSE-1g	400	80	42	3	**34**	5	300	21.5	**314**	31	1172	INAA	**1235**	45
^{53}Cr	GSE-1g	400	80	42	3	**37**	3	300	21.5	**318**	32	1172	INAA	**1212**	35
^{55}Mn	GSE-1g	590	20	220	20	**179**	21	1255	93	**1250**	174	2125	INAA	**1956**	133
^{56}Fe	GSE-1g	98717	2332	103381	777	**85708**	7750	72598	13310	**71935**	7930	571806	INAA	**525165**	30955
^{57}Fe	GSE-1g	98717	2332	103381	777	**85807**	7708	72598	13310	**71915**	8013	571806	INAA	**526305**	34954
^{59}Co	GSE-1g	380	20	40	2	**30**	5	47	3.51	**42**	8	241	INAA	**235**	16
^{60}Ni	GSE-1g	58	4	58	4	**48**	4	146	18.9	**150**	12	573	INAA	**585**	42
^{63}Cu	GSE-1g	380	40	42	2	**33**	4	90	20.31	**70**	9	33	INAA	**10**	15
^{65}Cu	GSE-1g	380	40	42	2	**35**	3	90	20.31	**75**	6	33	INAA	**12**	16
^{66}Zn	GSE-1g	460	10	54	2	**43**	3	71	16.6	**73**	5	588	INAA	**506**	101
^{71}Ga	GSE-1g	490	70	54	7	**39**	6	16	2	**13**	2	41.088	LA (MASS-1)	**34**	2
^{72}Ge	GSE-1g	320	80	32	8	**26**	2	1.3	0.41	**1.3**	0	0.856	LA (MASS-1)	**1.45**	0.24
^{74}Ge	GSE-1g	320	80	32	8	**26**	2	1.3	0.41	**1.1**	0.11	0.856	LA (MASS-1)	**0.98**	0.13
^{75}As	GSE-1g	260	90	27	8	**22**	2	N.A.		**1.8**	0	N.A.	N.A.	**0.21**	0.56
^{88}Sr	GSE-1g	447	5	69	1	**52**	7	167	26.1	**136**	20	N.A.	N.A.	**0.21**	0.27

^{89}Y	GSE-1g	42	2	42	2	**30**	3	19	1.78	**14**	2	0.08	LA (BCR2g)	**0.07**	0.10
^{90}Zr	GSE-1g	42	2	42	2	**31**	4	55	2.4	**41**	6	27.50	LA (BCR2g)	**18**	3.33
^{91}Zr	GSE-1g	42	2	42	2	**35**	2	55	2.4	**47**	3	27.50	LA (BCR2g)	**20.9175**	3
^{93}Nb	GSE-1g	42	3	42	3	**31**	4	4.16	0.41	**3.01**	0.53	1.72	LA (BCR2g)	**1.76**	0.09
^{95}Mo	GSE-1g	390	30	39	3	**32**	3	N.A.		**0.36**	0.06	0.76	LA (NIST361)	**0.35**	0.03
^{118}Sn	GSE-1g	29	6	29	6	**22**	2	1.33	0.71	**0.99**	0.16	2.20	LA (MASS-1)	**1.52**	0.11
^{121}Sb	GSE-1g	450	110	43	7	**33**	5	0.13	0.01	**0.12**	0.02	0.02	INAA	**0.02**	0.01
^{178}Hf	GSE-1g	395	7	39	2	**29**	4	1.52	0.15	**1.14**	0.17	0.58	INAA	**0.69**	0.09
^{181}Ta	GSE-1g	390	40	40	4	**28**	2	0.28	0.03	**0.18**	0.02	0.07	INAA	**0.11**	0.00
^{182}W	GSE-1g	430	50	43	4	**32**	5	N.A.		**0.22**	0.03	0.51	LA (NIST361)	**0.01**	0.01
^{208}Pb	GSE-1g	378	12	50	2	**36**	6	3.28	0.78	**3.04**	0.50	1.98	LA (MASS-1)	**0.05**	0.06

Abbreviations: Ave, average; Stdev, standard deviation; bdl, below detection limit; N.A., not analyzed

The internal standard used is the 47 Ti with the following values : 450 ppm (GSE-1g), 0.7 wt.% (GSD-1g), 0.7 wt.% (Gprob6) and 8.8 wt.% (BC28)

Working values for BC28 are taken from Dare et al. (2012). INAA data have been recalculated to 100 % magnetite with a factor of 1.07 from values of Barnes et al. (2004)

Table A.5 LA-ICP-MS analyses of reference material used for calibration and to monitor the data quality of pyrite

Isotope	Calibration			Monitor (reference material)				In-house reference material			
				GSE-1g (synthetic basalt glass)				JB-MSS5 (synthetic FeS)			
	Reference Material	Certificate value		Certificate value		This study		Working value		This study	
		Ave	Stdev	Ave	Stdev	Ave (n=7)	Stdev	Ave	Stdev	Ave (n=7)	Stdev
^{34}S	po-727	390900	1600					404700		**394014**	18584
^{59}Co	MASS-1	60	10	380	20	**397**	28	0.28	0.02	**0.02**	0.002
^{60}Ni	MASS-1	440	30	440	30	**461**	21	10487	N.D.	**11768**	558
^{62}Ni	MASS-1	440	30	440	30	**422**	37	10487	N.D.	**12117**	354
^{63}Cu	MASS-1	134000	500	380	40	**421**	21	208	24	**190**	11
^{65}Cu	MASS-1	134000	500	380	40	**378**	17	208	24	**173**	8.11
^{66}Zn	MASS-1	210000	5000	460	10	**383**	13	N.A.		**2.47**	1.15
^{72}Ge	MASS-1	50	N.D.	320	80	**363**	21	N.A.		**0.63**	0.09
^{74}Ge	MASS-1	50	N.D.	320	80	**369**	16	N.A.		**0.55**	0.06
^{75}As	MASS-1	65	3	260	90	**315**	16	79	11	**55**	3.71
^{78}Se	MASS-1	51	4	20	16	**19**	11	47.27	13.39	**56**	6.02
^{95}Mo	MASS-1	59	9	390	30	**412**	26	0.23	0.02	**0.33**	0.02
^{100}Ru	po-727	36.5	0.3	N.A.		**361**	22	21.68	2.31	**22.08**	1.06
^{101}Ru	po-727	36.5	0.3	N.A.		**0**	0	21.68	2.31	**21.39**	1.09
^{103}Rh	po-727	41.6	0.3	N.A.		**70**	20	61.4	7.2	**72.86**	3.72
^{105}Pd	po-727	43.4	0.3	N.A.		**154**	22	65.2	5.1	**57.92**	5.31
^{106}Pd	po-727	43.4	0.3	N.A.		**163**	22	65.2	5.1	**58.35**	5.13
^{107}Ag	MASS-1	50	5	200	20	**220**	18	53	4.9	**46.73**	3.66
^{108}Pd	po-727	43.4	0.3	N.A.		**155**	18	65.2	5.1	**58.36**	4.92
^{111}Cd	MASS-1	60	7	160	50	**182**	20	0.13	0.04	**0.10**	0.03
^{113}Cd	MASS-1	60	7	160	50	**253**	22	0.13	0.04	**0.06**	0.01
^{115}In	MASS-1	50	N.D.	370	60	**377**	29	N.A.		**bdl**	
^{118}Sn	MASS-1	59	6	280	50	**404**	18	0.34	0.03	**0.05**	0.02

^{121}Sb	MASS-1	60	9	450	110	**403**	13	61.3	7.3	**49.47**	2.51
^{125}Te	MASS-1	15	N.D.	N.A.		**189**	9	44	3	**26.82**	1.70
^{182}W	MASS-1	20	2	430	50	**472**	23	N.A.		**0.02**	0.003
^{185}Re	GSE	120	N.D.	Used in calibration				20.7	N.D.	**30.62**	3.59
^{189}Os	po-727	46.7	2.6	N.A.		**bdl**		42.58	0.93	**53.62**	2.78
^{190}Os	po-727	46.7	2.6	N.A.		**bdl**		42.58	0.93	**53.76**	2.96
^{191}Ir	po-727	48	1.2	120		**52**	19	40.21	0.53	**40.27**	2.11
^{193}Ir	po-727	48	1.2	120		**51**	18	40.21	0.53	**40.72**	2.98
^{194}Pt	po-727	35.5	0.8	30		**33**	11	39.9	1	**40.58**	3.99
^{195}Pt	po-727	35.5	0.8	30		**33**	12	39.9	1	**40.56**	4.20
^{197}Au	po-727	45.8	2.4	7		**8**	1	35.9	4.8	**35.00**	3.54
^{205}Tl	MASS-1	50	N.D.	2		**1**	0	N.A.		**bdl**	
^{208}Pb	MASS-1	68	7	378	12	**407**	33	71.5	4.5	**62.41**	4.34
^{209}Bi	MASS-1	60	N.D.	320	30	**307**	16	76.1	2.9	**64.63**	3.38

Abbreviations: Ave, average; Stdev, standard deviation; bdl, below detection limit; N.A., not analyzed; N.D., not determined
The internal standard used is the ^{57} Fe with the following values : 9.8 wt.% (GSE-1g), 15.6 wt.% (MASS-1), 61 wt.% (LAF po-727) and 57 wt.% (JB-MSS5)

Table A.6 Electron microprobe analyses of Fe-Ti oxides from gabbros of the Semnon Sb-Au deposit

Wt. Oxides %	SiO2	Al2O3	TiO2	V2O3	Cr2O3	FeO	Fe2O3	MnO	MgO	CaO	Total	**A.p.f.u.**	Si	Al	Ti	V	Cr	Fe 3+	Fe 2+	Mn	Mg	Ca	Total
Ilmenite																							
D.L.	0.01	0.01	0.02	0.27	0.04	0.17	0.13	0.01	0.01	-													
MF1 c4-1	0.04	0.02	49.54	0.15	0.02	42.80	4.91	1.61	0.05	-	99.22		0.00	0.00	1.90	0.01	0.00	0.19	1.82	0.07	0.00	-	4
MF1 c4-2	0.02	bdl	49.11	0.42	bdl	42.22	7.01	1.73	0.05	-	100.66		0.00	-	1.86	0.02	-	0.27	1.78	0.07	0.00	-	4
MF1 c4-3	0.02	0.05	49.68	0.40	0.02	42.59	4.85	2.01	0.02	-	99.66		0.00	0.00	1.90	0.02	0.00	0.19	1.81	0.09	0.00	-	4
MF1 c3-1	0.06	0.17	49.33	0.55	0.04	42.42	5.49	1.72	0.09	-	99.99		0.00	0.01	1.88	0.02	0.00	0.21	1.79	0.07	0.01	-	4
MF1 c3-2	0.02	0.16	50.13	0.15	0.09	43.07	4.84	1.80	0.07	-	100.40		0.00	0.01	1.90	0.01	0.00	0.18	1.81	0.08	0.01	-	4
MF1 c3-3	0.02	0.03	49.41	0.37	0.01	42.72	5.89	1.62	0.06	-	100.12		0.00	0.00	1.88	0.01	0.00	0.22	1.81	0.07	0.00	-	4
MF1 c3-4	0.01	0.03	49.12	0.35	0.06	42.08	6.03	2.03	0.03	-	99.78		0.00	0.00	1.87	0.01	0.00	0.23	1.79	0.09	0.00	-	4
MF1 c3-5	bdl	0.14	49.10	0.14	0.06	42.38	5.81	1.69	0.04	-	99.43		-	0.01	1.88	0.01	0.00	0.22	1.80	0.07	0.00	-	4
MF1 c3-6	0.00	bdl	49.44	0.35	0.03	42.59	5.07	1.74	0.03	-	99.37		0.00	0.00	1.89	0.01	0.00	0.19	1.81	0.08	0.00	-	4
MF1 c3-7	0.05	0.03	49.59	0.35	0.01	42.75	5.21	1.70	0.04	-	99.77		0.00	0.00	1.89	0.01	0.00	0.20	1.81	0.07	0.00	-	4
MF1 c2-1	0.05	0.01	48.13	0.79	0.05	41.38	7.89	1.74	0.05	-	100.15		0.00	0.00	1.83	0.03	0.00	0.30	1.75	0.07	0.00	-	4
MF1 c2-2	0.01	0.18	48.47	0.27	0.03	41.56	7.13	1.82	0.06	-	99.60		0.00	0.01	1.85	0.01	0.00	0.27	1.77	0.08	0.00	-	4
MF1 c2-3	0.02	0.04	49.55	0.50	0.01	42.37	5.47	1.78	0.05	-	99.90		0.00	0.00	1.89	0.02	0.00	0.21	1.79	0.08	0.00	-	4
MF1 c2-4	0.03	0.10	50.18	0.12	bdl	43.06	4.65	1.62	0.08	-	99.96		0.00	0.01	1.91	0.00	-	0.18	1.82	0.07	0.01	-	4
MF1 c2-5	0.03	0.10	48.66	0.42	bdl	41.43	6.97	2.05	0.05	-	99.76		0.00	0.01	1.86	0.02	-	0.27	1.76	0.09	0.00	-	4
MF1 c2-6	0.01	0.04	48.63	0.54	0.06	41.76	6.68	1.74	0.07	-	99.54		0.00	0.00	1.86	0.02	0.00	0.26	1.78	0.07	0.01	-	4
MF1 c1-1	0.06	bdl	49.13	0.16	0.01	42.23	7.01	1.80	0.05	-	100.58		0.00	-	1.86	0.01	0.00	0.27	1.78	0.08	0.00	-	4
MF1 c1-2	0.02	bdl	49.19	0.40	0.02	42.26	6.20	1.77	0.05	-	99.94		0.00	0.00	1.87	0.02	0.00	0.24	1.79	0.08	0.00	-	4
MF1 c1-3	0.00	0.04	49.01	0.24	bdl	42.13	6.20	1.84	0.04	-	99.53		0.00	0.00	1.88	0.01	-	0.24	1.79	0.08	0.00	-	4
MF1 c1-4	0.05	0.02	49.41	0.10	0.02	42.62	5.48	1.78	0.05	-	99.53		0.00	0.00	1.89	0.00	0.00	0.21	1.81	0.08	0.00	-	4
MF1 c1-5	0.01	0.09	49.01	0.40	0.10	42.22	6.76	1.67	0.08	-	100.35		0.00	0.01	1.86	0.02	0.00	0.26	1.78	0.07	0.01	-	4
BAN1 c1-3	0.01	0.00	50.11	0.06	bdl	41.08	4.34	3.83	0.05	-	99.50		0.00	0.00	1.92	0.00	-	0.17	1.75	0.16	0.00	-	4
BAN1 c2-7	0.02	0.06	48.92	0.14	0.03	40.68	6.32	3.01	0.11	-	99.31		0.00	0.00	1.87	0.01	0.00	0.24	1.73	0.13	0.01	-	4
BAN1 c2-8	bdl	bdl	48.54	0.23	bdl	40.54	7.52	2.76	0.09	-	99.84		-	0.00	1.85	0.01	-	0.29	1.72	0.12	0.01	-	4
BAN1 c3-5	0.01	0.01	48.81	0.11	0.01	39.40	7.13	4.15	0.12	-	99.87		0.00	0.00	1.86	0.00	0.00	0.27	1.67	0.18	0.01	-	4
Average	0.02	0.07	49.21	0.31	0.04	42.01	6.03	2.04	0.06	-	99.83		0.00	0.00	1.88	0.01	0.00	0.23	1.78	0.09	0.00	-	4

Stdev	0.02	0.06	0.52	0.18	0.03	0.87	0.99	0.67	0.02	-	0.39	0.00	0.00	0.02	0.01	0.00	0.04	0.04	0.03	0.00	-	-
Titanohematite																						
D.L.	0.01	0.01	0.02	0.27	0.04	0.17	0.13	0.01	0.01	-												
TOU1 c1-1	0.11	0.93	21.65	0.50	bdl	17.42	56.95	1.81	0.03	-	99.47	0.01	0.06	0.85	0.02	0.00	2.23	0.76	0.08	0.00	-	4
TOU1 c1-2	0.10	0.14	22.88	0.61	0.24	20.31	54.25	0.29	bdl	-	98.85	0.01	0.01	0.90	0.03	0.01	2.14	0.89	0.01	-	-	4
TOU1 c1-3	0.09	0.08	16.71	0.52	0.04	13.44	68.18	1.53	0.02	-	100.66	0.00	0.00	0.65	0.02	0.00	2.66	0.58	0.07	0.00	-	4
TOU1 c1-4	0.07	1.03	22.16	0.76	0.77	16.95	55.39	2.78	0.02	-	100.01	0.00	0.06	0.86	0.03	0.03	2.15	0.73	0.12	0.00	-	4
TOU1 c2-1	0.10	0.50	18.36	0.67	0.41	15.69	63.93	0.83	0.01	-	100.53	0.01	0.03	0.71	0.03	0.02	2.49	0.68	0.04	0.00	-	4
TOU1 c2-3	0.12	0.80	22.09	0.54	0.05	18.82	56.33	1.07	0.02	-	99.92	0.01	0.05	0.86	0.02	0.00	2.19	0.81	0.05	0.00	-	4
TOU1 c2-4	0.14	0.26	18.57	0.62	0.36	15.87	63.38	0.93	bdl	-	100.17	0.01	0.02	0.73	0.03	0.01	2.48	0.69	0.04	0.00	-	4
TOU1 c3-1	0.08	0.09	19.16	0.91	0.36	16.42	62.94	0.53	0.03	-	100.71	0.00	0.01	0.75	0.04	0.01	2.45	0.71	0.02	0.00	-	4
TOU1 c3-3	1.10	0.36	16.36	0.47	0.36	14.57	65.31	1.04	0.22	-	99.81	0.06	0.02	0.64	0.02	0.01	2.55	0.63	0.05	0.02	-	4
TOU1 c3-4	0.10	0.20	21.72	0.56	0.05	19.12	56.86	0.37	0.04	-	99.08	0.00	0.01	0.86	0.02	0.00	2.24	0.84	0.02	0.00	-	4
TOU1 c3-5	0.09	1.40	22.14	0.46	0.23	18.04	55.70	1.67	0.03	-	99.82	0.00	0.08	0.86	0.02	0.01	2.16	0.78	0.07	0.00	-	4
BAN1 c1-1	0.10	0.06	18.84	0.79	bdl	16.21	64.49	0.83	bdl	-	101.39	0.01	0.00	0.73	0.03	0.00	2.49	0.70	0.04	0.00	-	4
BAN1 c1-2	0.08	0.07	20.99	0.56	bdl	18.08	59.42	0.79	0.02	-	100.12	0.00	0.00	0.82	0.02	0.00	2.32	0.79	0.03	0.00	-	4
BAN1 c1-5	0.06	0.09	15.08	0.48	bdl	12.39	72.35	1.01	0.06	-	101.66	0.00	0.01	0.58	0.02	0.00	2.80	0.53	0.04	0.00	-	4
BAN1 c1-6	0.11	0.09	20.20	0.34	bdl	17.20	61.53	0.91	0.04	-	100.55	0.01	0.01	0.79	0.01	-	2.40	0.74	0.04	0.00	-	4
BAN1 c1-7	0.10	0.15	19.07	0.74	bdl	15.71	64.65	1.38	0.02	-	101.87	0.01	0.01	0.73	0.03	-	2.49	0.67	0.06	0.00	-	4
BAN1 c1-8	0.09	bdl	17.93	0.33	bdl	15.33	67.21	0.85	0.02	-	101.76	0.00	-	0.69	0.01	-	2.59	0.66	0.04	0.00	-	4
BAN1 c2-1	0.10	0.03	20.24	0.54	bdl	17.01	62.15	1.22	0.02	-	101.34	0.01	0.00	0.78	0.02	0.00	2.40	0.73	0.05	0.00	-	4
BAN1 c2-2	0.12	bdl	19.82	0.98	bdl	16.33	62.44	1.45	bdl	-	101.22	0.01	-	0.77	0.04	0.00	2.42	0.70	0.06	0.00	-	4
BAN1 c2-3	0.10	0.18	19.85	0.63	bdl	16.85	61.98	1.06	0.02	-	100.71	0.01	0.01	0.77	0.03	0.00	2.41	0.73	0.05	0.00	-	4
BAN1 c2-4	0.09	0.40	19.19	0.49	0.05	16.40	63.89	0.63	0.02	-	101.30	0.00	0.02	0.74	0.02	0.00	2.47	0.70	0.03	0.00	-	4
BAN1 c2-5	0.10	0.13	21.68	0.45	bdl	19.37	57.51	0.20	bdl	-	99.50	0.01	0.01	0.85	0.02	0.00	2.26	0.85	0.01	0.00	-	4
BAN1 c2-6	0.08	0.79	22.47	0.63	bdl	19.96	56.64	0.24	0.02	-	100.93	0.00	0.05	0.87	0.03	0.00	2.18	0.86	0.01	0.00	-	4
BAN1 c3-2	0.09	0.72	20.52	0.31	bdl	17.47	60.85	0.93	0.03	-	100.96	0.00	0.04	0.79	0.01	0.00	2.35	0.75	0.04	0.00	-	4
BAN1 c3-3	0.12	0.08	21.37	0.39	bdl	18.26	60.04	0.79	0.03	-	101.27	0.01	0.00	0.83	0.02	0.00	2.32	0.78	0.03	0.00	-	4
BAN1 c3-4	0.08	0.07	20.39	bdl	bdl	17.25	61.12	1.00	0.01	-	100.13	0.00	0.00	0.80	0.01	0.00	2.39	0.75	0.04	0.00	-	4
Average	0.13	0.36	19.98	0.57	0.27	16.94	61.37	1.01	0.03	-	100.53	0.01	0.02	0.78	0.02	0.01	2.39	0.73	0.04	0.00	-	4
Stdev	0.20	0.38	2.01	0.20	0.19	1.86	4.41	0.55	0.04	-	0.83	0.01	0.02	0.08	0.01	0.01	0.17	0.08	0.02	0.00	-	-

CG rutile

D.L.	0.04	0.04	0.05	0.01	0.01	0.08	0.08	0.03	0.03	0.02											
SEM9-c1-1	0.09	0.13	99.31	0.74	0.01	-	0.28	bdl	bdl	bdl	101.16	0.00	0.00	1.97	0.02	0.00	0.01	-	-	-	-	2
SEM9-c1-2	0.14	0.09	99.30	0.81	0.03	-	0.21	bdl	bdl	0.07	100.70	0.00	0.00	1.97	0.02	0.00	0.00	-	-	-	0.00	2
SEM9-c1-3	0.16	0.07	99.27	0.71	0.03	-	0.12	bdl	bdl	0.08	100.46	0.00	0.00	1.97	0.02	0.00	0.00	-	-	-	0.00	2
SEM9-c1-4	0.08	bdl	100.03	0.57	bdl	-	0.20	bdl	bdl	0.30	101.24	0.00	-	1.97	0.01	-	0.00	-	-	-	0.01	2
SEM9-c1-5	0.08	bdl	99.05	0.79	0.03	-	0.25	bdl	bdl	0.19	100.44	0.00	-	1.97	0.02	0.00	0.00	-	-	-	0.01	2
SEM9-c1-6	bdl	bdl	99.68	0.80	0.02	-	0.00	bdl	bdl	0.14	100.63	-	-	1.98	0.02	0.00	-	-	-	-	0.00	2
SEM9-c1-7	0.12	bdl	98.69	0.73	bdl	-	0.12	bdl	bdl	0.15	99.84	0.00	-	1.97	0.02	-	0.00	-	-	-	0.00	2
SEM9-c2-1	bdl	bdl	99.71	0.74	0.06	-	0.20	bdl	bdl	bdl	100.98	-	-	1.98	0.02	0.00	0.00	-	-	-	-	2
SEM9-c2-2	bdl	bdl	100.12	0.81	0.04	-	0.20	bdl	bdl	bdl	101.22	-	-	1.98	0.02	0.00	0.00	-	-	-	-	2
SEM9-c2-3	0.13	0.07	99.62	0.81	0.07	-	0.14	bdl	bdl	0.06	101.09	0.00	0.00	1.97	0.02	0.00	0.00	-	-	-	0.00	2
SEM9-c2-4	bdl	0.08	99.25	0.70	bdl	-	0.20	bdl	bdl	0.05	100.72	-	0.00	1.97	0.01	-	0.00	-	-	-	0.00	2
SEM9-c2-5	0.10	0.25	98.38	0.59	bdl	-	0.95	bdl	bdl	0.05	100.92	0.00	0.01	1.95	0.01	-	0.02	-	-	-	0.00	2
SEM9-c3-1	bdl	bdl	99.17	0.94	bdl	-	0.13	bdl	bdl	0.07	100.59	-	-	1.97	0.02	-	0.00	-	-	-	0.00	2
SEM9-c3-3	bdl	0.08	96.17	0.71	0.02	-	3.60	bdl	bdl	0.09	100.86	-	0.00	1.91	0.01	0.00	0.07	-	-	-	0.00	2
SEM9-c3-4	bdl	1.40	97.25	0.65	0.03	-	0.46	bdl	bdl	bdl	99.80	-	0.04	1.93	0.01	0.00	0.01	-	-	-	-	2
SEM9-c3-6	0.15	bdl	99.11	0.38	bdl	-	0.42	bdl	bdl	0.72	100.84	0.00	-	1.96	0.01	-	0.01	-	-	-	0.02	2
SEM9-c3-7	bdl	bdl	99.31	0.40	bdl	-	0.48	bdl	bdl	1.03	101.30	-	-	1.95	0.01	-	0.01	-	-	-	0.03	2
SEM9-c3-8	bdl	bdl	100.52	0.47	bdl	-	0.35	bdl	bdl	0.46	101.84	-	-	1.97	0.01	-	0.01	-	-	-	0.01	2
SEM9-c3-9	bdl	bdl	100.26	0.45	bdl	-	0.28	bdl	bdl	0.18	101.30	-	-	1.98	0.01	-	0.01	-	-	-	0.01	2
SEM9-c3-10	bdl	bdl	100.20	0.60	bdl	-	0.27	bdl	bdl	bdl	101.25	-	-	1.98	0.01	-	0.01	-	-	-	-	2
SEM9-c3-11	bdl	bdl	99.97	0.52	bdl	-	0.26	bdl	bdl	bdl	100.79	-	-	1.98	0.01	-	0.01	-	-	-	-	2
SEM9-c3-12	0.16	0.20	99.97	0.48	bdl	-	0.32	bdl	bdl	0.05	101.37	0.00	0.01	1.97	0.01	-	0.01	-	-	-	0.00	2
SEM9-c3-13	bdl	bdl	99.17	0.45	bdl	-	0.41	bdl	bdl	0.04	100.47	-	-	1.98	0.01	-	0.01	-	-	-	0.00	2
SEM9-c3-15	0.16	bdl	100.39	0.80	0.00	-	bdl	bdl	bdl	bdl	101.43	0.00	-	1.98	0.02	0.00	0.00	-	-	-	-	2
SEM9-c3-16	bdl	bdl	100.06	0.81	bdl	-	bdl	bdl	bdl	bdl	101.15	-	-	1.98	0.02	-	0.00	-	-	-	-	2
SEM9-c3-18	bdl	bdl	100.14	0.58	bdl	-	0.23	bdl	bdl	0.09	101.04	-	-	1.98	0.01	-	0.00	-	-	-	0.00	2
SEM9-c3-19	bdl	bdl	100.37	0.28	bdl	-	0.23	bdl	bdl	0.08	101.14	-	-	1.99	0.01	-	0.00	-	-	-	0.00	2
SEM9-c3-20	bdl	bdl	99.96	0.56	bdl	-	0.20	bdl	bdl	0.10	101.01	-	-	1.98	0.01	-	0.00	-	-	-	0.00	2
SEM9-c3-21	bdl	bdl	100.07	0.72	bdl	-	0.14	bdl	bdl	0.04	101.00	-	-	1.98	0.02	-	0.00	-	-	-	0.00	2

SEM9-c3-22	bdl	bdl	99.83	0.67	bdl	-	0.21	bdl	bdl	bdl	100.93	-	-	1.98	0.01	-	0.00	-	-	-	-	2
SEM9-c3-23	bdl	bdl	99.79	0.78	bdl	-	0.16	bdl	bdl	0.06	100.97	-	-	1.98	0.02	-	0.00	-	-	-	0.00	2
SEM9-c4-1	bdl	0.14	99.32	0.77	0.08	-	0.13	bdl	bdl	0.04	100.66	-	0.00	1.97	0.02	0.00	0.00	-	-	-	0.00	2
SEM9-c4-2	bdl	0.18	99.04	0.84	0.03	-	0.21	bdl	bdl	bdl	100.61	-	0.01	1.97	0.02	0.00	0.00	-	-	-	-	2
SEM9-c4-3	bdl	bdl	99.36	0.80	0.06	-	0.25	bdl	0.06	0.06	100.60	-	-	1.97	0.02	0.00	0.00	-	-	0.00	0.00	2
SEM9-c4-4	bdl	bdl	99.41	0.80	0.07	-	0.20	bdl	bdl	bdl	100.84	-	-	1.97	0.02	0.00	0.00	-	-	-	-	2
SEM9-c4-5	0.21	0.08	98.78	0.54	0.03	-	0.18	bdl	bdl	0.14	100.09	0.01	0.00	1.97	0.01	0.00	0.00	-	-	-	0.00	2
SEM9-c4-7	bdl	bdl	100.13	0.69	0.06	-	0.27	bdl	bdl	0.17	101.38	-	-	1.97	0.01	0.00	0.01	-	-	-	0.00	2
SEM9-c4-8	bdl	bdl	98.41	0.65	bdl	-	1.09	bdl	bdl	0.19	100.69	-	-	1.96	0.01	-	0.02	-	-	-	0.01	2
SEM9-c4-9	bdl	bdl	99.16	0.70	bdl	-	0.15	bdl	bdl	0.04	100.21	-	-	1.98	0.01	-	0.00	-	-	-	0.00	2
SEM9-c5-1	bdl	bdl	100.40	0.77	0.04	-	0.12	bdl	bdl	0.20	101.53	-	-	1.98	0.02	0.00	0.00	-	-	-	0.01	2
SEM9-c5-2	0.16	0.10	99.55	0.74	0.02	-	0.18	bdl	bdl	0.23	101.07	0.00	0.00	1.97	0.02	0.00	0.00	-	-	-	0.01	2
SEM9-c5-3	bdl	bdl	99.87	0.61	bdl	-	bdl	bdl	bdl	0.11	100.63	-	-	1.98	0.01	-	-	-	-	-	0.00	2
SEM9-c5-4	bdl	bdl	99.62	0.85	bdl	-	0.12	bdl	bdl	0.22	100.89	-	-	1.97	0.02	-	0.00	-	-	-	0.01	2
SEM9-c5-5	0.09	0.07	99.34	0.85	0.02	-	0.14	bdl	bdl	0.21	100.86	0.00	0.00	1.97	0.02	0.00	0.00	-	-	-	0.01	2
SEM9-c5-6	bdl	bdl	99.48	0.79	0.01	-	bdl	bdl	bdl	0.04	100.34	-	-	1.98	0.02	0.00	-	-	-	-	0.00	2
SEM9-c5-8	bdl	bdl	99.93	0.37	0.03	-	0.31	bdl	bdl	0.15	100.83	-	-	1.98	0.01	0.00	0.01	-	-	-	0.00	2
SEM9-c6-1	bdl	bdl	99.22	0.37	bdl	-	0.14	bdl	bdl	0.12	99.93	-	-	1.99	0.01	-	0.00	-	-	-	0.00	2
SEM9-c6-2	bdl	bdl	98.68	0.61	0.02	-	0.20	bdl	bdl	0.41	100.33	-	-	1.97	0.01	0.00	0.00	-	-	-	0.01	2
SEM9-c6-3	bdl	0.08	99.85	0.55	0.03	-	0.17	bdl	bdl	0.12	100.82	-	0.00	1.98	0.01	0.00	0.00	-	-	-	0.00	2
SEM9-c6-4	bdl	0.11	99.19	0.50	bdl	-	0.22	bdl	bdl	0.17	100.44	-	0.00	1.97	0.01	-	0.00	-	-	-	0.00	2
SEM9-c6-5	bdl	0.20	98.12	0.63	bdl	-	0.26	bdl	bdl	0.13	99.83	-	0.01	1.97	0.01	-	0.01	-	-	-	0.00	2
SEM9-c6-8	0.16	0.24	98.35	0.73	0.11	-	0.39	bdl	bdl	0.14	100.30	0.00	0.01	1.96	0.02	0.00	0.01	-	-	-	0.00	2
SEM9-c6-9	bdl	0.21	98.40	0.73	0.05	-	bdl	bdl	bdl	0.07	99.76	-	0.01	1.97	0.02	0.00	-	-	-	-	0.00	2
SEM9-c6-10	0.10	bdl	99.20	0.67	0.03	-	0.15	bdl	bdl	0.10	100.43	0.00	-	1.97	0.01	0.00	0.00	-	-	-	0.00	2
SEM11-c1-1	bdl	0.11	99.80	0.75	0.03	-	0.18	bdl	bdl	0.30	101.23	-	0.00	1.97	0.02	0.00	0.00	-	-	-	0.01	2
SEM11-c1-3	bdl	bdl	99.38	0.64	0.04	-	0.25	bdl	bdl	0.45	100.89	-	-	1.97	0.01	0.00	0.00	-	-	-	0.01	2
SEM11-c1-5	bdl	0.13	99.32	0.82	0.08	-	0.22	bdl	bdl	0.59	101.17	-	0.00	1.96	0.02	0.00	0.00	-	-	-	0.02	2
SEM11-c1-6	0.12	0.21	98.42	0.82	0.03	-	0.13	bdl	bdl	0.61	100.54	0.00	0.01	1.95	0.02	0.00	0.00	-	-	-	0.02	2
SEM11-c1-7	bdl	bdl	99.80	0.54	bdl	-	0.23	bdl	bdl	0.48	101.15	-	-	1.97	0.01	-	0.00	-	-	-	0.01	2
SEM11-c1-8	bdl	bdl	99.45	0.57	bdl	-	bdl	bdl	bdl	0.82	100.92	-	-	1.96	0.01	-	-	-	-	-	0.02	2
SEM11-c2-1	bdl	0.19	99.33	0.74	bdl	-	0.27	bdl	bdl	0.33	100.97	-	0.01	1.96	0.02	-	0.01	-	-	-	0.01	2

SEM11-c2-2	bdl	0.29	98.77	0.75	0.03	-	0.37	bdl	bdl	0.64	101.03	-	0.01	1.95	0.02	0.00	0.01	-	-	-	0.02	2
SEM11-c2-3	0.08	0.14	99.20	0.72	0.02	-	bdl	bdl	bdl	1.01	101.50	0.00	0.00	1.95	0.02	0.00	-	-	-	-	0.03	2
SEM11-c2-4	0.14	0.41	97.73	0.79	0.02	-	1.37	bdl	bdl	0.44	101.17	0.00	0.01	1.92	0.02	0.00	0.03	-	-	-	0.01	2
SEM11-c2-5	0.00	0.07	99.41	0.93	0.03	-	0.16	bdl	bdl	0.47	101.10	-	0.00	1.96	0.02	0.00	0.00	-	-	-	0.01	2
SEM11-c2-6	0.19	0.10	98.62	0.52	bdl	-	0.28	bdl	bdl	0.77	100.65	0.01	0.00	1.95	0.01	-	0.01	-	-	-	0.02	2
SEM11-c2-8	bdl	bdl	99.21	0.73	bdl	-	0.47	bdl	bdl	0.13	100.59	-	-	1.97	0.02	-	0.01	-	-	-	0.00	2
SEM11-c2-10	bdl	bdl	100.08	0.86	0.01	-	bdl	bdl	bdl	0.53	101.70	-	-	1.96	0.02	0.00	-	-	-	-	0.01	2
SEM11-c2-11	0.10	0.07	99.85	0.90	0.01	-	0.13	bdl	bdl	0.64	101.87	0.00	0.00	1.95	0.02	0.00	0.00	-	-	-	0.02	2
SEM11-c2-13	bdl	0.06	100.26	0.57	0.02	-	0.32	bdl	bdl	0.70	101.99	-	0.00	1.96	0.01	0.00	0.01	-	-	-	0.02	2
SEM11-c2-15	bdl	bdl	99.55	0.61	bdl	-	0.20	bdl	bdl	0.78	101.53	-	-	1.96	0.01	-	0.00	-	-	-	0.02	2
SEM11-c3-1	0.32	0.07	99.02	0.64	0.07	-	0.20	bdl	bdl	0.56	100.92	0.01	0.00	1.95	0.01	0.00	0.00	-	-	-	0.02	2
SEM11-c3-2	bdl	bdl	98.10	0.69	0.06	-	0.14	bdl	bdl	0.57	99.58	-	-	1.96	0.01	0.00	0.00	-	-	-	0.02	2
SEM11-c3-3	bdl	bdl	98.57	0.86	0.02	-	0.16	bdl	bdl	0.83	101.15	-	-	1.95	0.02	0.00	0.00	-	-	-	0.02	2
SEM11-c3-4	bdl	bdl	99.18	0.81	0.01	-	0.13	bdl	bdl	0.46	100.80	-	-	1.96	0.02	0.00	0.00	-	-	-	0.01	2
SEM11-c4-1	bdl	bdl	100.08	0.64	0.02	-	0.18	bdl	bdl	0.71	101.93	-	-	1.96	0.01	0.00	0.00	-	-	-	0.02	2
SEM11-c4-2	bdl	bdl	99.48	0.75	0.03	-	0.16	bdl	bdl	0.61	101.34	0.00	-	1.96	0.02	0.00	0.00	-	-	-	0.02	2
SEM11-c4-3	bdl	0.10	99.29	0.62	0.00	-	0.08	bdl	bdl	0.52	100.97	-	0.00	1.96	0.01	-	0.00	-	-	-	0.01	2
SEM11-c4-4	bdl	0.07	99.52	0.59	0.00	-	0.23	bdl	bdl	0.69	101.59	-	0.00	1.96	0.01	-	0.00	-	-	-	0.02	2
SEM11-c5-1	bdl	bdl	99.92	0.64	0.01	-	bdl	bdl	bdl	0.53	101.24	-	-	1.97	0.01	0.00	-	-	-	-	0.01	2
SEM11-c5-2	bdl	bdl	99.08	0.86	0.00	-	bdl	bdl	bdl	0.80	101.35	-	-	1.95	0.02	0.00	-	-	-	-	0.02	2
SEM11-c5-4	bdl	0.13	98.15	0.63	0.01	-	bdl	bdl	bdl	0.89	99.87	-	0.00	1.96	0.01	0.00	-	-	-	-	0.03	2
SEM11-c5-5	bdl	0.08	98.67	0.59	0.00	-	0.12	bdl	bdl	0.76	100.60	-	0.00	1.96	0.01	-	0.00	-	-	-	0.02	2
SEM11-c5-6	bdl	0.07	99.17	0.75	0.02	-	0.18	bdl	bdl	0.67	101.23	-	0.00	1.95	0.02	0.00	0.00	-	-	-	0.02	2
SEM11-c5-9	bdl	bdl	99.40	0.41	0.00	-	0.22	bdl	bdl	0.86	101.17	-	-	1.96	0.01	-	0.00	-	-	-	0.02	2
SEM11-c5-10	bdl	0.18	98.73	0.38	0.00	-	0.72	bdl	bdl	0.51	100.89	-	0.01	1.95	0.01	-	0.01	-	-	-	0.01	2
SEM11-c6-1	bdl	bdl	99.74	0.77	0.00	-	0.26	bdl	bdl	0.52	101.50	-	-	1.96	0.02	-	0.01	-	-	-	0.01	2
SEM11-c6-3	bdl	0.12	99.05	0.77	0.11	-	0.13	bdl	bdl	0.66	100.89	-	0.00	1.96	0.02	0.00	0.00	-	-	-	0.02	2
SEM11-c6-4	bdl	bdl	98.76	0.79	0.08	-	0.16	bdl	bdl	0.62	100.49	-	-	1.96	0.02	0.00	0.00	-	-	-	0.02	2
SEM11-c6-5	bdl	bdl	98.95	0.66	0.09	-	bdl	bdl	bdl	0.84	101.10	-	-	1.95	0.01	0.00	-	-	-	-	0.02	2
SEM11-c7-2	bdl	bdl	99.56	0.88	0.02	-	0.12	bdl	bdl	0.51	101.27	-	-	1.96	0.02	0.00	0.00	-	-	-	0.01	2
Average	0.13	0.17	99.31	0.68	0.03	-	0.30	-	0.06	0.37	100.89	0.00	0.01	1.97	0.01	0.00	0.01	-	-	-	0.01	2.000
Stdev	0.06	0.16	0.72	0.14	0.03	-	0.41	-	-	0.30	0.50	0.00	0.01	0.01	0.00	0.00	0.01	-	-	-	0.01	-

FG rutile

D.L.	0.04	0.04	0.05	0.01	0.01	0.08	0.08	0.03	0.03	0.02												
SEM11-c1-2	6.34	5.17	74.92	0.46	bdl	6.60	bdl	bdl	2.58	0.51	96.83	-	-	-	-	-	-	-	-	-	-	-
SEM11-c1-4	6.92	5.97	72.44	0.41	bdl	7.78	bdl	bdl	2.85	0.40	97.02	-	-	-	-	-	-	-	-	-	-	-
SEM11-c1-9	9.43	8.40	62.14	0.24	bdl	11.35	bdl	bdl	4.00	0.19	95.89	-	-	-	-	-	-	-	-	-	-	-
SEM11-c1-10	7.46	6.22	69.09	0.26	bdl	8.10	bdl	bdl	3.27	0.21	94.85	-	-	-	-	-	-	-	-	-	-	-
SEM11-c2-7	7.37	5.97	73.12	0.41	bdl	7.62	bdl	bdl	2.76	0.32	97.74	-	-	-	-	-	-	-	-	-	-	-
SEM11-c5-7	6.45	5.32	75.91	0.49	bdl	6.69	bdl	bdl	2.50	0.17	97.67	-	-	-	-	-	-	-	-	-	-	-
SEM11-c6-2	bdl	bdl	85.85	0.55	0.02	12.69	bdl	0.51	bdl	0.59	101.25	-	-	-	-	-	-	-	-	-	-	-
SEM11-c7-3	4.74	4.53	79.50	0.59	0.02	5.51	bdl	bdl	1.76	0.06	96.90	-	-	-	-	-	-	-	-	-	-	-
SEM11-c7-4	2.54	2.08	87.65	0.68	0.06	2.71	bdl	bdl	0.61	0.19	96.68	-	-	-	-	-	-	-	-	-	-	-
SEM9-c2-6	7.39	5.91	76.31	0.33	bdl	6.57	bdl	bdl	2.65	0.06	99.22	-	-	-	-	-	-	-	-	-	-	-
SEM9-c3-2	bdl	0.12	90.33	0.79	0.01	9.83	bdl	bdl	bdl	0.04	101.18	-	-	-	-	-	-	-	-	-	-	-
SEM9-c3-14	13.34	2.38	77.54	0.45	bdl	3.06	bdl	bdl	1.00	0.84	98.94	-	-	-	-	-	-	-	-	-	-	-
SEM9-c3-17	9.19	4.70	76.33	0.34	bdl	6.31	bdl	bdl	1.86	0.10	99.06	-	-	-	-	-	-	-	-	-	-	-
SEM9-c5-7	11.66	7.74	77.55	0.38	bdl	0.36	bdl	bdl	0.09	0.10	98.14	-	-	-	-	-	-	-	-	-	-	-
SEM9-c6-7	7.52	7.18	65.19	0.28	0.08	10.51	bdl	bdl	2.89	0.08	94.01	-	-	-	-	-	-	-	-	-	-	-
Average	7.72	5.12	76.26	0.44	0.04	7.05	-	0.51	2.22	0.26	97.69	-	-	-	-	-	-	-	-	-	-	-
Stdev	3.74	2.56	7.71	0.16	0.03	3.33	-	0.13	1.29	0.23	2.05	-	-	-	-	-	-	-	-	-	-	-

Abbreviations: D.L., detection limit; Stdev, standard deviation; bdl, below detection limit

Values below the detection limit are not taken into account for the calculation of average

Table A.7 Electron microprobe analyses of arsenopyrite and pyrite from gabbros of the Semnon Sb-Au deposit

Element	S	Fe	As	Sb	Au	Zn	Cu	Co	Ni	Total
	%	%	%	%	%	%	%	%	%	
Arsenopyrite										
D.L.	0.12	0.08	0.08	0.09	0.08	0.11	0.17	0.06	0.06	
SEM45-Pt-c2-37	21.75	34.85	42.86	bdl	bdl	bdl	bdl	bdl	bdl	99.77
SEM45-Pt-c2-38	21.28	33.60	43.54	0.27	bdl	bdl	bdl	0.65	bdl	99.99
SEM45-Pt-hc-40	21.60	34.74	43.27	0.30	bdl	bdl	bdl	bdl	bdl	100.05
SEM45-Pt-hc-41	21.16	34.66	43.55	0.31	bdl	bdl	bdl	bdl	bdl	99.91
SEM45-Pt-hc-44	21.39	34.95	42.97	1.01	bdl	bdl	bdl	bdl	bdl	100.38
SEM45-Pt-hc-45	21.13	34.98	43.30	0.33	bdl	bdl	bdl	bdl	bdl	99.94
SEM45-Pt-c6-47	21.30	34.80	42.01	1.26	bdl	bdl	bdl	bdl	bdl	99.60
SEM45-Pt-c6-48-1	20.92	34.21	43.08	0.16	bdl	bdl	bdl	bdl	bdl	98.44
SEM45-Pt-c6-48-2	21.58	34.92	43.39	bdl	bdl	bdl	bdl	bdl	0.08	100.11
SEM45-Pt-c6-48-3	21.24	35.10	43.38	0.20	bdl	bdl	bdl	bdl	bdl	100.05
SEM45-Pt-c6-48-4	21.58	34.78	43.38	0.10	bdl	bdl	bdl	bdl	bdl	99.93
SEM45-Pt-c6-48-5	21.91	34.89	42.98	bdl	bdl	bdl	bdl	bdl	bdl	99.99
SEM45-Pt-c6-48-6	21.43	34.89	43.20	0.19	bdl	bdl	bdl	bdl	bdl	99.84
SEM45-Pt-c6-48-7	21.43	35.13	43.26	bdl	bdl	bdl	bdl	bdl	bdl	100.12
SEM45-Pt-c6-48-8	21.29	34.99	43.60	0.24	bdl	bdl	bdl	bdl	bdl	100.25
SEM45-Pt-c6-48-9	20.99	34.51	44.31	0.35	bdl	bdl	bdl	bdl	bdl	100.30
SEM45-Pt-c6-48-10	21.41	34.73	43.48	0.29	bdl	bdl	bdl	bdl	bdl	100.03
SEM45-Pt-c6-48-11	20.79	34.57	43.97	0.40	bdl	bdl	bdl	bdl	bdl	99.81
SEM45-Pt-c6-48-12	21.13	34.43	43.79	0.18	bdl	bdl	bdl	bdl	bdl	99.64
SEM45-Pt-c6-48-13	21.29	34.58	43.84	bdl	bdl	bdl	bdl	bdl	bdl	99.86
SEM45-Pt-c6-48-14	21.06	35.05	43.65	0.38	bdl	bdl	bdl	bdl	bdl	100.15
SEM45-Pt-c6-48-15	21.21	34.88	43.60	0.33	bdl	bdl	bdl	bdl	bdl	100.09
SEM45-Pt-c6-48-16	20.89	34.78	43.91	0.32	bdl	bdl	bdl	bdl	bdl	100.04
SEM45-Pt-c6-48-17	21.36	35.11	43.83	0.26	bdl	bdl	bdl	bdl	bdl	100.71
SEM45-Pt-c6-48-18	20.99	34.72	43.67	0.32	bdl	bdl	bdl	bdl	bdl	99.90
SEM45-Pt-c6-48-19	21.11	34.93	43.76	0.31	bdl	bdl	bdl	bdl	bdl	100.21
SEM45-Pt-c6-48-20	21.40	34.93	43.49	0.28	bdl	bdl	bdl	bdl	bdl	100.15
SEM45-Pt-c6-48-21	21.08	34.64	44.00	0.19	bdl	bdl	bdl	bdl	bdl	99.94
SEM45-Pt-c6-48-22	21.72	35.22	43.09	0.46	bdl	bdl	bdl	bdl	bdl	100.60
SEM45-Pt-c6-48-23	21.60	34.86	43.46	bdl	bdl	bdl	bdl	bdl	bdl	100.19
SEM45-Pt-c6-48-24	21.18	35.04	43.59	0.39	bdl	bdl	bdl	bdl	bdl	100.28
SEM45-Pt-c6-48-25	21.31	34.72	43.55	0.44	bdl	bdl	bdl	bdl	bdl	100.17
SEM45-Pt-c6-48-26	21.54	34.65	43.67	0.41	bdl	bdl	bdl	bdl	bdl	100.35
SEM45-Pt-c6-48-27	20.80	34.94	43.92	0.36	bdl	bdl	bdl	bdl	bdl	100.27
SEM45-Pt-c6-48-28	20.97	34.69	43.89	0.34	bdl	bdl	bdl	bdl	bdl	100.08
SEM45-Pt-c6-48-29	20.83	34.78	44.04	0.27	bdl	bdl	bdl	bdl	bdl	100.02
SEM45-Pt-c6-48-30	21.22	34.71	43.74	0.27	bdl	bdl	bdl	bdl	bdl	100.06
SEM45-Pt-c6-48-31	21.16	35.08	43.40	0.19	bdl	bdl	bdl	bdl	bdl	99.94
SEM45-Pt-c6-48-32	21.51	35.33	43.41	0.11	bdl	bdl	bdl	bdl	bdl	100.55
SEM45-Pt-c6-48-33	21.42	35.27	43.11	bdl	bdl	bdl	bdl	bdl	bdl	100.01
SEM45-Pt-c6-48-34	22.32	35.65	42.14	bdl	bdl	bdl	bdl	bdl	bdl	100.23
SEM45-Pt-c6-48-35	21.67	35.15	42.33	0.62	bdl	bdl	bdl	bdl	bdl	99.82
SEM45-Pt-c6-48-36	20.76	34.74	42.67	1.31	bdl	bdl	bdl	bdl	bdl	99.49

SEM45-Pt-c6-48-37	21.46	35.37	43.36	0.30	bdl	bdl	bdl	bdl	bdl	100.70
SEM45-Pt-c6-48-38	21.73	35.01	43.35	0.09	bdl	bdl	bdl	bdl	bdl	100.29
SEM45-Pt-c6-48-39	21.35	35.05	43.23	0.09	bdl	bdl	bdl	bdl	bdl	99.74
SEM45-Pt-c6-48-40	21.94	35.32	43.51	bdl	bdl	bdl	bdl	bdl	bdl	101.00
SEM45-Pt-c6-48-41	22.95	35.50	41.17	0.11	bdl	bdl	bdl	bdl	bdl	99.83
SEM45-Pt-c6-48-42	21.74	35.19	42.34	0.66	bdl	bdl	bdl	bdl	bdl	100.04
SEM45-Pt-c6-48-43	21.73	34.86	42.81	0.27	bdl	bdl	bdl	bdl	bdl	99.84
SEM45-Pt-hc-49	21.85	35.03	42.05	0.59	bdl	bdl	bdl	bdl	bdl	99.59
SEM45-Pt-hc-50	21.47	35.54	43.10	bdl	bdl	bdl	bdl	bdl	bdl	100.28
SEM45-Pt-hc-51	21.69	35.48	43.07	0.18	bdl	bdl	bdl	bdl	bdl	100.50
SEM45-Tr-hc-52-1	20.98	34.78	43.30	1.10	bdl	bdl	bdl	bdl	bdl	100.32
SEM45-Tr-hc-52-2	21.29	34.87	43.68	0.23	bdl	bdl	bdl	bdl	bdl	100.17
SEM45-Tr-hc-52-3	21.42	34.98	43.81	0.17	bdl	bdl	bdl	bdl	bdl	100.49
SEM45-Tr-hc-52-4	21.32	34.88	43.52	bdl	bdl	bdl	bdl	bdl	bdl	99.90
SEM45-Tr-hc-52-5	20.97	34.54	42.98	0.82	bdl	bdl	bdl	bdl	bdl	99.40
SEM45-Tr-hc-52-6	21.43	34.83	42.79	0.82	bdl	bdl	bdl	bdl	0.16	100.18
SEM45-Tr-hc-52-7	22.52	35.30	42.04	bdl	bdl	bdl	bdl	bdl	bdl	99.97
SEM45-Tr-hc-52-8	21.69	34.96	43.23	bdl	bdl	bdl	bdl	bdl	0.13	100.16
SEM45-Tr-hc-52-9	20.39	34.85	43.54	0.90	bdl	bdl	bdl	bdl	bdl	99.90
SEM45-Tr-hc-52-10	20.68	34.75	43.66	0.87	bdl	bdl	bdl	bdl	bdl	99.97
SEM45-Tr-hc-52-11	20.62	34.89	43.94	0.24	bdl	bdl	bdl	bdl	bdl	99.74
SEM45-Tr-hc-52-12	21.10	34.90	42.92	0.97	bdl	bdl	bdl	bdl	bdl	100.03
SEM45-Tr-hc-52-13	20.86	35.17	43.77	0.27	bdl	bdl	bdl	bdl	bdl	100.12
SEM45-Tr-hc-52-14	20.93	34.91	43.81	0.30	bdl	bdl	bdl	bdl	bdl	100.08
SEM45-Tr-hc-52-15	20.60	35.09	43.98	0.31	bdl	bdl	bdl	bdl	bdl	100.19
SEM45-Tr-hc-52-16	20.75	34.39	43.86	0.31	bdl	bdl	bdl	bdl	bdl	99.42
SEM45-Tr-hc-52-17	21.71	34.84	42.23	0.09	bdl	bdl	bdl	bdl	bdl	98.99
SEM45-Tr-hc-52-18	20.89	35.09	43.83	bdl	bdl	bdl	bdl	bdl	bdl	99.97
SEM45-Tr-hc-52-19	20.61	34.75	44.26	0.44	bdl	bdl	bdl	bdl	bdl	100.14
SEM45-Tr-hc-52-20	21.13	34.96	43.81	0.23	bdl	bdl	bdl	bdl	bdl	100.29
SEM45-Tr-hc-52-21	20.97	34.72	43.76	0.52	bdl	bdl	bdl	bdl	bdl	100.07
SEM45-Tr-hc-52-22	20.99	34.97	43.76	0.19	bdl	bdl	bdl	bdl	bdl	100.08
SEM45-Tr-hc-52-23	21.04	34.79	43.95	0.34	bdl	bdl	bdl	bdl	bdl	100.29
SEM45-Tr-hc-52-24	21.28	34.84	43.68	0.40	bdl	bdl	bdl	bdl	bdl	100.27
SEM45-Tr-hc-52-25	20.94	35.04	43.94	bdl	bdl	bdl	bdl	bdl	bdl	100.03
SEM45-Tr-hc-52-26	21.13	34.13	43.65	0.09	bdl	bdl	bdl	0.62	0.11	99.79
SEM45-Tr-hc-52-27	21.22	35.17	43.48	0.53	bdl	bdl	bdl	bdl	bdl	100.52
SEM45-Tr-hc-52-28	20.73	35.04	44.06	0.23	bdl	bdl	bdl	bdl	bdl	100.19
SEM45-Tr-hc-52-29	21.11	34.93	43.61	0.21	bdl	bdl	bdl	bdl	bdl	100.09
SEM45-Tr-hc-52-30	21.54	34.92	43.43	0.25	bdl	bdl	bdl	bdl	bdl	100.19
SEM45-Tr-hc-52-31	21.46	34.83	43.30	0.26	bdl	bdl	bdl	bdl	bdl	99.93
SEM45-Tr-hc-52-32	21.21	35.13	43.26	0.27	bdl	bdl	bdl	bdl	bdl	99.98
SEM45-Tr-hc-52-33	20.93	34.45	43.14	0.27	bdl	bdl	bdl	bdl	bdl	98.85
SEM45-Tr-hc-52-34	20.99	35.05	43.71	0.17	bdl	bdl	bdl	bdl	bdl	99.94
SEM45-Tr-hc-52-35	20.93	35.21	43.64	0.25	bdl	bdl	bdl	bdl	bdl	100.08
SEM45-Tr-hc-52-36	22.17	35.29	42.43	bdl	bdl	bdl	bdl	bdl	bdl	100.11
SEM45-Tr-hc-52-37	21.20	34.93	43.40	bdl	bdl	bdl	bdl	bdl	bdl	99.61
SEM45-Tr-hc-52-38	21.42	35.06	43.53	bdl	bdl	bdl	bdl	bdl	bdl	100.21
SEM45-Tr-hc-52-39	20.09	34.27	46.28	0.21	bdl	bdl	bdl	bdl	bdl	101.00

SEM45-Tr-hc-52-40	21.68	35.33	43.05	0.09	bdl	bdl	bdl	bdl	bdl	100.18
SEM45-Tr-hc-52-41	21.02	34.88	43.61	0.14	bdl	bdl	bdl	bdl	bdl	99.73
SEM45-Tr-hc-52-42	21.40	34.78	43.54	0.12	bdl	bdl	bdl	bdl	bdl	99.89
SEM45-Tr-hc-52-43	21.35	35.06	43.96	bdl	bdl	bdl	bdl	bdl	bdl	100.53
SEM45-Tr-hc-52-44	21.38	34.72	43.69	0.15	bdl	bdl	bdl	bdl	bdl	99.95
SEM45-Tr-hc-52-45	21.75	34.97	42.83	0.20	bdl	bdl	bdl	bdl	bdl	99.84
SEM45-Tr-hc-52-46	20.29	34.07	46.91	0.14	bdl	bdl	bdl	bdl	bdl	101.64
SEM45-Tr-hc-52-47	21.17	35.09	43.57	bdl	bdl	bdl	bdl	bdl	bdl	100.05
SEM45-Tr-hc-52-48	21.31	34.90	43.32	bdl	bdl	bdl	bdl	bdl	bdl	99.57
SEM45-Tr-hc-53-1	22.21	35.46	42.17	bdl	bdl	bdl	bdl	bdl	bdl	100.14
SEM45-Tr-hc-53-2	21.27	34.92	43.49	0.13	bdl	bdl	bdl	bdl	bdl	99.87
SEM45-Tr-hc-53-3	21.68	35.09	43.12	bdl	bdl	bdl	bdl	bdl	bdl	99.98
SEM45-Tr-hc-53-4	21.74	35.40	42.75	bdl	bdl	bdl	bdl	bdl	bdl	99.93
SEM45-Tr-hc-53-5	22.00	35.24	42.84	0.12	bdl	bdl	bdl	bdl	bdl	100.30
SEM45-Tr-hc-53-6	21.95	35.16	43.10	bdl	bdl	bdl	bdl	bdl	bdl	100.42
SEM45-Tr-hc-53-7	21.15	35.34	43.62	0.17	bdl	bdl	bdl	bdl	bdl	100.49
SEM45-Tr-hc-53-8	21.50	35.03	43.09	0.11	bdl	bdl	bdl	bdl	bdl	99.77
SEM45-Tr-hc-53-9	21.58	34.93	43.38	bdl	bdl	bdl	bdl	bdl	bdl	100.00
SEM45-Tr-hc-53-10	22.06	35.55	42.62	bdl	bdl	bdl	bdl	bdl	bdl	100.38
SEM45-Tr-hc-53-11	21.68	35.00	43.34	0.26	bdl	bdl	bdl	bdl	bdl	100.31
SEM45-Tr-hc-53-12	21.14	35.05	43.50	0.35	bdl	bdl	bdl	bdl	bdl	100.26
SEM45-Tr-hc-53-13	20.95	34.93	43.82	0.25	bdl	bdl	bdl	bdl	bdl	100.12
SEM45-Tr-hc-53-14	21.34	34.80	43.53	0.42	bdl	bdl	bdl	bdl	bdl	100.15
SEM45-Tr-hc-53-15	20.94	34.50	43.63	0.43	bdl	bdl	bdl	bdl	bdl	99.53
SEM45-Tr-hc-53-16	21.01	35.01	43.66	0.32	bdl	bdl	bdl	bdl	bdl	100.02
SEM45-Tr-hc-53-17	20.86	34.96	43.67	0.22	bdl	bdl	bdl	bdl	bdl	99.80
SEM45-Tr-hc-53-18	21.15	35.05	43.56	0.25	bdl	bdl	bdl	bdl	bdl	100.16
SEM45-Tr-hc-53-19	20.99	34.66	43.50	0.27	bdl	bdl	bdl	bdl	bdl	99.58
SEM45-Tr-hc-53-20	20.18	34.36	45.26	0.30	bdl	bdl	bdl	bdl	bdl	100.16
SEM45-Tr-hc-53-21	21.44	35.17	43.69	0.24	bdl	bdl	bdl	bdl	bdl	100.55
SEM45-Tr-hc-53-22	20.93	34.88	43.55	0.31	bdl	bdl	bdl	bdl	bdl	99.72
SEM45-Tr-hc-53-23	20.89	34.74	43.94	0.30	bdl	bdl	bdl	bdl	bdl	100.00
SEM45-Tr-hc-53-24	21.15	34.63	43.82	0.34	bdl	bdl	bdl	bdl	bdl	99.98
SEM45-Tr-hc-53-25	21.18	34.90	43.59	0.46	bdl	bdl	bdl	bdl	bdl	100.25
SEM45-Tr-hc-53-26	20.32	34.71	44.33	0.32	bdl	bdl	bdl	bdl	bdl	99.92
SEM45-Tr-hc-53-27	20.60	34.66	44.04	0.47	bdl	bdl	bdl	bdl	bdl	99.93
SEM45-Tr-hc-53-28	20.72	34.75	44.01	0.38	bdl	bdl	bdl	bdl	bdl	99.99
SEM45-Tr-hc-53-29	21.07	35.07	43.64	0.49	bdl	bdl	bdl	bdl	bdl	100.38
SEM45-Tr-hc-53-30	20.99	34.88	43.06	1.01	bdl	bdl	bdl	bdl	bdl	100.01
SEM45-Tr-hc-53-31	20.70	35.03	43.58	0.51	bdl	bdl	bdl	bdl	bdl	99.82
SEM45-Tr-hc-53-32	21.20	35.06	43.67	0.30	bdl	bdl	bdl	bdl	bdl	100.49
SEM45-Tr-hc-53-33	21.02	35.08	43.78	0.20	bdl	bdl	bdl	bdl	bdl	100.16
SEM45-Tr-hc-53-34	21.91	35.10	42.62	bdl	bdl	bdl	bdl	bdl	bdl	99.98
SEM45-Tr-hc-53-35	20.70	34.90	44.01	0.24	bdl	bdl	bdl	bdl	bdl	99.87
SEM45-Tr-hc-53-36	21.06	34.91	43.76	0.21	bdl	bdl	bdl	bdl	bdl	100.03
SEM45-Tr-hc-53-37	20.65	34.60	43.88	0.40	bdl	bdl	bdl	bdl	bdl	99.74
SEM45-Tr-hc-53-38	20.68	34.58	43.74	0.39	bdl	bdl	bdl	bdl	0.09	99.68
SEM45-Tr-hc-53-39	20.52	34.65	43.80	0.40	bdl	bdl	bdl	bdl	0.09	99.56
SEM45-Tr-hc-53-40	20.99	34.96	43.66	0.48	bdl	bdl	bdl	bdl	bdl	100.14

SEM45-Tr-hc-53-41	20.82	35.01	43.82	0.36	bdl	bdl	bdl	bdl	bdl	100.07
SEM45-Tr-hc-53-42	20.79	34.88	43.84	0.43	bdl	bdl	bdl	bdl	bdl	99.95
SEM45-Tr-hc-53-43	20.64	35.03	43.85	0.22	bdl	bdl	bdl	bdl	bdl	99.84
SEM45-Tr-hc-53-44	21.78	35.02	42.91	bdl	bdl	bdl	bdl	bdl	bdl	99.81
SEM45-Tr-hc-53-45	21.11	34.85	43.33	0.33	bdl	bdl	bdl	bdl	bdl	99.75
SEM45-Tr-hc-53-46	21.43	34.94	43.41	0.16	bdl	bdl	bdl	bdl	bdl	100.04
SEM45-Tr-hc-53-47	21.67	34.98	43.18	0.17	bdl	bdl	bdl	bdl	bdl	100.26
SEM45-Tr-hc-53-48	21.41	35.02	43.21	0.17	bdl	bdl	bdl	bdl	bdl	99.83
Average	21.23	34.92	43.48	0.35	-	-	-	0.64	0.11	100.04
Stdev	0.45	0.29	0.64	0.25	-	-	-	0.07	0.02	0.36

Magmatic pyrite

D.L.	0.09	0.10	0.01	0.05	0.03	0.12	0.05	0.03	0.05	
TOU1 c4-1	52.23	46.28	bdl	bdl	bdl	0.15	bdl	0.11	bdl	98.81
TOU1 c4-2	51.70	46.51	bdl	bdl	bdl	bdl	bdl	0.09	0.10	98.46
TOU1 c4-3	51.68	46.79	bdl	bdl	bdl	bdl	bdl	0.03	0.06	98.57
TOU1 c4-4	52.31	46.77	bdl	bdl	bdl	bdl	0.08	bdl	bdl	99.22
TOU1 c4-5	52.83	47.53	bdl	bdl	bdl	0.24	bdl	bdl	bdl	100.64
TOU1 c4-6	52.63	47.33	bdl	bdl	bdl	bdl	0.07	bdl	bdl	100.06
TOU1 c4-7	52.50	47.33	bdl	0.06	bdl	bdl	bdl	0.06	0.10	100.06
TOU1 c5-1	51.78	46.71	bdl	0.06	bdl	bdl	0.06	bdl	bdl	98.64
TOU1 c5-2	52.80	48.71	0.01	bdl	bdl	bdl	bdl	bdl	bdl	101.58
TOU1 c5-3	52.39	47.49	bdl	bdl	bdl	bdl	bdl	bdl	bdl	100.02
TOU1 c5-4	52.79	47.73	0.02	bdl	bdl	bdl	bdl	0.14	bdl	100.76
TOU1 c5-5	52.79	47.71	bdl	bdl	0.05	bdl	bdl	bdl	bdl	100.66
TOU1 c5-6	52.61	47.89	0.01	bdl	bdl	0.26	bdl	bdl	bdl	100.84
TOU1 c5-7	52.68	47.50	0.07	bdl	bdl	bdl	bdl	bdl	bdl	100.33
MF1 c6-1	53.17	47.71	bdl	bdl	bdl	bdl	bdl	0.05	bdl	101.07
MF1 c6-2	53.01	47.44	bdl	bdl	bdl	bdl	bdl	0.27	0.06	100.84
MF1 c6-3	53.02	46.20	0.03	bdl	bdl	bdl	bdl	0.80	bdl	100.05
MF1 c5-1	52.18	46.20	0.05	bdl	bdl	bdl	bdl	0.12	bdl	98.56
MF1 c5-2	52.85	47.94	0.06	bdl	bdl	0.13	bdl	bdl	bdl	101.05
MF1 c5-3	52.76	47.78	bdl	bdl	bdl	bdl	bdl	0.30	bdl	100.86
MF1 c5-4	52.91	47.40	bdl	bdl	bdl	bdl	bdl	bdl	bdl	100.44
Average	52.55	47.28	0.04	0.06	0.05	0.19	0.07	0.20	0.08	100.07
Stdev	0.43	0.66	0.02	0.02	0.01	0.08	0.03	0.18	0.03	0.97

Hydrothermal pyrite

D.L.	0.16	0.08	0.04	0.08	0.07	0.11	0.20	0.06	0.06	
SEM45-Tr-hc-43-1	53.42	45.98	0.26	bdl	bdl	bdl	bdl	bdl	bdl	99.82
SEM45-Tr-hc-43-2	54.04	46.26	0.18	bdl	bdl	bdl	bdl	bdl	bdl	100.63
SEM45-Tr-hc-43-3	53.05	46.14	0.70	bdl	bdl	bdl	bdl	bdl	bdl	100.14
SEM45-Tr-hc-43-4	54.12	45.89	0.02	bdl	bdl	bdl	bdl	bdl	bdl	100.18
SEM45-Tr-hc-43-5	53.43	46.10	0.05	bdl	bdl	bdl	bdl	bdl	bdl	99.71
SEM45-Tr-hc-43-6	53.53	46.10	0.14	bdl	bdl	bdl	bdl	bdl	bdl	99.91
SEM45-Tr-hc-43-7	53.71	46.05	0.04	bdl	bdl	bdl	bdl	bdl	bdl	100.04
SEM45-Tr-hc-43-8	54.72	45.88	0.11	bdl	bdl	bdl	bdl	0.10	bdl	100.92
SEM45-Tr-hc-43-9	53.74	46.20	0.52	bdl	bdl	bdl	bdl	bdl	bdl	100.60

SEM45-Tr-hc-43-10	52.40	46.48	0.55	bdl	bdl	bdl	bdl	bdl	bdl	99.64
SEM45-Tr-hc-43-11	53.34	46.43	0.22	bdl	bdl	bdl	bdl	bdl	bdl	100.08
SEM45-Tr-hc-43-12	53.40	46.39	0.32	bdl	bdl	bdl	bdl	bdl	bdl	100.17
SEM45-Tr-hc-43-13	53.63	46.15	0.65	bdl	bdl	bdl	bdl	bdl	bdl	100.49
SEM45-Tr-hc-43-14	53.25	46.26	0.61	bdl	bdl	bdl	bdl	bdl	bdl	100.31
SEM45-Tr-hc-43-15	53.36	46.02	0.76	bdl	bdl	bdl	bdl	bdl	0.07	100.28
SEM45-Tr-hc-43-16	52.99	46.34	0.89	bdl	bdl	bdl	bdl	bdl	bdl	100.45
SEM45-Tr-hc-43-17	52.94	46.26	0.60	bdl	bdl	bdl	bdl	bdl	bdl	99.86
SEM45-Tr-hc-43-18	52.43	46.09	0.81	bdl	bdl	bdl	bdl	bdl	bdl	99.45
SEM45-Tr-hc-43-19	52.85	46.06	0.49	bdl	bdl	bdl	bdl	bdl	bdl	99.46
SEM45-Tr-hc-43-20	52.13	45.91	1.10	bdl	bdl	bdl	bdl	bdl	bdl	99.41
SEM45 c3-1	52.77	47.63	0.75	bdl	bdl	bdl	bdl	bdl	bdl	101.30
SEM45 c3-2	53.85	47.88	0.02	bdl	bdl	bdl	bdl	bdl	bdl	101.79
SEM45 c3-3	53.11	47.23	0.79	bdl	bdl	0.14	bdl	bdl	bdl	101.29
SEM45 c3-4	52.98	46.64	1.01	bdl	bdl	bdl	bdl	bdl	0.08	100.81
SEM45 c3-5	53.49	47.78	0.02	bdl	bdl	bdl	bdl	bdl	bdl	101.33
SEM45 c2-1	53.52	47.11	0.00	bdl	bdl	bdl	bdl	bdl	bdl	100.74
SEM45 c2-2	53.40	47.69	0.01	bdl	bdl	bdl	bdl	bdl	bdl	101.17
SEM45 c2-3	53.57	47.34	0.33	bdl	bdl	bdl	bdl	bdl	bdl	101.31
SEM45 c1-1	52.60	46.30	0.00	bdl	bdl	bdl	bdl	0.18	bdl	99.22
SEM45 c1-2	53.10	47.43	0.75	bdl	bdl	bdl	bdl	bdl	bdl	101.30
SEM45 c1-3	52.66	47.67	0.90	bdl	bdl	bdl	bdl	bdl	bdl	101.26
SEM45 c1-4	53.13	47.62	1.16	bdl	bdl	bdl	bdl	bdl	bdl	101.94
SEM45 c1-5	53.78	47.22	0.01	bdl	bdl	bdl	bdl	bdl	bdl	101.09
SEM45 c1-6	53.34	47.16	0.01	bdl	bdl	bdl	bdl	bdl	bdl	100.61
SEM45 c1-7	53.47	47.14	0.38	bdl	bdl	bdl	bdl	bdl	bdl	101.07
LS4A c1-2	52.79	47.43	1.08	bdl	bdl	0.17	bdl	bdl	bdl	101.51
LS4A c1-3	52.67	47.44	0.48	bdl	bdl	bdl	bdl	bdl	bdl	100.71
LS4A c1-4	53.06	47.41	0.52	bdl	bdl	bdl	bdl	bdl	bdl	101.03
LS4A c1-6	53.15	47.46	0.53	bdl	bdl	bdl	bdl	bdl	bdl	101.20
LS4A c1-7	53.21	47.23	0.56	bdl	bdl	bdl	bdl	bdl	bdl	101.06
LS4A c2-1	52.64	47.40	1.04	bdl	bdl	bdl	bdl	bdl	bdl	101.17
LS4A c2-2	52.66	47.48	0.76	bdl	bdl	0.12	bdl	bdl	bdl	101.05
LS4A c2-5	53.45	47.62	0.08	bdl	bdl	bdl	bdl	bdl	bdl	101.22
LS4A c2-6	51.80	46.65	1.26	bdl	bdl	bdl	bdl	bdl	bdl	99.78
Average	53.20	46.79	0.49			0.14		0.14	0.08	100.60
Stdev	0.54	0.67	0.38			0.04		0.03	0.02	0.70

Abbreviations: D.L., detection limit; Stdev, standard deviation; bdl, below detection limit

Values below the detection limit are not taken into account for the calculation of average

Table A.8 LA-ICP-MS results for trace elements composition of pyrite from the altered gabbro of Semnon Sb-Au deposit

Isotope	^{34}S	^{59}Co	^{60}Ni	^{62}Ni	^{63}Cu	^{65}Cu	^{66}Zn	^{72}Ge	^{74}Ge	^{75}As	^{78}Se	^{95}Mo	^{100}Ru	^{101}Ru	^{103}Rh	^{105}Pd	^{106}Pd	^{107}Ag	^{108}Pd	^{111}Cd	^{113}Cd	^{115}In	^{118}Sn
	ppm																						
D.L.	148.3457	0.0004	0.0147	0.0530	0.0043	0.0054	0.0186	0.0265	0.0117	0.0972	0.4245	0.0003	0.0004	0.0001	0.0001	0.0005	0.0005	0.0019	0.0004	0.0052	0.0038	0.0005	0.0086
LS4A-C1-PY1-1	532000	21.1	23	26.7	14	1.77	0.49	0.7	0.069	7590	bdl	0.369	0.357	bdl	bdl	bdl	bdl	0.0182	0.0007	0.0059	0.0043	0.0051	0.015
LS4A-C1-PY1-3	545000	9.9	6.5	5.9	0.92	0.84	0.076	0.387	0.012	10370	bdl	0.066	0.062	bdl	bdl	bdl	bdl	0.0061	0.0008	bdl	bdl	0.0062	0.0153
LS4A-C1-PY1-5	556000	11.8	25.3	23.7	0.483	0.55	0.16	0.385	0.0101	12200	bdl	0.0027	0.003	bdl	bdl	0.0013	bdl	bdl	bdl	bdl	bdl	0.008	0.029
LS4A-C1-PY1-8	563000	1.4	1.23	1.6	0.48	0.47	0.106	0.434	0.0132	15780	bdl	0.017	0.015	bdl	bdl	0.0006	bdl	0.0027	bdl	bdl	0.0008	0.0128	0.0236
LS4A-C1-PY1-10	528000	5.09	2.42	2.51	1.17	1.3	0.068	0.546	0.073	1790	bdl	0.157	0.145	bdl	bdl	0.001	bdl	0.0089	0.0013	bdl	0.0007	0.0019	0.0177
LS4A-C1-PY1-12	580000	21.3	16.1	18.7	1.2	1.26	0.228	0.49	0.037	10140	bdl	0.036	0.025	bdl	bdl	0.004	0.107	0.035	0.044	0.035		0.0079	0.058
LS4A-C1-PY1-13	600000	40	58	69	2.1	2	2.14	0.412	0.045	10520	bdl	0.129	0.106	bdl	0.00025	0.0049	0.228	0.066	0.09	0.06	0.0054	0.0094	0.084
LS4A-C2-PY2-1	561000	5.96	5.1	5.44	3.49	3.73	0.6	0.416	0.036	6390	bdl	0.0026	0.0008	bdl	0.00058	0.0014	0.0018	0.0271	0.0015	0.0119	0.0132	0.0054	0.0174
LS4A-C2-PY2-4	554000	93	82.2	86	12.2	12.3	1.9	0.541	0.101	12470	bdl	0.7	0.59	bdl	0.00053	0.0034	0.0094	0.057	0.0025	0.0201	0.0138	0.0135	1.16
LS4A-C2-PY2-3	606000	7.1	10.4	10.4	3.26	3.66	8.5	0.504	0.12	6150	bdl	0.0027	0.0076	bdl	0.00053	0.0036	0.0009	0.0265	0.0007	0.0094	0.0092	0.0054	0.053
LS4A-C2-PY2-7	604000	37	24.8	27.1	2.36	2.25	4	0.551	0.092	7320	bdl	0.001	0.0052	bdl	0.0044	0.0039	0.012	0.0101	0.0011	0.0052	0.0085	0.01	0.048
D.L.	120.29480	0.00049	0.01844	0.06897	0.00668	0.00894	0.02300	0.03293	0.01567	0.12621	0.48376	0.00066	0.00048	0.00014	0.00005	0.00043	0.00041	0.00233	0.00050	0.00704	0.00483	0.00077	0.00935
SEM45-C1-PY1-1	505000	0.86	10.99	13.8	7.97	9.4	0.49	0.51	0.062	8230	bdl	0.0067	0.0077	bdl	0.00025	bdl	0.0121	0.0263	0.0027	bdl	bdl	0.0075	0.272
SEM45-C1-PY1-2	476000	35.9	79	89	5.7	5.59	2.79	0.55	0.068	9440	bdl	0.06	0.072	bdl	0.0005	0.0027	0.0155	0.032	0.0037	bdl	bdl	0.008	0.168
SEM45-C1-PY-3	528000	680	111	109	6.09	5.23	1.54	5.9	1.27	6430	1	0.038	0.038	bdl	0.00021	0.067	0.084	0.04	0.0047	0.053	0.015	0.0054	0.119
SEM45-C1-PY2-1	521000	5.7	7.8	9.3	20.4	21.6	0.163	0.356	bdl	12280	bdl	0.0072	0.0013	bdl	0.00034	0.0009	bdl	bdl	bdl	bdl	bdl	0.008	bdl
SEM45-C1-PY2-2	483000	204	40	43.7	5.03	5.47	4.4	0.448	0.055	1210	2.3	0.34	0.332	bdl	0.00016	0.0029	0.019	0.063	0.0118	0.015	0.0058	0.00209	0.067
SEM45-C1-PY2-3	493000	417	114	110	7.87	8.2	9	0.58	0.249	296	8.9	0.026	0.025	bdl	0.00073	0.0007	0.0017	0.137	0.0023	0.038	0.024	0.01	0.046
SEM45-C1-PY2-4	525000	363	154	165	10.6	10.4	18.1	0.467	0.07	4510	bdl	0.473	0.423	bdl	0.0006	0.0008	0.019	0.098	0.0062	0.027	0.0116	0.0079	0.084
SEM45-C2-PY3-1	449000	1200	204	175	11.72	11.32	5.05	0.471	0.182	123.6	17.7	0.196	0.195	bdl	0.00166	0.0012	0.0035	0.251	0.0017	0.038	0.0227	0.0052	0.0391
SEM45-C2-PY3-2	456000	469	374	313	13.2	13.05	7.04	0.489	0.214	114	17.3	0.55	0.45	bdl	0.00164	0.001	0.0006	0.243	0.0013	0.0126	0.0114	0.003	0.035
SEM45-C2-PY3-3	533000	1320	137	140	6.25	6.9	3.09	0.55	0.127	2230	5.6	0.0017	0.014	bdl	0.0016	0.001	0.0009	0.103	bdl	bdl	0.008	0.0042	0.014
SEM45-C3-PY4-1	566000	10.3	41.1	44.3	2.01	2.27	0.31	0.396	bdl	10120	bdl	0.0039	bdl	bdl	bdl	0.0019	0.0046	0.0066	bdl	bdl	bdl	0.0063	0.074
SEM45-C3-PY4-2	465000	840	103	89	5.6	5.8	5.5	0.422	0.133	330	14.1	0.54	0.63	bdl	0.0008	0.0018	0.0044	0.079	0.002	0.0085	0.0123	0.016	0.13
SEM45-C3-PY4-3	539000	790	80	86.9	4.62	4.56	1.32	0.422	0.067	7400	9.3	bdl	0.0044	bdl	0.00083	bdl	0.002	0.09	bdl	bdl	0.0058	0.0064	0.0204
SEM45-C3-PY4-4	546000	11.3	11.1	13.5	5.8	5.7	6.9	0.45	0.018	9000	bdl	0.66	0.76	bdl	0.00047	bdl	bdl	0.0108	bdl	bdl	bdl	0.0057	bdl
SEM45-C3-PY4-5	449000	632	109	112.4	10.5	10.5	6.8	0.53	0.283	1020	16.7	0.346	0.293	bdl	0.00093	0.0006	0.0039	0.124	0.0007	0.0094	0.013	0.0038	0.023
Average	529346	278	70.4	68.9	6.35	6.00	3.49	0.69	0.13	6671	10.3	0.189	0.182		0.001	0.005	0.028	0.060	0.009	0.017	0.01	0.01	0.10
Stdev	46420	397	82.8	72.4	5.04	5.00	4.14	1.07	0.24	4584.64	6.20	0.232	0.229		0.001	0.013	0.049	0.068	0.019	0.02	0.01	0.00	0.22

Abbreviations: D.L., detection limit; Stdev, standard deviation; bdl, below detection limit

Values below the detection limit are not taken into account for the calculation of average

Table A.8 (suite)

Isotope	^{121}Sb	^{125}Te	^{182}W	^{185}Re	^{194}Pt	^{195}Pt	^{197}Au	^{205}Tl	^{208}Pb	^{209}Bi
D.L.	0.0026	0.0113	0.0002	0.0006	0.0002	0.0004	0.0004	0.0006	0.0007	0.0003
LS4A-C1-PY1-1	2.99	0.033	0.02	0.007	bdl	bdl	0.74	0.015	2.37	0.0249
LS4A-C1-PY1-3	0.83	0.029	0.0008	bdl	bdl	bdl	0.184	0.0043	1.38	0.0179
LS4A-C1-PY1-5	1.2	0.02	0.0027	bdl	bdl	bdl	0.94	0.0035	0.354	0.0013
LS4A-C1-PY1-8	3.81	0.018	0.008	bdl	bdl	bdl	0.66	0.009	1.13	0.0057
LS4A-C1-PY1-10	4.96	0.04	0.0094	bdl	bdl	bdl	0.159	0.0106	1.75	0.0219
LS4A-C1-PY1-12	13.3	0.024	0.137	bdl	0.0088	0.0035	0.666	0.0146	1.32	0.0039
LS4A-C1-PY1-13	13.2	0.03	0.51	bdl	0.0149	0.0119	1.26	0.0052	1.51	0.0159
LS4A-C2-PY2-1	57.4	0.039	0.78	bdl	bdl	bdl	1.01	0.0182	14.1	0.0159
LS4A-C2-PY2-4	217	0.026	31.1	bdl	0.0016	0.0015	2.77	0.0079	10.6	0.0366
LS4A-C2-PY2-3	74	0.055	0.12	bdl	bdl	bdl	1.11	0.0228	11.7	0.0154
LS4A-C2-PY2-7	38	0.041	0.078	bdl	0.0005	bdl	0.699	0.0431	4.13	0.0073
D.L.	0.00396	0.01119	0.00024	0.00089	0.00021	0.00007	0.00040	0.00072	0.00094	0.00037
SEM45-C1-PY1-1	124.1	0.014	18.7	bdl	0.0016	0.001	3.39	0.0041	0.545	0.0044
SEM45-C1-PY1-2	390	bdl	8.4	bdl	bdl	bdl	4.02	0.0052	2.71	0.0259
SEM45-C1-PY-3	191	0.085	5	0.001	0.0019	0.002	2.36	0.0026	8	0.094
SEM45-C1-PY2-1	8.7	bdl	0.11	bdl	bdl	bdl	22.5	bdl	0.165	bdl
SEM45-C1-PY2-2	515	0.089	0.59	bdl	0.0005	0.0022	0.598	0.0029	10.4	0.15
SEM45-C1-PY2-3	37	0.145	0.051	bdl	bdl	bdl	0.321	0.0052	54.7	1.158
SEM45-C1-PY2-4	606	0.159	2.88	bdl	0.0007	0.0011	1.27	0.0169	33.9	0.573
SEM45-C2-PY3-1	91	0.347	0.0279	bdl	bdl	bdl	0.0419	0.0153	167	2.58
SEM45-C2-PY3-2	134	0.167	0.037	bdl	bdl	bdl	0.06	0.02	168.8	1.365
SEM45-C2-PY3-3	9.4	0.093	0.0073	bdl	bdl	bdl	1.18	0.0097	75	0.78
SEM45-C3-PY4-1	14.5	bdl	0.85	bdl	bdl	bdl	2.45	0.0075	0.46	0.0168
SEM45-C3-PY4-2	310	0.15	0.115	bdl	0.0004	bdl	0.18	0.008	20.7	0.598
SEM45-C3-PY4-3	27.2	0.123	0.0127	bdl	bdl	bdl	1.27	0.0084	40.8	0.709
SEM45-C3-PY4-4	350	0.025	0.015	bdl	bdl	bdl	4.8	0.0062	0.84	0.028
SEM45-C3-PY4-5	414	0.267	0.18	bdl	0.0006	bdl	0.087	0.0136	66.9	1.111
Average	140.33	0.08	2.68	0.004	0.003	0.003	2.10	0.011	26.972	0.360
Stdev	178.98	0.09	7.03	0.001	0.003	0.002	4.3	0.01	46.68	0.62

Abbreviations: D.L., detection limit; Stdev, standard deviation; bdl, below detection limit

Values below the detection limit are not taken into account for the calculation of average

Table A.9 LA-ICP-MS results for trace elements composition of Fe-Ti oxides from the gabbro dyke of Semnon Sb-Au deposit

Isotope	^{24}Mg	^{25}Mg	^{27}Al	^{29}Si	^{31}P	^{44}Ca	^{43}Ca	^{45}Sc	^{47}Ti	^{49}Ti	^{51}V	^{52}Cr	^{53}Cr	^{55}Mn	^{56}Fe	^{57}Fe	^{59}Co	^{60}Ni	^{63}Cu	^{65}Cu	^{66}Zn
	ppm	ppm	ppm	ppm	ppm	ppm	ppm	ppm	ppm	ppm	ppm	ppm	ppm	ppm	ppm	ppm	ppm	ppm	ppm	ppm	ppm
Ilmenite																					
D.L.	0.0400	0.0988	0.1552	182	3.1	42	7.9	0.0265	0.0872	0.1288	0.0203	0.2990	0.2856	0.3193			0.0011	0.0559	0.0215	0.0337	0.0837
MF1-C1-IL1	2570	2370	2220	7000	12	3000	2700	40	350000	346100	1765	85	111	13660			18.18	7.1	0.9	3.96	255
MF1-C1-IL3-2	4700	4400	6600	36300	64	22200	22700	25.01	381400	381500	1355	55.3	63.3	15580			17.73	14.7	0.96	3.58	75.6
MF1-C1-IL3-3	15400	15200	15600	46100	63	24700	24400	50.6	369000	365000	1515	118.1	131.9	15200			25.2	30.3	1.35	4.33	108
MF1-C1-IL4	870	750	1660	2400	14	2700	2200	25.7	340000	342000	1560	111.5	136	14460			21.74	7.7	1.2	4.02	1660
MF1-C1-IL2	3300	3100	3000	9300	bdl	3500	3060	62.8	354000	350300	2263	195	222	14820			16.97	8.8	0.76	3.49	147.3
MF1-C1-IL3-4	2990	2410	3700	20000	45	17300	15400	35	369000	375000	1900	160	195	16720			12.91	9.6	0.72	3.59	88.2
MF1-C2-IL5-1	1500	1310	2750	13900	8.8	2290	1950	54	367300	366700	2105	214.4	219.8	14340			22.25	6.05	1.8	4.9	279
MF1-C2-IL5-2	1510	1212	1120	12900	52	4940	4190	49.6	364500	368500	2124	235.4	231.3	14380			18.43	4.88	0.751	12	252
MF1-C2-IL5-3	1980	1670	1640	14800	bdl	4340	3680	35.6	364800	367200	2533	207.8	212.2	13310			20.21	5.46	0.504	3.32	375
MF1-C2-IL6	1370	1050	2000	5500	27	4000	3480	31.7	364000	359000	1304	115	130	13590			22.61	6.09	0.513	3.14	155
MF1-C2-IL8	673	545	559	1370	bdl	290	277	26.35	356000	354900	2096	108.6	119.6	13570			22.95	7.8	0.541	3.1	561
MF1-C2-IL7	387	336	339	416	8	106	96	35	346500	348500	2260	158.1	175.4	13350			20.59	6.4	2	3.09	557
MF1-C3-IL9	1640	1340	2470	12100	21	14500	13800	41.6	367000	360000	1598	167	196	14610			15.16	7.5	0.556	3.19	98.6
MF1-C3-IL10	1890	1550	2100	9700	18.8	5900	5200	36.2	365000	365000	1878	278	271	13840			19.1	7.1	0.449	3.05	153.2
MF1-C3-IL11	2500	2300	4000	13400	9	5200	4600	12.91	378000	373000	1690	120.1	142.9	13810			20.5	8	0.421	3.17	107
MF1-C3-IL13	6900	6600	7700	17400	37	4430	3720	40.8	345400	343800	1976	153	173.1	13150			21.89	13.4	0.513	6.4	521
MF1-C3-IL14-1	500	425	325	2240	19	1160	960	46.7	354300	363000	1754	85.2	104.2	14950			14.75	4.6	0.468	2.99	121.8
MF1-C3-IL14-2	701	519	927	4090	9.4	3910	3250	28.5	358000	364000	2128	98.3	124	14840			13.42	5.77	0.496	3.15	426
MF1-C4-IL15-1	485	389	304	980	bdl	2870	2400	43	372700	372100	1647	97.3	113.8	16200			18.15	4.41	0.53	3.12	206
MF1-C4-IL15-2	1500	1118	696	15300	bdl	6930	5930	36	373000	376000	1556	64	77.8	14420			18.8	5.09	0.54	3.3	88.9
Average	2668	2430	2986	12260	27	6713	6200	38	361995	362080	1850	141	158	14440			19.1	8.5	0.80	4.0	312
Stdev	3390	3374	3571	11627	21	7103	7081	12	11157	11353	330	60	56	967			3.3	5.8	0.46	2.0	357
Titanohematite																					
D.L.	0.0336	0.0884	0.1103	113	2.3	32	6.0	0.0183	0.0655	0.1171	0.0151	0.2190	0.2212	0.2355			0.0008	0.0417	0.0124	0.0194	0.0625
BAN1-C1-IL1-1	5600	5000	5700	26800	33	46300	45800	28.42	863000	863000	2939	9.04	9.48	21400			36.9	38.2	82	91	165
BAN1-C1-IL2-1	1850	1528	8450	6450	3.9	7560	6420	7.81	159900	159800	4067	6.04	7.9	5477			32.1	80.8	45.4	47.6	811
BAN1-C1-IL3-1	4310	4220	5210	6380	bdl	1530	1250	6.96	151500	151600	4230	5.7	6.67	10280			27.81	59.2	24.8	26.8	248.2
BAN1-C1-IL3-2	692	559	13840	2080	bdl	930	730	6.07	137700	137300	3620	6.75	7.92	4920			31.62	68.3	42.4	44.7	661
BAN1-C1-IL6	726	578	8930	560	bdl	354	299	6.59	152600	151300	3428	3.69	4.48	6560			22.82	61.3	25.4	27.5	252.8
BAN1-C1-IL7-1	2350	2060	5810	5650	12	4650	4220	6.12	139400	139700	2768	13.03	15.3	6250			30	60.1	26	27.6	482
BAN1-C1-IL7-2	10810	10490	12100	23700	3.7	6240	5430	9.17	168700	170400	3580	3.96	4.6	6840			37	80	16.4	17.8	128.9
BAN1-C1-IL5	1746	1393	11430	3460	32.7	1100	920	4.24	141300	140300	3647	3.83	3.69	6070			30.34	71	20	21.6	701
BAN1-C2-IL8	3210	3100	5240	6720	22.8	2440	2050	6.64	146100	146900	4440	5.16	5.34	5960			23.67	62.8	41.1	43.9	366
BAN1-C2-IL9	1860	1710	10920	4200	249	910	790	7.18	146500	146600	3328	5.03	5.53	7010			31.74	65.5	30.1	32.2	305
BAN1-C2-IL10	7660	7570	12120	10900	bdl	3000	2490	8.6	152400	151800	3965	8.12	9.24	10680			31.9	87.2	31.6	32.8	393
BAN1-C2-IL11-2	566	463	13210	bdl	bdl	1830	1520	7.43	145500	144600	3990	4.44	6.15	5050			33	48.6	33.2	33.7	686
BAN1-C2-IL11-1	3600	3410	4370	7750	bdl	3630	3140	7.17	138800	138200	2922	2.05	3.24	7480			35.4	51.1	15.9	15.71	173.3
BAN1-C2-IL12	2710	2330	5450	3520	bdl	760	700	7.39	142900	144600	3220	4.7	5.3	7150			35.4	66.2	34.1	34.9	464
Average	3406	3172	8770	8321	51	5802	5411	9	199021	199007	3582	6	7	7938			31	64	33	36	417
Stdev	2914	2886	3434	7986	65	11856	11776	6	191301	191320	514	3	3	4232			4	13	17	19	224
D.L.	0.0618	0.1719	0.2645	254	11	78	13	0.0465	0.1302	0.1899	0.0321	0.5176	0.4948	0.5392			0.0034	0.0852	0.0257	0.0345	0.1520
TOU1-C1-IL2	14100	13600	18300	30100	1090	16800	14800	8.6	186200	184500	3330	1297	1375	7970			45.3	62.1	45	45.4	2480
TOU1-C1-IL3	384	352	4780	1690	bdl	460	362	4.48	164500	164200	2500	7560	8800	14700			32	52.6	20.4	22.7	7330
TOU1-C1-IL6	1340	1070	9070	10450	27	3680	3210	3.33	191000	185200	3900	630	570	1580			23.4	58.3	34	35.8	3160
TOU1-C2-IL18	205	195	5440	1410	bdl	930	800	3.58	172000	168300	3380	11020	12750	10170			34.4	49.6	28.2	29.3	6880
TOU1-C2-IL21	18800	18200	80000	164000	3800	49400	47600	9.8	188000	192000	4340	1469	1476	5130			47	97.3	17.2	18.9	430
TOU1-C2-IL20	1180	1070	4060	4480	bdl	3820	3110	3.15	179200	178500	3680	438	441	6250			25.5	70.8	40.7	43.2	3210
TOU1-C3-IL29-2	5300	5000	6700	9500	bdl	2950	2510	4.47	172700	177000	3410	930	940	9730			29.9	60.3	17.4	18.5	1210
TOU1-C3-IL27-1	4050	3560	7260	15600	40	6680	5700	5.88	187300	192400	4930	1804	1744	5870			24.92	66.2	48.3	50.9	5500
TOU1-C3-IL31-2	3100	2590	6600	22200	37	1200	1110	3.52	182000	181000	3390	841	836	4350			25.27	55.5	28.4	30.7	700
Average	5384	5071	15801	28826	999	9547	8800	5	180322	180344	3651	2888	3215	7306			32.0	64	31	33	3433
Stdev	6603	6438	24444	51580	1268	15757	15201	2	8930	9636	689	3755	4419	3851			8.8	14	12	12	2593

CG rutile																				
D.L.	0.0743	0.2295	0.3332	214	2.4	91	17	0.0661			0.0419	0.6743	0.5334	0.6413	1.0942	1.3569	0.0015	0.0876	0.0249	0.0276	0.1469
SEM9-C1-RU1-1	279	220	2700	2690	17	308	243	92			3537	253	256	14.4	1260	1089	0.024	0.142	0.8	4.12	3.16
SEM9-C1-RU1-2	320	238	370	1700	6	210	220	49.7			3780	320	299	16.3	2940	2540	0.022	0.07	0.627	3.84	14.3
SEM9-C2-RU5-1	820	830	47000	39000	13	1400	1330	86.7			3940	246	252	52	1340	1130	0.014	0.23	1.13	4.9	3.02
SEM9-C3-RU7-4	388	340	12600	9900	15	760	900	75.3			3881	621	544	15.1	920	810	0.019	0.08	0.98	4.23	6.1
SEM9-C4-RU10	3890	3490	1690	22000	bdl	9500	9900	127			3508	223.5	216.4	267	8000	6800	0.319	0.89	0.46	3.4	8.1
Average	1139	1024	12872	15058	12.8	2436	2519	86			3729	333	313	73	2892	2474	0.08	0.28	0.80	4.10	6.94
Stdev	1553	1401	19682	15648	7.0	3977	4153	28			197	165	132	110	2960	2511	0.13	0.35	0.27	0.55	4.63
D.L.	0.0714	0.2382	0.3214	192	2.0	84	17	0.0564			0.0405	0.5744	0.5156	0.6591	0.9408	1.3405	0.0033	0.0850	0.0228	0.0270	0.1347
SEM11-C1-RU1-1	590	488	800	450	10	29400	32500	92.8			4120	389	348.2	980	4590	4050	0.216	bdl	0.53	3.69	5.1
SEM11-C1-RU1-2	226	172	270	380	8	13400	14400	124			4289	477	423	410	1600	1400	0.151	0.13	0.451	3.45	2.39
SEM11-C1-RU1-3	188.4	124.4	372	287	12.7	170	159	116.8			4063	298	276.8	48.2	1250	1090	0.153	0.086	0.552	3.72	2.26
SEM11-C2-RU2-1	185.7	125.3	1144	330	bdl	61	54.1	152.4			3930	219	215.4	172	4060	3480	0.126	bdl	0.451	3.77	3.91
SEM11-C2-RU2-2	820	790	1090	440	15	135000	151000	115.7			4080	324	307	3600	4280	3690	0.179	0.25	0.6	3.59	3.05
SEM11-C2-RU2-3	610	600	245	380	bdl	127000	144000	102.2			4700	370	352	3360	2690	2440	0.054	0.3	0.45	3.9	3.76
SEM11-C5-RU8-2	636	624	316		bdl	88000	99000	125.9			2936	145.6	146.7	1950	2730	2440	0.195	0.124	0.512	3.54	4.9
SEM11-C6-RU9-1	299	250	410	510	bdl	14600	15200	111.2			4890	824	714	344	890	810	0.21	0.35	0.82	3.9	3.03
SEM11-C8-RU11	212	150	610	340	12.6	8000	7800	106			3637	444	390	249	1030	920	0.062	bdl	0.528	3.39	2.31
SEM11-C9-RU12	3500	3100	3200	3400	102	239000	265000	129			2149	157.1	151	5700	11200	9800	0.87	2.3	1.51	4.37	9.1
Average	727	642	846	724	27	65463	72911	118			3879	365	332	1681	3432	3012	0.22	0.51	0.64	3.73	3.98
Stdev	1001	897	890	1006	31	80060	89417	17			812	197	164	1933	3058	2667	0.23	0.70	0.32	0.28	2.07
FG rutile																				
D.L.	0.0878	0.2421	0.4239	218	2.7	105	20	0.0766	0.1839	0.2220	0.0543	0.7538	0.6160	0.7637			0.0042	0.1048	0.0277	0.0370	0.1604
SEM11-C1-LC1	18170	19520	29900	38900	16	14100	13200	102	522000	543000	2690	344	344	326			4.52	13.9	0.78	3.91	126.2
SEM11-C2-LC6	16720	18290	31570	49500	23	4700	4600	69.6	482000	480000	2490	238	239	138			4.04	14.18	0.59	3.22	126.1
SEM11-C6-LC8	16780	18380	30440	33200	36	40000	44000	92.8	495000	512000	2590	410	401	1050			5.71	20.67	3.2	5.6	142
SEM11-C9-LC10	17100	18660	32900	31900	45	32100	33900	169	502000	497000	1980	340	340	670			5.45	13.4	2.91	6.01	144
SEM11-C9-LC11	18460	20210	30070	55400	21	9800	9600	96.6	580000	580000	3760	390	386	223			5.11	10.7	10.7	12.7	127.6
Average	17446	19012	30976	41780	28	20140	21060	106	516200	522400	2702	344	342	481			5.0	14.6	3.6	6.3	133.2
Stdev	813	827	1257	10303	12	15160	16994	37	38486	39665	652	67	63	377			0.7	3.7	4.1	3.8	9.0

Abbreviations: D.L., detection limit; Int. Standard, internal standard; Stdev, standard deviation; bdl, below detection limit
Values below the detection limit are not taken into account for the calculation of average

Table A.9 (suite)

Isotope	^{71}Ga	^{72}Ge	^{74}Ge	^{75}As	^{88}Sr	^{89}Y	^{90}Zr	^{91}Zr	^{93}Nb	^{95}Mo	^{118}Sn	^{121}Sb	^{178}Hf	^{181}Ta	^{182}W	^{208}Pb
	ppm	ppm	ppm	ppm	ppm	ppm	ppm	ppm	ppm	ppm	ppm	ppm	ppm	ppm	ppm	ppm
Ilmenite																
D.L.	0.0017	0.0809	0.0402	0.3052	0.0005	0.0004	0.0004	0.0061	0.0000	0.0022	0.0240	0.0082	0.0001	0.0000	0.0008	0.0030
MF1-C1-IL1	1.24	0.66	0.358	bdl	6.3	11.5	835	919	103.6	1.04	1.58	0.216	12	6.16	0.13	0.32
MF1-C1-IL3-2	3.5	3.45	2.27	0.56	56.1	28	1379	1595	220	1.62	2.93	2.41	20.3	12.48	1.5	2.21
MF1-C1-IL3-3	6.1	1.77	1.24	0.53	34.6	48.2	1670	1940	197	3.05	4.73	1.24	30.9	9.24	0.67	1.33
MF1-C1-IL4	1.47	1	0.56	bdl	2.77	4.1	853	856	122.5	1.2	1.47	0.3	11.81	4.56	0.05	0.9
MF1-C1-IL2	2.22	0.84	0.51	bdl	8.5	10.6	696	701	48.6	0.466	1.14	0.275	8.04	3.85	0.13	0.31
MF1-C1-IL3-4	2.4	2.45	1.74	0.55	39.9	22.8	1006	1020	75	0.89	2.95	1.88	15	4.7	0.85	1.74
MF1-C2-IL5-1	1.28	0.73	0.359	bdl	7.7	14.7	1053	1226	73	0.88	1.53	0.188	15.5	4.67	0.2	0.292
MF1-C2-IL5-2	0.78	0.88	0.409	0.34	9.2	11.1	943	1099	62.2	0.606	1.48	0.346	12.06	4.47	0.16	0.411
MF1-C2-IL5-3	0.99	0.524	0.239	bdl	6.71	4.03	407	406	99	0.657	1.75	0.117	7.54	6.2	0.11	0.263
MF1-C2-IL6	0.83	0.8	0.51	bdl	7.7	6.51	757	768	53.6	0.55	1.43	0.291	10.45	3.34	0.13	0.39
MF1-C2-IL8	0.51	0.513	0.171	bdl	0.52	4.29	730	723	62.7	0.585	1.03	0.015	8.91	4.68	0.04	0.02
MF1-C2-IL7	0.41	0.528	0.16	bdl	0.29	7.81	677	671	49.7	0.426	0.837	0.016	7.57	3.91	0.02	0.019
MF1-C3-IL9	1.24	1.83	1.21	bdl	33.1	17.6	1060	1260	63.2	0.64	1.74	1.102	13.4	4.46	0.73	1.188
MF1-C3-IL10	0.78	0.77	0.4	bdl	3.86	12.6	1008	1160	62	0.53	2	0.179	12.38	4.22	0.24	0.279
MF1-C3-IL11	1.06	0.52	0.38	bdl	23	6.1	666	666	94	1.45	2.21	0.194	12.57	5.05	0.13	0.28
MF1-C3-IL13	2.91	0.78	0.417	bdl	17	8.38	470	464	47.3	0.7	1.4	0.345	6.11	3.59	0.12	0.383
MF1-C3-IL14-1	0.288	0.59	0.301	bdl	3.17	7.73	976	1051	90.6	0.85	1.26	0.154	11.56	5.97	0.11	0.145
MF1-C3-IL14-2	0.624	0.76	0.37	bdl	8.7	8.05	675	691	70.1	0.591	1.095	0.356	8.2	5.22	0.16	0.313
MF1-C4-IL15-1	0.349	0.503	0.69	bdl	12.6	6.7	940	1030	115	0.98	2.41	0.156	13.5	6.25	0.11	0.111
MF1-C4-IL15-2	0.58	0.83	0.49	bdl	10.2	8.46	1107	1298	119.2	0.889	1.95	0.362	14.33	6.98	0.27	0.439
Average	1.48	1.04	0.64	0.50	14.6	12.5	895	977	91	0.93	1.85	0.51	13	5.5	0.29	0.57
Stdev	1.40	0.77	0.55	0.21	15.1	10.5	293	375	47	0.59	0.89	0.65	5	2.1	0.37	0.60
Titanohematite																
D.L.	0.0008	0.0643	0.0304	0.1892	0.0004	0.0001	0.0000	0.0000	0.0000	0.0011	0.0161	0.0059	0.0002	0.0000	0.0004	0.0022
BAN1-C1-IL1-1	4.1	4.02	3.4	17.2	62.9	57.1	2306	2726	178	5.24	4.55	2.9	30.39	11.05	0.53	5.79
BAN1-C1-IL2-1	5.21	2.13	1.63	4.66	5.21	12.3	283	290	70.6	3.25	5.78	1.67	6.46	3.4	0.27	13.1
BAN1-C1-IL3-1	5.5	1.71	1.242	2.41	12.4	11.03	265.2	266	54.5	0.948	3.36	1	4.74	1.626	0.08	8.5
BAN1-C1-IL3-2	5.93	1.49	1.207	3.26	1.25	1.06	182.8	186.1	32.28	0.74	3.29	0.87	3.54	1.244	0.03	9.08
BAN1-C1-IL6	4.62	1.54	1.225	0.3	3.55	3.75	265	268	113.1	2.8	4.51	0.217	6.33	3.53	0.03	1.96
BAN1-C1-IL7-1	4.6	1.56	1.27	3.73	8.3	6.96	205	205	54	2.96	5.5	1.19	4.98	2.839	0.33	12.86
BAN1-C1-IL7-2	8.58	2.55	1.99	16.37	18.1	10.22	238	238	152.5	6.9	6.26	5.84	6.56	4.51	0.25	49.2
BAN1-C1-IL5	4.99	1.37	1.03	5.86	4.9	2.59	209.8	207.4	40.24	0.995	3.75	1.63	3.95	1.648	0.09	21
BAN1-C2-IL8	5.36	2.08	1.429	2.35	11.3	10.56	251	252	80.4	1.35	4.1	0.879	5.48	1.891	0.15	4.39
BAN1-C2-IL9	5.62	1.5	1.128	1.67	1.8	2.29	218	222	93	2.01	3.84	0.56	4.99	2.39	0.3	6.3
BAN1-C2-IL10	6.79	1.7	1.291	11.95	11.9	7.36	222	219.8	40.5	0.57	4.69	4.02	3.98	1.294	0.18	41.5
BAN1-C2-IL11-2	5.66	1.54	1.192	1.65	3.28	1.1	247	247	100.7	1.155	3.72	0.56	5.07	1.953	0.01	7.1
BAN1-C2-IL11-1	4.59	1.94	1.5	8.67	7.72	6.28	220	224	137.8	4.12	5.78	2.84	5.55	3.93	0.16	34.8
BAN1-C2-IL12	5.47	1.89	1.45	1.13	5.18	6.9	285	297	156.6	4.89	7.37	0.406	6.59	4.51	0.08	3.84
Average	5.5	1.9	1.5	5.8	11	10	386	418	93	2.7	4.8	1.8	7.0	3.3	0.18	16
Stdev	1.1	0.7	0.6	5.6	16	14	554	665	48	2.0	1.2	1.6	6.8	2.5	0.15	15
D.L.	0.0035	0.1360	0.0702	0.5317	0.0004	0.0003	0.0004	0.0026	0.0002	0.0050	0.0351	0.0193	0.0000	0.0000	0.0010	0.0054
TOU1-C1-IL2	9.66	3.77	3.04	4.75	20.5	28.3	425	484	79.4	1.96	4.78	10.24	8.95	2.03	0.1	31
TOU1-C1-IL3	7.38	2.87	2.35	1.43	6.76	4.84	177.5	218	105.5	5.67	9.6	2.92	5.55	3.33	0.03	5.69
TOU1-C1-IL6	6.57	2.36	1.98	2.36	23.2	4.98	196	241	98.4	5.55	5.63	2.7	6.2	3.31	0.09	3.36
TOU1-C2-IL18	7.75	1.7	1.23	0.6	9.4	2.03	203	227	75.8	2.62	2.9	5.94	5.57	1.99	0.05	2.85
TOU1-C2-IL21	21.3	3.7	2.58	8.02	237	38	325	373	75.2	3.2	4.67	5.14	6.04	2.91	0.33	16.9
TOU1-C2-IL20	6.05	3.08	2.51	6.58	16.8	6.27	222	272	92.8	4.58	6.7	7.05	6.35	3.05	0.05	8.4
TOU1-C3-IL29-2	6.6	2.09	1.75	3.03	7.64	4.5	183	216	99.6	8.3	8.5	2.21	5.59	3.63	0.26	7.05
TOU1-C3-IL27-1	7.47	2.75	2.31	3.69	16.1	10.81	229	272	54.5	1.21	3.36	7.44	4.71	1.22	0.08	5.2
TOU1-C3-IL31-2	4.7	1.91	1.63	0.82	6.2	3.71	340	360	110	5.05	3.58	0.94	6.6	3.02	0.05	3.3
Average	8.6	2.7	2.2	3.5	38	11	256	296	88	4.2	5.5	5.0	6.2	2.7	0.12	9.3
Stdev	4.9	0.7	0.6	2.6	75	13	87	91	18	2.2	2.3	3.0	1.2	0.8	0.10	9.2

CG rutile																
D.L.	0.0045	0.1421	0.0687	0.4206	0.0006	0.0000	0.0000	0.0080	0.0000	0.0017	0.0368	0.0425	0.0016	0.0000	0.0030	0.0052
SEM9-C1-RU1-1	1.05	0.67	0.79	3.54	35.9	8.6	520	450	172	0.26	0.706	541	11.3	10.38	7.85	1.18
SEM9-C1-RU1-2	0.45	0.4	0.48	1.71	12.6	4.13	791	666	196	0.85	1.77	226	13.11	10.83	10.8	1.037
SEM9-C2-RU5-1	11.9	0.97	0.78	1.65	34.9	12.01	681	618	146.7	0.53	1.33	252	10.06	9.66	17.7	1.83
SEM9-C3-RU7-4	3.2	0.41	0.4	0.76	15.4	3.51	384	347	104.2	0.239	1.16	261	8.3	5.91	12.8	1
SEM9-C4-RU10	0.9	0.51	0.48	0.7	40	9.1	880	770	180.4	1.36	1.6	135	16.6	9.5	10.9	0.99
Average	3.50	0.59	0.59	1.67	28	7.5	651	570	160	0.65	1.31	283	11.9	9.3	12.0	1.21
Stdev	4.81	0.24	0.18	1.15	13	3.6	201	170	36	0.47	0.41	153	3.2	1.9	3.6	0.36
D.L.	0.0030	0.1399	0.0679	0.3882	0.0011	0.0000	0.0020	0.0019	0.0009	0.0049	0.0333	0.0311	0.0004	0.0001	0.0008	0.0049
SEM11-C1-RU1-1	0.93	0.44	0.405	0.49	135	13.7	820	710	136.8	0.119	0.668	7.7	13.6	9.73	12.5	1.52
SEM11-C1-RU1-2	0.473	0.35	0.323	0.48	69	14.4	1240	1130	144	0.176	0.587	5.6	16.8	8.92	4.1	1.89
SEM11-C1-RU1-3	0.474	0.39	0.46	0.61	12.8	6.21	1620	1480	221	0.197	1.33	4.88	33.3	11.68	4.2	1.11
SEM11-C2-RU2-1	1.37	0.25	0.278	0.2	9.6	1.95	1262	1067	346	0.124	1.52	2.02	31.2	17.55	0.09	0.736
SEM11-C2-RU2-2	1.3	0.41	0.279	0.18	590	21.6	640	564	102.5	0.64	0.75	3.17	10.5	7.68	3.6	3.3
SEM11-C2-RU2-3	0.89	0.87	0.69	1.11	430	23	469	426	86.4	0.46	0.69	112	7.98	6.76	7.4	1.89
SEM11-C5-RU8-2	0.476	0.47	0.42	0.19	600	15.1	1980	1790	250	0.91	0.948	7.2	22.5	14.6	6.9	3.05
SEM11-C6-RU9-1	0.5	0.39	0.41	0.66	61.2	12.81	435	397	51.8	0.19	0.369	7.6	6.21	5	3.73	2.96
SEM11-C8-RU11	0.399	0.3	0.237	0.26	35.7	12.7	1670	1500	107.4	0.51	0.95	1.99	26.7	7.65	0.46	0.79
SEM11-C9-RU12	3.6	1.15	0.84	1.7	930	29.7	1150	1040	227	0.9	3.2	91	20.7	12.44	6.8	4.9
Average	1.04	0.50	0.43	0.59	287	15.1	1129	1010	167	0.42	1.10	24	19	10.2	5.0	2.2
Stdev	0.97	0.28	0.19	0.49	327	8.1	531	482	91	0.31	0.81	41	10	3.9	3.6	1.3
FG rutile																
D.L.	0.0035	0.1823	0.0758	0.4587	0.0016	0.0007	0.0000	0.0000	0.0000	0.0066	0.0378	0.0330	0.0010	0.0000	0.0010	0.0049
SEM11-C1-LC1	13.45	3.22	2.55	5.74	102	145	1800	1580	278	3.3	56.1	227	29.7	12.1	34.9	3.02
SEM11-C2-LC6	11.34	2.27	1.96	3.81	44	92.6	1550	1340	201	1.2	23.4	184	24.1	10.25	30.3	2.74
SEM11-C6-LC8	12.7	3.32	2.57	7.34	156	113	1240	1060	131.3	1.44	28.5	173.6	24.6	7.7	38.1	3.57
SEM11-C9-LC10	11.9	2.52	2.15	7.9	132	125	2750	2550	251	2.64	25.1	246	45.1	8.55	42.5	2.64
SEM11-C9-LC11	14.39	3.12	2.71	9.6	77	116	1152	1003	127.2	1.5	35.9	238	17.2	8.37	23.6	17.6
Average	12.8	2.9	2.4	6.9	102	118	1698	1507	198	2.0	34	214	28	9.4	33.9	5.9
Stdev	1.2	0.5	0.3	2.2	44	19	642	627	68	0.9	13	33	10	1.8	7.3	6.5

Abbreviations: D.L., detection limit; Int. Standard, internal standard; Stdev, standard deviation; bdl, below detection limit

Values below the detection limit are not taken into account for the calculation of average

Annexe 3

Supporting information for:

Hydrothermal history of Variscan Sb-Au mineralisation in Central Brittany (France)

Anthony Pochon[1], Eric Gloaguen[2, 3], Yannick Branquet[1, 2], Marc Poujol[1], Gilles Ruffet[1], Philippe Boulvais[1], Marie-Christine Boiron[4], Charles Gumiaux[2], Florence Cagnard[3], Fanny Gouazou[4], Denis Gapais[1]

[1] Géosciences Rennes, UMR 6118, Université de Rennes 1, OSUR, Campus de Beaulieu, 35042 Rennes Cedex, France

[2] Institut des Sciences de la Terre d'Orléans, UMR 7327, Université d'Orléans, Campus Géosciences, 1A rue de la Férollerie, 45071 Orléans Cedex 2, France

[3] Bureau de Recherche Géologique et Minière (BRGM), UMR 7327, 3 avenue Claude-Guillemin, BP 36009, 45060 Orléans Cedex 02, France

[4] GeoRessources, CNRS, Université de Lorraine, CREGU, Faculté des Sciences et Technologies, Campus des Aiguillettes, Rue Jacques Callot, B.P. 70239, F-54506, Vandœuvre-lès-Nancy cedex, France

Table ESM 1 Operating conditions for the LA-ICP-MS equipment

	U-Pb apatite and rutile analyses
Laboratory & Sample Preparation	
Laboratory name	Géosciences Rennes, UMR CNRS 6118, Rennes, France
Sample type/mineral	Apatite and rutile
Imaging	CL: RELION CL instrument, Olympus Microscope BX51WI, Leica Color Camera DFC 420C
Laser ablation system	
Make, Model & type	ESI NWR193UC, Excimer
Ablation cell	ESI NWR TwoVol2
Laser wavelength	193 nm
Pulse width	< 5 ns
Fluence	6.5 J/cm-2
Repetition rate	5 Hz
Spot size	100x20 µm (apatite) or 65x20 µm (rutile)
Sampling mode / pattern	Single spot
Carrier gas	100% He, Ar make-up gas and N2 (3 ml/mn) combined using in-house smoothing device
Background collection	20 seconds
Ablation duration	60 seconds
Wash-out delay	15 seconds
Cell carrier gas flow (He)	0.75 l/min
ICP-MS Instrument	
Make, Model & type	Agilent 7700x, Q-ICP-MS
Sample introduction	Via conventional tubing
RF power	1350W
Sampler, skimmer cones	Ni
Extraction lenses	X type
Make-up gas flow (Ar)	0.87 l/min
Detection system	Single collector secondary electron multiplier
Data acquisition protocol	Time-resolved analysis
Scanning mode	Peak hopping, one point per peak
Detector mode	Pulse counting, dead time correction applied, and analog mode when signal intensity > ~ 10^6 cps
Masses measured	^{43}Ca, ^{204}(Hg + Pb), ^{206}Pb, ^{207}Pb, ^{208}Pb, ^{232}Th, ^{238}U
Integration time per peak	10-30 ms
Sensitivity / Efficiency	28000 cps/ppm Pb (50µm, 10Hz)
Dwell time per isotope	5-70 ms depending on the masses
Data Processing	
Gas blank	20 seconds on-peak
Calibration strategy	Madagascar apatite R10 rutile used as primary reference material, Durango and McClure apatites and R19 rutile used as secondary reference material (quality control)
Reference Material info	Madagascar (Thomson et al. 2012) Durango (McDowell et al. 2005) McClure (Schoene and Bowring 2006) R10 and R19 (Zack et al. 2011)
Data processing package used	Iolite (Paton et al. 2010) and VizualAge_UcomPbine (Chew et al. 2014) for apatite, GLITTER® (Van Achterbergh et al. 2001) for rutile
Quality control / Validation	Durango: Weighted average ^{207}Pb corrected age = 31.47 ± 0.87 Ma (MSWD = 2.7) McClure: Weighted average ^{207}Pb corrected age = 529.7 ± 5.7 Ma (MSWD = 3.1) R19: Weighted average ^{207}Pb corrected age = 476 ± 30 Ma (MSWD = 1.6)

Table ESM 2 Illite 40Ar/39Ar analytical data

Laser power	$^{40}Ar_{Atm}$	Error ^{40}Ar	$^{39}Ar_K$	Error ^{39}Ar	^{38}Ar	Error ^{38}Ar	^{37}Ar	Error ^{37}Ar	^{36}Ar	Error ^{36}Ar	$^{40}Ar^*/^{39}ArK$	Error $^{40}Ar^*/^{39}ArK$	Apparent age (Ma)	Error Age (Ma)	Delay to irradiation (day)
SEMAP1															
250	816.38	1.04	27.49	0.05	0.000001	0.021	0.134	0.027	1.056998	0.01565	18.81	0.19	324.7	3.4	130.81
290	799.39	1.17	26.61	0.11	0.001524	0.017	0.157	0.024	0.896185	0.02471	20.53	0.30	351.9	4.9	130.83
350	2298.02	0.80	95.64	0.16	0.005911	0.017	0.281	0.026	1.285517	0.031079	20.34	0.11	348.8	2.3	130.85
380	2819.00	1.31	127.56	0.20	0.000001	0.019	0.376	0.029	1.01807	0.015962	19.98	0.06	343.1	1.8	130.87
410	7227.58	3.75	341.81	0.22	0.000001	0.015	0.579	0.039	1.646808	0.02515	19.93	0.04	342.4	1.7	130.92
430	21383.03	5.36	1058.56	0.49	0.043513	0.020	1.280	0.048	2.659947	0.032937	19.64	0.03	337.9	1.6	130.94
440	12845.64	5.72	649.87	0.55	0.010434	0.016	0.682	0.037	0.822936	0.015681	19.57	0.03	336.7	1.6	130.96
460	7509.28	2.46	381.84	0.40	0.005548	0.020	0.402	0.042	0.432606	0.020409	19.51	0.04	335.8	1.6	130.98
520	11888.06	3.41	607.51	0.47	0.000001	0.028	0.434	0.022	0.445808	0.015795	19.52	0.03	336.0	1.6	131.02
600	2915.15	1.53	149.62	0.22	0.000001	0.025	0.111	0.021	0.106685	0.013259	19.44	0.05	334.8	1.7	131.04
Fusion	1775.93	1.02	92.28	0.11	0.001013	0.027	0.110	0.024	0.115471	0.016571	19.05	0.06	328.5	1.8	131.06
J parameter		1.05E-02													
error J		4.32E-05													
Mass Discrimination (1+e)		1.009405													
Err Discrimination		1.32E-03													
SEMAP2															
270	1741.38	1.56	48.66	0.13	0.004504	0.017	0.335	0.027	2.660967	0.01681	20.24	0.16	347.2	3.0	125.81
310	1740.97	1.32	71.77	0.13	0.000001	0.016	0.340	0.034	0.973687	0.023989	20.53	0.12	351.9	2.4	125.83
340	568.64	0.75	26.04	0.08	0.000001	0.016	0.209	0.031	0.205898	0.034122	19.74	0.39	339.4	6.3	125.85
380	5543.66	4.00	212.94	0.34	0.000001	0.013	0.745	0.017	4.289048	0.041519	20.42	0.09	350.0	2.1	125.89
390	11356.38	4.19	501.78	0.71	0.009879	0.020	0.896	0.035	5.050279	0.01327	19.91	0.05	342.1	1.7	125.91
400	1883.93	1.18	94.28	0.16	0.000001	0.014	0.207	0.030	0.232753	0.013274	19.44	0.06	334.7	1.8	125.94
430	16691.55	3.31	829.38	1.44	0.000001	0.021	0.966	0.052	2.173236	0.032711	19.54	0.05	336.3	1.7	125.96
450	3432.90	6.17	176.91	0.37	0.000001	0.017	0.244	0.032	0.158468	0.018172	19.31	0.07	332.7	1.8	126.01
500	21648.25	7.91	1108.12	0.67	0.000001	0.022	0.979	0.042	0.981094	0.018892	19.45	0.03	334.8	1.6	126.03
530	2863.08	1.25	147.81	0.21	0.02671	0.019	0.241	0.028	0.159458	0.014879	19.22	0.05	331.3	1.7	126.05
580	1022.15	1.07	52.73	0.12	0.00152	0.020	0.195	0.041	0.131628	0.014825	18.83	0.10	325.1	2.1	126.06
660	3342.57	1.83	172.09	0.22	0.000001	0.027	0.307	0.027	0.112444	0.023429	19.40	0.05	334.1	1.7	126.11
900	1102.06	0.47	56.88	0.14	0.000001	0.023	0.148	0.021	0.092196	0.020647	19.07	0.12	328.9	2.4	126.13
Fusion	111.58	0.25	5.71	0.04	0.000001	0.015	0.055	0.034	0.024372	0.025146	18.49	1.29	319.7	20.5	126.15
J parameter		1.05E-02													
error J		4.32E-05													
Mass Discrimination (1+e)		1.009405													
Err Discrimination		1.32E-03													

Table ESM 2 (suite)

Laser power	$^{40}Ar_{Atm}$	Error ^{40}Ar	$^{39}Ar_K$	Error ^{39}Ar	^{38}Ar	Error ^{38}Ar	^{37}Ar	Error ^{37}Ar	^{36}Ar	Error ^{36}Ar	$^{40}Ar^*/^{39}ArK$	Error $^{40}Ar^*/^{39}ArK$	Apparent age (Ma)	Error Age (Ma)	Delay to irradiation (day)
SEMJB1															
250	2573.95	1.50	93.43	0.16	0.000001	0.019	0.158	0.033	1.464003	0.016109	23.24	0.08	394.6	2.2	126.81
290	1606.17	1.26	75.55	0.17	0.000001	0.020	0.266	0.031	0.255574	0.018926	20.46	0.09	351.8	2.1	126.83
340	7563.07	3.45	366.84	0.34	0.013741	0.016	0.783	0.038	0.382759	0.031591	20.49	0.04	352.2	1.7	126.85
360	6802.98	4.39	338.36	0.37	0.001098	0.018	1.099	0.028	0.270121	0.02208	20.05	0.04	345.3	1.7	126.87
380	8098.36	3.84	407.39	0.37	0.000001	0.027	0.566	0.026	0.267335	0.027785	19.86	0.04	342.3	1.7	126.91
400	6031.85	7.88	303.83	0.25	0.025192	0.026	0.285	0.030	0.265596	0.028062	19.77	0.05	340.9	1.7	126.93
430	73561.24	17.23	3744.77	0.98	0.000001	0.033	1.199	0.046	1.297761	0.042699	19.71	0.03	340.0	1.6	126.95
450	4647.32	2.40	237.86	0.29	0.000001	0.029	0.207	0.029	0.134299	0.034961	19.54	0.06	337.3	1.8	126.97
550	15667.84	7.31	799.90	0.39	0.000001	0.016	0.213	0.052	0.236918	0.02732	19.67	0.03	339.3	1.6	127.01
650	7692.52	5.73	379.51	0.23	0.000001	0.014	0.129	0.028	0.207782	0.021844	20.28	0.04	348.9	1.7	127.03
Fusion	245.74	0.35	5.18	0.08	0.000001	0.014	0.000	0.030	0.148326	0.01155	39.52	0.89	627.4	12.2	127.06
J parameter		1.05E-02													
error J		4.33E-05													
Mass Discrimination (1+e)		1.009405													
Err Discrimination		1.32E-03													
SEMJB2															
250	953.63	1.24	42.06	0.06	0.000001	0.020	0.119	0.026	0.635087	0.026891	18.49	0.20	320.7	3.4	129.92
290	731.94	1.10	32.49	0.07	0.000001	0.015	0.109	0.025	0.220874	0.020326	20.75	0.19	356.3	3.4	129.94
330	1352.82	3.71	62.80	0.19	0.00161	0.020	0.165	0.026	0.169883	0.022591	20.94	0.14	359.2	2.7	129.96
370	3101.13	1.32	147.64	0.26	0.016112	0.033	0.317	0.027	0.161954	0.024211	20.87	0.07	358.1	1.9	129.98
390	14126.15	5.50	696.60	0.46	0.000001	0.025	0.606	0.036	0.468199	0.034892	20.26	0.03	348.5	1.7	130.02
400	12963.31	5.25	647.87	0.43	0.039613	0.027	0.360	0.038	0.640459	0.022881	19.89	0.03	342.8	1.6	130.03
410	13575.98	4.60	684.86	0.35	0.012567	0.021	0.344	0.045	0.484444	0.031885	19.79	0.03	341.2	1.6	130.05
420	7290.09	3.01	367.52	0.24	0.029654	0.025	0.237	0.049	0.271824	0.024256	19.79	0.04	341.2	1.6	130.07
440	10831.13	6.01	546.67	0.55	0.024987	0.022	0.235	0.028	0.351777	0.013941	19.79	0.04	341.3	1.6	130.11
470	38012.52	18.64	1943.00	0.83	0.014356	0.019	0.397	0.035	0.574473	0.033209	19.64	0.03	338.9	1.6	130.13
490	1180.59	1.56	60.13	0.14	0.000001	0.019	0.110	0.021	0.082683	0.023982	19.40	0.13	335.2	2.5	130.15
Fusion	7093.09	3.58	359.88	0.28	0.000001	0.026	0.174	0.029	0.203966	0.026686	19.71	0.04	340.0	1.6	130.17
J parameter		1.05E-02													
error J		4.33E-05													
Mass Discrimination (1+e)		1.009405													
Err Discrimination		1.32E-03													

Table ESM 2 (suite)

Parameters				
(36Ar/37Ar)Ca	0.000322	3	%	
(39Ar/37Ar)Ca	0.000788	4	%	
(38Ar/37Ar)Ca	0.000026	100	%	
(40Ar/37Ar)Ca	0.0006	100	%	
(40Ar/39Ar)K	0.00085	4	%	
(38A/39Ar)K	0.011	91	%	
(36Cli/38Cl)	316	5	%	[3]
(40Ar/36Ar)Atm	298.56	0.104	%	[1] and [1']
(38Ar/36Ar)Atm	0.1885	0.159	%	[1] and [1']
Lambda 40	5.53E-10	1.35E-12	y-1	[2]
Lambda 39	2.58E-03		y-1	
Lambda 37	1.98E-02		d-1	
Lambda 36Cl	2.26E-06		y-1	

References:

[1] Lee, JY, Marti, K, Severinghaus, JP, Kawamura, K, Yoo, HS, Lee, JB, Kim, JS (2006). A redetermination of the isotopic abundances of atmospheric Ar. Geochimica Cosmochimica Acta, 70, 4507-4512.

[1'] Mark, DF, Stuart, FM, De Podesta, M (2011). New high-precision measurements of the isotopic composition of atmospheric argon. Geochimica Cosmochimica Acta, 75, 7494-7501.

[2] Renne, PR, Balco, G, Ludwig, RL, Mundil, R, Min, K, . (2011). Response to the comment by W.H. Schwarz et al. on "Joint determination of (40)K decay constants and (40)Ar*/(40)K for the Fish Canyon sanidine standard, and improved accuracy for (40)Ar/(39)Ar geochronology" by PR Renne et al. (2010). Geochimica Cosmochimica Acta, 75, 5097-5100.

[3] York, D, Personnal Communication - McMaster reactor

Regression method: York, D. (1969). Least-squares fitting of a straight line with correlated errors. Earth Planet. Sci. Lett. 5, 320-4.

Ages and errors of Hb3gr and TCs monitors refers to: Rennes, PR, Balco, G, Ludwig, Mundil, R, Min, K, . (2011). Response to the comment by W.H. Schwarz et al. on "Joint determination of (40)K decay constants and (40)Ar*/(40)K for the Fish Canyon sanidine standard, and improved accuracy for (40)Ar/(39)Ar geochronology" by PR Renne et al. (2010). Geochimica Cosmochimica Acta, 75, 5097-5100.

Table ESM3-1 Electron microprobe analyses of ankerite from the Semnon Sb-Au deposit

Wt. Oxides %	SiO2	Al2O3	TiO2	FeO T	MgO	MnO	CaO	BaO	Na2O	K2O	Total	**A.p.f.u.**	Si	Al	Ti	Fe2+	Mg	Mn	Ca	Ba	Na	K	Total	CaCO3	FeCO3	MnCO3	MgCO3
D.L.	0.03	0.03	0.06	0.07	0.04	0.07	0.06	0.14	0.05	0.02																	
Wallrock between vein & dolerite																											
LS6-c6-13	0.05	bdl	0.02	14.45	11.41	0.56	27.91	bdl	bdl	bdl	54.42		0.00	0.00	0.00	0.41	0.57	0.02	1.00	0.00	0.00	0.00	2.00	50.28	20.32	0.79	28.61
LS6-c6-14	bdl	bdl	0.03	15.08	11.45	0.58	28.08	bdl	bdl	bdl	55.33		0.00	0.00	0.00	0.42	0.57	0.02	1.00	0.00	0.00	0.00	2.00	49.92	20.93	0.82	28.33
LS6-c6-15	bdl	bdl	0.00	13.61	9.80	2.00	29.51	bdl	0.05	bdl	55.01		0.00	0.00	0.00	0.38	0.49	0.06	1.06	0.00	0.00	0.00	2.00	53.36	19.13	2.86	24.65
LS6-c6-16	bdl	bdl	0.00	16.13	8.76	3.02	27.21	bdl	bdl	bdl	55.24		0.00	0.00	0.00	0.46	0.45	0.09	1.00	0.00	0.00	0.00	2.00	50.04	23.16	4.39	22.41
LS6-c6-18	bdl	bdl	0.00	14.59	10.03	0.45	30.04	bdl	bdl	bdl	55.22		0.00	0.00	0.00	0.41	0.50	0.01	1.08	0.00	0.00	0.00	2.00	53.89	20.43	0.64	25.03
LS6-c6-19	bdl	0.04	0.00	12.89	11.30	0.70	29.89	bdl	bdl	bdl	54.90		0.00	0.00	0.00	0.36	0.56	0.02	1.06	0.00	0.00	0.00	2.00	53.16	17.89	0.98	27.97
LS6-c6-20	bdl	bdl	0.02	14.90	10.20	0.42	29.32	bdl	bdl	bdl	54.92		0.00	0.00	0.00	0.42	0.51	0.01	1.06	0.00	0.00	0.00	2.00	52.85	20.97	0.60	25.58
LS6-c5-8	bdl	0.05	0.00	12.93	12.03	0.53	28.68	bdl	bdl	bdl	54.28		0.00	0.00	0.00	0.36	0.60	0.02	1.02	0.00	0.00	0.00	2.00	51.27	18.05	0.75	29.93
LS6-c5-9	0.03	bdl	0.00	13.98	11.49	0.60	29.22	bdl	bdl	bdl	55.39		0.00	0.00	0.00	0.39	0.56	0.02	1.03	0.00	0.00	0.00	2.00	51.63	19.28	0.84	28.25
LS6-c4-7	bdl	0.03	0.00	15.20	11.09	0.54	27.53	bdl	bdl	bdl	54.43		0.00	0.00	0.00	0.43	0.56	0.02	1.00	0.00	0.00	0.00	2.00	49.83	21.47	0.78	27.93
LS6-c4-8	0.06	0.03	0.00	12.72	11.66	0.58	29.59	bdl	bdl	bdl	54.64		0.00	0.00	0.00	0.35	0.58	0.02	1.05	0.00	0.00	0.00	2.00	52.65	17.67	0.81	28.87
LS6-c4-9	bdl	0.05	0.06	12.36	12.27	0.62	28.86	bdl	bdl	bdl	54.23		0.00	0.00	0.00	0.34	0.61	0.02	1.03	0.00	0.00	0.00	2.00	51.48	17.21	0.87	30.45
LS6-c4-10	bdl	bdl	0.03	12.39	11.84	0.61	29.49	bdl	bdl	bdl	54.43		0.00	0.00	0.00	0.34	0.59	0.02	1.05	0.00	0.00	0.00	2.00	52.54	17.23	0.86	29.36
LS6-c4-11	0.04	bdl	0.00	12.58	11.36	0.48	29.96	bdl	bdl	bdl	54.51		0.00	0.00	0.00	0.35	0.56	0.01	1.07	0.00	0.00	0.00	2.00	53.52	17.55	0.68	28.25
LS6-c3-4	bdl	0.03	0.02	13.81	10.75	0.59	29.61	bdl	bdl	bdl	54.88		0.00	0.00	0.00	0.39	0.54	0.02	1.06	0.00	0.00	0.00	2.00	53.05	19.31	0.84	26.80
LS6-c3-5	0.13	bdl	0.00	13.90	10.25	0.50	29.90	bdl	bdl	bdl	54.76		0.00	0.00	0.00	0.39	0.51	0.01	1.08	0.00	0.00	0.00	2.00	53.96	19.58	0.72	25.74
LS6-c3-10	0.05	0.03	0.00	13.01	12.35	0.47	28.62	bdl	bdl	bdl	54.56		0.00	0.00	0.00	0.36	0.61	0.01	1.01	0.00	0.00	0.00	2.00	50.81	18.04	0.66	30.50
LS6-c3-11	bdl	0.07	0.00	12.82	11.90	0.53	28.66	bdl	bdl	bdl	54.07		0.00	0.00	0.00	0.36	0.59	0.01	1.03	0.00	0.00	0.00	2.00	51.50	17.99	0.75	29.76
LS6-c3-12	bdl	0.05	0.00	14.23	11.36	0.45	28.72	bdl	bdl	bdl	54.87		0.00	0.00	0.00	0.40	0.56	0.01	1.02	0.00	0.00	0.00	2.00	51.30	19.84	0.63	28.22
LS6-c2-5	bdl	0.03	0.02	12.11	12.11	0.55	29.65	bdl	bdl	bdl	54.59		0.00	0.00	0.00	0.33	0.60	0.02	1.05	0.00	0.00	0.00	2.00	52.58	16.76	0.77	29.89
LS6-c2-6	0.04	bdl	0.02	13.04	12.16	0.51	29.27	bdl	bdl	bdl	55.15		0.00	0.00	0.00	0.36	0.60	0.01	1.03	0.00	0.00	0.00	2.00	51.56	17.93	0.71	29.80
LS6-c2-9	0.04	0.04	0.01	13.84	11.40	0.47	28.64	bdl	bdl	bdl	54.47		0.00	0.00	0.00	0.39	0.57	0.01	1.03	0.00	0.00	0.00	2.00	51.45	19.40	0.66	28.49
LS6-c2-10	bdl	bdl	0.00	16.30	9.43	0.39	28.92	bdl	bdl	bdl	55.08		0.00	0.00	0.00	0.46	0.48	0.01	1.05	0.00	0.00	0.00	2.00	52.51	23.10	0.56	23.83
Tension gashes																											
SEM39-c1-6	0.06	0.03	0.00	12.95	11.77	0.77	29.15	bdl	bdl	bdl	54.74		0.00	0.00	0.00	0.36	0.58	0.02	1.03	0.00	0.00	0.00	2.00	51.83	17.97	1.08	29.11
SEM39-c1-7	0.07	0.03	0.00	13.06	10.43	0.70	30.34	bdl	bdl	bdl	54.71		0.00	0.00	0.00	0.37	0.52	0.02	1.09	0.00	0.00	0.00	2.00	54.57	18.33	0.99	26.11
SEM39-c2-5	0.07	0.06	0.03	15.00	11.16	0.56	27.55	bdl	bdl	bdl	54.51		0.00	0.00	0.00	0.42	0.56	0.02	0.99	0.00	0.00	0.00	2.00	49.88	21.20	0.80	28.11
SEM39-c2-6	bdl	0.03	0.00	13.35	10.85	0.62	29.31	bdl	bdl	bdl	54.18		0.00	0.00	0.00	0.38	0.55	0.02	1.06	0.00	0.00	0.00	2.00	52.98	18.84	0.88	27.29
SEM39-c2-8	0.04	0.03	0.00	12.76	11.07	0.68	30.19	bdl	bdl	bdl	54.85		0.00	0.00	0.00	0.35	0.55	0.02	1.07	0.00	0.00	0.00	2.00	53.82	17.76	0.95	27.46
SEM42-c1-4	bdl	0.04	0.05	9.90	14.79	0.68	28.36	bdl	bdl	bdl	53.83		0.00	0.00	0.00	0.27	0.72	0.02	0.99	0.00	0.00	0.00	2.00	49.58	13.51	0.94	35.98
SEM42-c1-5	bdl	0.05	0.02	16.44	10.08	0.73	28.06	bdl	bdl	bdl	55.41		0.00	0.00	0.00	0.46	0.50	0.02	1.01	0.00	0.00	0.00	2.00	50.57	23.13	1.04	25.27
SEM42-c2-3	bdl	0.03	0.00	15.35	11.42	0.68	27.52	bdl	bdl	bdl	55.05		0.00	0.00	0.00	0.43	0.57	0.02	0.98	0.00	0.00	0.00	2.00	49.21	21.42	0.96	28.41
SEM42-c3-3	bdl	bdl	0.00	13.29	10.81	0.52	29.69	bdl	bdl	bdl	54.37		0.00	0.00	0.00	0.37	0.54	0.01	1.07	0.00	0.00	0.00	2.00	53.49	18.68	0.74	27.10

Table ESM3-1 (suite)

Wt. Oxides %	SiO2	Al2O3	TiO2	FeO T	MgO	MnO	CaO	BaO	Na2O	K2O	Total	**A.p.f.u.**	Si	Al	Ti	Fe2+	Mg	Mn	Ca	Ba	Na	K	Total	CaCO3	FeCO3	MnCO3	MgCO3
Deformed vein in slates																											
LS8b-c5-1	bdl	bdl	0.04	14.74	10.63	0.55	28.97	bdl	bdl	0.03	55.05		0.00	0.00	0.00	0.41	0.53	0.02	1.04	0.00	0.00	0.00	2.00	52.01	20.65	0.78	26.56
LS8b-c5-2	bdl	0.04	0.00	15.62	9.96	0.84	27.81	bdl	bdl	bdl	54.34		0.00	0.00	0.00	0.45	0.51	0.02	1.02	0.00	0.00	0.00	2.00	51.00	22.37	1.21	25.42
LS8b-c5-5	bdl	0.05	0.04	15.95	9.88	0.88	28.12	bdl	bdl	0.02	55.00		0.00	0.00	0.00	0.45	0.50	0.03	1.02	0.00	0.00	0.00	2.00	51.12	22.62	1.27	25.00
LS8b-c5-6	bdl	0.04	0.00	17.46	8.70	1.09	27.67	bdl	bdl	0.02	55.06		0.00	0.00	0.00	0.50	0.45	0.03	1.02	0.00	0.00	0.00	2.00	51.00	25.09	1.59	22.32
Dolerite																											
SEM45-c2-2	0.15	0.09	0.01	13.21	10.22	0.54	30.76	bdl	bdl	0.02	55.08		0.00	0.00	0.00	0.37	0.51	0.02	1.10	0.00	0.00	0.00	2.00	55.21	18.50	0.76	25.53
Average	0.06	0.04	0.01	13.94	11.03	0.70	28.94		0.05	0.02	54.75		0.00	0.00	0.00	0.39	0.55	0.02	1.04	0.00	0.00	0.00	2.00	51.93	19.55	1.00	27.52
Stdev	0.04	0.02	0.02	2.71	2.11	0.48	4.78		0.01	0.01	8.89		0.00	0.00	0.00	0.08	0.10	0.01	0.17	0.00	0.00	0.00	0.32	8.55	3.89	0.70	5.13

Abbreviations: D.L., detection limit; Stdev, standard deviation; bdl, below detection limit

Table ESM3-2 Electron microprobe analyses of phyllosilicates from the Semnon Sb-Au deposit

Wt. Oxides %	SiO2	Al2O3	TiO2	V2O3	Cr2O3	FeO	MgO	K2O	CaO	Na2O	BaO	Total	**A.p.f.u.**	Si	Al IV	Al VI	Cr	V	Fe3+	Fe2+	Ti	Mg	K	Na	Ca	Ba	Σ Tetra	Σ Octa	Σ Inter	Total
Illite																														
D.L.	0.04	0.04	0.06	0.03	0.02	0.07	0.03	0.03	0.05	0.04	0.14																			
Wallrock between vein & dolerite																														
LS6-c6-1	47.42	37.02	-	0.08	-	0.37	0.29	7.86	0.08	0.63	0.20	93.99		3.13	0.87	2.00	0.00	0.00	0.00	0.02	0.00	0.03	0.66	0.08	0.01	0.01	4.00	2.05	0.75	6.81
LS6-c6-2	47.14	36.79	0.08	0.08	-	0.41	0.38	7.65	-	0.46	-	93.11		3.13	0.87	2.01	0.00	0.00	0.00	0.02	0.00	0.04	0.65	0.06	0.00	0.00	4.00	2.07	0.71	6.78
LS6-c6-3	47.07	37.20	0.09	0.06	-	0.34	0.33	7.35	-	0.48	-	93.09		3.12	0.88	2.02	0.00	0.00	0.00	0.02	0.00	0.03	0.62	0.06	0.00	0.00	4.00	2.08	0.68	6.77
LS6-c6-4	47.12	36.75	0.12	0.09	-	0.39	0.31	7.50	0.07	0.51	-	92.97		3.13	0.87	2.01	0.00	0.00	0.00	0.02	0.01	0.03	0.64	0.07	0.00	0.00	4.00	2.07	0.71	6.78
LS6-c6-5	47.49	36.47	0.07	0.07	-	0.40	0.37	7.03	0.11	0.41	-	92.53		3.16	0.84	2.01	0.00	0.00	0.00	0.02	0.00	0.04	0.60	0.05	0.01	0.00	4.00	2.08	0.66	6.73
LS6-c6-6	47.04	36.64	-	0.08	-	0.43	0.37	7.59	0.07	0.50	-	92.85		3.13	0.87	2.00	0.00	0.00	0.00	0.02	0.00	0.04	0.64	0.06	0.01	0.00	4.00	2.07	0.71	6.78
LS6-c6-7	47.61	36.78	0.10	0.06	-	0.39	0.33	7.35	-	0.35	-	93.16		3.15	0.85	2.02	0.00	0.00	0.00	0.02	0.00	0.03	0.62	0.05	0.00	0.00	4.00	2.08	0.67	6.74
LS6-c6-8	47.39	36.85	-	0.07	-	0.38	0.34	7.58	bdl	0.38	-	93.09		3.14	0.86	2.02	0.00	0.00	0.00	0.02	0.00	0.03	0.64	0.05	0.00	0.00	4.00	2.07	0.69	6.76
LS6-c6-9	45.76	35.35	-	0.08	-	0.43	0.35	7.42	-	0.47	-	89.99		3.14	0.86	2.00	0.00	0.00	0.00	0.02	0.00	0.04	0.65	0.06	0.00	0.00	4.00	2.07	0.71	6.78
LS6-c6-10	46.98	36.53	0.07	0.08	-	0.41	0.37	7.75	0.06	0.50	0.17	92.92		3.13	0.87	2.00	0.00	0.00	0.00	0.02	0.00	0.04	0.66	0.06	0.00	0.00	4.00	2.06	0.73	6.79
LS6-c6-11	47.21	37.19	-	0.05	-	0.33	0.34	7.85	0.06	0.50	bdl	93.71		3.12	0.88	2.01	0.00	0.00	0.00	0.02	0.00	0.03	0.66	0.06	0.00	0.00	4.00	2.07	0.73	6.80
LS6-c6-12	46.85	36.89	-	0.07	-	0.24	0.33	7.84	-	0.51	-	92.83		3.12	0.88	2.01	0.00	0.00	0.00	0.01	0.00	0.03	0.67	0.07	0.00	0.00	4.00	2.07	0.73	6.80
LS6-c5-1	46.61	36.86	0.06	0.08	-	0.33	0.35	7.44	0.13	0.44	-	92.40		3.11	0.89	2.02	0.00	0.00	0.00	0.02	0.00	0.03	0.63	0.06	0.01	0.00	4.00	2.08	0.70	6.78
LS6-c5-2	47.00	36.75	0.09	0.06	-	0.35	0.35	7.60	0.07	0.41	-	92.74		3.13	0.87	2.01	0.00	0.00	0.00	0.02	0.00	0.03	0.64	0.05	0.00	0.00	4.00	2.07	0.70	6.77
LS6-c5-3	47.09	36.49	0.15	0.05	-	0.38	0.33	7.46	0.10	0.52	-	92.60		3.14	0.86	2.00	0.00	0.00	0.00	0.02	0.01	0.03	0.63	0.07	0.01	0.00	4.00	2.06	0.71	6.77
LS6-c5-4	46.94	37.03	0.07	0.09	-	0.35	0.31	7.35	0.19	0.48	-	92.92		3.12	0.88	2.01	0.00	0.00	0.00	0.02	0.00	0.03	0.62	0.06	0.01	0.00	4.00	2.07	0.70	6.77
LS6-c5-6	46.62	36.72	0.06	0.06	-	0.28	0.32	7.57	-	0.50	-	92.22		3.12	0.88	2.02	0.00	0.00	0.00	0.02	0.00	0.03	0.65	0.06	0.00	0.00	4.00	2.07	0.71	6.78
LS6-c5-7	46.89	36.67	0.08	0.09	-	0.29	0.33	7.76	-	0.54	-	92.79		3.12	0.88	2.01	0.00	0.00	0.00	0.02	0.00	0.03	0.66	0.07	0.00	0.00	4.00	2.06	0.73	6.79
LS6-c5-10	47.49	36.97	-	0.06	-	0.30	0.32	7.59	0.12	0.58	-	93.58		3.13	0.87	2.01	0.00	0.00	0.00	0.02	0.00	0.03	0.64	0.07	0.01	0.00	4.00	2.06	0.72	6.78
LS6-c5-11	46.92	36.81	0.12	0.10	-	0.37	0.34	7.64	0.07	0.47	0.22	93.05		3.12	0.88	2.00	0.00	0.01	0.00	0.02	0.01	0.03	0.65	0.06	0.01	0.01	4.00	2.07	0.72	6.79
LS6-c5-12	46.82	37.03	0.10	0.07	-	0.30	0.31	7.89	0.06	0.56	-	93.21		3.11	0.89	2.01	0.00	0.00	0.00	0.02	0.01	0.03	0.67	0.07	0.00	0.00	4.00	2.06	0.74	6.81
LS6-c5-13	47.25	36.86	-	0.09	-	0.35	0.33	7.77	0.08	0.53	-	93.36		3.13	0.87	2.01	0.00	0.01	0.00	0.02	0.00	0.03	0.66	0.07	0.01	0.00	4.00	2.06	0.73	6.79
LS6-c4-1	47.35	36.93	-	0.06	-	0.37	0.28	7.67	-	0.55	-	93.38		3.13	0.87	2.01	0.00	0.00	0.00	0.02	0.00	0.03	0.65	0.07	0.00	0.00	4.00	2.07	0.72	6.78
LS6-c4-2	47.43	36.88	-	0.08	-	0.33	0.32	7.64	0.05	0.60	-	93.41		3.14	0.86	2.01	0.00	0.00	0.00	0.02	0.00	0.03	0.64	0.08	0.00	0.00	4.00	2.06	0.72	6.79
LS6-c4-3	47.45	36.74	0.13	0.09	-	0.33	0.36	7.22	0.08	0.47	-	93.04		3.14	0.86	2.01	0.00	0.00	0.00	0.02	0.01	0.04	0.61	0.06	0.01	0.00	4.00	2.08	0.68	6.75
LS6-c4-4	46.81	36.25	-	0.09	-	0.48	0.32	7.32	0.15	0.53	0.17	92.16		3.14	0.86	2.00	0.00	0.00	0.00	0.03	0.00	0.03	0.63	0.07	0.01	0.00	4.00	2.07	0.71	6.78
LS6-c4-5	46.93	37.01	-	0.10	-	0.41	0.35	7.61	0.13	0.57	-	93.19		3.11	0.89	2.01	0.00	0.01	0.00	0.02	0.00	0.03	0.64	0.07	0.01	0.00	4.00	2.07	0.73	6.80
LS6-c4-6	46.91	36.75	-	0.08	-	0.39	0.33	7.49	0.09	0.53	0.14	92.78		3.12	0.88	2.01	0.00	0.00	0.00	0.02	0.00	0.03	0.64	0.07	0.01	0.00	4.00	2.07	0.72	6.78
LS6-c3-1	47.67	37.18	0.09	0.08	0.03	0.38	0.36	7.39	0.06	0.43	0.14	93.83		3.13	0.87	2.01	0.00	0.00	0.00	0.02	0.00	0.04	0.62	0.06	0.00	0.00	4.00	2.08	0.68	6.76
LS6-c3-2	47.49	36.76	0.11	0.08	-	0.41	0.36	7.11	-	0.47	-	92.89		3.14	0.86	2.01	0.00	0.00	0.00	0.02	0.01	0.04	0.60	0.06	0.00	0.00	4.00	2.08	0.66	6.74
LS6-c3-3	47.15	37.24	0.06	0.08	-	0.49	0.33	7.10	0.10	0.46	-	93.10		3.12	0.88	2.02	0.00	0.00	0.00	0.03	0.00	0.03	0.60	0.06	0.01	0.00	4.00	2.09	0.66	6.75
LS6-c3-6	47.03	36.92	0.07	0.09	-	0.44	0.33	7.27	0.09	0.62	-	92.88		3.12	0.88	2.01	0.00	0.00	0.00	0.02	0.00	0.03	0.62	0.08	0.01	0.00	4.00	2.07	0.70	6.78
LS6-c3-7	47.53	37.03	-	0.07	-	0.44	0.37	6.66	0.13	0.34	-	92.64		3.15	0.85	2.03	0.00	0.00	0.00	0.02	0.00	0.04	0.56	0.04	0.01	0.00	4.00	2.10	0.62	6.71
LS6-c3-8	47.17	37.02	-	0.10	-	0.52	0.34	7.65	0.13	0.52	-	93.57		3.12	0.88	2.00	0.00	0.01	0.00	0.03	0.00	0.03	0.65	0.07	0.01	0.00	4.00	2.07	0.72	6.79
LS6-c3-9	46.99	36.68	0.07	0.08	-	0.62	0.33	7.70	0.25	0.61	-	93.43		3.12	0.88	1.99	0.00	0.00	0.00	0.03	0.00	0.03	0.65	0.08	0.02	0.00	4.00	2.06	0.75	6.81

Table ESM3-2 (suite)

Wt. Oxides %	SiO2	Al2O3	TiO2	V2O3	Cr2O3	FeO	MgO	K2O	CaO	Na2O	BaO	Total	**A.p.f.u.**	Si	Al IV	Al VI	Cr	V	Fe3+	Fe2+	Ti	Mg	K	Na	Ca	Ba	Σ Tetra	Σ Octa	Σ Inter	Total
LS6-c2-1	47.57	36.72	0.10	0.08	-	0.49	0.39	7.35	0.11	0.48	-	93.35		3.14	0.86	2.00	0.00	0.00	0.00	0.03	0.00	0.04	0.62	0.06	0.01	0.00	4.00	2.07	0.69	6.76
LS6-c2-2	47.15	36.87	-	0.08	-	0.35	0.29	7.33	0.07	0.57	-	92.88		3.13	0.87	2.02	0.00	0.00	0.00	0.02	0.00	0.03	0.62	0.07	0.00	0.00	4.00	2.07	0.70	6.77
LS6-c2-3	47.21	36.57	0.07	0.08	-	0.38	0.35	7.10	0.08	0.51	-	92.42		3.14	0.86	2.01	0.00	0.00	0.00	0.02	0.00	0.04	0.60	0.07	0.01	0.00	4.00	2.08	0.67	6.75
LS6-c2-4	47.18	36.35	0.10	0.09	-	0.50	0.38	7.35	0.10	0.49	bdl	92.68		3.14	0.86	1.99	0.00	0.00	0.00	0.03	0.00	0.04	0.62	0.06	0.01	0.00	4.00	2.07	0.70	6.77
LS6-c2-7	47.34	36.74	0.06	0.06	-	0.43	0.33	7.13	0.10	0.52	-	92.79		3.14	0.86	2.01	0.00	0.00	0.00	0.02	0.00	0.03	0.60	0.07	0.01	0.00	4.00	2.08	0.68	6.75
LS6-c2-8	46.93	37.46	-	0.08	0.04	0.33	0.30	7.35	-	0.49	-	93.13		3.11	0.89	2.03	0.00	0.00	0.00	0.02	0.00	0.03	0.62	0.06	0.00	0.00	4.00	2.09	0.68	6.77
Tension gashes																														
SEM39-c1-1	47.47	37.56	0.08	0.05	-	0.42	0.35	6.86	0.18	0.37	0.15	93.52		3.12	0.88	2.03	0.00	0.00	0.00	0.02	0.00	0.03	0.57	0.05	0.01	0.00	4.00	2.09	0.64	6.73
SEM39-c1-2	46.32	37.23	0.06	0.04	-	0.39	0.36	7.46	0.22	0.47	-	92.63		3.09	0.91	2.02	0.00	0.00	0.00	0.02	0.00	0.04	0.63	0.06	0.02	0.00	4.00	2.08	0.71	6.79
SEM39-c1-3	46.70	37.33	-	0.03	-	0.35	0.33	7.50	0.12	0.43	0.16	93.02		3.10	0.90	2.02	0.00	0.00	0.00	0.02	0.00	0.03	0.64	0.06	0.01	0.00	4.00	2.08	0.70	6.78
SEM39-c1-5	46.93	37.08	0.16	0.04	-	0.34	0.30	7.65	0.10	0.47	-	93.21		3.11	0.89	2.01	0.00	0.00	0.00	0.02	0.01	0.03	0.65	0.06	0.01	0.00	4.00	2.07	0.71	6.78
SEM39-c1-8	46.70	36.82	-	0.04	-	0.38	0.34	7.42	0.11	0.48	-	92.42		3.12	0.88	2.02	0.00	0.00	0.00	0.02	0.00	0.03	0.63	0.06	0.01	0.00	4.00	2.07	0.70	6.78
SEM39-c1-9	46.34	37.07	-	0.04	-	0.39	0.31	7.62	0.14	0.63	-	92.64		3.10	0.90	2.01	0.00	0.00	0.00	0.02	0.00	0.03	0.65	0.08	0.01	0.00	4.00	2.07	0.74	6.81
SEM39-c2-1	46.54	37.31	-	0.04	-	0.35	0.29	7.42	0.14	0.56	-	92.79		3.10	0.90	2.03	0.00	0.00	0.00	0.02	0.00	0.03	0.63	0.07	0.01	0.00	4.00	2.08	0.71	6.79
SEM39-c2-3	47.87	37.53	-	0.04	-	0.31	0.32	6.85	0.13	0.37	-	93.53		3.14	0.86	2.04	0.00	0.00	0.00	0.02	0.00	0.03	0.57	0.05	0.01	0.00	4.00	2.09	0.63	6.72
SEM39-c2-4	47.19	37.32	0.10	0.06	-	0.40	0.36	7.27	0.10	0.37	-	93.31		3.12	0.88	2.02	0.00	0.00	0.00	0.02	0.00	0.04	0.61	0.05	0.01	0.00	4.00	2.09	0.67	6.75
SEM39-c2-7	47.82	37.24	-	0.06	-	0.47	0.33	6.31	0.19	0.28	-	92.82		3.15	0.85	2.04	0.00	0.00	0.00	0.03	0.00	0.03	0.53	0.04	0.01	0.00	4.00	2.10	0.58	6.68
SEM39-c3-3	47.02	36.82	-	0.05	-	0.51	0.28	7.76	0.06	0.62	-	93.25		3.12	0.88	2.00	0.00	0.00	0.00	0.03	0.00	0.03	0.66	0.08	0.00	0.00	4.00	2.06	0.74	6.80
SEM42-c3-2	46.66	36.77	0.08	0.04	-	0.34	0.38	7.26	0.14	0.40	-	92.22		3.12	0.88	2.01	0.00	0.00	0.00	0.02	0.00	0.04	0.62	0.05	0.01	0.00	4.00	2.08	0.68	6.76
Wallrock between vein & slates																														
LS2-c3-1	46.52	36.73	0.07	0.04	-	0.35	0.34	7.67	0.12	0.61	0.22	92.68		3.11	0.89	2.00	0.00	0.00	0.00	0.02	0.00	0.03	0.65	0.08	0.01	0.01	4.00	2.06	0.75	6.81
Deformed vein in slates																														
LS8b-c7-1	47.05	37.40	0.12	0.04	-	0.33	0.30	6.75	0.05	0.28	-	92.37		3.12	0.88	2.05	0.00	0.00	0.00	0.02	0.01	0.03	0.57	0.04	0.00	0.00	4.00	2.10	0.61	6.71
LS8b-c7-2	47.20	37.33	-	0.04	-	0.40	0.29	7.25	0.24	0.60	-	93.49		3.11	0.89	2.02	0.00	0.00	0.00	0.02	0.00	0.03	0.61	0.08	0.02	0.00	4.00	2.07	0.70	6.78
LS8b-c6-2	47.10	36.90	0.17	0.03	-	0.62	0.50	7.16	0.09	0.41	-	93.05		3.12	0.88	2.00	0.00	0.00	0.00	0.03	0.01	0.05	0.61	0.05	0.01	0.00	4.00	2.10	0.66	6.76
LS8b-c5-8	47.04	35.95	0.10		-	0.90	0.59	7.16	0.05	0.44	-	92.35		3.15	0.85	1.98	0.00	0.00	0.00	0.05	0.00	0.06	0.61	0.06	0.00	0.00	4.00	2.09	0.67	6.77
Dolerite																														
SEM45-c1-1	46.34	36.69	0.79	0.08	-	0.47	0.38	6.19	0.13	1.52	-	92.64		3.08	0.92	1.96	0.00	0.00	0.00	0.03	0.04	0.04	0.53	0.20	0.01	0.00	4.00	2.07	0.73	6.80
SEM45-c5-1	46.30	36.75	0.09	0.08	-	0.62	0.43	7.67	0.08	0.60	-	92.64		3.10	0.90	1.99	0.00	0.00	0.00	0.03	0.00	0.04	0.65	0.08	0.01	0.00	4.00	2.08	0.74	6.82
SEM45-c5-2	46.85	36.82	0.24	0.07	-	0.46	0.38	7.23	0.05	0.50	-	92.65		3.12	0.88	2.00	0.00	0.00	0.00	0.03	0.01	0.04	0.61	0.06	0.00	0.00	4.00	2.08	0.68	6.76
SEM45-c5-3	47.48	37.44	0.13	0.05	-	0.27	0.33	6.94	0.08	0.46	0.15	93.35		3.12	0.88	2.03	0.00	0.00	0.00	0.01	0.01	0.03	0.58	0.06	0.01	0.00	4.00	2.09	0.65	6.74
Average	47.06	36.88	0.12	0.07	0.04	0.40	0.34	7.38	0.11	0.51	0.17	92.92		3.12	0.88	2.01	0.00	0.00	0.00	0.02	0.00	0.03	0.63	0.07	0.01	0.00	4.00	2.07	0.70	6.77
Stdev	5.94	4.66	0.11	0.02	0.01	0.11	0.06	0.99	0.06	0.17	0.06	11.72		0.39	0.11	0.25	0.00	0.00	0.00	0.01	0.01	0.01	0.08	0.02	0.00	0.00	0.50	0.26	0.09	0.85

Table ESM3-2 (suite)

Wt. Oxides %	SiO2	Al2O3	TiO2	V2O3	Cr2O3	FeO	MgO	K2O	CaO	Na2O	BaO	Total
Allophane												
D.L.	0.04	0.04	0.06	0.03	0.02	0.06	0.02	0.03	0.04	0.04	0.13	
Around Apy in slates												
LS2-c1-2	37.50	45.74	-	-	bdl	1.15	0.37	bdl	0.18	bdl	bdl	84.96
LS2-c1-3	36.93	46.13	-	bdl	-	0.76	0.28	0.03	0.21	bdl	-	84.52
LS2-c2-1	36.24	46.54	-	bdl	bdl	0.26	0.08	0.05	0.25	0.05	bdl	83.52
LS2-c2-2	36.21	46.38	bdl	bdl	-	0.52	0.28	0.03	0.17	bdl	-	83.72
Mineralized vein in contact with Stn												
SEM42-c1-1	36.49	46.76	bdl	bdl	bdl	0.32	0.12	bdl	0.21	bdl	bdl	83.92
SEM42-c1-2	36.05	46.65	bdl	-	bdl	0.20	0.14	0.03	0.13	bdl	-	83.25
SEM42-c1-3	36.09	46.84	bdl	bdl	bdl	0.31	0.08	-	0.11	bdl	-	83.51
SEM42-c1-6	34.63	45.54	-	0.03	bdl	0.13	0.10	-	0.10	bdl	bdl	80.58
SEM42-c2-1	36.44	47.78	bdl	bdl	bdl	0.17	0.12	-	0.07	bdl	-	84.67
SEM42-c2-2	36.72	47.24	bdl	0.03	bdl	0.30	0.13	-	0.16	bdl	bdl	84.63
Average	36.33	46.56		0.03		0.41	0.17	0.04	0.16	0.05		83.73
Stdev	0.74	0.67		0.01		0.32	0.10	0.02	0.05	0.02		1.25

Abbreviations: D.L., detection limit; Stdev, standard deviation; bdl, below detection limit; Apy, arsenopyrite; Stn, stibnite

Table ESM3-3 Electron microprobe analyses of sulfides from mineralization of the Semnon Sb-Au deposit

Element	S	Fe	As	Sb	Au	Bi	Zn	Cu	Co	Ni	Ag	Se	Total
	%	%	%	%	%	%	%	%	%	%	%	%	
Arsenopyrite													
D.L.	0.12	0.07	0.07	0.09	0.08	0.16	0.11	0.18	0.06	0.06	0.12	0.06	
LS2-Tr-c1-1	21.16	34.23	43.55	0.26	-	0.03	-	-	-	0.27	bdl	-	99.54
LS2-Tr-c1-1	21.31	34.57	43.27	0.34	bdl	-	bdl	bdl	-	-	-	-	99.56
LS2-Tr-c1-1	21.26	34.57	43.02	0.33	-	-	-	bdl	-	-	-	-	99.21
LS2-Tr-c1-1	21.27	34.19	42.87	0.34	-	-	bdl	bdl	-	-	-	-	98.71
LS2-Tr-c1-1	21.17	34.01	42.77	-	-	0.04	bdl	bdl	-	-	bdl	-	98.12
LS2-Tr-c1-1	21.17	34.47	42.85	0.33	bdl	0.02	-	-	-	-	bdl	-	98.92
LS2-Tr-c1-1	21.06	34.95	43.09	0.34	bdl	-	-	bdl	-	-	-	-	99.50
LS2-Tr-c1-1	21.73	34.47	42.91	0.21	bdl	-	bdl	-	-	-	bdl	-	99.42
LS2-Tr-c1-1	21.33	34.62	43.02	0.26	-	-	-	bdl	-	-	bdl	-	99.27
LS2-Tr-c1-1	21.21	34.31	43.03	0.26	bdl	-	bdl	-	-	-	bdl	-	98.92
LS2-Tr-c1-1	21.43	34.56	42.74	0.40	bdl	0.03	bdl	bdl	-	-	-	-	99.21
LS2-Tr-c1-1	21.06	34.73	43.03	0.67	-	-	bdl	bdl	-	-	bdl	-	99.59
LS2-Tr-c1-1	22.15	34.58	41.13	1.23	-	-	-	bdl	-	0.10	-	-	99.25
LS2-Tr-c1-1	20.87	34.21	42.89	0.86	bdl	-	-	bdl	-	-	bdl	-	98.98
LS2-Tr-c1-1	21.69	34.26	42.57	0.17	-	0.03	-	bdl	-	-	bdl	-	98.83
LS2-Tr-c1-1	20.92	34.29	43.16	0.39	-	-	-	-	-	-	bdl	-	98.80
LS2-Tr-c1-1	20.97	33.96	42.76	0.35	-	0.05	bdl	bdl	-	-	bdl	-	98.28
LS2-Tr-c1-1	21.07	34.61	43.32	0.56	-	-	-	-	-	-	bdl	-	99.60
LS2-Tr-c1-1	20.84	34.61	43.33	0.34	bdl	-	-	-	-	-	bdl	-	99.18
LS2-Tr-c1-1	20.99	34.35	42.83	0.47	bdl	0.01	bdl	bdl	-	-	-	-	98.79
LS2-Tr-c1-1	21.51	34.67	42.84	0.43	bdl	-	bdl	bdl	-	-	-	-	99.60
LS2-Tr-c1-1	21.07	34.64	43.34	0.19	-	-	bdl	bdl	-	-	bdl	-	99.41
LS2-Tr-c1-1	20.84	33.89	43.37	0.31	bdl	-	-	bdl	-	-	bdl	-	98.51
LS2-Tr-c1-1	21.34	34.09	42.96	0.10	-	0.01	-	bdl	-	-	-	-	98.52
LS2-Tr-c1-1	21.20	34.52	43.10	0.31	-	-	bdl	bdl	-	-	-	-	99.22
LS2-Tr-c1-1	20.75	34.37	43.39	0.21	bdl	-	-	bdl	-	-	bdl	-	98.79
LS2-Tr-c1-1	20.61	33.96	42.95	0.37	bdl	0.05	-	bdl	-	-	-	-	98.03
LS2-Tr-c1-1	21.15	34.78	43.20	0.41	bdl	-	-	bdl	-	-	bdl	-	99.62
LS2-Tr-c1-1	20.91	34.26	43.10	0.10	bdl	-	bdl	-	-	0.14	-	-	98.55
LS2-Tr-c1-1	21.08	34.30	43.25	0.30	bdl	-	-	bdl	-	-	bdl	-	99.05
LS2-Tr-c1-1	21.21	34.50	43.41	-	-	-	bdl	-	-	-	bdl	-	99.14
LS2-Tr-c1-1	21.19	34.28	42.87	0.38	-	0.01	-	-	-	-	bdl	-	98.83
LS2-Tr-c1-1	21.06	34.61	43.03	0.29	bdl	-	bdl	-	-	-	-	-	99.02
LS2-Tr-c1-1	21.73	34.39	41.60	1.22	-	0.08	-	bdl	-	-	-	-	99.07
LS2-Tr-c1-1	21.04	34.56	43.29	0.53	-	-	bdl	bdl	-	-	bdl	-	99.60

Table ESM3-3 (suite)

Element	S	Fe	As	Sb	Au	Bi	Zn	Cu	Co	Ni	Ag	Se	Total
LS2-Tr-c1-1	21.03	34.29	43.17	0.51	bdl	0.04	-	-	-	-	-	-	99.04
LS2-Tr-c1-1	21.09	34.15	42.78	0.60	bdl	-	bdl	bdl	-	-	-	-	98.70
LS2-Tr-c1-1	20.80	34.08	43.22	0.33	-	-	bdl	-	-	-	bdl	-	98.46
LS2-Tr-c1-1	20.85	34.19	43.41	0.31	-	-	-	bdl	-	-	bdl	-	98.86
LS2-Tr-c1-1	20.69	34.42	43.18	0.88	-	-	-	bdl	-	-	bdl	-	99.20
LS2-Tr-c1-1	21.47	34.64	43.02	0.29	-	-	-	bdl	-	-	bdl	-	99.56
LS2-Tr-c1-1	21.28	34.43	43.08	0.18	-	-	bdl	bdl	-	-	-	-	99.02
LS2-Tr-c1-1	21.34	33.94	42.97	0.56	-	-	bdl	bdl	-	0.09	bdl	-	98.93
LS2-Tr-c1-1	21.04	33.94	42.95	0.26	-	-	bdl	bdl	-	-	bdl	-	98.41
LS2-Tr-c1-2	21.29	34.11	43.24	0.24	bdl	-	bdl	-	-	-	-	-	98.95
LS2-Tr-c1-2	21.11	33.87	43.40	0.11	-	-	bdl	bdl	-	0.13	-	-	98.67
LS2-Tr-c1-2	20.96	34.33	43.44	0.29	-	0.02	bdl	-	-	-	-	-	99.05
LS2-Tr-c1-2	20.93	34.02	43.55	0.33	-	-	bdl	-	-	-	bdl	-	98.93
LS2-Tr-c1-2	21.55	33.99	42.71	0.59	-	-	bdl	-	-	-	-	-	98.91
LS2-Tr-c1-2	21.56	34.62	42.80	0.17	-	-	-	bdl	-	-	-	-	99.21
LS2-Tr-c1-2	21.08	34.02	43.14	0.21	-	-	bdl	bdl	-	-	-	-	98.66
LS2-Tr-c1-2	20.96	34.24	43.11	0.30	-	-	-	bdl	-	-	bdl	-	98.69
LS2-Tr-c1-2	20.90	34.21	43.32	0.25	-	-	-	bdl	-	-	-	-	98.71
LS2-Tr-c1-2	21.29	34.24	43.18	0.38	-	-	-	bdl	-	-	bdl	-	99.18
LS2-Tr-c1-2	21.44	34.36	42.92	0.42	-	-	-	bdl	-	-	bdl	-	99.31
LS2-Tr-c1-2	21.06	34.04	43.32	0.14	-	0.01	-	bdl	-	-	bdl	-	98.65
LS2-Tr-c1-2	20.83	34.16	43.23	0.38	-	-	-	bdl	-	-	-	-	98.64
LS2-Tr-c1-2	21.21	34.04	43.16	0.41	bdl	-	bdl	bdl	-	-	bdl	-	98.94
LS2-Tr-c1-2	21.07	34.14	43.02	0.19	-	-	bdl	bdl	-	-	bdl	-	98.57
LS2-Tr-c1-2	21.67	34.17	42.73	0.11	bdl	-	-	-	-	0.09	-	-	98.84
LS2-Tr-c1-2	21.62	34.27	41.96	0.20	-	-	-	bdl	-	-	-	-	98.10
LS2-Pt-c1-3	21.08	33.74	43.23	0.21	-	-	-	bdl	-	-	bdl	-	98.40
LS2-Pt-c2-12	21.44	34.09	43.22	0.20	-	-	-	-	-	-	-	-	99.02
LS8b-Tr-hc-14	21.36	34.62	43.05	0.16	bdl	0.05	bdl	-	-	-	bdl	-	99.35
LS8b-Tr-hc-14	21.05	34.91	43.08	0.10	-	-	-	bdl	-	-	bdl	-	99.21
LS8b-Tr-hc-14	20.82	34.42	43.30	-	-	-	-	bdl	-	-	-	-	98.60
LS8b-Tr-hc-14	21.06	34.53	42.87	-	bdl	-	bdl	bdl	-	-	bdl	-	98.59
LS8b-Tr-hc-14	21.78	34.65	42.74	-	-	-	-	bdl	-	0.10	bdl	-	99.33
LS8b-Tr-hc-14	21.94	34.73	42.72	-	-	-	bdl	bdl	-	-	bdl	-	99.58
LS8b-Tr-hc-14	21.88	34.84	42.61	0.28	-	0.01	-	bdl	-	-	bdl	-	99.68
LS8b-Tr-hc-14	21.90	34.66	42.51	0.13	-	-	-	-	-	-	-	-	99.20
LS8b-Tr-hc-14	21.54	34.54	42.76	0.15	bdl	-	bdl	-	-	-	bdl	-	99.08
LS8b-Tr-hc-14	21.74	34.92	42.45	0.17	-	-	-	bdl	-	-	bdl	-	99.37

Table ESM3-3 (suite)

Element	S	Fe	As	Sb	Au	Bi	Zn	Cu	Co	Ni	Ag	Se	Total
LS8b-Tr-hc-14	22.00	34.91	42.45	0.11	-	0.02	-	-	-	-	-	-	99.50
LS8b-Tr-hc-14	21.69	34.45	39.17	0.16	-	-	-	bdl	-	-	-	-	95.59
LS8b-Tr-hc-14	21.61	34.66	42.37	0.35	-	-	-	bdl	-	-	-	-	99.01
LS8b-Tr-hc-14	21.63	34.50	42.65	0.11	-	0.02	bdl	bdl	-	-	bdl	-	99.10
LS8b-Tr-hc-14	21.31	34.46	42.67	0.25	-	0.06	-	bdl	0.09	0.19	-	-	99.05
LS8b-Tr-hc-14	21.44	34.79	42.50	0.25	-	0.02	bdl	-	-	-	-	-	99.05
LS8b-Tr-hc-14	21.71	34.62	42.78	0.19	-	-	-	bdl	-	-	bdl	-	99.43
LS8b-Tr-hc-14	21.38	34.23	43.00	0.13	-	-	-	bdl	-	0.13	bdl	-	98.92
LS8b-Tr-hc-14	21.24	34.59	43.14	0.20	bdl	-	-	bdl	-	0.20	bdl	-	99.48
LS8b-Tr-hc-14	21.21	34.45	43.09	0.87	bdl	0.08	bdl	bdl	-	-	bdl	-	99.93
LS8b-Tr-hc-14	21.40	34.81	42.65	0.69	-	-	-	-	-	-	bdl	-	99.57
LS8b-Tr-hc-14	21.37	34.52	42.98	0.39	-	-	-	-	-	-	bdl	-	99.28
LS8b-Tr-hc-14	20.95	34.51	43.28	0.45	-	0.03	-	-	-	-	bdl	-	99.25
LS8b-Tr-hc-14	20.81	34.28	43.27	0.48	-	-	bdl	bdl	-	-	bdl	-	98.93
LS8b-Tr-hc-14	20.77	34.27	43.28	0.44	-	-	-	-	-	-	bdl	-	98.83
LS8b-Tr-hc-14	20.84	34.49	43.17	0.44	-	-	-	bdl	-	-	bdl	-	99.04
LS8b-Tr-hc-14	21.32	34.34	43.15	0.50	-	-	bdl	bdl	-	-	-	-	99.38
LS8b-Tr-hc-14	21.11	34.52	43.03	0.42	-	-	-	-	-	-	bdl	-	99.10
LS8b-Tr-hc-14	21.24	34.42	43.36	0.51	-	-	-	bdl	-	-	bdl	-	99.59
LS8b-Tr-hc-14	21.35	34.64	42.96	0.43	-	-	-	-	-	-	-	-	99.41
LS8b-Tr-hc-14	20.51	34.32	43.37	0.31	-	0.01	bdl	-	-	-	-	-	98.53
LS8b-Tr-hc-14	21.47	34.47	42.72	0.59	bdl	-	bdl	-	-	-	bdl	-	99.33
LS8b-Tr-hc-14	21.31	34.60	42.34	0.96	bdl	-	-	bdl	-	-	-	-	99.24
LS8b-Tr-hc-14	21.29	34.26	42.21	1.01	bdl	-	-	bdl	-	-	bdl	-	98.85
LS8b-Tr-hc-14	21.37	33.96	42.33	1.00	-	-	-	bdl	-	0.10	bdl	-	98.87
LS8b-Tr-hc-14	21.94	34.61	41.69	0.66	-	0.01	bdl	bdl	-	-	bdl	-	99.04
LS8b-Tr-hc-14	21.56	34.17	42.17	0.66	bdl	0.02	-	bdl	-	-	-	-	98.66
LS8b-Tr-hc-14	21.53	34.55	41.92	0.66	-	-	-	-	-	-	-	-	98.68
LS8b-Tr-hc-14	22.01	34.67	42.07	0.58	-	-	bdl	bdl	-	-	-	-	99.36
LS8b-Tr-hc-14	21.42	34.53	42.03	0.68	bdl	-	bdl	bdl	-	-	bdl	-	98.81
LS8b-Tr-hc-14	22.01	34.53	41.70	0.62	-	-	-	bdl	-	-	bdl	-	98.97
LS8b-Tr-hc-14	21.56	34.52	42.23	0.30	-	-	bdl	bdl	-	-	-	-	98.68
LS8b-Tr-hc-14	22.15	34.53	41.95	0.19	-	-	-	bdl	-	-	bdl	-	98.88
LS8b-Tr-hc-15	21.52	34.40	42.75	0.12	-	0.02	-	-	-	-	-	-	98.82
LS8b-Tr-hc-15	21.17	34.54	43.06	0.10	-	0.02	-	-	-	-	-	-	98.90
LS8b-Tr-hc-15	18.54	33.58	46.60	-	-	-	-	bdl	-	-	bdl	-	98.84
LS8b-Tr-hc-15	21.83	34.41	42.53	0.11	-	-	bdl	-	-	-	bdl	-	99.01
LS8b-Tr-hc-15	21.71	34.59	42.34	0.14	-	-	-	-	-	-	-	-	98.84

Table ESM3-3 (suite)

Element	S	Fe	As	Sb	Au	Bi	Zn	Cu	Co	Ni	Ag	Se	Total
LS8b-Tr-hc-15	21.50	34.45	42.88	-	-	-	-	-	-	-	-	-	98.91
LS8b-Tr-hc-15	21.79	34.38	42.61	-	bdl	-	-	bdl	-	-	bdl	-	98.94
LS8b-Tr-hc-15	21.80	34.37	42.46	0.19	bdl	-	-	bdl	-	0.09	-	-	99.04
LS8b-Tr-hc-15	21.90	34.45	42.43	-	-	-	bdl	-	-	0.17	bdl	-	99.11
LS8b-Tr-hc-15	21.85	34.66	41.74	0.24	-	0.01	bdl	bdl	-	-	bdl	-	98.62
LS8b-Tr-hc-15	22.08	34.65	41.51	-	-	-	bdl	-	-	0.08	bdl	-	98.41
LS8b-Tr-hc-15	22.03	34.45	42.05	0.17	bdl	-	bdl	bdl	-	-	bdl	-	98.83
LS8b-Tr-hc-15	22.44	34.66	41.58	-	-	-	-	bdl	-	0.08	-	-	98.87
LS8b-Tr-hc-15	21.58	33.99	42.76	0.16	-	-	-	-	0.15	0.60	-	-	99.24
LS8b-Tr-hc-15	21.72	34.44	42.43	0.28	-	-	bdl	bdl	-	-	-	-	98.91
LS8b-Tr-hc-15	21.53	34.07	42.33	0.18	-	-	-	bdl	-	0.39	bdl	-	98.61
LS8b-Tr-hc-15	21.01	34.52	42.79	0.39	-	0.05	-	bdl	-	0.18	bdl	-	99.10
LS8b-Tr-hc-15	21.70	34.23	41.73	1.01	bdl	0.02	bdl	bdl	-	-	-	-	98.80
LS8b-Tr-hc-15	20.87	34.53	43.01	0.51	-	-	-	-	-	-	-	-	98.93
LS8b-Tr-hc-15	20.85	34.11	42.61	0.48	-	-	bdl	bdl	-	-	-	-	98.18
LS8b-Tr-hc-15	21.43	34.66	42.64	0.47	bdl	-	bdl	bdl	-	-	bdl	-	99.29
LS8b-Tr-hc-15	21.09	34.51	43.25	0.46	bdl	-	-	-	-	-	-	-	99.32
LS8b-Tr-hc-15	21.73	34.23	42.79	0.11	-	-	-	-	-	-	-	-	98.87
LS8b-Tr-hc-15	21.29	34.51	42.62	0.54	-	-	-	bdl	-	-	bdl	-	99.06
LS8b-Tr-hc-15	21.56	34.42	42.47	0.68	-	-	-	bdl	-	-	-	-	99.17
LS8b-Tr-hc-15	21.59	34.67	42.71	0.76	bdl	0.01	-	-	-	-	-	-	99.80
LS8b-Tr-hc-15	21.79	34.78	41.90	0.80	bdl	-	bdl	bdl	-	-	bdl	-	99.42
LS8b-Tr-hc-15	21.25	34.52	42.59	0.61	-	0.09	-	bdl	-	-	bdl	-	99.13
LS8b-Tr-hc-15	21.64	34.63	42.75	-	-	-	bdl	-	-	0.13	-	-	99.22
LS8b-Tr-hc-15	21.22	34.79	43.03	0.18	-	0.01	bdl	bdl	-	-	-	-	99.26
LS8b-Tr-hc-15	21.09	34.65	42.68	0.55	-	-	bdl	bdl	-	-	bdl	-	99.07
LS8b-Tr-hc-15	21.19	34.85	42.72	0.34	-	-	-	bdl	-	-	bdl	-	99.20
LS8b-Tr-hc-15	21.32	34.42	42.78	0.62	-	-	bdl	bdl	-	-	bdl	-	99.32
LS8b-Tr-hc-15	21.30	34.68	42.56	0.74	-	-	-	bdl	-	-	-	-	99.36
LS8b-Tr-hc-15	21.24	34.67	42.29	0.27	-	0.02	bdl	-	-	-	bdl	-	98.57
LS8b-Tr-hc-15	21.48	34.48	41.89	0.89	-	-	-	bdl	-	0.09	bdl	-	98.90
LS8b-Tr-hc-15	21.56	34.65	41.76	0.69	bdl	-	bdl	-	-	-	-	-	98.76
LS8b-Tr-hc-15	21.10	34.39	42.87	0.73	-	0.05	bdl	bdl	-	-	-	-	99.23
LS8b-Tr-hc-15	21.56	34.37	41.82	0.50	bdl	-	bdl	bdl	-	-	-	-	98.34
LS8b-Tr-hc-15	21.28	34.61	42.57	0.58	-	-	-	bdl	-	-	bdl	-	99.14
LS8b-Tr-hc-15	21.50	34.49	42.40	0.61	bdl	-	-	bdl	-	-	bdl	-	99.08
LS8b-Tr-hc-15	21.70	34.56	42.39	0.44	-	-	-	bdl	-	-	bdl	-	99.18
LS8b-Pt-hc-34	21.15	34.16	42.61	0.18	-	-	-	bdl	-	-	-	-	98.15

Table ESM3-3 (suite)

Element	S	Fe	As	Sb	Au	Bi	Zn	Cu	Co	Ni	Ag	Se	Total
8A.z1.Apyb	21.71	35.35	41.80	-	0.15	-	-	-	-	-	-	0.09	99.13
8A.z1.Apybc	21.38	35.49	42.63	0.04	-	-	-	-	-	-	-	0.07	99.60
8A.z1.Apybc	21.60	35.56	42.14	0.06	-	0.20	-	-	-	-	-	-	99.55
8A.z1.Apybc	21.70	35.73	42.85	0.08	-	-	-	-	-	-	-	-	100.36
8A.z1.Apybc	20.17	35.82	42.59	0.09	-	-	-	-	-	-	-	0.09	98.75
8A.z1.Apybc	21.69	35.61	42.13	0.14	-	0.22	-	-	-	-	-	0.11	99.90
8A.z1.Apybc	21.85	35.72	41.75	0.14	-	-	-	-	-	0.11	-	0.13	99.69
8A.z1.Apybc	21.62	35.68	41.96	0.52	-	-	-	-	-	-	-	0.13	99.91
8A.z1.Apybc	21.10	35.52	42.34	0.68	-	0.17	-	-	-	-	-	-	99.81
8A.z1.Apybc	21.85	35.69	41.87	0.57	-	-	-	-	-	-	-	-	99.98
8A.z1.Apybc	21.44	35.58	42.46	0.32	-	-	-	-	-	-	-	-	99.80
8A.z1.Apybc	21.37	35.63	42.42	0.28	0.09	0.12	-	-	-	-	-	0.13	100.05
8A.z1.Apybc	21.13	35.78	42.83	0.26	-	-	-	-	-	-	-	0.12	100.11
8A.z1.Apybc	21.12	35.38	42.30	0.20	0.16	-	-	-	-	-	-	0.10	99.25
8A.z1.Apybc	21.26	35.21	42.97	0.24	-	-	-	-	-	-	-	0.13	99.81
8A.z1.Apybc	21.25	35.03	42.58	0.35	-	-	-	-	-	-	-	-	99.22
8A.z1.Apybc	20.99	35.29	42.81	0.71	-	0.21	-	-	-	0.12	-	-	100.11
8A.z1.Apybc	21.30	35.83	43.05	0.23	0.10	0.15	-	-	-	0.12	-	0.07	100.84
8A.z1.Apybc	21.51	35.55	42.77	0.25	-	-	-	-	-	0.06	-	0.15	100.29
8A.z1.Apybc	21.74	35.70	42.14	0.24	-	-	-	-	-	-	0.07	0.07	99.95
8A.z1.Apybc	21.02	35.60	42.25	0.52	-	-	-	-	-	-	-	0.08	99.46
8A.z1.Apybc	21.90	35.72	42.35	0.27	-	-	-	-	-	-	-	0.06	100.30
8A.z1.Apybc	21.27	35.74	42.45	0.11	0.09	0.17	-	-	-	-	-	0.07	99.90
8A.z1.Apybc	21.34	35.66	42.69	0.08	-	0.11	-	-	-	-	-	-	99.89
8A.z1.Apyb	21.40	36.21	42.70	-	0.10	0.24	-	-	-	-	-	0.16	100.81
Average	21.33	34.59	42.72	0.38	-	0.06	-	-	0.12	0.16	-	0.10	99.11
Stdev	3.20	5.16	6.38	0.26	-	0.04	-	-	0.01	0.07	-	0.03	14.74
Pyrrhotite													
SEM38-c1-2	39.36	58.93	bdl	-	-	bdl	-	bdl	-	-	-	-	98.43
SEM38-c1-4	39.34	59.13	bdl	-	-	bdl	bdl	bdl	-	-	-	-	98.68
SEM38-c1-5	38.99	58.93	bdl	bdl	bdl	bdl	-	bdl	bdl	-	bdl	-	98.15
SEM38-c1-7	39.09	59.80	bdl	bdl	bdl	bdl	-	bdl	-	bdl	-	-	99.17
SEM38-c1-10	39.61	59.36	bdl	bdl	-	bdl	-	bdl	-	-	bdl	-	99.22
SEM38-c1-14	39.33	59.42	bdl	bdl	bdl	bdl	bdl	0.21	-	-	-	-	99.09
SEM38-c1-15	39.76	58.32	bdl	0.19	-	bdl	-	bdl	-	bdl	-	-	98.49
Average	39.35	59.13	-	0.19	-	-	-	0.21	-	-	-	-	98.75
Stdev	0.27	0.47	-	0.07	-	-	-	0.08	-	-	-	-	0.42

Table ESM3-3 (suite)

Element	S	Fe	As	Sb	Au	Bi	Zn	Cu	Co	Ni	Ag	Se	Total
Berthierite													
LS2-Pt-hc-7	28.98	12.54	0.08	57.57	-	bdl	-	bdl	-	-	bdl	-	99.32
LS2-Pt-hc-11	27.81	3.26	0.09	68.36	-	-	-	bdl	-	-	-	-	99.57
SEM45-Pt-hc-39	29.13	15.30	3.76	53.04	-	-	bdl	bdl	-	-	-	-	101.39
SEM40-c1-1	29.74	12.75	0.11	57.74	-	-	-	0.22	-	-	bdl	-	100.58
SEM40-c1-4	29.45	12.86	0.10	57.65	bdl	-	-	bdl	-	bdl	-	-	100.24
SEM40-c1-5	29.78	12.90	0.12	57.77	-	bdl	bdl	bdl	-	-	bdl	-	100.75
SEM40-c1-6	29.32	12.84	0.10	57.49	-	bdl	bdl	0.26	-	bdl	bdl	-	100.12
SEM40-c1-8	29.89	12.71	0.07	57.70	bdl	-	bdl	0.20	-	-	bdl	-	100.60
SEM40-c2-1	29.51	12.66	bdl	57.68	bdl	bdl	-	bdl	-	-	bdl	-	99.97
SEM40-c2-3	29.53	12.92	0.09	57.66	-	-	-	bdl	-	-	bdl	-	100.33
SEM38-c1-16	30.30	13.12	0.11	54.48	-	-	bdl	bdl	-	-	-	-	98.15
Average	29.40	12.17	0.46	57.92	-	-	-	0.22	-	-	-	-	100.09
Stdev	0.64	3.05	1.11	3.81	-	-	-	0.11	-	-	-	-	0.86
Stibnite													
LS2-Pt-hc-5	27.44	0.06	bdl	72.41	bdl	-	-	bdl	-	-	bdl	-	100.04
LS2-Pt-hc-6	27.76	0.28	-	71.36	-	-	-	bdl	-	bdl	-	-	99.52
SEM42-Pt-c1-54	27.99	0.01	0.13	72.76	-	-	-	bdl	-	-	bdl	-	101.06
SEM42-Pt-c1-55	28.21	0.00	0.12	72.57	bdl	bdl	bdl	-	-	-	bdl	-	101.06
SEM42-Pt-hc-56	27.97	0.00	bdl	72.58	-	-	bdl	-	-	-	-	-	100.59
SEM42-Pt-hc-57	28.04	0.00	0.08	72.49	bdl	-	bdl	bdl	-	bdl	bdl	-	100.82
SEM40-c1-2	27.76	0.21	0.08	72.58	-	bdl	-	bdl	-	bdl	bdl	-	100.79
SEM40-c1-3	27.69	0.31	0.08	72.66	bdl	-	-	bdl	-	-	bdl	-	100.83
SEM40-c1-7	27.63	0.09	bdl	71.56	-	-	bdl	-	-	-	bdl	-	99.40
SEM40-c2-2	28.07	1.11	bdl	71.11	bdl	-	bdl	bdl	-	-	-	-	100.44
SEM40-c2-4	27.99	0.05	0.09	71.83	-	-	bdl	bdl	-	bdl	bdl	-	100.15
SEM38-c1-1	28.31	0.10	bdl	72.41	-	bdl	bdl	-	-	bdl	bdl	-	100.95
SEM38-c1-3	27.38	0.27	bdl	70.85	-	bdl	-	bdl	-	-	-	-	98.61
SEM38-c1-8	27.93	1.38	bdl	72.22	bdl	-	bdl	bdl	-	bdl	-	-	101.66
SEM38-c1-9	28.38	0.45	bdl	72.11	-	-	bdl	bdl	-	-	bdl	-	101.05
SEM38-c1-11	28.43	1.08	bdl	71.80	-	-	-	bdl	-	-	-	-	101.38
SEM38-c1-12	28.34	0.43	bdl	72.42	-	bdl	bdl	bdl	-	-	-	-	101.29
SEM38-c1-13	27.75	0.08	bdl	71.14	-	-	-	bdl	-	bdl	-	-	99.11
Average	27.95	0.33	0.10	72.05	-	-	-	-	-	-	-	-	100.49
Stdev	0.31	0.42	0.05	0.61	-	-	-	-	-	-	-	-	0.85

Abbreviations: D.L., detection limit; Stdev, standard deviation; bdl, below detection limit; Apy, arsenopryite; Stb, stibnite

ESM 4 Estimated crystallization temperatures of arsenopyrite formed at As-Fe-Au-Sb stage based on the projection of As activity (Kretschmar and Scott 1976, Sharp et al. 1985)

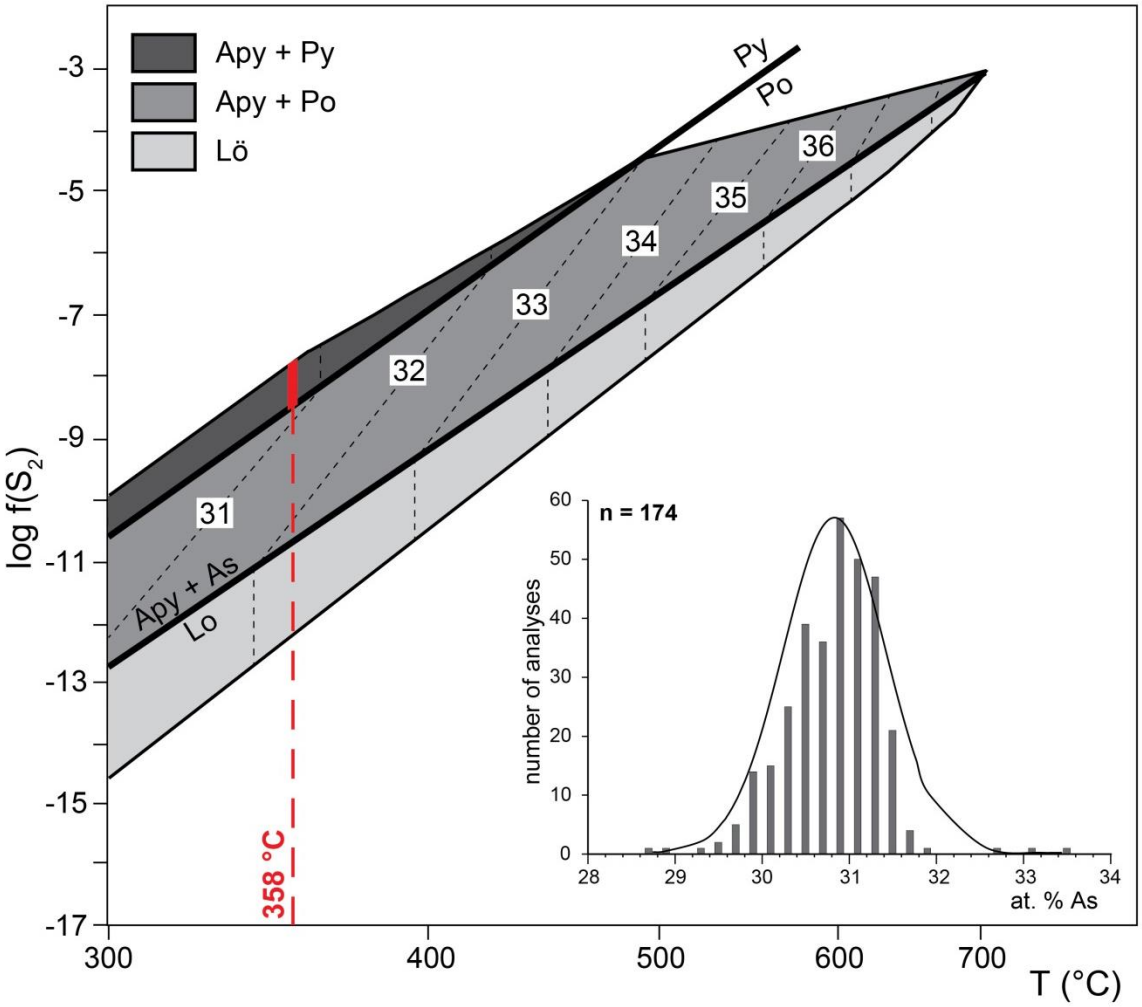

ESM 5 Chemical composition of representative aqueous-carbonic inclusions of the Le Semnon Sb-Au deposit obtained by Raman spectroscopy and corresponding microthermometric data

						Composition of the volatile phase (% mol)				Bulk composition (% mol)				Density (g/cm^3)
Sample	**Tm CO2**	**Tm H2O**	**TmCl**	**Th CO2**	**Th**	**CO_2**	**N_2**	**CH_4**	**H_2O**	**CO_2**	**N_2**	**CH_4**	**NaCl**	
Lc- w aqueous carbonic inclusions. LH2O-LCO2-VCO2 :														
L11-4.3	-57.4	-3.5	10.2	19.9	260*	90.1	9.2	0.7	82.9	14	1.25	0.1	1.8	0.85
L11-1b3	-57.6	n.o.	10.2	18.8	314	91.5	7.8	0.7	80.45	16.5	1.25	0.1	1.7	0.83
L11-1b7	-56.7	n.o.	10	22.8	306	92.1	7.4	0.5	74.8	21.9	1.6	0.1	1.6	0.77
Lw-c aqueous carbonic inclusions. LH2O-LCO2 :														
L11-1.3	-57.8	-3.2	9.9	-	255	88.7	10.5	0.8	94.9	4.2	0.19	0.01	0.7	0.79
L11-1.4	n.o.	-2.9	9.4	-	208	98.9	1.1	0	95.4	3.8	0.01	0	0.7	0.83
L11-1.9	n.o.	-3.2	9.9	-	158	99.7	0.3	0	95.8	3.4	<0.01	0	0.8	0.92
L11-4.8	-57.7	-3	9.8		275	91.5	8.7	0.8	95.69	3.5	0.1	0.01	0.7	0.88
L11-1b15	n.o.	-3.5	10	-	n.o.	70	28.8	1.1	95.8	3.1	0.26	0.01	0.83	0.93

Abbreviations: n = number of inclusions; Tm CO_2 = melting temperature of CO_2 solide; Tm H_2O = melting temperature of H20; Tm Cl = melting temperature of clathrates; Th CO_2 = Homogenization temperature of CO_2; Th = Homogenization temperature; L = liquid; * decrepitation temperature; n.o. = not observed. Temperatures are given in °C

Annexe 4

Supporting information for:

An Early Carboniferous Sb-Au mineralizing peak in a long-lived hydrothermal history: major tectono-magmatic implications for the Armorican Massif (France)

Anthony Pochon[1], Yannick Branquet[1, 2], Gilles Ruffet[1], Marc Poujol[1], Eric Gloaguen[2, 3], Philippe Boulvais[1], Charles Gumiaux[2], Florence Cagnard[2, 3], Denis Gapais[1], Jean-Marc Baele[4], Inoussa Kéré[1]

[1] Géosciences Rennes, UMR 6118, Université de Rennes 1, OSUR, Campus de Beaulieu, 35042 Rennes Cedex, France

[2] Institut des Sciences de la Terre d'Orléans, UMR 7327, Université d'Orléans, Campus Géosciences, 1A rue de la Férollerie, 45071 Orléans Cedex 2, France

[3] Bureau de Recherche Géologique et Minière (BRGM), UMR 7327, 3 avenue Claude-Guillemin, BP 36009, 45060 Orléans Cedex 02, France

[4.] Géologie Fondamentale et Appliquée, Université de Mons, Rue de Houdain, 9, 7000 Mons, Belgium

---

Supplementary Materials 1 (SM1)

Table SM1 Tobelite $^{40}Ar/^{39}Ar$ analytical data

Laser power	$^{40}Ar_{Atm}$	Error ^{40}Ar	$^{39}Ar_K$	Error ^{39}Ar	^{38}Ar	Error ^{38}Ar	^{37}Ar	Error ^{37}Ar	^{36}Ar	Error ^{36}Ar	$^{40}Ar^*/^{39}ArK$	Error $^{40}Ar^*/^{39}ArK$	Apparent age (Ma)	Error Age (Ma)	Delay to irradiation (day)
SADC76.a tobelite															
250	1386.02	0.91	2.75	0.02	0.000001	0.022	0.024	0.024	4.744664	0.024401	7.91	3.69	144.6	64.9	186.88
300	133.99	0.23	2.42	0.02	0.000001	0.024	0.066	0.021	0.352506	0.018282	13.70	2.21	243.6	36.8	186.90
370	182.75	0.25	5.50	0.07	0.000001	0.024	0.000	0.025	0.249114	0.020754	20.37	1.13	351.3	17.8	186.92
410	482.93	0.75	19.78	0.06	0.000001	0.023	0.033	0.020	0.27336	0.016225	20.61	0.25	355.1	4.3	186.94
430	7295.88	5.10	346.86	0.30	0.000001	0.022	0.025	0.017	0.44547	0.027615	20.83	0.04	358.5	1.7	186.98
460	4087.76	3.06	196.99	0.30	0.000001	0.019	0.068	0.021	0.037172	0.029196	20.86	0.06	359.1	1.9	187.00
510	23447.33	27.64	1126.63	1.12	0.000001	0.022	0.157	0.032	0.286386	0.02761	20.91	0.04	359.7	1.7	187.02
570	464.62	0.65	22.24	0.06	0.000001	0.019	0.066	0.025	0.029241	0.015328	20.69	0.21	356.4	3.7	187.04
650	1526.90	1.34	73.94	0.10	0.0332	0.023	0.051	0.029	0.014907	0.040499	20.76	0.16	357.5	3.0	187.08
Fusion	3.65	0.08	0.27	0.03	0.000001	0.024	0.075	0.028	0.033528	0.028366	-21.61	30.94	-466.7	762.4	187.10
SADC76.b tobelite															
250	834.58	1.05	5.96	0.04	0.000001	0.020	0.119	0.031	2.723412	0.026527	8.76	1.48	159.4	25.9	182.83
300	94.44	0.17	3.15	0.04	0.000001	0.016	0.001	0.020	0.117244	0.023277	19.44	2.16	336.7	34.1	182.85
350	410.52	0.79	17.74	0.08	0.000001	0.018	0.077	0.027	0.173854	0.016502	20.51	0.29	353.5	4.8	182.87
400	974.81	0.50	44.60	0.16	0.000001	0.018	0.041	0.028	0.192116	0.018117	20.79	0.14	357.8	2.8	182.91
400	644.45	0.61	30.64	0.05	0.000001	0.017	0.109	0.034	0.03358	0.040009	20.90	0.38	359.6	6.2	182.93
440	3088.71	1.80	146.89	0.19	0.007323	0.015	0.086	0.027	0.226004	0.015948	20.75	0.05	357.3	1.8	182.95
470	4628.97	3.01	227.55	0.18	0.010774	0.014	0.079	0.034	0.153909	0.012298	20.31	0.04	350.4	1.7	182.98
490	3285.32	1.50	164.86	0.25	0.000001	0.012	0.012	0.030	0.127399	0.021927	19.86	0.06	343.4	1.8	183.10
500	1885.28	1.21	94.63	0.19	0.018733	0.011	0.084	0.013	0.124605	0.021067	19.71	0.08	340.9	2.0	183.13
520	6082.64	2.40	301.63	0.26	0.000001	0.013	0.105	0.025	0.179847	0.011452	20.16	0.04	348.0	1.7	183.15
540	335.75	0.37	16.74	0.05	0.000956	0.015	0.033	0.014	0.043308	0.043436	19.48	0.76	337.3	12.0	183.17
650	3629.75	3.19	181.69	0.24	0.026601	0.013	0.076	0.039	0.049294	0.011799	20.06	0.05	346.5	1.7	186.81
Fusion	125.77	0.26	6.29	0.04	0.000001	0.021	0.017	0.036	0.000001	0.024069	20.17	1.12	348.1	17.6	186.84

Table SM 1 (suite)

Parameters				
$(^{36}Ar/^{37}Ar)_{Ca}$	0.000322	3	%	
$(^{39}Ar/^{37}Ar)_{Ca}$	0.000788	4	%	
$(^{38}Ar/^{37}Ar)_{Ca}$	0.000026	100	%	
$(^{40}Ar/^{37}Ar)_{Ca}$	0.0006	100	%	
$(^{40}Ar/^{39}Ar)_{K}$	0.00085	4	%	
$(^{38}Ar/^{39}Ar)_{K}$	0.011	91	%	
$(^{36}Cl/^{38}Cl)$	316	5	%	[3]
$(^{40}Ar/^{36}Ar)_{Atm}$	298.56	0.104	%	[1] and [1']
$(^{38}Ar/^{36}Ar)_{Atm}$	0.1885	0.159	%	[1] and [1']
λ_{40}	5.53E-10	1.35E-12	y-1	[2]
λ_{39}	2.58E-03		y-1	
λ_{37}	1.98E-02		d-1	
λ_{36Cl}	2.26E-06		y-1	

J parameter	0.01052934
Error J	0.00004349
Mass Discrimination (1+e)	1.009405
Error Discrimination	0.00132283

References:
[1] Lee, JY, Marti, K, Severinghaus, JP, Kawamura, K, Yoo, HS, Lee, JB, Kim, JS (2006). A redetermination of the isotopic abundances of atmospheric Ar. Geochimica Cosmochimica Acta, 70, 4507-4512.
[1'] Mark, DF, Stuart, FM, De Podesta, M (2011). New high-precision measurements of the isotopic composition of atmospheric argon. Geochimica Cosmochimica Acta, 75, 7494-7501.
[2] Renne, PR, Balco, G, Ludwig, RL, Mundil, R, Min, K, . (2011). Response to the comment by W.H. Schwarz et al. on "Joint determination of (40)K decay constants and (40)Ar*/(40)K for the Fish Canyon sanidine standard, and improved accuracy for (40)Ar/(39)Ar
[3] York, D, Personnal Communication - McMaster reactor
Regression method: York, D. (1969). Least-squares fitting of a straight line with correlated errors. Earth Planet. Sci. Lett. 5, 320-4.
Ages and errors of Hb3gr and TCs monitors refers to: Rennes, PR, Balco, G, Ludwig, Mundil, R, Min, K, . (2011). Response to the comment by W.H. Schwarz et al. on "Joint determination of (40)K decay constants and (40)Ar*/(40)K for the Fish Canyon sanidine standard, and

Table SM2 Representative LA-ICP-MS U-Pb analyses for fluorapatite IV

	U (ppm)	Pb (ppm)	$^{238}U/^{206}Pb$	Error (2σ)	$^{207}Pb/^{206}Pb$	Error (2σ)
StAubinApat_1	2	38	0.173	0.003	0.8668	0.0067
StAubinApat_2	2	34	0.230	0.006	0.8680	0.0052
StAubinApat_3	2	48	0.155	0.002	0.8724	0.0059
StAubinApat_4	2	48	0.164	0.004	0.8662	0.0068
StAubinApat_5	4	44	0.358	0.005	0.8589	0.0058
StAubinApat_7	3	66	0.184	0.004	0.8664	0.0057
StAubinApat_8	2	61	0.127	0.003	0.8637	0.0051
StAubinApat_9	23	41	2.128	0.140	0.8110	0.0061
StAubinApat_10	2	49	0.167	0.003	0.8667	0.0060
StAubinApat_11	5	27	0.729	0.033	0.8350	0.0063
StAubinApat_12	2	22	0.422	0.007	0.8601	0.0062
StAubinApat_13	8	3	6.435	0.430	0.6230	0.0120
StAubinApat_14	15	4	9.116	0.110	0.5456	0.0070
StAubinApat_15	4	3	5.227	0.077	0.6960	0.0120
StAubinApat_16	19	3	11.848	0.150	0.4351	0.0120
StAubinApat_17	3	3	4.198	0.120	0.7460	0.0130
StAubinApat_18	16	4	9.470	0.250	0.5290	0.0100
StAubinApat_19	2	3	3.128	0.058	0.7460	0.0130
StAubinApat_20	2	13	0.685	0.011	0.8538	0.0071
StAubinApat_21	1	10	0.613	0.026	0.8650	0.0089
StAubinApat_22	3	19	0.721	0.018	0.8600	0.0061
StAubinApat_23	0	15	0.022	0.001	0.8671	0.0076

Annexe 5

Water pumping in mantle shear zones

Jacques Précigout[1], Cécile Prigent[2], Laurie Palasse[3], Anthony Pochon[4]

[1] *Institut des Sciences de la Terre d'Orléans, UMR 7327, Université d'Orléans, Campus Géosciences, 1A rue de la Férollerie, 45071 Orléans Cedex 2*

[2] *Univ. Grenoble Alpes, CNRS, ISTerre, F-38000 Grenoble, France.*

[3] *Bruker Nano Analytics, Am Studio 2D, 12489 Berlin, Germany*

[4] *Géosciences Rennes, UMR 6118, Université de Rennes 1, Campus de Beaulieu, 35042 Rennes Cedex*

Publié à *Nature communications*, vol. 8, doi: 10.1038/ncomms15736 (2017)

---

nature COMMUNICATIONS

ARTICLE

Received 25 Aug 2016 | Accepted 25 Apr 2017 | Published 8 Jun 2017

DOI: 10.1038/ncomms15736 OPEN

Water pumping in mantle shear zones

Jacques Précigout[1], Cécile Prigent[2], Laurie Palasse[3] & Anthony Pochon[4]

Water plays an important role in geological processes. Providing constraints on what may influence the distribution of aqueous fluids is thus crucial to understanding how water impacts Earth's geodynamics. Here we demonstrate that ductile flow exerts a dynamic control on water-rich fluid circulation in mantle shear zones. Based on amphibole distribution and using dislocation slip-systems as a proxy for syn-tectonic water content in olivine, we highlight fluid accumulation around fine-grained layers dominated by grain-size-sensitive creep. This fluid aggregation correlates with dislocation creep-accommodated strain that localizes in water-rich layers. We also give evidence of cracking induced by fluid pressure where the highest amount of water is expected. These results emphasize long-term fluid pumping attributed to creep cavitation and associated phase nucleation during grain size reduction. Considering the ubiquitous process of grain size reduction during strain localization, our findings shed light on multiple fluid reservoirs in the crust and mantle.

[1] Institut des Sciences de la Terre d'Orléans (ISTO), CNRS-UMR 7327, Université d'Orléans, Campus Géosciences, 1A rue de la Férollerie, 45071 Orléans Cedex 2, France. [2] Univ. Grenoble Alpes, CNRS, ISTerre, F-38000 Grenoble, France. [3] Bruker Nano Analytics, Am Studio 2D, 12489 Berlin, Germany. [4] Géosciences Rennes, UMR 6118, Université de Rennes 1, Campus de Beaulieu, 35042 Rennes, France. Correspondence and requests for materials should be addressed to J.P. (email: jacques.precigout@univ-orleans.fr).

Water is one of the main characteristic components of the Earth. It significantly influences geological processes such as partial melting, ore genesis and the production of earthquakes. Deformation experiments have also shown that water may weaken single crystals and mineral aggregates during ductile flow[1–4], with key implications for plate tectonics. For instance, water/hydrolytic weakening of quartz in the lower crust and of olivine in the uppermost mantle may change the mode of lithospheric deformation from localized (subduction zone, narrow rift) to distributed (ridge plateau, wide rift), or vice versa[5–7]. Although the physical process of this phenomenon remains to be resolved, intra-grain water is thought to enhance the glide or climb of line defects (dislocations) during plastic flow, resulting in mechanical weakening[8,9].

Conversely, rock deformation may have an impact on water distribution. While brittle faults are accepted as controlling the circulation of fluids at shallow depth (< 10 km depth), natural observations—mainly of mid-crustal rocks—suggest that ductile shear zones also drive fluids at greater depth[10]. In the brittle regime, the presence of faults controls the migration of fluids by providing structural conduits or through seismic pumping[11]. But at deeper levels and higher temperatures, these fault-related processes are unlikely owing to plastic flow. At present, two possible mechanisms have been proposed to account for water draining in ductile shear zones, including a 'passive' convergence due to an increase of porosity where grain size is being reduced[12], or 'dynamic' pumping through opening of micro-cavities[13]. Fluid migration is indeed particularly observed where mineral aggregates dominantly deform by grain-size-sensitive (GSS) creep, commonly including a component of grain boundary sliding (GBS)[13–15]. When GBS cannot be fully compensated by diffusive or plastic processes, some micro-cavities open and close in a continuous process because of local dilatancies, giving rise to creep cavitation[16–18]. This might result in fluid pumping—including water—towards the shear zone centre. Nevertheless, only a few vestiges of syn-tectonic water draining have been reported so far, and exclusively for crustal rocks[13,19], allowing doubts to persist about the validity of this latter mechanism.

In this paper, we describe systematic changes in dislocation slip-system and related olivine fabric, combined with enrichments in amphibole, that document syn-tectonic water draining in natural mantle shear zones (Ronda massif, Spain). While water accumulates around ultramylonites that deform by GSS creep, fluid aggregation is coeval with multi-scale strain partitioning between water-poor and water-rich layers during olivine dislocation creep. Providing evidence of long-term water pumping during shear strain localization in upper mantle peridotites, our findings strongly suggest that water converges through the opening of micro-cavities coupled with phase nucleation processes.

Results

The Ronda mylonitic complexes. Located in the internal domain of the Betic Cordillera in southern Spain, the Ronda massif encompasses several kilometre-scale lenses of sub-continental ultramafic bodies (Fig. 1a). During continental extension and subsequent thrusting onto continental crust[20,21], these mantle peridotites were affected by several stages of deformation[21,22] including the development of ductile shear zones in the southwestern massif (Fig. 1a)[23]. In this region, the outcrop-scale features consist of alternating protomylonitic and mylonitic layers within so-called mylonitic complexes. These complexes range from a few centimetres to more than 10 m in thickness and extend up to several hundred meters along strike (Fig. 1b,c). They developed from a protolith of porphyroclastic, spinel-bearing

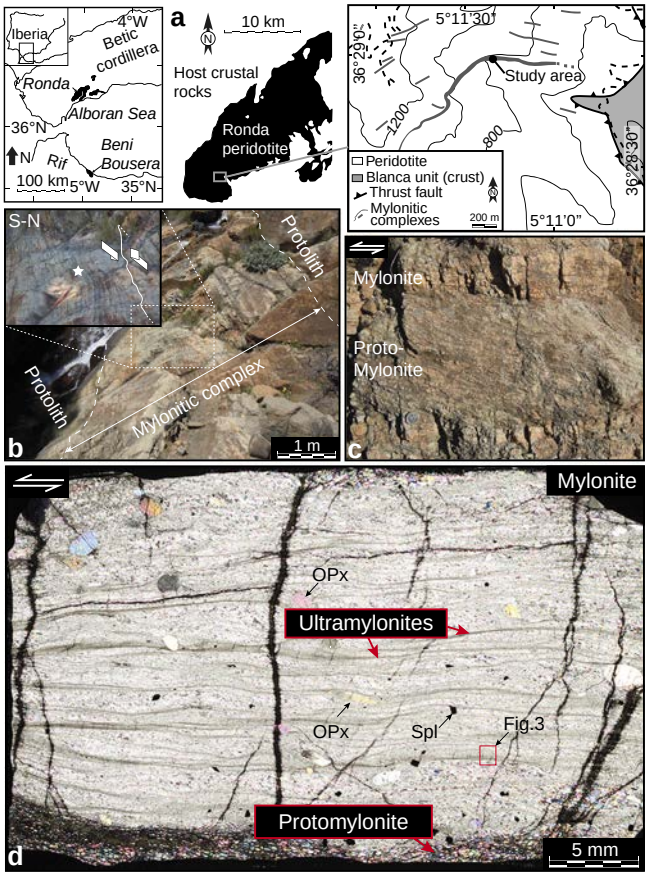

Figure 1 | The Ronda mantle shear zones. (**a**) Location of the Ronda peridotite massif (Betic cordillera, southern Spain) and its mylonitic complexes, including the study area (modified from Hidas *et al.*[23]). (**b**) Studied area of a 5-m-thick mylonitic complex of spinel-bearing harzburgite (protolith) with top-to-the-SW kinematics (inset). (**c**) Detailed view of the strain partitioning between protomylonitic and (ultra)mylonitic spinel-bearing peridotites in the mylonitic complex. (**d**) Photomicrograph (plane polarized light) of a mylonite layer highlighting very fine-grained anastomosing ultramylonite bands adjacent to pyroxene porphyroclasts. The thin section has been cut in the XZ structural plane, that is, the plane normal to the shear plane and parallel to the shear direction. All ductile horizontal structures are crosscut by post-tectonic serpentine. The thin section is 50 μm thick. Opx = orthopyroxene; Spl = spinel.

harzburgite with a foliation oriented 110°/50°NE with top-to-the-SW shear sense criteria (Fig. 1b). The transition from the protolith to a mylonitic complex is progressive and characterized by a thickening of mylonitic and protomylonitic layers (see Supplementary Fig. 1).

In thin section, the mylonitic peridotites contain several ultramylonitic bands of very fine grains that always wrap around pyroxene porphyroclasts (Fig. 1d). Indeed, the protolith and protomylonites have a mean grain size >1 mm for all phases, but the grain size substantially decreases to ~150 μm close to mylonitic layers, ~30–50 μm in mylonitic layers (that is, in between ultramylonites) and <15 μm in ultramylonitic layers, except for a few porphyroclasts of pyroxene (see the Methods section for grain size calculation). At the centre of mylonitic complexes, the density and size of ultramylonitic bands substantially increase, and mylonitic layers contain coarse spinel grains (chromite) with many mode-I cracks sealed by olivine and amphibole (tremolite) (Fig. 2). The occurrence of cracks resulting from tensile stress and sealed by a hydrous phase strongly suggests that the cracking process was the result of high fluid

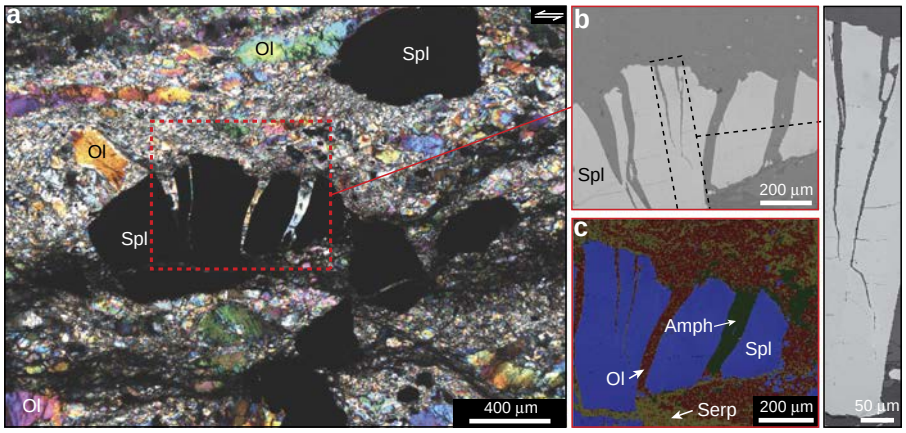

Figure 2 | Mode-I cracks in spinel located near the centre of a mylonitic complex. (**a**) Thin section (polarized light) of a mylonite layer containing cracked spinel (Spl; chromite) in between ultramylonite layers (a white star shows the field location in Fig. 1b). (**b**) Backscatter electron (BSE) image showing the mode-I cracks in spinel. See the methods section for analytical conditions. (**c**) Element map of the BSE image using energy-dispersive X-ray spectroscopy (EDX). The colour coding is based on the relative amounts of O, Mg, Si, Fe, Al, Ca and Cr. This map highlights olivine (Ol) and amphibole (Amph) as filling the mode-I cracks. Serp = serpentine.

pressure[24]. Post-tectonic serpentine is also present in the protolith and protomylonites, but is less abundant in mylonites and is quasi-absent in ultramylonites.

Through high-resolution element maps collected by electron microprobe, we further demonstrate enrichment in secondary phases and the presence of amphiboles (pargasite ± tremolite) in fine-grained ultramylonites (Fig. 3a,b). Most peridotites of the shear zones (protolith, protomylonites and mylonites) are indeed composed of olivine (85%) with a small amount of orthopyroxene (13%) ± clinopyroxene (1%) ± spinel (1%), whereas the ultramylonites contain far more orthopyroxene (~30%) and ~4.5% of calcium-bearing phases. These latter include either clinopyroxene (diopside) or amphiboles with local intergrowths (Fig. 3b). The amount of amphibole generally increases with reducing grain size, but we also document higher content of amphibole in some mylonitic areas located along ultramylonitic layers (see Supplementary Fig. 2). In ultramylonites, all phases are strongly mixed with a low-porosity, with backscatter electron (BSE) images revealing only a few pores of ~1 µm size (Fig. 3c). Very little amphibole is present in the protolith[25].

Based on mineral compositions in the mylonites and ultramylonites and using available geothermobarometers (see Supplementary Tables 1–6), we appraise (1) a pressure reducing from ~1.2 GPa to ~0.5 GPa, and (2) a coeval decrease in temperature from >1,000 °C to below 600 °C with reducing grain size (Fig. 3d). These conditions are consistent with previous estimates that documented decompression and cooling from ~1 GPa/1,000 °C to ~0.5 GPa/<700 °C in the study area[22,25,26]. Using Perple_X calculations to construct a P–T diagram of phase equilibrium (pseudosection), we further give an estimate of the ultramylonites water content. Focusing on a very fine grain size area, we estimated the mineral modal proportions through point counting using element map. This gives 65.9% for olivine, 28.8% for orthopyroxene, 3.0% for amphiboles, 1.5% for clinopyroxene and 0.8% for spinel, which was subsequently converted into oxide percentages. Based on our P–T estimates, as well as calculated isopleths for amphibole and clinopyroxene on the pseudosection, we need ~600 p.p.m. H_2O to reach 3% amphibole (2.25% pargasite + 0.75% tremolite) and <2% clinopyroxene in the ultramylonites (Fig. 3e). As 3% amphibole is close to the maximum that we found in ultramylonites, a lower water content may be expected. However, the absence of plagioclase necessarily implies a minimum of 400 p.p.m. H_2O (see Supplementary Fig. 3). For further information about microstructures, phase compositions and P–T estimates, the readers may refer to Hidas *et al.*[25].

Olivine fabric and lattice misorientations. Through electron backscatter diffraction (EBSD) analyses, we documented lattice preferred orientation (LPO) and related features for olivine. All LPOs are characterized by olivine [100] axis maxima at low angles to the shear direction (X) and [001] axes close to the pole to the shear plane (Z), which is typical of an E-type fabric (Fig. 4a)[27]. This feature differs from the distal protolith where an A-type fabric has been documented[22,25]. Moreover, in some layers, the [010] and [001] axes are more dispersed and distributed as girdles normal to the shear direction. Together with a strong [100] axis maximum that is close to the shear direction, these features are typical of an axial-[100] fabric or D-type fabric[28,29], giving rise to a combined type of olivine LPO between E- and D-type fabrics.

To better characterize this combined LPO, here referred to as D/E-type fabric (Fig. 4a), we used the eigenvalues of each pole figure to calculate the BA index[30,31]. This index indicates a degree of combination between axial-[100] fabric (BA = 1) and axial-[010] fabric (BA = 0). A point maximum LPO such as an E-type fabric will have an intermediate value, typically around 0.5. Across the Ronda shear zones, the BA index indicates pure E-type fabric at the edge of the protolith along mylonitic complexes (BA = 0.48), and at the edge of the mylonitic layers adjacent to ultramylonites (BA = 0.49) (Fig. 4b). Elsewhere, olivine developed a D/E-type fabric with significant components of D-type fabric, including in the protomylonites (BA = 0.67), the core of the mylonites (BA = 0.73) and the core of the protolith layers located between mylonitic complexes (BA = 0.81) (Fig. 4a,b). We also found D/E-type fabric in the ultramylonites (BA = 0.70), but this value remains uncertain because of their very weak and dispersed LPOs (Fig. 4a).

In relation to this, the strength of olivine fabrics was investigated using the texture[32] (J) and misorientation[33] (M) indices. These both give the degree of mineral alignment from random (J = 1; M = 0) to single crystal-like LPO (J = ∞; M = 1). Across the Ronda shear zones, olivine fabrics range from moderately weak LPOs in the protolith (J = 3.87; M = 0.14) to very strong LPOs at the edge of mylonitic areas adjacent to ultramylonites (J = 16.80; M = 0.46). They also systematically

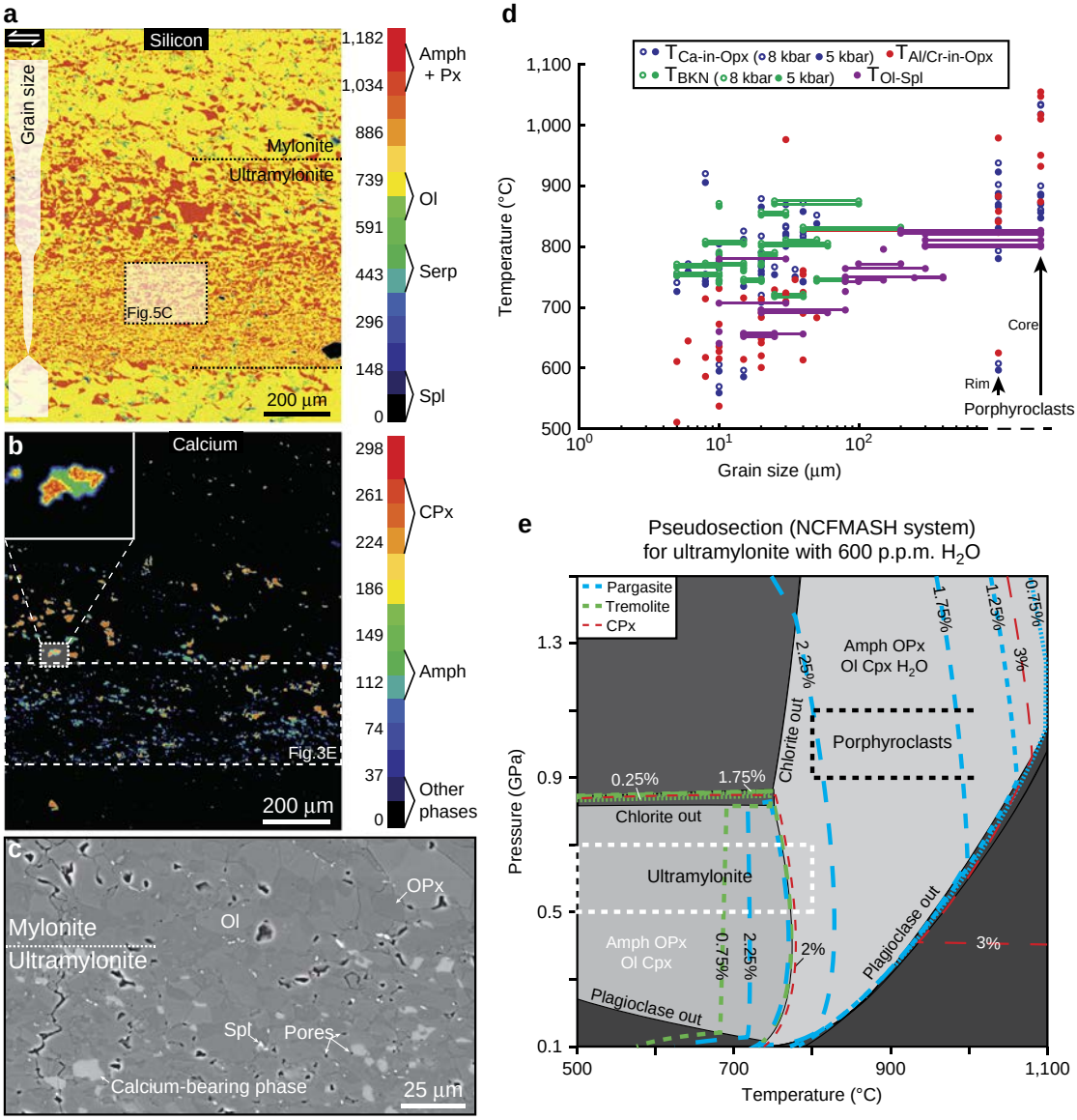

Figure 3 | Phase enrichment and pressure-temperature-water content estimates. (**a**,**b**) Element maps (electron microprobe) that show the distribution of silicon (**a**) and calcium (**b**) across an ultramylonite layer (location in Fig. 1d). The step size is 1 µm and the colour scale refers to the number of counts (see the methods section). These maps highlight enrichment in secondary phases (pyroxene (Px) and amphibole (Amph)) and increasing amphibole (pargasite ± tremolite) content with decreasing grain size. The top inset in **b** gives a detailed view of phase intergrowth between clinopyroxene and amphibole. (**c**) BSE image of an ultramylonite where very few micro-pores (<1 µm) have been identified. The calcium-bearing phases are either amphibole or clinopyroxene grains. (**d**) Calculated temperature in mylonites and ultramylonites as a function of mineral grain size, except for the rim and core of porphyroclasts. For calculations, we applied four geothermometers based on major-element mineral compositions measured by microprobe (see Supplementary Tables 1–6). These geothermometers include the Ca-in-OPx thermometer[65], Al/Cr-in-OPx thermometer[66], two-pyroxenes thermometer[65] (BKN) and olivine-spinel thermometer[67]. The horizontal lines link the two different grain sizes in the case of the two-phase thermometers. For pressure-dependent thermometers, we calculated temperatures at pressures of 5 (empty dot) and 8 (full dot) kbar. Pressure estimates are from Putirka *et al.*[68] (see Supplementary Tables 1–6). (**e**) Equilibrium phase diagram (pseudosection) for an ultramylonite. The pseudosection has been constructed using modal amounts of the phases in the ultramylonite layer shown in **b** (see text and methods section). Based on the P-T conditions recorded in the ultramylonites (dotted white rectangle) and using isopleths of clinopyroxene (dotted red line), pargasite (dotted blue line) and tremolite (dotted green line), we estimate a water content of ~600 p.p.m. during deformation of this ultramylonite band. For comparison, we also show the predicted conditions before deformation based on the P-T data recorded in porphyroclasts (dotted black rectangle). Amph = amphibole; Chl = chlorite; CPx = clinopyroxene; Ol = Olivine; OPx = orthopyroxene; Pl = plagioclase; Serp = serpentine; Spl = spinel.

strengthen from centre to edge within each layer (Fig. 4b). Indeed, the J and M indices never exceed 5 and 0.2, respectively, in the centres of the protolith layers between mylonitic complexes, the protomylonites and the mylonites. In contrast, the fabric strength largely exceeds J = 10 and M = 0.3 at the edge of these layers (Fig. 4a). This distribution (using M index) correlates with the distribution of shear strain (γ) across the Ronda shear zones, deduced from the angle between the long shape axis of olivine grains and the shear plane (Fig. 4b)[34]. It is also important to note that despite high shear strain in ultramylonites ($\gamma > 5$), the olivine LPO remains extremely weak (J = 1.64; M = 0.01).

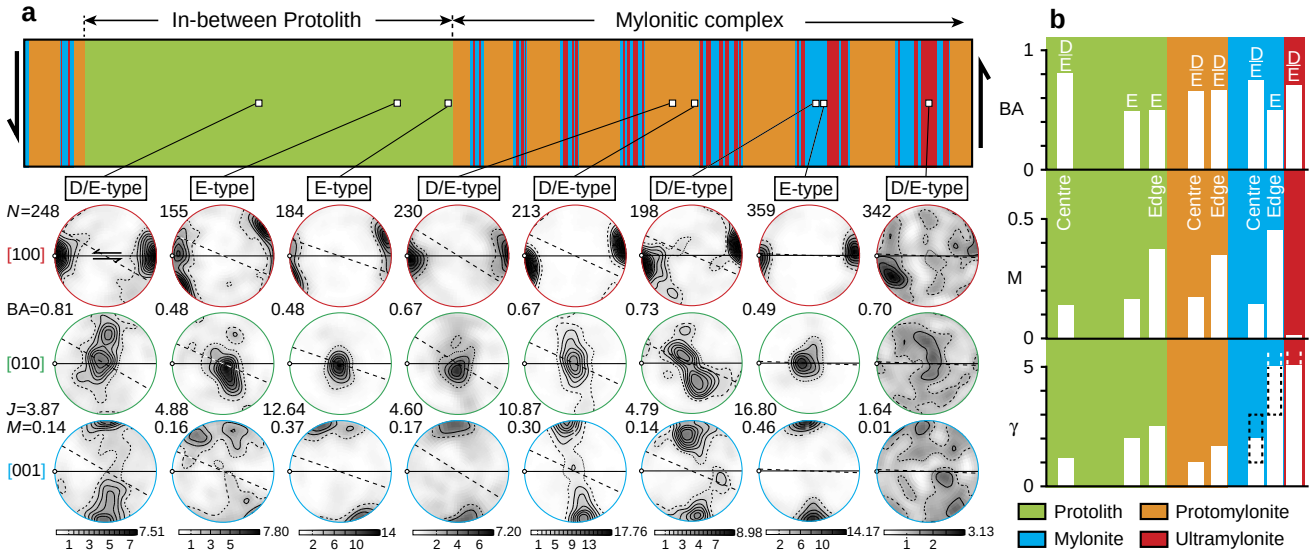

Figure 4 | Olivine fabric across a mylonitic complex. (**a**) Olivine lattice preferred orientation (LPO) across a mylonitic complex, including an in-between protolith. For the protolith, protomylonites and mylonites, we show LPO patterns from centre to edge. LPOs are displayed in equal-area lower-hemisphere pole figures with respect to the shear plane (horizontal line defined by ultramylonitic bands), shear direction (white dot) and foliation plane (dotted line) for the three principal axes of olivine ([100], [010] and [001]). The iso-contours and grey shading are multiples of a uniform distribution based on one point per grain (linear scale). While E-type fabric is identified at the edges of the protolith and mylonites, we observe a combination of E-type and D-type fabrics in other layers[27,28,44]. The BA index gives the degree of combination from ~0.5 (E-type fabric) to 1 (D-type fabric)[30]. N = number of grains; J = texture index[32]; M = misorientation index[33]; X = shear direction; Z = pole to the shear plane. (**b**) From top to bottom, distribution of the BA index, M index and finite shear strain (γ)[34] across the protolith and mylonitic complex. We only show the values from centre to edge for each type of layer. In mylonite and ultramylonite layers, the finite strain may strongly vary, including to values higher than 5 (dotted box).

EBSD maps were used to document intra- and inter-granular structural features across the shear zones. These measurements identify olivine sub-grain boundaries in mylonites, with a sub-grain size (~20 μm) that far exceeds olivine grain size in the ultramylonites (Fig. 5a). Sub-grain boundaries are also prevalent in both the protolith and protomylonitic bands, in contrast to ultramylonitic layers where only a few sub-grains are observed. The parameters used for the definition of grain boundaries and sub-grain boundaries are available in the methods section.

Of further interest, EBSD maps combined with inverse pole figures (IPF) emphasize different LPOs for olivine as a function of the distance from ultramylonite layers. In Fig. 5a, we display the distribution of olivine crystallographic axes with respect to the Y direction, that is, the deformation axis normal to the shear direction and parallel to the shear plane. As sketched in Fig. 5b, this map highlights different areas that include: (1) ultramylonitic layers with a very weak LPO (J = 2.54; M = 0.04) and a mean grain size of ~12 μm (B_1 area); (2) mylonitic connected bands adjacent to the ultramylonites with a strong LPO (J = 16.80; M = 0.46) and a grain size of ~34 μm (B_2 area) and (3) mylonitic areas with a moderate LPO (J = 4.79; M = 0.14) and a grain size of ~33 μm (B_3 area). The colour coding in Fig. 5a indicates that olivine [010]-axes are parallel to Y in the B_2 bands, consistent with the dominant E-type fabric in these areas. This feature is supported by a BA index of 0.49 (Fig. 5b and Supplementary Fig. 4). In contrast, olivine [001]-axes are mostly aligned with Y in B_3 areas, giving rise to a different olivine fabric. With a BA index of 0.74 (Fig. 5b), the corresponding LPO is characterized by a combined pattern between E- and D-type fabrics (see Supplementary Fig. 4). Olivine grains in ultramylonites do not show a noticeable LPO, but their LPOs also display a combined pattern of D/E-type fabric with BA = 0.60 (Fig. 5b and Supplementary Fig. 4). Moreover, detailed maps in ultramylonite layers highlight tiny grains of orthopyroxene (~2 μm) located at quadruple junctions of grain boundaries. These quadruple junctions only occur in very fine-grained ultramylonites (Fig. 5c).

For each area (B_1, B_2 and B_3) and the whole map of Fig. 5a, we show the distribution of olivine misorientation axes and related dislocation slip-systems at sub-grain boundaries (Fig. 6). As shown experimentally[35], most sub-grain boundaries are related to tilt boundaries instead of twist boundaries. Plotting misorientation axes on IFPs provides a key to identifying the rotation axis of the main dislocation slip-system[36,37] (Fig. 6a). In Fig. 6b, IPF are displayed for the whole map (in black) and specific areas from B_1 to B_3, as referred to in Fig. 5b. For the whole map and the B1 (blue) and B_2 (purple) areas, the distribution of misorientation axes indicates rotation around the [010] axis, consistent with dominant dislocation slip on the (001)[100] slip-system. On the other hand, misorientation axes are highly concentrated around the [001] axis at intermediate distances from the ultramylonites (red B_3 area). This rotation axis is related to activation of the (010)[100] slip-system in olivine[35]. These results reveal, therefore, a change in dislocation slip-system from (001)[100] to (010)[100] in mylonitic layers with increasing distance from ultramylonites.

Discussion

During mantle flow, olivine aggregates deform by several competing mechanisms that include grain-size-insensitive creep, typically dislocation creep, and GSS creep, such as diffusion creep. GSS creep is also referred to as superplastic flow when GBS significantly contributes to the deformation[15,38]. During grain size reduction, the dominant deformation mechanism commonly switches from dislocation creep to GSS creep, causing a substantial drop in strength[3,4]. Furthermore, intense grain size reduction is often coeval with phase mixing. This provides conditions to keep grain size small by inhibiting grain growth through grain boundary pinning, enhancing GSS creep[39].

In the Ronda shear zones, weak olivine LPO and phase mixing indicate that deformation occurred dominantly by GSS creep in ultramylonites[39,40], and most likely by superplastic flow as suggested by quadruple junctions. These junction types arise when grain boundaries align with the shear plane due to significant GBS[41]. The crystallization of new orthopyroxene grains at quadruple junctions also suggests that phase nucleation occurred during ductile flow. Based on recent experiments[42], it is very likely that strain localization in ultramylonites results from this phase nucleation process and associated grain size reduction. In contrast, strong olivine LPOs and numerous sub-grains indicate that dislocation creep is the dominant deformation mechanism for the rest of the Ronda shear zones (protolith, protomylonites and mylonites). Using the size of sub-grains and an olivine piezometer[43], we estimate a stress between 100 and 200 MPa during deformation.

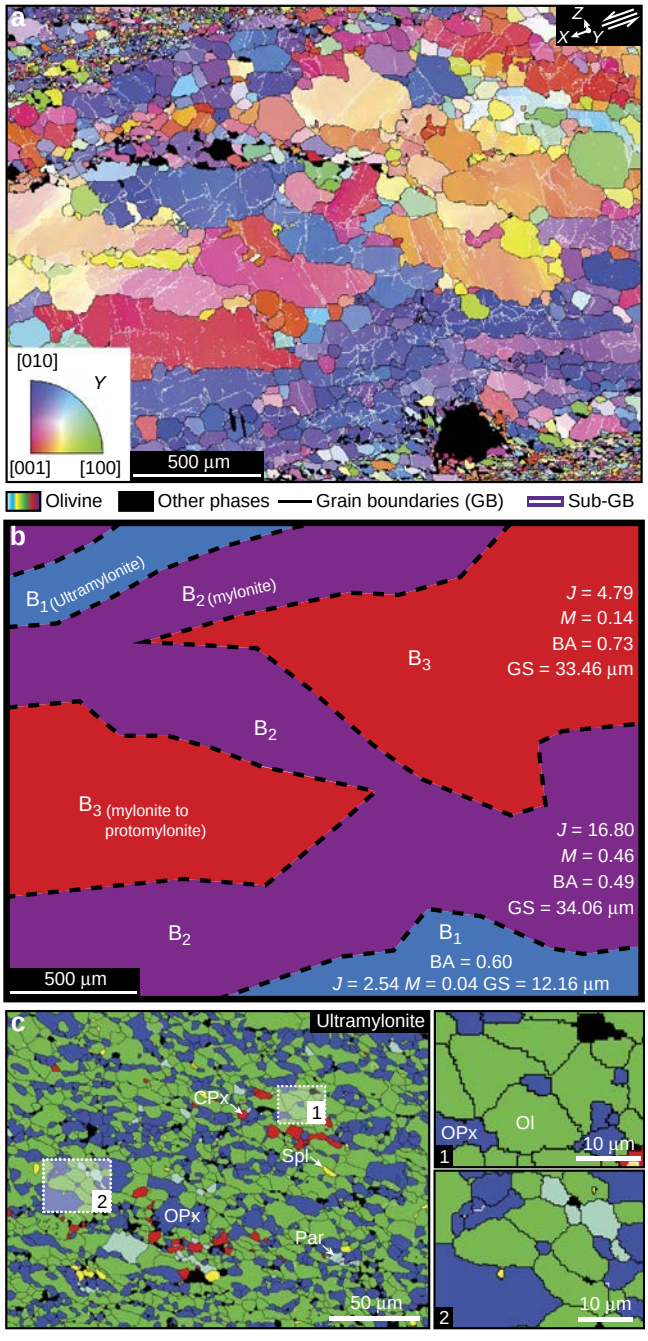

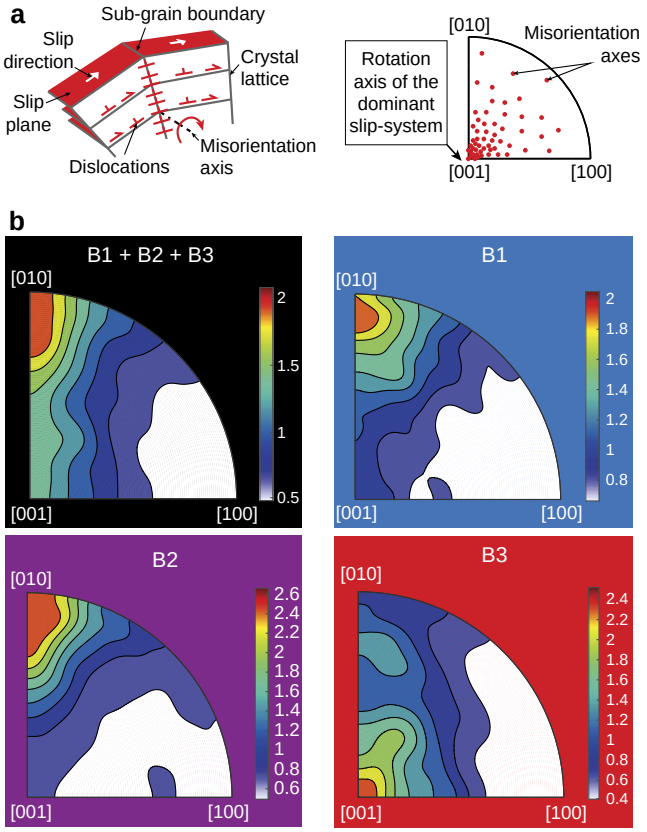

Figure 6 | Olivine dislocation slip-systems deduced from the distribution of misorientation axes. (**a**) Sketch illustrating characteristic features of sub-grain tilt boundaries. Inverse pole figures (IPFs) of the olivine axes ([100], [010] and [001]) provide information on the lattice rotation axis induced by the slip of dislocations on a lattice-controlled slip plane and slip direction, that is, on a specific slip-system[35,36]. (**b**) Olivine IPFs showing the distribution of correlated misorientation axes (between 2° and 10°) in olivine for each area illustrated in Fig. 5b, including the whole map ($B_1+B_2+B_3$), ultramylonites (B_1), purple bands (B_2) and isolated areas (B_3). The iso-contours and colour scale are multiples of a uniform distribution (linear scale). These IPFs show that isolated areas (B_3) differ from the other areas (whole map, B_1 and B_2) in terms of the dislocation slip-system (see text).

Figure 5 | Olivine sub-grain boundaries and distribution of lattice misorientation distributions between ultramylonites. (**a**) EBSD map coloured as a function of the inverse pole figure (bottom left inset) of the [100]-, [010]- and [001]-axes of olivine. The colour coding refers to the orientation of the olivine lattice with respect to the *Y* axis, that is, the deformation axis normal to the shear direction (*X*) and to the pole of the shear plane (*Z*). The black and white lines highlight grain boundaries (GB) and sub-grain boundaries (sub-GB), respectively (the parameters used to define GB and sub-GB are given in the methods section). Black areas are other phases and non-indexed points (see Supplementary Fig. 4). (**b**) Sketch of the different areas defined by the variation in olivine LPO in **a**, including ultramylonites (B_1), adjacent connected bands in the mylonite (B_2), and isolated areas between ultramylonites (B_3). For each area, we give the texture index (*J*), misorientation index (*M*), BA index (BA) and mean olivine grain size (GS). The corresponding olivine LPOs are available in Supplementary Fig. 4. (**c**) Detailed EBSD map highlighting tiny phases of orthopyroxene (enstatite) surrounded by quadruple junctions of olivine grain boundaries. The location of the EBSD map is shown in Fig. 3a. Black area = pores; CPx = clinopyroxene; Ol = olivine; OPx = orthopyroxene; Par = pargasite; Spl = spinel.

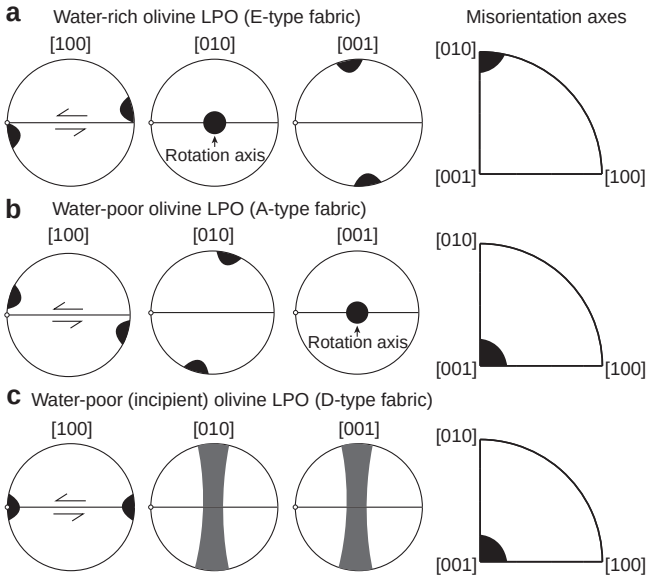

Figure 7 | Lab-based olivine LPOs and related misorientation axes distribution. (**a**) Olivine LPO ([100], [010] and [001] axes) produced in water-rich conditions (E-type fabric) with a moderate amount of water[27]. (**b**) Olivine LPO produced in water-poor conditions (A-type fabric)[44]. (**c**) Incipient olivine LPO produced in water-poor conditions (D-type fabric)[29]. While LPOs are displayed in equal-area lower-hemisphere pole figures with respect to the shear plane (horizontal line) and shear direction (white dot), inverse pole figures show the main rotation axis of tilt boundaries for E-type, A-type and D-type fabrics (see text).

When olivine mainly deforms by dislocation creep, several dislocation slip-systems are involved to accommodate plastic strain, but generally, one dominant slip-system governs the development and geometry of the olivine LPO. So far, five olivine fabrics and associated slip-systems have been described (resulting in A-, B-, C-, D- and E-type fabrics). Their preferential activation depends on the deformation conditions including stress, pressure and/or water content[27,44,45]. While E-type fabric is generally recognized as resulting from activation of the (100)[001] slip-system during deformation of olivine containing a moderate amount of water[27] (Fig. 7a), the (010)[100] slip-system is preferentially activated during deformation of dry or poorly hydrated olivine, giving rise to an A-type fabric[44] (Fig. 7b). As for the D-type fabric, it has only been observed for dry or poorly hydrated olivine[28,46] and recent experiments have described it as an incipient A-type fabric resulting from the activation of the same water-poor slip-system[29] (Fig. 7c). All of these fabrics can develop at pressures lower than 3 GPa and below a stress of 300 MPa (refs 27,46).

The development of E-type fabric in Ronda indicates that water was present during strain localization. This is confirmed by the presence of amphibole and our estimate of $\sim$600 p.p.m. H_2O in the ultramylonites (Fig. 3e). However, the occurrence of combined D/E-type fabric shows that water content has changed during deformation, either from dry to wet conditions (that is, from D- to E-type) or vice versa (that is, from E- to D-type). The occurrence of millimetre-scale water gradients preserved in the mineral fabric (Fig. 5) does not support progressive hydration through water infiltration. Indeed, even in shear zones where very high deformation rates are expected (10^{-12}–10^{-10} s^{-1}), many years of deformation are needed to generate a mineral fabric, particularly with high fabric strength[29,30]. At a millimetre scale, it is a matter of days to diffuse water through an olivine aggregate, even through the crystal lattice[47]. This rate of water diffusion excludes *in situ* measurements of water content in our samples (see the methods section). The systematic occurrence of E-type fabric, more or less combined with D-type fabric, also suggests that water was present everywhere in the study area before strain localization, contrary to the distal protolith where a dry A-type fabric has been described[22,25]. The most likely scenario is, therefore, that the D-type fabric overprinted the E-type fabric during strain localization.

The distribution of olivine fabrics implies that water progressively converged towards the ultramylonites during deformation. This gave rise to water accumulation at the edge of the mylonites (E-type fabric), and overprinting of E-type fabric by D-type fabric where olivine was progressively dried (Fig. 8a). Assuming that water mainly diffuses along grain boundaries—grain boundary diffusion is indeed one order of magnitude faster than volume diffusion in olivine[48]—this overprinting is attributed to a switch in the dislocation slip-system where water is being exsolved from olivine, that is, where interstitial water is no longer available (Fig. 8a). We further attribute the D/E-type fabric in ultramylonites to grain size reduction and subsequent water distribution through increasing grain boundary abundance. While water content increases per volume unit, as shown by the distribution of amphibole, it decreases per unit of grain boundary (Fig. 8a). Water convergence is also expected at a larger scale considering the higher density of ultramylonites at the centre of mylonitic complexes. This results in partially dried olivine (D/E-type fabric) in between mylonitic complexes, as well as strain partitioning between water-poor and water-rich layers because of water/hydrolytic weakening (Fig. 8b). The sole exception concerns the ultramylonitic layers, where the expected strain hardening due to olivine drying is far outweighed by grain size reduction and phase mixing, both of which promote weakening by leading to dominant GSS creep[49]. The high amount of water at the centre of complexes further accounts for the occurrence of mode-I cracks in this area, particularly in mylonites where we expect to have the highest amount of water at grain boundaries (Fig. 8b).

Altogether, these features show that water draining in ductile shear zones does not only occur in the crust, but also in the upper mantle, and necessarily on a long-term basis in order to be preserved into the olivine fabric. Our documentation of water accumulation around ultramylonites further excludes grain size reduction as a unique 'passive' process accounting for water draining. They show instead that water converged as a result of 'dynamic' pumping during ductile flow. Although we have no direct evidence of strain-induced cavities, the convergence of water towards layers dominated by superplastic flow supports creep cavitation as the source responsible for water-rich fluid pumping (Fig. 8a). GBS-induced quadruple junctions are also typical sites for cavitation[41]. In addition, the presence of nucleated phases at quadruple junctions, as well as a low porosity, suggests that opening cavities are filled by new precipitating phases, which may enhance long-term water pumping. While creep cavitation is a transient process that first opens cavities, by pumping fluid, and then closes cavities by expelling fluid too[13], the filling of opening cavities by new solid phases precludes fluid expulsion. Lateral fluid-assisted diffusion of mineral components is likewise expected to compensate for the local deficit of fluid solute induced by phase nucleation[25,50]. This accounts for enrichment in secondary phases within ultramylonites, particularly for orthopyroxene, which only relies on increasing silica content.

To conclude, we here ascribe dynamic long-term fluid pumping during the deformation process of GBS and related creep cavitation, both arising from grain size reduction through phase nucleation. As grain size reduction is a ubiquitous feature

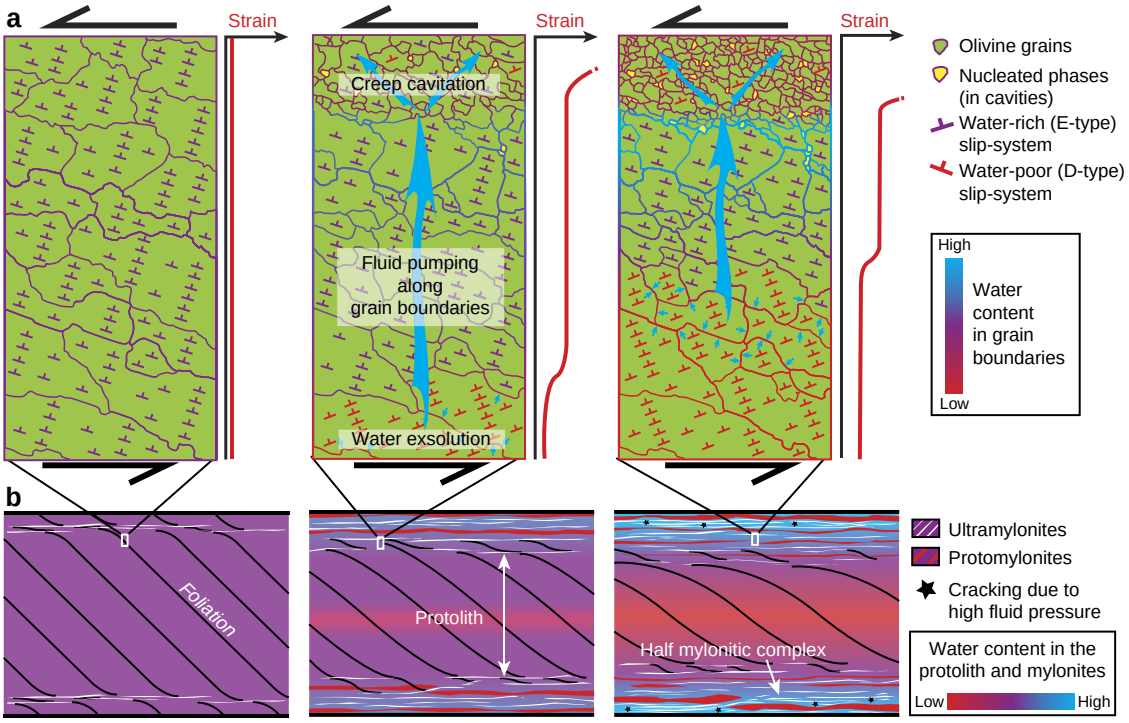

Figure 8 | Olivine fabric and strain partitioning resulting from water pumping in mantle shear zones. (**a**) Water distribution in grain boundaries during strain localization, grain size reduction and related water pumping (top part). While water equally distributes on olivine grain boundaries during incipient strain localization, giving rise to an overall E-type fabric, the fluid subsequently accumulates in ultramylonites because of 'dynamic' pumping. The blue arrows refer to water migration through grain boundaries. Accordingly, where water is no longer available at grain boundaries, olivine grains are progressively dried out through water exsolution, leading to strain partitioning (middle and right panels) and E-type fabric that is then overprinted by D-type fabric (change in dislocation slip-system). The D-type fabric also arises in ultramylonites as fluid distributes in new grain boundaries. We here attribute water pumping to creep cavitation and related phase nucleation in layers dominated by grain-size-sensitive creep (ultramylonites). (**b**) Large-scale fluid pumping and strain partitioning in mylonitic complexes. From left to right, water converges towards the centre of the mylonitic complexes, which progressively widen through lateral production of further ultramylonite layers. As a consequence, the olivine fabric switches from an E-type to a D-type LPO in the centre of the protolith and water accumulates in the mylonites, where the density of ultramylonites increases. This gives rise to cracking (black stars) due to high fluid pressure in these zones.

of mantle and crustal shear zones[39,40,51,52], this process is expected to occur wherever strain highly localizes, such as plate boundaries and at the base of the lithosphere-asthenosphere boundary. Our study therefore confirms a ductile process that could provide important fluid reservoirs, impacting the water distribution and related features of both the crust and mantle.

Methods

Scanning electron microscope. BSE images were acquired on polished (using 1 µm diamond paste) and carbon coated (20 nm) thin sections using a TESCAN scanning electron microscope (SEM) at ISTO/BRGM (University of Orléans, France). The SEM was set at an accelerating voltage of 20 kV, a probe current of ~6 nA and a working distance of 10 mm. We also used the TESCAN SEM at ISTO/BRGM with an accelerating voltage of 15 kV to perform energy-dispersive X-ray spectroscopy (EDS) on cracked spinel.

Microprobe. Major-element compositions and element maps were acquired using a CAMECA SX-five electron microprobe at ISTO/BRGM (University of Orléans, France). The analyses were performed on carbon-coated (20 nm), polished (using 1 µm diamond paste) thin sections using an accelerating voltage of 15 kV, a probe current of 10 nA and a beam diameter of 1 µm. For point analyses, we applied a counting time of 10 and 5 s for peak and background signals, respectively. Calibration was carried out against natural and synthetic minerals, including albite, $MnTiO_3$, Fe_2O_3, MgO, Al_2O_3, andradite, orthose, Cr_2O_3, NiO and vanadinite.

Perple_X calculations. The pseudosections were calculated using Perple_X (ref. 53) with the thermodynamic database of Holland and Powell[54]. It was built in the NCFMASH (Na_2O-CaO-FeO-MgO-Al_2O_3-SiO_2-H_2O) chemical system. The weight percent of oxides was calculated by combining the volume percent of mineral modes, which were determined by point counting on elements maps, and the composition of mineral phases determined at the microprobe. No phase was excluded, but we did not consider chromium in spinel for simplicity. The solution models are from Holland and Powell[54,55] and Holland *et al.*[56], except for antigorite[57], amphibole[58] and plagioclase[59].

Electron backscatter diffraction. The EBSD data were collected using an SEM either coupled to an EDAX Pegasus system at ISTO/BRGM, or using an e$^-$Flash^{HR} detector at Bruker Nano Analytics GmbH (Berlin, Germany). Crystallographic information was also combined with EDX (Energy-Dispersive X-ray) spectroscopy to identify phases. The EBSD measurements were performed at a working distance of 15 or 20 mm with an accelerating voltage of 20 kV and a probe current of ~6 nA on polished thin sections (diamond paste of 0.25 µm followed by colloidal silica). In order to avoid indexing errors, we constructed pole figures using one measurement per grain collected manually. The iso-contours and grey shadings on pole figures were plotted using the Unicef careware software package written by David Mainprice (www.gm.univ-montp2.fr/PERSO/mainprice/W_data/CareWare_Unicef_Programs). We further used the open-source matlab-based MTEX toolbox to construct IPF of misorientation axes and to calculate the texture (J) and misorientation (M) indices[30,60]. To plot pole figures and calculate the J index, we used a Gaussian half-width angle of 10°.

For acquisition data processing and analysis of EBSD maps, we used the OIM Analysis 7 software (EDAX) and/or HKL Tango channel 5 system (Oxford Instruments). The indexing hit rates were higher than 80% for all maps, including cavities. We used a minimum of six indexed bands and a maximum band mismatch of 2°. The outlier pixels and zero solutions were removed up to a maximum pixel count of 10. Grain detection was performed using correlated misorientation angles higher than 10° for grain boundaries and between 2 and 10° for sub-grain boundaries. Each grain contains a minimum of five pixels considering a hexagonal grid. The average grain size corresponds to the mean equivalent diameter calculated using the grain ellipsoid fit. EBSD maps were used only to calculate the grain size in the protomylonites (edge), mylonites and ultramylonites. In the protolith and centre of protomylonites, we applied the length-intercept method on BSE images because of their larger grain sizes.

***In situ* water content.** A major problem with *in situ* measurements of water content in natural rocks is how far the measured value reflects the water content at lithosphere depths. It has been demonstrated that for orogenic peridotites where the exhumation is slow compared to xenoliths, there are limits in the use of Fourier transform infrared spectroscopy—or other analytical methods—in the determination of olivine water content[61,62]. Water from crustal fluids may be indeed introduced or may precipitate as fluid inclusions and hydrated phases in olivine during exhumation[63]. Note that the Ronda peridotites have been lying on the crust of the internal Betics since more than 20 Ma (ref. 21). Furthermore, lab experiments have demonstrated that water diffusion is fast in olivine (10^{-10} m^2 s^{-1}) relative to geological strain rates[47]. If water was originally present in olivine grains, it could have been easily diffused out during the peridotite exhumation stage[64]. The presence of post-tectonic serpentine in the studied peridotites may also have strongly modified olivine water content after deformation. It is therefore very likely that *in situ* measurements in olivine of the Ronda peridotites would not reflect the water content of the minerals prior to exhumation, and particularly during their deformation. In contrast, lab experiments have shown that olivine LPOs are sensitive to water content[27,44]. As they directly arise from rock deformation, they provide a more robust method—yet qualitative—to document syn-tectonic water content in upper mantle rocks[61].

Data availability. The authors declare that most of the data supporting the findings of this study are available within the paper (and its Supplementary Information files). The source files of EBSD data are available from the corresponding author on reasonable request.

References

1. Kronenberg, A. K. & Tullis, J. Flow strengths of quartz aggregates: grain size and pressure effects due to hydrolytic weakening. *J. Geophys. Res.* **89,** 4281–4297 (1984).
2. Mackwell, S. J., Kohlstedt, D. L. & Paterson, M. S. The role of water in the deformation of olivine single crystal. *J. Geophys. Res.* **90,** 11,319–11,333 (1985).
3. Karato, S.-I., Paterson, M. S. & FitzGerald, J. D. Rheology of synthetic olivine aggregates: influence of grain size and water. *J. Geophys. Res.* **91,** 8151–8176 (1986).
4. Hirth, G. & Kohlstedt, D. L. Rheology of the upper mantle and the mantle wedge: a view from the experimentalists. *Geophys. monogr.* **138,** 83–105 (2003).
5. Jackson, J. Strength of the continental lithosphere: time to abandon the jelly sandwich? *GSA today* **12,** 4–10 (2002).
6. Burov, E. B. & Watts, A. B. The long-term strength of continenal lithosphere: 'Jelly sandwich' or 'crème brûlée'. *GSA Today* **16,** 4–10 (2006).
7. Gueydan, F., Morency, C. & Brun, J.-P. Continental rifting as a function of lithosphere mantle strength. *Tectonophysics* **460,** 83–93 (2008).
8. Griggs, D. T. Hydrolytic weakening of quartz and other silicates. *Geophys. J. R. Astro. Soc.* **14,** 19–31 (1967).
9. Kohlstedt, D. L. The role of water in high-temperature rock deformation. *Rev. Min. Geochem.* **62,** 377–396 (2006).
10. McCaig, A. M. Deep fluid circulation in fault zones. *Geology* **16,** 867–870 (1988).
11. Sibson, R. H., Moore, J., McM. & Rankin, A. H. Seismic pumping—a hydrothermal fluid transport mechanism. *J. Geol. Soc. Lond.* **131,** 653–659 (1975).
12. Wark, D. A. & Watson, E. B. Effect of grain size on the distribution and transport of deep-seated fluids and melts. *Geophys. Res. Lett.* **27,** 2029–2032 (2000).
13. Fusseis, F., Regenauer-Lieb, K., Liu, J., Hough, R. M. & De Carlo, F. Creep cavitation can establish a dynamic granular fluid pump in ductile shear zones. *Nature* **459,** 974–977 (2009).
14. Chokshi, A. H. Cavity nucleation and growth in superplasticity. *Mater. Sci. Eng. A* **410–411,** 95–99 (2005).
15. Oliot, E., Goncalves, P., Schulmann, K., Marquer, D. & Lexa, O. Mid-crustal shear zone formation in granitic rocks: constraints from quantitative textural and crystallographic preferred orientations analyses. *Tectonophysics* **612–613,** 63–80 (2014).
16. Kassner, M. E. & Hayes, T. A. Creep cavitation in metals. *Int. J. Plast.* **19,** 1715–1748 (2003).
17. Dimanov, A., Rybacky, E., Wirth, R. & Dresen, G. Creep and strain-dependent microstructures of synthetic anorthite-diopside aggregates. *J. Struct. Geol.* **29,** 1049–1069 (2007).
18. Rybacki, E., Wirth, R. & Dresen, G. High-strain creep of feldspar rocks: Implications for cavitation and ductile failure in the lower crust. *Geophys. Res. Lett.* **35,** L04304 (2008).
19. Menegon, L., Fusseis, F., Stünitz, H. & Xiao, X. Creep cavitation bands control porosity and fluid flow in lower crustal shear zones. *Geology* **43,** 227–230 (2015).
20. Garrido, C. J. *et al.* Garnet lherzolite and garnet-spinel mylonite in the Ronda peridotite: vestiges of oligocene backarc mantle lithospheric extension in the western Mediterranean. *Geology* **39,** 927–930 (2011).
21. Précigout, J., Gueydan, F., Garrido, C. J., Cogné, N. & Booth-Rea, G. Deformation and exhumation of the Ronda peridotite (Spain). *Tectonics* **32,** 1011–1025 (2013).
22. Van der Wal, D. & Vissers, R. L. M. Structural petrology of the Ronda peridotite, SW spain: deformation history. *J. Petrol.* **37,** 23–43 (1996).
23. Hidas, K. *et al.* Backarc basin inversion and subcontinental mantle emplacement in the crust: kilometre-scale folding and shearing at the base of the proto-Alborán, lithospheric mantle (Betic Cordillera, southern Spain). *J. Geol. Soc. Lond.* **170,** 47–55 (2012).
24. Hubbert, M. K. & Willis, D. G. Mechanics of hydraulic fracturing. *AAPG special volumes* **A075,** 239–257 (1972).
25. Hidas, K. *et al.* Fluid-assisted strain localization in the shallow subcontinental lithospheric mantle. *Lithos* **262,** 636–650 (2016).
26. Hidas, K. *et al.* Strain localization in pyroxenite by reaction-enhanced softening in the shallow subcontinental lithospheric mantle. *J. Petrol.* **54,** 1997–2031 (2013).
27. Katayama, I., Jung, H. & Karato, S.-I. New type of olivine fabric from deformation experiments at modest water content and low stress. *Geology* **32,** 1045–1048 (2004).
28. Bystricky, M., Kunze, K., Burlini, L. & Burg, J.-P. High shear strain of olivine aggregates: rheological and seismic consequences. *Science* **290,** 1564–1567 (2000).
29. Hansen, L. N., Zhao, Y.-H., Zimmerman, M. E. & Kohlstedt, D. L. Protracted fabric evolution in olivine: implications for the relationship among strain, crystallographic, and seismic anisotropy. *Earth Planet. Sci. Lett.* **387,** 157–158 (2014).
30. Mainprice, D., Bachmann, F., Hielscher, R. & Schaeben, H. in *Rock Deformation from Field, Experiments and Theory: A Volume in Honour of Ernie Rutter* Vol. 409, 251–271 (eds Faulkner, D. R., Mariani, E. & Mecklenburg, J.) (Geological Society, 2014).
31. Chatzaras, V. *et al.* Axial-type olivine crystallographic preferred orientations: the effect of strain geometry in mantle texture. *J. Geophys. Res. Solid Earth* **121,** 1–28 (2016).
32. Bunge, H. *Texture Analysis in Materials Science: Mathematical Models* 593 (Butterworths, 1982).
33. Skemer, P., Katayama, I., Jiang, Z. & Karato, S.-I. The misorientation index: development of a new method for calculating the strength of lattice-preferred orientation. *Tectonophysics* **411,** 157–167 (2005).
34. Ramsay, J. G. Shear zone geometry: a review. *J. Struct. Geol.* **2,** 83–99 (1980).
35. Hansen, L. N., Zimmerman, M. E. & Kohlstedt, D. L. The influence of microstructure on deformation of olivine in the grain-boundary sliding regime. *J. Geophys. Res.* **117,** B09201 (2012).
36. Mehl, L., Hacker, B. R., Hirth, G. & Kelemen, P. B. Arc-parallel flow within the mantle wedge: evidence from the accreted Talkeetna arc, south central Alaska. *J. Geophys. Res.* **108,** 2375 (2003).
37. Précigout, J. & Hirth, G. B-type olivine fabric induced by grain boundary sliding. *Earth Planet. Sci. Lett.* **395,** 231–240 (2014).
38. Langdon, T. G. Grain boundary sliding revisited: development in sliding over four decades. *J. Mater. Sci.* **41,** 597–609 (2006).
39. Warren, J. M. & Hirth, G. Grain size sensitive deformation mechanisms in naturally deformed peridotites. *Earth Planet. Sci. Lett.* **248,** 438–450 (2006).
40. Drury, M. R., Ave'Lallemant, H. G., Pennock, G. M. & Palasse, L. N. Crystal preferred orientation in peridotite ultramylonites deformed by grain size sensitive creep, Etang de Lers, Pyrenees, France. *J. Struct. Geol.* **33,** 1776–1789 (2011).
41. Ree, J.-H. Grain boundary sliding and development of grain boundary openings in experimentally deformed octachloropropane. *J. Struct. Geol.* **16,** 403–418 (1994).
42. Précigout, J. & Stünitz, H. Evidence of phase nucleation during olivine diffusion creep: a new perspective for mantle strain localisation. *Earth Planet. Sci. Lett.* **455,** 94–105 (2016).
43. Van der Wal, D., Chopra, P., Drury, M. & Fitz Gerald, J. Relationships between dynamically recrystallized grain size and deformation conditions in experimentally deformed olivine rocks. *Geophys. Res. Lett.* **20,** 1479–1482 (1993).
44. Jung, H. & Karato, S.-I. Water-induced fabric transitions in olivine. *Science* **293,** 1460–1463 (2001).
45. Ohuchi, T., Kawazoe, T., Nishihara, Y., Nishiyama, N. & Irifune, T. High pressure and temperature fabric transitions in olivine and variations in upper mantle seismic anisotropy. *Earth Planet. Sci. Lett.* **304,** 55–63 (2011).
46. Demouchy, S., Tommasi, A., Barou, F., Mainprice, D. & Cordier, P. Deformation of olivine in torsion under hydrous conditions. *Phy. Earth Planet. Int.* **202–203,** 56–70 (2012).
47. Demouchy, S. & Mackwell, S. Water diffusion in synthetic iron-free olivine. *Phys. Chem. Minerals* **30,** 486–494 (2003).
48. Demouchy, S. Diffusion of hydrogen in olivine grain boundaries and implications for the survival of water-rich zones in the Earth's mantle. *Earth Planet. Sci. Lett.* **295,** 305–313 (2010).

49. Fei, H., Wiedenbeck, M., Yamazaki, D. & Katsura, T. Small effect of water on upper-mantle rheology based on silicon self-diffusion coefficients. *Nature* **498,** 213–216 (2013).
50. Linckens, J., Herwegh, M., Müntener, O. & Mercolli, I. Evolution of a polymineralic mantle shear zone and the role of second phases in the localisation of deformation. *J. Geophys. Res.* **116,** B06210 (2011).
51. Drury, M. R., Vissers, R. L. M., Van der Wal, D. & Hoogerduijn Strating, E. H. Shear localisation in upper mantle peridotites. *Phys. App. Geophys.* **137,** 439–460 (1991).
52. Rutter, E. H. & Brodie, K. H. The role of tectonic grain size reduction in the rheological stratification of the lithosphere. *Geologische Rundschau* **77,** 295–308 (1988).
53. Connolly, J. A. D. The geodynamic equation of state: what and how. *Geochem. Geophys. Geosyst.* **10,** Q10014 (2009).
54. Holland, T. & Powell, R. An internally consistent thermodynamic data set for phases of petrological interest. *J. Metam. Geol.* **16,** 309–343 (1998).
55. Holland, T. & Powell, R. Thermodynamics of order-disorder in minerals. 2. Symmetric formalism applied to solid solutions. *Am. Mineral.* **81,** 1425–1437 (1996).
56. Holland, T., Baker, J. & Powell, R. Mixing properties and activity-composition relationships of chlorites in the system MgO-FeO-Al_2O_3-SiO_2-H_2O. *Eur. J. Mineral.* **10,** 395–406 (1998).
57. Padrón-Navarta, J. A. *et al.* Tschermak's substitution in antigorite and consequences for phase relations and water liberation in high-grade serpentinites. *Lithos* **178,** 186–196 (2013).
58. Dale, J., Powell, R., White, R. W., Elmer, F. L. & Holland, T. J. B. A thermodynamic model for Ca-Na clinoamphiboles in Na_2O-CaO-FeO-MgO-Al_2O_3-SiO_2-H_2O for petrological calculations. *J. Metam. Geol.* **23,** 771–791 (2005).
59. Newton, R. C., Charlu, T. V. & Kleppa, O. J. Thermochemistry of the high structural state plagioclases. *Geochem. Cosmochim. Acta* **44,** 933–941 (1980).
60. Bachmann, F., Hielscher, R. & Schaeben, H. Texture analysis with MTEX—free and open software toolbox. *Solid State Phenomena* **160,** 63–68 (2010).
61. Palasse, L. N. Microstructural evolution and seismic anisotropy of upper mantle rocks in rift zones. *Geologica Ultraiectina*. Vol. 300 (PhD thesis, Utrecht Univ. Repository, 2008).
62. Warren, J. M. & Hauri, E. H. Pyroxenes as tracers of mantle water variations. *J. Geophys. Res. Solid Earth* **119,** 1851–1881 (2014).
63. Kostenko, O., Jamtveit, B., Austrheim, H., Pollok, K. & Putnis, C. The mechanism of fluid infiltration in peridotites at Almklovdalen, western Norway. *Geofluids* **2,** 203–215 (2002).
64. Peslier, A. H. & Luhr, J. F. Hydrogen loss from olivines in mantle xenoliths from Simcoe (USA) and Mexico: mafic alkali magma ascent rates and water budget of the sub-continental lithosphere. *Earth Planet. Sci. Lett.* **242,** 302–319 (2006).
65. Brey, G. P. & Köhler, T. Geothermobarometry in four-phase Lherzolites II. New thermobarometers, and practical assessment of existing thermobarometers. *J. Petrol.* **31,** 1353–1378 (1990).
66. Witt-Eickschen, G. & Seck, H. A. Solubility of Ca and Al in orthopyroxene from spinel peridotite: an improved version of an empirical geothermometer. *Contrib. Min. Petrol.* **106,** 431–439 (1991).
67. Jianping, L., Kornprobst, J., Vielzeuf, D. & Fabriès, J. An improved experimental calibration of the olivine-spinel geothermometer. *Chinese J. Geochem.* **14,** 68–77 (1995).
68. Putirka, K. D. Thermometers and barometers for volcanic systems. *Rev. Min. Geochem.* **69,** 61–120 (2008).

Acknowledgements

We thank Carlos J. Garrido for his help in acquiring field data. We also thank Holger Stünitz, Nicole Le Breton, Alexandra R. L. Kushnir and Jessica M. Warren for their help and comments, as well as Florian Fusseis for his fruitful reviews. This project has been funded by the ETH Zürich (ETH fellowship application FEL01 09-3), ERC RHEOLITH (Grant n° 290864), Labex Voltaire (ANR-10-LABX-100-01) and ANR DSP-Tibet (ANR-13-BS06-0012).

Author contributions

J.P., C.P. and A.P. contributed to acquire field data. J.P., C.P. and L.P. contributed to performed EBSD analyses. J.P. and C.P. contributed to performed microprobe analyses. C.P. contributed to perform pseudo-sections with Perplex. All authors contributed to the conception of the study and writing of the manuscript.

Additional information

Supplementary Information accompanies this paper at http://www.nature.com/naturecommunications

Competing interests: The authors declare no competing financial interests.

Reprints and permission information is available online at http://npg.nature.com/reprintsandpermissions/

How to cite this article: Précigout, J. *et al.* Water pumping in mantle shear zones. *Nat. Commun.* **8,** 15736 doi: 10.1038/ncomms15736 (2017).

Publisher's note: Springer Nature remains neutral with regard to jurisdictional claims in published maps and institutional affiliations.

Open Access This article is licensed under a Creative Commons Attribution 4.0 International License, which permits use, sharing, adaptation, distribution and reproduction in any medium or format, as long as you give appropriate credit to the original author(s) and the source, provide a link to the Creative Commons license, and indicate if changes were made. The images or other third party material in this article are included in the article's Creative Commons license, unless indicated otherwise in a credit line to the material. If material is not included in the article's Creative Commons license and your intended use is not permitted by statutory regulation or exceeds the permitted use, you will need to obtain permission directly from the copyright holder. To view a copy of this license, visit http://creativecommons.org/licenses/by/4.0/

© The Author(s) 2017

Supporting information for:

Water pumping in mantle shear zones

Jacques Précigout[1], Cécile Prigent[2], Laurie Palasse[3], Anthony Pochon[4]

[1] *Institut des Sciences de la Terre d'Orléans, UMR 7327, Université d'Orléans, Campus Géosciences, 1A rue de la Férollerie, 45071 Orléans Cedex 2*

[2] *Univ. Grenoble Alpes, CNRS, ISTerre, F-38000 Grenoble, France.*

[3] *Bruker Nano Analytics, Am Studio 2D, 12489 Berlin, Germany*

[4] *Géosciences Rennes, UMR 6118, Université de Rennes 1, Campus de Beaulieu, 35042 Rennes Cedex*

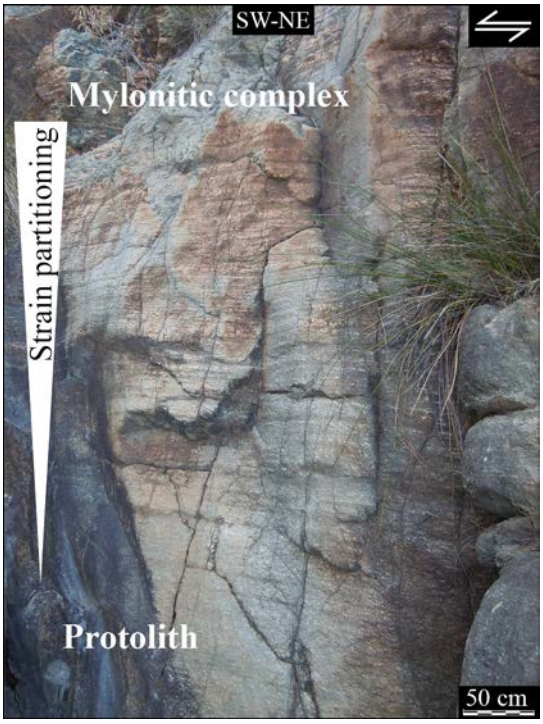

Supplementary Figure 1 | Strain partitioning at the edge of mylonitic complexes. From the protolith to the mylonitic complexes, the strain partitioning between the protomylonite layers (dark) and the mylonite layers (bright) progressively strengthens.

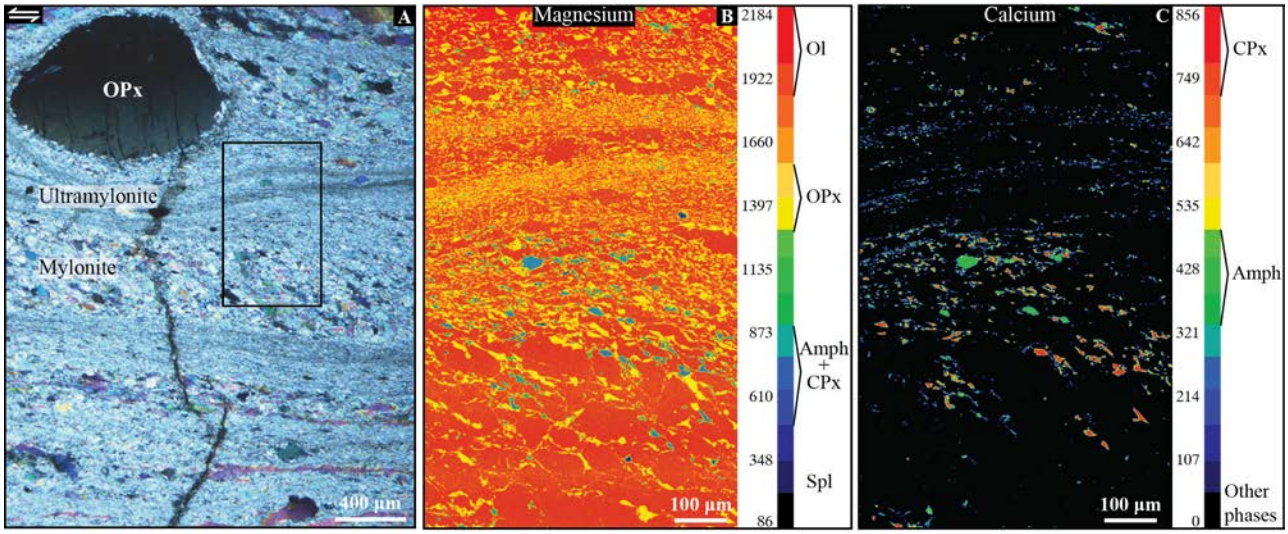

Supplementary Figure 2 | Element maps across ultramylonite layers. A) Thin section (polarized light) of a mylonitic peridotite, including ultramylonites. **B)** Distribution of magnesium (microprobe) across (ultra)mylonitic layers. Location in supplementary figure 2A. The colour coding refers to point counting. The step size is 0.8 µm and the analytical conditions are 15 kV and 10 nA on polished thin section (diamond paste of 1 µm). Ol = olivine; Amph = amphibole; CPx = clinopyroxene; Spl = Spinel. **C)** Distribution of calcium across the same area. This map highlights an enrichment in amphibole nearby ultramylonite layers. OPx = orthopyroxene.

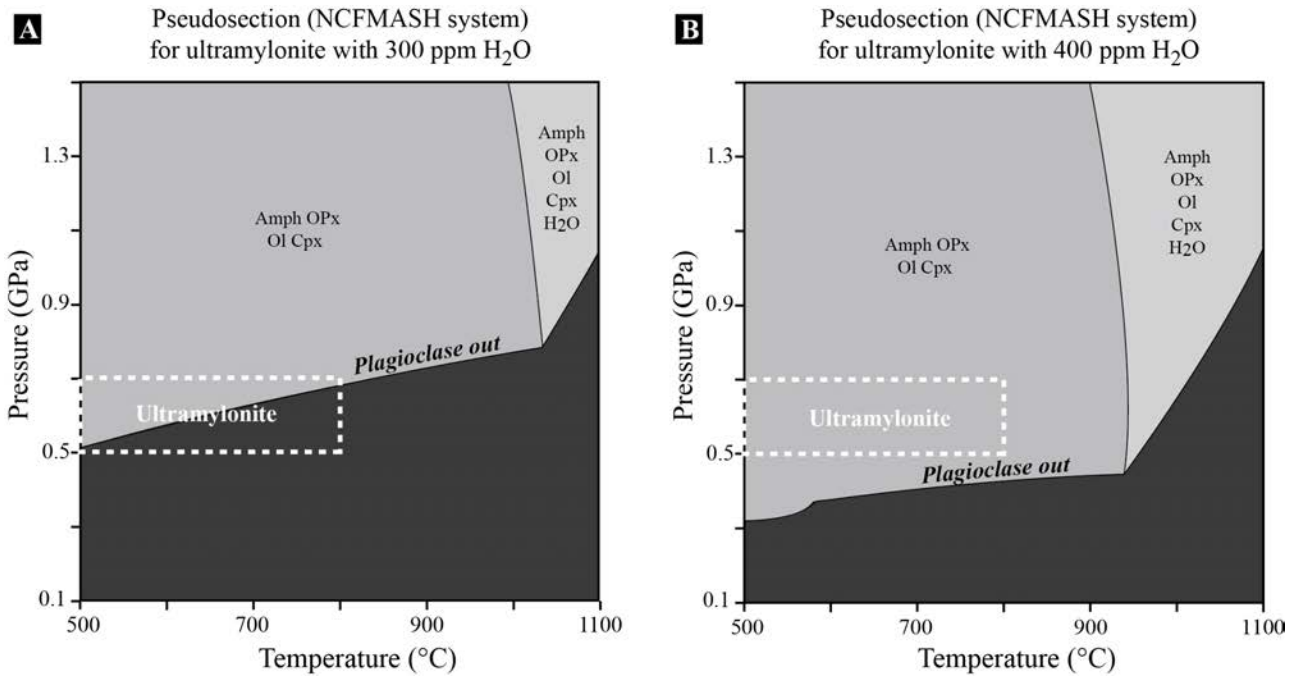

Supplementary Figure 3 | Equilibrium phase diagrams (pseudosections) for ultramylonites. A) Pseudosection with 300 ppm H_2O. **B)** Pseudosection with 400 ppm H_2O. The pseudosections were produced using Perple_X calculations in the NCFMASH (Na_2O-CaO-FeO-MgO-Al_2O_3-SiO_2-H_2O) chemical system, and based on the modal proportions that include olivine (65.9%), orthopyroxene (28.8%), amphibole (3.0%), clinopyroxene (1.5%) and spinel (0.8%). For comparison, we show the calculated conditions of deformation for the ultramylonites (dotted white rectangle). Based on the absence of plagioclase in the Ronda shear zones, our Perple_X calculations indicate a minimum of ~400 ppm H_2O in the ultramylonite layers. Amph = amphibole; OPx = orthopyroxene; Ol = Olivine; CPx = clinopyroxene.

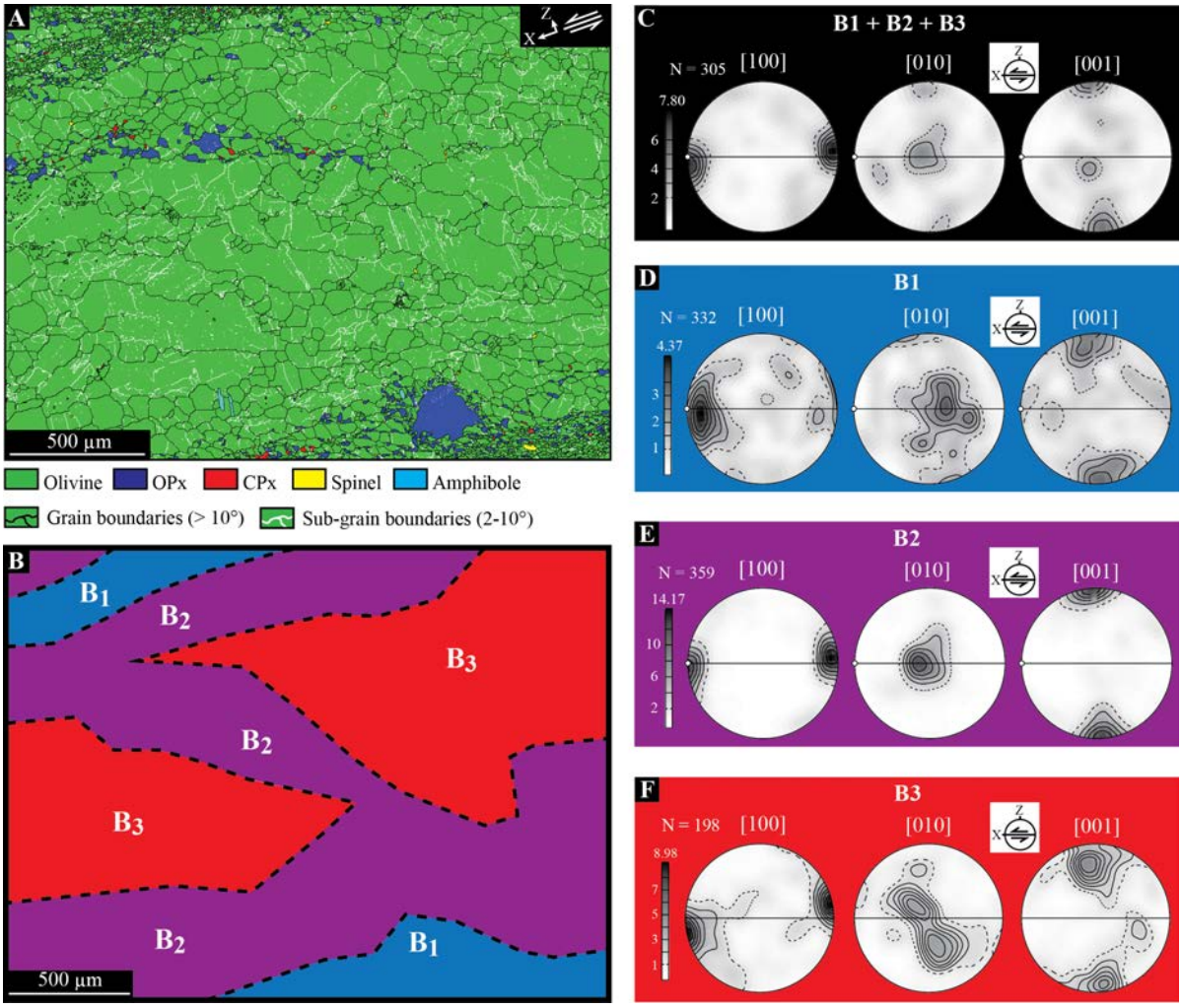

Supplementary Figure 4 | Phase distribution and olivine fabric between ultramylonites. A) EBSD map (phases) of the mylonitic layer shown in figure 5A of the paper. The step size is 1 µm and the analytical conditions are described in the methods section of the paper. While grain boundaries (black lines) are defined by correlated misorientation angles of more than 10°, the lattice tilt boundaries (white lines) are defined by correlated misorientation angles between 2° and 10°. X = shear direction; Z = pole to the shear plane. The black points within grains are non-indexed points. **B)** Sketch of the different areas highlighted in figure 5A of the paper and based on the olivine LPO distribution, including ultramylonites (B1), connected bands of strong LPO in the mylonite (B2), and isolated areas of moderate LPO between the ultramylonites (B3). **From C to F)** Olivine LPOs for each area, including the whole map (C), B1 area (D), B2 area (E) and B3 area (F). The three orthorhombic axes for olivine ([100], [010] and [001]) are shown in lower-hemisphere pole figures with respect to the shear plane (horizontal line) and shear direction (white dot). The iso-contours and grey shading (linear scale) are multiples of a uniform distribution. They were constructed using a Gaussian half-width angle of 10° and based on one point per grain. N = number of grains; OPx = orthopyroxene; CPx = clinopyroxene.

Supplementary Table 1 | Major-element compositions (in weight percent) and grain size of olivine (Ol) grains in the mylonites and ultramylonites. Por = porphyroclasts.

Oxides (%)	Ol_1	Ol_2	Ol_3	Ol_4	Ol_5	Ol_6	Ol_7	Ol_8	Ol_9	Ol_{10}	Ol_{11}	Ol_{12}
SiO_2	40.86	40.96	41.11	41.00	41.03	41.13	41.2	40.85	40.38	40.80	40.91	40.89
TiO_2	0.00	0.00	0.00	0.00	0.00	0.00	0.00	0.00	0.00	0.00	0.00	0.00
Al_2O_3	0.00	0.00	0.00	0.00	0.00	0.00	0.00	0.00	0.00	0.00	0.00	0.00
Cr_2O_3	0.00	0.03	0.01	0.01	0.01	0.00	0.00	0.00	0.00	0.00	0.00	0.01
FeO	8.03	7.82	7.69	7.80	8.39	8.30	8.25	8.34	8.19	7.95	7.96	7.79
MnO	0.12	0.12	0.11	0.12	0.13	0.13	0.12	0.13	0.12	0.12	0.12	0.12
MgO	50.32	50.32	50.31	50.16	50.32	50.72	50.65	50.51	50.66	50.87	50.59	51.36
CaO	0.02	0.03	0.06	0.02	0.00	0.00	0.01	0.02	0.00	0.00	0.02	0.00
Na_2O	0.00	0.00	0.00	0.00	0.00	0.00	0.00	0.01	0.00	0.00	0.00	0.00
NiO	0.40	0.40	0.41	0.38	0.38	0.39	0.40	0.40	0.39	0.40	0.40	0.39
Total	99.75	99.66	99.69	99.50	100.3	100.7	100.7	100.3	99.74	100.1	100.0	100.6
Grain size (μm)	250	40	25	25	80	60	300	400	Por	Por	Por	10

Oxides (%)	Ol_{13}	Ol_{14}	Ol_{15}	Ol_{16}	Ol_{17}	Ol_{18}	Ol_{19}	Ol_{20}	Ol_{21}	Ol_{22}
SiO_2	40.88	41.47	41.28	41.12	41.21	41.15	40.92	41.21	41.10	40.92
TiO_2	0.00	0.00	0.00	0.00	0.00	0.00	0.00	0.00	0.00	0.00
Al_2O_3	0.00	0.00	0.00	0.00	0.00	0.00	0.00	0.00	0.00	0.00
Cr_2O_3	0.00	0.03	0.02	0.00	0.01	0.01	0.00	0.21	0.00	0.00
FeO	7.78	7.11	7.44	8.13	8.08	7.91	8.06	7.75	7.71	8.06
MnO	0.11	0.11	0.11	0.12	0.12	0.12	0.12	0.13	0.11	0.12
MgO	51.48	50.85	50.48	50.94	51.15	50.48	50.39	50.49	50.43	50.39
CaO	0.00	0.03	0.05	0.01	0.01	0.14	0.01	0.01	0.01	0.01
Na_2O	0.00	0.00	0.00	0.00	0.00	0.00	0.00	0.01	0.00	0.00
NiO	0.41	0.43	0.39	0.40	0.42	0.39	0.40	0.39	0.42	0.4
Total	100.7	100.0	99.77	100.7	101.0	100.2	99.90	100.2	99.77	100.0
Grain size (μm)	10	100	80	150	80	30	200	30	100	200

Supplementary Table 2 | Major-element compositions (oxides in weight percent) and grain size of enstatite (En) grains in the mylonites and ultramylonites. Por = porphyroclasts.

Oxides	En_1	En_2	En_3	En_4	En_5	En_6	En_7	En_8	En_9	En_{10}	En_{11}	En_{12}
SiO_2	55.43	55.84	55.68	55.54	56.00	55.80	56.59	56.70	56.63	55.47	55.91	57.57
TiO_2	0.01	0.01	0.02	0.00	0.00	0.01	0.02	0.00	0.01	0.00	0.01	0.00
Al_2O_3	2.20	1.70	1.79	2.03	1.39	1.35	1.01	0.54	0.50	0.54	1.97	0.13
Cr_2O_3	0.71	0.48	0.56	0.61	0.27	0.27	0.16	0.04	0.07	0.09	0.75	0.05
FeO	5.49	5.61	5.52	5.71	5.62	5.62	5.62	5.69	5.30	5.85	5.41	5.55
MnO	0.13	0.14	0.15	0.15	0.14	0.14	0.14	0.12	0.12	0.12	0.14	0.14
MgO	34.34	34.81	34.90	34.91	35.25	35.25	35.51	35.73	36.07	37.10	34.89	36.00
CaO	1.05	0.71	0.54	0.55	0.51	0.53	0.33	0.27	0.24	0.26	0.51	0.09
Na_2O	0.03	0.02	0.02	0.02	0.03	0.01	0.00	0.00	0.02	0.00	0.00	0.00
K_2O	0.00	0.01	0.00	0.00	0.00	0.00	0.01	0.00	0.00	0.00	0.00	0.00
Total	99.39	99.33	99.16	99.52	99.20	98.99	99.38	99.09	98.95	99.45	99.59	99.53
Grain size (μm)	Por (rim)	Por (core)	Por (rim)	Por (core)	30	20	20	40	5	5	Por (core)	Por (rim)

Oxides	En_{13}	En_{14}	En_{15}	En_{16}	En_{17}	En_{18}	En_{19}	En_{20}	En_{21}	En_{22}	En_{23}	En_{24}
SiO_2	56.82	57.39	57.77	56.44	56.66	57.06	56.64	56.34	56.66	57.14	56.78	56.92
TiO_2	0.01	0.00	0.02	0.00	0.02	0.01	0.01	0.02	0.02	0.01	0.01	0.00
Al_2O_3	0.17	0.24	0.14	0.85	1.39	0.55	1.01	0.83	1.05	0.55	0.95	1.84
Cr_2O_3	0.03	0.04	0.05	0.16	0.30	0.08	0.15	0.12	0.17	0.09	0.14	0.80
FeO	5.73	5.80	5.76	5.96	5.66	5.45	5.57	5.86	5.64	5.57	5.61	5.67
MnO	0.14	0.13	0.15	0.15	0.13	0.12	0.13	0.14	0.15	0.16	0.14	0.16
MgO	36.94	36.00	36.19	36.41	35.42	35.98	35.34	36.03	35.56	35.79	35.68	33.71
CaO	0.06	0.08	0.09	0.27	0.40	0.28	0.39	0.33	0.47	0.30	0.31	0.49
Na_2O	0.00	0.00	0.00	0.00	0.00	0.00	0.01	0.04	0.00	0.00	0.01	0.02
K_2O	0.00	0.00	0.00	0.00	0.00	0.00	0.00	0.01	0.00	0.00	0.01	0.00
Total	99.89	99.66	100.16	100.23	99.99	99.51	99.26	99.70	99.72	99.61	99.65	99.59
Grain size (μm)	10	15	10	8	40	10	20	10	50	6	10	Por (core)

Oxides	En_{25}	En_{26}	En_{27}	En_{28}	En_{29}	En_{30}	En_{31}	En_{32}	En_{33}	En_{34}	En_{35}	En_{36}
SiO_2	57.13	56.72	57.33	57.62	56.94	57.11	57.63	57.12	57.12	57.60	57.37	57.27
TiO_2	0.01	0.00	0.01	0.00	0.01	0.01	0.00	0.02	0.01	0.00	0.00	0.01
Al_2O_3	1.75	0.42	1.08	0.45	1.30	1.98	1.46	1.19	1.15	0.39	0.67	0.60
Cr_2O_3	0.68	0.03	0.17	0.07	0.24	0.81	0.62	0.19	0.18	0.04	0.07	0.05
FeO	5.23	5.34	5.53	5.55	5.51	5.62	5.76	5.50	5.61	5.45	5.46	5.80
MnO	0.26	0.13	0.14	0.14	0.11	0.15	0.12	0.13	0.16	0.13	0.14	0.13
MgO	33.91	36.10	35.55	36.00	35.31	33.68	34.14	35.48	35.45	36.15	35.84	35.82
CaO	0.55	0.65	0.36	0.28	0.43	1.07	0.34	0.42	0.41	0.29	0.26	0.25
Na_2O	0.02	0.01	0.03	0.00	0.01	0.04	0.00	0.02	0.02	0.02	0.00	0.03
K_2O	0.02	0.00	0.00	0.00	0.00	0.00	0.00	0.00	0.00	0.00	0.00	0.01
Total	99.55	99.39	100.2	100.1	99.85	100.5	100.1	100.1	100.1	100.1	99.80	99.98
Grain size (μm)	Por (core)	8	20	35	30	Por (core)	Por (rim)	30	15	20	15	10

Supplementary Table 2 (continued)

Oxides	En_{37}	En_{38}	En_{39}	En_{40}	En_{41}	En_{42}	En_{43}	En_{44}	En_{45}	En_{46}	En_{47}	En_{48}	En_{49}
SiO_2	57.08	57.49	58.23	55.89	57.06	56.70	56.88	55.81	57.61	56.70	57.55	57.29	57.71
TiO_2	0.01	0.05	0.00	0.01	0.02	0.01	0.01	0.01	0.02	0.02	0.01	0.00	0.05
Al_2O_3	1.13	1.44	1.35	0.89	0.91	1.33	1.16	0.62	0.64	1.02	0.48	1.82	1.17
Cr_2O_3	0.22	0.36	0.31	0.18	0.21	0.29	0.22	0.08	0.09	0.16	0.05	0.69	0.31
FeO	5.51	5.46	5.98	5.72	5.33	5.52	5.48	5.73	5.42	5.51	5.36	5.85	5.50
MnO	0.14	0.18	0.10	0.14	0.11	0.14	0.15	0.12	0.14	0.14	0.13	0.09	0.26
MgO	35.49	33.97	34.56	36.57	35.46	35.20	35.43	35.92	35.41	35.13	35.90	33.71	34.33
CaO	0.36	0.55	0.61	0.30	0.29	0.52	0.39	0.26	0.27	0.38	0.21	0.60	0.45
Na_2O	0.00	0.03	0.00	0.00	0.00	0.00	0.01	0.02	0.00	0.00	0.00	0.02	0.02
NiO	0.00	0.00	0.00	0.00	0.00	0.00	0.00	0.00	0.00	0.01	0.00	0.01	0.00
Total	99.95	99.52	101.1	99.72	99.39	99.71	99.73	98.58	99.59	99.07	99.71	100.1	99.90
Grain size	10	Por (rim)	Por (rim)	20	25	40	40	8	40	30	20	Por (core)	Por (rim)

Supplementary Table 3 | Major-element compositions (oxides in weight percent) and grain size of diopside (Di) grains in the mylonites and ultramylonites. Por = porphyroclasts.

Oxides (%)	Di_1	Di_2	Di_3	Di_4	Di_5	Di_6	Di_7	Di_8	Di_9	Di_{10}	Di_{11}	Di_{12}
SiO_2	54.24	53.95	53.95	54.26	53.70	54.24	53.87	53.57	53.30	53.95	54.12	53.44
TiO_2	0.03	0.03	0.02	0.02	0.05	0.01	0.01	0.04	0.06	0.07	0.04	0.05
Al_2O_3	1.57	1.94	1.90	1.20	2.23	1.55	1.60	1.97	2.21	1.78	1.28	1.55
FeO	2.11	2.26	2.22	2.13	2.27	2.15	2.19	2.15	2.31	2.22	2.03	2.19
MnO	0.06	0.08	0.06	0.08	0.09	0.07	0.06	0.08	0.07	0.07	0.05	0.07
MgO	17.32	17.34	17.38	17.66	16.86	17.45	17.16	17.35	17.39	17.07	17.45	17.16
CaO	23.14	22.85	23.07	23.38	23.21	23.32	23.33	22.72	22.53	23.18	23.44	23.47
Na_2O	0.59	0.59	0.63	0.53	0.67	0.60	0.58	0.71	0.65	0.58	0.52	0.47
K2O	0.00	0.00	0.00	0.00	0.00	0.00	0.00	0.00	0.01	0.00	0.00	0.00
Cr_2O_3	0.55	0.72	0.65	0.39	0.81	0.55	0.55	0.89	0.99	0.70	0.33	0.44
Total	99.59	99.75	99.88	99.66	99.88	99.95	99.35	99.48	99.52	99.61	99.27	98.85
Grain size (μm)	15	30	50	8	15	5	10	200	100	25	15	25

Oxides (%)	Di_{13}	Di_{14}	Di_{15}	Di_{16}	Di_{17}	Di_{18}
SiO_2	54.14	53.27	53.12	53.96	54.10	53.55
TiO_2	0.04	0.02	0.01	0.03	0.01	0.02
Al_2O_3	1.36	1.73	1.93	1.69	1.29	1.82
FeO	2.20	2.26	2.30	2.29	2.13	2.19
MnO	0.06	0.07	0.07	0.07	0.07	0.05
MgO	17.23	17.38	17.33	17.36	17.55	17.22
CaO	23.34	23.33	23.00	23.29	23.81	23.23
Na_2O	0.49	0.51	0.54	0.59	0.51	0.65
K2O	0.00	0.01	0.00	0.00	0.00	0.00
Cr_2O_3	0.38	0.65	0.73	0.59	0.42	0.68
Total	99.25	99.22	99.02	99.86	99.89	99.42
Grain size (μm)	15	10	60	10	10	80

Supplementary table 4 | Major-element compositions (oxides in weight percent) and grain size of spinel (Spl) grains in the mylonites and ultramylonites. Por = porphyroclasts.

Oxides (%)	Spl_1	Spl_2	Spl_3	Spl_4	Spl_5	Spl_6	Spl_7	Spl_8	Spl_9	Spl_{10}	Spl_{11}	Spl_{12}
SiO_2	0.05	0.20	0.04	0.01	0.01	0.00	0.03	0.04	0.05	0.01	0.84	0.02
TiO_2	0.04	0.02	0.01	0.01	0.01	0.07	0.03	0.03	0.08	0.08	0.04	0.02
Al_2O_3	22.13	20.62	30.47	26.08	27.20	20.48	28.38	27.71	24.24	23.69	24.68	24.12
Cr_2O_3	43.16	41.45	36.02	41.28	39.80	45.57	36.96	36.07	41.91	42.48	39.30	42.71
V2O3	0.15	0.16	0.18	0.18	0.19	0.15	0.17	0.16	0.15	0.16	0.15	0.19
FeO	17.19	19.84	17.60	14.78	16.85	16.05	17.92	18.06	15.72	15.69	17.12	15.73
Fe2O3	6.02	7.38	2.77	4.43	3.71	5.61	4.46	5.56	5.16	5.51	4.21	4.63
MnO	0.22	0.28	0.21	0.19	0.21	0.21	0.22	0.22	0.20	0.20	0.21	0.20
MgO	11.91	9.88	12.13	13.90	12.58	12.45	11.83	11.54	13.13	13.10	12.59	13.03
NiO	0.11	0.10	0.08	0.12	0.10	0.11	0.09	0.11	0.12	0.12	0.10	0.11
ZnO	0.25	0.24	0.49	0.17	0.25	0.13	0.42	0.39	0.13	0.16	0.17	0.19
Total	101.2	100.2	100.0	101.2	101.0	100.8	100.5	99.90	100.9	101.2	99.41	100.9
Grain size (μm)	400	15	20	Por	80	Por	10	10	150	300	80	150

Oxides (%)	Spl_{13}	Spl_{14}	Spl_{15}	Spl_{16}	Spl_{17}	Spl_{18}
SiO_2	0.01	0.07	0.03	0.00	0.00	0.02
TiO_2	0.02	0.02	0.05	0.06	0.04	0.05
Al_2O_3	26.10	30.72	21.46	21.28	23.35	21.61
Cr_2O_3	39.82	35.14	45.03	44.93	42.89	44.91
V2O3	0.19	0.19	0.16	0.17	0.17	0.17
FeO	16.32	16.24	15.33	16.42	16.00	15.49
Fe2O3	4.91	3.87	5.32	5.28	5.12	5.22
MnO	0.21	0.19	0.20	0.22	0.20	0,.20
MgO	12.75	13.18	13.05	12.30	12.75	12.96
NiO	0.12	0.12	0.12	0.10	0.11	0.11
ZnO	0.22	0.27	0.13	0.15	0.17	0.14
Total	100.7	100.0	100.9	100.1	100.8	100.9
Grain size (μm)	100	10	Por	10	200	Por

Supplementary Table 5 | Major-element compositions (oxides in weight percent) of amphibole grains (Amp) in the mylonites and ultramylonites. Por = porphyroclasts.

Oxides (%)	Amp1	Amp2	Amp3	Amp4	Amp5	Amp6	Amp7	Amp8	Amp9	Amp10
SiO_2	44.81	43.92	44.28	43.81	44.00	44.16	44.27	43.89	44.40	43.62
TiO_2	0.34	0.44	0.40	0.21	0.21	0.21	0.36	0.49	0.42	0.50
Al_2O_3	13.11	13.42	13.23	13.05	13.01	12.85	12.99	13.39	12.64	13.22
Cr_2O_3	1.56	2.17	1.90	2.11	2.04	2.24	1.83	1.91	1.58	1.91
Fe_2O_3	3.73	3.95	3.91	3.82	3.75	3.86	4.08	3.91	4.22	4.22
FeO	0.00	0.00	0.00	0.00	0.00	0.00	0.00	0.00	0.00	0.00
MnO	0.06	0.05	0.04	0.05	0.06	0.06	0.01	0.04	0.04	0.05
MgO	19.02	18.42	18.73	18.93	18.90	18.76	18.75	18.19	18.68	18.37
CaO	12.04	11.99	12.03	11.95	11.93	11.87	12.14	12.04	11.96	12.10
Na_2O	2.77	2.88	2.85	3.01	3.24	3.28	3.12	2.85	2.88	2.94
K_2O	0.09	0.09	0.08	0.08	0.07	0.07	0.17	0.21	0.19	0.20
H_2O	2.13	2.12	2.12	2.11	2.11	2.12	2.12	2.11	2.11	2.11
Total	99.66	99.44	99.58	99.12	99.34	99.47	99.84	99.03	99.12	99.25

Supplementary Table 6 | Pressure (P in kbar) and temperature (T in °C) data estimated in the mylonites and ultramylonites based on the major-elements compositions and geothermobarometers. Each number refers to the phase number shown in previous tables (from tables S1 to S5). The temperature data are summarized in the figure 3D of the paper. (1) = Ca in OPx at 5 kbar[1]; (2) = Ca in OPx at 8 kbar[1]; (3) = Al and Cr in OPx[2]; (4) = Two-pyroxene thermometer at 5 kbar[1] (TBKN); (5) = two-pyroxene thermometer at 8 kbar[1]. (6) = Olivine-spinel thermometer[3]. (7) = Two-pyroxene barometer[4].

Phase(s)	En_1	En_2	En_3	En_4	En_5	En_6	En_7	En_8	En_9	En_{10}	En_{11}	En_{12}	En_{13}	En_{14}	En_{15}	En_{16}	En_{17}	En_{18}
T (1)	1016.9	923.4	866.7	871.6	855.2	865.5	777.2	742.0	726.0	740.5	856.3	596.7	559.5	586.0	595.2	742.5	811.3	752.1
T (2)	1032.5	937.8	880.5	885.4	868.9	879.3	789.9	754.2	738.1	752.8	870.0	607.3	569.6	596.4	605.7	754.8	824.4	764.4
T (3)	932.05	823.6	858.1	873.9	723.8	713.7	683.9	613.3	610.9	510.9	950.2	624.4	537.6	614.1	615.1	617.4	754.1	635.6

Phase(s)	En_{19}	En_{20}	En_{21}	En_{22}	En_{23}	En_{24}	En_{25}	En_{26}	En_{27}	En_{28}	En_{29}	En_{30}	En_{31}	En_{32}	En_{33}	En_{34}	En_{35}	En_{36}
T (1)	804.5	776.2	838.4	759.6	766.5	847.3	869.6	905.8	790.6	750.4	821.5	1018.0	780.4	818.9	812.2	754.8	734.8	731.0
T (2)	817.5	788.7	851.9	772.1	779.0	860.8	883.4	920.0	803.5	762.8	834.7	1033.6	793.2	832.1	825.3	767.2	747.0	743.1
T (3)	691.0	616.2	683.3	644.6	672.3	1054.9	1009.9	714.2	641.7	746.1	976.4	1047.4	978.6	720.6	715.4	619.9	654.0	627.2

Phase(s)	En_{37}	En_{38}	En_{39}	En_{40}	En_{41}	En_{42}	En_{43}	En_{44}	En_{45}	En_{46}	En_{47}	En_{48}	En_{49}	Di_1/ En_{26}	Di_2/ En_{27}	Di_3/ En_{32}	Di_4/ En_{34}	Di_5/ En_{35}
T (1)	791.5	869.5	887.6	759.7	753.9	858.0	804.7	737.8	742.9	800.3	708.4	886.5	830.5					
T (2)	804.4	883.3	901.6	772.2	766.3	871.7	817.7	750.0	755.2	813.3	720.3	900.5	843.8					
T (3)	730.6	883.0	840.4	601.3	728.8	760.8	724.7	586.5	690.7	709.4	647.7	1017.2	841.9					
T (4)														804.6	852.3	806.7	769.2	759.9
T (5)														809.1	857.1	811.3	773.5	764.3

Phase(s)	Di_6/ En_{36}	Di_7/ En_{37}	Di_8/ En_{42}	Di_9/ En_{41}	Di_{10}/ En_{40}	Di_{11}/ En_{47}	Di_{12}/ En_{45}	Di_{13}/ En_{44}	Di_{14}/ En_{10}	Di_{15}/ En_6	Di_{16}/ En_{18}	Di_{17}/ En_{20}	Di_{18}/ En_{21}	Ol_1/ SPl_1	Ol_2/ SPl_2	Ol_3/ SPl_2	Ol_4/ SPl_2	Ol_5/ SPl_3
T (4)	766.8	740.2	827.8	870.4	785.6	742.8	717.5	768.9	752.2	800.8	786.7	866.4	743.1					
T (5)	771.1	744.5	832.4	875.2	790.1	747	721.6	773.3	756.5	805.4	791.2	871.3	747.3					
T (6)														749.0	656.0	652.0	657.0	696.0

Phase(s)	Ol_4/ SPl_2	Ol_5/ SPl_3	Ol_6/ SPl_3	Ol_7/ SPl_4	Ol_8/ SPl_5	Ol_9/ SPl_6	Ol_{10}/ SPl_6	Ol_{11}/ SPl_6	Ol_{12}/ SPl_7	Ol_{13}/ SPl_8	Ol_{14}/ SPl_9	Ol_{15}/ SPl_{10}	Ol_{15}/ SPl_{11}	Ol_{16}/ SPl_{12}	Ol_{17}/ SPl_{13}	Ol_{18}/ SPl_{14}	Ol_{19}/ SPl_{15}	Ol_{20}/ SPl_{16}	Ol_{21}/ SPl_{17}	Ol_{22}/ SPl_{18}
T (6)	657.0	696.0	691.0	821.0	750.0	811.0	800.0	802.0	660.0	641.0	745.0	764.0	726.0	796.0	743.0	707.0	827.0	780.0	772.0	822.0

Phase(s)	Di_1/ En_{26}	Di_2/ En_{27}	Di_3/ En_{32}	Di_4/ En_{34}	Di_5/ En_{35}	Di_6/ En_{36}	Di_7/ En_{37}	Di_8/ En_{42}	Di_9/ En_{41}	Di_{10}/ En_{40}	Di_{11}/ En_{47}	Di_{12}/ En_{45}	Di_{13}/ En_{44}	Di_{14}/ En_{10}	Di_{15}/ En_6	Di_{16}/ En_{18}	Di_{17}/ En_{20}	Di_{18}/ En_{21}
P (7)	4.8	9.0	6.9	8.8	10.6	10.7	6.5	5.9	11.8	9.0	10.8	7.7	9.6	9.2	4.9	8.9	6.1	5.1

Supplementary References

1. Brey, G. P., & Köhler, T. Geothermobarometry in four-phase lherzolites II. New thermobarometers, and practical assessment of existing thermobarometers. *J. Petrol.* **31,** 1353-1378 (1990).
2. Witt-Eickschen, G. & Seck, H. A. Solubility of Ca and Al in orthopyroxene from spinel peridotite: an improved version of an empirical geothermometer. *Contrib. Min. Petrol*. **106,** 431-439 (1991).
3. Jianping, L., Kornprobst, J., Vielzeuf, D. & Fabriès, J. An improved experimental calibration of the olivine-spinel geothermometer. *Chinese J. Geochem.* **14,** 68-77 (1995).
4. Putirka, K. D. Thermometers and barometers for volcanic systems. *Rev. Min. Geochem*. **69,** 61-120 (2008).